Rational Design of Solar Cells for Efficient Solar Energy Conversion

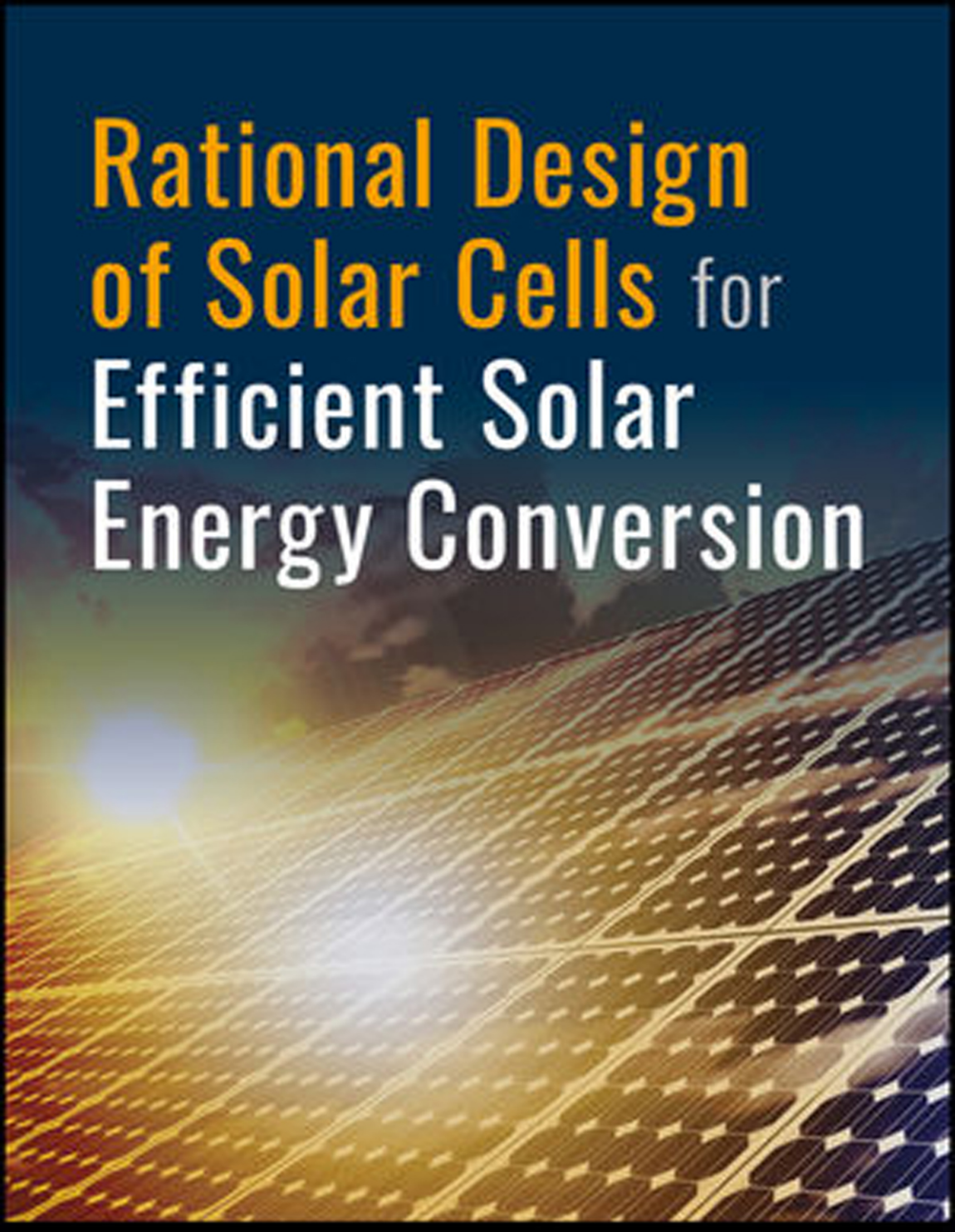

Edited by
Alagarsamy Pandikumar
Ramasamy Ramaraj

WILEY

Rational Design of Solar Cells for Efficient Solar Energy Conversion

Rational Design of Solar Cells for Efficient Solar Energy Conversion

Edited by

Alagarsamy Pandikumar
CSIR-Central Electrochemical Research Institute, Karaikudi, Tamil Nadu, India

and

Ramasamy Ramaraj
Madurai Kamaraj University, Madurai, Tamil Nadu, India

WILEY

This edition first published 2018

Registered Office
John Wiley & Sons, Inc., 111 River Street, Hoboken, NJ 07030, USA

Editorial Office
111 River Street, Hoboken, NJ 07030, USA

For details of our global editorial offices, customer services, and more information about Wiley products visit us at www.wiley.com.

Wiley also publishes its books in a variety of electronic formats and by print-on-demand. Some content that appears in standard print versions of this book may not be available in other formats.

Library of Congress Cataloging-in-Publication Data

Names: Pandikumar, Alagarsamy, editor. | Ramaraj, Ramasamy, editor.
Title: Rational design of solar cells for efficient solar energy conversion / edited by Alagarsamy Pandikumar, Ramasamy Ramaraj.
Description: First edition. | Hoboken, NJ : John Wiley & Sons, 2018. | Includes bibliographical references and index. |
Identifiers: LCCN 2018008636 (print) | LCCN 2018013539 (ebook) | ISBN 9781119437468 (pdf) | ISBN 9781119437451 (epub) | ISBN 9781119437406 (cloth)
Subjects: LCSH: Solar cells–Design and construction. | Direct energy conversion.
Classification: LCC TK2960 (ebook) | LCC TK2960 .R325 2018 (print) | DDC 621.31/244–dc23
LC record available at https://lccn.loc.gov/2018008636

Cover Design: Wiley
Cover Image: © EzumeImages/iStockphoto

Set in 10/12pt Warnock by SPi Global, Pondicherry, India

Printed in the United States of America

10 9 8 7 6 5 4 3 2 1

Contents

Biographies *xiii*
List of Contributors *xv*
Preface *xix*

1 Metal Nanoparticle Decorated ZnO Nanostructure Based Dye-Sensitized Solar Cells *1*
Gregory Thien Soon How, Kandasamy Jothivenkatachalam, Alagarsamy Pandikumar, and Nay Ming Huang
1.1 Introduction *1*
1.2 Metal Dressed ZnO Nanostructures as Photoanodes *3*
1.2.1 Metal Dressed ZnO Nanoparticles as Photoanodes *4*
1.2.2 Metal Dressed ZnO Nanorods as Photoanodes *6*
1.2.3 Metal Dressed ZnO Nanoflowers as Photoanodes *8*
1.2.4 Metal Dressed ZnO Nanowires as Photoanodes *8*
1.2.5 Less Common Metal Dressed ZnO Nanostructures as Photoanodes *10*
1.2.6 Comparison of the Performance of Metal Dressed ZnO Nanostructures in DSSCs *10*
1.3 Conclusions and Outlook *11*
References *13*

2 Cosensitization Strategies for Dye-Sensitized Solar Cells *15*
Gachumale Saritha, Sambandam Anandan, and Muthupandian Ashokkumar
2.1 Introduction *15*
2.2 Cosensitization *18*
2.2.1 Cosensitization of Metal Complexes with Organic Dyes *19*
2.2.1.1 Phthalocyanine-based Metal Complexes *19*
2.2.1.2 Porphyrin-based Metal Complexes *21*
2.2.1.3 Ruthenium-based Metal Complexes *27*

2.2.2 Cosensitization of Organic–Organic Dyes *41*
2.3 Conclusions *51*
Acknowledgements *51*
References *52*

3 Natural Dye-Sensitized Solar Cells – Strategies and Measures *61*
N. Prabavathy, R. Balasundaraprabhu, and Dhayalan Velauthapillai
3.1 Introduction *61*
3.1.1 Mechanism of the Dye-Sensitized Solar Cell Compared with the Z-scheme of Photosynthesis *62*
3.2 Components of Dye-sensitized Solar Cell *63*
3.2.1 Photoelectrode *63*
3.2.2 Dye *64*
3.2.3 Liquid Electrolyte *64*
3.2.4 Counterelectrode *65*
3.3 Fabrication of Natural DSSCs *65*
3.3.1 Preparation of TiO_2 Nanorods by the Hydrothermal Method *65*
3.3.2 Characterization of the Photoelectrode for DSSCs *66*
3.3.3 Preparation of Natural Dye *67*
3.3.4 Sensitization *68*
3.3.5 Arrangement of the DSSC *68*
3.4 Efficiency and Stability Enhancement in Natural Dye-Sensitized Solar Cells *68*
3.4.1 Effect of Photocatalytic Activity of TiO_2 Molecules on the Photostability of Natural Dyes *69*
3.4.1.1 Important Points to be Considered for the Preparation of Photoelectrodes *70*
3.4.2 Citric Acid – Best Solvent for Extracting Anthocyanins *70*
3.4.3. Algal Buffer Layer to Improve Stability of Anthocyanins in DSSCs *72*
3.4.3.1 Preparation of Buffer Layers – Sodium Alginate and Spirulina *73*
3.4.4 Sodium-doped Nanorods for Enhancing the Natural DSSC Performance *75*
3.4.4.1 Preparing Sodium-doped Nanorods as the Photoelectrode *75*
3.4.5 Absorber Material for Liquid Electrolytes to Avoid Leakage *77*
3.5 Other Strategies and Measures taken in DSSCs Using Natural Dyes *79*
3.6 Conclusions *82*
References *82*

4 Advantages of Polymer Electrolytes for Dye-Sensitized Solar Cells *85*
L.P. Teo and A.K. Arof
4.1 Why Solar Cells? *85*
4.2 Structure and Working Principle of DSSCs with Gel Polymer Electrolytes (GPEs) *86*
4.3 Gel Polymer Electrolytes (GPEs) *87*
4.3.1 Chitosan (Ch) and Blends *88*
4.3.2 Phthaloylchitosan (PhCh) and Blends *91*
4.3.3 Poly(Vinyl Alcohol) (PVA) *98*
4.3.4 Polyacrylonitrile (PAN) *105*
4.3.5 Polyvinylidene Fluoride (PVdF) *109*
4.4 Summary and Outlook *110*
Acknowledgements *111*
References *111*

5 Advantages of Polymer Electrolytes Towards Dye-sensitized Solar Cells *121*
Nagaraj Pavithra, Giovanni Landi, Andrea Sorrentino, and Sambandam Anandan
5.1 Introduction *121*
5.1.1 Energy Demand *121*
5.1.1.1 Generation of Solar Cells *122*
5.1.2 Types of Electrolyte Used in Third Generation Solar Cells *124*
5.1.2.1 Liquid Electrolytes (LEs) *124*
5.1.2.2 Room Temperature Ionic Liquids (RTILs) *125*
5.1.2.3 Solid State Hole Transport Materials (SS-HTMs) *126*
5.2 Polymer Electrolytes *127*
5.2.1 Mechanism of Ion Transport in Polymer Electrolytes *128*
5.2.2 Types of Polymer Electrolyte *129*
5.2.2.1 Solid Polymer Electrolytes *129*
5.2.2.2 Gel Polymer Electrolytes *129*
5.2.2.3 Composite Polymer Electrolyte *130*
5.3 Dye-sensitized Solar Cells *130*
5.3.1 Components and Operational Principle *131*
5.3.1.1 Substrate *133*
5.3.1.2 Photoelectrode *134*
5.3.1.3 Photosensitizer *135*
5.3.1.4 Redox Electrolyte *137*
5.3.1.5 Counter Electrode *140*
5.3.2 Application of Polymer Electrolytes in DSSCs *140*
5.3.2.1 Solid-state Dye-Sensitized Solar Cells (SS-DSSCs) *140*
5.3.2.2 Quasi-solid-state Dye-Sensitized Solar Cells (QS-DSSC) *142*

5.3.2.3 Types of Additives in GPEs *144*
5.3.3 Bifacial DSSCs *148*
5.4 Quantum Dot Sensitized Solar Cells (QDSSC) *150*
5.5 Perovskite-Sensitized Solar Cells (PSSC) *152*
5.6 Conclusion *153*
Acknowledgements *154*
References *154*

6 Rational Screening Strategies for Counter Electrode Nanocomposite Materials for Efficient Solar Energy Conversion *169*
Prabhakarn Arunachalam
6.1 Introduction *169*
6.2 Principles of Next Generation Solar Cells *171*
6.2.1 Dye-sensitized Solar Cells *171*
6.2.2 Principles of Quantum Dot Sensitized Solar Cells *173*
6.2.3 Principles of Perovskite Solar Cells *174*
6.3 Platinum-free Counterelectrode Materials *175*
6.3.1 Carbon-based Materials for Solar Energy Conversion *175*
6.3.2 Metal Nitride and Carbide Materials *178*
6.3.3 Metal Sulfide Materials *179*
6.3.4 Composite Materials *182*
6.3.5 Metal Oxide Materials *183*
6.3.6 Polymer Counterelectrodes *184*
6.4 Summary and Outlook *185*
References *186*

7 Design and Fabrication of Carbon-based Nanostructured Counter Electrode Materials for Dye-sensitized Solar Cells *193*
Jayaraman Theerthagiri, Raja Arumugam Senthil, and Jagannathan Madhavan
7.1 Photovoltaic Solar Cells – An Overview *193*
7.1.1 First Generation Solar Cells *194*
7.1.2 Second Generation Solar Cells *194*
7.1.3 Third Generation Solar Cells *194*
7.1.4 Fourth Generation Solar Cells *195*
7.2 Dye-sensitized Solar Cells *195*
7.2.1 Major Components of DSSCs *196*
7.2.1.1 Transparent Conducting Glass Substrate *197*
7.2.1.2 Photoelectrode *197*
7.2.1.3 Dye Sensitizer *198*
7.2.1.4 Redox Electrolytes *199*
7.2.1.5 Counterelectrode *200*
7.2.2 Working Mechanism of DSSCs *200*

7.3 Carbon-based Nanostructured CE Materials for DSSCs *201*
7.4 Conclusions *216*
References *217*

8 Highly Stable Inverted Organic Solar Cells Based on Novel Interfacial Layers *221*
Fang Jeng Lim and Ananthanarayanan Krishnamoorthy
8.1 Introduction *221*
8.2 Research Areas in Organic Solar Cells *222*
8.3 An Overview of Inverted Organic Solar Cells *224*
8.3.1 Transport Layers in Inverted Organic Solar Cells *227*
8.3.2 PEDOT:PSS Hole Transport Layer *227*
8.3.3 Titanium Oxide Electron Transport Layer *229*
8.4 Issues in Inverted Organic Solar Cells and Respective Solutions *232*
8.4.1 Wettability Issue of PEDOT:PSS in Inverted Organic Solar Cells *233*
8.4.2 Light-soaking Issue of TiOx-based Inverted Organic Solar Cells *234*
8.5 Overcoming the Wettability Issue and Light-soaking Issue in Inverted Organic Solar Cells *235*
8.5.1 Fluorosurfactant-modified PEDOT:PSS as Hole Transport Layer *235*
8.5.2 Fluorinated Titanium Oxide as Electron Transport Layer *239*
8.6 Conclusions and Outlook *245*
Acknowledgements *246*
References *246*

9 Fabrication of Metal Top Electrode via Solution-based Printing Technique for Efficient Inverted Organic Solar Cells *255*
Navaneethan Duraisamy, Kavitha Kandiah, Kyung-Hyun Choi, Dhanaraj Gopi, Ramesh Rajendran, Pazhanivel Thangavelu, and Maadeswaran Palanisamy
9.1 Introduction *255*
9.2 Organic Photovoltaic Cells *257*
9.3 Working Principle *258*
9.4 Device Architecture *260*
9.4.1 Single Layer or Monolayer Device *260*
9.4.2 Planar Heterojunction Device *261*
9.4.3 Bulk Heterojunction Device *261*
9.4.4 Ordered Bulk Heterojunction Device *261*
9.4.5 Inverted Organic Solar Cells *262*
9.5 Fabrication Process *263*
9.5.1 Hybrid-EHDA Technique *263*

9.5.1.1 Flow Rate *265*
9.5.1.2 Applied Potential *265*
9.5.1.3 Pneumatic Pressure *265*
9.5.1.4 Stand-off Distance *265*
9.5.1.5 Nozzle Diameter 266
9.5.1.6 Ink Properties *266*
9.5.2 Mode of Atomization *267*
9.5.2.1 Dripping Mode *267*
9.5.2.2 Unstable Spray Mode *267*
9.5.2.3 Stable Spray Mode *267*
9.6 Fabrication of Inverted Organic Solar Cells *267*
9.6.1 Deposition of Zinc Oxide (ZnO) on ITO Substrate *268*
9.6.2 Deposition of P3HT:PCBM *268*
9.6.3 Deposition of PEDOT:PSS *268*
9.6.4 Deposition of Silver as a Top Electrode *269*
9.7 Device Morphology *272*
9.8 Device Performance *273*
9.9 Conclusion *277*
Acknowledgements *277*
References *277*

10 Polymer Solar Cells – An Energy Technology for the Future *283*
Alagar Ramar and Fu-Ming Wang
10.1 Introduction *283*
10.2 Materials Developments for Bulk Heterojunction Solar Cells *284*
10.2.1 Conjugated Polymer–Fullerene Solar Cells *284*
10.2.2 Non-Fullerene Polymer Solar Cells *289*
10.2.3 All-Polymer Solar Cells *290*
10.3 Materials Developments for Molecular Heterojunction Solar Cells *291*
10.3.1 Double-cable Polymers *291*
10.4 Developments in Device Structures *293*
10.4.1 Tandem Solar Cells *295*
10.4.2 Inverted Polymer Solar Cells *297*
10.5 Conclusions *300*
Acknowledgements *300*
References *301*

11 Rational Strategies for Large-area Perovskite Solar Cells: Laboratory Scale to Industrial Technology *307*
Arunachalam Arulraj and Mohan Ramesh
11.1 Introduction *307*
11.2 Perovskite *308*
11.3 Perovskite Solar Cells *309*

11.3.1 Architecture *310*
11.3.1.1 Mesoporous PSCs *310*
11.3.1.2 Planar PSCs *313*
11.4 Device Processing *313*
11.4.1 Solvent Engineering *313*
11.4.2 Compositional Engineering *314*
11.4.3 Interfacial Engineering *314*
11.5 Enhancing the Stability of Devices *316*
11.5.1 Deposition Techniques *317*
11.5.1.1 Spin Coating *317*
11.5.1.2 Blade Coating *319*
11.5.1.3 Slot Die Coating *320*
11.5.1.4 Screen Printing *321*
11.5.1.5 Spray Coating *324*
11.5.1.6 Laser Patterning *324*
11.5.1.7 Roll-to-Roll Deposition *325*
11.5.1.8 Other Large Area Deposition Techniques *326*
11.6 Summary *329*
Acknowledgement *329*
References *329*

12 Hot Electrons Role in Biomolecule-based Quantum Dot Hybrid Solar Cells *339*
T. Pazhanivel, G. Bharathi, D. Nataraj, R. Ramesh, and D. Navaneethan
12.1 Introduction *339*
12.2 Classifications of Solar Cells *341*
12.2.1 Inorganic Solar Cells *342*
12.2.2 Organic Solar Cells (OSCs) *343*
12.2.3 Hybrid Solar Cells *344*
12.3 Main Losses in Solar Cells *344*
12.3.1 Recombination Loss *345*
12.3.2 Contact Losses *345*
12.4 Hot Electron Concept in Materials *346*
12.5 Methodology *347*
12.5.1 Hot Injection Method *348*
12.5.1.1 Nucleation and Growth Stages *349*
12.5.1.2 Merits of this Method *350*
12.6 Material Synthesis *350*
12.6.1 CdSe QD Preparation *350*
12.6.2 QD–βC Hybrid Formation *351*
12.7 Identification of Hot Electrons *351*
12.7.1 Photoluminescence (PL) Spectrum *351*
12.7.2 Time-correlated Single Photon Counting (TCSPC) *355*
12.7.3 Transient Absorption *357*

12.8 Quantum Dot Sensitized Solar Cells *360*
12.8.1 Working Principle *360*
12.8.2 Device Preparation *361*
12.8.2.1 Preparation of TiO2 Nanoparticle Electrode *361*
12.8.2.2 QDs Deposition on TiO_2 Nanoparticle *362*
12.8.2.3 Counterelectrode and Assembly of QDSSC *362*
12.8.3 Performance *362*
12.9 Conclusion *363*
References *363*

Index *369*

Biographies

Dr. Alagarsamy Pandikumar

Dr. Alagarsamy Pandikumar is currently working as a Scientist at the CSIR-Central Electrochemical Research Institute, Karaikudi, India. He obtained his PhD in chemistry (2014) from the Madurai Kamaraj University, Madurai, India. His doctoral research focused on the synthesis and characterization of plasmonic nanocomposite materials and the application of their photophysical/chemical properties in photocatalysis, photoelectrocatalysis, and dye-sensitized solar cells. He successfully completed his postdoctoral fellowship tenure (2014–2016) at the University of Malaya, Malaysia, under a high Impact Research Grant. During his postdoctoral research, he developed several graphene-based metal, metal oxide, polymeric nanocomposites for electrochemical sensors and dye-sensitized solar cell applications. He was appointed as a Research Assistant Professor in the Department of Chemistry & Research Institute at SRM University, India. His current research involves development of novel materials with graphene, graphitic carbon nitrides, transition metal chalcogenides in combination to metals, metal oxides, polymers, and carbon nanotubes for photocatalysis, photoelectrocatalysis dye-sensitized solar cells, and electrochemical sensor applications. His results outcomes have been documented in 95 peer-reviewed journals, including eight review articles; among them seven of the key articles have been cited more than 59 times and also have 1940 citations with the h – index of 26. On other side, he has served as Guest Editor for a special issue of the *Materials Focus* journal and edited four books for TransTech Publishers, Switzerland.

Professor Ramasamy Ramaraj

Professor Ramasamy Ramaraj is currently working as an Emeritus Scientist in the School of Chemistry and Centre for Photoelectrochemistry, Madurai Kamaraj University, Madurai, India. He obtained his PhD degree in chemistry from the Department of Inorganic Chemistry, University of Madras, Chennai, India. He had postdoctoral research experience at the Institute of Physical & Chemical Research (RIKEN), Japan, and the Max-Planck Institute for Radiation Chemistry, Mülheim an der Ruhr, Germany. His research interests are nanomaterials and their applications in catalysis, sensors and solar energy conversion, chemically modified electrodes, photoelectrochemistry, photoelectrocatalysis, artificial photosynthesis, and electron transfer reactions in organized assemblies. He was awarded a Doctor of Science (DSc) by Ibaraki University, Japan, in 2001 and a Doctor of Science (DSc) by Madurai Kamaraj University, Madurai, in 2004. He has published more than 160 research papers in peer-reviewed journals.

List of Contributors

Sambandam Anandan
Nanomaterials and Solar Energy Conversion Laboratory
National Institute of Technology
India

A.K. Arof
Centre for Ionics University of Malaya
Physics Department
Faculty of Science
University of Malaya
50603 Kuala Lumpur
Malaysia

Arunachalam Arulraj
University College of Engineering-Bharathidasan Institute of Technology (BIT) campus
Anna University
India

Prabhakarn Arunachalam
Electrochemistry Research Group
King Saud University
Saudi Arabia

Muthupandian Ashokkumar
School of Chemistry
University of Melbourne
Australia

R. Balasundaraprabhu
Centre for Surface Science
PSG College of Technology
India

G. Bharathi
Department of Physics
Bharathiyar University
India

Kyung-Hyun Choi
Department of Mechatronics Engineering
Jeju National University
Republic of Korea

Navaneethan Duraisamy
Department of Chemistry
Periyar University
India

Dhanaraj Gopi
Department of Chemistry
Periyar University
India

Gregory Thien Soon How
Department of Physics
University of Malaya
Malaysia

Kandasamy Jothivenkatachalam
Department of Chemistry
Anna University- BIT Campus
Tiruchirappalli- 620024
Tamilnadu
India

Kavitha Kandiah
Department of Microbiology
Periyar University
India

Ananthanarayanan Krishanamoorthy
SRM Research Institute and
Department of Chemistry
SRM University
India

Giovanni Landi
Department of Industrial
Engineering
University of Salerno
Italy
Institute for Polymers, Composites
and Biomaterials (IPCB),
National Research Council of Italy
(CNR), Italy

Fang Jeng Lim
Solar Energy Research Institute of
Singapore (SERIS)
National University of Singapore
Singapore

Jagannathan Madhavan
Solar Energy Laboratory
Thiruvalluvar University
India

Nay Ming Huang
Faculty of Engineering
University Xiamen Malaysia
Malaysia

D. Nataraj
Department of Physics
Bharathiyar University
India

D. Navaneethan
Department of Chemistry
Periyar University
India

Maadeswaran Palanisamy
Department of Energy Studies
Periyar University
India

Alagarsamy Pandikumar
Functional Materials Division
CSIR-Central Electrochemical
Research Institute
Karaikudi-630006
India

Nagaraj Pavithra
Nanomaterials and Solar Energy
Conversion Laboratory
National Institute of Technology
India

T. Pazhanivel
Department of Physics
Periyar University
India

N. Prabavathy
Centre for Surface Science
PSG College of Technology
India

Ramesh Rajendran
Department of Physics
Periyar University
India

Alagar Ramar
Graduate Institute of Applied Science and Technology
National Taiwan University of Science and Technology
Taiwan, R.O.C.

Mohan Ramesh
CSIR-Central Electrochemical Research Institute
India

R. Ramesh
Department of Chemistry
Periyar University
India

Gachumale Saritha
Nanomaterials and Solar Energy Conversion Laboratory
National Institute of Technology
India

Raja Arumugam Senthil
Solar Energy Laboratory
Thiruvalluvar University
India

Andrea Sorrentino
Institute for Polymers, Composites and Biomaterials (IPCB)
National Research Council of Italy (CNR), Italy

Jayaraman Theerthagiri
Centre of Excellence for Energy Research
Sathyabama Institute of Science and Technology
India

Solar Energy Laboratory
Thiruvalluvar University
India

L.P. Teo
Centre for Ionics University of Malaya
Physics Department
Faculty of Science
University of Malaya
50603 Kuala Lumpur
Malaysia

Pazhanivel Thangavelu
Department of Physics
Periyar University
India

Dhayalan Velauthapillai
Faculty of Engineering
Western Norway University of Applied Sciences
Norway

Fu-Ming Wang
Graduate Institute of Applied Science and Technology
National Taiwan University of Science and Technology
Taiwan, R.O.C.

Preface

Solar cell technology is a potential alternative to overcome the issues related to energy demand and environmental pollution caused by fossil fuels. Dye-sensitized solar cells, organic solar cells, polymer solar cells, perovskite solar cells, and quantum dot solar cells are promising next-generation alternative renewable energy technology to substitute for fossil fuels and other energy sources due to their high performance, ease of fabrication, long-term stability, and low manufacturing cost. This new book gathers and surveys a variety of novel ideas that have emerged in the fields of dye-sensitized solar cells, organic solar cells, polymer solar cells, perovskite solar cells, and quantum dot solar cells from over forty experts in the interdisciplinary areas of chemistry, physics, materials science, and engineering and widely explores the materials development and device fabrication in the field of solar cells to achieve higher solar energy conversion efficiency. This book presents a collection of twelve chapters written by researchers who are the leading experts in their fields of research and they explain the strategies needed to overcome the challenges in solar cell fabrication. The first chapter of this book is a succinct summary of the state of the art of the fabrication of plasmonic nanoparticles incorporated into photoanodes for dye-sensitized solar cells. Chapters 2 and 3 focus more on the aspects of sensitization processes with cosensitizer and natural dyes, and their impact in dye-sensitized solar cells. Chapters 4 and 5 explore the durability, stability, and performance enhancement strategies needed to adapt polymer and gel electrolytes for use in in dye-sensitized solar cells. Chapters 6 and 7 discuss the details of replacing the expensive platinum counterelectrode with alternative electrocatalysts to minimize the fabrication cost of dye-sensitized solar cells. Chapters 8–10 address the key challenges in the fabrication and possible strategies to improve the efficiency of the polymer solar cells with different approaches. Chapter 11 summarizes the possible methodologies to fabricate perovskite solar cells from laboratory scale to industrial scale. Chapter 12 presents the possible role of biomolecules and their charge transfer dynamics in quantum dot solar cells. Finally, we would like to express our sincere thanks to the all

contributing authors for sharing their knowledge on solar cells; this has made it possible to prepare this book for the benefit of those parties interested in light harvesting assemblies and applications.

Dr. Alagarsamy Pandikumar
Professor Ramasamy Ramaraj

1

Metal Nanoparticle Decorated ZnO Nanostructure Based Dye-Sensitized Solar Cells

Gregory Thien Soon How[1], *Kandasamy Jothivenkatachalam*[2], *Alagarsamy Pandikumar*[3], *and Nay Ming Huang*[4]

[1] *Department of Physics, University of Malaya, Malaysia*
[2] *Department of Chemistry, Anna University-BIT Campus, Tiruchirappalli-620024, Tamilnadu, India*
[3] *Functional Materials Division, CSIR-Central Electrochemical Research Institute, Karaikudi-630006, India*
[4] *Faculty of Engineering, University Xiamen Malaysia, Malaysia*

1.1 Introduction

Solar energy has always been an ideal renewable energy source that is clean, abundant, inexpensive, and widely distributed regionally in the world [1–3]. Understanding this, the emergence of dye-sensitized solar cells (DSSCs) for converting solar energy to electricity has been very promising due to the ease of the manufacturing process, the low fabrication cost, the fact that it is nonpolluting, and the relatively high efficiency [1, 4–6]. It is known that a typical DSSC consists of various subsections, includinng a nanocrystalline semiconductor oxide photoanode, dye sensitizer, redox couple electrolyte, and counterelectrode [3, 4]. The main idea behind the operating principle of DSSCs is based on the optical excitation of a dye that results in the injection of an electron into the conduction band of a wide band gap semiconductor oxide. The oxidized dye molecule is regenerated afterwards when it is reduced to its ground state by gaining one electron from a redox couple that is found in the electrolyte around the sensitized semiconductor oxide nanostructured film [3–5]. Since the first outstanding research work on DSSC was demonstrated by O'Regan and Gratzel in 1991 [5], each of its components has been extensively investigated and optimized, with the aim to maximize the power conversion efficiency (PCE) of DSSCs [4, 7, 8]. Recently, a PCE of 12.3% has been achieved by using the cosensitization of two dyes

Rational Design of Solar Cells for Efficient Solar Energy Conversion, First Edition.
Edited by Alagarsamy Pandikumar and Ramasamy Ramaraj.

and a Co(II/III) tris(bipyridyl)-based redox electrolyte [9]. Hence, study to find a suitable and high performance DSSC output has greatly increased over the years.

Amongst all the materials studied for use in DSSCs, nanocrystalline TiO_2 has been most commonly employed as the metal oxide semiconductor material in high efficiency DSSCs [4–6]. Several methods were used for the preparation of the TiO_2 nanoparticles in DSSCs, such as sol-gel [10, 11], gas-phase pyrolysis [12], or the commonly used hydrothermal synthesis method [13, 14]. However, hydrothermal methods are not ideal because both synthesis and purification processes take a prolonged time to achieve well-formed and highly crystalline TiO_2 particles [12]. To minimize the costs of metal oxide semiconductor materials for DSSCs, simple preparation methods are essential to control the formation of crystal structure, crystallization, and particle size [15]. Besides TiO_2, there are reports of other alternative metal oxides, such as SnO_2, Nb_2O_5, and ZnO, being used as porous semiconductor materials for DSSC photoelectrodes [16–20].

ZnO is an another attractive and alternative photoanode to replace TiO_2 as an electron conductor owing to its higher bulk electron mobility and easily tunable morphology, which allows the rational design and development of hierarchical ZnO nanostructures able to simultaneously optimize charge carrier path and dye loading [19, 20]. Hence, ZnO is considered an excellent backbone to produce high-efficiency DSSCs. The ZnO characteristic of higher electron mobility ($\sim 205–1000\,cm^2V^{-1}\,s^{-1}$) than TiO_2 ($\sim 0.1–4\,cm^2V^{-1}\,s^{-1}$), enables the rapid diffusion transport of photoinjected electrons when it is employed as a photoanode material in DSSCs. In addition, ZnO is a suitable material for the fabrication of mesoporous photoanodes in DSSCs; it has a band gap of 3.2 eV and a conduction band edge position of –4.3 eV, both of which are similar to TiO_2 [15–17]. Moreover, ZnO can be easily prepared into tunable nanostructures, such as nanoparticles, nanowires, nanotubes, nanorods, nanosheets, and tetrapods, providing numerous alternatives for optimizing photoanode morphology so as to improve the charge collection. However, the conversion efficiency of ZnO-based DSSCs reported so far still remains lower than those fabricated from TiO_2, leaving plenty of room to improve the efficiency through structural and morphology modifications of the ZnO nanostructures. Previous review articles [16, 17] have explored recent developments in ZnO nanostructures for application in DSSCs and suggest that the nanostructured ZnO can significantly enhance solar cell performance due to the large surface area for dye adsorption, direct transport pathways for photoexcited electrons, and efficient scattering centers for enhanced light-harvesting efficiency. Furthermore, the limitations of ZnO-based DSSCs are also discussed and a few suggestions are also given for the conversion efficiency improvement.

1.2 Metal Dressed ZnO Nanostructures as Photoanodes

One of the major challenges in the development of high efficiency DSSCs is the competition between the generation and recombination of photoexcited carriers. The use of low-dimensional nanostructures is able to support a direct pathway for the rapid collection of photogenerated electrons and, hence, reduce the charge recombination [21, 22]. Thus, the possible alternative way to improve the charge separation in DSSCs is to introduce a barrier layer at the semiconductor/electrolyte interface to block the back electron transfer from the semiconductor to the redox electrolyte. Doping of metals on ZnO nanostructures significantly reduces the charge recombination, which is another way to improve the charge separation in DSSCs. Rapid charge transfer and improved charge separation upon incorporation of metal nanoparticles on ZnO, leading to enhanced DSSC performance, have been demonstrated [23–33]. Moreover, the metal nanoparticles (namely silver and gold) that possess surface plasmon resonance can couple to visible light, which increases the optical absorption of the photoelectrode in the visible region.

Metal nanoparticles doped on ZnO exhibit unusual redox activity by readily accepting electrons either from a dye molecule or an electrode. Such metal nanoparticles, when in contact with a ZnO nanostructure, can equilibrate and undergo Fermi-level equilibration, thus forming a Schottky barrier at the metal/ZnO nanocomposite interfaces (Figure 1.1) [22].

The charge equilibration between the metal and ZnO nanocomposite interfaces in contact drives the Fermi level close to the conduction band edge of the semiconductor and, thus, influences the photovoltaic performance of DSSCs. So far, ZnO-based DSSC performance has been reviewed but there is no summary of the metal dressed ZnO based DSSC performance. In this review, the recent progress on metal dressed ZnO based DSSC and the role of metal nanoparticles on various ZnO nanostructures in DSSCs (Figure 1.2) in improving the device performance (through improved charge separation introduced by the Schottky barrier formed at the metal/ZnO nanocomposite interface) are

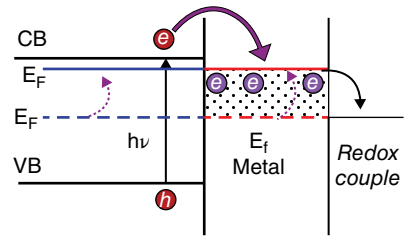

Figure 1.1 Schematic representation of photoinduced charge separation and charge distribution in ZnO/metal nanocomposites. E_F and E'_F represent Fermi levels attained before and after charge distribution. *Source:* Adapted from Subramanian 2003 [22]. Reprinted with permission of American Chemical Society.

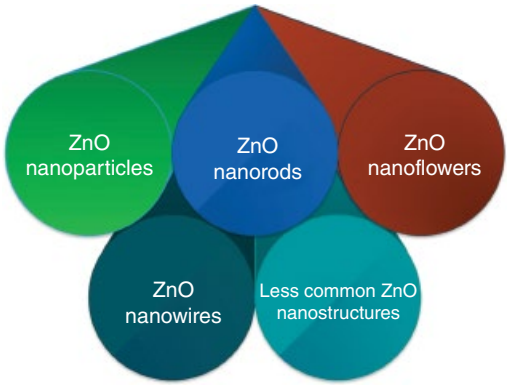

Figure 1.2 Various types of metal dressed ZnO nanostructure used as photoanodes in DSSCs.

discussed. Furthermore, the influence of silver and gold nanoparticles leading to enhanced optical absorption on the performance of DSSCs is also discussed.

1.2.1 Metal Dressed ZnO Nanoparticles as Photoanodes

There are few related works reported involving metal dressed ZnO nanoparticles as photoanodes in DSSC applications. Among them, Tripathi [23] and coworkers reported a bilayer TiO_2:Ag/ZnO:Ag (TZO:Ag) oxide film using a sol-gel process for DSSCs. They have investigated the effect of Eosin-Y dye and a cocktail dye (C) (Rhodamine B, Rose Bengal, Fast Green, Acridine Orange, Fast Green) for DSSC application. In comparison to the undoped ZnO/C film, their TZO/Ag/C film exhibits higher V_{oc}, J_{sc}, and PCE of 0.158%. This is due to the surface plasmon resonance effect of the silver nanoparticles in enhancing visible light absorption and also the Schottky barrier established at the semiconductor/metal interface. Sarkar *et al*. reported a nanocomposite consisting of gold and ZnO nanoparticles (NPs) for photocatalysis and DSSC applications [24]. Their ZnO–Au nanocomposite (NC) was synthesized based on the formation of gold NPs on the surface of ZnO NPs, using chloroauric acid ethanolic solution added into readily prepared ZnO NP colloid solution. To obtain the gold NPs, they added sodium borohydride (through a chemical reduction method) in order for gold chloride to undergo reduction. Interestingly, the ZnO–Au NC morphology (Figure 1.3) reveals the uniform distribution of gold on spherical ZnO nanoparticles, with average diameters of 6 nm and 8 nm, respectively. In their DSSC application, the ZnO–Au NC depicts a higher overall PCE of 0.8% than the pure ZnO (PCE = 0.012%). Such major difference in the PCE reported was claimed to be attributed to role of gold in increasing the electron mobility in ZnO–Au NC in addition to its plasmon resonance.

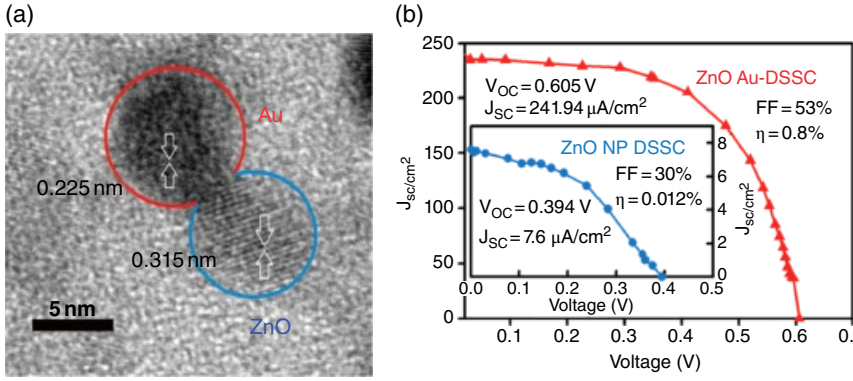

Figure 1.3 (a) TEM image of Au@ZnO nanoparticles and (b) *I–V* curves obtained for the modified photoanode-based DSSCs using N719 dye-sensitized Au@ZnO nanoparticles. Inset: *I–V* curves obtained for the N719 dye-sensitized ZnO nanoparticles based DSSCs. Adapted from [24] with permission of The Royal Society of Chemistry.

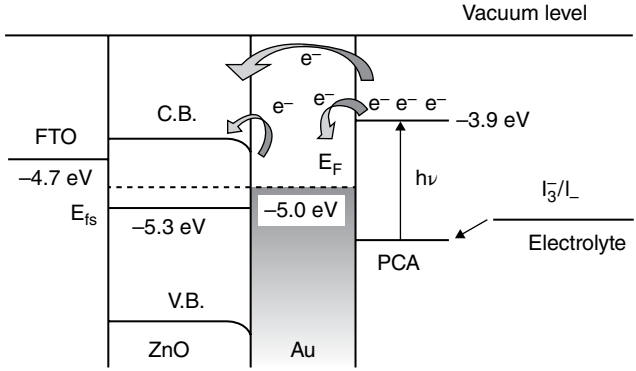

Figure 1.4 Energy level diagram and mechanism of photocurrent generation in the DSSC with FTO/ZnO/Au/PCA/polymer electrolyte. Adapted from [25] with permission of The Royal Society of Chemistry

Mikroyannidis and coworkers also reported gold-coated ZnO photoanodes for DSSC application using their own synthesized perylene monoimide derivative, PCA, as the sensitizer (Figure 1.4) [25]. Initially, they synthesized pure ZnO NPs using a sol-gel method and then immerse the preformed ZnO NPs in chloroauric acid to obtain ZnO NPs coated with gold nanoparticles. Later, the photoanodes were immersed in their own prepared PCA sensitizer, which is a metal-free dye. By comparing their DSSC obtained PCE, it was found that the PCE of their ZnO NPs coated with gold NPs was enhanced from 1.34 to 1.91%, which contributed to the fast transport of electrons from the gold NPs to the ZnO NPS through the Fermi-level equilibration and the

formation of a Schottky barrier at the ZnO/Au interface, which reduces the charge recombination rate, thus increasing the PCE as described earlier. The PCE was also improved by adding TiO_2 nanofillers into the ZnO–Au DSSC, which again increased the PCE values to 2.44%. It was reported that the increasing PCE value in the presence of nanofillers (TiO_2) is due to the enhancement of exchange charge density and diffusion coefficient of triiodide, which depress the concentration of I_3^-, and the suppression of the dark reaction by the polymer gel electrolyte with TiO_2. The improved PCE could be due to the incorporation ZnO into TiO_2 DSSCs as a result of the inhibition of the injected electrons from the dye molecules in recombining back with the electrolyte species [34].

1.2.2 Metal Dressed ZnO Nanorods as Photoanodes

Recently, great interest was shown in a ZnO nanorod (NR) structure (compared to other ZnO morphologies) due to its high surface area and its capability of rapid charge collection that enhances the overall short circuit current [35, 36]. Yin and coworkers [26] have reported on their ZnO nanorods array deposited with silver nanoparticles (Ag NPs/ZnO NRs) for DSSC application. This composite was synthesized through a combination of liquid phase epitaxial growth process and the reduction of silver on the surface of the ZnO NRs (Figure 1.5). According to this report, the role of silver NPs was seen to improve the DSSC efficiency (PCE = 0.81%) compared to the pure ZnO NRs; this can be related to the surface plasmon resonance of the silver NPs and the Schottky barrier at the Ag/ZnO interface.

Instead of using silver nanoparticles, a number of works related to dressing the ZnO nanorods with gold nanostructures have also appeared. Lou *et al.* reported the fabrication of gold NPs on hydrothermally prepared ZnO NR films using an ion sputtering technique [27]. Their work was mainly concerned with the effect of molecular modification on plasmon-enchanced DSSCs using the dodecanethiol molecule to protect the gold NPs from the electrolyte. The ZnO/Au/N719/dodecanethiol device recorded the highest IPCE in the range of 440–470 nm, which can be attributed to the "shielding" effect of the dodecanethiol molecules on the exposed gold nanoparticle sites that reduces the charge recombination rate. Similarly, Chen *et al.* reported the fabrication of a DSSC using vertically aligned ZnO nanorod arrays sensitized with gold nanoparticles [28]. Based on a low-temperature chemical seeding method, their composite was examined and compared with pure ZnO nanorod arrays, and also with and without the presence of ruthenium dye N719. Obviously, the composite photoanode in the presence of ruthenium dye exhibits the highest power conversion efficiency of 1.2%. They have claimed that the back electron transfer was significantly reduced by the interfacial ZnO–Au Schottky barrier that results in the increased efficiency.

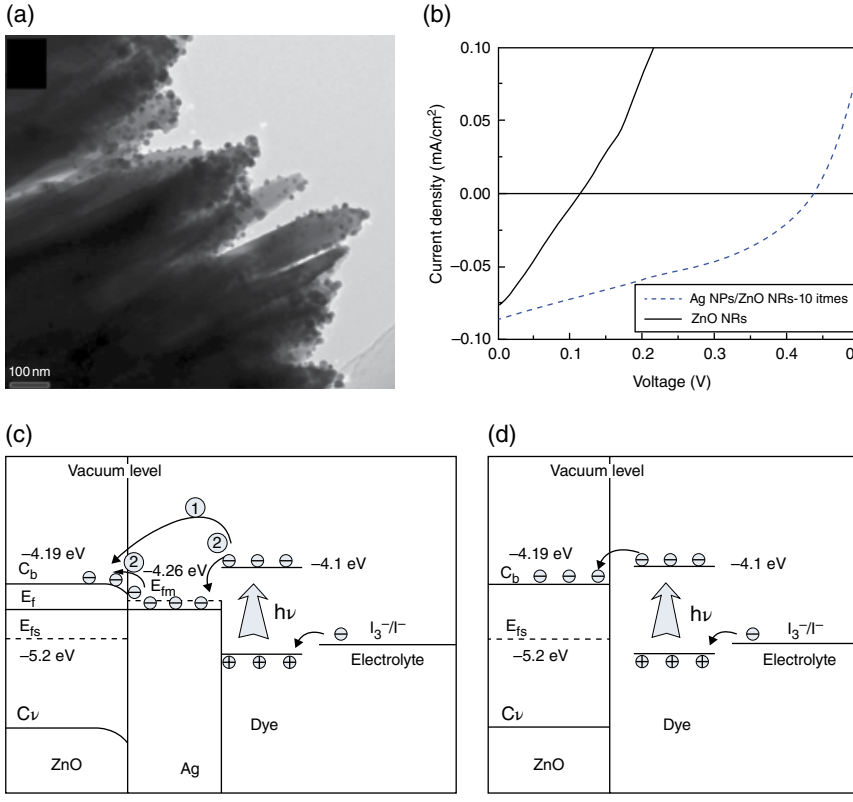

Figure 1.5 (a) TEM image of the Ag NPs/ZnO NRs composite arrays prepared by 10 adsorption–reduction cycles and (b) *J–V* characteristics of the solar cells prepared with the bare ZnO NR arrays and the Ag NPs/ZnO NR composite arrays (free dye). Energy level diagram and mechanism of the photocurrent generation in the photoelectrochemical cell prepared with (c) the Ag NPs/ZnO NR composite arrays and (d) the bare ZnO NRs array. Reprinted by permission from Springer Nature Copyright 2012 [26].

Although the surface plasmon resonance effect is known to significantly enhance the DSSC efficiency, Peh and coworkers reported that the addition of gold nanoparticles on their ZnO nanorods has substantially reduced the overall conversion efficiency [29]. The decrease of conversion efficiency of the pure ZnO nanorod device from 5.2 to 2.5% for the Au–ZnO device is attributed to the aggregation of the gold nanoparticles that distorts the plasmonic effect, thus broadening the spectral enhancement of the device. In addition, this also decreases the surface area of ZnO nanorods adhering to the dye molecules, which dramatically reduces the sunlight conversion process. In terms of the effect of the DSSC's active area, Bora *et al.* reported the presence of a highly efficient ZnO/Au Schottky barrier in their ZnO/Au nanocomposite DSSC

[30]. They studied the effects of various sizes of the active area in the DSSC, and also the amounts of gold nanoparticles incorporated in their ZnO nanorod photoelectrodes. Their results are in good agreement with the previous work as an approximately60% decrease in PCE was reported when the amount of gold nanoparticles increased by varying the dipping time of the ZnO nanorod photoelectrodes in $HAuCl_4 \cdot H_2O$ solution (0.01 mM). Furthermore, the impact of DSSC active area size was also reported, as increment in the size of the DSSC active area reveals higher sheet resistance of the used substrates. Therefore, the PCE values decrease as the active area of the DSSC increases. Through this reported work, the importance of optimizing the amount of metal nanoparticles to avoid excess aggregation occurring on the semiconductor layer, in order to fully harness the enhanced plasmonic effect of the DSSCs, is well understood, as is the size of the active area of DSSC to reduce the series resistance occurring on the substrates.

1.2.3 Metal Dressed ZnO Nanoflowers as Photoanodes

ZnO nanoflowers have been of considerable interest to some researchers due to their unique structure. Through the application of the ZnO nanoflowers, it is possible to benefit from the increased dye loading and light harvesting capability whilst still maintaining satisfactory electron conductivity in the DSSC [37, 38]. Although they are plenty of works involving ZnO nanoflowers for DSSCs, there is only one known work reporting on metal dressed ZnO nanoflowers used as a photoanode. This work, by Dhas and co-workers [31] involves the loading of ZnO nanoflowers on gold nanoparticles through a simple hydrothermal route. Initially, this one-step method involves the dissolution of zinc acetate, in which the morphology is controlled later by the addition of NaOH, and then loading of gold NPs using $HAuCl_4$. The wurzite structures of ZnO rod-like petal structures were embedded with gold NPs that are uniformly distributed with an average size of approximately 10 nm, as shown in Figure 1.6. In terms of their DSSC performance, the role of gold nanoparticles on the ZnO nanoflowers was compared with the pure ZnO nanoflower device. As expected, their *I–V* curves reveal that the bifunctional gold NP-loaded ZnO nanoflower shows enhanced properties (fill factor (FF) 0.33 and efficiency 2.5%) over the pure ZnO nanoflower device (FF 0.32 and efficiency 1.6%). Such an increase was attributed to the gold nanoparticles reducing the recombination spots due to the oxygen vacancies in ZnO in the surface layers and the surface plasmon resonance effect.

1.2.4 Metal Dressed ZnO Nanowires as Photoanodes

Similar to ZnO nanorods, one-dimensional ZnO nanowires also exhibits good photoconversion enhancement, which benefits from direct conduction paths for electrons to transport from the point of injection to the collection

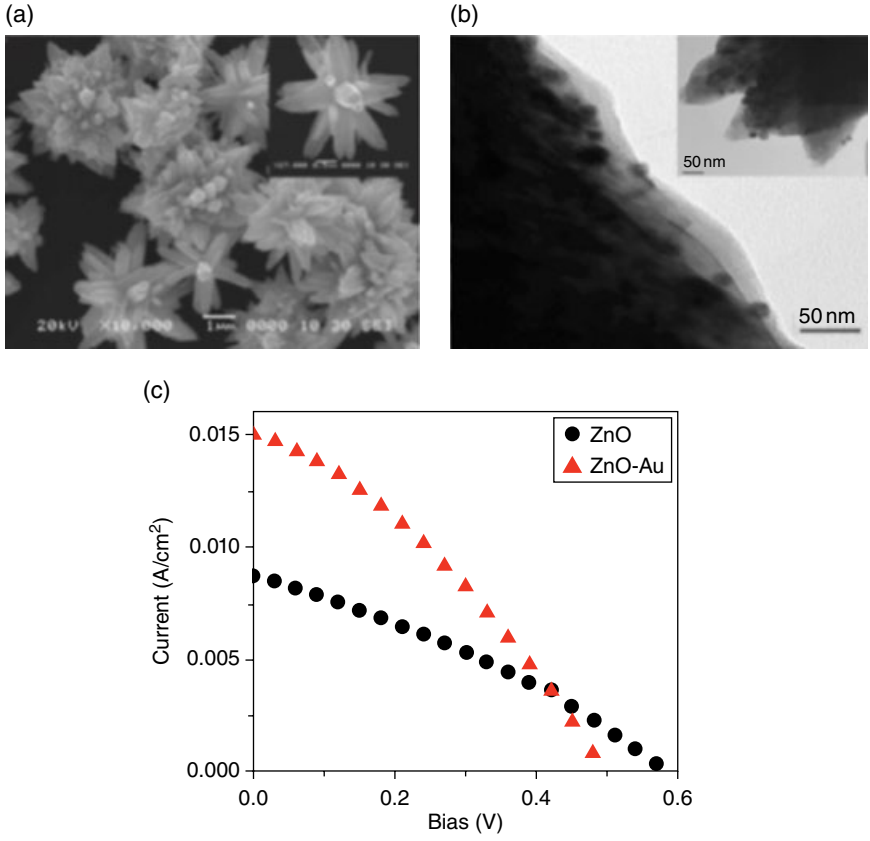

Figure 1.6 (a) SEM image of ZnO nanoflowers with gold nanoparticles and (b) HRTEM image of ZnO nanoflower petal surface loaded with gold nanoparticles. Inset (a) a single ZnO nanoflower with gold nanoparticles and (b) gold nanoparticles loaded ZnO nanoflower petals. (c) *J–V* curve obtained for N_3 dye-sensitized ZnO nanoflowers films with and without gold nanoparticles. Reprinted from [31] with the permission of AIP Publishing.

electrode, making them a much more preferable nanostructure in DSSC application [39, 40.] So far, they have only been reported once, by Lu and coworkers, in literature on metal dressed ZnO nanowires used in DSSC applications [32]. In their project, the synthesis was reported of vertically grown gold NPs on ZnO nanowire arrays (Au NPs @ZnO nanowire) through a two-step method. Their structure reveals that the size of the gold nanoparticles ranges from 5 to 10 nm and the shell is around 15 nm. Under solar simulation, bare ZnO nanowire arrays and the Au NPs @ZnO nanowires have been compared, with the latter displaying increased PCE values from 0.154 to 0.191% and from 0.269 to 0.387% using different length ZnO nanowire arrays (3 and 7.5 μm, respectively). Through this research, they have concluded that a plasmonic-enhanced DSSC

requires a lower thickness (about 20–40%) to achieve the same efficiency as conventional DSSCs. However, more experimental investigation is still needed in order to verify their conclusion.

1.2.5 Less Common Metal Dressed ZnO Nanostructures as Photoanodes

Although the most commonly reported ZnO nanostructures, such as nanorods and nanoparticles, are widely used in plasmonic-enhanced DSSCs, less common and unique ZnO nanostructures have also been reported during investigations into the use of other alternative rare nanostructures for enhancing DSSC properties. A *sheaf-like*-ZnO@Ag nanocomposite (*sheaf-like*-(ZnO@Ag)$_{NCM}$) has been reported as the photoanode in a DSSC application [33]. The synthesis of *sheaf-like*-(ZnO@Ag)$_{NCM}$ was made through a two-step method whereby ZnO NRs were synthesized using a microwave irradiation method at 150 W. Following this, the preformed ZnO NRs were mixed with $AgNO_3$ before undergoing a reduction process with NaOH to form the *sheaf-like*-(ZnO@Ag)$_{NCM}$, as shown in Figure 1.7a. The morphological structure obtained (Figure 1.7b) – the *sheaf-like*-(ZnO@Ag)$_{NCM}$ – was composed entirely of 1D closely-packed nanorods with a typical diameter of about 150–200 nm. It was well understood that the unique sheaf-like structure formation takes place during the conversion of Ag^+ to Ag NPs with NaOH as the reducing agent.

In terms of DSSC use, the *sheaf-like*-(ZnO@Ag)$_{NCM}$ was pasted on fluorine-doped tin oxide (ITO) through a doctor blade method and was dipped in two different sensitizers: eosin-Y and N719 dye. The *J*–*V* graph (Figure 1.7c) shows various photoanodes used to compare the different sensitizers and *sheaf-like*-(ZnO@Ag)$_{NCM}$ with pure ZnO photoanodes. Obviously, the ZnO NR–Ag photoanodes outperformed the pure ZnO NR photoanodes; this was attributed to the effective charge separation and charge transfer and the formation of a Schottky barrier due to the introduction silver nanoparticles on ZnO. As for the different sensitizers, ZnO NR–Ag/N719 exhibits a better PCE value (1.80%) than ZnO NR–Ag/EY (1.39%). Based on this work, the N719 dye remains a more appropriate sensitizer than the eosin-Y dye, as it has a broader absorption range in the entire visible region of the solar spectrum and the presence of silver NPs.

1.2.6 Comparison of the Performance of Metal Dressed ZnO Nanostructures in DSSCs

The performances of the various metal dressed ZnO nanostructures described in DSSCs are listed in Table 1.1. From this table, it can be seen that most of the ZnO nanostructure DSSCs incorporating plasmonic nanoparticles have yet to achieve a high benchmark in terms of PCE values. A wide range of study is still

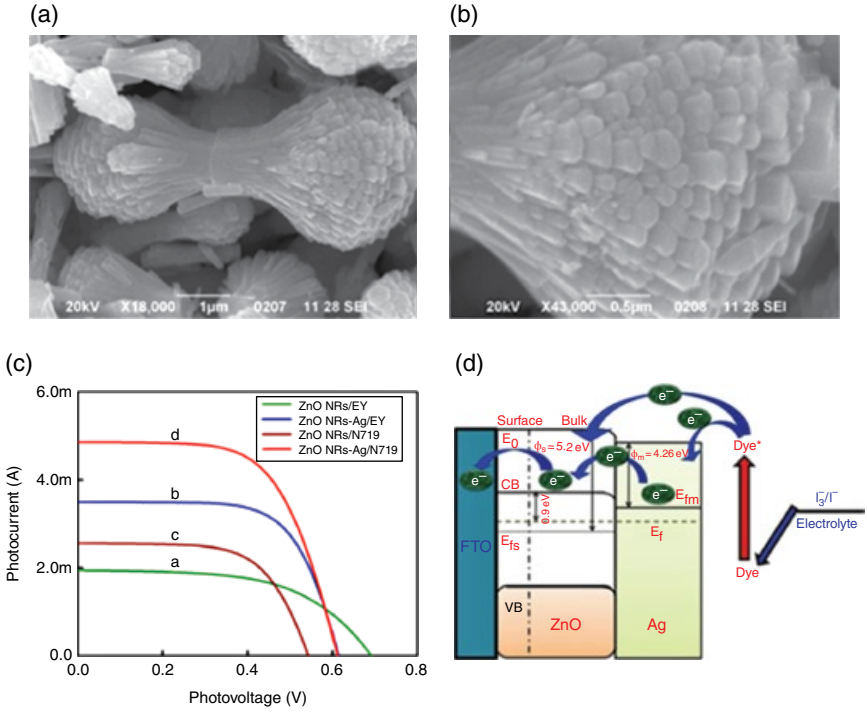

Figure 1.7 (a) and (b) SEM image of *sheaf-like*-$(ZnO@Ag)_{NCM}$. (c) *J–V* curves recorded for ZnO NRs/eosin-Y, *sheaf-like*-$(ZnO@Ag)_{NCM}$/eosin-Y, ZnO NRs/N719, and *sheaf-like* $(ZnO@Ag)_{NCM}$/N719 photoanodes with TiO_2 NPs modified PEO electrolyte based solid-state DSSCs under simulated AM 1.5 G solar irradiation of 100 mW/cm^2. Area of the cell was 1 cm^2. (d) Mechanism of photocurrent generation at *sheaf-like*-$(ZnO@Ag)_{NCM}$ modified photoelectrode based dye-sensitized solar cells. Where E_{fs} and E_{fm} are Fermi level of semiconductor and metal, respectively. ϕ_s and ϕ_m are work function of semiconductor and metal, respectively. Reprinted from [33] with the permission of AIP Publishing.

needed to enhance DSSCs performance for it to compete against recently reported photovoltaic cells. Among the reported DSSCs, the DSSC with ZnO/Au/N719/ dodecanethiol configuration showed an efficiency of 13.5 % due to the presence of gold nanoparticles, which enhanced the interfacial charge transfer process [27].

1.3 Conclusions and Outlook

This chapter has explained the use of plasmonic nanoparticle dressed ZnO nanostructures involving various structural designs (nanoparticles, nanorods, nanoflowers, nanowires, less common ZnO structures) used in DSSCs. As

Table 1.1 Comparison of various metal nanoparticle dressed ZnO nanostructure DSSCs.

Photoanode	Fabrication method	Sensitizer	Short-circuit photocurrent density, J_{sc} (mA/cm_2)	Open-circuit voltage, V_{oc} (V)	Fill factor, FF	Power conversion Efficiency, η (%)	Ref.
TZO/Ag/C	Sol-gel	Eosin-Y, Cocktail Dye	0.621	0.477	53	0.158	[23]
ZnO–Au NC	Chemical reduction	N719	0.26187	0.605	53	0.8	[24]
ZnO–Au + TiO_2 nanofiller	Chemical reduction	PCA	6.35	0.70	55	2.44	[25]
Ag NPs/ZnO NRs	Chemical reduction	N719	—	0.44	—	0.81	[26]
Zno/Au/N719/ dodecanethiol	Ion sputtering	N719	—	—	—	13.5*	[27]
Au/ZnO NR	Chemical reduction	N719	4.2	0.62	—	1.2	[28]
Au–ZnO	Mixing	N719	1.8	0.55	63.4	2.5	[29]
ZnO/Au nanocomposite	*In situ* precipitation	N719	14.89	0.67	65.06	6.49	[30]
ZnO-Au	Hydrothermal	N3	15.00	0.50	33	2.5	[31]
Au NPs @ZnO nanowire	—	—	—	—	—	0.191	[32]
sheaf-like-$(ZnO@Ag)_{NCM}$	Chemical reduction	Eosin-Y, N719	4.85	0.61	61	1.80	[33]

*η (%) based on IPCE measurements

reported, the role of the plasmonic nanoparticles was clearly observed enhancing the electrical properties of the photoanodes when attached to the ZnO nanostructures. Without a doubt, ZnO nanorods do possess a significant advantage over the other ZnO nanostructures when incorporated with plasmonic nanoparticles, as the structure itself promotes a more direct pathway for electron movement. Nonetheless, it also necessary to take into account other parameters, such as the size of the active area of the photoanode, the amount of plasmonic nanoparticles injected, and the type of sensitizer used, which could ultimately affect the final results of the DSSCs' efficiency.

Although some of the work has shown promising results for possible commercialization and applicability, these photoanodes still yield low PCE values when compared to TiO_2-based photoanodes. In order to achieve higher PCE values, other alternative materials are still to be explored, such as the incorporation of plasmonic nanoparticles on a mixture of various ZnO nanostructures (nanopellets, nanosheets, nanotubes, nanofibres). Only a few works on DSSCs based on plasmonic nanoparticles on ZnO nanostrucutures have been reported. Much work is still needed to be done and investigated, especially with different parameters, in order for it to be on par with recent DSSCs that have reported high performance and good stability.

References

1 R. Pike and P. Earis, *Energy Environ. Sci.*, 2010, **3**, 173.
2 P.V. Kamat, J. Phys. *Chem. C*, 2007, **111**, 2834–2860.
3 L.M. Gonçalves, V. de Zea Bermudez, H.A. Ribeiro, and A.M. Mendes, *Energy Environ. Sci.*, 2008, **1**, 655.
4 A. Hagfeldt, G. Boschloo, L. Sun, *et al.*, *Chem. Rev.*, 2010, **110**, 6595–6663.
5 B. O'Regan and M. Grätzel, *Nature*, 1991, **353**, 737–740.
6 C.J. Barbé, F. Arendse, P. Comte, *et al.*, *J. Am. Ceram. Soc.*, 1997, **80**, 3157–3171.
7 J. Cong, X. Yang, L. Kloo, and L. Sun, *Energy Environ. Sci.*, 2012, **5**, 9180.
8 N. Tétreault and M. Grätzel, *Energy Environ. Sci.*, 2012, **5**, 8506.
9 A. Yella, H.-W. Lee, H.N. Tsao, *et al.*, *Science*, 2011, **334**, 629–634.
10 D. Chen, F. Huang, Y.-B. Cheng, and R. A. Caruso, *Adv. Mater.*, 2009, **21**, 2206–2210.
11 M. Hočevar, U. Opara Krašovec, M. Berginc, *et al.*, *J. Sol-Gel Sci. Technol.*, 2008, **48**, 156–162.
12 X. Chen and S.S. Mao, *Chem. Rev.*, 2007, **107**, 2891–2959.
13 S. Lee, I.S. Cho, J.H. Lee, *et al.*, *Chem. Mater.*, 2010, **22**, 1958–1965.
14 H. Zhang, Y. Han, X. Liu, *et al.*, *Chem. Commun.*, 2010, **46**, 8395–8397.
15 Y.M. Evtushenko, S.V Romashkin, and V.V Davydov, *Theor. Found. Chem. Eng.*, 2011, **45**, 731–738.

16 K. Sayama, H. Sugihara, and H. Arakawa, *Chem. Mater.*, 1998, **100**, 3825–3832.
17 Y. Fukai, Y. Kondo, S. Mori, and E. Suzuki, *Electrochem. Commun.*, 2007, **9**, 1439–1443.
18 Q. Zhang and G. Cao, *Nano Today*, 2011, **6**, 91–109.
19 Q. Zhang, C.S. Dandeneau, X. Zhou, and G. Cao, *Adv. Mater.*, 2009, **21**, 4087–4108.
20 J. Anta, E. Guillén, and R. Tena-Zaera, *J. Phys. Chem. C*, 2012, **116**, 11413–11425.
21 C. Xu, J. Wu, U.V. Desai, and D. Gao, *J. Am. Chem. Soc.*, 2011, **133**, 8122–8125.
22 V. Subramanian, E.E. Wolf, and P.V Kamat, *J. Phys. Chem. B*, 2003, **107**, 7479–7485.
23 S.K. Tripathi, M. Rani, and N. Singh, *Electrochim. Acta*, 2015, **167**, 179–186.
24 S. Sarkar, A. Makhal, T. Bora, *et al.*, *Phys. Chem. Chem. Phys.*, 2011, **13**, 12488–12496.
25 J.A. Mikroyannidis, M.M. Stylianakis, P. Suresh, *et al.*, *Energy Environ. Sci.*, 2009, **2**, 1293.
26 X. Yin, W. Que, and F. Shen, *J. Sol-Gel Sci. Technol.*, 2012, **63**, 279–285.
27 Y. Lou, S. Yuan, Y. Zhao, *et al.*, *Dalton Trans.*, 2013, **42**, 5330–5337.
28 Z.H. Chen, Y.B. Tang, C.P. Liu, *et al.*, *J. Phys. Chem. C*, 2009, **113**, 13433–13437.
29 C.K.N. Peh, L. Ke, and G.W. Ho, *Mater. Lett.*, 2010, **64**, 1372–1375.
30 T. Bora, H.H. Kyaw, S. Sarkar, *et al.*, *Beilstein J. Nanotechnol.*, 2011, **2**, 681–690.
31 V. Dhas, S. Muduli, W. Lee, *et al.*, *Appl. Phys. Lett.*, 2008, **93**, 243108.
32 M.-Y. Lu, H.-A. Chen, S.-Y. Chen, *et al.*, *Honolulu PRIME Meeting*, 2012, **MA2012-02**, 2871.
33 A. Pandikumar, K.M. Saranya, and R. Ramaraj, *Appl. Phys. Lett.*, 2012, **101**. 10.1063/1.4748287
34 F. Al-juaid, A. Merazga, F. Abdel-wahab, and M. *Al-amoudi*, 2012, **2012**, 192–196.
35 M. Bokhari, A.K. Kasi, J.K. Kasi, *et al.*, *3M-NANO, International Conference on Manipulation, Manufacturing and Measurement on the Nanoscale*, 2013, **4**, 243–246.
36 M.H. Lai, M.W. Lee, G.J. Wang, and M.F. Tai, *Int. J. Electrochem. Sci.*, 2011, **6**, 2122–2130.
37 N. Mir, M. Salavati-Niasari, and F. Davar, *Chem. Eng. J.*, 2012, **181–182**, 779–789.
38 B. Kilic, T. Günes, I. Besirli, *et al.*, *Appl. Surf. Sci.*, 2014, **318**, 32–36.
39 J.B. Baxter and E.S. Aydil, *Sol. Energy Mater. Sol. Cells*, 2006, **90**, 607–622.
40 J.B. Baxter, A.M. Walker, K. Van Ommering, and E.S. Aydil, *Nanotechnology*, 2006, **17**, S304–S312.

2

Cosensitization Strategies for Dye-Sensitized Solar Cells

Gachumale Saritha[1], *Sambandam Anandan*[1], *and Muthupandian Ashokkumar*[2]

[1] *Nanomaterials and Solar Energy Conversion Laboratory, National Institute of Technology, India*
[2] *School of Chemistry, University of Melbourne, Australia*

2.1 Introduction

Increasing energy demand on a global stratum leads to extensive research focused on renewable energy sources. In addition, the depletion of fossil fuel-based energy sources and the undesirable environmental impacts of using them have created a greater need for renewable energy sources [1]. Photovoltaic cells are one of the renewable energy systems studied, as they convert the light energy into electrical energy. A photovoltaic cell or solar cell is a device based on the photovoltaic effect, discovered by French physicist Edmond Becquerel in 1839, and it has been the basis for different concepts of converting solar radiation into electricity [2].

Solar cell technologies are traditionally divided into three generation types [3, 4]. First generation solar cells are mainly based on crystalline silicon devices, whereas second generation solar cells based on the thin film solar cells consist of inorganic materials such as amorphous silicon (a-Si), cadmium telluride (CdTe), copper indium gallium selenide (CIGS), and others [5, 6]. The first two generation solar cells have achieved an efficiency of >20%, although the materials used are very expensive, which hampers large-scale production of the cells. During the last two decades, new generation solar cells, such as organic solar cells (OSCs) and dye-sensitized solar cells (DSSCs), known as third generation solar cells, have attracted much attention and have been regarded as a promising candidate for the utility of solar energy [7–13]. In the late 1960s, the dye-sensitization concept began when an organic dye, perylene, was used to generate electricity with an n-type semiconductor zinc oxide (ZnO) electrode

Rational Design of Solar Cells for Efficient Solar Energy Conversion, First Edition.
Edited by Alagarsamy Pandikumar and Ramasamy Ramaraj.

in an electrochemical cell [14]. In 1972, chlorophyll dye sensitization with a ZnO electrode was studied but the efficiency of these devices was poor due to poor light absorption efficiency [15]. The concept of dye sensitization with a wide bandgap semiconductor, TiO_2 (3.1 eV), is necessary for water splitting with a small bias voltage when exposed to light [16] was explored despite TiO_2 only in the ultraviolet region. The roughness factor of nanoporous TiO_2 electrodes – about 1000 – vividly augmented its light-harvesting efficiency. DSSCs have been alternatives to the conventional silicon solar cells since the pioneering work reported by O'Regan and Grätzel in 1991. The first dye-sensitized solar cells (DSSCs), fabricated using ruthenium-based dye (cisdithiocyanato bis(2,2'-bipyridine-4,4'-dicarboxylate)ruthenium-(II) (N3)) as photosensitizer, iodine/iodide (I^-/I_3^-) in an organic solvent as redox electrolyte, and platinum as a counterelectrode, had a conversion efficiency of 7.1% [17]. DSSCs have gained worldwide interest due to the following advantages: (i) the production costs and energy payback time are significantly reduced compared to standard silicon solar cells or other thin film cells; (ii) the color of the device could be easily modulated by choosing different dyes; (iii) flexibility; and (iv) simple fabrication and high performance [10–13,18,19]. DSSCs are multicomponent devices for the conversion of light into electricity.

Typically, DSSCs contain five major components (Figure 2.1):

1) conductive and transparent glasses,
2) nanocrystalline semiconductor film,
3) dye sensitizer,
4) redox couple,
5) counterelectrode.

Their efficiency depends critically on the individual properties of each of the materials used; these play a specific role in the process involved in converting sunlight into electricity. In DSSCs, the incident light is absorbed by the

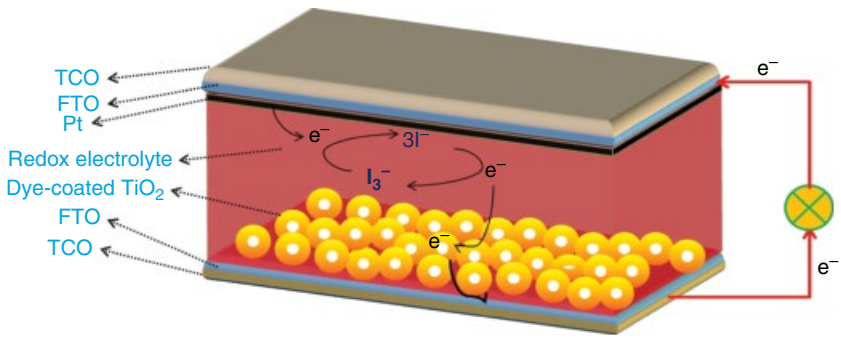

Figure 2.1 The composition of a dye-sensitized solar cell.

sensitizer, which injects electrons into the conduction band of TiO_2 from the excited state of the dye and charge separation take place at the interface of sensitizer and TiO_2. Further, the oxidized dye is regenerated by the electrolyte and the oxidation state of the electrolyte is regenerated at the counterelectrode by electrons through an external circuit.

The photosensitizer is one of the key components of a DSSC device, which is sensitive to the visible light region of the solar spectrum and attached to the semiconductor electrode by chemisorption. The performance of a DSSC depends on the relative energy levels of the sensitizer and kinetics of the electron transfer processes at the interface. An ideal sensitizer should meet the following requirements: (i) the absorption range of the dye should cover the whole UV–visible and near IR region with high molar extinction coefficient values; (ii) the lowest unoccupied molecular orbital (LUMO) of the dye should be above the conduction band edge of the semiconductor electrode and the highest occupied molecular orbital (HOMO) of the dye should be below the redox electrolyte for efficient electron injection and electron regeneration; (iii) a low tendency to aggregate on TiO_2 film; and (iv) excellent chemical, thermal, and electrochemical stability. Many new materials/dyes have been developed to improve device efficiency. The extensively used ruthenium-based sensitizers are di-tetrabutylammonium cis-bis(isothiocyanato)bis(2,2′-bipyridyl-4,4′-dicarboxylato) ruthenium(II) (N719) [20] and trithiocyanato (4,4′4′′-tricarboxy-2,2′:6′2′-terpyridine) ruthenium(II) (Black dye) [21], producing an efficiency (η) of >11%. However, Yella *et al*. obtained 12.3% efficiency by using zinc porphyrin (YD2-o-C8) dye as a sensitizer and Co(II/III)tris(bipyridyl) redox electrolytes [22]. Later, Mathew *et al*. achieved 13% efficiency by using zinc porphyrin-based SM315 dye [23] under AM 1.5G illumination. In the last two decades, a number of Ru(II) complexes have been developed with ancillary ligands; typically bipyridines or terpyridines can be tuned by different substituents (alkyl, aryl, heterocycle, etc.) to change the photophysical, electrochemical properties and, thus, improve the photovoltaic performance. In general, these dyes have shown good efficiency but there are certain limitations for DSSC [10]: (i) ruthenium metal shortage, (ii) high cost, (iii) low molar extinction coefficients, and (iv) difficulties in purification upon bulk production. Compared with traditional ruthenium-based dyes, metal-free organic dyes have become more promising due to their high molar absorption coefficient, low cost, easy synthesis and purification, no concern about resources, and tunable absorption spectra and energy levels through tailoring of molecular structure [11].

The basic structure of a metal-free organic dye is Donor-π-bridge-Acceptor (D-π-A) and it is a rod-like configuration. This architecture provides intramolecular charge transfer from donor to acceptor through a π-bridge to the conduction band of TiO_2. To further increase light harvesting ability, the

basic structure has been tuned by varying the donor, π-bridge or acceptor and studing their optical and electrochemical properties [24, 25]. For DSSCs based on metal-free organic dyes, the carboxy-anchor organic dye of LEG4 as the collaborative sensitizer to the silyl-anchor dye of ADEKA-1 gave a PCE >14%, V_{OC} above 1 V with the optimized Co(III/II) complex redox electrolyte solution [26]. The major drawback of pure organic dyes is a narrow region of absorption and failure to harness photons in the near infrared (NIR) region. Zhang *et al.* [2010] synthesized thieno[2, 3, 3–125]indole-based dyes, which exhibit their major electronic absorption in the range 400–600 nm in the visible region [27]. Later, Shi *et al.* [2011] synthesized squaraine-based sensitizer YR6, showing an absorption maximum at 659 nm with a high molar absorptivity of 279 000 M^{-1} cm^{-1} [28]. Liang and Chen [2013] showed high efficiency for the dyes having low energy absorption peaks [19]. Yang *et al.* [2014] synthesized indole-based dyes such as IQ4, YA421, and YA422, which showed the lowest energy absorption peak around 522 – 534 nm. The maximum efficiency (9.22%) was achieved for the dye YA422 in the presence of Co(II)/Co(III) redox electrolyte [29]. Using a single sensitizer, it may not be possible to cover a broad absorption spectrum from the UV–visible to NIR region. So, in order to achieve panchromatic sensitization, sensitized TiO_2 film is adsorbed by another dye with complementary spectral features to the cell sensitized by a primary dye. In both, metal complex and metal-free organic dyes, highest efficiencies of 12.3 and 14.3%, were obtained under cosensitization. In this chapter, the discussion is focused on the relationship between a structural property of metal-free organic dyes with metal complexes and in between two metal-free organic dyes under cosensitization. Further, the relationship between the molecular design and photovoltaic performances of DSSCs is discussed in order to develop new directions in achieving high efficiency for DSSCs.

2.2 Cosensitization

The major drawback of ruthenium-based metal complexes and organic sensitizers is their difficulty in achieving strong absorption in the red region of the visible spectrum. This problem can be rectified simply by cosensitization; this improves device performance by exhibiting complementary absorption in the visible and near-IR regions. For effective cosensitization, cosensitizers should meet the following conditions: (i) one of the sensitizers should have strong absorption in the near-IR region and the region about 400 nm to restore the dip in the incident photon-to-current conversion efficiency (IPCE) spectra induced by I_3^-; (ii) it should avoid competitive adsorption on TiO_2 film in mixed solution, which effectively avoids dye aggregation on TiO_2 film; and (iii) the cosensitizer should reduce the recombination of injected electrons with I_3^- and other

acceptor molecules. Dye aggregation may be inhibited by the mixing of two dyes with different size and shapes to form a mono compact layer and cover a large area on the TiO_2 film in order to enhance the light harvesting efficiency of the device. To avoid such unfavorable dye aggregation, the introduction of long alkyl chains or bulky substituted groups on sensitizer is used in the cosensitization application [30–34]. These alkyl chains reduce the charge recombination between the injected electrons in the TiO_2 conduction band and the electrolyte. Cosensitization not only increases the J_{SC} but also V_{OC}.

The cosensitization strategy can be achieved in two ways: stepwise sensitization and cocktail sensitization. The stepwise cosensitization involves sequential dipping of the TiO_2 electrode firstly in primary dye solution then in secondary dye solution. In this sequential adsorption, the primary dye adsorption is optimized with different time intervals and concentration. Afterward, the secondary dye effectively fills the vacant spaces on the TiO_2 film. By this method of cosensitization, there is no competitive adsorption between the sensitizers on the TiO_2 surface. However, optimization conditions, such as relative dye concentration, dipping time, dipping order, and other conditions of each dye solution, play an important role in achieving high efficiency. For the cocktail cosensitization method, the TiO_2 film is dipped into a solution containing a mixture of the dyes, hence there is the possibility of competitive adsorption between dyes on the TiO_2 surface. In this method, only the dye mixing ratio needs to be considered in addition to the usual dye adsorption process. Both cosensitization approaches have merits and drawbacks.

Usually, organic dyes have high molar absorption extinction coefficients and dyes showing an absorption maximum around 500 nm are used in cosensitization with ruthenium-based metal complexes and/or porphyrin-based metal complexes. Because ruthenium-based metal complexes have a low molar extinction coefficient, a thick film is needed for absorbing all the incident red photons. Due to high molar extinction coefficient values of organic dyes in cosensitization, thinner layers could be used in DSSCs without significantly reducing light-harvesting in any portion of the spectrum.

2.2.1 Cosensitization of Metal Complexes with Organic Dyes

2.2.1.1 Phthalocyanine-based Metal Complexes

The light harvesting efficiency (LHE) of a sensitizer having intense absorption in the near-IR region is an important factor. In this respect, phthalocyanine (Pc)-based sensitizers are more suitable for dye cosensitization because the LHE of the phthalocyanines is in the far red region. In addition, they have high molar extinction coefficient. Therefore, phthalocyanines use the high energy absorbing sensitizers for cosensitization and they cover the whole absorption spectrum from UV–Vis to the near-IR region. Further, the large number of photons absorbed by the cosensitized device enhances the device performance

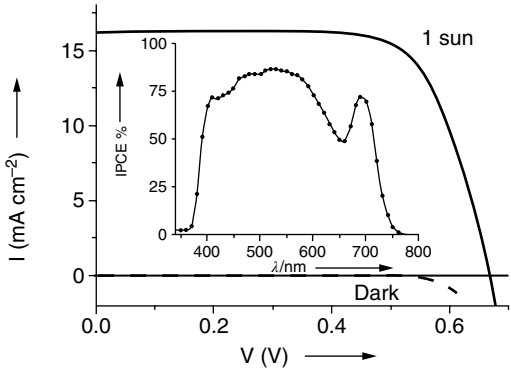

Figure 2.2 IPCE spectrum and *I–V* curve of a JK2/TT1/TiO_2 DSSC with an active area of 0.2 cm^2 [35]. Reproduced with permission of John Wiley & Sons.

better than the individually sensitized device. Based on this, Cid and coworkers [35] designed an efficient cosensitized DSSC system by using phthalocyanine (TT1) and efficient organic dye JK2. The photoresponse of the "molecular cocktail" extends up to 700 nm with photon-to-electron conversion efficiencies of 72% at 690 nm, which is higher than the individual dyes (Figure 2.2). The overall device efficiency was around 7.74%, with increased J_{SC} and V_{OC} values, which is the highest value reported for cosensitized DSSCs [35].

Clifford and coworkers reported that the cosensitized D2 + TT1 cells also show a better efficiency of 4.08% when compared to 3.43% for individual D2 sensitized solar cells (Figure 2.3) ($J_{SC} = 6.3\,mA\,cm^{-2}$; $V_{OC} = 780\,mV$; fill factor (FF) = 73.96%) and 2.37% for TT1 cells (Figure 2.3) ($J_{SC} = 6.3\,mA\,cm^{-2}$; $V_{OC} = 588\,mV$; FF = 63.31%) [36]. Cosensitized D2 + TT1 cells show increased light harvesting and overall improvement in cell efficiency compared to reference cells made with either D2 or TT1 only. The V_{OC} values of cosensitized D2 + TT1 cell are somewhat intermediate between D2 and TT1 cells and, in addition, these devices can be explained from both the charge extraction, transient photovoltage, and electron lifetimes data, which are of the order D2 > D2 + TT1 > TT1. The same trend was observed in the case of V_{OC} for cosensitized system D102 + TT1 using visible absorbing organic sensitizer D102 and a near-IR absorbing Zn–Pc complex (TT1) prepared by Brown and coworkers [37. Cosensitization improves the current density further to $9.4\,mA\,cm^{-2}$ while the overall power conversion efficiency increased to 4.7%; such increased photocurrent in the cosensitized devices is due to increased light harvesting ability by the Zn–Pc dye. The observed efficiency for the cosensitized system is higher than single dye D102 (Figure 2.3) or TT1 alone. Kimura and coworkers [38] reported a novel Zn–Pc dye PcS15 (Figure 2.3) having unsymmetrical and three-dimensional (3D) structure that prevented the cofacial aggregation of Zn–Pc adsorbed onto the TiO_2 surface. They applied

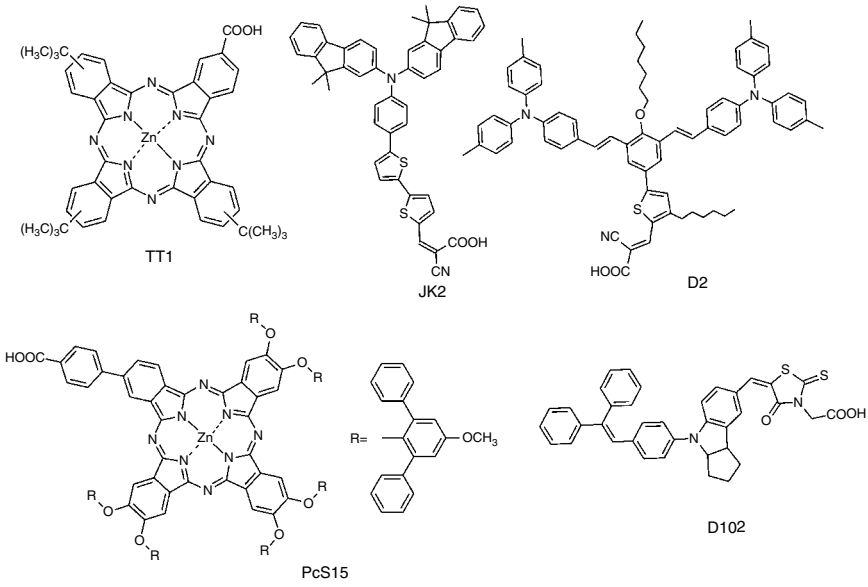

Figure 2.3 Molecular structures of cosensitized Zn–Phthalocyanine and organic sensitizers.

PcS15 cosensitization with red or orange organic dyes, D102 and D131. The DSSC performances of the cocktail-type PcS15 + D102 (5.6%) and PcS15 + D131 (6.2%) cells were significantly enhanced in comparison to that of the PcS15 cell (5.3%). Both J_{SC} and V_{OC} values increased upon cosensitization showing high IPCE values. Based on cosensitization, Robertson [39] stated that dyes should possess high molar extinction coefficients, allowing sufficient space on TiO_2 surface to attach other dyes with a complementary absorption spectrum [39]. Near-IR absorbing porphyrin sensitizers are thus perfect candidates for cosensitization to further improve the device performance.

2.2.1.2 Porphyrin-based Metal Complexes

The first porphyrin-based cosensitization was reported by Gratzel and coworkers in 2010 [40]. YD-2 [41 (Figure 2.4) cosensitization with D-205 [42] (Figure 2.5) dye improved the photovoltaic performance relative to that of a solar cell containing a single dye. Lack of light harvesting in the range of 480–630 nm by YD-2 leads to a reduction of J_{SC} and IPCE values were observed below 20% at 530 nm. Cosensitization with D-205 dye has an absorption maximum at 532 nm that coincides with the minimized IPCE response of the YD-2 dye and it showed complementary absorption spectrum. The photoconversion efficiency (PCE) of cosensitized system YD-2 + D-205 was 6.9% for 2.4 μm thick transparent titania film, which is higher compared to TiO_2 film sensitized by single dyes. Further, the best efficiency was reported by Yella and coworkers

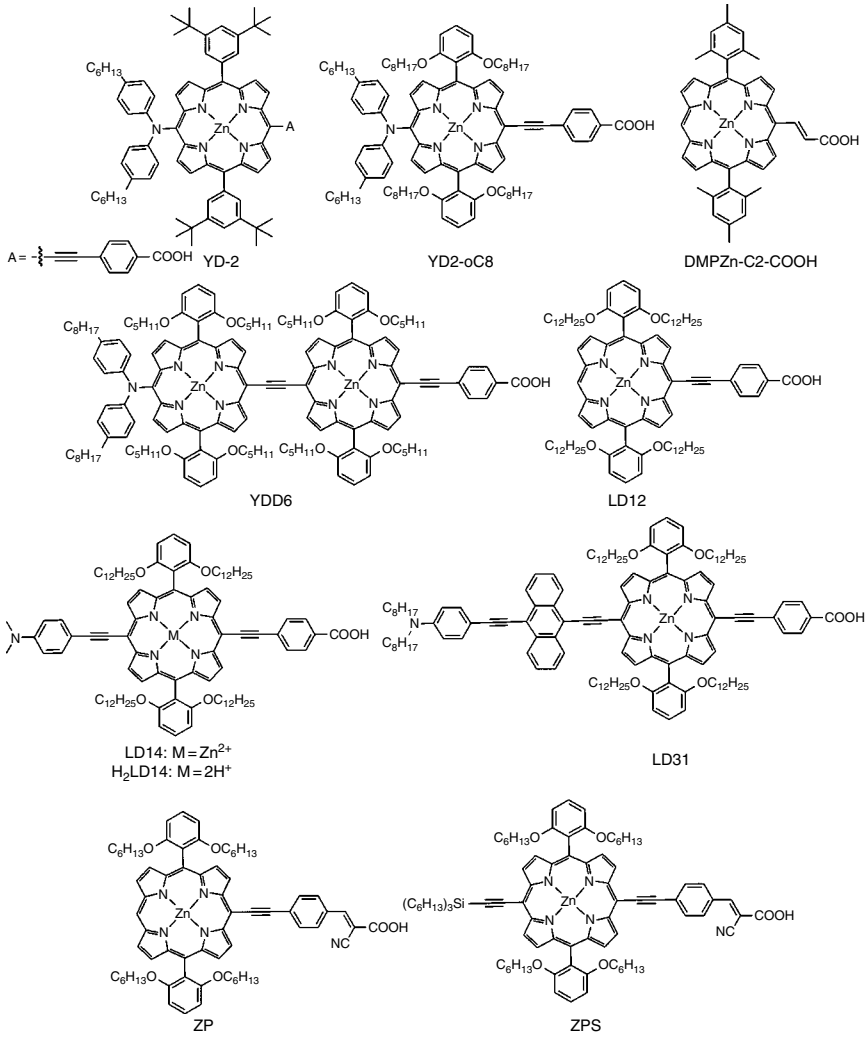

Figure 2.4 Molecular structures of porphyrin sensitizers.

[43] with a small variant of YD-2, i.e., incorporation of two octyloxy groups in the *ortho*-positions of each *meso*-phenyl ring, producing YD2-*o*-C8. The efficiency of YD2-*o*-C8 was 11.9%, which is higher than that of YD-2 (8.4%). The cosensitization of YD2-*o*-C8 with organic dye Y123 (Figure 2.5) yielded an efficiency of 12.3% when used in conjunction with the Co(II/III)tris(bipyridyl)-based redox electrolyte. The YD2-*o*-C8/Y123 cosensitization increases the J_{SC} and achieves incident photon-to-electron conversion efficiencies >90% in a large wavelength domain below 700 nm. Further, the V_{OC} decreased by about

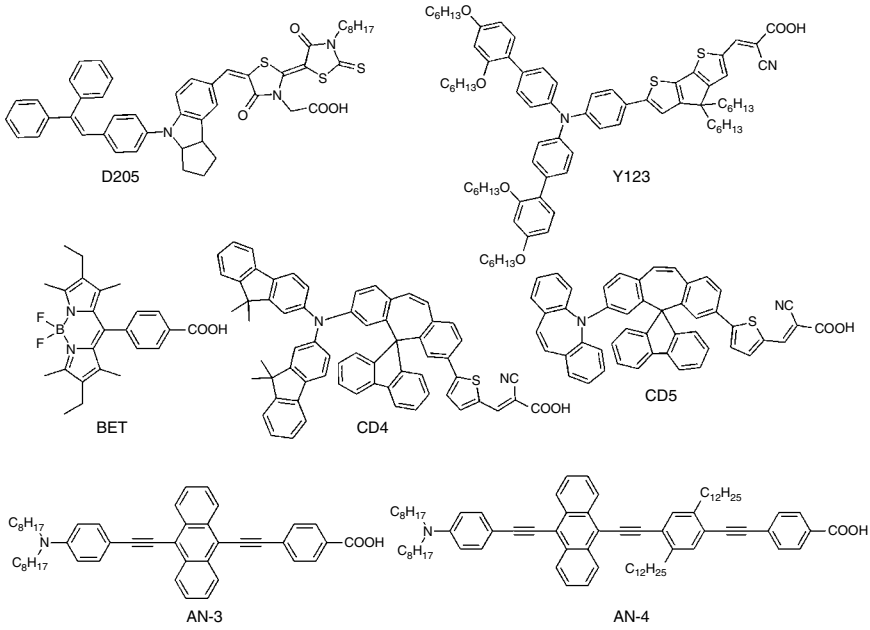

Figure 2.5 Molecular structures of cosensitized organic sensitizers with porphyrin dyes.

30 mV, which was consistent with electron lifetime compared to a film sensitized by YD2-*o*-C8 alone. Wu and coworkers reported that molecular cosensitization of TiO_2 films in a cocktail solution containing YD2-*o*-C8, an organic dye (CD4) (Figure 2.5), and a porphyrin dimer (YDD6) yielded 10.4% efficiency, which is superior to that obtained from the individual single-dye devices and the two-dye cosensitized systems [44]. The IPCE action spectrum is extended to the near-IR region.

The potential organic dye based on boron dipyrromethene (BET) (Figure 2.5) acted as a cosensitizer for DMPZn-C2-COOH, which had weak absorption between 450 and 550 nm; the IPCE spectrum of the cosensitized system revealed that photons between 450 and 550 nm are picked up by BET. A marginal improvement in energy conversion efficiency from 5.12 to 5.21% was achieved for the cosensitized system [45]. For the BET cosensitized with *ortho*-substituted porphyrin LD12 (Figure 2.4), both J_{SC} (14.7 mA cm^{-2}) and efficiency (7.5%) improved relative to the device made of LD12 (6.65%) dye alone [46]. The IPCE of the cosensitized LD12 + BET device was enhanced to ~70% compared to the individual BET and LD12 devices (at ~500 nm ~5% and ~40%, respectively). Zinc porphyrin dye LD12 was cosensitized with hole conducting characteristic of a spirally configured organic dye CD5 by Lan and coworkers [47] (Figure 2.5). The cosensitized LD12 + CD5 device showed significantly enhanced V_{OC} and J_{SC} relative to its individual single-dye sensitized devices.

A cosensitized LD12 + CD5 device yielded $J_{SC} = 16.7\,mA\,cm^{-2}$, $V_{OC} = 740\,mV$, FF = 73% and $\eta = 9.0\%$; this performance is superior to that of devices made from LD12 ($\eta = 7.5\%$) or CD5 ($\eta = 5.7\%$) [47]. The gap of the IPCE response, about 500 nm for the LD12 device, was completely filled in the action spectrum of LD12 + BET or LD12 + CD5 devices with the contribution of BET or CD5 that shows maximum photoresponse in that spectral region. For a LD12 + CD5 device, the V_{OC} was enhanced through retarded charge recombination overwhelming the downward shift of the TiO_2 potential.

The additional substitution at the *meso*-position of porphyrin LD12 yields LD14 sensitizer (Figure 2.4). Wang and coworkers [48] reported that the cosensitized system LD14/H_2LD14/AN-3 exhibited $J_{SC} = 18.76\,mA\,cm^{-2}$, $V_{OC} = 716\,mV$, FF = 72%, and an overall device efficiency $\eta = 9.72\%$ which is superior to that obtained from the individual single-dye devices and the two-dye cosensitized system LD14/H_2LD14 (8.31%). The V_{OC} of the LD14/H_2LD14/AN-3 device is greater than that of the LD14/H_2LD14 device (698 mV) due to the presence of additional AN-3 dye. By attaching a 4-dioctylaminophenyl-ethynyl-anthracenyl group via an acetylene bridge at the *meso*-position of the porphyrin core LD14 opposite to the anchoring group, the molecular design of LD31 was prepared (Figure 2.4). Further, LD31 was used for cosensitization with AN-4 (Figure 2.5) and the cosensitized device LD31/AN-4 shows the highest efficiency (10.26%) relative to that of individual dyes [49]. The J_{SC} was enhanced with the IPCE response of LD31/AN-4 cosensitized device. Jeong and coworkers reported that the spatially separated and mixed cosensitization of zinc porphyrin ZP or ZPS with highly efficient organic dye JK2 [50]. In spatially separated cosensitization, $JK2_{bottom}/ZPS_{top}$ on 4.5 μm thick TiO_2 film exhibited $J_{SC} = 13.67\,mA\,cm^{-2}$, $V_{OC} = 670\,mV$, FF = 70%; the the overall device performance $\eta = 6.41\%$ is finer than $JK2_{bottom}/ZP_{top}$, which exhibited an efficiency of 5.24%. In mixed cosensitization, JK2 + ZPS or JK2 + ZP exhibited efficiency 4.27 or 3.51%, respectively; these efficiency values are lesser than JK2 dye alone ($\eta = 4.74\%$) but for spatially separated cosensitization the efficiency values are superior to the individual single dye alone.

Three Zn(II)-porphyrin sensitizers, denoted as HP, EHOP and HOP (Figure 2.6), were based on additional hexyl (H), ethylhexyloxy (EHO,) and hexyloxy (HO) groups in the diphenylamine substituted Zn(II)-porphyrin position opposite to the anchoring cyanoacrylic acid group in work reported by Kang and coworkers in 2013 [51]. PTZ1 (Figure 2.7) used as coadsorbant and developed through the modification of HCA1, was used to prevent π–π stacking of dyes. The highest efficiency among three dyes was observed for HOP (4.7%) and, furthermore, mixed with PTZ1 both J_{SC} and V_{OC} values were enhanced and overall device efficiency increased to 7.6% using the I^-/I_3^- redox couple. Chang and coworkers used cosensitization of ZnP (Figure 2.6) with phenothiazine molecule PT-C6 (Figure 2.7), which has a strong light response in the visible range [52]. A stepwise cosensitization was performed for a

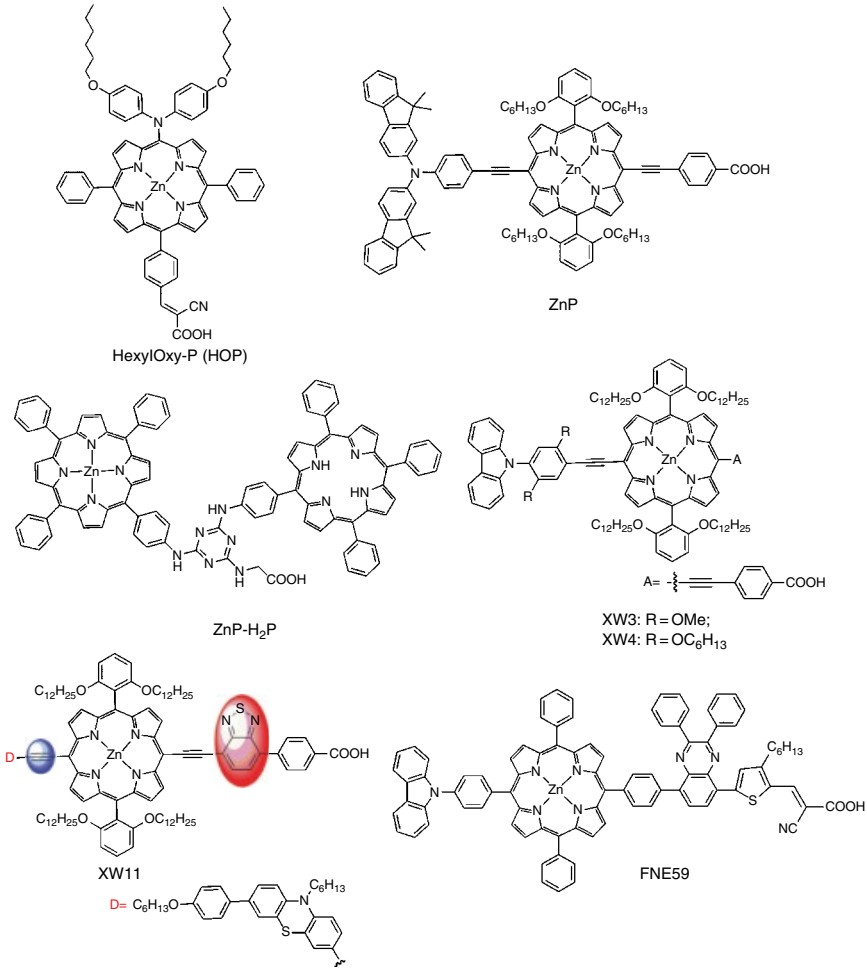

Figure 2.6 Molecular structures of porphyrin sensitizers.

ZnP + PT-C6 device; firstly, the TiO_2 film was soaked in a ZnP solution for 10 h, followed by incubation in PT-C6 solution for 1, 2, 3, 4 and 10 h, respectively. ZnP cosensitization with a 4 h or 10 h incubation in PT-C6 exhibits the highest efficiency (10.10%), with increased J_{SC} values that are finer than individual dyes. The metallated and free-base porphyrin unit ZnP-H_2P (Figure 2.6) is an unsymmetrical porphyrin dyad used for cosensitization with a tertiary arylamine compound (DC); it was reported by Sharma and coworkers [53]. A ZnP-H_2P/DC cosensitized device showed $J_{SC} = 11.72\,mA\,cm^{-2}$, $V_{OC} = 720\,mV$, FF = 73%, and the overall device performance $\eta = 6.16\%$; it was further improved up to 7.68%, by using a formic acid treated TiO_2 photoanode. Both J_{SC} and V_{OC}

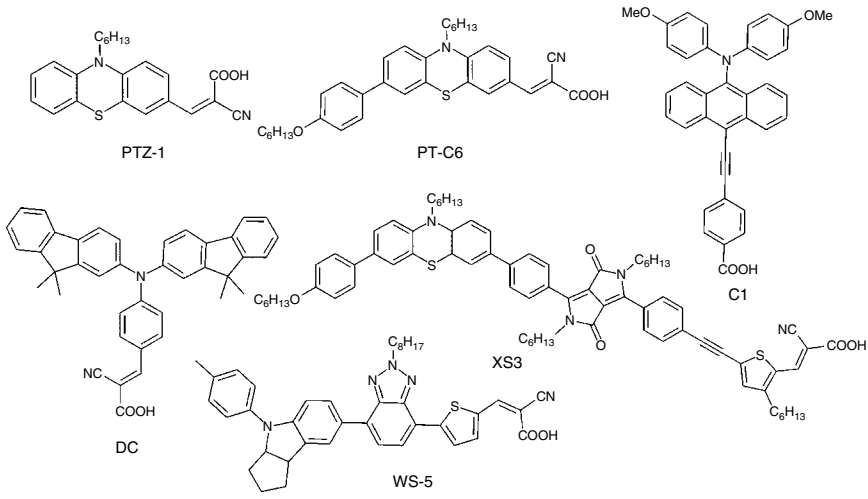

Figure 2.7 Molecular structures of cosensitized organic sensitizers.

values were enhanced and the V_{OC} values are consistent with the electron lifetime. Carbazole donor based zinc porphyrin sensitizer XW4 cosensitized with C1 (Figure 2.7), whose absorption peak lies at approximately $\lambda = 500$ nm, affords the highest efficiency of 10.45%; it was reported by Wang and coworkers [54].

The cosensitization approach results in enhanced J_{SC}, $V_{OC,}$ and efficiencies for solar cells fabricated using porphyrin dyes compared to standard ruthenium dye N719 (9.63%). Further, Sun and coworkers used phenothiazine-based cosensitizer XS3 (Figure 2.7) for XW3 and XW4 dye. The cosensitized devices XS3 + XW3 and XS3 + XW4 exhibited efficiencies of 10.45 and 10.75%, respectively; these values well exceed that of 9.63% obtained for the ruthenium dye N719 [55]. Further, Liu and coworkers reported XW4 dye cosensitization with WS-5 [56]; XW4 + WS-5 showed $J_{SC} = 18.79\ mA\ cm^{-2}$, $V_{OC} = 774$ mV, FF = 72%, and an overall device efficiency of 10.41% [57]. Xie and coworkers synthesized cosensitizers to attain enhanced efficiency by introducing the phenothiazine moiety as the electron donor at the meso-position of the porphyrin core (opposite to the anchoring group) [58]. Compared with XW9, the additional ethynylene bridge and the auxiliary benzothiadiazole group in XW10 and XW11 red-shifted the absorption onset wavelengths and exhibited efficiencies from 8.2 to 8.6 and 7.8%, respectively. Further, these sensitizers used for cosensitization with C1 and WS-5 organic sensitizers and the cosensitized device XW11 + WS-5 ($\eta = 11.5\%$ with $J_{SC} = 20.33\ mA\ cm^{-2}$, $V_{OC} = 760$ mV, FF = 74.4%) showed high efficiencies compared to XW11 + C1 ($\eta = 10.6\%$ with $J_{SC} = 19.52\ mA\ cm^{-2}$, $V_{OC} = 746$ mV, FF = 74%), which are superior to the individual single dyes.

Generally, V_{OC} values of cosensitized solar cells are in between those obtained for the individual dyes. Improvement of V_{OC} values for cosensitized devices was seen for XW11 + C1 and XW11 + WS-5 due to the large V_{OC} of C1 (780 mV) and WS-5 (791 mV). The quasi-solid-state DSSCs cosensitized by FNE57 (or FNE59) with FNE46 on TiO_2 films of thickness 15 μm were reported by Fan and coworkers [59]. The stepwise cosensitization was performed for devices, i.e. firstly immersed in the FNE57 (or FNE59) solution for six hours and then immersed in the FNE46 solution for 12 h [59]. Upon cosensitization, the quasi-solid-state DSSCs based on a FNE59 + FNE46 device showed $\eta = 8.14\%$ with $Jsc = 17.03\ mA\ cm^{-2}$, $V_{OC} = 683$ mV, and fill factor FF = 70%; it has good long-term stability during light soaking.

2.2.1.3 Ruthenium-based Metal Complexes

The main drawback of ruthenium-based sensitizers is the weak absorption in the red region of the visible spectrum; this limits their light harvesting capacity. Greater than 11% efficiency was observed for ruthenium-based N3, black dye, and N719 dyes. Further, device performance was improved simply by combination with another dye absorbing in the range from the red region of visible to near-IR part of the spectrum. In 1999, Zhao and coworkers reported that squarylium cyanine dye Sq3 (Figure 2.8) doped with N3 dye improved the efficiency by 12% relative to that of single N3 dye by extending the visible region from 400 to 800 nm [60]. Ehret and coworkers used di-carboxylated cyanine dyes and showed the photocurrent for a mixture of three dyes (B1G7R4) covering altogether most of the visible light region [61]. Further, *cis*-configured squaraine dye HSQ1 (Figure 2.8) was used for cosensitization with N3 dye by Qin and coworkers [62]. It has high IPCE response in the near-IR region and it is a suitable cosensitizer for DSSCs with high power

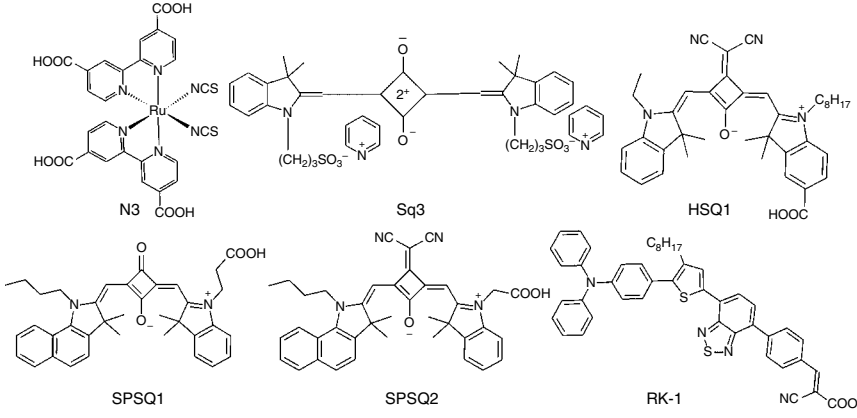

Figure 2.8 Molecular structures of N3 and cosensitized organic sensitizers.

conversion efficiency. HSQ1 showed efficiency around 4.1% and it increased up to 8.14% for a N3 + HSQ1 cosensitized device that exhibited $J_{SC} = 15.76\,mA\,cm^{-2}$, $V_{OC} = 680\,mV$, and FF = 76%, values that well exceed those of N3 and HSQ1 dyes. Both J_{SC} and V_{OC} values are increased upon cosensitization relative to that of individual sensitizers. The IPCE value for the cosensitized cell was 66% at 700 nm, compared to 41% for a cell sensitized by N3 dye alone. Combinations of squaraine-based dyes SPSQ1 or SPSQ2 (Figure 2.8) with N3 dye have been chosen for cosensitization by Hanumantha Rao and coworkers [63]. Cosensitized devices based on SPSQ1 + N3 and SPSQ2 + N3 showed enhanced IPCE spectra covering the spectral region from 350 to 800 nm, which led to the highest J_{SC} when compared to individual organic dyes (SPSQ1 and SPSQ2) [63]. The PCE of 7.20% for SPSQ1 + N3 and 8.20% for SPSQ2 + N3 are 42% and 48% increments on the isolated SPSQ1 and SPSQ2 dyes. The highest efficiency of 9.23% observed for ruthenium complex N3 dye was cosensitized with organic dye RK-1 [64] (Figure 2.8). The PCE of the cosensitized device is significantly enhanced compared to that of individual dyes N3 (6.10%) or RK-1 (5.82%) with both the J_{SC} and V_{OC} values improved.

Ruthenium-based black dye (BD or N749) is one of the most efficient sensitizers and is used for cosensitization to further improve the efficiency. Layered cosensitization of black dye in dye-bilayer (TiO_2/BD/NK3075) [65] (Figure 2.9) or dye-triple layer (TiO_2/P5/N719/N749) [66] (Figure 2.10) was used to improve the device efficiency and these values well exceed that of a

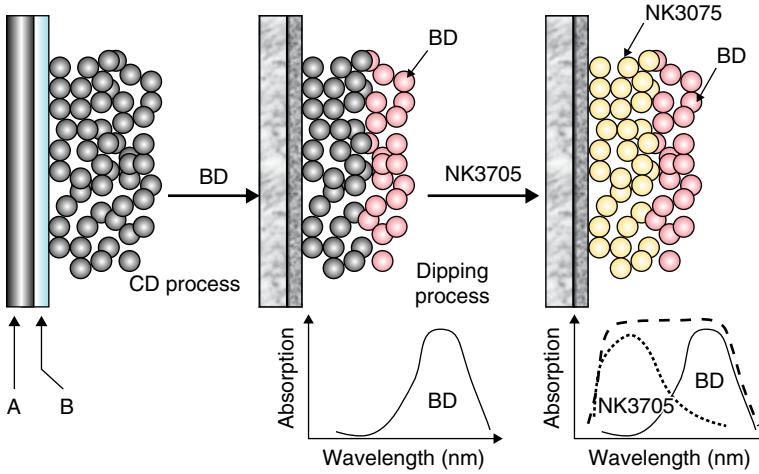

Figure 2.9 The fabrication process of DSC-2-TiO and image of light-harvesting with a wide range of wavelength. A: glass; B: F-doped SnO_2; BD: black dye and CD process: pressurized CO_2 condition [65]. Reproduced with permission of AIP Publishing.

solar cell sensitized by a monolayer dye; however, the PCE of these devices are less than 10%.

Furthermore, a successful cosensitization was reported by Ogura and coworkers using different adsorption sites of BD and D131 dyes on a TiO_2 surface [67]. There was no competition between the adsorption of dye molecules on the TiO_2 surface for mixed dye solution; as well D131 act as coadsorbant and improves the BD dispersion on TiO_2. Both J_{SC} and V_{OC} values were increased for the multiple dye system and the overall device efficiency was 11%. Later, a significant improvement was observed in the conversion efficiency of a cosensitized BD + D131 device, from 11.08 to 11.33% and 11.57%, with the use of deoxycholic acid (DCA) as coadsorbant (Figure 2.11) and use of DCA with an antireflection film and a black mask, respectively [68]. The V_{OC} value was enhanced for a device with DCA as coadsorbant due to decreased dye loading on the TiO_2 surface, which suppresses black dye aggregation and prevenst the backward electron transfer from the conduction band of TiO_2. A small coadsorbant Y1 (Figure 2.11) molecule that has intense absorption maxima between 350 and 400 nm forms a compact monolayer on the bare TiO_2 surface with BD [69]. The combination of a BD + Y1 device exhibited efficiency around 11.28% with an increment of J_{SC} and V_{OC} values corresponding to the IPCE spectra and effectively suppress the recombination of electrons in the TiO_2 film with I_3^-. The highest certified conversion efficiency of 11.4% was obtained with the use of a black metal mask.

Akhtaruzzaman and coworkers reported that the simple indoline-based organic dye (D-1) cosensitized with the black dye (BD + D-1) showed an efficiency of about 9.80%, which is superior to that of a solar cell sensitized by a

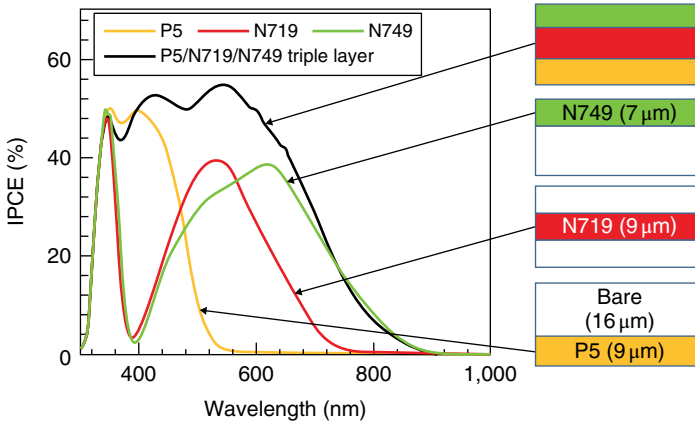

Figure 2.10 IPCE spectrum of the selectively positioned three-dye-sensitized solar cell and those of the single-dye cell with P5 on the bottom, N719 in the middle, and N749 on the top of the TiO_2 film [66]. Reproduced with permission of Nature Publishing Group.

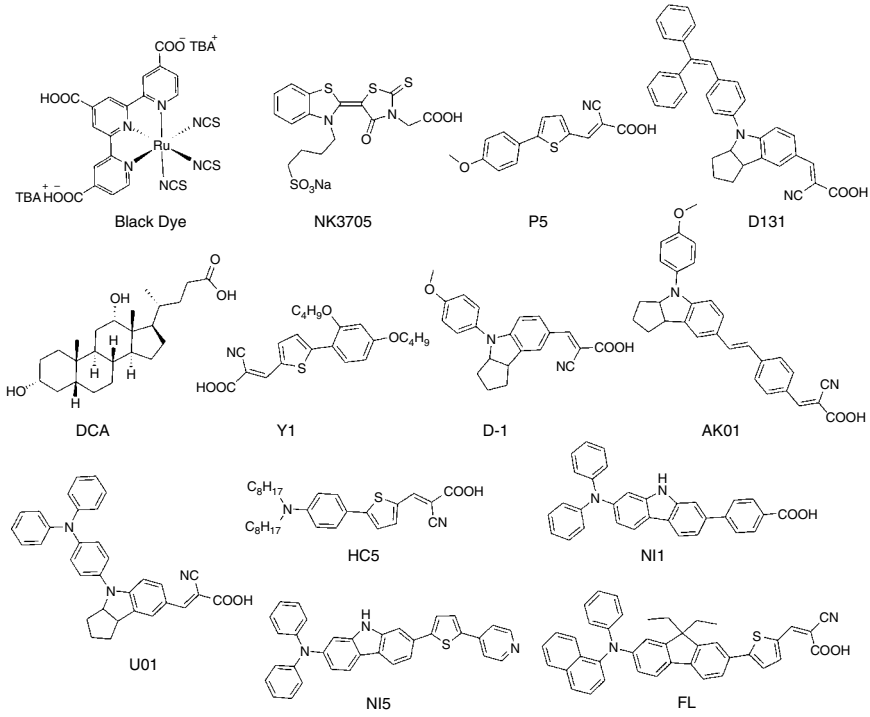

Figure 2.11 Molecular structures of black dye and cosensitized organic sensitizers.

single dye [70]. The addition of D-1 sensitizer enhanced the IPCE in the wavelength range 350–600 nm and enhanced the overall device performance. Other indoline-based sensitizers AK01 and U01 (Figure 2.11) cosensitized with black dye enhanced the efficiency from 9.8 to 10.21% and 10.56%, respectively [71]. Both J_{SC} and V_{OC} values were enhanced for a BD + U01 device compared to those of BD + D-1 device, which correspond to IPCE spectra and electron lifetime, respectively. The BD + HC5 cosensitized device system improves the efficiency from 11.2 to 11.6% using an antireflection film, as reported by Zhang and coworkers [72]. With respect to the cell using BD alone, J_{SC} was improved to 8.5%, efficiency was improved to 12% in a BD + HC5 cosensitized device, and the V_{OC} values are also slightly increased. The site-selective adsorption behavior of two different dyes on TiO_2 film without competitive adsorption for the cosensitized system was reported by Shibayama and coworkers [73]. Stepwise cosensitization was performed for the DSSC to avoid a ligand substitution reaction between the NCS ligands of the adsorbed black dye and the pyridine-anchor units of NI5 (Figure 2.11). Cosensitization of BD with a pyridine anchor dye (NI5) enhanced the J_{SC} values, with the improvement of 10% relative to that of black dye, and the overall device efficiency was 10% superior due to

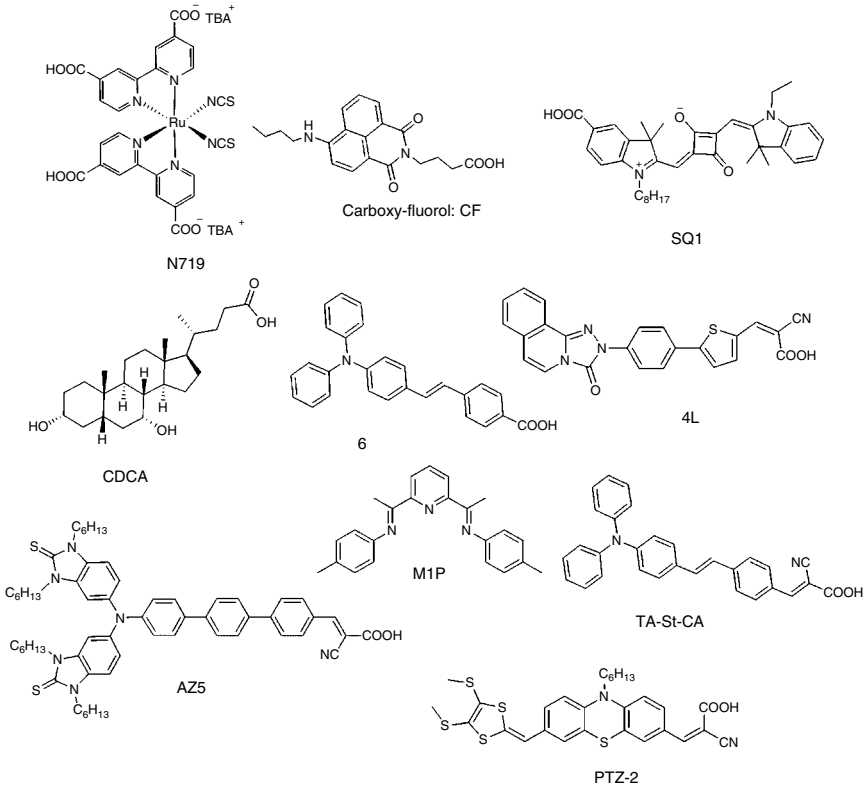

Figure 2.12 Molecular structures of N719 and cosensitized organic sensitizers.

cosensitization of the carboxyl anchor unit of NI1 (Figure 2.11) with BD ($\eta = 8.8\%$). A quasi-solid-state cosensitized DSSC based on ruthenium complex BD and PT-C6 organic dye was reported by Chang and coworkers [74]. The highest PCE of 8.0% for the cosensitized device was achieved by firstly dipping the electrode in BD solution for eight hours followed by immersing it in PT-C6 for three hours. Lee and coworkers [75] reported stepwise cosensitization of BD or N719 with organic dye FL for plastic DSSCs. The conversion efficiencies of cosensitized devices for plastic DSSCs with BD/FL and N719/FL are found to be 3.78 and 5.10%, respectively, which are higher than those of cell sensitized with a single dye.

The efficiency observed for ruthenium-based N719 dye was 11.18%; to further improve the PCE, cosensitization was applied with different organic dyes to achieve panchromatic absorption spectrum. To the best of our knowledge, the first cosensitization of N719 with an organic dye carboxy-fluorol (CF) (Figure 2.12) was reported by Siegers and coworkers in 2008. The cosensitized N719 + CF

device showed a similar J_{SC} value and a slightly decreased V_{OC} value, leading to a lower device efficiency compared to the solar cell sensitized by N719 single dye alone [76]. A similar observation for N719 cosensitization with SDA1570 was reported by Colonna and coworkers [77]. The cosensitized device was first saturated with N719 and then dipped into SDA1570 solution for 15 minutes. It exhibited 4.3% efficiency with decreased J_{SC} and V_{OC} values due to intermolecular interactions between SDA and N719; these values are lower than those of cell sensitized by the saturated N719 dye alone ($\eta = 5.2\%$). A successful cosensitization was reported by Holliman and coworkers using a fast dyeing method [78]. The cosensitization of N719 with SQ1-CDCA dye exhibited an efficiency of about 7.9%, which exceeded that of cell sensitized by N719 ($\eta = 6.4\%$) or SQ1-CDCA ($\eta = 2.9\%$) using "passive" dyeing techniques. The fast dyed cosensitization of N719 with triarylamine dye (6) (Figure 2.12) showed superior efficiency to a cell sensitized by a single dye, either by a passive or fast dyed method [79]. The triazole isoquinoline-based organic dye (4L) (Figure 2.12) has absorption in the blue part of the visible region when it is cosensitized with N719; this results in an increased IPCE in the region between 350 and 500 nm. The overall device efficiency of 8.83% was observed for a cosensitized device with the increment of J_{SC} and V_{OC} values [80].

Wu and coworkers reported that cosensitization with cyclic thiourea functionalized organic dye AZ5 (Figure 2.12) resulted in an improved power conversion efficiency (PCE) of 7.91% in comparison with that of N719 (PCE = 7.28%) sensitized alone [81]. Both J_{SC} and V_{OC} values increased upon cosensitization and intensive absorption in the ultraviolet region. AZ5 could compensate the loss of light harvest induced by triiodide, thereby improving the IPCE spectrum of cosensitized (N719 + AZ5) DSSC. Wei and coworkers studied different numbers and positions of methyl groups on their phenyl rings (M1*o*, M1*p* and M2) employed as cosensitizers for DSSC [82]. The more methyl groups in the cosensitizers (M0-M2) improve the J_{SC} value from 13.09 to 16.53 mA cm^{-2}, with the position of the methyl group playing a decisive role in the power conversion efficiency. The highest efficiency shown by methyl groups at the *para*-position of the imine group (M1P) (Figure 2.12) cosensitized with N719 sensitizer yielded an overall efficiency of 7.32%, which is 35% higher than that of the device sensitized only by N719 (5.43%). Stepwise cosensitization of N719/TA-St-CA achieved 8.27% overall efficiency, which was higher compared to those solar cells based on either TA-St-CA (4.45%) or N719 (5.78 %) sensitizer [83]. A different anchoring unit of the two dyes sensitized on the TiO_2 surface results in the mono compact layer and large coverage of the TiO_2 surface, thereby enhancing J_{SC} and reducing the back electron recombination with triiodide.

Furthermore, Luo and coworkers reported cosensitization of N719 with PTZ-2 and PTZ-3 by modifying the simple reference dye PTZ-1 [84]. Cosensitized DSSC (PTZ–2 + N719) gave the highest efficiency of 8.12%,

exhibiting an improvement of 16.5% compared to the device sensitized with N719 alone ($\eta = 6.97\%$), with increased J_{SC} values [84]. However, the efficiencies based on ruthenium complex dye N719 involved in cosensitization with different organic dyes gave unsatisfactory results, i.e. efficiency was less than 9%. Saritha and coworkers reported carbazole-based sensitizers CCC and CTC upon cosensitization with N719 dye [85]. Upon cosensitization with N719 dye, a fabricated solar cell with CCC dye showed the highest short circuit current density of 19.33 mA cm^{-2}, open circuit voltage of 0.745 V, and fill factor of 0.473, resulting in the highest power conversion efficiency (PCE) of 8.01%, which is higher than DSSCs based on individual dyes, due to greater incident photon current conversion efficiency and broader visible light absorption. The reason for such higher V_{OC} values is due to the better charge transport properties and the higher molar extinction coefficient values. The PCE of the N719 cosensitized CCC device showed higher performance than a N719 cosensitized CTC device, due to the occupation of planar CCC molecules in the voids between N719 molecules and reduced electron recombination compared to the nonplanar CTC molecule (Figure 2.13). The increased J_{SC} values correspond to enhanced IPCE spectrum for cosensitized devices, which showed higher efficiency than cell sensitized by individually sensitized dye as well as N719 dye alone.

Other ruthenium-based metal complexes were developed to achieve high efficiency and these complexes were subjected to cosensitization with various organic sensitizers to further improve the PCE of the device. Nguyen and coworkers reported a stepwise cosensitization of C106 metal complex (Figure 2.14) with organic dye D131 [86]. A cell sensitized by C106 dye has vacant spaces in

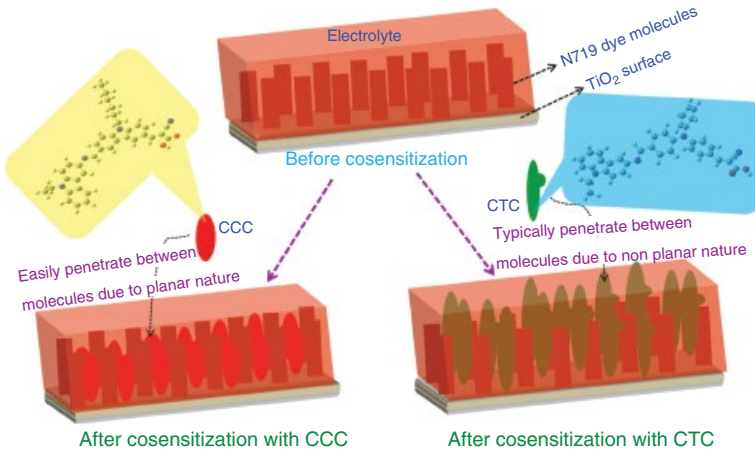

Figure 2.13 Cosensitization of CCC and CTC dye molecules with N719 dye [85]. Reproduced with permission of Elsevier.

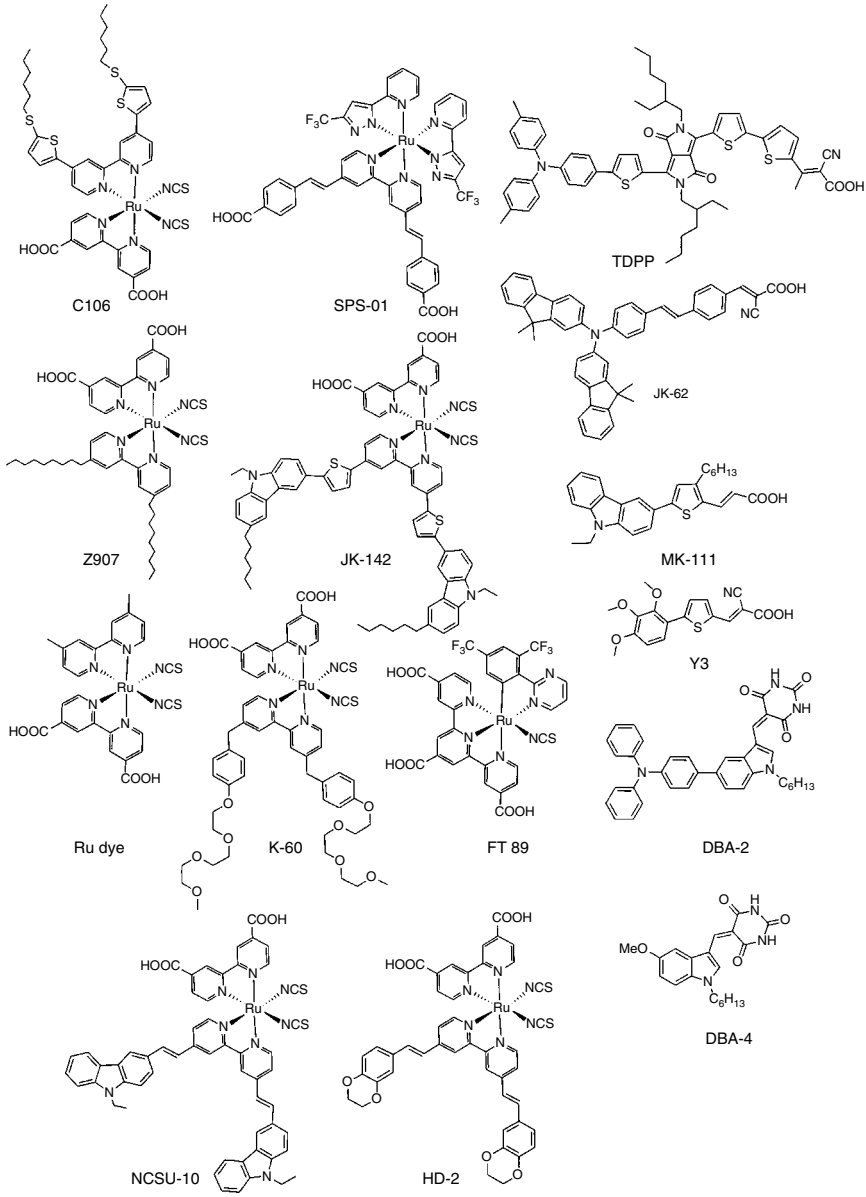

Figure 2.14 Molecular structures of ruthenium and cosensitized organic sensitizers.

between the molecules; when filled by D131 dye molecules, this thereby effectively suppresses the charge recombination. Both J_{SC} and V_{OC} values were improved and, hence, the overall device efficiency was 11.1% for a C106 + D131 cosensitized device, which is higher compared to the fabricated solar cell sensitized with either C106 (9.5%) or D131 (5.6%) alone. A similar phenomenon was observed for a cosensitized SPS-01 + JD1 device [87]. The cosensitized cell showed PCE of 8.30%, which is superior to that of the individual dyes (either SPS-01 or JD1) sensitized on the TiO_2 surface. Further, results are available regarding stepwise cosensitization of SPS-01 and a diketopyrrolopyrrole (DPP)-based TDPP (Figure 2.14) sensitizer [88]. The cosensitized device showed significant improvement in both J_{SC} and V_{OC} and the overall device efficiency was 6.9%, which was further improved up to 8.1% by the addition of DCA as a coadsorbent in the SPS-01 + TDPP dye solution.

A cosensitized cell based on Z907 (Figure 2.14) and NK3705 showed a PCE of 7.1%, which is higher than a cell sensitized by the single dyes Z907 (6.9%) and NK3705 (1.8%) [89]. The PCE of this cosensitized device is lower than a cosensitized cell based on black dye and NK3705 (Table 2.1, entry 25). Fan and coworkers reported cosensitization of ruthenium-based metal complex dye JK-142 and organic dye JK-62 [90]. The large size of the JK-142 sensitizer ineffectively penetrates into the inner surface of the TiO_2 film, which results in a lower PCE for the cell sensitized by the single dye. PCE was increased, with the improvement of J_{SC} and V_{OC} values, by sequential adsorption of JK-142 followed by the small molecular of JK-62. The cosensitized device exhibited an efficiency of 10.2%, which is superior to that of individual dyes as well as standard N719 (8.82%) dye [90]. The higher PCE of the cyclometalated ruthenium complex (FT89) compared to black dye was found upon cosensitization with carbazole-based sensitizers MK-45 and MK-111, respectively. A PCE of 10.2% was marked for a FT89 + MK-111 cosensitized device with DCA coadsorbent, which was further improved to 11.1% with an antireflection film and a mask without DCA coadsorbent [91]. MK-111 was more effective than MK-45 for cosensitization with FT89 due to a structural difference in their anchoring groups. A combination of amphiphilic ruthenium (II) sensitizer dye and Y3 possessing three methoxy groups on the donor moiety improves J_{SC} value and the PCE (6.29%) compared to that of individual ruthenium dye (5.21%) and Y3 (3.30%) [92]. Cosensitization of metal complex K60 and Y1 organic dye showed an efficiency of 8.19% with $J_{SC} = 18.26\ mA\ cm^{-2}$ and $V_{OC} = 650\ mV$, which is higher than the solar cell sensitized with pristine K60 (6.26%) dye [93]. Dickson and coworkers reported cosensitization of ruthenium complex HD-2 with indole-based dye DBA-2 slightly improves the J_{SC} and V_{OC} values and the device efficiency (8.06%); however, it is superior to a cell sensitized by N719 dye under the same conditions [94]. A similar observation was made when using cosensitization of ruthenium complex NCSU-10 with DBA-4, which exhibited a PCE of 10.12% with CDCA coadsorbent [95].

Table 2.1 Photovoltaic properties of metal complexes cosensitized with organic sensitizers.

Entry	Sensitizer	J_{sc} ($mAcm^{-2}$)	V_{oc} (mV)	FF	η (%)	Reference efficiency (η%)	Electrolyte	Ref.
1	JK2/TT1	16.20	666	72	7.74	JK2, 7.08; TT1, 3.52	I_3^-/I^-	35
2	D2/TT1	8.6	643	72.4	4.08	D2, 3.43; TT1, 2.37	I_3^-/I^-	36
3	D102/TT1	9.4	800	60	4.7	D102, 3.9; TT1, 1.1	gel electrolyte	37
4	PcS15/D131 PcS15/D102	15.3 13.9	630 625	64 64	6.2 5.6	PcS15, 5.3	I_3^-/I^-	38
5	YD-2/D-205	12.6	742	73.2	6.9	D-205, 5.7; YD-2, 5.6	I_3^-/I^-	40
6	YD2-o-C8/ Y123	17.66	935	74	12.3	YD2-o-C8, 11.9;	Co(II/III)	43
7	YD2-o-C8/CD4/YDD6	19.28	753	71.9	10.4	YD2-o-C8, 8.8; CD4, 5.8; YDD6, 4.7; CD4/YDD6, 8.2; YD2-oC8/YDD6, 9.6; YD2-oC8/CD4, 9.2	I_3^-/I^-	44
8	DMPZn-C2-COOH/BET	9.40	753	73.6	5.21	DMPZn-C2-COOH, 5.12	I_3^-/I^-	45
9	LD12/BET	14.66	705	72.6	7.50	LD12, 6.6; BET, 0.15	I_3^-/I^-	46

10	LD12/CD5	16.74	736	73.1	9.0	LD12, 7.5; CD5, 5.7	I_3^-/I^-	47
11	LD14/H2LD14 LD14/H2LD14/AN-3	16.71 18.76	698 716	71.2 72.2	8.31 9.72	LD14, 9.25; H_2LD14, 5.62; AN – 3, 4.68	I_3^-/I^-	48
12	LD31/AN – 4	20.27	704	71.8	10.26	LD31, 9.95; AN-4, 4.44	I_3^-/I^-	49
13	JK2\ZPS (sep) JK2\ZP (sep)	13.67 11.36	670 650	70 71	6.41 5.24	ZP, 2.49; ZPS, 4.16; JK2, 4.74	—	50
14	HOP/PTZ1	15.9	678	70.3	7.6	HOP, 4.7	I_3^-/I^-	51
15	ZnP/PT-C6	19.36	735	71.0	10.1	ZnP, 7.4; PT-C6, 8.2	I_3^-/I^-	52
16	ZnP-H_2P/DC	13.45	760	75.0	7.68	ZnP-H_2P, 4.56; DC, 4.06	I_3^-/I^-	53
17	XW4/C1	20.15	736	71.0	10.45	XW4, 7.94; C1, 5.67	Co(II/III)	54
18	XS3/XW3 XS3/XW4	19.89 19.96	720 728	73.0 74.0	10.45 10.75	XS3, 8.02; XW3, 7.32; XW4, 7.94	Co(II/III)	55
19	XW4/WS-5	18.79	774	72.0	10.41	XW4, 6.42; WS-5, 8.64	I_3^-/I^-	57
20	XW11/C1 XW11/WS-5	19.52 20.33	746 760	74.0 74.4	10.6 11.5	XW11, 7.8	I_3^-/I^-	58
21	FNE59/FNE46	17.03	683	70.0	8.14	FNE59, 6.02; FNE46, 6.8	gel electrolyte	59

(*Continued*)

Table 2.1 (Continued)

Entry	Sensitizer	J_{sc} ($mAcm^{-2}$)	V_{oc} (mV)	FF	η (%)	Reference efficiency (η%)	Electrolyte	Ref.
22	N3/HSQ1	15.76	680	76.0	8.14	N3, 6.52; HSQ1, 4.10	I_3^-/I^-	62
23	N3/SPSQ1 N3/SPSQ2	15.60 17.10	635 656	73.0 73.0	7.20 8.20	N3, 7.13	I_3^-/I^-	63
24	N3/RK-1	18.10	888	57.4	9.23	N3, 6.10; RK-1, 5.82	I_3^-/I^-	64
25	BD/NK3075	21.80	600	70.0	9.16	BD, 7.28; NK3705, 1.85	I_3^-/I^-	65
26	P5/N719/N749	10.6	618	72.5	4.8	P5,1.0; N719, 2.6; N749, 3.6	I_3^-/I^-	66
27	BD/D131	22.59	696	70.0	11.0	BD, 10.04; D131, 5.06	I_3^-/I^-	67
28	BD/D131/DCA BD/D131/DCA (anti ref. film)	23.34 23.49	685 683	70.9 72.1	11.33 11.57	BD, 10.0; D131, 4.73	I_3^-/I^-	68
29	BD/Y1	20.88	743	72.7	11.28	BD, 10.70	I_3^-/I^-	69
30	BD/D-1	19.54	703	71.4	9.80	BD, 9.18; D-1, 3.34	I_3^-/I^-	70
31	BD/AK01 BD/U01	20.98 20.44	685 722	71.1 71.5	10.21 10.56	BD, 9.18; AK01, 6.20; U01,6.01	I_3^-/I^-	71
32	BD/HC5 BD/HC5 (A.R.Film)	22.08 22.36	705 710	71.7 72.9	11.2 11.6	BD, 10.3; HC5, 5.3	I_3^-/I^-	72

33	BD/NI5 BD/NI1	20.7 18.3	680 670	71.0 72.0	10.0 8.8	BD, 9.5	I_3^-/I^-	73
34	BD/PT-C6	17.59	645	70.0	8.0	BD, 6.3 PT-C6, 6.5	gel electrolyte	74
35	BD/FL N719/FL	9.77 11.42	650 715	59.5 62.5	3.78 5.10	BD, 2.66; FL, 2.67; N719, 4.89	I_3^-/I^-	75
36	N719/SQ1-CDCA	15.0	820	63.0	7.9	N719,6.4; SQ1-CDCA, 2.9	—	78
37	N719/6	15.45	740	65.0	7.5	N719,5.6 (passive), 6.0 (fast); 6, 1.2 (passive), 2.6 (fast)	I_3^-/I^-	79
38	N719/4L	16.39	770	70.0	8.83	N719, 8.36; 4L, 3.70	I_3^-/I^-	80
39	N719/AZ5	17.9	698	63.3	7.91	N719, 7.28; AZ5, 4.37	I_3^-/I^-	81
40	M1P/N719	16.48	720	59.0	7.00	N719, 5.43	I_3^-/I^-	82
41	N719/TA-St-CA	16.22	680	75.0	8.27	TA-St-CA, 4.45; N719, 5.78	I_3^-/I^-	83
42	N719/PTZ-2	16.37	670	74.0	8.12	PTZ-2, 5.81; N719, 6.97	I_3^-/I^-	84
43	CCC/N719 CTC/N719	19.33 18.75	745 742	47.3 41.0	8.01 6.71	CCC, 3.12; CTC, 2.63; N719, 6.6	I_3^-/I^-	85
44	C106/D131	20.6	766	70.0	11.1	C106, 9.5; D131, 5.6	—	86]

(*Continued*)

Table 2.1 (Continued)

Entry	Sensitizer	J_{sc} ($mAcm^{-2}$)	V_{oc} (mV)	FF	η (%)	Reference efficiency (η%)	Electrolyte	Ref.
45	SPS-01/JD1	15.28	720	76.0	8.30	SPS-01, 5.98; JD1, 4.76	I_3^-/I^-	87]
46	SPS-01/TDPP SPS-01/TDPP/ DCA	13.7 15.2	700 720	72.0 74.0	6.9 8.1	SPS-01, 5.47 TDPP, 4.82	I_3^-/I^-	88
47	Z907/NK3705	15.68	700	64.0	7.1	Z907, 6.9; NK3705, 1.8	I_3^-/I^-	89
48	JK-142/JK-62	18.61	740	74.0	10.20	N719, 8.82; JK-142, 7.28; JK-62, 5.36.	I_3^-/I^-	90
49	FT89/MK-111/DCA FT89/ MK-111	21.2 22.4	710 710	68.0 69.0	10.2 11.1	FT89, 9.1; MK-111, 3.4	I_3^-/I^-	91
50	Ru dye/Y3	14.32	602	73.0	6.29	Ru dye, 5.21; Y3, 3.30	I_3^-/I^-	92
51	K60/Y1	18.26	650	69.0	8.19	K60, 6.26	I_3^-/I^-	93
52	HD-2/DBA-2	16.54	732	66.5	8.06	HD-2, 7.61; DBA-2, 1.01	I_3^-/I^-	94
53	NCSU-10/DBA-4/CDCA	22.69	715	62.4	10.12	NCSU-10, 8.84	I_3^-/I^-	95

2.2.2 Cosensitization of Organic–Organic Dyes

Organic sensitizers are promising potential candidates for DSSC applications due to high molar extinction coefficients, because they can be prepared and purified more easily, and they are cost effect compared to Ru(II) polypyridyl complexes. But, the major drawback of organic sensitizers is sharp and narrow absorption characteristics that limit the light harvesting capacity. Unfortunately, there is no single sensitizer with strong absorption covering a spectral region from visible to near-IR; hence, the cosensitization strategy was applied by mixing two or more dyes that have different absorption wavelengths to broaden the absorption spectrum (Table 2.2). Less of the dye is required to sensitize a TiO_2 film due to the high molar extinction coefficient of organic sensitizers and, thereby, the combined dyes exhibit complementary absorption spectra. Several groups have been examined; a combination of blue and red absorbing sensitizers facilitates panchromatic sensitization of DSSCs. Sayama and coworkers [96] reported sensitization of TiO_2 film with cyanine and merocyanine organic dyes having short anchoring groups to show enhanced efficiency. Cells sensitized with such dyes were found to adsorb simultaneously and, in addition, attained improved J_{SC} (11.5 mA cm^{-2}) and efficiency (3.10%) compared to cells sensitized with single dye. Guo and coworkers reported that cell sensitized with a mixture of pentamethylcyanine derivative (A) and trimethylcyanine derivative (B), with the volume ratio of 1:3 (A:B), generated the highest photoelectric conversion yield of 3.4% [97].

Chen and coworkers explored solar cells fabricated with three dyes Y, R, and B (Figure 2.15) with different absorbance maxima (380, 535, and 642 nm), leading to an efficient light harvesting over a wide spectrum covering the whole visible region and part of near-IR. The highest efficiency observed was 6.5% for cell sensitized with three kind of dyes [98]. The cosensitization of dye absorbing light in the blue part of the visible spectrum (JK2) and red/near-IR absorption of SQ1 (Figure 2.15) was reported by Yum and coworkers [99]. The cosensitized device showed a promising conversion efficiency of 7.43% for a mixed solution; this is higher than sequential adsorption of cosensitizers SQ1 and JK2 (7.38%) as well as cells sensitized by the individual dyes JK2 (7.00%) and SQ1 (4.23%). Complementary absorption of these two dyes results in a higher and broader IPCE spectrum for the cosensitized device, which, in turn, improved the J_{SC} value and the overall device efficiency [99]. Clifford and coworkers reported the novel cosensitization strategy, i.e. cosensitization of primary and secondary dye was distinct by deposition of secondary metal oxide (Al_2O_3) whose cell architecture was TiO_2/Dye1/Al_2O_3/Dye2 [100]. This strategy was further used for cell sensitized with JK2 and SQ1 and the cell architecture TiO_2/JK2/Al_2O_3/SQ1 was developed by Choi and coworkers [101]. The stepwise cosensitized JK2/Al_2O_3/SQ1 device showed J_{SC} and efficiency (η) of 17.6 mA cm^{-2} and 8.65%, respectively, which is higher than the cell based on cocktail cosensitization of JK2 and

Table 2.2 Photovoltaic properties of organic–organic sensitizer cosensitization.

Entry	Sensitizer	J_{sc} ($mAcm^{-2}$)	V_{oc} (mV}	FF	η (%)	Reference efficiency (η)	Electrolyte	Ref
1	Cy0/Cy1/SQ	11.5	470	57	3.1	Cy0, 0.8; Cy1, 2.3; SQ, 2.4	I_3^-/I^-	96
2	A1/B3	15.8	520	47	3.4	A, 1.3; B, 2.9	I_3^-/I^-	97
3	Y/R/B	15.8	525	63	6.5	Y, 2.8; R, 4.6; B, 3.9	I_3^-/I^-	98
4	JK2/SQ1 (seqential) JK2/SQ1(mixed)	16.1 15.5	655 685	70 70	7.38 7.43	JK2, 7.0; SQ1, 4.23	I_3^-/I^-	99
5	JK2/SQ1 JK2/Al_2O_3/SQ1	16.9 17.6	662 696	71 70	8.01 8.65	JK2, 7.48; SQ1, 4.02	I_3^-/I^-	101
6	SQ1/JK2	13.62	665	70.8	6.41	JK2, 6.02; SQ1, 3.78	ionic liq. electrolyte	102
7	A3/B1	15.18	444	45	3.0	A, 2.42; B, 1.56	I_3^-/I^-	103
8	NKX2677/HC-Acid	18.01	663	76.16	9.09	NKX2677, 6.59; HC-Acid, 1.21	I_3^-/I^-	104
9	BP-2/SQ2	21.33	660	58	8.14	BP-2, 5.95; SQ2, 3.78	I_3^-/I^-	105
10	CMR103/CM203/HY113	20.1	597	68.3	8.2	CMR103, 3.1; CM203, 5.0; HY113, 4.4	I_3^-/I^-	106
11	JD1/SQ2	15.13	640	66	6.36	JD1, 5.44; SQ2, 4.11	I_3^-/I^-	107
12	SQ2/5c	17.76	610	57	6.24	—	I_3^-/I^-	108
13	JD10/D35	18.0	653	67	7.9	JD10, 7.30	I_3^-/I^-	109

14	Y1/HSQ5	8.36	629	69.5	3.66	Y1, 2.16; HSQ5, 2.30	I_3^-/I^-	110
15	T4BTD-A /HSQ3 T4BTD-A /HSQ4	17.21 18.09	611 588	67 73	7.05 7.77	T4BTD-A, 6.38; HSQ3, 4.81; HSQ4, 5.78	I_3^-/I^-	111
16	D131/SQ2(cocktail) D131/ SQ2 (layered)	8.78 9.73	600 650	62 65	3.3 4.1	D131, 3.4; SQ2, 2.7	I_3^-/I^-	112
17	XS41/TC2	16.1	770	66	8.18	XS41, 6.73; TC2, 5.19	I_3^-/I^-	113
18	WS-26/S1	18.25	731	71	9.72	WS-26, 8.61	I_3^-/I^-	114
19	IQ21/S2	19.8	731	72	10.4	IQ21, 9.0	I_3^-/I^-	115
20	WS-1/VG1-C8 WS-1/HSQ4	17.73 18.71	701 657	72 71	9.0 8.7	VG1-C8, 3.5; WS-1, 6.3; HSQ4, 5.0	I_3^-/I^-	116
21	WS-39/WS-2	18.25	731	71	9.48	WS-39, 8.67; WS-2, 8.48	I_3^-/I^-	117
22	TA-St-CA/D TA-St-CA/D/DCA	12.40 12.96	660 730	76 76	6.26 7.19	TA-St-CA, 4.98, D, 4.22	I_3^-/I^-	118
23	C258/C239 C259/C239	18.28 17.85	856 891	71.5 72.2	11.2 11.5	C258, 8.9	Co(bpy)	119
24	FNE46/FNE53	18.12	634	70	8	FNE46, 7.03; FNE53, 5.19	I_3^-/I^-	120
25	WS64 /S2	14.9	738	72	7.9	WS64, 5.6; S2, 6.3	I_3^-/I^-	121
26	TP3/YR6	19.18	721	71.2	9.84	TP3, 8.0; YR6, 2.16	I_3^-/I^-	122

(*Continued*)

Table 2.2 (Continued)

Entry	Sensitizer	J_{SC} ($mAcm^{-2}$)	V_{OC} (mV}	FF	η (%)	Reference efficiency (η)	Electrolyte	Ref
27	LI-102/SQ2	16.62	714	63	7.44	LI-102, 5.98 SQ2, 4.28	I_3^-/I^-	123
28	ADEKA-1/SFD-5.	16.0	>1000	—	12.8	ADEKA-1, 12.5	Co(II/III)	124
29	ADEKA-1/ LEG4	17.77	1018	76.6	13.8	ADEKA-1, 12.5	Co(II/III)	125
	ADEKA-1/ LEG4 (GNP counter electrode)	18.27	1014	77.1	14.3			

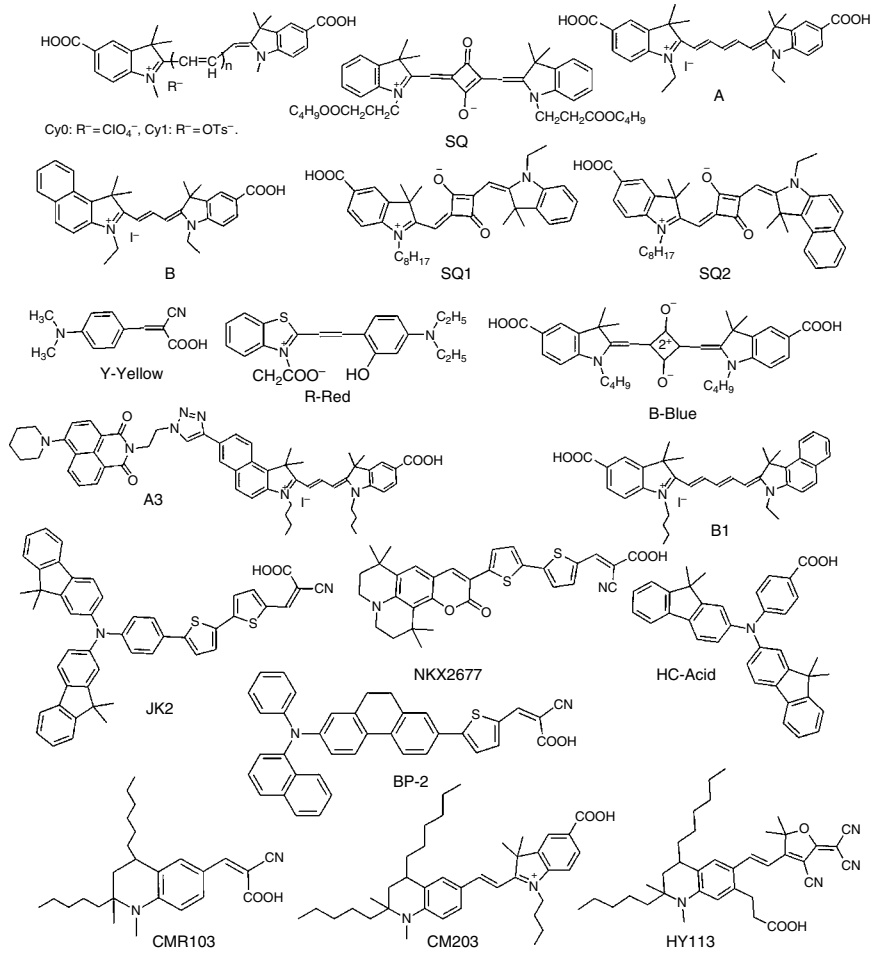

Figure 2.15 Molecular structures of cosensitized organic dyes.

SQ1 [101]. This improvement was observed due to retardation of the interfacial recombination dynamics. Kuang and coworkers also reported the cosensitization of organic dyes JK2 and SQ1 for efficient ionic liquid electrolyte based DSSCs [102]. Cosensitization of TiO_2 films was first carried by dipping for four hours in the SQ1 dye solution and then by dipping for two hours in the JK2 dye solution; this resulted in a PCE of 6.41%, which is superior to individually sensitized JK2 (6.02%) and SQ1 (3.78%) dyes.

Wu and coworkers reported that the trimethine cyanine dye (A3) and a near-IR absorbing pentamethine cyanine dye (B1) (Figure 2.15) were employed to cosensitize a solar cell over the entire visible spectrum and the solar-cell

performance was improved to 3.0% in the volume ratio 3:1 for A3:B1 when compared to individually sensitized dye on TiO_2 film [103]. A successful PCE of 9.09% was achieved by NKX2677 organic dye coadsorbed by Y-shaped triarylamine HC-Acid (J_{SC} = 18.01 mA cm^{-2}, V_{OC} = 663 mV, and FF = 76.16%); these values well exceed that of individual NKX2677 and HC-Acid dyes. The overall conversion efficiency (η) of 38% occurred in comparison to the NKX2677-based solar cell [104]. HC-Acid caused the breakup of π-stacked aggregates, which reduced the recombination process at the TiO_2 surface and improved the J_{SC} and V_{OC} values. Lin and coworkers reported that the cosensitization of organic dye containing 9,10-dihydrophenanthrene unit in the spacer (BP-2) and SQ2 is 8:2 (v/v), yielding a high efficiency of 8.14% as compared to individually sensitized cell [105]. Cheng and coworkers synthesized novel cyanine dyes CM201-CM204, in which a tetrahydroquinoline derivative is used as an electron donor, and the CM203 was also applied to cosensitize with other two organic dyes, CMR103 and HY113. CMR103 and HY113 have strong absorption in the range 400–500 nm and intense absorption in the near-IR region (600–700 nm), respectively, and the cell sensitized by three dyes showed broad absorption in the range of 400–700 nm. For such a cosensitized device, the TiO_2 film was firstly dipped in the CMR103 dye solution (0.5 h), then dipped in the CM203 dye solution (0.5 h), followed by dipping in the HY113 dye solution (4 h), resulting in a PCE of 8.2% [106].

Furthermore, cosensitization of squaraine dye (SQ2) and a diarylaminofluorene-based organic dye (JD1); SQ2 dye has high molar extinction coefficient values and absorption maximum at 662 nm, which affords complementary spectral characteristics for JD1 dye [107] (Figure 2.16). A wide absorption wavelength (400–750 nm) for the cosensitized device JD1 + SQ2 at the molar ratio of 6:4 showed a PCE of 6.36%, which is much higher than those of the cells sensitized with individual dyes absorbing narrow wavelength of light, i.e. η of 5.44% and 4.11% for the DSSC sensitized with JD1 and SQ2 dyes, respectively. Chang and coworkers used SQ2 cosensitization with pyrenoimidazole-based dye (5C) (Figure 2.16), which has absorption maximum at 464 nm, thereby producing panchromatic sensitization in the 400–750 nm region for the molar ratio of 4:6 (SQ2:5C) and the observed PCE was 6.24% [108]. Delcamp and coworkers utilized another squaraine-based dye (JD10) for cosensitization with metal-free organic dye D35 [109]. The PCE of 7.3% attained for JD10 dye alone sensitized on TiO_2 film is further improved to 7.9% when cosensitized with D35 in a 1:1 molar ratio with improved J_{SC} and V_{OC} values. Zhang and coworkers reported that the cocktail cosensitization of Y1 and HSQ5 (Figure 2.16) in 1:1 molar ratio showed two strong absorption peaks around 400 and 700 nm; these are attributed to Y1 and HSQ5 dyes, respectively[111]. The IPCE of such a cocktail cell (Y1/HSQ5) covers a fairly broad absorption region up to 770 nm, which corresponds to the larger J_{SC} of the cocktail cell (8.36 mA cm^{-2}) compared to those of the Y1 (4.67 mA cm^{-2}) and HSQ5

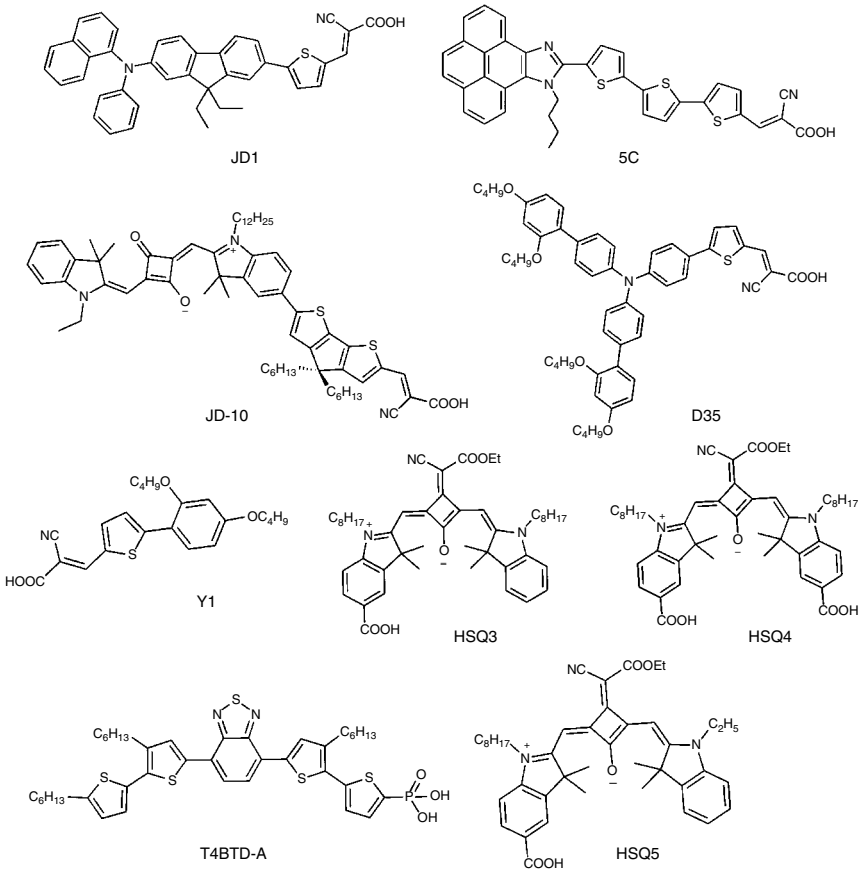

Figure 2.16 Molecular structures of the JD1, 5C, JD-10, D35, Y1, HSQ3, HSQ4, T4BTD-A, and HSQ5 organic dyes.

(5.47 mA cm^{-2}) single-dye cells. The overall Y1/HSQ5 device efficiency was 3.66%, which is significantly higher than the efficiencies of Y1 (2.16%) and HSQ5 (2.30%) single-dye cells. Other *cis*-configured squaraine rings HSQ3 or HSQ4 organic dyes cosensitized by oligothienylene dye containing benzothiadiazole (T4BTD-A) dye (Figure 2.16) shows improved J_{SC} and V_{OC} values; these are attributed to complementary absorption spectra and suppression of charge recombination of the injected electrons, respectively. The improved PCE of 7.0% for T4BTD-A + HSQ3 and 7.7% for T4BTD-A + HSQ4 are superior to DSSCs sensitized with the individual dyes [111].

Xue and coworkers [112] reported cosensitized plastic DSSCs using D131 (Figure 2.17) and SQ2 dyes. D131 exhibits an absorption maximum at 430 nm while SQ2 has absorption maxima at 610 nm and 670 nm on TiO_2 film. Both

cocktail cosensitization and layered cosensitization (using multiple electrophoretic deposition, EPD) were studied and a PCE of 4.1% achieved for layered cosensitization of D131 and SQ2, which is higher than that of cocktail cosensitization as well as cell sensitized with individual dyes D131 and SQ2 [112]. Li and coworkers [113] used indoline-based organic dyes XS41-XS44, which can notably retard the charge recombination at the titania/electrolyte interface. These dyes were coadsorbed with TC1 and TC2 organic dyes and results of XS41, upon co-adsorption with TC2, produce higher J_{SC} (16.1 mA cm^{-2}), V_{OC} (770 mV), and fill factor (0.66), corresponding to a PCE of 8.18% [113]. Further, another indoline-based dye WS-26 (Figure 2.17), cosensitized with metal-free

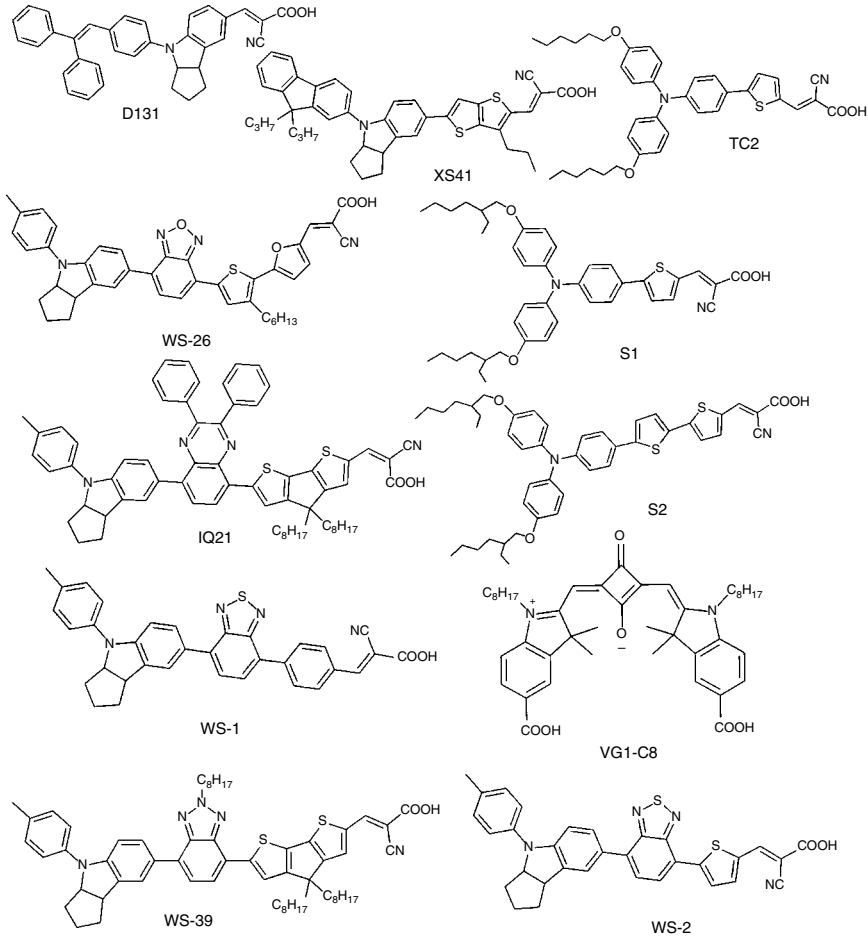

Figure 2.17 Molecular structures of the D131, XS41, TC2, WS-26, S1, IQ21, S2, WS-1, VG1-C8, WS-39, and WS-2 organic dyes.

organic dye S1 by immersing a TiO_2 film in the solution of WS-26 for 12 h and then in S1 for one hour results better performance. That is, the cosensitized WS-26/S1 improves the photovoltaic efficiency from 8.61 to 9.72%, with $J_{SC} = 19.84\,mA\,cm^{-2}$, $V_{OC} = 694\,mV$, and FF = 0.706 [114]. Pei and coworkers reported that cosensitization of indoline-based IQ21 dye with S2 dye (i.e. S2 dye has an additional thiophene unit compared to the S1 dye) (Figure 2.17) exhibited a PCE of 10.41% ($J_{SC} = 19.8\,mA\,cm^{-2}$, $V_{OC} = 731\,mV$, FF = 0.72), which is superior to a cell sensitized with single dye IQ21 (9.0%) with improved J_{SC} value [115]. Zhang and coworkers used indoline dye WS-1 cosensitized with squaraine dyes VG1-C8 or HSQ4. For cosensitization, the TiO_2 electrodes were first immersed in a dye bath of WS-1 for two hours, followed by immersion in dye solution containing VG1-C8 (Figure 2.17) or HSQ4 (Figure 2.16) at different time intervals. Incorporating an electron-withdrawing group in HSQ4 efficiently broadens the IPCE action spectra and increases the photocurrent compared to VG1-C8 cosensitization with WS-1 [116]. But the V_{OC} value of the cosensitized device WS-1 + HSQ4 was low compared to the cosensitized device WS-1 + VG1-C8; the PCE of 8.7% for WS-1 + HSQ4 and 9.0% for WS-1 + VG1-C8 are much higher than those for individually sensitized WS-1(6.3%), HSQ4 (5.0%), and VG1-C8 (3.5%) dyes. Further, the high J_{SC} value of WS-2 dye and high V_{OC} value of WS-39 dyes were involved in cosensitization, as reported by Liu and coworkers [117]. For such a cosensitized device, the cell is sensitized first with high V_{OC} value WS-39 then WS-2 improves the PCE of 9.48% [117].

Sharma and coworkers reported cosensitization of two metal-free organic dyes, TA-St-CA (Figure 2.18) and D, which results in complementary absorption bands in the visible and near infrared regions, and, in addition, showed an improved PCE of 6.26% compared to DSSCs based on individual dyes TA-St-CA (4.98%) or D (4.22%). Furthermore, the PCE was improved to 7.19% by using DCA coadsorbent [118]. Triphenylamine-based organic dye C258 or C259 cosensitized with metal-free organic dye C239 (Figure 2.18) showed the highest PCE of 11.2 and 11.5%, respectively [119] under $100\,mW\,cm^{-2}$ light illumination in the presence of (Co-bpy) redox couple. The PCE of 8.9% for C258 individually sensitized dye was improved to 11.2% when cosensitized with C239 dye, with an 8% increment in J_{SC} value. Lu and coworkers [120] reported near-infrared organic sensitizers FNE53 and FNE46 used as cosensitizers for metal-free cocktail-type quasi-solid-state DSSCs. The sensitizer FNE53 not only extends the photoresponse range but also suppresses the intermolecular interactions and gives overall efficiency of 8.04% with photovoltaic parameters $J_{SC} = 18.12\,mA\,cm^{-2}$, $V_{OC} = 634\,mV$, and FF = 0.70 for a quasi-solid-state DSSC cosensitized with FNE46 and FNE53. Triphenylamine-based dyes S0-S2 have different lengths of π-bridge have been developed as cosensitizers for WS62 and WS64 dye, as investigated by Li and coworkers [121]. The promising efficiency of 7.9% by the cosensitization of WS64 and S2 shows $J_{SC} = 14.9\,mA\,cm^{-2}$,

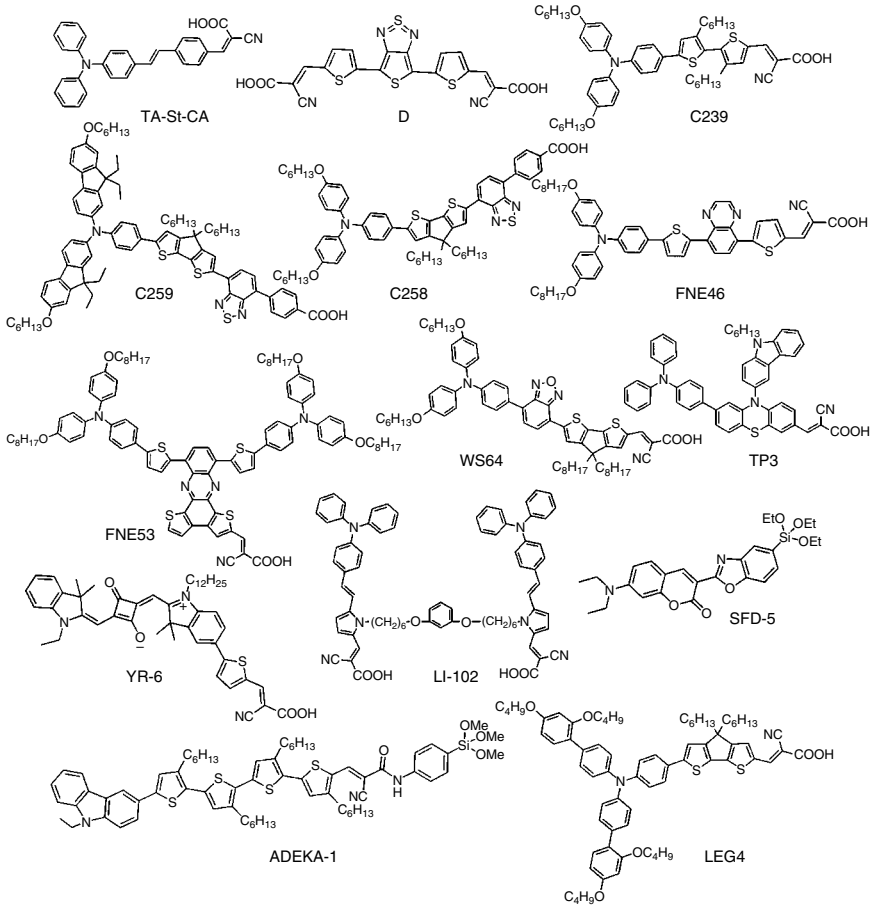

Figure 2.18 Molecular structures of the TA-St-CA, D, C239, C259, C258, FNE46, FNE53, WS64, TP3, YR-6, LI-102, SFD-5, ADEKA-1, and LEG4 organic dyes.

V_{OC} = 738 mV, and FF = 0.72, which is 41% higher than the individually sensitized WS64 dye. Phenothiazine-cored 3D bulky organic sensitizer TP3 was cosensitized with a near-infrared-absorbing squaraine dye YR6 to suppress the dye aggregation and retarded the charge recombination in DSSCs. The highest PCE of 9.84% was achieved at the TP3/YR6 (Figure 2.18) molar ratio of 25:1, which exhibited remarkable efficiency enhancement of 33% compared with the device solely based on TP3 dye [122]. Fang and coworkers synthesized H-type organic dyes LI-101, LI-102, and LI-103 and used these for cosensitization with SQ2. Among the three dyes, *meta*-linkage model LI-102 cosensitized with SQ2 showed the best photovoltaic performance of 7.44%, much higher than SQ2

itself (4.28%) and LI-102 (5.98%) [123]. Kakiage and coworkers reported cosensitization of organic silyl-anchor dyes using carbazole (ADEKA-1) and coumarin dyes (SFD-5) (Figure 2.18) with organosilicon tethers [124]. The ADEKA-1-sensitized solar cell exhibited the highest η of 12.5%, which is further improved to 12.8% while cosensitize with SFD-5 using cobalt (III/II) complex electrolyte [124]. Moreover, the same group reported that ADEKA-1 (Figure 2.18) cosensitized with LEG4 (Figure 2.18), gave a PCE of 13.5%, which is further improved to 14.3% with the optimized cobalt (III/II) complex redox electrolyte solution and the GNP (graphene nanoplatelets) counterelectrode [125]. This is highest efficiency among all cosensitized and individually sensitized devices.

2.3 Conclusions

In conclusion, DSSCs are promising photovoltaic devices and a plausible alternative to conventional photovoltaic systems. The sensitizer is one of the key components in achieving high efficiency. Many type of metal complexes and metal-free organic dyes can be used in DSSC fabrication. However, the major drawback of using a single sensitizer is failure to harness photons either from visible or near infrared (NIR) region. In this regard, cosensitization is found to be alternative method. Cosensitization is an effective method, forming a mono compact layer on TiO_2 film of two or more sensitizers with different sizes and shapes. Cosensitized device efficiency was augmented with enhanced photovoltaic parameters. Cosensitized device efficiency was augmented with enhanced photovoltaic parameters, which is clearly visible from the IPCE. Some classes of cosensitizers, particularly phthalocyanine, porphyrin, ruthenium-based metal complexes, and metal free organic sensitizers have been discussed in this chapter. The highest efficiency of 12.3% was observed for metal complex YD2-*o*-C8 with organic dye Y123 using cobalt redox electrolyte. The metal-free organic sensitizer ADEKA-1 cosensitized with another organic dye LEG4 achieved 14.3% using cobalt redox electrolyte and the GNP (graphene nanoplatelets) counterelectrode. This is the highest efficiency among all cosensitized and individually sensitized devices. These cosensitized strategies are promising candidates to replace individually sensitized devices.

Acknowledgements

The author Sambandam Anandan thanks DST-SERB (EMR/2014/000009), New Delhi for the sanction of research funds towards the development of new facilities.

References

1 J. Perlin, *From Earth to Space: The Story of Solar Electricity*; Routledge: Cambridge, 1999.
2 A.E. Becquerel, Memoire sur les effets électriques produits sous l'influence des rayons solaires, *C.R. Acad. Sci.*, **9**, 1839, 561–567.
3 R.C. Neville, *Solar Energy Conversion: The Solar Cell*, Elsevier: Amsterdam, 1995.
4 M. A. Green, *Third Generation Photovoltaics: Advanced Solar Energy Conversion*; Springer Verlag, Berlin, 2005.
5 D.M. Chapin, C.S. Fuller, and G.L. Pearson, A new silicon p-n junction photocell for converting solar radiation into electrical power, *J. Appl. Phys.*, **25**, 1954, 676–677.
6 A. Shah, Photovoltaic technology: The case for thin-film solar cells, *Science*, **285**, 1999, 692–698.
7 S. Günes, H. Neugebauer, and N.S. Sariciftci, Conjugated polymer-based organic solar cells, *Chem. Rev.*, **107**, 2007, 1324–1338.
8 G. Li, R. Zhu, and Y. Yang, Polymer solar cells, *Nat. Photonics*, **6**, 2012, 153–161.
9 Y. Lin, Y. Li, X. Zhan, Small molecule semiconductors for high-efficiency organic photovoltaics, *Chem. Soc. Rev.*, **41**, 2012, 4245–4272.
10 M. Grätzel, Recent advances in sensitized mesoscopic solar cells, *Acc. Chem. Res.*, **42**, 2009, 1788–1798.
11 A. Mishra, M.K.R. Fischer, and P. Bäuerle, Metal-free organic dyes for dye-sensitized solar cells: from structure: property relationships to design rules, *Angew. Chem., Int. Ed.*, **48**, 2009, 2474–2499.
12 A. Hagfeldt, G. Boschloo, L. Sun, *et al*., Dye-sensitized solar cells, *Chem. Rev.*, **110**, 2010, 6595–6663.
13 M. Urbani, M. Grätzel, M.K. Nazeeruddin, and T. Torres, Meso-substituted porphyrins for dye-sensitized solar cells, *Chem. Rev.*, **114**, 2014, 12330–12396.
14 H. Gerischer, M. Michel-Beyerle, E. Rebentrost, and H. Tributsch, Sensitization of charge-injection into semiconductors with large band gap, *Electrochim. Acta*, **13**, 1968, 1509–1515.
15 H. Tributsch, Reaction of excited chorophyll molecules at electrodes and in photosynthesis, *Photochem. Photobiol.*, **16**, 1972, 261–269.
16 A. Fujishima and K. Honda, Electrochemical photolysis of water at a semiconductor electrode, *Nature*, **238**, 1972, 37–38.
17 B. O'Regan, and M. Gratzel, A low-cost, high-efficiency solar cell based on dye sensitized colloidal TiO_2 films. *Nature*, **353**, 1991, 737–740.
18 Z. Ning and H. Tian, Triarylamine: A promising core unit for efficient photovoltaic materials, *Chem. Commun.*, 2009, 5483–5495.
19 M. Liang and J. Chen, Arylamine Organic Dyes for Dye-Sensitized Solar Cells, *Chem. Soc. Rev.*, **42**, 2013, 3453–3488.

20 M.K. Nazeeruddin, P. Pechy, T. Renouard, *et al.*, Engineering of efficient panchromatic sensitizers for nanocrystalline TiO_2-based solar cells, *J. Am. Chem. Soc.*, **123**, 2001,1613–1624.

21 M.K. Nazeeruddin, F. De Angelis, S. Fantacci, *et al.*, Combined experimental and DFT-TDDFT computational study of photoelectrochemical cell ruthenium sensitizers, *J. Am. Chem. Soc.*, **127**, 2005, 16835–16847.

22 A. Yella, H.W. Lee, H.N. Tsao, *et al.*, Porphyrin-sensitized solar cells with cobalt (II/III)–based redox electrolyte exceed 12 percent efficiency, *Science*, **334**, 2011, 629–633.

23 S. Mathew, A. Yella, P. Gao, *et al.*, Dye-sensitized solar cells with 13% efficiency achieved through the molecular engineering of porphyrin sensitizers, *Nature Chem.*, **6**, 2014, 242–247.

24 Y. Ooyama and Y. Harima, Molecular designs and syntheses of organic dyes for dye-sensitized solar cells, *Eur. J. Org. Chem.*, **18**, 2009, 2903–2934.

25 M.K.R. Fisher, S. Wenger, M. Wang, *et al.*, D-π-A sensitizers for dye-sensitized solar cells: linear vs branched oligothiophenes, *Chem. Mater.*, **22**, 2010, 1836–1845.

26 K. Kakiage, Y. Aoyama, T. Yano, *et al.*, Highly-efficient dye-sensitized solar cells with collaborative sensitization by silyl-anchor and carboxy-anchor dyes, *Chem. Commun.*, **51**, 2015, 15894–15897.

27 X.-H. Zhang, Y. Cui, R. Katoh, *et al.*, Organic dyes containing thieno[3,2-] bindole donor for efficient dye-sensitized solar cells, *J. Phys. Chem. C*, **114**, 2010, 18283–18290.

28 Y. Shi, R.B.M. Hill, J-H. Yum, *et al.*, A high-efficiency panchromatic squaraine sensitizer for dye-sensitized solar cells, *Angew. Chem. Int. Ed.*, **50**, 2011, 6619–6621.

29 J. Yang, P. Ganesan, J. Teuscher, *et al.*, Influence of the donor size in D-π-A organic dyes for dye- sensitized solar cells, *J. Am. Chem. Soc.*, **136**, 2014, 5722–5730.

30 N. Koumura, Z.-S. Wang, S. Mori, *et al.*, Alkyl-functionalized organic dyes for efficient molecular photovoltaics, *J. Am. Chem. Soc.*, **128**, 2006, 14256.

31 A. Islam, S.P. Singh, M. Yanagida, *et al.*, Amphiphilic ruthenium(II) terpyridine sensitizers with long alkyl chain substituted β-diketonato ligands: an efficient coadsorbent-free dye-sensitized solar cells, *Int. J. Photoenergy*, 2011, **757421**.

32 Y.J. Chang, P.-T. Chou, S.-Y. Lin, *et al.*, High-performance organic materials for dye-sensitized solar cells: triarylene-linked dyads with a 4-tert-butylphenylamine donor, *Chem. Asian J.*, **7**, 2012, 572.

33 Y. Numata, A. Islam, H. Chen, and L. Han, Aggregation-free branch-type organic dye with a twisted molecular architecture for dye-sensitized solar cells, *Energy Environ. Sci.*, **5**, 2012, 8548–8552.

34 Y. Wu, X. Zhang, W. Li, *et al.*, Hexylthiophene-featured D–A–π–A structural indoline chromophores for coadsorbent-free and panchromatic dye-sensitized solar cells, *Adv. Energy Mater.*, **2**, 2012, 149.

35 J.-J. Cid, J.-H Yum, S.-R Jang, *et al*., Molecular cosensitization for efficient panchromatic dye-sensitized solar cells, *Angew. Chem.*, **119**, 2007, 8510–8514; *Angew. Chem. Int. Ed.*, **46**, 2007, 8358–8362.

36 J.N. Clifford, A. Forneli, H. Chen, *et al*., Cosensitized DSCs: dye selection criteria for optimized device V_{OC} and efficiency, *J. Mater. Chem.*, **21**, 2011, 1693–1696.

37 M.D. Brown, P. Parkinson, T. Torres, *et al*., Surface energy relay between cosensitized molecules in solid-state dye-sensitized solar cells, *J. Phys. Chem. C*, 2011, **115**, 23204–23208.

38 M. Kimura, H. Nomoto, N. Masaki, and S. Mori, Dye molecules for simple cosensitization process: fabrication of mixed-dye-sensitized solar cells, *Angew. Chem. Int. Ed.*, **51**, 2012, 4371–4374.

39 N. Robertson, Catching the rainbow: light harvesting in dye sensitized solar cells, *Angew. Chem. Int. Ed.*, **47**, 2008, 101–1014.

40 T. Bessho, S.M. Zakeeruddin, C.-Y. Yeh, *et al*., Highly efficient mesoscopic dye-sensitized solar cells based on donor–acceptor-substituted porphyrins, *Angew. Chem. Int. Ed.*, **49**, 2010, 6646–6649.

41 H.-P. Lu, C.-Y. Tsai, W.-N. Yen, *et al*., *J. Phys. Chem. C*, Control of dye aggregation and electron injection for highly efficient porphyrin sensitizers adsorbed on semiconductor films with varying ratios of coadsorbate, **113**, 2009, 20990–20997; C.-P. Hsieh, H.-P. Lu, C.-L. Chiu, *et al*., Synthesis and characterization of porphyrin sensitizers with various electron-donating substituents for highly efficient dye-sensitized solar cells, *J. Mater. Chem.*, **20**, 2010, 1127–1134

42 D. Kuang, S. Uchida, R. Humphry-Baker, *et al*., Organic dye-sensitized ionic liquid based solar cells: remarkable enhancement in performance through molecular design of indoline sensitizers, *Angew. Chem.*, 120, 2008, 1949; *Angew. Chem. Int. Ed.*, **47**, 2008, 1923.

43 A. Yella, H.-W. Lee, H.N. Tsao, *et al*., Porphyrin-sensitized solar cells with cobalt (II/III)-based redox electrolyte exceed 12 percent efficiency, *Science*, **334**, 2011, 629.

44 H.-P. Wu, Z.-W. Ou, T.-Y. Pan, *et al*., Molecular engineering of cocktail cosensitization for efficient panchromatic porphyrin-sensitized solar cells, *Energy Environ. Sci.*, **5**, 2012, 9843–9848.

45 M. Shrestha, L. Si, C.-W. Chang, *et al*., Dual functionality of BODIPY chromophore in porphyrin-sensitized nanocrystalline solar cells, *J. Phys. Chem. C*, **116**, 2012, 10451–10460.

46 H. He, A. Gurung, L. Si, and A.G. Sykes, A simple acrylic acid functionalized zinc porphyrin for cost-effective dye-sensitized solar cells, *Chem. Commun.*, **48**, 2012, 7619–7621.

47 C.-M. Lan, H.-P. Wu, T.-Y. Pan, *et al*., Enhanced photovoltaic performance with cosensitization of porphyrin and an organic dye in dye-sensitized solar cells, *Energy Environ. Sci.*, **5**, 2012, 6460–6464.

48 C.-L. Wang, J.-W. Shiu, Y.-N. Hsiao, *et al.*, Cosensitization of zinc and free-base porphyrins with an organic dye for efficient dye-sensitized solar cells, *J. Phys. Chem. C*, **118**(48), 2014, 27801–27807.
49 C.-L. Wang, J.-Y. Hu, C.-H. Wu, *et al.*, Highly efficient porphyrin-sensitized solar cells with enhanced light harvesting ability beyond 800 nm and efficiency exceeding 10%, *Energy Environ. Sci.*, **7**, 2014, 1392–1396.
50 N.C. Jeong, H.-J. Son, C. Prasittichai, *et al.*, Effective panchromatic sensitization of electrochemical solar cells: strategy and organizational rules for spatial separation of complementary light harvesters on high-area photoelectrodes, *J. Am. Chem. Soc.*, **134**, 2012, 19820–19827.
51 S.H. Kang, I.T. Choi, M.S. Kang, *et al.*, Novel D–π–A structured porphyrin dyes with diphenylamine derived electron-donating substituents for highly efficient dye-sensitized solar cells, *J. Mater. Chem. A*, **1**, 2013, 3977–3982.
52 S. Chang, H. Wang, Y. Hua, *et al.*, Conformational engineering of cosensitizers to retard back charge transfer for high-efficiency dye-sensitized solar cells, *J. Mater. Chem. A*, **1**, 2013, 11553–11558.
53 G.D. Sharma, G.E. Zervaki, P.A. Angaridis, *et al.*, Stepwise cosensitization as a useful tool for enhancement of power conversion efficiency of dye-sensitized solar cells: The case of an unsymmetrical porphyrin dyad and a metal-free organic dye, *Organic Electronics*, **15**, 2014, 1324–1337.
54 Y. Wang, B. Chen, W. Wu, X. Li, *et al.*, Efficient solar cells sensitized by porphyrins with an extended conjugation framework and a carbazole donor: from molecular design to cosensitization, *Angew. Chem. Int. Ed.*, **53**, 2014, 10779–10783; *Angew. Chem.*, **126**, 2014, 10955–10959.
55 X. Sun, Y. Wang, X. Li, *et al.*, Cosensitizers for simultaneous filling up both absorption valleys of porphyrins: a novel approach for developing efficient panchromatic dye-sensitized solar cells, *Chem. Commun.*, **50**(98), 2014, 15609–15612.
56 W.Q. Li, Y.Z. Wu, Q. Zhang, *et al.*, D-A-π-A Featured sensitizers bearing phthalimide and benzotriazole as auxiliary acceptor: effect on absorption and charge recombination dynamics in dye-sensitized solar cells, *ACS Appl. Mater. Interfaces*, **4**, 2012, 1822–1830.
57 J. Liu, B. Liu, Y. Tang, *et al.*, Highly efficient cosensitization of D–A–π–A benzotriazole organic dyes with porphyrin for panchromatic dye-sensitized solar cells, *J. Mater. Chem. C*, **3**, 2015, 11144–11150.
58 Y. Xie, Y. Tang, W. Wu, *et al.*, Porphyrin cosensitization for a photovoltaic efficiency of 11.5%: a record for non-ruthenium solar cells based on iodine electrolyte, *J. Am. Chem. Soc.*, **137**(44), 2015, 14055–14058.
59 S. Fan, X. Lu, H. Sun, *et al.*, Effect of cosensitization sequence on the performance of dye- sensitized solar cells with porphyrin and organic dyes, *Phys. Chem. Chem. Phys.*, **18**, 2016, 932–938.
60 W. Zhao, Y.J. Hou, X.S. Wang, *et al.*, Study on squarylium cyanine dyes for photoelectric conversion, *Sol. Energy Mater. Sol. Cells*, **58**, 1999, 173–183.

61 A. Ehret, L. Stuhl, and M.T. Spitler, Spectral sensitization of TiO_2 nanocrystalline electrodes with aggregated cyanine dyes, *J. Phys. Chem. B*, **105**, 2001, 9960–9965.

62 C. Qin, Y. Numata, S. Zhang, *et al*., A near-infrared cis-configured squaraine cosensitizer for high-efficiency dye-sensitized solar cells, *Adv. Funct. Mater.*, **23**, 2013, 3782–3789.

63 G.H. Rao, A. Venkateswararao, G. Lingamallu, *et al*. Near-infrared squaraine cosensitizer for high efficiency dye-sensitized solar cells, *Phys. Chem. Chem. Phys.*, **18**, 2016, 14279–14285.

64 U. Mehmood, I.A. Hussein, K. Harrabi, *et al*., Enhanced photovoltaic performance with cosensitization of a ruthenium(II) sensitizer and an organic dye in dye-sensitized solar cells, *RSC Adv.*, **6**, 2016, 7897–7901.

65 F. Inakazu, Y. Noma, Y. Ogomi and S. Hayase, Dye-sensitized solar cells consisting of dye-bilayer structure stained with two dyes for harvesting light of wide range of wavelength, *Appl. Phys. Lett.*, **93**, 2008, 093304.

66 K. Lee, S.W. Park, M.J. Ko, *et al*., Selective positioning of organic dyes in a mesoporous inorganic oxide film, *Nat. Mater.*, **8**, 2009, 665–671.

67 R.Y. Ogura, S. Nakane, M. Morooka, *et al*., High-performance dye-sensitized solar cell with a multiple dye system, *Appl. Phys. Lett.*, **94**, 2009, 073308.

68 H. Ozawa, R. Shimizu, and H. Arakawa, Significant improvement in the conversion efficiency of black-dye-based dye-sensitized solar cells by cosensitization with organic dye, *RSC Adv.*, **2**, 2012, 3198–3200.

69 L. Han, A. Islam, H. Chen, *et al*., High-efficiency dye-sensitized solar cell with a novel coadsorbent, *Energy Environ. Sci.*, **5**, 2012, 6057–6060.

70 Md. Akhtaruzzaman, A. Islam, M. R. Karim, *et al*., Improving the spectral response of black dye by cosensitization with a simple indoline based dye in dye-sensitized solar cell, *J. Chem.*, 2013, 910527.

71 A. Islam, T. Swetha, M.R. Karim, *et al*., Tuning of spectral response by cosensitization in black-dye based dye-sensitized solar cell, *Phys. Status Solidi A*, 2014, 1–6.

72 S. Zhang, A. Islam, X. Yang, *et al*., Improvement of spectral response by cosensitizers for high efficiency dye-sensitized solar cells, *J. Mater. Chem. A*, **1**, 2013, 4812.

73 N. Shibayama, H. Ozawa, M. Abe, *et al*., A new cosensitization method using the Lewis acid sites of a TiO_2 photo electrode for dye-sensitized solar cells, *Chem. Commun.*, **50**, 2014, 6398.

74 S. Chang, K.Y. Wong, X. Xiao, and T. Chen, Effective improvement of the photovoltaic performance of black dye sensitized quasi-solid state solar cells, *RSC Adv.*, **4**, 2014, 31759–31763.

75 K.-M. Lee, Y.-C. Hsu, *et al*., Cosensitization promoted light harvesting for plastic dye-sensitized solar cells, *J. Power Sources*, **196**, 2011, 2416–2421.

76 C. Siegers, U. Wurfel, M. Zistler, *et al.*, Overcoming kinetic limitations of electron injection in the dye solar cell via co-adsorption and FRET, *ChemPhysChem*, **9**, 2008, 793–798.
77 D. Colonna, V. Capogna, A. Lembo, *et al.*, Efficient cosensitization strategy for dye-sensitized solar cells, *Appl. Phys. Express*, **5**, 2012, 022303.
78 P.J. Holliman, M.L. Davies, A. Connell, *et al.*, Ultra-fast dye sensitisation and co-sensitisation for dye sensitized solar cells, *Chem. Commun.*, **46**, 2010, 7256–7258.
79 P.J. Holliman, M. Mohsen, A. Connell, *et al.*, Ultra-fast cosensitization and tri-sensitization of dye-sensitized solar cells with N719, SQ1 and triarylamine dyes, *J. Mater. Chem.*, **22**, 2012, 13318–13327.
80 C.-L. Lee, W.-H. Lee, and C.-H. Yang, The effects of cosensitization in dye-sensitized solar cells, *J. Mater. Sci.*, **48**, 2013, 3448–3453.
81 Z. Wu, Y. Wei, Z. An, *et al.*, Cosensitization of N719 with an organic dye for dye-sensitized solar cells application, *Bull. Korean Chem. Soc.*, **35**, 2014, 1449.
82 L. Wei, Y. Na, Y. Yang, *et al.*, Efficiency of ruthenium dye sensitized solar cells enhanced by 2,6-bis[1-(phenylimino)ethyl]pyridine as a cosensitizer containing methyl substituents on its phenyl rings, *Phys. Chem. Chem. Phys.*, **17**, 2015, 1273–1280.
83 M. Singh, R. Kurchania, R.J. Ball, and G.D. Sharma, Efficiency enhancement in dye sensitized solar cells through step wise cosensitization of TiO_2 electrode with N719 and metal free dye, *Indian J. Pure Appl. Phys.*, **54**(10), 2016, 656–664.
84 J. Luo, Z. Wan, C. Jia, *et al.*, Cosensitization of dithiafulvenyl-phenothiazine based organic dyes with N719 for efficient dye-sensitized solar cells, *Electrochim. Acta*, **211**, 2016, 364–374.
85 G. Saritha, R.V. Mangalaraja, and S. Anandan, High-efficiency dye-sensitized solar cells fabricated using D-D-π-A (donor-donor/π-spacer-acceptor) architecture, *Solar Energy*, **146**, 2017, 150–160.
86 L.H. Nguyen, H.K. Mulmudi, D. Sabba, *et al.*, A selective cosensitization approach to increase photon conversion efficiency and electron lifetime in dye-sensitized solar cells, *Phys. Chem. Chem. Phys.*, **14**, 2012, 16182–16186.
87 G.D. Sharma, S.P. Singh, R. Kurchania, and R.J. Ball, Cosensitization of dye sensitized solar cells with thiocyanate free Ru dye and metal free dye containing thienyfluorene conjugation, *RSC Adv.*, **3**, 2013, 6036–6043.
88 G.D. Sharma, M.S. Roy, and S.P. Singh, Improvement in the power conversion efficiency of thiocyanate-free Ru(II) based dye sensitized solar cells by cosensitization with a metal-free dye, *J. Mater. Chem.*, **22**, 2012, 18788–18792.
89 Y. Ogomi, S.S. Pandey, S. Kimura, and S. Hayase, Probing mechanism of dye double layer formation from dye-cocktail solution for dye-sensitized solar cells, *Thin Solid Films*, **519**, 2010, 1087–1092.
90 S.-Q. Fan, C. Kim, B. Fang, *et al.*, Improved efficiency of over 10% in dye-sensitized solar cells with a ruthenium complex and an organic dye heterogeneously positioning on a single TiO_2 electrode, *J. Phys. Chem. C*, **115**, 2011, 7747–7754.

91 T. Funaki, N. Koumura, and K. Sayama, Cosensitization of cyclometalated ruthenium complex and organic dyes for high-efficiency dye-sensitized solar cells, *Chem. Lett.*, **42**, 2013, 1371–1373.

92 S.P. Singh, M. Chandrasekharam, K.S.V. Gupta, *et al*., Cosensitization of amphiphilic ruthenium (II) sensitizer with a metal free organic dye: Improved photovoltaic performance of dye sensitized solar cells, *Organ. Electron.*, **14**, 2013, 1237–1241.

93 G. Koyyada, S. Shome, M. Chandrasekharam, *et al*., High performance dye-sensitized solar cell from cocktail solution of ruthenium dye and metal free organic dye, *RSC Adv.*, **6**, 2016, 41151.

94 D.D. Babu, R. Su, A. El-Shafei, and A.V. Adhikari, From molecular design to cosensitization; high performance indole based photosensitizers for dye-sensitized solar cells, *Electrochim. Acta*, **198**, 2016, 10–21.

95 D.D. Babu, R. Su, A. El-Shafei, and A.V. Adhikari, New indole based cosensitizers for dye sensitized solar cells exceeding 10% efficiency, *RSC Adv.*, **6**, 2016, 30205–30216.

96 K. Sayama, S. Tsukagoshi, T. Mori, *et al*., Efficient sensitization of nanocrystalline TiO_2 films with cyanine and merocyanine organic dyes, *Sol. Energy Mater. Sol. Cells*, **80**, 2003, 47–71.

97 M. Guo, P. Diao, Y.-J. Ren, *et al*., Photoelectrochemical studies of nanocrystalline TiO_2 cosensitized by novel cyanine dyes, *Sol. Energy Mater. Sol. Cells*, **88**, 2005, 23–35.

98 Y. Chen, Z. Zeng, C. Li, *et al*., Highly efficient cosensitization of nanocrystalline TiO_2 electrodes with plural organic dyes, *New J. Chem.*, **29**, 2005, 773–776.

99 J.-H. Yum, S.-R. Jang, P. Walter, *et al*., Efficient cosensitization of nanocrystalline TiO_2 films by organic sensitizers, *Chem. Commun.*, 2007, 4680–4682.

100 J.N. Clifford, E. Palomares, M.K. Nazeeruddin, *et al*., Multistep electron transfer processes on dye cosensitized nanocrystalline TiO_2 films, *J. Am. Chem. Soc.*, **126**, 2004, 5670–5671.

101 H. Choi, S. Kim, S.O. Kang, *et al*., Stepwise cosensitization of nanocrystalline TiO_2 films utilizing Al_2O_3 layers in dye-sensitized solar cells, *Angew. Chem.*, **120**, 2008, 8383–8387; *Angew. Chem. Int. Ed.*, **47**, 2008, 8259–8263.

102 D. Kuang, P. Walter, F. Nuesch, *et al*., Cosensitization of organic dyes for efficient ionic liquid electrolyte-based dye-sensitized solar cells, *Langmuir*, **23**, 2007, 10906–10909.

103 W. Wu, F. Meng, J. Li, X. Teng and J. Hua, Cosensitization with near-IR absorbing cyanine dye to improve photoelectric conversion of dye-sensitized solar cells, *Synth. Met.*, **159**, 2009, 1028–1033.

104 H.M. Song, K.D. Seo, M.S. Kang, *et al*., A simple triaryl amine-based dual functioned coadsorbent for highly efficient dye-sensitized solar cells, *J. Mater. Chem.*, **22**, 2012, 3786–3794.

105 R.Y.-Y. Lin, Y.-S. Yen, Y.-T. Cheng, *et al*., Dihydrophenanthrene-based metal-free dyes for highly efficient cosensitized solar cells, *Org. Lett.*, **14**, 2012, 3612–3615.

106 M. Cheng, X. Yang, J. Li, *et al*., Cosensitization of organic dyes for efficient dye-sensitized solar cells, *ChemSusChem*, **6**, 2013, 70–77.

107 L.–Y. Lin, M.-H. Yeh, C.-P. Lee, *et al*., Insights into the cosensitizer adsorption kinetics for complementary organic dye-sensitized solar cells, *J. Power Sources*, **247**, 2014, 906–914.

108 J. Chang, C.-P. Lee, D. Kumar, *et al*., Cosensitization promoted light harvesting for organic dye-sensitized solar cells using unsymmetrical squaraine dye and novel pyrenoimidazole-based dye, *J. Power Sources*, **240**, 2013, 779–785.

109 J.H. Delcamp, Y. Shi, J.–H. Yum, *et al*., The role of π bridges in high-efficiency DSCS based on unsymmetrical squaraines, *Chem. Eur. J.*, **19**, 2013, 1819–1827.

110 K. Zhang, C. Qin, X. Yang, *et al*., High-performance, transparent, dye-sensitized solar cells for see-through photovoltaic windows, *Adv. Energy Mater.*, 2014, **1301966**.

111 A. Islam, Md. Akhtaruzzaman, T.H. Chowdhury, *et al*., Enhanced photovoltaic performances of dye-sensitized solar cells by cosensitization of benzothiadiazole and squaraine-based dyes, *ACS Appl. Mater. Interfaces*, **8**, 2016, 4616–4623.

112 Z. Xue, L. Wang, and B. Liu, Facile fabrication of cosensitized plastic dye-sensitized solar cells using multiple electrophoretic deposition, *Nanoscale*, **5**, 2013, 2269–2273.

113 G. Li, M. Liang, H. Wang, *et al*., Significant enhancement of open-circuit voltage in indoline-based dye-sensitized solar cells via retarding charge recombination, *Chem. Mater.*, **25**(9), 2013, 1713–1722.

114 H. Zhu, Y. Wu, J. Liu, *et al*., D–A–π–A featured sensitizers containing auxiliary acceptor of benzoxadiazole: molecular engineering and cosensitization, *J. Mater. Chem. A*, **3**, 2015, 10603–10609.

115 K. Pei, Y. Wu, H. Li, *et al*., Cosensitization of D-A-π-A quinoxaline organic dye: efficiently filling the absorption valley with high photovoltaic efficiency, *ACS Appl. Mater. Interfaces*, **7**(9), 2015, 5296–5304.

116 W. Zhang, W. Li, Y. Wu, *et al*., Novel squaraine cosensitization system of panchromatic light- harvesting with synergistic effect for highly efficient solar cells, *ACS Sustainable Chem. Eng.*, **4**, 2016, 3567–3574.

117 B. Liu, Q. Chai, W. Zhang, *et al*., Cosensitization process effect of D-A-π-A featured dyes on photovoltaic Performances, *Green Energy & Environment*, **1**, 2016, 84–90.

118 G.D. Sharma, S.P. Singh, P. Nagarjuna, *et al*., Efficient dye-sensitized solar cells based on cosensitized metal free organic dyes with complementary absorption spectra, *J. Renewable Sustainable Energy*, **5**, 2013, 043107.

119 M. Zhang, Y. Wang, M. Xu, *et al*., Design of high-efficiency organic dyes for titania solar cells based on the chromophoric core of cyclopentadithiophene-benzothiadiazole, *Energy Environ. Sci.*, **6**, 2013, 2944–2949.

120 X. Lu, T. Lan, Z. Qin, *et al*., A near-infrared dithieno[2,3-a:3′,2′-c] phenazine-based organic cosensitizer for highly efficient and stable quasi-solid-state dye-sensitized solar cells, *ACS Appl. Mater. Interfaces*, **6**, 2014, 19308–19317.

121 H. Li, Y. Wu, Z. Geng, *et al*., Cosensitization of benzoxadiazole based D–A–π–A featured sensitizers: compensating light harvesting and retarding charge recombination, *J. Mater. Chem. A*, **2**, 2014, 14649–14657.

122 Y. Hua, L.T.L. Lee, C. Zhang, *et al*., Cosensitization of 3D bulky phenothiazine-cored photosensitizer with planar squaraine dye for efficient dye-sensitized solar cells, *J. Mater. Chem. A*, **3**, 2015, 13848–13855.

123 M. Fang, H. Li, Q. Li, and Z. Li, Cosensitization of "H"-type dyes with planar squaraine dyes for efficient dye-sensitized solar cells, *RSC Adv.*, **6**, 2016, 40750–40759.

124 K. Kakiage, Y. Aoyama, T. Yano, *et al*., Fabrication of a high-performance dye-sensitized solar cell with 12.8% conversion efficiency using organic silyl-anchor dyes, *Chem. Commun.*, **51**, 2015, 6315–6317.

125 K. Kakiage, Y. Aoyama, T. Yano, *et al*., Highly-efficient dye-sensitized solar cells with collaborative sensitization by silyl-anchor and carboxy-anchor dyes, *Chem. Commun.*, **51**, 2015, 15894–15897.

3

Natural Dye-Sensitized Solar Cells – Strategies and Measures

N. Prabavathy[1], *R. Balasundaraprabhu*[1], *and Dhayalan Velauthapillai*[2]

[1] *Centre for Surface Science, PSG College of Technology, India*
[2] *Faculty of Engineering, Western Norway University of Applied Sciences, Norway*

3.1 Introduction

Although the first and second generation solar cell technologies based on silicon and inorganic materials such as CdTe, GaAs have reached appreciable efficiencies, the current production and installation costs of these solar technologies hardly make it competitive on an energy market still dominated by cheap fossil fuels. In the last few decades, there has been a lot of research interest on various other materials and structures to produce low cost, flexible, and easily manufactured photovoltaics. Dye-sensitized solar cells (DSSCs) have been the center of new research interests in the solar energy field ever since Graetzel and O'Regan reported that a thin film of titanium dioxide (TiO_2) could work as an effective solar cell when it is dye-sensitized. The principle of DSSC is artificial photosynthesis as in plants [1]. Plants follow a set of light-dependent reactions to prepare their own food in the form of energy. These reactions are called the Z-scheme of photosynthesis. Studying nature helps in understanding the science. One such comparison of the Z-scheme of photosynthesis in plants with dye-sensitized solar cells helps in understanding the working mechanism of DSSCs.

Generally, DSSC are prepared using synthetic dyes. However, there are drawbacks with these dyes because of high cost, their toxic nature, and stability issues in longer runs. To commercialize DSSCs, these drawbacks have to be taken care of by using natural dyes, as they are cheap, eco-friendly, and available in abundance. But, the biggest challenge is that DSSCs fabricated using natural dyes have shown very low efficiency compared to synthetic dyes.

Rational Design of Solar Cells for Efficient Solar Energy Conversion, First Edition.
Edited by Alagarsamy Pandikumar and Ramasamy Ramaraj.

Tackling the efficiency issue of natural DSSCs will contribute immensely to the photovoltaics field. The natural pigments in plants play an imperative part in the photosynthesis process. They serve uniquely for the production of starch in various ways. In this work, the functions of the plant pigments are analyzed and effectively used in the fabrication of natural DSSCs. This helps in increasing the efficiency of natural DSSCs enabling their commercialization to meet the future needs.

In this chapter the reasons for the low efficiency of natural DSSCs is listed and the solutions to overcome the drawbacks are explained in detail, referring to works by Prabavathy *et al*. [2–5]. Two dyes namely from *Caesalpinnia. Pulcherrima (C.Pulcherrima)* and rose flower are used as natural dye for sensitization of titania rod film prepared by the hydrothermal method for DSSC fabrication. This chapter extensively reports the enhancement in the natural DSSC, by adopting the strategies and measures reported by Prabavathy *et al*.

3.1.1 Mechanism of the Dye-Sensitized Solar Cell Compared with the Z-scheme of Photosynthesis

The Z-scheme of photosynthesis has four important elements – chlorophyll dye, accessory pigments, water from external sources, and the nucleotide adenine dihydrogen phosphate ($NADP^+$) enzyme molecule [6]. The chlorophyll pigment absorbs sunlight at 680 and 720 nm and is excited to higher energy level. The excited dye molecule loses an electron and returns to the oxidized state. This free electron is then transferred by the accessory pigments and finally reaches the $NADP^+$ molecule. The water from an external source is used by the plants, dissociating and giving electron to the oxidized dye, H^+ ions to the $NADP^+$ molecule. This liberates fresh O_2 molecules to the environment. The H^+ ions and the free electrons reacts with $NADP^+$ molecule, being reduced and forming the NADPH molecule. This is used in the Calvin cycle for the preparation of starch in plants. Figure 3.1 shows a working sketch of the Z-scheme of photosynthesis and the dye-sensitized solar cell.

The components of a DSSC function similarly to the above mentioned elements in the Z-scheme of photosynthesis. Generally the DSSC has four main components namely: photoelectrode, dye or sensitizer, liquid electrolyte and counterelectrode [7]. The sensitizer or dye functions similarly to the chlorophyll pigments in plants. It absorbs sunlight in the visible region and is excited to higher energy level, where it injects electron to the photoelectrode and returns to the oxidized dye state. This free electron is transferred by the photoelectrode and finally reaches the counterelectrode through the outer circuit. In the meantime, the redox electrolyte containing an iodine ion gives the electron to the oxidized dye and becomes triiodide molecule. The oxidized dye returns to its original state (dye regeneration). The triiodide molecule, being heavy, reaches the counterelectrode, from where it gains an electron and is converted

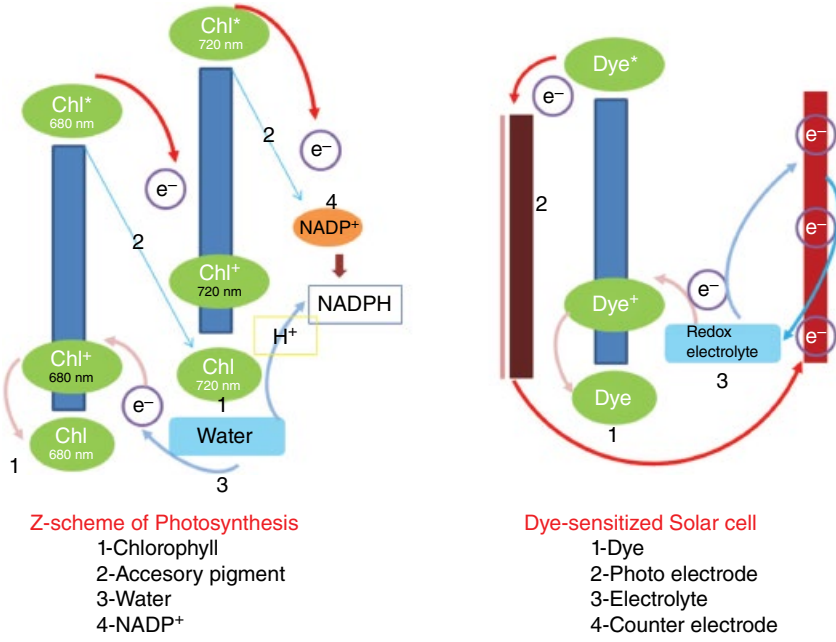

Figure 3.1 Comparison of the Z–scheme of photosynthesis and the dye-sensitized solar cell.

back to iodine ions (electrolyte regeneration). Since the flow of electrons is completed by employing a redox electrolyte in DSSC, current is generated as output. But there is a possibility that the oxidized dye molecule and the triiodide molecule may react with the free electron generated in the dye excitation process (electron recombination processes) [8]. This causes break down in the DSSC. Hence, tailoring each component to the DSSC requirements as described in later sections helps to increase the photovoltaic performance of the cell by decreasing the electron recombination in the DSSC.

3.2 Components of Dye-sensitized Solar Cell

3.2.1 Photoelectrode

The function of the photoelectrode is to directly transfer the injected electron from the excited state dye molecule to the counterelectrode. Wide bandgap semiconductors such as TiO_2, ZnO, and SnO_2 were used as a direct electron transfer medium because of their less corrosive nature in the presence of liquid electrolyte for DSSCs. Among them, TiO_2 is mostly preferred as photoelectrode because of its inertness, high refractive index, high porosity, and high

stability [9]. Bulk TiO_2 shows least surface area, which made dye adsorption unfeasible. So, TiO_2 nanoparticles were employed as photoelectrode for DSSCs. The TiO_2 nanoparticle has high surface area and good porosity. This help in increasing the dye concentration in the TiO_2 film. But due to more grain boundaries, the injected electron is trapped and it causes electron recombination in DSSCs, which reduces the open circuit voltage in DSSCs. Hence, TiO_2 with 1D morphology (TiO_2 nanorod, TiO_2 nanotube) was employed as photoelectrode. The TiO_2 nanorods have a good roughness factor that improves dye absorption; their vertical alignment on the substrate increases the light scattering effect in the film, which enhances the photon absorbance in the film; they have high stability, as the morphology of rods is not affected at higher temperature, whereas the nanotube morphology perishes at high temperature; the high crystallinity and cylindrical solid structure help in creating radial electric field that separates the electron from recombination [10]. Due to these advantages, the TiO_2 nanorod was preferred as photoelectrode for DSSC fabrication in the research work by Prabavathy *et al*.

3.2.2 Dye

The dye functions as the sensitizer for a DSSC. It absorbs sunlight in the visible region and injects the electron to the photoelectrode. The main characteristics required for a dye in a DSSC are: high absorption coefficient, broad visible spectrum, appropriate functional groups to anchor with the OH groups of TiO_2 molecules, high molar extinction coefficient, good stability, nonhazardous nature, and low cost [11].

Generally ruthenium complexes (synthetic dyes) are used as dye for a DSSC. However, they are toxic, not available in abundance, are high cost, and have poor stability on longer runs [12]. Due to these reasons natural dyes are becoming significant for DSSCs. The photovoltaic performance of a DSSC using natural dye is very low compared to DSSCs based on synthetic ruthenium dyes. But research work on natural dyes has shown fruitful results in enhancing the efficiency of the DSSC. Taking this factor into consideration, if the research study is directed towards identifying the possible reasons for their low performance, this will help in increasing the DSSC performance. One such work is reported here with the possible strategies and measures taken to enhance the efficiency and stability of DSSC using natural dyes. Natural dyes extract from *rose* and *C. Pulcherimma* are used as anthocyanin dye in this work.

3.2.3 Liquid Electrolyte

A vital component in a DSSC is the electrolyte. They function similarly to the water in photosynthesis of plants. Additionally, due to their redox nature, they can be reduced and oxidized easily, which favors electrolyte regeneration that

produces current in the cell. The characteristics of liquid electrolyte for DSSCs are: high transparency, good conductivity, fast redox reaction, high stability, high diffusion coefficients, and high inertness [13]. A liquid electrolyte containing iodine ions is commonly used as electrolyte for DSSC in this chapter work by Prabavathy *et al.*

3.2.4 Counterelectrode

The counterelectrode works as a catalyst to reduce the redox species, the triiodide molecule, to iodine ions. The counterelectrode in a DSSC must have high conductivity, high electron mobility, chemical inertness, high temperature resistance, and high stability in liquid electrolyte [14]. The properties of the counterelectrode are met by platinum, which is generally used as the counterelectrode for DSSCs.

3.3 Fabrication of Natural DSSCs

In the present work TiO_2 nanorods prepared by a hydrothermal method are employed as photoelectrode; natural dye extracted from a known rose flower and a new dye from the *C.Pulcherrima* flower is used as anthocyanin dyes; iodine/iodide solution as redox liquid electrolyte and platinum film as counterelectrode are considered for DSSC fabrication.

Titanium tetra isopropoxide (TTIP) and concentrated hydrochloric acid (36 wt-%) were purchased from Sigma Aldrich. Fluorine doped tin oxide (14 Ω sheet resistance), the platinum counterelectrode, and liquid redox electrolyte are purchased from Dye Sol.

3.3.1 Preparation of TiO_2 Nanorods by the Hydrothermal Method

Equal portions of water and concentrated hydrochloric acid are stirred in a beaker for one hour. This adjusts the pH of the solution to 1. To the solution in the beaker, 0.5 ml of TTIP are added in drops and stirred for one hour. On adding TTIP to the acid solution, the TTIP is hydrolyzed to give titanium hydroxide and alcohol. After stirring, the solution is carefully transferred to a Teflon container in an autoclave. The fluorine-doped tin oxide (FTO) substrates are cleaned and introduced into the container such that the FTO coating side faces the wall of the Teflon container in the autoclave. Finally, the autoclave is heated in a muffle furnace at 180 °C for four hours. The titanium hydroxide thus formed condenses to form a complex titanium dioxide with water. The FTO atoms on the substrates act as nucleating sites for the TiO_2 molecules. The chloride ions present in the HCl influence the growth of film in the (011) direction on the FTO substrates and the lattice mismatch between

the FTO and TiO_2 results in nanorod morphology in the film with rutile phase. The rods formed show a uniform distribution with good roughness and good porosity. The length of nanorod thus prepared varies from 2 to 3 μm.

3.3.2 Characterization of the Photoelectrode for DSSCs

X-ray diffraction, field emission scanning electron microscopy (SEM), transmission electron microscopy (TEM), and UV-Vis spectrum studies are widely analyzed for the characterization of the photoelectrode. Figures 3.2a, 3.2b, and 3.2c show the morphology of TiO_2 films at different temperatures: 160 °C, 180 °C and 190 °C. Figure 3.2b shows the morphology and alignment of nanorods on the FTO substrates prepared at 180 °C. The surface roughness of the film can be noticed from the blisters at the tip of each nanorod. This

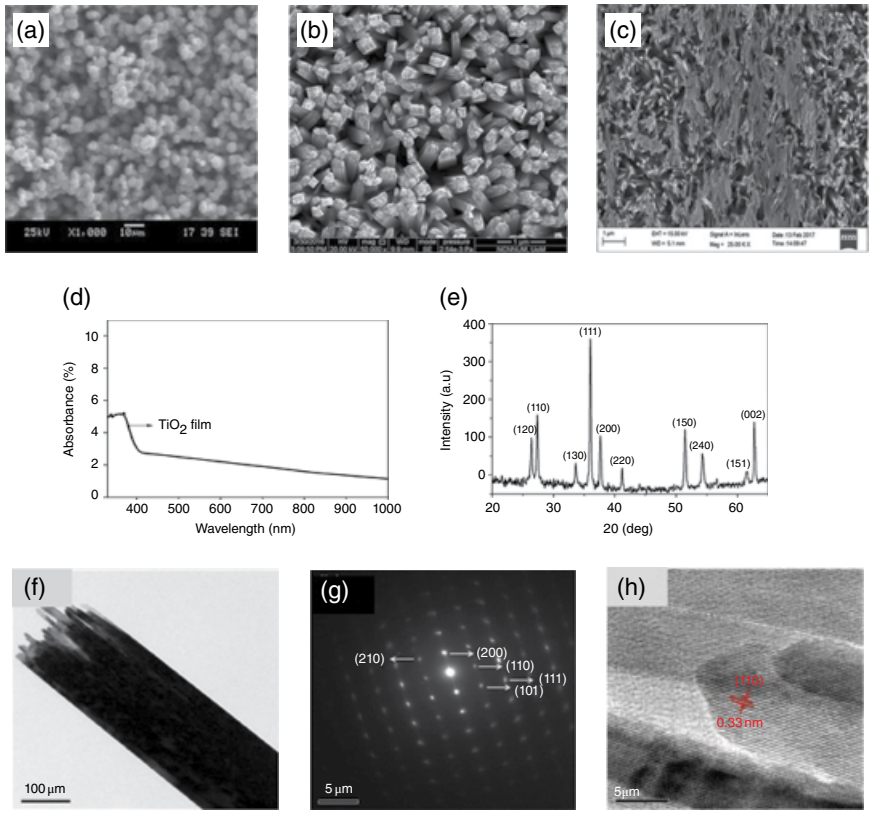

Figure 3.2 (a), (b), (c) SEM image of TiO_2 film prepared at 160 °C, 180 °C, and 190 °C, respectively; (d) XRD spectra of TiO_2 film (180 °C); (e) UV-VIS spectra of TiO_2 film (180 °C); (f), (g), (h) TEM image of TiO_2 nanorods

decreases the photocatalytic activity (PCA) of the film and improves dye anchoring to the surface of TiO_2. The length of nanorod can be measured from the cross-sectional image of the SEM, which shows 2.5 μm. On lowering the operating temperature of furnace to 160 °C, the nucleating centers collide with each other and form TiO_2 nanoparticles on the FTO substrates. At 190 °C, the TiO_2 nanorods are overgrown on the nanorod film in a horizontal plane to the FTO substrates. This confirms that formation of nanorods takes place only at 180 °C. Figure 3.2d shows the X-ray diffraction (XRD) spectra of TiO_2 film prepared at 180 °C. The XRD peaks confirm good crystallinity in the film with pure rutile phase. Rutile phase is the stable phase among all other TiO_2 polymorphs [15]. The surface area of the film can be enhanced by increasing the length of the nanorods. The absorbance spectra show a maximum peak in the range 200–400 nm, i.e. the UV region, as shown in Figure 3.2e, which clearly states the characteristic of photoelectrode. Figures 3.2f, 3.2 g, and 3.2 h show the TEM image of TiO_2 film prepared at 180 °C. The TEM image clearly shows that a single rod comprises small rods bundled together. The selected area electron diffraction (SAED) pattern confirms the presence of TiO_2 nanorods in the film surface.

3.3.3 Preparation of Natural Dye

Natural dye preparation requires adequate information about the type of pigment present in it. The anthocyanins present in flowers can be dissolved in polar solvents such as methanol, ethanol, and acetone. To choose among the polar solvents a small quantity of the flower is soaked in different solvents for 24 h and the maximum absorbance and color intensity is noted. The solvent that shows good absorbance and color intensity is used as the polar solvent to extract the natural dye.

The natural dye for DSSC is prepared by taking 20 g of anthocyanin-rich flower fragments into an airtight opaque container with 20 ml of desired polar solvent. The petals are gently pressed for complete immersion of the petals. The container is left in dark for 48 h. The dye is filtered out and stored in a refrigerator in an air sealed glass bottle. On the day of sensitization with TiO_2 nanorods, one or two drops of HCl is added to make the dye stable; the dye is used without further purification. The root and stem part of plants cannot be extracted using polar solvents. Hence, a small amount of stem, root is immersed in warm distilled water for overnight. The next day it is heated to 70 °C for 30 min. The solution is filtered out and boiled well until the solution becomes concentrated. One or two drops of lemon are squeezed into the solution. This is used as dye for the DSSC without further purification. The dye from fruits is easier to prepare. The juice from the fruits is extracted and is concentrated by adding a mordant such as common salt. This helps in increasing the concentration of the juice and this is used as dye for the DSSC.

3.3.4 Sensitization

Prior to sensitization, the TiO_2 film is heated for ten minutes to remove any air molecules that are trapped between the nanorods in the film. Sensitization of TiO_2 film with the extracted natural dye can be carried out in one of several ways:

- immersing the TiO_2 film in dye for 24 h;
- dipping the TiO_2 film in the dye solution for two minutes and air drying for three minutes, then repeating this cycle a maximum of 40 times;
- heating the TiO_2 film at 50 °C on a hot plate and adding the dye solution in drops over the film, repeat this a maximum of 20 times;
- placing the dye in a Teflon container along with the TiO_2 film in an autoclave and heating in a muffle furnace to 70 °C for one hour; the pressure and temperature helps in the sensitization of dye molecules on the surface of the TiO_2 film;
- as the dye becomes older, the concentration of the solution increases, which helps in easier sensitization, so the film can be immersed in the dye solution for 15 days or more.

If all the above steps are not satisfactory, then change the solvent used for extraction of anthocyanin dye.

3.3.5 Arrangement of the DSSC

The TiO_2 film is peeled out from the FTO substrates leaving an effective area for preparing the DSSC. Now the film is sensitized with the natural dye. After sensitization the film is heated at 40 °C for 10 min to stabilize the dye layer. A platinum electrode with hole for inserting the electrolyte is placed on the effective area of the TiO_2 film such that the hole is placed on a corner of the TiO_2 layer. The films are then sealed by a surlyn (polymer film) gasket. Now the electrolyte is inserted in the hole in drops. The electrolyte is pushed inside by heating the film slightly. This evacuates air and creates space for electrolyte. The excess electrolyte is cleaned and the hole is close by a cover slip. Thus, the DSSC is fabricated.

3.4 Efficiency and Stability Enhancement in Natural Dye-Sensitized Solar Cells

The efficiency and stability of natural dye DSSCs can be enhanced by listing the reasons for their low efficiency. The present work highlights the major points for the cause. Also, remedial measures are updated in the DSSC framework to produce a cot effective and eco-friendly solar cell. The probable reasons for the low efficiency of DSSCs using natural dyes as sensitizer are:

- photoinstability of natural dyes due to the photocatalytic activity (PCA) of titanium dioxide, which is generally used as the photoelectrode in the DSSC;
- the solvents used for the extraction of the natural dye from the plants;
- inefficient anchoring between the dye molecules and the titanium dioxide molecules;
- lower absorbance of sunlight in the visible region;
- leakage and dissolution of liquid electrolyte in dye.

3.4.1 Effect of Photocatalytic Activity of TiO_2 Molecules on the Photostability of Natural Dyes

The TiO_2 molecules are a superior photocatalyst in the presence of sunlight. They absorb sunlight in the UV region, i.e. 200–400 nm, and this, in turn, excites an electron to the surface of the TiO_2 film. The free electron being reactive, it reacts with the moisture in air and produces free radicals such as $O_2^{\bullet}$ and $H^{\bullet}$. These radicals are dangerous to the organic matter present nearby. Hence, it affects the natural dye sensitized on the TiO_2 film very easily and degrades the pigments in seconds. This causes breakdown in a DSSC.

By reducing the photocatalytic activity (PCA) of TiO_2 molecules, the photostability of dyes can be enhanced. The function of TiO_2 molecules in a DSSC is to directly transfer the injected electron to the FTO substrates, from where it finally reaches the counterelectrode. The electron injection kinetics in a DSSC is independent of the properties of TiO_2 molecules. Hence, reducing the PCA of TiO_2 molecules does not affect the mechanism of the DSSC [3]. Figure 3.3

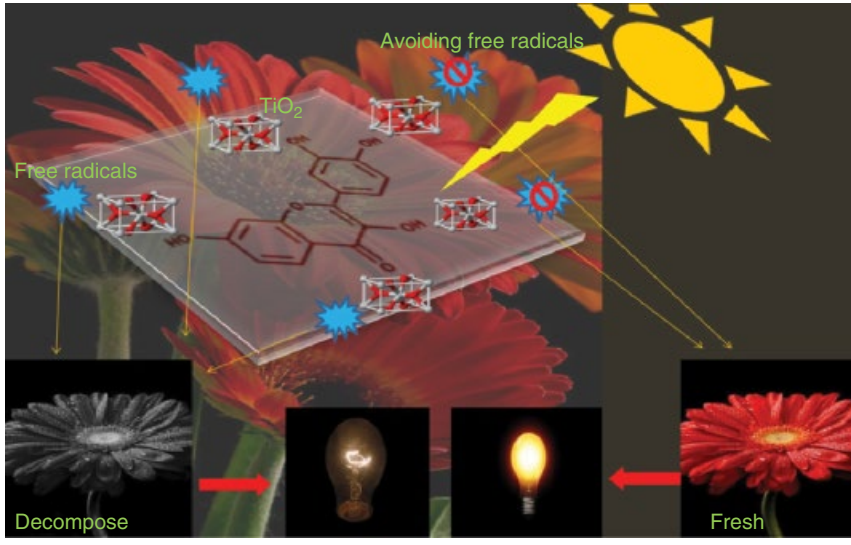

Figure 3.3 Graphical abstract on the effect of PCA in a DSSC [3].

shows a graphical abstract on the effect of PCA in a photoelectrode that affects the dye molecules in a DSSC. The PCA of TiO_2 molecules can be reduced by their synthesis, introducing a passivation layer and choosing the appropriate dye molecules for sensitization.

3.4.1.1 Important Points to be Considered for the Preparation of Photoelectrodes

- The PCA of TiO_2 can be reduced by decreasing the thickness and increasing the surface roughness of TiO_2 film.
- The concentration TiO_2 should be below 0.1 mg for the PCA to be absent.
- The antioxidant property present in the anthocyanins pigment can effectively improve the photostability of dye by fighting back with the free radicals.
- The rutile phase of TiO_2 molecules shows lower PCA compared to the anatase phase of TiO_2 molecules.
- The dye solution for sensitization must have higher intensity, so that the light can enter only at the surface of TiO_2 and reduce the free electron excitation. Thus, the PCA of the film is reduced.
- The PCA of TiO_2 film reduces with an increase in the crystallinity of the film.

From the above, the following recommendation are to be considered for the fabrication of a DSSC: the titania nanorods (1D morphology) with good crystallinity and roughness are prepared by hydrothermal method; anthocyanin-rich natural dyes – rose and *C.Pulcherrima* – are used as natural dye because of their high antioxidant activity.

3.4.2 Citric Acid – Best Solvent for Extracting Anthocyanins

The natural dye used as sensitizer for a DSSC is extracted from plant parts such as the root, stem, fruit, and flower. The plants have a wide variety of natural pigments that serve uniquely for their subsistence. The major pigments are chlorophylls, flavonoids, carotenoids and betalains.

The chlorophylls are the major pigments for the process of photosynthesis. They absorb light mostly in the blue and red wavelengths of the spectrum, hence they reflect back green color, which gives the greenish color appearance to the leaves in plants. Their major function is to absorb the sunlight and use it for the preparation of starch through Z-scheme of photosynthesis and the Calvin cycle.

The next important pigments are the flavonoids. They constitute anthocyanins, which are responsible for coloration in the petals of flowers and skin of fruits. They are good antioxidants. In this respect they fight against the free radicals generated in the plants and make them fresh all the time. Due to the antioxidant property, the ability to absorb a wide range of light in

the visible region, and the presence of the carboxyl group (which anchors easily with the hydroxyl group of TiO_2 molecules), they are widely used as sensitizers in DSSCs [16].

The carotenoids is a huge family. They constitute xanthophylls and carotenes. Excess sunlight entering the plants may damage the tissues and cells of plants, so it is maintained and dissipated back by the carotenoid. They keep in check the excess energy and, in that case, use it in the xanthophylls cycle [17].

The other pigment group is betalains. They are present in plants where the anthocyanins are absent. They work with carotenoids to remove excess energy generated. Comprehending the function of the plant pigment helps in building an eco-friendly solar cell.

The important part in the dye preparation lies in the extraction procedure and the solvents used for extraction. Usually methanol, ethanol, and acetone are used as solvents. Chemically, the anthocyanins in *in vitro* condition lose their stability. To maintain their stability the pH should be adjusted towards 1. This produces flavylium cations that make them highly stable in acidic conditions [18]. This can be done by adding one or two drops of HCl to the extracted dye. Unfortunately, the dye molecules become degraded in minutes due to the corrosive nature of HCl. Also, the addition of HCl in the dye extract promotes the production of the enzyme phenyl propoxidase (PPO), which causes faster biodegradation; additionally, the carboxylate group (essential group for anchoring with TiO_2 molecules) is hydrolyzed in the presence of HCl, which results in poor sensitization with TiO_2 molecules in a DSSC. Hence, a new solvent, namely citric acid, was used effectively for extracting anthocyanins from the flowers. The reason for choosing citric acid as solvent is because it is a safe solvent containing natural ingredients; it interacts well with the anthocyanins that help in stabilizing the dye and inhibit the production PPO [2]. Figure 3.4 shows the color of the extracted dye and the sensitized film from rose and *C.Pulcherrima* flowers

To understand the effect of the solvent in the extraction of anthocyanin, five different solvents were used, namely ethanol, ethanol and 1% HCl (Aci.ethanol), water, water and 1% HCl (Aci.water), and citric acid. Among them the solvent using citric acid showed the highest absorption spectra in the visible region, which allows more sunlight to pass through; a higher anthocyanin content contributes a higher antioxidant property, higher color intensity, and high quantum yield efficiency for maximum photon absorption. Figures 3.5a and 3.5b show the J-V characteristics of a DSSC prepared using *C. Pulcherimma and rose dye.* The photovoltaic performance of the natural dyes using different solvents is shown in Table 3.1. The solvent citric acid shows good photovoltaic performance compared to other solvents.

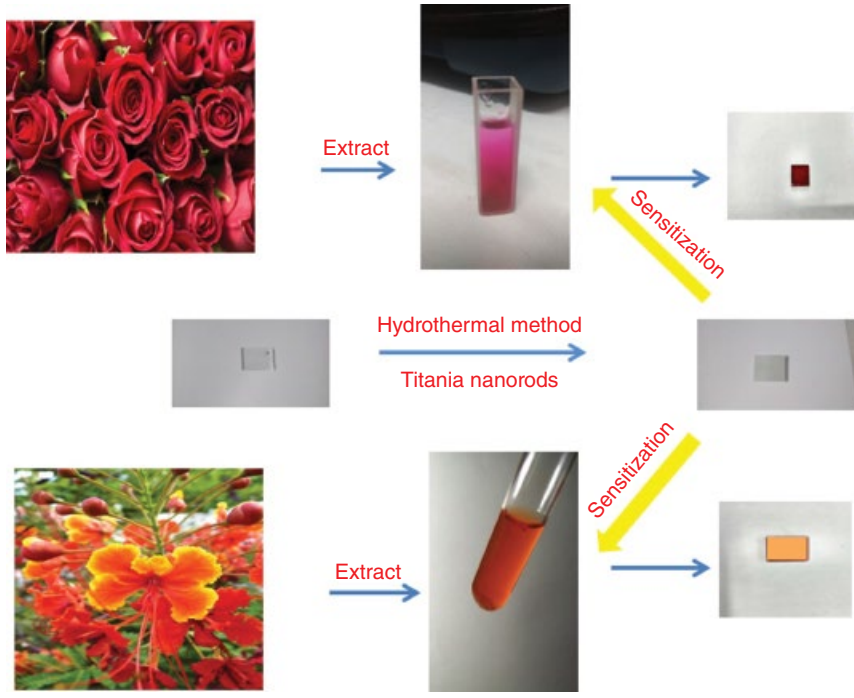

Figure 3.4 Extraction of natural dye from the flowers rose (top) and *C.Pulcherrima* (bottom) using citric acid as solvent and sensitizing the TiO_2 film with the natural extract.

3.4.3. Algal Buffer Layer to Improve Stability of Anthocyanins in DSSCs

One major problem with natural DSSC is their dye anchoring ability. Due to the scarcity of functional groups, steric hindrance, and planar distribution of anthocyanin molecules, the anchoring of anthocyanins with the TiO_2 molecules is not efficient. The dye anchoring and the stability of anthocyanins can be enhanced by the introduction of algal buffer layers in the DSSC framework. The algal buffer layers are prepared from the byproducts of algae: sodium alginate extracted from the cell walls of brown algae, spirulina extracted from green algae *Spirulina.Platensis.* There are several reasons for choosing the algal buffer layers [5]:

- they are nontoxic and natural byproducts;
- sodium alginate has rich functional groups and they are also used as a binder for fixing anthocyanins dye molecules to the surface of TiO_2 nanorod films;
- the spirulina has four different constituents, namely chlorophyll, xanthophyll, phycocyanin, and amino acid that serve uniquely for improving the stability of the DSSC.

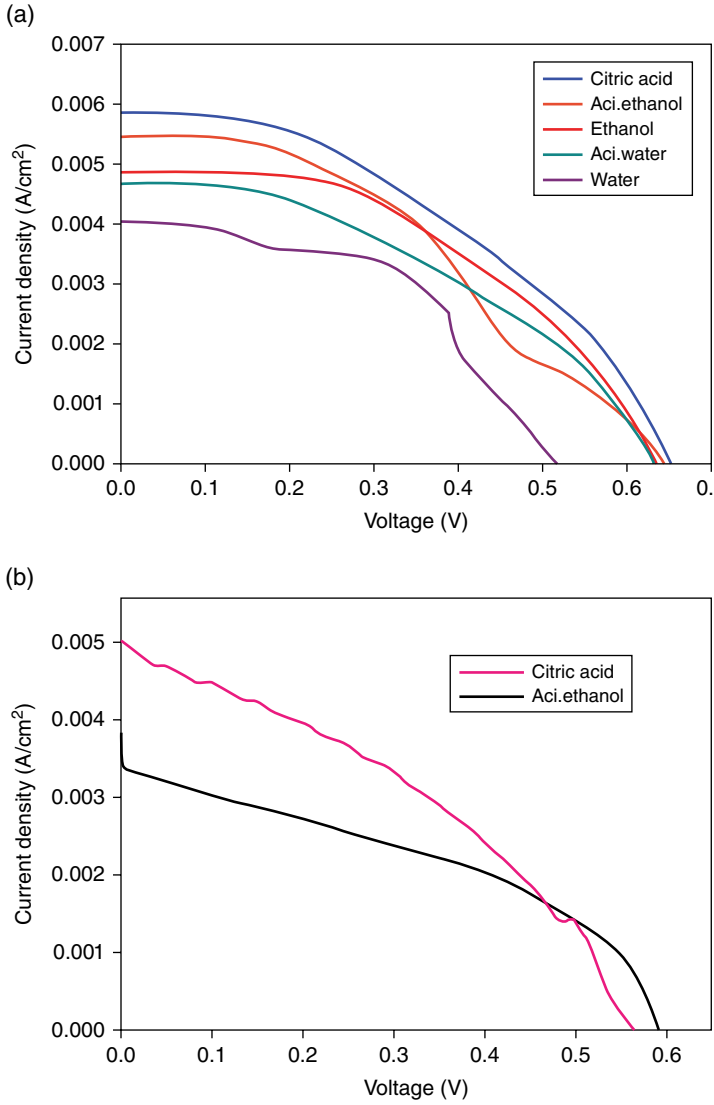

Figure 3.5 J-V characteristics of (a) *C.Pulcherrima* and (b) rose sensitized DSSCs using different solvents respectively.

3.4.3.1 Preparation of Buffer Layers – Sodium Alginate and Spirulina

Sodium alginate in powder form is made into a transparent paste by the application of water. The paste is then applied to the surface of TiO_2 film prepared by a hydrothermal method. The film is then UV treated. This causes the sodium alginate layer to disintegrate and produce polysaccharides. The polysaccharide

Table 3.1 Photovoltaic parameters of natural DSSCs using solvents citric acid and acidified ethanol.

TiO_2-based solar cell	J_{sc} (mA/cm^2)	V_{oc} (V)	FF	η (%)
C. Pulcherrima (aci.ethanol)	5.5	0.64	0.30	0.71
C. Pulcherrima (citric acid)	5.9	0.65	0.33	0.83
Rose dye (aci.ethanol)	3.3	0.59	0.34	0.62
Rose dye (citric acid)	5.0	0.57	0.35	0.99

has more functional groups [19]. These groups, along with the hydroxyl groups of TiO_2 molecules, help in the dye fixation on the film. The presence of functional groups was confirmed by the FTIR studies. Also, the dye concentration in the anthocyanin sensitized film using sodium alginate showed a higher concentration compared to the film in the absence of sodium alginate.

After application of first buffer layer the film is sensitized with the spirulina extract. The spirulina extract is prepared by taking commercially available spirulina pills and dissolving with water (1 g spirulina /100 ml water). After sensitization the film is air dried for 48 h. The film is now prepared with the algal buffer layers for the sensitization of anthocynin dye. Figure 3.6 shows the fabrication of a rose sensitized DSSC with algal buffer layers.

The constituents of Spirulina serve uniquely for anthocyanin stability. The chlorophylls assist the anthocyanins by absorbing more photons [20]. This is confirmed by the maximum absorbance in the UV absorption spectra of spirulina-sensitized TiO_2 film compared to anthocyanin-sensitized film. In addition, absorbing excess energy causes the breakdown in DSSCs; this is kept in check by the xanthophylls of the spirulina. The phycocyanin present in spirulina is a natural blue-greenish pigment that helps to increase the absorption of sunlight in the visible region [21]. Additionally, they have functional groups that assist the sodium alginate TiO_2 film for the sensitization of anthocyanins. The amino acids (constituent of Spirulina) have amine groups that also take part in the sensitization of anthocyanins. Hence, the algal buffer layers help to increase the dye concentration and the stability of a DSSC. Figures 3.7a and 3.7b show the J-V characteristics of rose and *C.Pulcherrima* sensitized DSSCs with algal buffer layers and citric acid as solvent. The color change of the TiO_2 film after sensitization with rose dye along with the buffer layers is also shown in the figure. The photovoltaic performances of the natural dyes with algal buffer layers are shown in Table 3.2. The DSSCs with algal buffer layers show higher efficiency compared to the DSSC without buffer layers

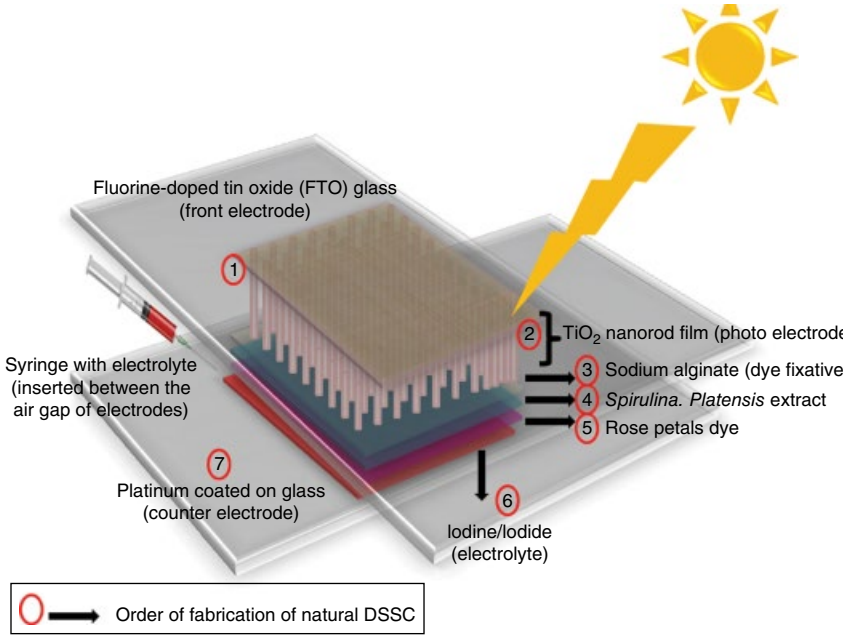

Figure 3.6 Fabrication of natural DSSC with algal buffer layers [5].

3.4.4 Sodium-doped Nanorods for Enhancing the Natural DSSC Performance

The efficiency of DSSCS is enhanced by surface modification of the TiO_2 nanorod film. In this context the surface modification is personalized by doping. The selection of dopant is very crucial for increasing or decreasing the bandgap of the TiO_2 film. In DSSCs the rutile TiO_2 film prepared by the hydrothermal method has an energy bandgap of 3.2 eV, i.e. in the UV region. When this bandgap is reduced the TiO_2 film can absorb light in the visible region. This helps in increasing the quantum efficiency of DSSCs. Consequently, a natural element, sodium, is chosen as dopant in DSSCs. Also, as the sodium ionic radius is comparable with the ionic radii of titanium atoms, Na^+ ions can effectively replace the Ti^{4+} ions without creating much stress in the film. Another important reason for selecting sodium is that, in textile industries, a sodium salt is used as mordant for the fixation of dye molecules on the surface of the fiber. In this context the sodium atoms doped on TiO_2 nanorods can act as mordant for the fixation of anthocyanin molecules in the film [4].

3.4.4.1 Preparing Sodium-doped Nanorods as the Photoelectrode

Take concentrated HCl and distilled water in equal amounts in a beaker and stir for one hour. 0.5 ml of TTIP is added to the beaker in drops and stirred for

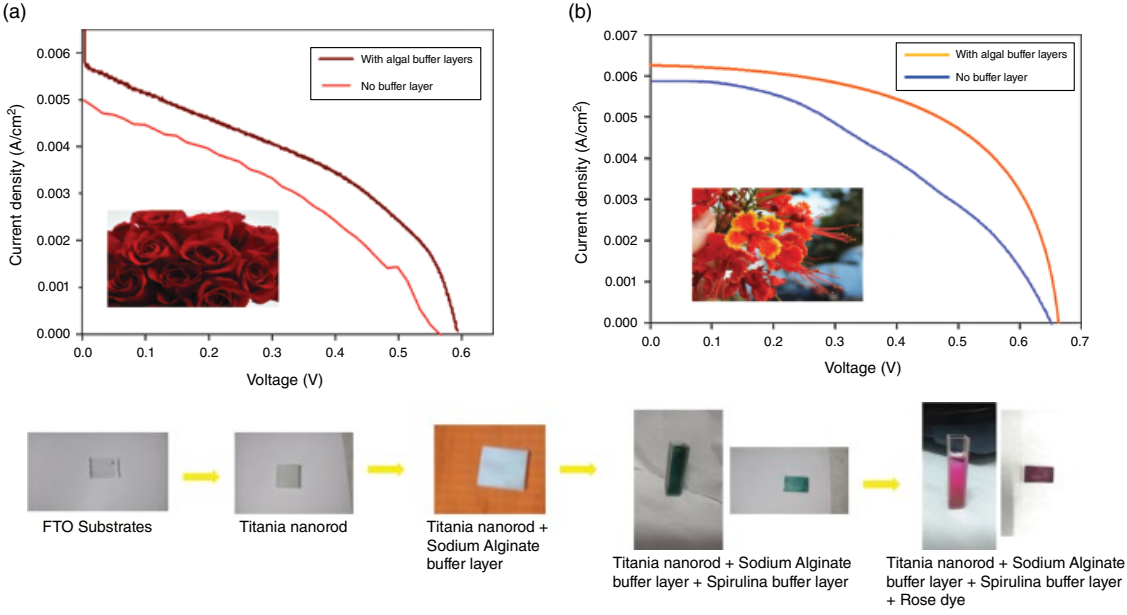

Figure 3.7 J-V characteristics of DSSCs with algal buffer layers sensitized by (a) rose and (b) *C.Pulcherrima* dye (citric acid as solvent).

Table 3.2 Photovoltaic parameters of natural DSSCs with algal buffer layers using citric acid as solvent.

TiO_2-based solar cell	J_{sc} (mA/cm^2)	V_{oc} (V)	FF	η (%)
C. Pulcherrima	5.9	0.65	0.33	0.83
C. Pulcherrima with algal buffer layers	6.4	0.66	0.71	1.81
Rose	5.0	0.57	0.35	0.99
Rose with algal buffer layers	5.8	0.60	0.52	1.47

30 min. A varying percentage of NaCl is added to the initial solution: 2, 4, and 6%. The solution is stirred for one hour. When a sufficient quantity of the dopant is added to the initial solution, the sodium forms complexes with hydroxyl ions. The initial solution is transferred to a Teflon container and place in an autoclave. The FTO substrates are kept inside the Teflon container such that they face the wall of the container. The autoclave is heated to 180 °C for four hours. On heating the TiO_2 nanorods starts nucleating. On increasing the percentage of doping to 6%, the sodium complexes form nodes at certain places such that the rods start to grow from such places giving a 3D flower-like appearance. These flower-shaped rods act as scattering layers by absorbing more photons through multiple light scattering [22]. Also, he sodium-doped nanorods have dots on their surface. These are sodium ions, and they act as mordants for enhanced sensitization of natural dye molecules. Figures 3.8a, 3.8b, and 3.8c show the SEM images of nanorods prepared by the hydothermal method and and Figure 3.8d, 3.8e, and 3.8f shows the SEM image of sodium-doped nanorods (6% dopant concentration). The SEM image shows the appearance of nanoflowers on naorods that act as scattering layer in a DSSC. Also, the bandgap of sodium-doped nanorods is reduced from 3.2 to 2.75 eV by increasing the dopant concentration from 2 to 6%. Figure 3.9 shows the J-V characteristics of rose and *C.Pulcherrima* sensitized DSSCs prepared with 6% doped sodium nanorods as photoelectrode, algal buffer layers, and citric acid as solvent for the extraction of dyes. The photovoltaic performance of the natural dyes with 6% sodium doping is shown in Table 3.3. The DSSC fabricated shows an enhanced efficiency by employing sodium-doped nanorods as photoelectrode.

3.4.5 Absorber Material for Liquid Electrolytes to Avoid Leakage

The liquid redox electrolyte used in DSSCs is the best known electrolyte. But they face drawbacks such as leakage and dissolution in the natural dye [23]. So sealing the solar cell becomes a major concern. Many research advances have been progressed but the performance of the liquid electrolyte is not met by

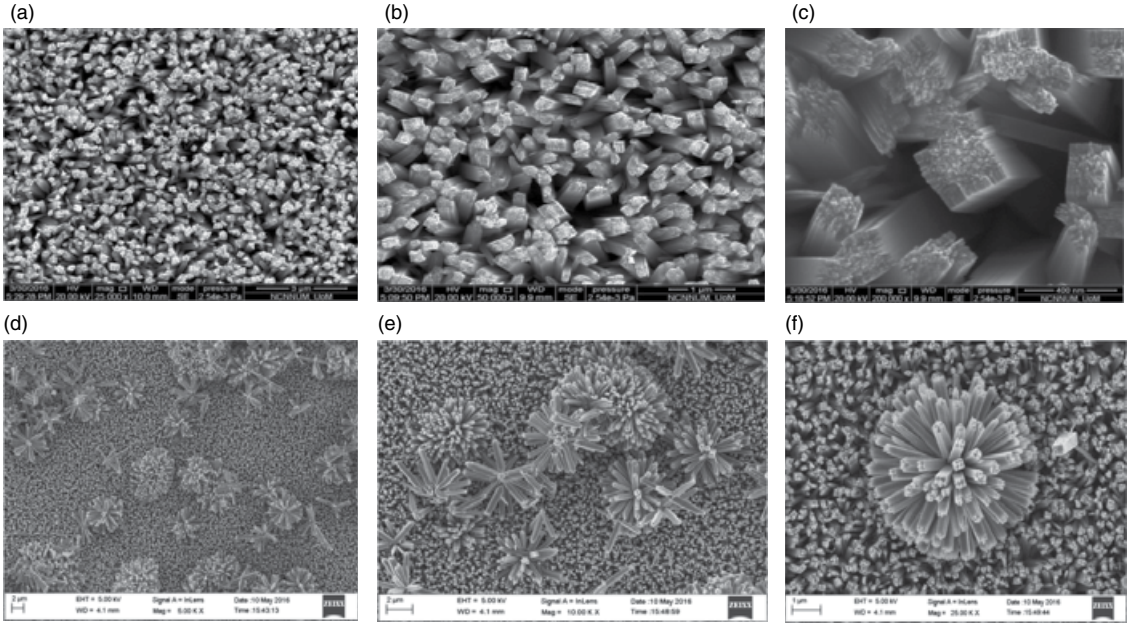

Figure 3.8 (a), (b), (c) FESEM image of TiO_2 nanorods prepared by the hydrothermal method; (d), (e), (f) FESEM images of sodium-doped TiO_2 nanorods prepared by the hydrothermal method (6% dopant concentration).

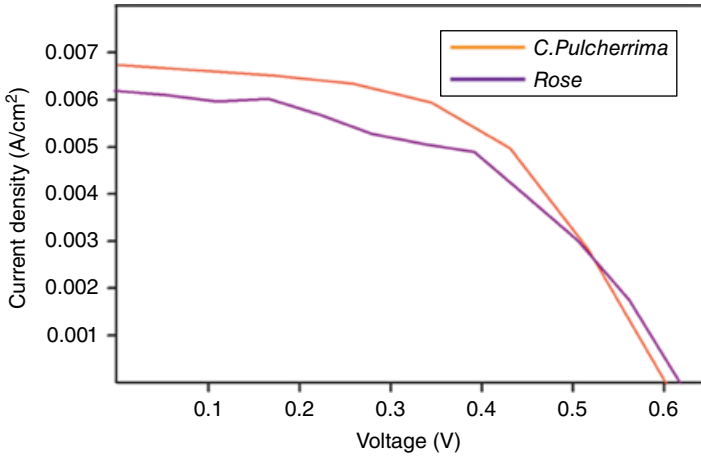

Figure 3.9 J-V characteristics of rose and *C.Pulcherrima* sensitized DSSCs with sodium-doped nanorods as photoelectrode (with algal buffer layers and citric acid as solvent).

Table 3.3 Photovoltaic parameters of natural DSSCs with sodium-doped nanorods as photoelectrode (with algal buffer layers and citric acid as solvent).

TiO_2-based solar cell	J_{sc} (mA/cm^2)	V_{oc} (V)	FF	η (%)
Rose	6.1	0.63	0.57	1.97
C. Pulcherrima	6.7	0.60	0.60	2.15

them. Therefore, in this work we have introduced an absorber material made of cotton. The absorber material is like a thin sheet of cotton.It is cut into shape according to the effective area of solar cell and a drop of electrolytes is introduced which is easily absorbed. This is used as the electrolyte layer between the front electrode and counterelectrode. This reduces the leakage of electrolyte and dissolution of the electrolyte to an extent. The sealing of DSSC becomes easier with this absorber.

3.5 Other Strategies and Measures taken in DSSCs Using Natural Dyes

Some of the various strategies and measures used to enhance the efficiency of natural DSSCs are shown in Table 3.4.

Table 3.4 Enhanced reported efficiencies of natural DSSCs with various strategies and measures.

Photoelecrode	Natural dye	Electrolyte, Counterelectrode	Initial efficiency (%)	Measure taken to enhance DSSC efficiency	Final efficiency (%)	References
TiO_2 nanorods	*Caesalpinnia Pulcherrima* petals	Iodine redox electrolyte Platinum films	0.43	The solvent used for extraction of anthocyanins from the flowers is changed from water to citric acid.	0.83	[2]
TiO_2 nanorods	Petals of rose petals	Iodine/iodide redox electrolyte Platinum films	0.99	Introduction of algal buffer layers – sodium alginate, spirulina for enhancing the dye concentration, and anchoring ability of rose dye to the photoelectrode using citric acid as solvent	1.47	[5]
TiO_2 nanorods	1) *Sesbania (S) Grandiflora* petals 2) *Camelia Sinensis* leaves 3) *Rubis (R) Tinctorum* roots	Iodine/iodide redox electrolyte Platinum films	—	The nanorods are prepared using surfactant that resulted in broccoli-shaped nanorods. Mordants such as potash alum are used as a dye fixative before sensitization. This helps in increasing the dye concentration in the photoelectrode.	1.38 1.65 1.45	[24]
TiO_2 nanorods	1) *Sesbania (S) Grandiflora* petals 2) *Camelia Sinensis* leaves 3) *Rubis (R) Tinctorum* roots	Iodine/iodide redox electrolyte Platinum films	—	Trirthoxy ethyl silane is used as a primer for the FTO substrates for the growth of nanorods. The silane acts a coupling agent to enhance the adhesion rods to the substrates.	0.65 1.53 1.28	[25]
1% Tin-doped TiO_2 nanorods	*Camelia Sinensis* leaves	Iodine/iodide redox electrolyte Platinum films	1.68	Posttreatment of photoelectrode with Zr and HNO_3 to enhance dye adsorption.	2.09	[26]

TiO_2 nanoparticles	Pomegranate fruit pulp	Iodine/iodide redox electrolyte Graphite	—	$TiCl_4$ treatment and the use of graphite as counterelectrode enhanced the efficiency of DSSC.	2.0	[27]
TiO_2 nanoparticles	Astaxanthin pigment algae *Haematococcus. Pluvialis*	Iodine/iodide redox electrolyte Platinum films	—	An algal pigment is used as a sensitizer for reducing electron recombination and dye aggregation.	0.1	[28]
TiO_2 nanoparticles	Monascus Yellow food dye	Iodine/iodide redox electrolyte Platinum films	—	An acetic acid treatment is given to the dye for dye sensitization.	2	[29]
TiO_2 nanoparticle	Mangosteen pericarp peel	Iodine/iodide redox electrolyte Carbonized natural counterelectrode	1.755 using Pt electrode	The mangosteen peel has a high surface area with high roughness and honeycomb structure that increase the catalytic activity of the carbonized peel.	1.99	[30]

Table 3.5 The enhanced photovoltaic performance of *C. Pulcherrima* and rose dye-sensitized DSSCs.

	DSSC efficiency with (TiO_2 nanorod/natural dye/liquid electrolyte/Pt films)			
Dye name	**Water as solvent η (%)**	**Citric acid as solvent η (%)**	**Algal buffer layers + citric acid η (%)**	**Na doping + algal buffer layer + citric acid η (%)**
C. Pulcherrima	0.43	0.83	1.81	2.15
Rose	0.31	0.99	1.47	1.97

3.6 Conclusions

This chapter has focused on improving the efficiency and stability of DSSC using natural dyes. TiO_2 nanorods prepared by the hydrothermal method, anthocyanins from *C. Pulcherrima*, rose dye extract, iodine/iodide redox electrolyte and platinum films used as photoelectrode, natural dye, electrolyte and counterelectrode, respectively for DSSC fabrication. Photoinstability of dye due to the PCA of the photoelectrode, effect of solvent in the extraction of anthocyanins, inefficient dye anchoring, lower absorbance in the visible region, and electrolyte leakage are the major problems met in DSSCs using natural dyes. The photostability of the dye can be enhanced by reducing the PCA of the photoelectrode. The recommendations for preparing the photoelectrode with low PCA are detailed in this chapter. Citric acid is used as an alternative solvent to reduce the corrosive nature of the dye resulting from the use of hydrochloric acid. The introduction of algal buffer layers helps in improving the dye concentration in the film. Nanoflowers on the surface of TiO_2 nanorods act as scattering layers for absorbing more photons by sodium doping. The leakage of electrolyte is controlled using a thin absorber material. These strategies and measures helps in building an eco-friendly solar cell with enhanced efficiencies from 0.43 and 0.31% to 2.15 and 1.97% for *C.Pulcherrima* and rose dye extract. Table 3.5 shows the enhanced efficiency of the flowers for the work carried out in this chapter.

References

1 Grätzel, C. and Zakeeruddin, S.M., Recent trends in mesoscopic solar cells based on molecular and nanopigment light harvesters, *Mater. Today*, **16**, 2013, 11–18.

2 Prabavathy, N., Shalini, S, Balasundaraprabhu, R., *et al*. Effect of solvents in the extraction and stability of anthocyanin from the petals of *Caesalpinia*

pulcherrima for natural dye sensitized solar cell applications, *J. Mater. Sci. Mater. Electron.*, 2017. doi: 10.1007/s10854-017-6743-7.

3 Prabavathy, N., Shalini, S, Balasundaraprabhu, R., *et al*. Enhancement in the photostability of natural dyes for dye-sensitized solar cell (DSSC) applications: a review, *Int. J. Energy Res.*, **41**(10), 2017. doi: 10.1002/er.3703.

4 Shalini, S., Prabavathy, N., Balasundaraprabhu, R., *et al*. Effect of Na doping on structure, morphology and properties of hydrothermally grown one dimensional TiO_2 nanorod structures, *J. Mater. Sci. Mater. Electron.*, **28**(4), 2017, 3500–3508.

5 Prabavathy, N., Shalini, S, Balasundaraprabhu, R., *et al*. Algal buffer layers for enhancing the efficiency of anthocyanins extracted from rose petals for natural dye-sensitized solar cell (DSSC), *Int. J. Energy Res.,* 2017. doi: 10.1002/er.3866.

6 Barber, J., Tran,. P.D., and Barber, J., From natural to artificial photosynthesis, *J. R. Soc. Interface*, **10**(81), 2013, 20120984.

7 Gong, J., Liang, J., and Sumathy, K., Review on dye-sensitized solar cells (DSSCs): Fundamental concepts and novel materials, *Renew. Sustain. Energy Rev.*, **16**, 2012, 5848–5860.

8 Narayan, M.R., Review: Dye sensitized solar cells based on natural photosensitizers, *Renew. Sustain. Energy Rev.*, **16**(1), 2012, 208–215.

9 Hsiao, P.T. and Teng, H., Coordination of Ti^{4+} sites in nanocrystalline TiO_2 films used for photoinduced electron conduction: Influence of nanoparticle synthesis and thermal necking, *J. Am. Ceram. Soc.*, **92**(4), 2009, 888–893.

10 Tacchini, I., Ansón-Casaos, A., Yu, Y. *et al*., Hydrothermal synthesis of 1D TiO_2 nanostructures for dye sensitized solar cells, *Mater. Sci. Eng. B*, **177**(1), 2012, 19–26.

11 Shalini, S., Balasundara Prabhu, R., Prasanna, S., *et al*., Review on natural dye sensitized solar cells: Operation, materials and methods, *Renew. Sustain. Energy Rev.*,**51**, 2015, 1306–1325.

12 Richhariya, G., Kumar, A., Tekasakul, P., and Gupta, B., Natural dyes for dye sensitized solar cell: A review, *Renew. Sustain. Energy Rev.*, **69**, 2015, 705–718.

13 Gmetzel, N.M., Influence of dye chemistry and electrolyte solution on interfacial processes at nanostructured ZnO in dye-sensitized solar cells, *J. Photochem. Photobiol. A Chem.*, **264**, 2013, 26–33.

14 Gong, J., Liang, J., and Sumathy, K., Review on dye-sensitized solar cells (DSSCs): Fundamental concepts and novel materials, *Renew. Sustain. Energy Rev.*, **16**(8), 2012, 5848–5860.

15 Mital, G.S. and Manoj, T., A review of TiO_2 nanoparticles, *Chin. Sci. Bull.*, **56**(16), 2011, 1639–1657.

16 Vankar, P.S. and Shukla, D., Natural dyeing with anthocyanins from *Hibiscus rosa sinensis* flowers, *Appl. Polym. Sci.*, **122**, 2016, 3361–3368.

17 Demmig-Adams, B. and Adams, W., The role of xanthophyll cycle carotenoids in the protection of photosynthesis, *Trends Plant Sci.*, **1**(1), 1996, 21–26.

18 Sirimanne, P.M., Senevirathna, M.K.I., Premalal, E.V.A., *et al*., Utilization of natural pigment extracted from pomegranate fruits as sensitizer in solid-state solar cells, *J. Photochem. Photobiol. A Chem.*, **177**(2–3), 2006, 324–327.

19 Burana-osot, J., Hosoyama, S., Nagamoto, Y., *et al*., Photolytic depolymerization of alginate, *Carbohydr. Res.*, **344**(15), 2009, 2023–2027.

20 A. Lim, A. Manaf, N.H., Tennakoon, K., *et al.*, Higher performance of DSSC with Dyes from *Cladophora* sp. as mixed cosensitizer through synergistic effect, *J. Biophys.*, 2015, 510467.

21 A. Kathiravan, A. and R. Renganathan, R., "Photosensitization of colloidal TiO_2 nanoparticles with phycocyanin pigment," *J. Colloid Interface Sci.*, **335**, 2, 2009, 196–202.

22 Li, Y., Guo, M., Zhang, M., and Wang, X., Hydrothermal synthesis and characterization of TiO_2 nanorod arrays on glass substrates, *Mater. Res. Bull.*, **44**, 2009, 1232–1237.

23 Wu, J., Lan, Z., Hao, S., et al., Progress on the electrolytes for dye-sensitized solar cells, *Pure Appl. Chem.*, **80**(11), 2008, 2241–2258.

24 Yuvapragasam, Y., Muthukumarasamy, N., Agilan, S., et al., Natural dye sensitized TiO_2 nanorods assembly of broccoli shape based solar cells, *J. Photochem. Photobiol. B Biol.*, **148**, 2015, 223–231.

25 Akila, Y., Muthukumarasamy, N., Agilan, S., et al., Enhanced performance of natural dye sensitised solar cells fabricated using rutile TiO_2 nanorods, *Opt. Mater. (Amst).*, **58**, 2016, 76–83.

26 Akilavasan, J., Wijeratne, K., Gannoruwa, A., *et al*. Significance of $TiCl_4$ post-treatment on the performance of hydrothermally synthesized titania nanotubes-based dye-sensitized solar cells, *Appl. Nanosci.*, **4**(2), 2014, 185–188.

27 W. Ghann, W., Kang, H., Sheikh, T., *et al.*, Fabrication, optimization and characterization of natural dye sensitized solar cell, *Sci. Rep.*, **7**, 2016, 41470.

28 Orona-Navar, A., Aguilar-Hernández, I., Cerdán-Pasarán, A., and Ornelas-Soto, N., Astaxanthin from *Haematococcus pluvialis* as a natural photosensitizer for dye-sensitized solar cell, *Algal Res.*, **26**, 2017, 15–24.

29 Ito, S., Saitou, T., Imahori, H., et al., Fabrication of dye-sensitized solar cells using natural dye for food pigment: Monascus yellow, *Energy Environ. Sci.*, **3**, 2010, 905–909.

30 Maiaugree, W., Lowpa, S., Towannang, M., et al., A dye sensitized solar cell using natural counterelectrode and natural dye derived from mangosteen peel waste., *Sci. Rep.*, **5**, 2015. doi:10.1038/srep15230.

4

Advantages of Polymer Electrolytes for Dye-Sensitized Solar Cells

L.P. Teo and A.K. Arof

Centre for Ionics University of Malaya, Physics Department, Faculty of Science, University of Malaya, 50603 Kuala Lumpur, Malaysia

4.1 Why Solar Cells?

Solar cells convert sunlight into electricity. Currently, the world's supply of electricity is derived from fossil fuels such as oil, coal, and natural gas. However, the reserves of these conventional energy sources are being depleted. Solar power generation is one of the fast expanding sources of renewable electricity. There are many benefits of solar power production. Solar power generation does not require fossil fuels. Compared to other methods of producing electricity, it does not pose serious environmental issues. Solar energy could adequately complement electricity provision from an electricity transmission grid during peak hours. Solar technology applications are easily adaptable and installation at the customer site is also possible. The Malaysian government has placed emphasis on solar energy application since *Rancangan Malaysia ke-9* or the Ninth Malaysia Plan.

Solar cells have come a long way and dye-sensitized solar cell (DSSC) is a third generation photovoltaic system. The first generation is the silicon solar cell and the second generation is the thin film technology. Although the price of the first generation solar cell has reduced, the emerging third generation technology promises to be less expensive. The advantage of the DSSC is that it is still functional in diffused light at intensities less than 1 Sun. Furthermore, silicon is not a good absorber of sunlight.

Rational Design of Solar Cells for Efficient Solar Energy Conversion, First Edition.
Edited by Alagarsamy Pandikumar and Ramasamy Ramaraj.

4.2 Structure and Working Principle of DSSCs with Gel Polymer Electrolytes (GPEs)

A DSSC consists of an electrolyte sandwiched between a photoanode and a counter electrode, as shown in Figure 4.1.

The photoanode consists of a compact titanium dioxide (TiO_2) layer on top of which is deposited mesoporous TiO_2. The two layers are deposited on the same transparent conducting oxide (TCO) glass or plastic substrate. The substrate is coated with either an indium-doped tin oxide (ITO) or a fluorine-doped tin oxide (FTO) to make it conducting. The TiO_2 particles making up both layers are of nanosize. The TiO_2 nanocrystals for the compact layer are smaller in size (about 14 nm) than the nanocrystals of the mesoporous layer TiO_2 (about 21 nm). The TCO/compact TiO_2 layer/mesoporous TiO_2 layer assembly is then soaked in a dye. The second layer is porous in order to enlarge the surface area for adsorbance of the dye molecules. Following the absorption of photons and the excitation of dye molecules from the highest occupied molecular orbital (HOMO) to the lowest unoccupied molecular orbital (LUMO) states is the release of electrons into the nano-TiO_2 layer. The nano-TiO_2 is a wide bandgap semiconductor; on injection of the released electrons into its conduction band, a hole is left in the dye molecule and the dye molecule becomes oxidized. The electron exits the TiO_2 nanoparticles (NP) and delivers electrical energy to a load.

Electrolytes used contain iodide/triiodide (I^-/I_3^-) redox ions to transfer electrons between the counter electrode (CE) (usually platinum (Pt)) and the photoanode. The I^-/I_3^- couple is a popular redox mediator because it has good solubility, does not absorb too much light, enables fast dye regeneration, has suitable redox potential, and the triiodide ion does not recombine easily with electrons that have been injected into TiO_2 semiconductor [1]. Discussion on electrolytes in this chapter deals only with gel polymer electrolytes (GPEs). The GPEs should exhibit (i) good interfacial properties with the photoanode and CE or cathode, (ii) good interfacial, optical, thermal, chemical, and electrochemical stabilities to prevent dye degradation, (iii) compatibility with the dye sensitizer, (iv) high conductivity to ensure fast charge transfer, and (v) little

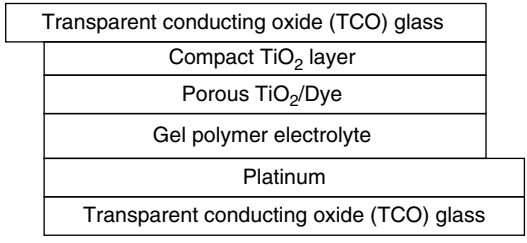

Figure 4.1 Schematic diagram of the DSSC configuration.

absorption in the visible region [2]. The CEs tested include platinum [3, 4], carbon [5], carbon nanotube [6], graphite [7], conducting polymers (e.g. polypyrrole (PPy), polyaniline (PANI), poly(3,4-ethylenedioxythiophene) (PEDOT)) [8–10], metal sulfide such as MoS_2 [11], NiS [12], and $NiCo_2S_4$ [13] to name a few. The regeneration of the oxidized photosensitizer occurs when the holes receive electrons from the iodide ions. The iodide ions become triiodide ions again. The triiodide ion then replaces the electron donated by the iodide ion with an electron that has reached the cathode and will be reduced to an iodide ion again. The function of the redox mediator is to complete the electron circuit.

Ni *et al.* [14] developed a Schottky barrier model based on the theory of thermionic emission and diffusion differential model. This model relates current density (J) and voltage (V) for a DSSC:

$$V = \frac{kTm}{q} ln\left[\frac{(J_{sc} - J)L\,cosh(d/L)}{qDn_0 sinh(d/L)} + 1\right] - \frac{kT}{q} ln\left[1 + \frac{J}{A^* T^2 \exp(-q\phi_b / kT)}\right] \quad (4.1)$$

Here ϕ_b is the Schottky barrier height; k is Boltzmann constant; T is temperature in Kelvin; m is the nonideality factor; q is 1.60×10^{-19} C (electron charge), and A^* is given by:

$$A^* = \frac{4\pi m^* q k^2}{h^3} \quad (4.2)$$

with h as Planck's constant and m^* is equal to 5.6 times the free electron mass of TiO_2 [14]. A^* is the Richardson constant of TiO_2; its value is equal to 6.71×10^6 A m^{-2} K^{-2}. D is the electron diffusion coefficient; n_0 is the dark electron concentration ($n_0 = 10^{16}$ cm^{-3}); L is the electron diffusion length given by $\sqrt{D\tau}$, where τ is the conduction band free electrons lifetime and d is thickness of the thin film. J_{sc} is the short circuit current density. As an example, ϕ_b may take values of magnitude a few tenths of an eV, $\tau = 10$ ms and $m = 2$ [15]; $D = 2.0 \times 10^{-4}$ cm^2 s^{-1} [16]. The model investigated the TiO_2/transparent conducting oxide interfacial effects on the open circuit voltage (V_{oc}) and J-V characteristics.

4.3 Gel Polymer Electrolytes (GPEs)

A gel polymer electrolyte (GPE) basically contains liquid electrolyte, i.e. salt dissolved in solvent but entrapped in the polymer network. As mentioned earlier, redox couple should be included in the GPE for DSSC applications.

Other ingredients that can be incorporated into it are a secondary polymer host, plasticizers, additives, and fillers to name a few. These ingredients are able to improve the characteristics of the GPE. The condition where the liquid electrolyte is trapped in a polymer network in GPE can reduce the possibility of leakage compared to DSSCs made from liquid electrolytes, making it more stable for long term use [17, 18]. GPEs, also known as quasi-solid state polymer electrolytes, have both the cohesive feature of solids and diffusive characteristic of liquids. GPEs also have high ionic conductivity and good interfacial contact with electrodes as with liquid electrolytes. High ionic conductivity is known to have a constructive effect on DSSC performance [19].

There are two important characteristics that govern the selection of polymer host in an electrolyte system [20, 21]. These are (i) the ability of the polymer to solvate salts and (ii) glass transition temperature, T_g. To solvate salts, the polymer must contain polar groups to form dative bonds with cations of the dissociated salt. The low T_g eases segmental motion and, thereby, facilitates conduction. Although polymers of low glass transition temperature are advantageous, there are reports on the use of polymers with high T_g in the literature [22, 23]. When choosing a salt, its low lattice energy and large anion radius should be taken into account. Low salt lattice energy will enable the salt to dissolve easily in the polymer matrix. On the other hand, the choice of the solvent is influenced by its properties, such as high boiling point, high dielectric constant, low viscosity, and low melting temperature, to assist in dissociating the salt [24, 25]. Some of the polymers used in GPEs for DSSC application reported in the literature include poly(ethylene oxide) (PEO) [26], polyacrylonitrile (PAN) [19], poly(vinyl alcohol) (PVA) [27], poly(vinylidene fluoride-hexafluoropropylene) (PVdF-HFP) [28], poly(methyl methacrylate) (PMMA) [29], hydroxypropyl cellulose (HPC) [30], poly(methyl methacrylate-co-ethyl acrylate) (PMMA-EA) [31], PAN-co-vinyl acetate [4], and blends of PEO/PVdF-HFP [32]. In our work, the DSSCs fabricated used GPEs based on chitosan (Ch), phthaloylchitosan (PhCh), PAN, PVA, poly(vinylidene fluoride) (PVdF), and polymer blends. Each component with their properties and role in the electrolyte will be discussed in detail, as understanding of polymer electrolytes is essential in designing good GPEs for DSSCs. Although the main focus in this chapter is the gel polymer electrolytes for application in DSSCs, the choice and role of other constituents in DSSCs will also be elaborated.

4.3.1 Chitosan (Ch) and Blends

Chitosan (Ch) is a deacetylated byproduct of chitin, which is a plentiful polysaccharide or biopolymer found in nature. Chitin exists in arthropod exoskeletons, crustacean shells (e.g. in shrimps, lobsters, and crabs), insect cuticles (e.g. in ants, beetles, and butterflies), the cephalopod beaks (e.g. in squids and octopuses) and the cell walls of fungi. Ch is an inert, hydrophilic,

odorless, nontoxic, biodegradable, and biocompatible polymer that has high mechanical strength with a glass transition temperature of 480 K [33–35]. In the structure of Ch, there is amine group (NH_2) that differentiates it from chitin. Due to the amine and hydroxyl groups (OH) on the Ch chain, it has been described as a suitable biopolymer for the formation of dative bonds with metal ions [36, 37]. The nitrogen and oxygen atoms in the amine and hydroxyl groups, respectively, each have a pair of unused electrons that can complex with cations of the doping salt. Hence, Ch can be considered as a good choice to serve as a polymer electrolyte to host ionic conduction, as it is a relatively inexpensive material that does not require complicated apparatus to manufacture; it is environmental friendly, too. Moreover, using a waste material such as chitosan will minimize environmental stress. Table 4.1 summarizes the Ch-based polymer electrolytes and their performance in DSSCs under 1 Sun illumination unless stated otherwise. The photoanode used comprises two

Table 4.1 Photovoltaic performance of DSSCs using chitosan-based GPEs with their ambient conductivities.

GPE	Dye	σ (S cm^{-1})	J_{sc} (mA cm^{-2})	V_{oc} (V)	*FF*	η (%)	Ref.
27.5 wt-% Ch 22.5 wt-% $NH_4I(+I_2)$ 50 wt-% BMII	Anthocyanin (black rice)	1.51×10^{-4}	0.76	0.38	0.48	0.14	[38]
27.5 wt-% Ch 22.5 wt-% $NH_4I(+I_2)$ 50 wt-% BMII	Anthocyanin (red cabbage)	1.51×10^{-4}	1.43	0.31	0.45	0.20	[38]
11 wt-% Ch 9 wt-% $NH_4I(+I_2)$ 80 wt-% BMII	Anthocyanin (black rice)	3.02×10^{-4}	0.90	0.37	0.45	0.15	[38]
11 wt-% Ch 9 wt-% $NH_4I(+I_2)$ 80 wt-% BMII	Anthocyanin (red cabbage)	3.02×10^{-4}	2.09	0.61	0.30	0.38	[38]
3.3 wt-% Ch 7.7 wt-% PEO 9 wt-% $NH_4I(+I_2)$ 80 wt-% BMII	Anthocyanin (black rice)	5.52×10^{-4}	1.21	0.40	0.47	0.23	[38]
3.3 wt-% Ch 7.7 wt-% PEO 9 wt-% $NH_4I(+I_2)$ 80 wt-% BMII	Anthocyanin (red cabbage)	5.52×10^{-4}	2.52	0.40	0.39	0.39	[38]

I_2 = iodine; BMII = 1-butyl-3-methylimidazolium iodide

TiO_2 layers (compact and mesoporous) deposited on ITO glass substrate while the CE was platinum coated on ITO. Their conductivity (σ) values at room temperature have also been included in the table.

From Table 4.1, it may be inferred that the efficiency (η) of DSSCs is influenced by the type of dye and also by the source of dye. These are based on the results that cells using the same electrolyte composition but different anthocyanin sources gave different performance. A DSSC with anthocyanin extracted from red cabbage exhibited higher efficiency than that of anthocyanin from black rice due to the structural difference in which the cyanidin-3-(sinapoyl)diglucoside-5-glucoside in red cabbage has more sites to bind with TiO_2 [38]. Ionic liquid (IL) addition, namely 1-butyl-3-methylimidazolium iodide (BMII), also affects the DSSC performance. As can be seen in Table 4.1, the conductivity of 27.5 wt-% Ch/22.5 wt-% $NH_4I(+I_2)$/50 wt-% BMII was doubled when more BMII (80 wt-%) was added and subsequently increased the J_{sc} and η [38]. BMII is basically a molten salt at ambient temperature and is in the liquid state. IL, in general, does not evaporate easily, is nonflammable, has good chemical and thermal stabilities, high ionic conductivity, excellent solvating capability and wide potential windows [39]. Also, ionic liquids do not undergo crystallization due to their low melting point making them more attractive. They can offer extra charge carriers in the electrolytes and also serve as plasticizer. BMII was selected as it has higher conductivity at room temperature as compared to its counterpart, i.e. 1-propyl-3-methylimidazolium iodide (PMII) [40]. On the other hand, ammonium iodide (NH_4I) salt has been chosen [38] due to its low lattice energy (605.3 kJ mol^{-1}) [41] enabling the salt to dissolve easily in the polymer matrix and resulting in reasonably good conductivity. As a comparison, NH_4I is known to exhibit higher conductivity than sodium iodide (NaI) and lithium iodide (LiI) [42]. Lee and coworkers [43] also reported a similar observation and tested phosphazene-based liquid electrolyte containing the three salts in DSSCs. They found that the phosphazene-based liquid electrolyte containing NH_4I salt exhibited the highest J_{sc} and η of 1.28 mA cm^{-2} and 0.45%, respectively, when compared with that employing NaI and LiI. The σ, J_{sc}, and η of the three salts follow the order $NH_4I > NaI > LiI$.

Other than that, the efficiency is dependent on factors such as the type of polymer host and whether one or two polymers are being used in the GPE. It is well known that the ionic conductivity of polymer electrolytes can be enhanced by blending two polymers. It has been anticipated that better properties in terms of higher conductivity, improved flexibility and better mechanical strength will be obtained in blended polymer electrolytes when compared to electrolytes having single polymer matrix. As can be seen from Table 4.1, the conductivity has been increased to 5.52×10^{-4} S cm^{-1} from 3.02×10^{-4} S cm^{-1} when Ch has been blended with PEO in the weight ratio of 30:70, as blending provides more donor sites for the ions to conduct [38]. As a result,

improvement in J_{sc}, fill factor (*FF*) and η can be observed for both black rice and red cabbage DSSCs with Ch–PEO blend GPE. PEO, the most commonly used polymer host, is a synthetic polymer that has the monomer unit –CH_2CH_2O– in which the oxygen atom has lone pair electrons to interact with the salt to form polymer–salt complexes. PEO has the benefit of solvating a wide variety of salts in high concentration with its glass transition temperature around 209 K [44]. Nonetheless, PEO has the drawbacks of having high degree of crystallinity (70–85%) and poor ionic conductivity of about 10^{-8} S cm^{-1} at ambient temperature [45]. Hence, it is used as cohost in reference [38]. Furthermore, Ch and PEO are known to be miscible in one another and, thus, well-suited for blending [46].

4.3.2 Phthaloylchitosan (PhCh) and Blends

The use of chitosan has been restricted because of its insolubility in almost all ordinary solvents, such as water, alkali and organic solvents, but it is soluble in dilute acetic and formic acids. The rigid crystalline structure that resulted through both intra- and intermolecular hydrogen bonding accounts for the insolubility of chitosan in some common organic solvents. Nevertheless, the presence of the amine groups in chitosan enables modification of the biopolymer to impart the desired property of solubility. As mentioned earlier, apart from the amine groups, chitosan has two hydroxyl groups, which are also eligible to be modification sites to enhance solubility. In preparing the chitosan-based electrolytes shown in Table 4.1, the solvent used was 1% acetic acid solution. However, the presence of water in the solvent aided by oxygen will result in the formation of iodate (IO_3^-) ions and lesser triiodide ions to mediate the transport of electrons from the CE to the photoanode; this is detrimental to DSSC performance. The process of IO_3^- formation is [47]:

$$2D^+ + 3I^- + 4O_2 + H_2O \rightarrow 2D + 3IO_3^- + 2H^+ \tag{4.3}$$

To reduce the resistivity of the electrolytes derived from chitosan, increase the solubility of chitosan in aprotic solvents, and, consequently, the efficiency of the DSSC, modification of the chitosan is required. N-phthaloylation is one of the chemical methods used to bestow hydrophobicity to the framework of chitosan. Phthaloylchitosan (PhCh) is an N-phthaloyl derivative of chitosan. PhCh has shown boosted solubility in organic solvents, while the phthaloyl group could easily regenerate free amino groups. PhCh can dissolve in solvents such as dimethyl formamide (DMF), dimethylacetamide (DMAc), dimethyl sulfoxide (DMSO), and pyridine [48]. Film containing PhCh has been reported to exhibit the glass transition temperature of 260 K [49]. Table 4.2 lists the conductivity and photovoltaic parameters of GPEs employing PhCh as polymer host. The DSSCs were illuminated at 1 Sun whereas the photoanode used

Table 4.2 Photovoltaic performance of DSSCs using PhCh-based GPEs with their ambient conductivities.

GPE	Dye	σ (S cm^{-1})	J_{sc} (mA cm^{-2})	V_{oc} (V)	FF	η (%)	Ref.
11 wt-% PhCh 9 wt-% $NH_4I(+I_2)$ 80 wt-% BMII	Anthocyanin (red cabbage)	5.86×10^{-4}	3.47	0.37	0.34	0.43	[38]
16.1 wt-% PhCh 32.3 wt-% EC 32.3 wt-% PC 12.9 wt-% TPAI 6.4 wt-% $LiI(+I_2)$	N719	4.14×10^{-3}	7.25	0.77	0.67	3.71	[53]
18.18 wt-% PhCh 27.27 wt-% EC 36.37 wt-% PC 18.18 wt-% $TBAI(+I_2)$	N3	4.45×10^{-3}	5.58	0.65	0.63	2.29	[60]
16.1 wt-% PhCh 32.3 wt-% EC 32.3 wt-% PC 19.3 wt-% $TPAI(+I_2)$	N719	5.27×10^{-3}	7.38	0.72	0.66	3.50	[53]
12.2 wt-% PhCh 36.6 wt-% EC 36.6 wt-% DMF 14.6 wt-% $TPAI(+I_2)$	N3	5.46×10^{-3}	12.72	0.60	0.66	5.00	[54,55]
18.18 wt-% PhCh 27.27 wt-% EC 36.37 wt-% PC 18.18 wt-% $TPAI(+I_2)$	N3	5.53×10^{-3}	7.65	0.67	0.64	3.28	[60]
12.2 wt-% PhCh 36.6 wt-% EC 36.6 wt-% DMF 7.3 wt-% TPAI 7.3 wt-% $LiI(+I_2)$	N3	6.09×10^{-3}	17.29	0.59	0.62	6.36	[55]
18.18 wt-% PhCh 27.27 wt-% EC 36.37 wt-% PC 3.64 wt-% KI 14.54 wt-% $TBAI(+I_2)$	N3	6.71×10^{-3}	8.70	0.80	0.63	4.36	[60]
18.18 wt-% PhCh 27.27 wt-% EC 36.37 wt-% PC 3.64 wt-% KI 14.54 wt-% $TPAI(+I_2)$	N3	8.45×10^{-3}	8.72	0.80	0.63	4.37	[60]

Table 4.2 (Continued)

GPE	Dye	σ (S cm^{-1})	J_{sc} (mA cm^{-2})	V_{oc} (V)	FF	η (%)	Ref.
18.18 wt-% PhCh 27.27 wt-% EC 36.37 wt-% PC 18.18 wt-% KI(+I_2)	N3	1.37×10^{-2}	7.71	0.67	0.63	3.23	[60]
3.3 wt-% PhCh 7.7 wt-% PEO 9 wt-% NH_4I(+I_2) 80 wt-% BMII	Anthocyanin (red cabbage)	6.24×10^{-4}	3.50	0.34	0.39	0.46	[38]
4.79 wt-% PhCh 11.16 wt-% PEO 70.97 wt-% DMF 13.08 wt-% TPAI(+I_2)	Anthocyanin (black rice)	7.36×10^{-3}	2.24	0.41	0.58	0.53	[56]
4.79 wt-% PhCh 11.16 wt-% PEO 70.97 wt-% DMF 13.08 wt-% TPAI(+I_2)	Anthocyanin (black rice)	7.36×10^{-3}	2.71	0.40	0.68	0.74	[56]
4.79 wt-% PhCh 11.16 wt-% PEO 70.97 wt-% DMF 13.08 wt-% TPAI(+I_2)	N3	7.36×10^{-3}	13.04	0.58	0.61	4.61	[56]
4.79 wt-% PhCh 11.16 wt-% PEO 70.97 wt-% DMF 13.08 wt-% TPAI(+I_2)	N3	7.36×10^{-3}	15.24	0.60	0.57	5.21	[56]
5.04 wt-% PhCh 1.26 wt-% PEO 31.5 wt-% EC 37.8 wt-% DMF 24.4 wt-% TPAI(+I_2)	Chlorophyll (screwpine leaves) + Anthocyanin (black rice) (sequential deposition)	1.11×10^{-2}	1.64	0.52	0.66	0.56	[57]
5.04 wt-% PhCh 1.26 wt-% PEO 31.5 wt-% EC 37.8 wt-% DMF 24.4 wt-% TPAI(+I_2)	Anthocyanin (black rice)	1.11×10^{-2}	1.83	0.50	0.65	0.59	[57]
5.04 wt-% PhCh 1.26 wt-% PEO 31.5 wt-% EC 37.8 wt-% DMF 24.4 wt-% TPAI(+I_2)	Chlorophyll (screwpine leaves)	1.11×10^{-2}	1.19	0.49	0.63	0.39	[57]

(*Continued*)

Table 4.2 (Continued)

GPE	Dye	σ (S cm^{-1})	J_{sc} (mA cm^{-2})	V_{oc} (V)	FF	η (%)	Ref.
5.04 wt-% PhCh 1.26 wt-% PEO 31.5 wt-% EC 37.8 wt-% DMF 24.4 wt-% TPAI(+I_2)	Anthocyanin (black rice) + Chlorophyll (screwpine leaves) (sequential deposition)	1.11×10^{-2}	2.64	0.46	0.63	0.81	[57]
5.09 wt-% PhCh 1.32 wt-% PEO 38.45 wt-% EC 32.05 wt-% DMF 23.09 wt-% TPAI(+I_2)	N3	—	12.71	0.68	0.69	5.96	[59]
5.09 wt-% PhCh 1.32 wt-% PEO 38.45 wt-% EC 32.05 wt-% DMF 23.09 wt-% TPAI(+I_2)	N3	—	17.21	0.65	0.64	7.15	[59]
5.09 wt-% PhCh 1.32 wt-% PEO 38.45 wt-% EC 32.05 wt-% DMF 23.09 wt-% TPAI(+I_2)	N3	—	17.32	0.66	0.63	7.20	[59]
5.04 wt-% PhCh 1.26 wt-% PEO 31.5 wt-% EC 37.8 wt-% DMF 24.4 wt-% TPAI(+I_2)	N3	1.11×10^{-2}	16.56	0.66	0.67	7.10	[58]
4.64 wt-% PhCh 1.16 wt-% PEO 29 wt-% EC 34.8 wt-% DMF 22.4 wt-% TPAI(+I_2) 8 wt-% BMII	N3	1.35×10^{-2}	19.68	0.71	0.69	9.61	[58]

consists of two layers of TiO_2 deposited on FTO glass and CE was platinum coated on FTO unless stated otherwise.

Whether it is ITO or FTO used in Table 4.2, the TCO glass substrate not only acts as a support for both electrodes but also as current collector [50]. In order to have a good performance, TCO substrates should exhibit high transparency, excellent transmittance, low sheet resistance, and good heat stability [51]. ITO can transmit 80% of light that falls on it while the transmittance percentage of FTO is 70%. Nevertheless, ITO is more expensive than FTO due to the scarce indium element and also the resistivity of ITO will be increased after thermal treatment of TiO_2 deposited on it, which subsequently leads to decrement in performance [52]. ITO glass substrate has been used in reference [38] whereas the rest of the data in Table 4.2 were obtained using FTO glass [53–59]. Note also that diisopropxytitanium bis(acetylacetonate) was deposited on TCO glass before the mesoporous TiO_2 coated on it in references [38, 60]. As stated earlier, this layer, which is known as compact or blocking layer, plays the role of preventing electron recombination. Also, with its presence, better TiO_2 adhesion on TCO and larger contact area between TiO_2 and TCO can be achieved resulting in efficient electron transfer and improved performance [61]. The compact blocking layer can also be prepared from nanoporous P90 Degussa TiO_2 [54–59]. In contrast, the photoanode used in reference [53] consists only one layer of TiO_2, i.e. without the compact layer.

As can be observed from Table 4.2, the 11 wt-% PhCh / 9 wt-% NH_4I / 80 wt-% BMII GPE gave higher ambient conductivity (5.86×10^{-4} S cm^{-1}) than the same composition GPE but with chitosan as polymer matrix instead (3.02×10^{-4} S cm^{-1}) (Table 4.1) [38]. Again, higher conductivity is accompanied by increment in J_{sc}, *FF*, and η [38]. The conductivity and efficiency can be further enhanced when PhCh has been blended with PEO in weight ratio of 30:70, thus delivering the conductivity of 6.24×10^{-4} S cm^{-1} and efficiency of 0.46% [38]. Yet, the efficiency is still low, which may be attributed to the use of natural resources as sensitizers. In fact, it is clear that all the DSSCs employing natural dyes listed in Table 4.2 yielded the efficiencies of not more than 1%. This may be due to the photoinstability issue of the natural dyes, which makes them easily degradable, as well as their weak binding interaction with the photoanode. Nonetheless, natural dyes are easily accessible, environmental friendly, and inexpensive, which can help reduce the price of DSSCs. It is worth mentioning that the highest efficiency of 0.81% obtained for a natural DSSC using PhCh-PEO GPE listed in Table 4.2 was using the combination of anthocyanin extracted from black rice and chlorophyll from screwpine leaves [57]. The two layers of TiO_2 has been firstly sensitized in anthocyanin black rice solution for 24 h followed by immersion in chlorophyll solution for another 24 h. Interestingly, when the sensitization procedure was reversed, a lower efficiency of 0.56% was obtained. This is attributable to anthocyanin having both carbonyl and hydroxyl functional groups that can bind more efficiently with the porous

TiO_2 surface as compared to the chlorophyll molecule that has only the carbonyl group. It is to be noted that the PhCh-PEO GPE that delivered efficiency of 0.81% used TPAI salt.

Organic salts, such as tetrapropylammonium iodide (TPAI or $(C_3H_7)_4NI$), tetramethylammonium iodide (TMAI or $(CH_3)_4NI$), and tetrabutylammonium iodide (TBAI or $(C_4H_9)_4NI$) to name a few, have been employed as they are nonvolatile and stable in atmospheric condition [62]. In contrast, inorganic salts (e.g. NH_4I) have restricted solubility at ambient temperature [63]. The type of salt is also a factor in influencing DSSCs performance. It can also be observed in reference [60] that the ambient conductivity of PhCh-based GPE containing potassium iodide (KI), TPAI, and TBAI salts increases in the order of TBAI (4.45 mS cm^{-1}) < TPAI (5.53 mS cm^{-1}) < KI (13.7 mS cm^{-1}), which is attributed to the reduction in cationic radius in the same order. The ionic radii of K^+, TPA^+ (or $C_{12}H_{28}N^+$), and TBA^+ (or $C_{16}H_{36}N^+$) are 138, 460, and 500 pm, respectively. Hence, TBAI has the lowest lattice energy, enabling the salt dissociation to take place more easily compared to TPAI and KI. Among the three salts, the TBA^+ cation is largest in size and, thus, it is expected to be less mobile and impedes the movement of ions, thereby decreasing the ionic mobility and conductivity. From Table 4.2, J_{sc} can be seen to increase in the same order as conductivity trend. However, the J_{sc} and efficiency do not follow the same trend but increase in the mode of J_{sc}/η (TPAI) > J_{sc}/η (KI) > J_{sc}/η (TBAI). Bandara and coworkers [64] have also reported that TPAI is the best performing salt in a PAN-based GPE system among other quaternary ammonium iodide salts including NH_4I, TBAI, tetraethylammonium iodide (TEAI or $(C_2H_5)_4NI$), tetrapentylammonium iodide (TPentAI or $(C_5H_{11})_4NI$), and tetrahexylammonium iodide (THAI or $(C_6H_{13})_4NI$). The efficiency follows the order of THAI ($\eta = 3.16\%$) < TPentAI ($\eta = 3.48\%$) < NH_4I ($\eta = 3.69\%$) < TEAI ($\eta = 4.11\%$) < TBAI ($\eta = 4.16\%$) < TPAI ($\eta = 4.30\%$). Similar to this work [60], their efficiency variation also does not follow the conductivity trend. As for KI, efficiency approximately 3% was obtained in a PAN-based GPE [65]. Note that Bandara *et al.* [64, 65] employed N719 sensitizer whereas in the PhCh-based GPE DSSCs, N3 dye was used [60].

In DSSCs, both the cations and anions of the salt are equally important. For the case of iodide salts, more iodide ions are beneficial in enhancing the J_{sc} and, subsequently, efficiency. As for the cations, small cations are able to absorb better on TiO_2 surface and improve electron injection rate while large cations, on the other hand, decrease the cationic conduction due to their bulkiness and, thereby, increase the iodide concentration. Both the improved electron injection rate and increase in iodide concentration will usually lead to enhancement in J_{sc} and efficiency. V_{oc} can also be enhanced with a large cation that shifts the conduction band to more positive potentials and decreases the electron recombination process. This means that with the right combination of salts, the small cation increases J_{sc} whereas, at the same time, the large cation is able to improve the V_{oc}. Therefore, based on this mixed cation effect, the usage of double salts

with large and small cations can definitely yield better DSSC performance. In the GPE systems containing both KI-TPAI and KI-TBAI binary salts, improvement in J_{sc}, V_{oc}, and efficiency were observed compared to a GPE containing KI salt only [60]. Conversely, conductivity decreased as expected. Nevertheless, the DSSCs using the two binary salts electrolyte systems with N3 dye gave almost identical efficiency of about 4.4% with both KI:TPAI/TBAI weight percentage ratio at 20:80 [60]. It is to be noted that part of the KI has been substituted with TPAI/TBAI so that the total weight of the salts in the electrolyte are maintained. Using N719 dye, the DSSC with gel electrolyte containing 16.1 wt-% PhCh / 32.3 wt-% EC / 32.3 wt-% PC / 12.9 wt-% TPAI / 6.4 wt-% LiI(+I_2) exhibits lower ionic conductivity but higher efficiency compared to the PhCh-based electrolyte having single salt, i.e. TPAI only [53], as can be seen from Table 4.2. Interestingly, the V_{oc} increased while J_{sc} decreased for the GPE containing TPAI-LiI double salts when compared to single TPAI salt electrolyte. The smaller Li^+ cation size enabled it to move through segmental motion of the polymer chain and decreased the flexibility of the polymer backbone, thereby increasing the viscosity and obstructing the mobility leading to conductivity decrement [53]. On the contrary, the small Li^+ cation can adhere well onto the TiO_2 surface and change the Fermi level of TiO_2, thus improving the V_{oc} leading to better efficiency.

Modification of the photoanode is another effective way to boost the efficiency besides tuning the components in the electrolyte. We have studied the plasmonic effect of silver (Ag) nanoparticles (10 nm in size) in both natural and synthetic DSSC with PhCh-PEO-DMF-TPAI gel electrolyte [56]. Increments of 39.6% and 13% in efficiency were observed in the anthocyanin and N3 DSSCs, respectively. This can be ascribed to the localized surface plasmon resonance behavior of the metal nanoparticles to the photoanode, which enhances the light absorption, thereby improving the performance [66, 67]. On the other hand, it can be observed in Table 4.1 that NiS and $Ni_{0.95}Mo_{0.05}S$ have also been tried as CE, as metal sulfides have attractive features, such as good electrocatalytic activity, decent conductivity, stability, nontoxicity, and abundance in nature [59]. Although platinum is commonly used as CE, it is very expensive due to its scarcity; it also suffers from dissolution due to I^-/I_3^- corrosion in the electrolyte [68]. Based on the performance listed in Table 4.1, it can be concluded that $Ni_{0.95}Mo_{0.05}S$/FTO CE prepared via an electrochemical deposition technique displayed comparable efficiency with that of Pt/FTO, thus showing its potential as a low cost CE material.

It is worth highlighting that an N3 DSSC using GPE with the composition of 4.64 wt-% PhCh / 1.16 wt-% PEO / 29 wt-% EC / 34.8 wt-% DMF / 22.4 wt-% TPAI(+I_2) / 8 wt-% BMII having the high conductivity of 1.35×10^{-2} S cm^{-1} [58] is the best performing DSSC among the others. Here, ethylene carbonate (EC) and DMF play the role of both solvent and plasticizer. The dielectric constant, viscosity, boiling and melting temperatures of EC are 95.3 (at 25 °C), 2.56 cP, 246 °C and 36 °C, respectively. DMF has a dielectric constant of 36.7, viscosity

of 0.802 cP (at 25 °C), boiling point of 153 °C, and melting point of −60.4 °C. These values indicate that DMF and EC meet the requirements of high dielectric constant and high boiling point with low viscosity and low melting point to serve as solvent and plasticizer. To our knowledge, this efficiency is the highest efficiency ever recorded for DSSCs employing gel polymer electrolytes found in literature. Figure 4.2 shows the *J-V* characteristics of best performing DSSC employing 4.64 wt-% PhCh / 1.16 wt-% PEO / 29 wt-% EC / 34.8 wt-% DMF / 22.4 wt-% TPAI(+I_2) / 8 wt-% BMII GPE. Fitted points (represented by unfilled circles) are based on Equation (4.1) with m value taken to be 2.35. The value of Schottky barrier used was 0.1 eV. The model shows small deviation in V_{oc} by 0.0247 V from the experimental data points (represented by line).

4.3.3 Poly(Vinyl Alcohol) (PVA)

As a synthetic polymer, PVA is semicrystalline with chemical formula of $[CH_2CH(OH)]_n$. PVA has hydroxyl and carbonyl functional groups that can interact with the dissociated salt. Similar to chitosan, PVA is nontoxic, hydrophilic, biocompatible, inexpensive, biodegradable, and has good mechanical strength. It is also thermally and chemically stable, adhesive, and has good film forming ability [69]. PVA has the glass transition temperature of 355 K [35]. The GPEs using PVA as polymer host with their application in DSSCs under 1 Sun illumination have been tabulated in Table 4.3. The photoanode used was double-layered TiO_2 deposited on FTO glass and CE was Pt/FTO unless stated otherwise. It is to be noted that DMSO was also used as solvent and plasticizer

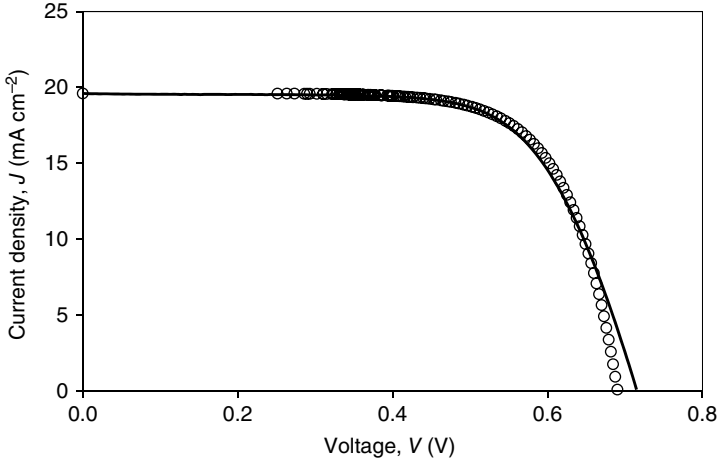

Figure 4.2 *J-V* characteristics of best performing N3 DSSC using PhCh-PEO-EC-DMF-TPAI(+I_2)-BMII GPE.

other than EC and propylene carbonate (PC) in the preparation of GPEs listed in the table. DMSO has high boiling point of 189 °C, high dielectric constant of 47.24, low melting temperature of 18.45 °C and low viscosity of 1.987 cP at 25 °C. PC, on the other hand, has dielectric constant of 64.4, boiling point of 240 °C, melting point of –55 °C and viscosity of 2.53 cP at 25 °C.

Synthetic ruthenium-based complexes are the most popular and successful sensitizers that are capable of absorbing light in the visible, ultraviolet and near-infrared (NIR) regions. N719 (*cis*-diisothiocyanato-*bis*(2,2'-bipyridyl-4,4'-dicarboxylato)ruthenium(II)*bis*(tetrabutyl-ammonium or simply ruthenizer 535-*bis* TBA) and N3 (*cis*-diisothiocyanato-*bis*(2,2'-bipyridyl-4,4'-dicarboxylic acid)ruthenium(II) or simply ruthenizer 535) dyes are two examples of ruthenium-based sensitizers. The chemical structure of N3 dye, also known as red dye, contains four carboxylic (–COOH) functional groups whereas the N719 or the blue dye has two carboxylic groups and two tetrabutylammonium (COO – TBA) groups. This means that N3 dye has four free carboxylic groups for anchoring while N719 has two. Nonetheless, it is known that N719 dye exhibits superior performance to N3 dye due to reduction in electrostatic repulsion owing to larger structure of the former, thus resulting in enhanced dye adsorption [81]. Moreover, the molar absorption coefficient of N719 is higher than that of N3. Gratzel's group has also stated that N719 DSSC attained better photovoltaic performance than N3 and gave a higher V_{oc} but comparable J_{sc} [82]. Based on Table 4.3, it is evident that the η of cell using N719 dye with electrolyte composition of 15.15 wt-% PVA / 22.73 wt-% EC / 30.3 wt-% PC / 31.82 wt-% KI(+I_2) is higher than the cell using the same electrolyte composition but with N3 dye [74, 79]. The usage of N719 has resulted in increment in V_{oc}, *FF*, and η [79]. These findings seem to be contradicting those reported by Bandara *et al.* [81]. Although Bandara and coauthors have also observed improvement in efficiency when using N719 dye in DSSC with GPE containing PAN-EC-PC-CsI-TPAI(+I_2)-MPII-TBP, it was J_{sc} and η that increased [81]. Nevertheless, N719 has one shortcoming – it cannot absorb in the red range of visible spectrum whereas N3 can [82].

The results obtained in references [71, 74, 75, 77] demonstrated the importance of a compact TiO_2 layer in ensuring good performance by suppressing the electron recombination. Using the same electrolyte (15.15 wt-% PVA / 22.73 wt-% EC / 30.3 wt-% PC / 22.27 wt-% KI / 9.55 wt-% TPAI(+I_2)) and N3 dye, the cell with a compact TiO_2 layer beneath the mesoporous TiO_2 layer gave higher efficiency of 5.51% [71] compared to that without the compact layer (η = 3.12%) [77]. Similarly, for the case of a single salt KI electrolyte, the N3 DSSC with a double-layered TiO_2 exhibited better performance (η = 3.83%) [75] than the cell using a photoanode consisting of only one TiO_2 mesoporous layer (η = 2.64%) [74]. J_{sc} and *FF* have increased along with η but V_{oc} has decreased with the existence of compact blocking layer in the photoanode [75]. Note that the compact layer was also present in the work in references [70, 72, 73, 76, 78]

whereas in references [79, 80] the TiO_2 photoanode is without the compact layer. Note also that ITO has been used as substrate in the work in reference [73]. The mixed cation effect has also been examined in the PVA-EC-PC based GPEs containing KI, TMAI, TPAI, and TBAI salts. It is found that both electrolytes containing the same ratio of 70% KI / 30% TPAI and 70% KI / 30% TMAI showed the best performance with the efficiencies of 3.12% and 3.45%, respectively [74, 77]. Better performance of KI-TMAI electrolyte may be due to the fact that it has higher ambient conductivity of 12.91 mS cm^{-1}, thereby leading to higher J_{sc} (9.12 mA cm^{-2}) and η [74]. In contrast, the best efficiency of 5.80% was achieved by the DSSC using 30% KI / 70% TBAI electrolyte [75]. When part of the KI salt has been substituted with TBAI, improvement in photovoltaic parameters in terms of J_{sc}, V_{oc}, *FF*, and η of the cell can be observed with expected decrement in conductivity. For single salt electrolyte systems, PVA-KI GPE exhibited higher conductivity but lower efficiency than PVA-TBAI GPE [75]. J_{sc} and V_{oc} followed the efficiency trend whereas *FF* followed the conductivity variation.

One viable way to boost the efficiency is to incorporate additives such as TBP, pyridine, and guadinium thiocyanate, to name a few. There are various means for the incorporation of additives; for instance, treating the TiO_2 photoanode with TBP and adding TBP into electrolyte system with the mutual aim to suppress dark current and hinder electron recombination from taking place at the electrode/electrolyte interface [73]. By just immersing the TiO_2 into TBP solution for a mere 15 s has resulted in a 28%, 83%, and 87% increase in V_{oc}, *FF*, and η, respectively, compared to the cell without TBP treatment [73]. TBP can improve the V_{oc} by shifting the TiO_2 conduction band upon interacting its N atom at pyridine ring with Lewis acid sites of TiO_2 surface [83]. In most cases, in the presence of TBP increase in V_{oc} is detected with decrement in J_{sc} [84,85]. For DSSC using natural chlorophyll extracted from *Hyophila involuta* moss [72], V_{oc} has been enhanced from 0.58 to 0.64 V whereas J_{sc} decreased from 5.96 to 3.71 mA cm^{-2} when the photoanode was immersed in TBP solution for one hour. However, overall the efficiency did not increase but reduced to 1.69%. Nevertheless, when TBP was incorporated into the PVA-EC-PC-KI-TPAI electrolyte, the chlorophyll cell showed increment in *FF* and η by 26 and 8.5%, respectively. The V_{oc}, on the other hand, decreased slightly from 0.58 to 0.55 V along with the decrement in J_{sc} as expected. Hence, it can be said that adding TBP into a PVA-based electrolyte system is a better way to enhance the efficiency rather than subjecting the photoanode to TBP treatment. In another unrelated case with a PVA-EC-PC-KI-TPAI electrolyte system, the opposite effect was observed with increment in J_{sc} of 0.14 mA cm^{-2} and decrement in V_{oc} of 0.03 V upon the addition of TBP in the electrolyte [75]. The *FF*, however, remained the same but the efficiency was enhanced to 6.03% for the N3 cell using TBP added electrolyte [75].

To further enhance cell efficiency with PVA-KI-TPAI GPE, the addition of third salt can be an alternative. Upon incorporation of BMII as ternary salt, the efficiency has been further increased to 6.40% with an increment percentage of 10.3% [75]. From Table 4.3, this can be seen to be accompanied by enhancement in J_{sc} of 26.4% whereas V_{oc} can be seen to decrease while *FF* remains the same. Although its conductivity is unknown, it can be expected that the conductivity will be increased with the addition of BMII as BMII contributes to the number density of mobile ions, reduces the rigidity of polymer chains, thus improving its flexibility and mobility of ions. A usual method of increasing the conductivity, and hence efficiency, is the inclusion of plasticizers in GPEs. Diethyl carbonate (DEC) has been added into PVA-based GPE with binary salts of KI and TPAI, as can be seen from Table 4.3 in reference [80]. DEC is in liquid form and has dielectric constant 3.1, boiling temperature 126 °C, melting temperature –43 °C, and viscosity of 0.749 cP at 25 °C. Notably, a 28.7% enhancement in conductivity was observed upon 5 wt-% DEC presence in GPE. Plasticizer can assist in ion dissociation and promote ion transfer for conduction. However, there is no improvement in J_{sc} while *FF* decreased slightly. Nevertheless, V_{oc} and efficiency showed increments of 11.1% and 4.2%, respectively [80].

Following the work [72], it is evident that that chenodeoxycholic acid (CDCA) has been added into the solution containing chlorophyll extracted from *Hyophila involuta* moss with the aim to improve the stability of the organic molecules. Additives such as CDCA assist in the binding of dye molecules to the TiO_2 surface in order to facilitate better electron injection and, thereby, improving J_{sc} and efficiency [86]. Furthermore, CDCA can help to block self-aggregation of the chlorophyll molecules,as dye aggregation is unfavorable to DSSC performance due to inefficient electron injection [87]. The presence of CDCA also aided in suppressing electron recombination reaction [88]. As a result, it is obvious in Table 4.3 that J_{sc} and efficiency have been increased to 8.44 mA cm^{-2} and 2.62% from 5.96 mA cm^{-2} and 2%, respectively, when 5 mM CDCA was incorporated into the chlorophyll solution [72]. Besides CDCA, ferulic acid (FA) has also been used in *Hyophila involuta* chlorophyll and demonstrated an improvement in the performance for cells having PVA-based single and double salt GPEs [70, 71]. For single salt KI PVA GPE, increase in J_{sc}, *FF*, and efficiency by 9.9, 86.7, and 67.5%, respectively, was observed whereas *FF* and efficiency were enhanced by 9.3 and 2.5% only in a cell with double salt KI-TPAI GPE. Yet, at the same time, J_{sc} did not show any improvement. It is to be noted that an excessive amount of FA added into the dye would lead to deterioration in DSSC performance [70]. It can be inferred that CDCA works better in improving the performance than FA in the chlorophyll sensitized cell using PVA-binary salt GPE.

As for PVA-based GPE, highest efficiency obtained to date in our group is 7.49% using N3 dye with the electrolyte having a composition of 5.7 wt-% PVA / 5.7 wt-% PEO / 24.4 wt-% EC / 24.4 wt-% DMSO / 19.5 wt-% TBAI(+I_2) / 20.3 wt-% BMII

Table 4.3 Photovoltaic performance of DSSCs using PVA-based GPEs with their ambient conductivities.

GPE	Dye	σ (S cm^{-1})	J_{sc} (mA cm^{-2})	V_{oc} (V)	*FF*	η (%)	Ref.
15.15 wt-% PVA 22.73 wt-% EC 30.3 wt-% PC 31.82 wt-% KI(+I_2)	Chlorophyll (*Hyophila involuta* moss)	1.25×10^{-3}	4.53	0.61	0.30	0.83	[70]
15.15 wt-% PVA 22.73 wt-% EC 30.3 wt-% PC 31.82 wt-% KI(+I_2)	Chlorophyll (*Hyophila involuta* moss) + 3 wt-% FA	1.25×10^{-3}	4.98	0.50	0.56	1.39	[70,71]
15.15 wt-% PVA 22.73 wt-% EC 30.3 wt-% PC 31.82 wt-% KI(+I_2)	Chlorophyll (*Hyophila involuta* moss)	1.25×10^{-2}	4.59	0.61	0.64	1.77	[72]
15.15 wt-% PVA 22.73 wt-% EC 30.3 wt-% PC 22.27 wt-% KI 9.55 wt-% TPAI(+I_2)	Chlorophyll (*Hyophila involuta* moss)	9.72×10^{-3}	5.96	0.58	0.58	2.00	[72]
15.15 wt-% PVA 22.73 wt-% EC 30.3 wt-% PC 22.27 wt-% KI 9.55 wt-% TPAI(+I_2)	Chlorophyll (*Hyophila involuta* moss)	9.72×10^{-3}	3.71	0.64	0.72	1.69	[72]
15.15 wt-% PVA 22.73 wt-% EC 30.3 wt-% PC 22.27 wt-% KI 9.55 wt-% TPAI(+I_2)	Chlorophyll (*Hyophila involute* moss) + 3 wt-% FA	9.72×10^{-3}	5.94	0.55	0.63	2.05	[71]
15.15 wt-% PVA 22.73 wt-% EC 30.3 wt-% PC 22.27 wt-% KI 9.55 wt-% TPAI(+I_2) + 0.7 M TBP	Chlorophyll (*Hyophila involuta* moss)	—	5.37	0.55	0.73	2.17	[72]

Table 4.3 (Continued)

GPE	Dye	σ (S cm^{-1})	J_{sc} (mA cm^{-2})	V_{oc} (V)	*FF*	η (%)	Ref.
15.15 wt-% PVA 22.73 wt-% EC 30.3 wt-% PC 22.27 wt-% KI 9.55 wt-% TPAI(+I_2)	Chlorophyll (*Hyophila involuta* moss) + 5 mM CDCA	9.72×10^{-3}	8.44	0.54	0.58	2.62	[72]
10.5 wt-% PVA 42.4 wt-% EC 42.4 wt-% PC 4.7 wt-% KI(+I_2)	N3	1.83×10^{-3}	2.31	0.56	0.36	0.47	[73]
10.5 wt-% PVA- 42.4 wt-% EC 42.4 wt-% PC 4.7 wt-% KI(+I_2)	N3	1.83×10^{-3}	1.87	0.72	0.66	0.88	[73]
9.9 wt-% PVA 39.6 wt-% EC 39.6 wt-% PC- 6.5 wt-% KI 4.4 wt-% TPAI (+I_2)	N3	2.18×10^{-3}	9.66	0.77	0.44	3.27	[73]
15.15 wt-% PVA 22.73 wt-% EC 30.3 wt-% PC 31.82 wt-% TMAI(+I_2)	N3	3.94×10^{-3}	5.80	0.60	0.58	2.02	[74]
9.9 wt-% PVA 39.6 wt-% EC 39.6 wt-% PC 10.9 wt-% KI(+I_2)	N3	4.08×10^{-3}	6.27	0.72	0.44	1.97	[73]
15.15 wt-% PVA 22.73 wt-% EC 30.3 wt-% PC 31.82 wt-% TBAI(+I_2)	N3	4.68×10^{-3}	11.13	0.67	0.63	4.70	[75]
15.15 wt-% PVA 22.73 wt-% EC 30.3 wt-% PC 9.55 wt-% KI- 22.27 wt-% TBAI(+I_2)	N3	5.25×10^{-3}	12.56	0.65	0.71	5.80	[75]

(*Continued*)

Table 4.3 (Continued)

GPE	Dye	σ ($S\,cm^{-1}$)	J_{sc} ($mA\,cm^{-2}$)	V_{oc} (V)	*FF*	η (%)	Ref.
7.14 wt-% PVA 7.14 wt-% PEO 30.61 wt-% EC 30.61 wt-% DMSO 24.5 wt-% TBAI(+I_2)	N3	5.50×10^{-3}	12.31	0.66	0.66	5.36	[76]
15.2 wt-% PVA 22.73 wt-% EC 30.3 wt-% PC 31.82 wt-% TPAI(+I_2)	N3	6.24×10^{-3}	6.80	0.71	0.57	2.75	[77]
5.7 wt-% PVA 5.7 wt-% PEO 24.4 wt-% EC 24.4 wt-% DMSO 19.5 wt-% TBAI(+I_2) 20.3 wt-% BMII	N3	8.38×10^{-3}	14.25	0.79	0.67	7.49	[78]
15.15 wt-% PVA 22.73 wt-% EC 30.3 wt-% PC 22.27 wt-% KI 9.55 wt-% TPAI(+I_2)	N3	9.72×10^{-3}	8.01	0.63	0.62	3.12	[77]
15.15 wt-% PVA 22.73 wt-% EC 30.3 wt-% PC 22.27 wt-% KI 9.55 wt-% TPAI(+I_2)	N3	9.72×10^{-3}	14.10	0.63	0.62	5.51	[71]
15.15 wt-% PVA 22.73 wt-% EC 30.3 wt-% PC 31.82 wt-% KI(+I_2)	N3	1.25×10^{-2}	11.03	0.51	0.68	3.83	[75]
15.15 wt-% PVA 22.73 wt-% EC 30.3 wt-% PC 31.82 wt-% KI(+I_2)	N719	1.25×10^{-2}	5.08	0.68	0.79	2.74	[79]
15.15 wt-% PVA 22.73 wt-% EC 30.3 wt-% PC 31.82 wt-% KI(+I_2)	N3	1.25×10^{-2}	6.60	0.63	0.64	2.64	[74]

Table 4.3 (Continued)

GPE	Dye	σ (S cm^{-1})	J_{sc} (mA cm^{-2})	V_{oc} (V)	*FF*	η (%)	Ref.
14.39 wt-% PVA 21.59 wt-% EC 28.79 wt-% PC 21.16 wt-% KI 9.07 wt-% TPAI(+I_2) 5 wt-% DEC	N3	1.26×10^{-2}	8.00	0.70	0.58	3.25	[80]
15.15 wt-% PVA 22.73 wt-% EC 30.3 wt-% PC 22.27 wt-% KI 9.55 wt-% TMAI(+I_2)	N3	1.29×10^{-2}	9.12	0.62	0.61	3.45	[74]
14.17 wt-% PVA 21.26 wt-% EC 28.34 wt-% PC 8.93 wt-% KI 20.83 wt-% TBAI(+I_2) 6.47 wt-% TBP	N3	—	13.70	0.62	0.71	6.03	[75]
14.46 wt-% PVA 21.69 wt-% EC 28.92 wt-% PC-9.11 wt-% KI 21.26 wt-% TBAI(+I_2) 4.56 wt-% BMII	N3	—	15.88	0.57	0.71	6.40	[75]

FA = ferulic acid; TBP = 4-tert-butylpyridine; CDCA = chenodeoxycholic acid; DEC = diethyl carbonate

[78]. Also, it is to be noted that the DSSC using natural dye from *Hyophila involuta* moss chlorophyll with PVA-EC-PC-KI-TPAI(+I_2) GPE exhibited remarkably high efficiency of 2.62% [72] compared to many other chlorophyll DSSCs employing liquid electrolytes [89–91].

4.3.4 Polyacrylonitrile (PAN)

PAN is a synthetic semicrystalline organic polymer with chemical formula $(C_3H_3N)_n$, dielectric constant of 4.2 and glass transition temperature around 104 °C [92]. It is understood that PAN as polymer matrix does not take part in ionic conduction but offers a host medium for structural stability [93]. Due to the polar feature, the nitrile groups in PAN can hold more free cations [94].

Moreover, PAN is suitable with polar substances such EC and PC and, thus, can dissolve easily [95]. Many researchers worldwide have employed PAN as polymer host in GPE for application in DSSCs [64, 65, 81, 93, 96–99]. Wanninayake *et al.* [100] reported a DSSC with efficiency of 6.40% using GPE with composition 13.64 wt-% PAN / 31.82 wt-% EC / 45.45 wt-% PC / 3.03 wt-% TPAI / 6.06 wt-% LiI(+I_2). In the work of Bandara *et al.* [97], PAN-based GPE containing double salts, i.e. THAI and magnesium iodide (MgI_2), exhibited an efficiency of 3.50%. The GPE composition was 9.8 wt-% PAN / 39.22 wt-% EC / 39.22 wt-% PC / 1.96 wt-% MgI_2 / 9.8 wt-% THAI(+I_2). As mentioned earlier, TPAI is capable of accomplishing the best performance in terms of highest J_{sc} and highest η among other quaternary ammonium iodide salts [64] whereas, among the alkaline metal iodide salts, cesium iodide (CsI) has been reported to deliver optimal efficiency of 3.48% [65]. But the highest J_{sc} was obtained by rubidium iodide (RbI) salt with the value of 9.43 mA cm^{-2} [65]. Table 4.4 shows some works done by our group on PAN-based GPEs in DSSCs. Similarly, the DSSCs having double-layered TiO_2/FTO photoanode and Pt/FTO CE were irradiated at 1 Sun unless stated otherwise.

Again, it can be inferred that with CDCA as coadsorbent in chlorophyll dye, better J_{sc} and efficiency can be obtained due to enhanced chlorophyll adsorption on TiO_2 photoanode [101], as can be seen from Table 4.4. In reference [103], we have also attempted an unconventional way of preparing GPE, i.e. without the inclusion of iodine as redox mediator in PAN-BMII-LiBOB electrolyte. Lithium bis(oxalato)borate (LiBOB) is a unique salt that has been used for lithium-ion batteries application rather than in DSSCs. It has good electrochemical and thermal stabilities with decomposition temperature of 302 °C. The BOB^- anion, which consists of four carbonyl oxygen and four ether oxygen atoms that are loosely bound to the B atom, has only one single negative charge, making it weakly coordinating; thus, it can dissociate easily. Consequently, LiBOB is expected to offer good ionic conductivity due to its high dissociation. LiBOB is also known to form good interfacial contact with graphite/anode in lithium-ion batteries [106] and therefore, it is expected that it will do the same in DSSCs. The rationale behind the utilization of LiBOB in DSSCs is to study the effect of cations without I^- ions interfering so that the effect is more pronounced. Hence, a larger number of smaller lithium cations will be provided with the use of LiBOB as it has low lattice energy with a large BOB anion. It was anticipated that the triiodide I_3^- ions can still be produced from I^- ions resulting from BMII dissociation. Although the efficiency obtained was low at only 0.41%, it shows that the PAN-BMII-LiBOB GPE is still useful and functional in DSSCs [103]. Nevertheless, the efficiency was enhanced to 0.65% with the presence of iodine in the GPE. It is interesting to note that a noniodide salt, i.e. tetraethylammonium tetrafluoroborate (Et_4NBF_4), has been employed by Cui *et al.* [32] and used for the first time in a DSSC. The GPE

Table 4.4 Photovoltaic performance of DSSCs using PAN-based GPEs with their ambient conductivities.

GPE	Dye	σ (S cm^{-1})	J_{sc} (mA cm^{-2})	V_{oc} (V)	*FF*	η (%)	Ref.
9.99 wt-% PAN 41.46 wt-% EC 38.46 wt-% PC 4.41 wt-% LiI 4.43 wt-% TPAI(+I_2 1.25 wt-% BMII	Carotenoid (saffron)	3.91×10^{-3}	0.61	0.54	0.74	0.24	[101]
9.99 wt-% PAN 41.46 wt-% EC 38.46 wt-% PC 4.41 wt-% LiI 4.43 wt-% TPAI(+I_2) 1.25 wt-% BMII	Carotenoid (saffron) + 30 wt-% CDCA	3.91×10^{-3}	1.26	0.48	0.51	0.31	[101]
10 wt-% PAN 40 wt-% EC 40 wt-% PC 10 wt-% TPAI(+I_2)	Chlorophyll (*Hyophila involuta* moss)	5.25×10^{-3}	5.78	0.60	0.57	1.97	[102]
20 wt-% PAN 30 wt-% BMII-1 M LiBOB-DMSO	N3	3.50×10^{-3}	5.04	0.28	0.29	0.41	[103]
20 wt-% PAN 30 wt-% BMII-1 M LiBOB-DMSO + I_2	N3	—	2.65	0.51	0.48	0.65	[103]
10.45 wt-% PAN 43.37 wt-% EC 40.24 wt-% PC 4.63 wt-% TPAI(+I_2) 1.31 wt-% BMII	N3	2.32×10^{-3}	10.10	0.65	0.58	3.80	[104]
10.45 wt-% PAN 43.37 wt-% EC 40.24 wt-% PC 4.63 wt-% TPAI(+I_2) 1.31 wt-% BMII	N3	2.32×10^{-3}	12.72	0.61	0.54	4.16	[105]

(*Continued*)

Table 4.4 (Continued)

GPE	Dye	σ (S cm^{-1})	J_{sc} (mA cm^{-2})	V_{oc} (V)	*FF*	η (%)	Ref.
9.99 wt-% PAN 41.46 wt-% EC 38.46 wt-% PC 4.41 wt-% LiI 4.43 wt-% TPAI(+I_2) 1.25 wt-% BMII	N3	3.91×10^{-3}	21.00	0.48	0.53	5.40	[104]
9.99 wt-% PAN 41.46 wt-% EC 38.46 wt-% PC 4.41 wt-% LiI 4.43 wt-% TPAI(+I_2) 1.25 wt-% BMII	N3	3.91×10^{-3}	20.61	0.50	0.53	5.41	[105]

having configuration of (PEO/PVdF-HFP)-KI(+I_2)-Et_4NBF_4-SiO_2 exhibited better performance, with J_{sc} of 14.34 mA cm^{-2} and η of 6.24%, under illumination with intensity of 96.17 mW cm^{-2}, than GPE without Et_4NBF_4 (J_{sc} of 12.06 mA cm^{-2} and η of 4.51%) [32]. The authors attributed it to the increase in ionic conductivity and triiodide diffusion coefficient.

Based on the discussions in preceding sections, it can be concluded that the effect of mixed cations on improving the efficiency of DSSCs is similar/the same regardless of which polymer matrix being used in the electrolyte. In an attempt to test whether the mixed cation effect can also work in PAN-based GPEs with three iodide-based salts, GPE containing PAN polymer host and LiI, TPAI and BMII as ternary salts has been prepared and its performance compared with PAN-TPAI-BMII GPE [104]. Upon the addition of LiI as the third salt, the conductivity, as foreseen, has increased by 68.5% to 3.91×10^{-3} S cm^{-1} along with increment in J_{sc} and efficiency by 108% and 42%, respectively. It is evident in Table 4.4 that DSSCs in references [104] and [105] have employed the identical composition of PAN-based GPEs having double (TPAI-BMII) and ternary (TPAI-BMII-LiI) salts and the effect of mixed cations is also dominant, where better performance was attained by PAN-based GPE containing three salts with incremental percentages of 62% and 30% in J_{sc} and efficiency compared to having two salts [105]. The difference between [104] and [105] is that double-layered TiO_2 photoanode was used in [104] while the TiO_2 photoanode in [105] consists of only one layer, i.e. without the compact layer. Surprisingly, better efficiency is achieved for cells having a photoanode without the compact layer in both binary and tertiary salts GPEs [105]. This may be due to different

procedure of TiO_2 sensitization by N3 dye. The TiO_2 photoanodes were soaked in solution containing 0.5 mM N3 dye and ethanol solvent at 60 °C and then kept under ambient temperature for 24 h [105]. Meanwhile, in the work [104], TiO_2 sensitization was carried out by immersing the photoanode in 0.3 mM ethanol solution of N3 dye at room temperature for 24 h. Also to be taken into consideration is the active area of the cells for irradiation in [104] and [105], which is 0.20 cm^2 and 0.12 cm^2, respectively.

Nonetheless, based on the above results in [104] and [105], it implies that the mixed cation effect also works well in ternary iodide salts and has constructive effects on the DSSC performance. It is worthy to mention that using the same composition GPE having ternary iodide salts, a prototype solar panel comprising a parallel pair of eight solar cells connected in series has been fabricated and its feasibility tested in operating small decorative ornaments as well as calculator. Under low light illumination of 8 W m^{-2} intensity, V_{oc} of 5.4 V and short circuit current of 6.4 mA were produced by the solar panel. In other words, this means that a maximum output power of 17.1 mW with average power of conversion efficiency of 3.7% has been achieved [104].

4.3.5 Polyvinylidene Fluoride (PVdF)

PVdF has the chemical formula C_2H_2F in which the fluorine atom has lone electron pairs to interact with the cation of the salt. Having small ionic radius, the fluorine atom (–C–F) has very high electronegativity and, thus, can enhance the ion transport due to reduced recombination rate at the TiO_2/polymer electrolyte interface in DSSCs [107]. PVdF, which is semicrystalline in nature, has dielectric constant of 8.4 and glass transition temperature of 235 K [108]. It offers good flexibility and is resistant against corrosion, making it attractive for use in polymer electrolyte for application in devices [109]. Table 4.5 lists the preliminary work done by our group on DSSCs utilizing PVdF-based GPEs with N719 sensitizer under irradiance of 1 Sun. Again, the CE is Pt deposited on FTO glass substrate whereas the photoanode consists of only one layered TiO_2.

The mixed cation effect has again been verified in N719 DSSCs using PVdF-based GPE systems with double salts of KI and TPAI [110]. When part of the smaller KI salt has been replaced with the larger TPAI salt, J_{sc} and efficiency showed large incremental percentage of 98.6% and 65.4% with minimal decrement in V_{oc}. Conversely, its conductivity decreased. Although PVdF-based GPE with single KI salt exhibited the highest conductivity, its efficiency is the lowest among PVdF-TPAI and PVdF-binary salt GPEs [110]. PVdF-based GPE containing THAI has been reported to achieve ambient conductivity of 3.43 mS cm^{-1} and efficiency of 2.08% [111]. Efficiencies of 6.74% [112] and 7.30% [28] have been obtained by PVdF counterparts, i.e. PVdF-HFP based GPEs indicating reasonably good performance but it employed volatile solvents,

Table 4.5 Photovoltaic parameters of DSSCs using PVdF-based GPEs with their ambient conductivities.

GPE	σ (S cm^{-1})	J_{sc} (mA cm^{-2})	V_{oc} (V)	*FF*	η (%)	Ref.
10 wt-% PVdF 40 wt-% EC 40 wt-% PC 10 wt-% KI(+I_2)	1.07×10^{-2}	4.61	0.75	0.69	2.37	[110]
10 wt-% PVdF 40 wt-% EC 40 wt-% PC 10 wt-% TPAI(+I_2)	4.38×10^{-3}	6.15	0.68	0.69	2.90	[110]
10 wt-% PVdF 40 wt-% EC 40 wt-% PC 1.66 wt-% KI 8.34 wt-% TPAI(+I_2)	5.53×10^{-3}	9.16	0.67	0.63	3.92	[110]

namely acetonitrile and acetone, which may pose flammability issues, thus making it less favorable. Comparatively, other polymers such as PhCh, PVA, and PAN are more attractive and advantageous for use as polymer host without the need to use such solvents.

4.4 Summary and Outlook

As a summary, polymers, namely Ch, PhCh, PAN, PVA and PVdF, have potential for use as polymer matrix in GPEs and tested in DSSCs. Factors such as the type of polymer host, single or dual polymers, type of salt, single/binary/ternary salts etc. are the parameters influencing the conductivity and subsequently the efficiency of DSSCs. In particular, the effect of a cation mix using small and large cations is significant in enhancing the DSSC performance regardless of the type of polymer host. Other than that, the type of sensitizers, condition of photoanode, and type of counter electrodes are also influencing factors in determining the DSSC performance. It is hoped that the information gathered will be useful in the design of good GPEs and DSSCs. Although the performance of DSSCs using GPEs looks promising, there is still room for improvements. Nonetheless, we remain hopeful and optimistic that DSSC efficiency can be further enhanced and their stability improved for practical use.

Acknowledgements

The authors thank the University of Malaya for UMRG grant awarded (Grant No. RP024C-AFR).

References

1 G. Wolfbauer, A.M. Bond, J.C Eklund, and D.R. MacFarlane, A channel flow cell system specifically designed to test the efficiency of redox shuttles in dye sensitized solar cells, *Solar Energy Material Solar Cells*, **70**, 2001, 85–101.
2 J. Wu, Z. Lan, S. Hao, *et al*., Progress on the electrolytes for dye-sensitized solar cells, *Pure and Applied Chemistry*, **80**, 2008, 2241–2258.
3 F. Bella, G. Griffini, M. Gerosa, and S. Turri, Performance and stability improvements for dye-sensitized solar cells in the presence of luminescent coatings, *Journal of Power Sources*, **283**, 2015, 195–203.
4 C.-L. Chen, T.-W. Chang, H. Teng, *et al*., Highly efficient gel-state dye-sensitized solar cells prepared using poly(acrylonitrile-co-vinyl acetate) based polymer electrolytes, *Physical Chemistry Chemical Physics*, **15**, 2013, 3640–3645.
5 G.P. Smestad, Education and solar conversion: Demonstrating electron transfer, *Solar Energy Materials and Solar Cells*, **55**, 1998, 157–178.
6 H. Zhu, H. Zeng, V. Subramanian, *et al*., Anthocyanin-sensitized solar cells using carbon nanotube films as counter electrodes, *Nanotechnology*, **19**, 2008, 465204 (5pp).
7 T. Denaro, V. Baglio, M. Girolamo, *et al*., Investigation of low cost carbonaceous materials for application as counter electrode in dye-sensitized solar cells, *Journal of Applied Electrochemistry*, **39**, 2009, 2173–2179.
8 S.S. Jeon, C. Kim, J. Ko, and S.S. Im, Speherical polypyrrole nanoparticles as highly efficient counter electrode for dye-sensitized solar cells, *Journal of Materials Chemistry*, **21**, 2011, 8146 –8151.
9 Q. Li, J. Wu, Q. Tang, *et al*., Application of microporous polyaniline counter electrode for dye-sensitized solar cells, *Electrochemistry Communications*, **10**, 2008, 1299 –1302.
10 K.-M. Lee, W.-H. Chiu, H.-Y. Wei, *et al*., Effects of mesoscopic poly(3,4-ethylenedioxythiophene) films as counter electrodes for dye-sensitized solar cells, *Thin Solid Films*, **518**, 2010, 1716–1721.
11 W. Wei, K. Sun, and Y.H. Hu, An efficient counter electrode material for dye-sensitized solar cells-flower-structured 1 T metallic phase MoS_2, *Journal of Materials Chemistry A*, **4**, 2016, 12398–12401.
12 X. Wang, B. Batter,Y. Xie, *et al*., Highly crystalline, small sized, monodisperse α-NiS nanocrystal ink as an efficient counter electrode for dye-sensitized solar cells, *Journal of Materials Chemistry A*, **3**, 2015, 15905–15912.

13 J.-Y. Lin, S.-W. Chou, Highly transparent $NiCo_2S_4$ thin film as an effective catalyst toward triiodide reduction in dye-sensitized solar cells, *Electrochemistry Communications*, **37**, 2013, 11 –14.

14 M. Ni, M.K.H. Leung, Dennis Y.C. Leung, and K. Sumathy, Theoretical modeling of TiO_2/TCO interfacial effect on dye-sensitized solar cell performance, *Solar Energy Materials & Solar Cells*, **90**, 2006, 2000–2009.

15 L. Dloczik, O. Ileperuma, I. Lauermann, *et al.*, Dynamic response of dye-sensitized nanocrystalline solar cells: Characterization by intensity-modulated photocurrent spectroscopy, *Journal of Physical Chemistry B*, **101**, 1997, 10281–10289.

16 K.D. Benkstein, N. Kopidakis, J. Van de Lagemaat, and A.J. Frank, Influence of the percolation network geometry on electron transport in dye-sensitized titanium dioxide solar cells, *Journal of Physical Chemistry B*, **107**, 2003, 7759–7767.

17 J. Shi, S. Peng, J. Pei, *et al.*, Quasi-solid-state dye-sensitized solar cells with polymer gel electrolyte and triphyenylamine-based organic dyes, *ACS Applied Materials & Interfaces*, **1**, 2009, 944–950.

18. Z. Huo, S. Dai, and C. Zhang, Low molecular mass organogelator based gel electrolyte with effective charge transport property for long-term stable quasi-solid-state dye-sensitized solar cells, *The Journal of Physical Chemistry B*, **112**, 2008, 12927–12933.

19 T.M.W.J. Bandara, T. Svensson, M.A.K.L. Dissanayake, *et al.*, Conductivity behavior in novel quasi-solid-state electrolyte based on polyacrylonitrile and tetrahexylammonium iodide intended for dye sensitized solar cells, *Journal of National Science Foundation Sri Lanka*, **41**, 2013, 175–184.

20 D. Golodnitsky, E. Strauss, E. Peled, and S. Greenbaum, Review – On order and disorder in polymer electrolytes, *Journal of The Electrochemical Society*, **162**, 2015, A2551–A2566

21 F.M. Gray, Solid Polymer Electrolytes, VCH, New York, 1991.

22 M. Forsyth, J. Sun, and D.R. MacFarlane, Novel high salt content polymer electrolytes based on high Tg polymers, *Electrochimica Acta*, **45**, 2000, 1249–1254.

23 X. Wei and D.F. Shriver, Highly conductive polymer electrolytes containing rigid polymers, *Chemistry of Materials*, **10**, 1998, 2307–2308.

24 R. Kumar, B. Singh, and S.S. Sekhon, Effect of dielectric constant of solvent on the conductivity behavior of polymer gel electrolytes, *Journal of Materials Science*, **40**, 2005, 1273–1275.

25 S. Sekhon, Conductivity behaviour of polymer gel electrolytes: Role of polymers, *Bulletin of Materials Science*, **26**, 321–328.

26 X. Shen, W. Xu, G. Liang, *et al.*, Quasi-solid-state dye-sensitized solar cells based on gel electrolytes containing different alkali metal iodide salts, *Solid State Ionics*, **179**, 2008, 2027–2030.

27 J.H. Kwon and J.S. Kim, Wire-shaped, dye-sensitized solar cells with poly(vinyl alcohol) gel electrolyte and metal filaments, *Journal of Applied Polymer Science*, **133**, 2016, 43439.

28 A.R.S. Priya, A. Subramania, Y.-S. Jung, and K.-J. Kim, High-performance quasi-solid-state dye-sensitized solar cell based on an electrospun PVdF-HFP membrane electrolyte, *Langmuir*, **24**, 2008, 9816–9819.

29 H. Yang, M. Huang, J. Wu, *et al*., The polymer gel electrolyte based on poly(methyl methacrylate) and its application in quasi-solid-state dye-sensitized solar cells, *Materials Chemistry and Physics*, **110**, 2008, 38–42.

30 M.H. Khanmirzaei, S. Ramesh, and K. Ramesh, Hydroxypropyl cellulose based non-volatile gel polymer electrolytes for dye-sensitized solar cell applications using 1-methyl-3-propylimidazolium iodide ionic liquid, *Scientific Reports*, **5**, 2015, 18056. doi: 10.1038/srep18056

31 Z. Seidalilir, R. Malekfar, H.-P. Wu, *et al*., High-performance and stable gel-state dye-sensitized solar cells using anodic TiO_2 nanotube arrays and polymer-based gel electrolytes, *ACS Applied Materials & Interfaces*, **7**, 2015, 12731–12739.

32 Y. Cui, X. Zhang, J. Feng, *et al*., Enhanced photovoltaic performance of quasi-solid-state dye-sensitized solar cells by incorporating a quarternized ammonium salt into poly(ethylene oxide)/poly(vinylidene fluoride-hexafluoropropylene) composite polymer electrolyte, *Electrochimica Acta*, **108**, 2013, 757–762.

33 M. Jumaa and B.W. Muller, Physicochemical properties of chitosan-lipid emulsions and their stability during the autoclaving process, *International Journal of Pharmaceutics*, **183**, 1999, 175–184.

34 Z. Zong, Y. Kimura, M. Takahashi, and H. Yamane, Characterization of chemical and solid state state structures of acylated chitosans, *Polymer*, **41**, 2009, 899–906.

35 K. Lewandowska, Miscibility and thermal stability of poly(vinyl alcohol)/chitosan mixtures, *Thermochimica Acta*, **493**, 2009, 42–48.

36 M.Z.A. Yahya and A.K. Arof, Studies on lithium acetate doped chitosan conducting polymer system, *European Polymer Journal*, **38**, 2002, 1191–1197.

37 Z. Osman, Z.A. Ibrahim, and A.K. Arof, Conductivity enhancement due to ion dissociation in plasticized chitosan based polymer electrolytes, *Carbohydrate Polymers*, **44**, 2001, 167–173.

38 M.H. Buraidah, L.P. Teo, S.N.F. Yusuf, *et al*., TiO_2/chitosan-$NH_4I(+I_2)$-BMII-based dye-sensitized solar cells with anthocyanin dyes extracted from black rice and red cabbage, *International Journal of Photoenergy*, **2011**, 2011, Article ID 273683.

39 T. Ueki and M. Watanabe, Macromolecules in ionic liquids: Progress, challenges and opportunities, *Macromolecules*, **41**, 2008, 3739–3749.

40 Y. Bai, Y. Cao, J. Zhang, *et al*., High-performance dye-sensitized solar cells based on solvent-free electrolytes produced from eutectic melts, *Nature Materials*, **7**, 2008, 626–630.

41 M.H. Buraidah and A.K. Arof, Characterization of chitosan/PVA blended electrolyte doped with NH_4I, *Journal of Non-Crystalline Solids*, **357**, 2011, 3261–3266.

42 M. Hema, S. Selvasekarapandian, D. Arunkumar, *et al*., FTIR, XRD and ac impedance spectroscopic study on PVA based polymer electrolyte doped with NH_4X (X = Cl, Br, I), *Journal of Non-Crystalline Solids*, **355**, 2009, 84–90.

43 S.-H.A. Lee, A.-M.S. Jackson, A. Hess, *et al*., Influence of different iodide salts on the performance of dye-sensitized solar cells containing phosphazene-based non-volatile electrolytes, *Journal of Physical Chemistry C*, **114**, 2010, 15234–15242.

44 A.M. Stephan, Review on gel polymer electrolytes for lithium batteries, *European Polymer Journal*, **42**, 2006, 21–42.

45 F.M. Gray, Polymer Electrolytes, Materials Monographs, The Royal Society of Chemistry, Cambridge, 1997.

46 N. Rakkapao, V. Vao-soongnern, Y. Masubuchi, and H. Watanabe, Miscibility of chitosan/poly(ethylene oxide) blends and effect of doping alkali and alkali earth metal ions on chitosan/PEO interaction, *Polymer*, **52**, 2011, 2618–2627.

47 H. Tributsch, Dye sensitization solar cells: a critical assessment of the learning curve, *Coordination Chemistry Reviews*, **248**, 2004, 1511–1530.

48 R. Yoksan, M. Akashi, S. Biramontri, and S. Chirachanchai, Hydrophobic chain conjugation at hydroxyl group onto γ–ray irradiated chitosan, *Biomacromolecules*, **2**, 2001, 1038–1044.

49 N.A. Aziz, S.R. Majid, and A.K. Arof, Synthesis and characterization of phthaloyl chitosan-based polymer electrolytes, *Journal of Non-Crystalline Solids*, **38**, 2012, 1581–1590.

50 S. Ngamsinlapasathian, T. Sreethawong, Y. Suzuki, and S. Yoshikawa, Doubled layered ITO/SnO_2 conducting glass for substrate of dye-sensitized solar cells. *Solar Energy Materials and Solar Cells*, **90**, 2006, 2129–2140.

51 K. Hara and H. Arakawa, Dye-sensitized solar cells in A. Luque and S. Hegedus (eds), Handbook of Photovoltaic Science and Engineering, John Wiley & Sons Ltd, Chichester, 2003, pp. 663–700.

52 W.-Y. Rho, H. Jeon, H.-S. Kim, *et al*., Recent progress in dye-sensitized solar cells for improving efficiency: TiO_2 nanotube arrays in active layer, *Journal of Nanomaterials*, **2015**, 2015, Article ID 247689.

53 S.N.F. Yusuf, M.F. Aziz, H.C. Hassan, *et al*., Phthaloylchitosan-based gel polymer electrolytes for efficient dye-sensitized solar cells, *Journal of Chemistry*, **2014**, 2014, Article ID 783023.

54 S.N.F. Yusuf, A.D. Azzahari, R. Yahya, *et al*., From crab shell to solar cell: a gel polymer electrolyte based on N-phthaloylchitosan and its application in dye-sensitized solar cells, *RSC Advances*, **6**, 2016, 27714–27724.

55 S.N.F. Yusuf, A.D. Azzahari, V. Selvanathan, *et al*., Improvement of N-phthaloylchitosan based gel polymer electrolyte in dye-sensitized solar cells using a binary salt system, *Carbohydrate Polymers*, **157**, 2017, 938–944.

56 S. Shah, I.M. Noor, J. Pitawala, *et al*., Plasmonic effects of quantum size metal nanoparticles on dye-sensitized solar cell, *Optical Materials Express*, **7**, 2017, 2069–2083.

57 S. Shah, M.H. Buraidah, L.P. Teo, *et al*., Dye-sensitized solar cells with sequentially deposited anthocyanin and chlorophyll dye as sensitizers, *Optical and Quantum Electronics*, **48**, 2016, 219 (8 pp).

58 M.H. Buraidah, S. Shah, L.P. Teo, *et al*., High efficient dye sensitized solar cells using phthaloylchitosan based gel polymer electrolytes, *Electrochimica Acta*, **245**, 2017, 846–853.

59 J. Theerthagiri, R.A. Senthil, M.H. Buraidah, *et al*., One-step electrochemical deposition of $Ni_{1-x}Mo_xS$ ternary sulfides as an efficient counter electrode for dye-sensitized solar cells, *Journal of Materials Chemistry A*, **4**, 2016, 16119–16127.

60 M.H. Buraidah, S. Shah, L.P. Teo, *et al*., Dye-sensitized solar cells utilizing phthaloylchitosan based gel polymer electrolytes containing binary salts, in A.K. Arof, M.A. Careem, and M.H. Buraidah (eds), Proceedings of the 2nd International Conference on Solar Energy Materials, Solar Cells and Solar Energy Applications, 22–24 August 2013, Centre for Ionics University of Malaya, ISBN 978-967-12067-0-6, pp. 217–222.

61 H. Yu, S. Zhang, H. Zhao, *et al*., An efficient and low-cost TiO_2 compact layer for performance improvement of dye-sensitized solar cells, *Electrochimica Acta*, **54**, 2009, 1319–1324.

62 X. Liu, D. Qin, Y. Fan, *et al*., An alternative electrolyte based on acetylacetone–pyridine–iodine for dye-sensitized solar cells, *Electrochemistry Communications*, **9**, 2007, 1735–1738.

63 J. Theerthagiri, R.A. Senthil, M.H. Buraidah, *et al*., Effect of tetrabutylammonium iodide content on PVDF-PMMA polymer blend electrolytes for dye-sensitized solar cells, *Ionics*, **21**, 2015, 2889–2896.

64 T.M.W.J. Bandara, W.J.M.J.S.R. Jayasundara, M.A.K.L. Dissanayake, *et al*., Effect of cation size on the performance of dye sensitized nanocrystalline TiO_2 solar cells based on quasi-solid state PAN electrolytes containing quarternary ammonium iodides, *Electrochimica Acta*, **109**, 2013, 609–616.

65 T.M.W.J. Bandara, H.D.N.S. Fernando, M. Furlani, *et al*., Effect of the alkaline cation size on the conductivity in gel polymer electrolytes and their influence on photo electrochemical solar cells, *Physical Chemistry Physical Physics*, **18**, 2016, 10873–10881.

66 S. Chang, Q. Li, X. Xiao, *et al*., Enhancement of low energy sunlight harvesting in dye-sensitized solar cells using plasmonic gold nanorods, *Energy& Environmental Science*, **5**, 2012, 9444–9448.

67 S.K. Tripathi, M. Rani, and N. Singh, ZnO:Ag and TZO:Ag plasmonic nanocomposite for enhanced dye sensitized solar cell performance, *Electrochimica Acta*, **167**, 2015, 179–186.

68 J. Theerthagiri, R.A. Senthil, M.H. Buraidah, *et al*., Synthesis and characterization of $(Ni_{1-x}Co_x)Se_2$ based ternary selenides as electrocatalyst for triiodide reduction in dye-sensitized solar cells, *Journal of Solid State Chemistry*, **238**, 2016, 113–120.

69 C.-C. Yang and G.M. Wu, Study of microporous PVA/PVC composite polymer membrane and its application to MnO_2 capacitors, *Materials Chemistry & Physics*, **114**, 2009, 948–955.

70 H.C. Hassan, Z.H.Z. Abidin, M.A. Careem, and A.K. Arof, Characterization of dye sensitized solar cell based on chlorophyll extracted from algae with $C_{10}H_{10}O_4$ as an additive, in A.K. Arof, M.A. Careem, and M.H. Buraidah (eds), Proceedings of the 2nd International Conference on Solar Energy Materials, Solar Cells and Solar Energy Applications, 22–24 August 2013, Centre for Ionics University of Malaya, ISBN 978-967-12067-0-6, pp. 187–192.

71 M.A. Careem, M.H. Buraidah, M.F. Aziz, *et al*., Polyvinyl alcohol gel polymer electrolyte based dye sensitized solar cells, *Proceedings of the 14th Asian Conference on Solid State Ionics*, 2014, ISBN 978-981-09-1137-9, pp. 159–168.

72 H.C. Hassan, Z.H.Z. Abidin, F.I. Chowdhury, and A.K. Arof, A high efficiency chlorophyll sensitized solar cell with quasi solid PVA based electrolyte, *International Journal of Photoenergy*, **2016**, 2016, Article ID 3685210.

73 A.K. Arof, M. Naeem, F. Hameed, *et al*., Quasi solid state dye-sensitized solar cells based on polyvinyl alcohol (PVA) electrolytes containing I^-/I_3^- redox couple, *Optical and Quantum Electronics*, **46**, 2014, 143–154.

74 M.F. Aziz, I.M. Noor, M.H. Buraidah, *et al*., PVA-based gel polymer electrolytes doped with $(CH_3)_4NI$/KI for application in dye-sensitized solar cells, *15th International Conference on Transparent Optical Networks*, 2013, Article 6602906.

75 M.F. Aziz, M.H. Buraidah, M.A. Careem, and A.K. Arof, PVA based gel polymer electrolytes with mixed iodide salts (K^+I^- and $Bu_4N^+I^-$) for dye-sensitized solar cell application, *Electrochimica Acta*, **182**, 2015, 217–223.

76 T.S. Tiong, M.H. Buraidah, L.P. Teo, and A.K. Arof, Conductivity studies of poly(ethylene oxide)(PEO)/poly(vinyl alcohol) (PVA) blend gel polymer electrolytes for dye-sensitized solar cells, *Ionics*, **22**, 2016, 2133–2142.

77 M.F. Aziz, M.H. Buraidah, and A.K. Arof, Dye-sensitized solar cells using binary iodide-PVA gel electrolyte, *15th International Conference on Transparent Optical Networks*, 2013, Article 6602808.

78 M.N.S.M. Sri, M.H. Buraidah, and L.P. Teo, Effect of 1-butyl-3-methylimidazolium iodide on the performance of dye-sensitized solar cell having PEO-PVA based gel polymer electrolyte, *Materials Today: Proceedings*, **4**, 2017, 5161–5168.

79 M.F. Aziz, I.M. Noor, B. Sahraoui, and A.K. Arof, Dye-sensitized solar cells with PVA-KI-EC-PC gel electrolytes, *Optical and Quantum Electronics*, **46**, 2013, 133–141.

80 M.F. Aziz, M.H. Buraidah, M.A. Careem, and A.K. Arof, PVA-based gel polymer electrolytes and their application in dye sensitized solar cells, in A.K. Arof, M.A. Careem, and M.H. Buraidah (eds), Proceedings of the 2nd International Conference on Solar Energy Materials, Solar Cells and Solar Energy Applications, 22–24 August 2013, Centre for Ionics University of Malaya, ISBN 978-967-12067-0-6, pp. 181–186.

81 T.M.W.J. Bandara, H.D.N.S. Fernando, E.J. Rupasinghe, *et al*., N719 and N3 dyes for quasi-solid state dye sensitized solar cells – A comparative study using polyacrylonitrile and CsI based electrolytes, *Ceylon Journal of Science*, **45**, 2016, 61–69.

82 J.-H. Yum, E. Baranoff, S. Wenger, *et al*., Panchromatic engineering for dye-sensitized solar cells, *Energy & Environmental Science*, **4**, 2011, 842–857.

83 T. Stergiopoulos, E. Rozi, C.-S. Karagianni, and P. Falaras, Influence of electrolyte co-additives on the performance of dye-sensitized solar cells, *Nanoscale Research Letters*, **6**, 2011, 307.

84 S. Zhang, M. Yanagida, X. Yang, and L. Han, Effect of 4-tert-butylpyridine on the quasi-Fermi level of dye sensitized TiO_2 films, *Applied Physics Express*, **4**, 2011, 042301.

85. F. Bella, A. Sacco, D. Pugliese, *et al*., Additives and salts for dye-sensitized solar cells electrolytes: What is the best choice?, *Journal of Power Sources*, **264**, 2014, 333–343.

86 G.D. Sharma, R. Kurchania, R.J. Ball, *et al*., Effect of deoxycholic acid on the performance of liquid electrolyte dye-sensitized solar cells using a perylene monoimide derivative, *International Journal of Photoenergy*, **2012**, 2012, Article ID 983081.

87 S. Tatay, S.A. Haque, B. O'Regan, *et al*., Kinetic competition in liquid electrolyte and solid-state cyanine dye sensitized solar cells, *Journal of Materials Chemistry*, **17**, 2007, 3037–3044.

88. Y.-S. Yen, T.-Y. Lin, and C.-Y. Hsu, A remarkable enhancement of efficiency by co-adsorption with CDCA on the bithiazole-based dye-sensitized solar cells, *Organic Electronics: Physics, Materials, Applications*, **14**, 2013, 2546–2554.

89 G.R.A. Kumara, S. Kaneko, M. Okuya, *et al*., Shiso leaf pigments for dye-sensitized solid-state solar cells, *Solar Energy and Solar Cells*, **90**, 2006, 1220–1226.

90 H. Chang and Y.-J. Lo, Pomegranate leaves and mulberry fruit as natural sensitizers for dye-sensitized solar cells, *Solar Energy*, **84**, 2010, 1833–1837.

91 B.-Q. Liu, X.-P. Zhao, and W. Luo, The synergistic effect of two photosynthetic pigments in dye-sensitized mesoporous TiO_2 solar cells, *Dye and Pigments*, **76**, 2008, 327–331.

92 W.R. Krigbaum and N. Tokita, Melting point depression study of polyacrylonitrile, *Journal of Polymer Science Part A: Polymer Chemistry*, **43**, 1960, 467–488.

93 O.A. Ilepruma, G.R.A. Kumara, H.-S. Yang, K. Murakami, Quasi-solid electrolyte based on polyacrylonitrile for dye-sensitized solar cells, *Journal of Photochemistry and Photobiology A: Chemistry*, **217**, 2011, 308–312.

94 K. Sada, K. Kokado, Y. Furukawa, Polyacrylonitrile (PAN), in S. Kobayashi and K. Müllen (eds), Encyclopedia of Polymeric Nanomaterials, Springer, 2014, pp. 1–7.

95 P.A.R.D. Jayathilaka, M.A.K.L. Dissanayake, I. Albinsson, and B.-E. Mellander, Dielectric relaxation, ionic conductivity and thermal studies of the gel polymer electrolyte system PAN/EC/PC/LiTFSI, *Solid State Ionics*, **156**, 2003, 179–195.

96 M.A.K.L. Dissanayake, C.A. Thotawatthage, G.K.R. Senadeera, *et al*., Efficiency enhancement by mixed cation effect in dye-sensitized solar cells with PAN based gel polymer electrolyte, *Journal of Photochemistry and Photobiology A: Chemistry*, **246**, 2012, 29–35.

97 T.M.W.J. Bandara, M.A.K.L. Dissanayake, W.J.M.J.S.R. Jayasundera, *et al*., Efficiency enhancement in dye-sensitized solar cells using gel polymer electrolytes based on a tetrahecylammonium iodide and MgI_2 binary iodide system, *Physical Chemistry Chemical Physics*, **14**, 2012, 8620–8627.

98 T.M.W.J. Bandara, H.D.N.S. Fernando, M. Furlani, *et al*., Dependence of solar cell performance on the nature of alkaline counterion in gel polymer electrolytes containing binary iodides, *Journal of Solid State Electrochemistry*, **21**, 2017, 1571–1578.

99 T.M.W.J. Bandara, W.J.M.J.S.R. Jayasundera, H.D.N.S. Fernando, *et al*., Efficiency enhancement of dye-sensitized solar cells with PAN:CsI:LiI quasi-solid state (gel) electrolytes, *Journal of Applied Electrochemistry*, **44**, 2014, 917–926.

100 W.M.N.M.B. Wanninayake, K. Premaratne, G.R.A. Kumara, and R.M.G. Rajapakse, Use of lithium iodide and tetrapropylammonium iodide in gel electrolytes for improved performance of quasi-solid-state dye-sensitized solar cells: Recording an efficiency of 6.40%, *Electrochimica Acta*, **191**, 2016, 1037–1043.

101 A.K. Arof, N.A. Mat Nor, N.R. Ramli, *et al*., Utilization of saffron (*Crocus sativus L*.) as sensitizer in dye-sensitized solar cells (DSSCs), *Optical and Quantum Electronics*, **49**, 2017, 37, (8 pp).

102 H.C. Hassan, Z.H.Z. Abidin, M.A. Careem, and A.K. Arof, Chlorophyll as sensitizer in I^-/I_3^--based solar cells with quasi-solid-state electrolytes, *High Performance Polymers*, **26**(6), 2014, 647–652.

103 A.K. Arof, H.K. Jun, L.N. Sim, *et al*., Gel polymer electrolyte based on LiBOB and PAN for the application in dye-sensitized solar cells, *Optical Materials*, **36**, 2014, 135–139.

104 A.K.Arof, I.M.Noor, M.H.Buraidah, *et al*., Polyacrylonitrile gel polymer electrolyte based dye sensitized solar cells for a prototype solar panel, *Electrochimica Acta*, **251**, 2017, 223–234.

105 T.M.W.J. Bandara, M.F. Aziz, H.D.N.S. Fernando, *et al*., Efficiency enhancement in dye-sensitized solar cells with a novel PAN-based gel polymer electrolyte with ternary iodides, *Journal of Solid State Elecrochemistry*, **19**, 2015, 2353–2359.

106 L.Z. Fan, T.F. Xing, R. Awan, and W.H. Qiu, Studies on lithium bis(oxalato)-borate/propylene carbonate-based electrolytes for Li-ion batteries, *Ionics*, **17**, 2011, 491–494.

107 S. Ganesan, V. Mathew, B.J. Paul, *et al*., Influence of organic nitrogenous compounds phenothiazine and diphyenyl amine in poly(vinylidene fluoride) blended with poly(ethylene oxide) polymer electrolyte in dye-sensitized solar cells, *Electrochimica Acta*, **102**, 2013, 219–224.

108 M. Muthuvinayagam and C. Gopinathan, Characterization of proton conducting polymer blend electrolytes based on PVdF-PVA, *Polymer*, **68**, 2015, 122–130.

109 S. Anandan, S. Pitchumani, B. Muthuraaman, and P. Maruthamuthu, Heteropolyacid-impregnated PVDF as a solid polymer electrolyte for dye-sensitized solar cells, *Solar Energy Materials and Solar Cells*, **90**, 2006, 1715–1720.

110 A.K. Arof, M.F. Aziz, M.M. Noor, *et al*., Efficiency enhancement by mixed cation effect in dye-sensitized solar cells with a PVdF based gel polymer electrolyte, *International Journal of Hydrogen Energy*, **39**, 2014, 2929–2935.

111 K.S. Perera and K.P. Vidanapathirana, Polyvinylidene fluoride based gel polymer electrolyte to be used in solar energy to electrical energy conversion, *Sri Lankan Journal of Physics*, **16**, 2016, 29–39.

112 K.-M. Lee, V. Suryanarayanan, and K.-C. Ho, High efficiency quasi-solid-state dye-sensitized solar cell based on polyvinylidene fluoride-co-hexafluoro propylene containing propylene carbonate and acetonitrile as plasticizers, *Journal of Photochemistry and Photobiology A: Chemistry*, **207**, 2009, 224–230.

5

Advantages of Polymer Electrolytes Towards Dye-sensitized Solar Cells

Nagaraj Pavithra[1], Giovanni Landi[2,3], Andrea Sorrentino[3], and Sambandam Anandan[1]

[1] *Nanomaterials and Solar Energy Conversion Laboratory, National Institute of Technology, India*
[2] *Department of Industrial Engineering, University of Salerno, Italy*
[3] *Institute for Polymers, Composites and Biomaterials (IPCB), National Research Council of Italy (CNR), Italy*

5.1 Introduction

5.1.1 Energy Demand

Energy demand headed the list entitled "top ten Global Concerns" by Richard Errett Smalley, Nobel laureate in chemistry for the year of 1996, at the 2004 Materials Research Society Fall Meeting in Boston [1]. The energy demand of our planet keeps on increasing due to improvements in technology and economic status, and also increasing population. The worldwide energy consumption is expected to be doubled in the next few decades and to be tripled by the end of this century [2]. Moreover, the energy economy is still highly dependent on three forms of fossil fuels – oil, natural gases, and coal – nearly 80% of the present energy needs are fulfilled by these nonrenewable energy sources [3]. Because of the nonrenewable nature of these conventional energy sources, researchers are urgently developing sustainable or renewable energy solutions to meet the current global energy demand [4]. At the present rate of consumption, all the fossil fuel available will be consumed completely around 2090.

Apart from the energy demand, another important problem caused by the use of fossil fuel is the environmental consequence and subsequent climatic changes due to the burning of fossil fuel. This releases greenhouse gases like CO_2, SO_2, etc. into the atmosphere and results in the greenhouse effect, which leads to the global warming. Nuclear energy sources were one of the important energy sources not involving any release of toxic gases that has gained attention in

Rational Design of Solar Cells for Efficient Solar Energy Conversion, First Edition.
Edited by Alagarsamy Pandikumar and Ramasamy Ramaraj.

recent years but has the drawback of disposal of radioactive wastes and safety issues. Hence, researchers are focusing on nonpolluting renewable energy sources. The energy sources that are naturally replenished on a human timescale, such as sunlight, wind, rain, tides, waves, and geothermal, are referred as renewable energy sources and are usually much more environmentally friendly than fossil fuels [5]. The most commonly known renewable energy sources include the wind, wave, hydroelectric, biomass, and solar energy. Among various available renewable energy sources, solar energy is the most promising renewable energy because the energy provided by the sun is enormous and is available year-round. Energy released from the sun for an hour is greater than the global energy required for the year.

5.1.1.1 Generation of Solar Cells

A **solar cell or photovoltaic cell** is the device that converts solar energy into electrical energy and works on the principle of "**photovoltaic effect**". Photovoltaic effect is the phenomenon of excitation of electrons from a metal surface by the photons of light and was first discovered by a French physicist, Edmund Becquerel in 1839 [6]. He observed an increase in electrical energy when the apparatus used for an electrochemical experiment involving two metal plates in acidic solution is exposed to sunlight. The photovoltaic cell provides the direct use of solar radiation to produce electricity and is close to an ideal way to use nature's renewable energy flow. It has the advantages of avoiding transmission losses and costs, and the solar panels themselves operate without noise, toxic and greenhouse gas emissions, and require very little maintenance.

Photovoltaic cells are divided into three main categories and referred to as generations of photovoltaic cells (Figure 5.1a) [7]. The first generation of photovoltaic includes the monocrystalline silicon and multicrystalline silicon-based solar cells; these achieved efficiencies up to 25%. The first silicon-based solar cells [8] were reported by Chapin *et al*. in 1954. The solar cell consisted of an arsenic-doped silicon substrate with a boron-doped layer, a p-i-n device. This solar cell had an efficiency of 6%, which was rapidly increased to 10%. For many years, the main application of the technology was in space vehicle power supplies but it did not gain any significant public attention due to the high cost. The poor availability of pure silicon and tedious fabrication process made it costlier. The second generation solar cells include amorphous silicon-based thin film solar cells – cadmium telluride/cadmium sulfide (CdTe/CdS) solar cells and copper indium gallium selenide (CIGS) solar cells. Comparatively, these are cheaper to produce but their efficiencies are lower than that of first generation solar cells and they use hazardous materials like cadmium and rare elements such as telluride and indium. The implementation of a technology marketed as environmentally friendly that uses hazardous metals is quite controversial.

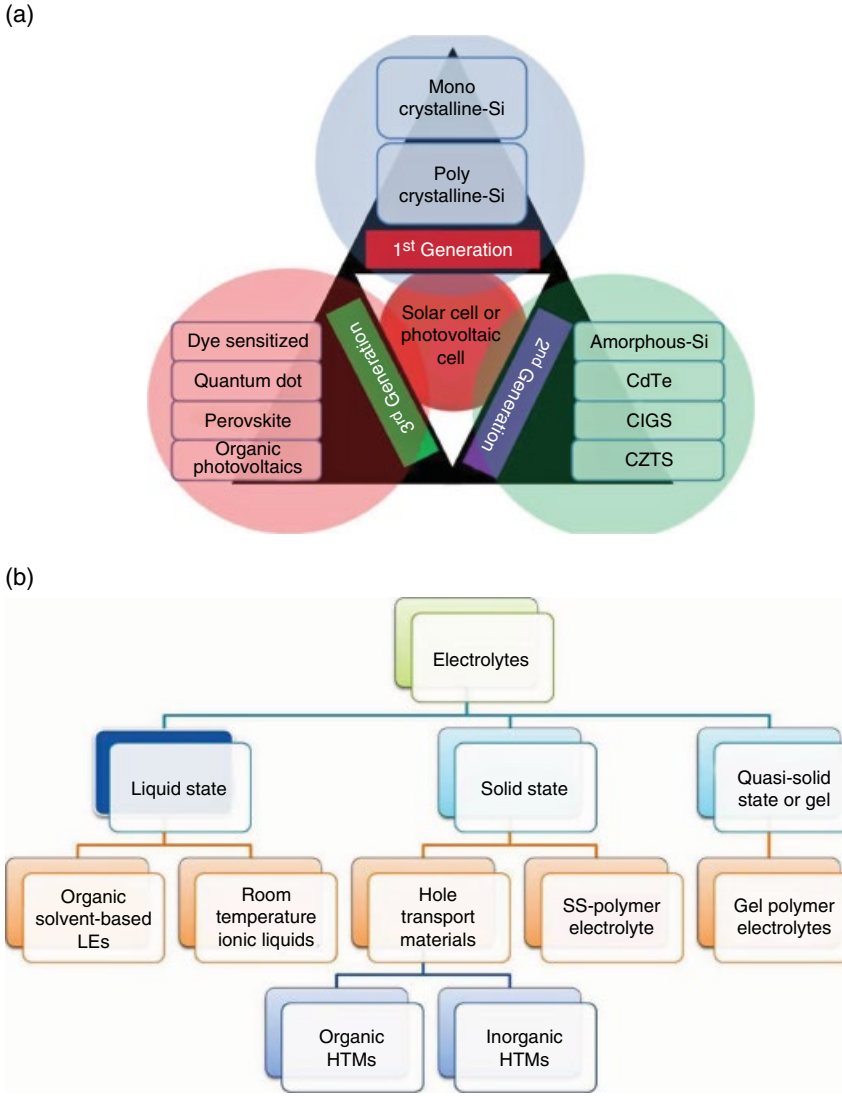

Figure 5.1 (a) Various generations of solar cell; (b) types of electrolytes used in third generation solar cells.

Among the emerging technologies investigated for the fabrication of a solar cell, such as the quantum dot solar cell [9] and the hot carrier solar cell [10], only the multijunction III-V concentrator cells have demonstrated solar power conversion efficiency over 40% since 2006, and represent the only third-generation photovoltaic technology to enter commercial power generation

markets so far [11]. These are called as double- or triple-junction cells, i.e. these devices are fabricated by superimposing various cells based on materials with a different band gap that absorb in distinct wavelength regions [12]. It is worth noting that the light splitting process within the solar cell has been recently applied to the intermediate band solar cell concept. In this respect, the light absorption occurs in the same bulk material, compared to the multijunction solar cell, with a theoretical power conversion efficiency over 60% [13]. However, few studies have been reported in literature regarding the use of the defect engineering to create an intermediate band within the forbidden band, such as iron atom incorporation in the $CuGaS_2$ bulk material [14]. It should be noted that another emerging technology, concentrator photovoltaics (CPV), uses high-efficiency multijunction solar cells in combination with optical lenses and a tracking system with an efficiency from 40 to 50% in production cells [11, 15]. Hence, to make the solar cells more eco-friendly and flexible, researchers are focused on the third generation solar cell, which includes nanocrystal-based solar cells, bulk heterojunction (BHJ) solar cells, dye-sensitized solar cells (DSSCs), quantum dot-sensitized solar cells (QDSSCs), and Perovskite-sensitized solar cells (PSSCs). The basic structure of this type of solar cell includes two electrodes (a photoanode and cathode) separated by an electrolyte. Either a redox couple or a hole transport layer can act as the electrolyte.

5.1.2 Types of Electrolyte Used in Third Generation Solar Cells

In third generation solar cells, the electrolyte plays a vital role in deciding the power conversion efficiency as well as stability. The electrolyte is responsible for charge transport between the photoanode and the cathode and it completes the internal circuit by being oxidized and, subsequently, reduced. The basic requirements for the electrolyte include:

- electrochemical potential should match with the quasi-Fermi level of the semiconductor to maximize the photovoltage;
- it should possess higher conductivity for fast diffusion of charge of ions or holes;
- it should not absorb in the UV-Vis and near-IR range;
- it should be chemically and thermally stable under light irradiation.

Various types of electrolytes used are illustrated in Figure 5.1b.

5.1.2.1 Liquid Electrolytes (LEs)

Liquid electrolytes are the conventional type of electrolyte and the most widely used transport medium. LEs have some important features, such as easy preparation method, high conductivity due to low viscosity, and good interfacial contact with the electrodes, and, hence, give high conversion efficiencies to the

devices [16]. Generally, LEs consists of three components: organic solvent, redox couple, and additive. The organic solvent is the basic component in a LE; it is used for dissolution and diffusion of the redox couple. Low viscosity non-protonic organic solvents such as acetonitrile, 3-methoxy propionitrile, etc. are commonly used in LEs. Redox couple is shown based on the cell type, the energy levels of which should match with the sensitizer and the counterelectrode (CE) for better cell performance. Finally, additives such as 4-tertbutyl pyridine (TBP) and guanidium thiocyanate (GuSCN) were introduced to improve the device performance by varying the energies in working electrode/electrolyte interface.

DSSCs using porphyrin-based dye as sensitizer and a liquid-based electrolyte containing cobalt(II/III) redox shuttle have achieved an efficiency of 13% [17]. QDSSCs were fabricated with $CuInS_2$/ZnS quantum dots and a liquid electrolyte containing polysulfide (aqueous solution of 2.0 M Na_2S, 2.0 M sulfur, and 0.2 M KCl) was reported to have an efficiency of 7.04% [18]. PSSCs containing liquid-based iodide/iodine-based redox electrolyte have achieved efficiencies up to 6.54% [19]. The use of liquid electrolytes has many drawbacks, including lower stability and inflammability of volatile organic solvents, corrosion of electrodes, leakage and sealing issues for large scale manufacturing and outdoor applications. Therefore, significant research is going on to replace the conventional liquid electrolyte by a more suitable electrolyte for practical applications [20].

5.1.2.2 Room Temperature Ionic Liquids (RTILs)

Ionic liquid or molten salt is a salt in a liquid state, in other words, ionic liquids are liquid electrolyte entirely composed of ions [21]. They have melting points around 100 °C or below and are relatively low-viscosity, free-flowing liquids at room temperature. Hence, they are commonly referred to as room temperature ionic liquids (RTILs). Generally, RTILs are composed of bulky cations like ammonium, phosphonium, and heteroaromatics with weak intermolecular interactions, lower symmetry and low charge density [16]. The anions in RTILs are crudely divided into two types: halide/pseudohalide anions and complex anions like borates and triflate derivatives. RTILs were used widely due to their unique features of good chemical and thermal stability, high ionic conductivity, nonflammability and negligible vapor pressure. In DSSCs, RTILs can act as both solvents as well as redox ion source.

The first long-term stable DSSC using an ionic liquid in the electrolyte was reported by Papageorgiou *et al.* in 1996 [22]. This RTIL-based electrolyte consisted of methylhexyl-imidazolium iodide (MHImI) and 7 mM iodine has shown an excellent stability. About 83% initial photocurrent was retained; it was without a change in voltage after 80 days. A DSSC containing metal-free indoline dye D-149 as the sensitizer and an electrolyte containing acetylcholine iodide (ACI)/ethylene glycol (EG) (ratio 1:9) based quaternary

ammonium salt, 0.8 M LiI, 0.1 M I_2 and 0.05 M N-methyl benzimidazole has shown a power conversion efficiency of 3.36%. This value is about 82% of the performance of a conventional acetonitrile-based electrolyte under the same measurement conditions [23]. DSSCs with RTILs have achieved efficiencies up to 8.2% by using eutectic melt containing three imidazolium iodide salts with excellent stability of 93% conversion efficiency after 1000 hours light soaking [24]. A QDSSC, using CdSe quantum dots as sensitizer and pyrrolidinium ionic liquid has shown 1.86% efficiency and a good stability over 240 h [25]. But, the main issue with their use has been the resultant low short circuit current of the devices due to the low ionic mobility of the iodide species in high viscosity RTILs.

5.1.2.3 Solid State Hole Transport Materials (SS-HTMs)

SS-HTMs are semiconductors and the charge carrier transport is due to electrons and holes. In the case of SS-HTMs, along with the basic requirement of an electrolyte, pore filling ability and the deposition process of the SS-HTM are also important. It should be a nondestructive one. Only, a few p-type semiconductors are available to meet these requirements. Further, SS-HTMs are of two types: inorganic HTMs and organic HTMs.

Copper-based inorganic HTMs m*eet al*l of the above requirements and have received significant interest in this field. The first SS-DSSCwas reported in 1995 [26], using CuI as HTM with an efficiency of 2.4%. The lower conversion efficiency is due to fast crystallization of CuI [27]. By using 1-methyl-3-ethylimidazolium thiocyanate (MEISCN) as crystallization inhibitors the conversion efficiency is improved to 3.8% for SS-DSSC with CuIHTM [28]. However, the stability of the cell is greatly reduced under extended illumination due to crystallite formation [29]. CuSCN, which has greater stability and excellent pore filling ability, is chosen as an alternative to CuI [30], even though the maximum efficiency achieved was quite low due to fast charge recombination [31]. In 2012, Kanatzidis *et al*. reported a SS-DSSC employing caesium tin iodide ($CsSnI_3$, a type of perovskite) as an inorganic p-type semiconductor with the ruthenium dye (N719) and achieved an efficiency of 8.5% [32]. After this $CsSnI_3$ has attracted attention due to its excellently high solubility and hole mobility of 585 $cm^2 V^{-1} s^{-1}$ [33] but has the drawback of high sensitivity towards moisture and oxygen.

Organic HTMs have many attractive features over inorganic HTMs, such as low cost and ease of film formation. Among various organic HTMs, spiro-OMeTAD (2,2′,7,7′-tetrakis(*N,N*-di-*p*-methoxy phenyl-amine) 9,9′-spirobifluorene) is a system that has been thoroughly investigated [34]. The first report on SS-DSSC sensitized with N719 based on spiro-OMeTAD doping with $N(PhBr)_3SbCl_6$, and $Li[(CF_3SO_2)_2N]$ has shown an efficiency of 0.74% [35]. Tial *et al*. [36] reported a series of the triphenylamine-based small molecule as

organic hole transport materials (HTMs) in SS-DSSCs using the organic dye LEG4 as a photosensitizer. These compounds have low crystallinity and high hole mobility, and exhibited the desirable power conversion efficiencies up to 5.8%. An important strategy to improve the cell performance of HTMs is chemical doping. An outstanding efficiency of 7.2% was achieved by doping with Co(III) complexes as a p-type dopant in spiro-MeOTAD based SS-DSSCs [37]. SS-DSSCs have good long-term stability but the conversion efficiency is lower due to low conductivity, high probability of charge recombination from TiO_2, poor interfacial contact, and pore penetration.

Apart from the electrolyte types already mentioned, the one which gained attention due to its low cost and environmental friendliness is polymer electrolytes, which is discussed in detail in the following sections.

5.2 Polymer Electrolytes

Polymer electrolytes are ionic conductors prepared by the dissolution of salts in a suitable polymer. They are a promising substituent because they are less expensive; consume less energy in their production, and the stability of the electrolytes is excellent due to the trapping of ions in the polymer matrix. The investigation of polymer electrolytes started in 1973, after pioneering work by Wright and his group [38, 39]. They observed ionic conductivity in poly(ethylene) oxide (PEO) in complexes with sodium and potassium thiocyanates and sodium iodide. This work was followed by the demonstration of solid polymer electrolyte membrane containing PEO-Li salt in an all-solid-state battery in1979 [40]. After these novel discoveries, the field of polymer electrolyte has attracted attention from researchers working on electrochemical applications [41, 42]. Consequently, a number of polymer electrolytes containing various polymers involving different ions, such as H^+, Li^+, Na^+, K^+, Ag^+, Mg^{2+} etc., have been investigated.

Polymer electrolytes have shown its application in Li-ion batteries, sensors, electrochromic devices, fuel cells, supercapacitors and solar cells due to their stability and nonhazardous nature [41, 43]. A review in 1998 summarized the application of various polymer electrolytes for Li-ion batteries [42]. More recently, in 2014, a new highly ion-conductive organic–inorganic hybrid electrolyte based on the reaction of triblock copolymer poly(propylene glycol)-block-poly(ethylene glycol)-block-poly(propylene glycol) bis(2- aminopropylether) with 3-(glycidyloxypropyl)trimethoxysilane (GLYMO) was reported for application in electrochromic devices [44]. In general, the linear polymers like poly(ethylene oxide) or poly(ethylene glycol) (PEO or PEG), poly(acrylonitrile) (PAN), poly(vinyl pyrrolidinone) (PVP), polystyrene (PS), poly(vinyl chloride) (PVC), poly(vinylidene ester) (PVE), poly(vinylidene fluoride) (PVDF), poly(methyl methacrylate) (PMMA), etc., are often used in PEs.

5.2.1 Mechanism of Ion Transport in Polymer Electrolytes

In the case of PEs, the ionic mobility is due to the amorphous phase and the presence of crystalline nature restricts ionic motion [45]. Druger *et al*. developed a microscopic dynamic percolation model for the description of ion transport in PEs [46, 47]. In this model, the ionic motion is characterized as jumps between neighboring positions. For anions, which are weakly solvated by the polymer host, such a description is straightforward. For cations, the local coordination environment evolves slowly, as a single M^+.....B (M^+ = metal ion, B = Lewis base site on polymer) linkage is changed at a time. The mechanism of ionic transport [48–50] in some polymer electrolytes is shown in Figure 5.2. Xue *et al*. proposed an ion transport mechanism in PEO matrix in which lithium ions were coordinated with the ether oxygen atoms on a segmental PEO chain [51]. Li-ion transport occurs by intrachain or interchain hopping due to simultaneous breaking and forming of lithium–oxygen (Li–O) bonds followed by the replacement of ligands and continuous segmental rearrangement resulting in a long-range displacement of ions in PEs.

Conduction of both cations and anions take place simultaneously. But the mobility of the counterion is undesirable for device applications. For example, the mobility of the anion in the electrolytes interprets the performance of Li-ion batteries [52]. There are several approaches adapted to immobilize the counterion by using mixed salts or forming a polyelectrolyte, where the counterion is chemically bonded to the polymer backbone, or by using larger counter ion. For solar cell applications, a redox couple, most commonly I^-/I_3^- or Co(II)/Co(III), was dissolved in the polymer matrix. Call *et al*. studied the impact of I_2 additions on iodide ion transport and provided the evidence for

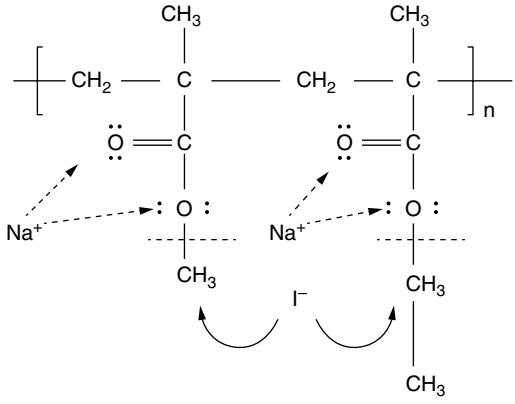

Figure 5.2 Mechanism of iodide ion transport in polymer electrolyte [P(MMA-co-EMA)] [51]. Reproduced with permission of the Royal Society of Chemistry.

the enhancement of charge transfer due to reduced cation–anion pair formation by the addition of I_2 with PEO/NaI [53].

5.2.2 Types of Polymer Electrolyte

Polymer electrolytes are further divided into the following categories based on preparation routes as well as their physical conditions [54]:

- solid polymer electrolyte (SPE);
- gel polymer electrolyte (GPE);
- composite polymer electrolyte (CPE).

5.2.2.1 Solid Polymer Electrolytes

Solid polymer electrolytes (SPEs), are commonly prepared by dissolving ionic salts with polar polymer hosts such as poly(ethylene oxide) (PEO), poly(propylene oxide) (PPO), etc. [55]. PEO is the most studied polymer because of its ability to dissolve ions due to the presences of oxygen–ether linkage. In general, SPE films were prepared either by solution cast method or by the hot-press method. SPEs have the advantages of high mechanical strength, stability, and inflammability over conventional liquid electrolytes; they are also nontoxic and noncorrosive [56]. Dey *et al.* reported an alkaline-based polymer electrolyte containing polyethylene oxide (PEO) complexed with potassium iodide (KI) and the effect of ceria (CeO_2 10 nm) fillers on ionic conductivity [57]. The addition of ceria nanoparticles enhances the conductivity by two orders of magnitude and maximum conductivity of 2.15×10^{-3} Scm^{-1} was achieved for SPEs containing 20 wt-% CeO_2. However, the performances of devices containing a SPE are poor due to the low ionic conductivity of SPEs due to the restriction of ionic motion in the solid matrix and also to crystallization of the ionic salt in the absence of a solvent.

5.2.2.2 Gel Polymer Electrolytes

Gel or quasi-solid state polymer electrolytes (GPEs) have been introduced to overcome the problems faced by SPEs without affecting mechanical strength and electrochemical stability [58]. GPEs are on the boundary between liquid and solid electrolytes and are prepared by trapping liquid electrolyte in the polymer. The polymer, which acts as a matrix or framework to gel, solidifies, absorbs, swells, holds, and interacts with liquid electrolyte. Polymers used in GPEs may vary from homopolymers, copolymers, polymer blends to modified polymers. A liquid electrolyte is prepared by dissolving suitable salts in high boiling organic solvents like low molecular weight polymers such as propylene carbonate (PC), ethylene carbonate (EC), di-ethylene carbonate (DEC), etc. to assure the nonvolatile nature of the GPE. These high boiling organic solvents provide the room and surroundings for ionic salt migration; it reduces the crystallization and glass transition temperature of the electrolyte, because it

exists between the adjacent polymer chains, decreases the polymer-polymer chain interaction, and increases the free volume and segmental mobility of the system. This gelation process between the polymer and liquid electrolyte includes weak interaction, like hydrogen bonds, van der Waals force, electrostatic interaction, etc., between the polymer matrixes (gelator) and the solvents. GPEs have received great attention because of the high conductivity and energy density, better possibility of geometrical variation, and safety [59]. GPEs exhibit, simultaneously, the cohesive properties of solids and the diffusive transport properties, high ionic conductivities, and the degree of pore-filling of liquids due to their unique hybrid network structure [60, 61].

5.2.2.3 Composite Polymer Electrolyte

Composite polymer electrolytes (CPEs) are very similar to GPEs in which a small fraction of additives, such as micro or nano-sized inorganic filler or plasticizer, is dispersed [62]. The ionic conductivity, mechanical stability and interfacial activity of GPEs is enhanced by the addition of these materials. The improvement in electrical properties of PEs by these additives is associated with an increment in the amorphous phase and segmental motion of polymer and availability of new conduction paths for charge carriers. Commonly, the inorganic fillers added are oxide micro/nanoparticles such as TiO_2, SiO_2, Al_2O_3, etc. The addition of inorganic fillers (i) increases amorphous phase of the polymer, (ii) provides a new path to charge carriers through polymer interaction and (iii) behaves as nucleation sites for small crystallites formation. In the case of inorganic fillers, size, surface area, and its fraction plays a significant role in improving the properties of CPEs [63].Recently, a gelatin-based polymer filled with a carbonaceous filler has been used as solid electrolyte for energy storage application[64, 65].

By definition, a plasticizer is an additive that changes the glass transition temperature and reduces the crystallinity degree of the polymer. Generally, plasticizers will have low molar mass, high boiling points and are routinely added to highly crystalline polymer matrixes to increase the flexibility of the polymer chains. For polymer electrolytes, the presence of these additives contributes to an increase in the ionic conductivity by several orders of magnitude [66]. For optimal properties the fraction of additive should be optimum, higher plasticizer content may lead to a loss of mechanical properties. Hence, in the following sections the application of various polymer electrolytes in the third generation thin film based solar cells such as dye-sensitized solar cells, quantum dot sensitized solar cell, and perovskite solar cells is summarized.

5.3 Dye-sensitized Solar Cells

The history of "dye sensitization" began in early days of photography. In 1883, Vogel discovered that silver halides could be sensitized by the use of dyes – this extended the photosensitization to longer wavelengths, thus enabling

"dye-sensitized" photographs. On the other hand, photoelectrochemistry began with Becquerel's observation of photoelectric effect. In 1887, the "sensitization" concept was borrowed from photography and extended to photoelectrochemistry, thus allowing much greater currents to be observed between the two electrodes. In 1950s after the creation of silicon-based solar cells, the newly acquired knowledge from silicon solar cells inspired researchers, and soon enough dyes started appearing in solar cells. This began with the work of Gerischer and Tributsch in 1968; they found adsorption of dye molecules on the surface of a wide bandgap semiconductor extended the absorption range of the system into the visible region [67]. This was the first attempt to construct solar cells using semiconductors such as titania or zinc oxide with Rose Bengal and fluoroescein dyes and a ferric/ferrous redox shuttle as a hole transporter. At the time, the operating mechanism was not fully understood, the semiconductors used were single crystal and the dyes were free in solution with only a small fraction of these dyes actually bound to the surface. The photocurrent observed was due to dyes in close proximity to the semiconductor absorbing incoming light and transferring the excited electron to the semiconductor conduction band; thus, they remained extremely inefficient and resulted in light absorption of less than 1%. As this field progressed, slowly, clues began emerging about how to improve the efficiency of the cells. One successful approach was to physically anchor the dyes to the semiconductor surface [68]. Another strategy was to increase the surface area of the semiconductor by texturing them, resulting in a 1.5% monochromatic efficiency [69]. In 1985, Desilvestro *et al*. observed that a rough-surfaced dye-sensitized electrode produced an improved efficiency due to the increased amount of dye adsorbed on the increased surface area [70]. Finally, the real breakthrough in the field came in 1991, when Brian O'Regan and Michael Gratzel reported the first dye-sensitized solar cells (DSSCs) with a conversion efficiency of 7.1% by using nanoparticles for the semiconductor phase as well as the use of previously reported optimized ruthenium dyes (cisdithiocyanatobis(2,2′-bipyridine-4,4′- dicarboxylate)ruthenium-(II) (N3)) as photosensitizer and iodine/iodide (I^-/I_3^-) in organic solvent as redox electrolyte. Platinum was used as a counterelectrode [71].

5.3.1 Components and Operational Principle

DSSCs consists of five major components: (i) conducting substrate, (ii) nanocrystalline semiconductor film, (iii) dye sensitizer, (iv) redox couple, and (v) counterelectrode (Figure 5.3a).

A schematic representation showing the working principle of the dye-sensitized solar cell (DSSCs) is given in Figure 5.3b. The conversion of light energy into electrical energy involves several steps.

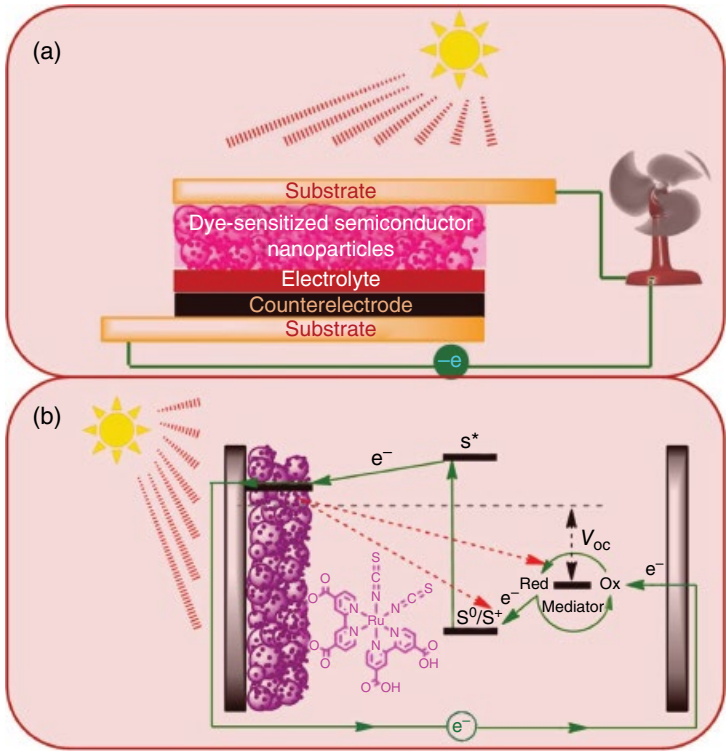

Figure 5.3 (a) Components of dye-sensitized solar cells; (b) operational principle of dye-sensitized solar cells.

i) Under light illumination, the ground state sensitizer molecule (S^0) harvests photons and goes to excited state (S^*) by the excitation of an electron from its highest occupied molecular orbital (HOMO) to the lowest unoccupied molecular orbital (LUMO).

$$S^0 + h\upsilon \rightarrow S^* \tag{5.1}$$

ii) These excited electrons from the sensitizer are injected into the conduction band of mesoporous TiO_2 film to form the oxidized dye (S^+). So, the charge separation is attained across the semiconductor interface where an electron is located in the TiO_2 and a hole is located in the oxidized dye molecule. The electrons in the TiO_2 film penetrate through the porous semiconductor network and, finally, reach the back contact of the working photoanode.

$$S^* \rightarrow S^+ + e^-\left(TiO_2\right) \tag{5.2}$$

iii) The oxidized dye (S^+) receives the electron from the reduced component (Red) of the redox mediator to regenerate dye (S^0) and to form oxidized form of redox couple (Ox).

$$S^+ + 3I^- \rightarrow S^0 + I_3^- \tag{5.3}$$

iv) The extracted electron from the photoanode immigrates to the cathode. The reduced form of redox couple is regenerated at the cathode and the cycle is completed.

$$I_3^- + 2e^- \rightarrow (Pt)\,3I^- \tag{5.4}$$

v) Meanwhile, there are two competitive reactions in the process. One is the recombination of electrons in the TiO_2 film by the oxidized dye (S^+).

$$S^+ + e^-(TiO_2) \rightarrow S^0 \tag{5.5}$$

vi) The other is the recombination of electrons in the TiO_2 film by the oxidized form of redox couple (Ox).

$$I_3^- + 2e^-(TiO_2) \rightarrow 3I^- \tag{5.6}$$

Overall, the device generates electric power from light without from any permanent chemical transformation [72, 73].

5.3.1.1 Substrate

A substrate material for DSSC is used as the support structure, current collector as well as sealing layer. It should provide combined physical properties of high visible light transmittance for light harvesting and also electrical conductivity for collecting current. Fluorine-doped tin oxide (FTO) coated glass is more commonly used in the fabrication of DSSCs [74]. In recent years, flexible transparent plastic substrates coated with conducting oxide layers have been introduced. Use of this flexible substrate makes the cells cheaper lighter, thinner, and easier to handle and transport than that of cells sandwiched between glass substrates; this makes the cells more suitable for the continuous roll-to-roll process for large scale production.

Vomiero *et al*. reported a flexible DSSC using poly(ethylene terephthalate) (PET) and Kapton HN substrate for the anode; a titanium film was deposited by means of DC magnetron sputtering at room temperature and platinum foil is used as counterelectrode [75]. The efficiency of 3.5% was obtained using N719 as a sensitizer. Kang *et al*. [76] reported a flexible DSSC using ITO- and SiO_x-sputtered stainless steel as supporting substrate for TiO_2 film and a transparent counterelectrode prepared by drop casting 10 mM hydrogen hexachloroplatinate(IV) hydrate in 2-propanol to

ITO-coated polyethersulfone plastic substrate; an overall solar conversion efficiency of 4.2% at 100 mW cm^{-2} was obtained. The flexible DSSC fabricated using the working and the counterelectrodes prepared by transferring high-temperature-annealed TiO_2 and platinum/carbon films, respectively, onto flexible PEN plastic substrates, has exhibited a remarkable efficiency of 7.27%. But these polymer substrates cannot withstand high-temperature steps required for transparent conducting oxide (TCO) layer coating, sintering of the TiO_2 film, and in the preparation of the platinum counterelectrode. It also has several other issues like permeability and low stability [77].

5.3.1.2 Photoelectrode

A nanocrystalline semiconductor film, supported on TCO where the light is illuminated and sensitized with dye molecules is referred to as a photoelectrode or working electrode.

5.3.1.2.1 Nanocrystalline Semiconductor Film

The performance of the DSSC depends significantly on the properties of the nanostructured semiconductor layer. There are several requirements for photoelectrode material: (i) it should be transparent to the visible spectrum, to maximize light harvesting; (ii) it should have high surface area for dye adsorption; (iii) the energy levels of the material should match with excited dye molecule to facilitate electron injection; (iv) it should have high charge carrier mobility to collect electrons efficiently; and (v) it should be easily available, stable, cheap, and environmentally friendly. More commonly, reported photoanode materials are TiO_2, ZnO, SnO_2, NiO, etc. [78–80]. Although numerous semiconductors were reported, TiO_2 is still the material of choice for DSSCS because of its chemical stability and relative inertness under light irradiation and ideal electronic structure with a band gap of 3.2 eV for anatase and 3.0 eV for rutile phase. It is nontoxic and inexpensive as well. ZnO, which is quite efficient in certain cells, has the drawback of poor stability [81] and use of SnO_2 results in lower performance due to faster recombination, which is in the order of 2–3 times higher in magnitude compared to TiO_2 [79]. Morphology of the TiO_2 plays a significant role and the interdependence of the properties of the TiO_2 film and the cell performance is diverse. For example, the internal surface area of the film determines the amount of dye uptake; how the pore size distribution affects the ion diffusion; how the particle size distribution determines the optical properties and the electron percolation depends on the interconnection of the TiO_2 particles. When the nanoparticles are stacked in a continuous network in the electrode, these effects become related and optimization of the properties with respect to cell performance arises as a key issue [82]. To achieve higher performance, the TiO_2 film should be efficiently attached to TCO layer and

also its surface area and interconnectivity between the particles should be high. Generally, the mesoporous TiO_2 films were prepared by sintering process or pressing semiconducting nanoparticles onto the TCO [83, 84].

5.3.1.3 Photosensitizer

Photosensitizer (dye) is regarded as the heart of the DSSC and acts as a molecular pump. It absorbs the photons of visible light and injects the electrons into a semiconductor and accepts an electron from the redox couple in the solution and then repeats the cycle. The properties of the dye strictly affect the light-harvesting efficiency and the overall photoelectric conversion efficiency of the solar cell. The dye molecules are coated onto the nanocrystalline semiconductor by immersing the porous film in a dye solution. There are certain requirements for a good sensitizer: (i) the absorption spectrum of the sensitizer should cover the whole visible and even part of the near-infrared (NIR) region; (ii) it should be strongly bonded with the semiconductor for efficient injection of electrons, generally carboxylic acid or phosphonic acid groups are used for this purpose [85]; (iii) it should have suitable energy levels to ensure electron injection and regeneration for redox couple; and (iv) it should have long-term stability [86]. For these reasons, an appropriate choice of the dye/semiconductor and dye/electrolyte pairs is of fundamental importance in order to have an efficient DSSC. Finally, another important requirement taken in account is dye aggregation on the oxide surface, particularly in the case of complex dye molecules, as this results in an increase in the decay from the excited state of the dye and, consequently, reduces the electron injection into the semiconductor conduction band (CB). Coadsorbent such as chenodeoxycholic acid (CDCA) [87] was used together with the sensitizer to decrease the dye aggregation. The dyes used in DSSCs are mainly classified into two categories: metal-based complexes and metal-free organic dyes.

5.3.1.3.1 Metal Complexes

The metal complexes used in DSSCs consist of a central metal ion with ancillary ligands with at least one anchoring group. Ancillary ligands can be tuned by different substituent to vary the photophysical, electrochemical, and photovoltaic properties. Anchoring groups are used to connect dye with the semiconductor through chemisorption. Anchoring causes a large electronic interaction between the ligand and the conduction band of the semiconductor, resulting in effective electron injection from the dye into the conduction band of an oxide material. Polypyridines and porphyrins were the commonly used ligands and the carboxylic acid is the anchoring group. The absorption of light in the visible region is due to theh metal-to-ligand charge transfer (MLCT) process and, hence, the metal ions play a vital role. Ruthenium polypyridyl complexes were the most commonly encountered metal based sensitizers (Figure 5.4).

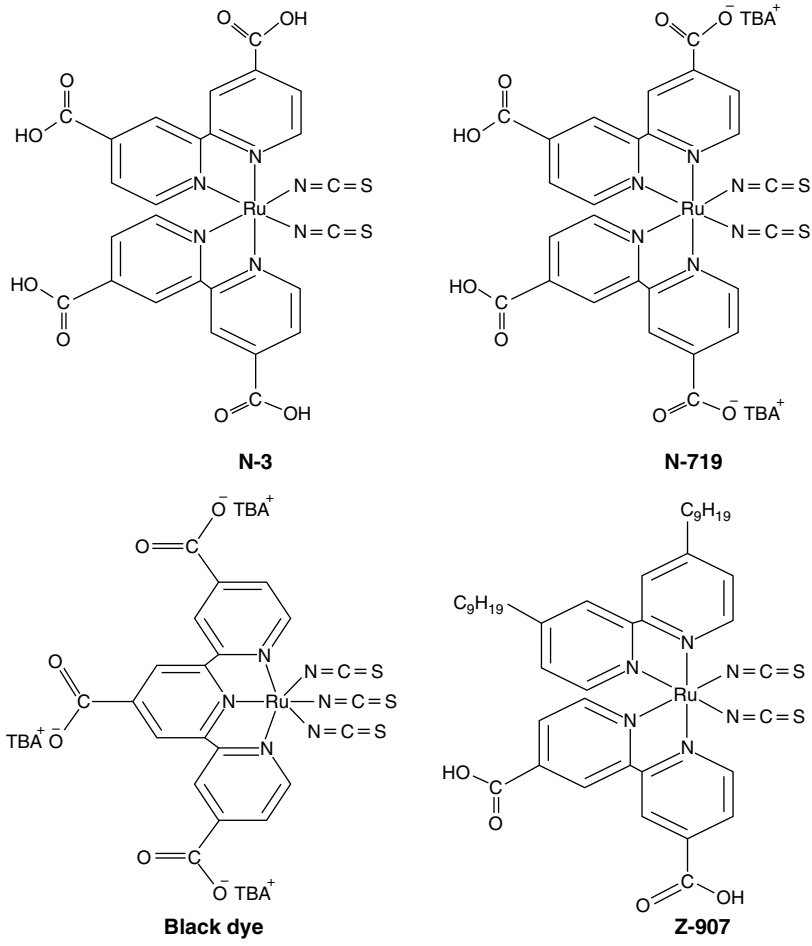

Figure 5.4 Ruthenium polypyridyl complexes as metal-based sensitizers.

After the discovery of N3 dye, $Ru(L)_2(SCN)_2$ (L = 2,2′-bipyridyl-4,4′-dicarboxylic acid), the fabricated solar cells using such ruthenium-based dye showed a conversion efficiency of 7.1% under solar illumination [86] compared to other numerous metal complexes containing various metals such as ruthenium [88], zinc [89], osmium [90], rhenium [91,] and iron [92]. Among the various reported ruthenium-based dyes, such as trithiocyanato (4,4′4′′-tricarboxy-2,2′:6′2′-terpyridine) ruthenium(II) (black dye) [93] and ditetrabutylammonium cis-bis(isothiocyanato) bis(2,2'-bipyridyl-4,4'-dicarboxylato) ruthenium(II) [94], power conversion efficiencies of 10–11% at 1.5 AM were achieved due to their broad absorption spectrum. N-719 is prepared by replacing two protons with tetra-n-butylammonium

(TBA) cation in the N-3 dye. Deprotonation changes the polarity at the TiO_2/dye interface, hence shifting the conduction band and increasing the open-circuit voltage (V_{OC}). The energy levels of ruthenium-based dyes are well matched with the conduction band of TiO_2 and redox potential of I^-/I_3^- redox electrolyte. In 2011, an efficiency of 12.3% was achieved using zinc porphyrin (YD2-*O*-C8) dye as a sensitizer and Co(II/III)tris(bipyridyl) redox electrolytes [89]. Metal-based sensitizers have some drawbacks, such as expensive synthesis, relatively lower molar extinction coefficients ($\varepsilon < 20\ 000\ lmol^{-1}cm^{-1}$), and limited availability of precursors.

5.3.1.3.2 Metal-free Organic Dyes

Metal-free organic sensitizers have been used to replace expensive metal-based sensitizers and to improve the electronic properties of DSSCs. Organic sensitizers have many advantages, which include (i) high molar extinction coefficients, (ii) easily tunable optoelectronic properties, (iii) enhanced environmental compatibility and abundance of their constituents, and (iv) reduced production costs [95]. Generally, organic dyes consist of donor-π-bridge-acceptor (D-π-A) structures, as shown in Figure 5.5 [96]. The photoelectric properties of these dyes can be tuned by altering or matching different substituents within the D-*π*-A structure.

The electron-rich aryl amines family, including phenylamine, aminocoumarin, indoline, and (difluorenyl)triphenylamine, were selected as the donor group. The *π*-conjugated connector is selected from compounds containing thiophene units, for example, oligothiophenes, thienylenevinylenes, or dithienothiophene, due to their outstanding charge transfer characteristics. Acrylic acid group is considered the best acceptor moiety. Hara *et al.* [97,98] reported a series of organicdyes (MK dyes), using carbazole derivatives as electron donors and a cyanoacrylic acid moiety as electron acceptor and an anchoring group, connected with *n*-hexyl-substituted oligothiophenes, as a π-conjugated system provides efficiency up to 8.3%. RK-1 dye containing triphenyl amine as electron donor and a phenyl ring in between the acceptor benzothiadiazole (BTD) and the cyanoacrylic acid group will stabilize the dye radical cation and decrease the recombination rate. Such system has shown 10.2% efficiency under standard conditions (AM 1.5G, 1000 Wm^2) using iodine/iodide as the electrolyte redox shuttle in the electrolyte [99]. However, the efficiency of DSSCs based on metal-free organic sensitizers is still low for industrial applications, due to the formation of dye aggregates on the semiconductor surface and to their narrow light absorption bands in the visible region.

5.3.1.4 Redox Electrolyte

In DSSCs, redox electrolyte injected in between the photoanode and the cathode plays one of the most crucial roles; it is responsible for charge transport between the electrodes. It completes the internal electrical circuit when it is

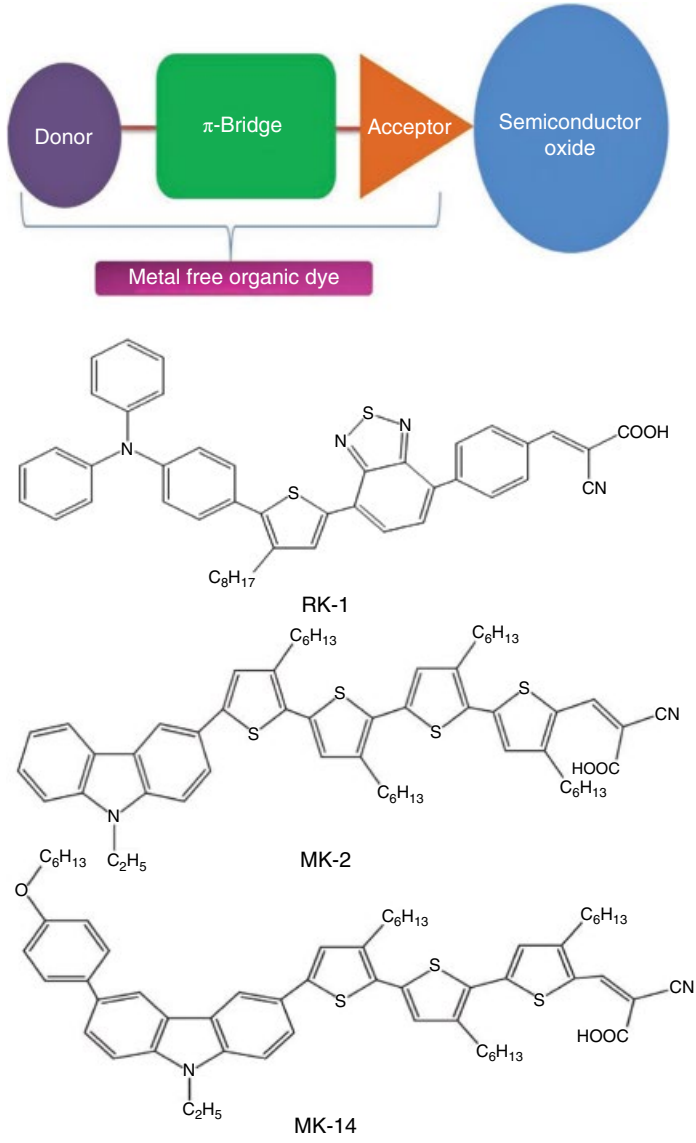

Figure 5.5 General donor-π-bridge-acceptor (D-π-A) structure of organic dyes and some examples of metal free dyes.

reduced to regenerate the oxidized dye and oxidized by receiving the electron from the counterelectrode. Hence, it has great influence in deciding the photocurrent conversion efficiency and stability of the devices. A review paper published in 2015 [100] stated that about one-third of DSSC research is based on redox electrolyte; this shows the importance of the electrolyte in a DSSC.

The redox couple used in the electrolyte plays a key role during the photoelectrochemical cycle of the DSSCs, i.e. the reduced state of the redox couple (RE) regenerates the photooxidized dye (D^+) and the oxidized state (OX) diffuse to the counterelectrode, where it is reduced. Hence, the reaction kinetics of the electron donation from RE to D^+ and electron acceptance from counterelectrode should be fast for efficient dye generation and to complete electrochemical cycle, respectively [101]. Also, electron recombination by the acceptance of electrons from TiO_2 film to OX should be slow [102]. The energy levels of redox electrolyte and dye should be close enough to increase the photovoltage of DSSCs but with sufficient driving force for dye regeneration. From the beginning of DSSCs, the iodide/triiodide couple has been the preferred redox couple due to its unique features, including suitable redox potential for rapid dye regeneration and slow electron recombination, good solubility, high conductivity, and favorable penetration ability into the mesoporous semiconductor film, and being proven to have long-term stability [103].

In recent years, new redox couples based on bromide/tribromide, interhalogens, pseudohalogens, and cobalt-based complexes have been reported. The bromide/tribromide couple has a more positive redox potential (about 1.1 V) in comparison to the iodide/ triiodide couple (about 0.35 V). Teng *et al.* [104] compared the performance of DSSCs based on the bromide/tribromide couple with the iodide/ triiodide couple and obtained a V_{OC} of 0.94 V and efficiency of 5.2% for Br^-/Br_3^--based electrolyte compared to V_{OC} of 0.62 V and efficiency of 4.1% for I^-/I_3^-[104]. Interhalogen redox systems, such as I^-/IBr_2^- and I^-/I_2Br^- were studied and obtained efficiencies up to 6.4% but complex equilibrium limits their full characterization [105]. Pseudo halogen redox couples, such as $SCN^-/(SCN)_3^-$ and $SeCN^-/(SeCN)_3^-$, have been studied as redox mediators for DSSCs. Wang *et al.* [106] achieved an efficiency of 7.5% for a DSSC containing an N3 dye in combination with an ionic liquid containing $SeCN^-$-based redox couple [105]. Organic redox couples disulfide/thiolate, disulfide, polysulfides, thiourea, cysteine, etc. were also tested in DSSCs. Redox system based on cocomplexes as one-electron redox couple and a power conversion efficiency of 2.2% were attained after Nusbaumer *et al.* [107] first report on charge-transfer dynamics of $Co(dbbip)_2^{2+/3+}$ in DSSCs. This one-electron outer sphere transition metal complex based redox couple has the advantages of being nonvolatile, noncorrosive, transparent, and having tunable potential (0.3–0.9 V) through modification of the ligands. However, due to the larger size of the complex and the higher viscosity, these electrolytes have disadvantages like mass-transport limitation and recombination loss. In order to overcome these disadvantages, research is going on and at present cocomplex based redox mediators are the most efficient redox couples for DSSCs. In 2011, Yella *et al.* [89] reported a DSSC using a cocomplex-based electrolyte in combination with Zn-porphyrin-based dye (YD2-o-C8) and achieved efficiency of 12.3%. Apart from cobalt-based redox couples, other metal complexes and clusters containing Ni(III)/Ni(IV), Cu(I)/Cu(II), and ferrocene/ferrocenium (Fc/Fc^+), have also been investigated in DSSCs.

Based on the physical state, the redox electrolytes were broadly classified into three categories: liquid electrolytes, solid-state electrolytes, and quasi-solid electrolytes. It completes the internal electrical circuit by regenerating the oxidized dye and receiving the electron from the counterelectrode. Hence, it has great influence in deciding the photocurrent conversion efficiency and stability of the devices.

5.3.1.5 Counter Electrode

The role of the counterelectrode is to transfer the electrons from the external circuit to the redox electrolyte and to catalyze the reduction of the oxidized ion in the redox couple [108]. Generally, the counterelectrode is fabricated onto the TCO substrate material like working photoanode. A catalyst layer with high electrocatalytic activity is necessary to ensure fast regeneration of redox electrolyte [72]. Platinum nanoparticles coated on a FTO substrate is the commonly used counterelectrode. Platinum counterelectrodes can be prepared by sputtering, pyrolytically, spin coating, etc. [109, 110]. These platinum-based CEs have the advantages of good electrocatalytic activity and low sheet resistance [108]. The research focused on counterelectrode materials shows that by varying the morphology the electrocatalytic properties and DSSC performance can be enhanced. In 2012, Jeong *et al.* [111] reported periodically aligned platinum nanocups (NC) with a controlled diameter (300–600 nm) for the enhancement of the surface area. These platinum NCs have a high surface area, greater catalytic activity towards the I^-/I_3^- redox species and, thus, lower impedance. DSSCs employing platinum NCs showed an efficiency of 9.75% whereas the planar platinum showed 7.87%. Platinum-based CEs have the drawback of extremely high cost, which is a problem for large-scale application. Carbon-based material, such as mesoporous carbon, graphene, carbon nanotubes, etc., polymer-based CEs, and other economically available metal sulfides, nitrides, etc., have advantages such as cost effectiveness, environmental friendliness, easy availability, corrosion resistance, and excellent catalytic activity. Even though the performance of carbon is not good as platinum, it can be improved by employing a porous film with high surface area. In 1996, Gratzel's group reported a DSSC by replacing the expensive platinum-coated FTO substrate with a mixture of graphite and carbon black as a catalyst as well as a lateral current collector with the efficiency of 6.7% [112].

5.3.2 Application of Polymer Electrolytes in DSSCs

5.3.2.1 Solid-state Dye-Sensitized Solar Cells (SS-DSSCs)

De Paoli and coworkers reported the first solid-state DSSC assembled with a SPE using a copolymer poly(epichlorohydrin-co-ethylene oxide) containing NaI/I_2 redox as electrolyte and using poly(*o*-methoxyaniline) doped with *p*-toluenesulfonic (PoAni-TSA) as sensitizer with short-circuit current

(J_{SC}) = 12.2 μA cm^{-2} and open-circuit voltage (V_{OC}) = 480 mV under illumination of 120 mW cm^{-2} [113]. One general approach for fabricating solid-state DSSCs is to place the polymer electrolyte membrane on top of the photoanode. In 2009 Rhee *et al.* reported a poly(ethylene oxide) (PEO) based solid polymer electrolyte membranes incorporated with 1-ethyl 3-methylimidazolium trifluoromethanesulfonate ($EMImTFO^-$) as ionic liquid (IL) [114]. Due to reduced crystallinity and free charge carriers provided by IL, the electrolyte membrane has shown improved ionic conductivity and efficiency of 2.45%.

In 2010, Buraidah *et al.* reported that a chitosan-based biopolymer electrolyte membrane complexed with ammonium iodide (NH_4I) and butyl-methyl-imidazolium-iodide (BMII) ionic liquid has shown conductivity of 3.43×10^5 S cm^{-1} at room temperature and J_{SC} of 0.07 mA cm^{-2} and V_{OC} of 230 mV for DSSCs fabricated using anthocyanin pigment extracted from black rice as sensitizer [115]. Imperiyka *et al.* studied the photoelectrochemical performance of poly(glycidyl methacrylate)-based solid polymer membrane with 30 wt-% $LiClO_4$ and 80 wt-% ethylene carbonate [116]. The assembled DSSC showed a conversion efficiency of 0.679% (J_{sc} = 3 mA cm^{-2}, V_{oc} = 0.48 V and FF = 0.47) under light intensity of 100 mW cm^{-2}. Even though the ionic conductivity of these polymer electrolyte membranes has reached up to 10^{-4} S cm^{-1}, the DSSC performance was very low due to the weak contact between the semiconductor–electrolytes interfaces [117].

Another approach is solution casting of polymer electrolyte solution onto the dye-sensitized photoanode. A 1-methyl 3-propyl imidazolium iodide (PMII) ionic liquid doped solid polymer electrolyte film prepared by the solution casting method using acetonitrile as a solvent with PEO polymer has shown an efficiency of 0.81% [119]. Sivakumar *et al.* reported a hybrid polymer electrolyte based on benzidine impregnated polyepichlorohydrin has shown an efficiency of 0.80% and reached 3.43% by using TiO_2 as nanofiller [120]. Also, a new inorganic–organic hybrid SPE consisting of hetero-polytungsticacid (HPA) impregnated polyepichlorohydrin and TiO_2 nanofiller has shown an efficiency of 3.9% [121]. HPA impregnated in the PE uses the back transferred electrons to get itself reduced to form heteropoly blue (HPB, photoreduced product) and again injects these electrons into the semiconductor, thus suppressing the back electron transfer as shown in Figure 5.6 [118]. Kim *et al.* reported a SPE consisting of poly(ethylene oxide dimethyl ether) (PEODME) with fumed SiO_2, 1-methyl-3-propylimidazolium iodide (MPII) and I_2 with one of the highest DSSC performance of 4.5% for SPE at 100 mW cm^{-2} [122].

Nogueira *et al.* [123] observed an increase in ionic conductivity by the addition of the plasticizer poly(ethylene glycol)methyl ether to the polymer electrolyte based on poly(epichlorohydrin-co-ethylene oxide), NaI, and I_2. A SS-DSSC assembled with this plasticized polymer electrolyte shows Jsc = 0.6 mA cm^{-2}, V_{OC} = 0.64 V, and η% = 1.75%; the efficiency remained unchanged for 30 days.

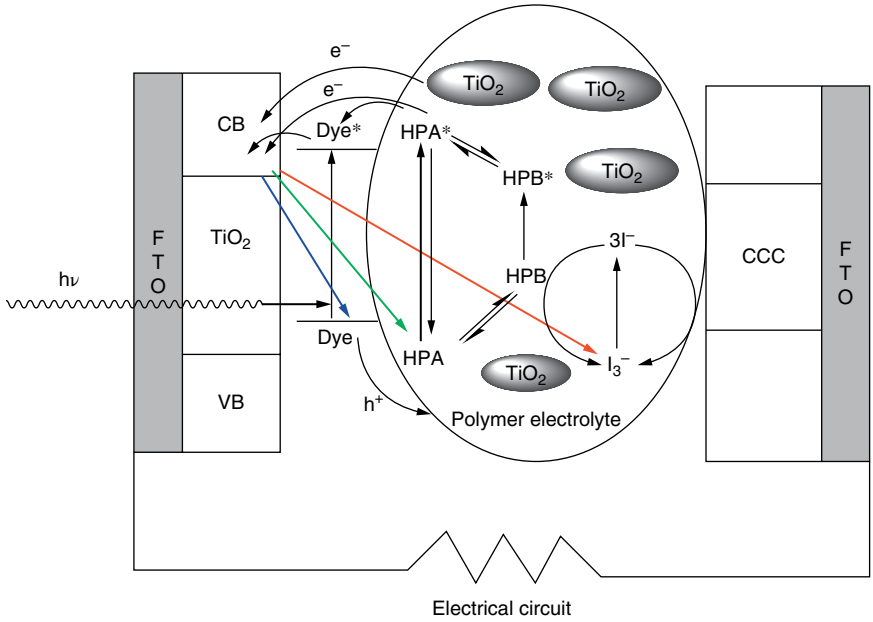

Figure 5.6 Schematic illustration of the dye-sensitized photovoltaic cell [FTO/TiO2/dye/E/CCC/FTO] where E is HPA impregnated PVDF polymer electrolyte with TiO_2nanofiller [118]. Reproduced with permission of John Wiley & Sons.

Bhattacharya *et al.* [124] investigated the effect of various cations on DSSC performance. They prepared the SPEs by complexing PEO:PEG blends in the weight ratio 40:60 with LiI, NaI, KI, NH_4I, 1-ethyl-3-methylimidazolium iodide (EMII), and 1-hexyl-3-methylimidazolium iodide (HMII). The SPE layer onto the photoanode was cast by a two-step method and the fabricated DSSCs showed a strong dependence on the cation radii. The maximum efficiency was around 2% for an SPE containing LiI and decreases with the increase in ionic radii of the cation.

De Paoli's group reported an 8 V solar module by connecting 13 DSSCs in series. The DSSCs were fabricated using an SPE consisting of NaI andI_2 in poly(ethylene oxide-co-epichlorohydrin) with ɣ-butyrolactone as a plasticizer [125]. The lower efficiencies of solid-state DSSCs is due to the crystallization of ionic salts and polymers because of the absence of solvent and lower ionic motion in a solid matrix.

5.3.2.2 Quasi-solid-state Dye-Sensitized Solar Cells (QS-DSSC)

Gel or quasi-solid-state electrolytes (GPEs) are introduced in order to improve the performance of polymer electrolyte based DSSCs without affecting the stability. Application of gel or quasi-solid-state electrolytes in DSSCs started in

1995 by Cao *et al.*'s pioneer work [126]. A QS-DSSC prepared by incorporating a liquid electrolyte containing ethylene carbonate, propylene carbonate, acetonitrile, NaI, and I_2 in polyacrylonitrile (PAN) polymer, exhibited photovoltaic efficiencies of 3–5% and higher stability compared to liquid electrolyte cells. General preparation techniques for GPEs include (i) gelation of liquid electrolyte using a polymer or oligomer, (ii) by swelling technique, and (iii) *in situ* sol-gel technique.

In gelation process, GPEs were prepared by dissolving a stoichiometric ratio of the polymer dissolved in conventional liquid electrolytes. Hence, stability is achieved trapping of liquid electrolyte in the polymer with good conductivity. Wang *et al.* reported a quasi-solid-state gel electrolyte in which poly(vinylidenefluoride-co-hexafluoropropylene) (PVDF–HFP), was used to solidify a 3-methoxypropionitrile (MPN)-based liquid electrolyte for a DSSC fabricated by using an amphiphilic ruthenium sensitizer [127]. The cell performance reached was >6% under 100 mW cm^{-2} and 94% of its initial cell performance cell was sustained for 1000 h at 80 °C. Also, an efficient GPE was prepared by using poly(acrylonitrile-co-vinyl acetate) (PAN–VA) as the gelator in 3-methoxypropionitrile (MPN)-based liquid electrolyte [128]. The presence of vinyl acetate segments accounts for the solubility of the polymer in electrolyte and formation of gel electrolytes and acrylonitrile segments account for the downward shift in the conduction band of TiO_2 in the DSSC. Photocurrent conversion efficiency of 8.34%, comparable with liquid electrolyte 8.63%, was achieved. A water-based thixotropic polymer gel electrolyte was prepared by mixing an aqueous solution of 3 wt-% xanthan gum with liquid electrolyte of 4 M propyl-methyl-imidazolium iodide (PMII), 0.3 M I_2, 1.5 M TBP, and 0.2 M GuSCN in MPN in the weight ratio of 1:1 [129]. The DSSC fabricated using a hydrophobic dye, TG6 as a sensitizer to prevent the dye desorption from the TiO_2 electrode has shown conversion efficiency of 4.78% under 100 mW cm^{-2} and an enhanced long-term stability compared to a water-based liquid electrolyte.

In the swelling technique, self-standing polymer films are swelled by a solution containing a redox couple that results in a stable gel. The polymeric network acts as a cage for liquid electrolytes and prevents its evaporation. A GPE prepared by soaking porous membrane containing acrylonitrile-methyl methacrylate copolymer in an organic electrolyte solution containing the triiodide/iodide redox couple yielded a conversion efficiency of 2.4%. The polymer encapsulated in the electrolyte solution well and maintains good mechanical properties without solvent leakage [130]. In 2014, Bella *et al.* reported new methacrylic-acrylic gel-polymer electrolytes prepared by soaking UV-cured poly(ethylene glycol) methyl ether methacrylate-polyethylene glycol diacrylate (PEGMA-PEGDA) membranes in a liquid electrolyte composed of 0.5 M NaI and 0.05 M I_2 in CH_3CN for 5 min [131]. A maximum photovoltaic conversion efficiency of 4.41% was achieved and only 10%

reduction in efficiency was observed after 250 h, while the cell based on the liquid electrolyte lost 43% of its initial efficiency. A gel-type electrolyte was prepared by soaking an electrospun poly(vinylidenefluoride-co-hexafluoropropylene) (PVdF–HFP) membrane in 0.6 M 1-hexyl-2,3-dimethylimidazolium iodide, 0.1 M LiI, 0.05 M I_2, and 0.5 M 4-*tert*-butylpyridine in ethylene carbonate/propylene carbonate (1:1 wt-%) liquid electrolyte. A conversion efficiency of 7.3% was obtained, which was slightly lower than the liquid-based electrolyte (7.8%) under similar conditions [132].

In situ polymerization may be induced in several ways, for example chemical, thermal or photochemical processes. Preparation of GPEs by *in situ* polymerization may result in good pore filling and wetting ability of electrolytes and restrict the electron-hole recombination and other parasitic current losses, thus improving the efficiency of DSSCs [133]. Yang *et al*. reported *in situ* ultra-thin porous membranes electrolytes prepared by a phase inversion method using porous poly(vinylidene fluoride-co-hexafluoropropylene) P(VDF–HFP) on N-719 sensitized TiO_2 electrodes followed by soaking in the organic liquid electrolyte [134]. Resulting DSSCs exhibited a $\eta = 8.35\%$ with $Jsc = 16.26\,mA\,cm^{-2}$, $V_{OC} = 0.751\,V$, and fill factor (FF) = 0.684 under $100\,mW\,cm^{-2}$. In 2010, Chen *et al*. reported a gel electrolyte containing poly-1,1′-(methylenedi-4,1-phenylene)bismaleimide (PBMI) prepared by *in situ* polymerization of the monomer without an initiator at 30 °C showing an efficiency of 6.24%; addition of 0.3 wt-% of the exfoliated alkyl modified-nanomica (EAMNM) resulted in an improvement in J_{SC} and efficiency to 7.05% [135]. Hong *et al*. reported an *in situ* gelation of a block copolymer containing hydroxystyrene and poly(ethylene oxide-co-propylene oxide) blocks under UV radiation in the presence of a typical liquid electrolyte [136]. The resultant GPE exhibited PCE of 5% and better stabilities compared to LE. Lee studied the ionic conductivities and performances of DSSCs of various GPEs prepared by *in situ* cross-linking of poly(imidazole-co-butylmethacrylate) with different cross-linkers [137]. Among various GPEs with various cross-linkers, 1,2,4,5-tetrakis(bromomethyl)-benzene (B4Br) showed higher cell performance of 3.61% because of microphase separation that resulted in an increase in ion transport paths in the GPE.

5.3.2.3 Types of Additives in GPEs

Apart from basic constituents such as polymer, solvent, and redox couple, some additives are also added to GPEs and such electrolytes led to further improvement in ionic conductivity and DSSC performance. Polymer electrolytes of this type of are referred as composite polymer electrolytes (CPEs). The role of additives in CPEs is to reduce the crystallinity of polymer by introducing a degree of disorder and segmental mobility, which, consequently, lowers the glass transition temperature [138]. In general, polymer electrolytes modified with additives will show better electrochemical properties and results in

DSSCs with higher conversion efficiency. There are several types of additives, including (i) plasticizers, (ii) nanofillers, (iii) inorganic proton donors, and (iv) ionic liquids.

5.3.2.3.1 Plasticizers

The plasticizer, usually a low molecular weight polyether or small organic molecules having hetero-atoms, is incorporated in the polymer matrix by small amounts in order to decrease the glass transition temperature and crystallinity [139]. Plasticizer exists in between the adjacent polymer chains, decreases the polymer–polymer interaction, and increases the free volume and, consequently, segmental mobility of the system. This results in the increment in ionic conductivity and cell performance. Commonly used plasticizers used in CPEs for the application of DSSCs are polyethylene glycol (PEG), polypropylene glycol (PPG), ethylene carbonate (EC), 1,2-dimethoxyethane (DME), γ-butyrolactone (BL), and propylene carbonate (PC).

GPE containing 8 wt-% poly(vinylenefluoride-hexafluoropropylene) P(VdF–HFP) as host polymer matrix and propylene carbonate (PC)–diethyl carbonate (DEC) as plasticizers in the ratio 1:1, with lithium iodide/iodine (LiI/I_2) as redox couple and tert-butylpyridine (TBP), has shown a maximum ionic conductivity of 5.25×10^{-3} Scm^{-1} at room temperature and an efficiency of 4.41% was obtained under 100 $mWcm^{-2}$ irradiation [60]. A DSSC constructed using GPE consisting of modified biopolymer N-phthaloylchitosan with tetrapropylammonium iodide, iodine, and ethylene carbonate as a plasticizer in dimethylformamide has shown an efficiency of 5.0%, with J_{SC} of 12.72 mA cm^{-2}, V_{OC} of 0.60 V, and fill factor of 0.66 [140]. With a composite polymer electrolyte having poly(hydroxyethyl acrylate)/poly(ethylene glycol) imbibed with polypyrrole, the DSSC showed a higher light-to-electric conversion efficiency of 7.02% compared to pure poly(hydroxyethyl acrylate)/poly(ethylene glycol) with 5.76% [141]. In our research group, we have studied GPEs containing acetamide and urea in various weight-percentages as a plasticizer for poly(ethylene oxide), LiI, I_2-based electrolyte in PC. By the addition of these plasticizers, the crystallinity of GPEs reduced due to electrostatic interactions of amino groups with PEO ether groups, as shown in Figure 5.7. Thus enhanced the ionic mobility and consequently, photocurrent conversion efficiency of 9.01 was achieved GPE with 5 wt-% acetamide in combination with N3 dye [142] and 6.82% for GPE with 4 wt-% urea in combination with N719 dye [143].

5.3.2.3.2 Nanofillers

Nanofillers (inert nano-sized materials) used as additives prevent crystal formation and, consequently, enhance the electrical and mechanical properties of CPEs. In general, the addition of a nanofiller results in more amorphous CPEs, thus the conductivity is enhanced. For application in DSSCs, the more commonly used nanofillers are Al_2O_3, TiO_2, ZrO_2, and SiO_2. Falaras *et al.*

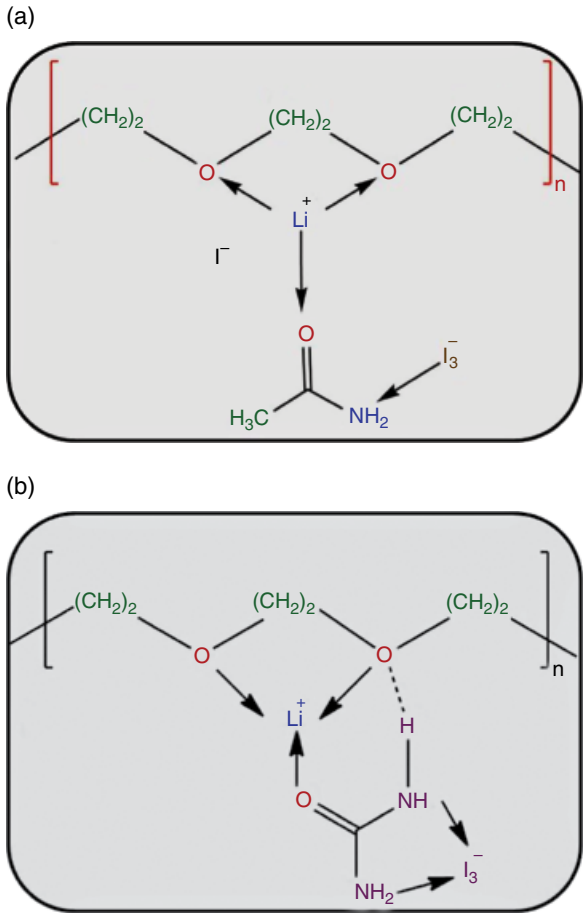

Figure 5.7 Electrostatic interactions of amino groups of (a) acetamide and (b) urea with PEO ether groups [142,143]. *Source:* Adapted from Pavithra 2015 [142].

studied the influence of metal cation and the TiO_2 nanofiller on the performance of DSSCs using PEO-based gel polymer redox electrolyte containing propylene carbonate as plasticizer and iodide/triiodide [144]. The iodide anion is introduced in the form of various metal salts: CsI, RbI, and LiI. The maximum performance was attained for PEO-TiO_2-PC (CsI/I_3^-) electrolyte, with $\eta = 2.87\%$ under standard AM1.5 simulated solar irradiation and for all the metal salts the electrolyte with the TiO_2 nanofiller has shown better performance.

Zebardastan *et al.* reported a GPE system PVdF-HFP/PEO:EC:PC:NaI:I_2 containing various weight-percentages of fumed silica (SiO_2) nanoparticles

and the optimum electrolyte, containing 13% SiO_2, has shown the highest ionic conductivity of 8.84 mS cm^{-1} and DSSC with the efficiency of 9.44%, compared to a GPE without SiO_2 which shows ionic conductivity 6.38 mS cm^{-1} and efficiency 5.67% [145]. A quasi-solid-state DSSC fabricated using poly(vinyl alcohol)/poly(ethylene glycol) gel electrolyte with 0.5% carboxy functionalized multiwalled carbon nanotubes (c-MWCNTs) has shown $J_{SC} = 8.80\,mA\,cm^{-2}$, $V_{OC} = 550\,mV$, and efficiency of 3.5% [146]. Huang *et al.* reported a PVDF–HFP-based GPE with different amounts of aluminum nitride (AlN) [147]. The addition of AlN increased the porosity and decreased the crystallinity of GPEs and the DSSC fabricated using 0.1 wt-% AIN showed the maximum conversion efficiency of 5.27%. Also, the DSSC showed an excellent stability for a period of 1000 h under both room temperatures as well at 40 °C.

5.3.2.3.3 Ionic Liquids

As mentioned earlier, ionic liquids are molten salts in liquid state and are replacements for volatile liquid electrolytes in several electrochemical applications. They have some drawbacks, such as leakage and sealing problems due to their liquid state at room temperature. But use of RTILs as an additive material in GPEs will result in better electrochemical and photoelectrochemical properties, and stability for DSSC applications. An ionic liquid based quasi-solid state electrolyte was prepared by solidifying a binary mixture of 1-hexyl-3-methylidazolium iodide (HMImI) and 1-ethyl-3-methylimidazolium tetrafluoroborate (EMImBF4) (weight ratio of 2:1) with 10 wt-% of the polymer poly(1-oligo(ethylene glycol)methacrylate-3-methylimidazolium chloride) (P(MOEMImCl)). The thermal stability of the electrolyte was examined by thermogravimetric analysis and has shown stability up to 200 °C, while the DSSC shows a conversion efficiency of 6.1% under the light intensity of 100 mW cm^{-2} [148].

A biopolymer-based quasi-solid state polymer electrolyte using agar, I_2, 50 wt-% of NaI and KI, 3.0 g of 1-methyl-3-propylimidazolium iodide (MPII) ionic liquid has been developed. Complexation of agar polymer with iodide salt and MPII results in the higher ionic conductivity of 1.48×10^{-3} S cm^{-1} and an efficiency of 2.16% was achieved [149]. GPEs consisting of poly[1-vinylpyrrolidone-co-vinyl acetate] (P[VP-co-VAc]), potassium iodide (KI), iodine (I_2), ethylene carbonate (EC), propylene carbonate (PC), and different weight-percentages of 1-methyl-3-propylimidazolium iodide (MPII) ionic liquid were prepared [150]. The resultant DSSC with GPE containing 15 wt-% MPII showed power conversion efficiency of 4.67% with maximum short-circuit current density (J_{SC}) of 11.98 mA cm^{-2}, open-circuit voltage (V_{OC}) of 0.59 V, and fill factor of 66%. Suryanarayanan *et al.* compared the DSSC performance of organic liquid electrolyte and PVDF-Co-HFP based GPE with different imidazolinum ionic liquids of the type 1-methyl-3-alkyl imidazolinium iodides (alkyl is C_nH_{2n+1}, where n = 3–10). In the case of GPEs containing various

1-methyl-3-alkyl imidazolinium iodides as ionic liquids, when the carbon chain length increases from C3 to C10 the cell performance decreases linearly, which is attributed to the increase in viscosity of ILs for alkyl chain lengths of C3 to C10 [151].

5.3.2.3.4 Inorganic Proton Donors

The addition of proton donor would improve the mobility and ionic conductivity of CPEs. Also, the presence of proton in the electrolyte medium will increase the open-circuit voltage (V_{OC}) and short-circuit current density (J_{SC}) due to the changes in the conduction band of TiO_2, and, consequently, the light harvesting efficiency of DSSCs [152]. Hetero poly acids (HPAs) are one of the commonly encountered inorganic proton donors used as an additive in polymer electrolytes because of desirable features such as tunable structural properties, excellent redox properties, and stability [153]. HPAs become reduced by receiving the back transferred electrons and return them back to the TiO_2 layer. Thus, the presence of HPAs in the electrolyte medium reduce the charge recombination reaction taking place in the TiO_2/dye/electrolyte interface and improve the cell performance of DSSCs.

Chen *et al.* reported a novel composite polymeric gel comprising RTILs(1-butyl-3-methyl-imidazolium-hexafluorophosphate, $BMImPF_6$) and hetero polyacid (phosphotungstic acid, PWA) in poly(2-hydroxyethyl methacrylate) matrix for quasi-solid state DSSCs [154]. GPE with 3 wt-% of PWA achieved the 1.68% under irradiation of $50\,mW\,cm^{-2}$ light intensity; this is more than three times higher than a DSSC with the blank $BMImPF_6$-based polymer electrolyte without PWA ($\eta = 0.52\%$). In our research group, we have reported silicotungustic acid (STA) modified gel polymer electrolytes (GPEs) with poly(ethylene oxide) as a polymer, PC as a plasticizer, and LiI/I_2 as a redox couple. The structural studies revealed the increment in amorphous nature of GPE by the addition of STA. Thus, increases the ionic conductivity and triiodide diffusion coefficient were also improved. The highest efficiency of 6.26% was achieved for the GPE containing 3 wt-% STA [155]. The improvement in efficiency of DSSC is due to suppression in charge recombination reaction in the TiO_2/dye/electrolyte interface. Further, the introduction of a LiI blocking layer improves the cell performance of STA free electrolyte. In DSSCs, the presence of this blocking layer of iodide salt will efficiently transfer holes from dye to electrolyte [156] and decrease the recombination of electron and holes. But, for the STA-modified GPE, the photovoltaic performance was decreased because of the two competing mechanisms.

5.3.3 Bifacial DSSCs

A new emerging technique developing in the recent years is bifacial DSSCs, which are capable of using the light from both sides to attain higher

efficiency in order to bring down the production cost [157]. This helps in the area of building integrated photovoltaic-like power generating windows using transparent DSSCs. Ito *et al*. reported a semitransparent photoanode using TiO_2 nanoparticles of diameter 42 nm and an SiO_2 layer to prevent generation of unwanted back current sensitized with ruthenium dye (Z907Na) and RTILs as the electrolyte [158]. The bifacial DSSCs achieved an efficiency of about 6% for illumination under the front and rear surface. Transparent polyaniline (PANI) electrodes as counterelectrodes for DSSCs prepared by a facile *in situ* polymerization method have shown conversion efficiency of 6.54% under front illumination, comparable with a platinum counterelectrode (6.69%), and an efficiency of 4.26% for rear illumination, which is 65% of that of front illumination [159]. Tang and coworkers reported a series of transparent counterelectrodes based on binary-alloy metal selenides consisting of Co, Ni, Cu, Fe, and Ru [160], among which FeSe yielded the highest front and rear efficiency of 9.22% and 5.90%, respectively.

Also reported is a bifacial quasi-solid-state DSSC containing a semitransparent gel electrolyte and a titanium-grid-supported metal selenide (MSe, M = Co, Ni, Ru) counterelectrode (CE). The semitransparent gel electrolyte was prepared by immersing polyacrylate-poly(ethylene glycol) in liquid electrolyte consists of 100 Mm tetramethylammonium iodide, 100 mM tetraethylammoniumiodide, 100 mM KI, 100 mM tetrabutylammonium iodide, 50 mM I_2, 100 mMLiI, 100 mM NaI, and 500 mM 4-tert-butylpyridine in 50 ml acetonitrile. The front and rear efficiencies of 6.51% and 1.84% were achieved for cost effective titanium-grid-supported RuSe counterelectrodes [161]. In the case of electrolytes containing conventional iodine-based redox couple, it is difficult to attain transparency due to the higher absorbance of iodine in the visible region. An iodine-free quasi-solid electrolyte containing poly(ethylene oxide) (PEO), NaI, and tertbutyl pyridine in acetonitrile for DSSCs fabricated using TiO_2 nanotube (NT) arrays grown on a flexible titanium foil as a working electrode and organichemi-squaraine-based dye as sensitizer has reached an efficiency of 2% under back illumination [162].

Recently, in our research group, we have reported transparent iodide/iodine redox couple based GPEs by incorporating thiourea (TU) in poly(ethylene oxide) (PEO) polymer matrix containing propylene carbonate (PC) as plasticizer as well as solvent. Highest efficiency of 7.17% was reached for the GPE modified with 1wt-% thiourea. GPE modified with 3 wt-% thiourea has shown rear illumination efficiency of 4.63%, which is about 90% as that of front illumination efficiency (5.17%). The improvement in DSSC performance in the presence of thiourea is attributed to a reduction in crystallinity and transparency is attained by the dimerization of thiourea and iodine in the electrolyte medium shown in Figure 5.8 [163].

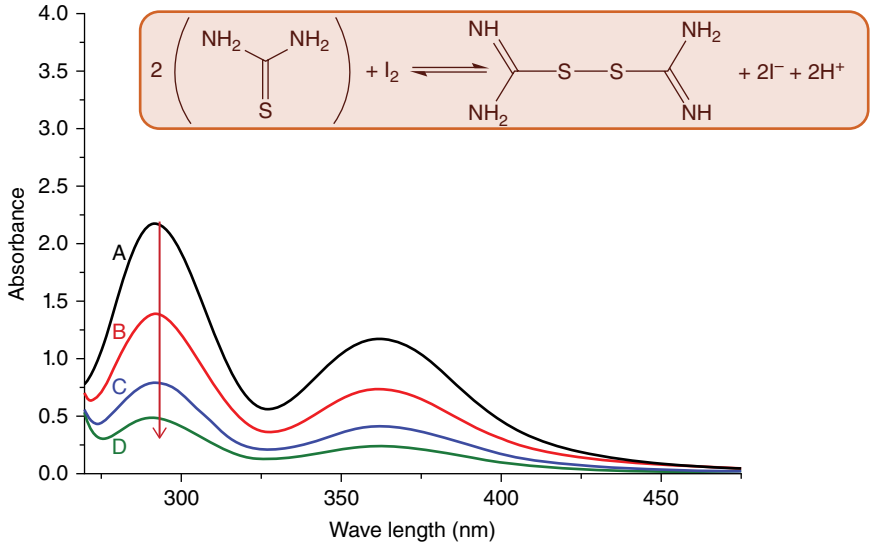

Figure 5.8 UV-Visible spectrum of 0.3% solution of GPEs in acetonitrile. A represents thiourea-free GPE. B, C, and D represent GPEs containing 1, 2, and 3 wt-% of thiourea, respectively (Inset: Dimerization reaction of thiourea (TU) with iodine molecule) [163].

5.4 Quantum Dot Sensitized Solar Cells (QDSSC)

Quantum dots (QDs) are narrow bandgap semiconductor nanoparticles, the physical and chemical properties of which depend on their size. QDs possess some excellent characteristics, such as higher absorption coefficient than organic dyes, good photostability, a tunable bandgap and multiple excitation generations. In quantum dot-sensitized solar cells (QDSSCs), QDs are used in the place of the sensitizer in the DSSC. Apart from this, the components and the working principle of the QDSSCs are very much similar to standard DSSCs. Another upcoming trend is "green" QDSSCs, in which QDs are prepared using less hazardous precursors [164]. The absorption range of QDs can be changed by varying the size [165]. Hence, by combining several types of QDs, it is possible to harvest the whole solar spectrum of infrared to ultraviolet [166]; QDs are capable of generating multiple electron-hole pairs for single photon absorption. This leads to the maximum theoretical conversion efficiency of 44% [167]. Use of I^-/I_3^- is limited to DSSCs because its corrosive nature towards most of the QDs, leading to poor performance of QDSSCs [168]. In order to improve the stability and performance of QDSSCs, iodine-free redox couples such as sulfide/polysulfide (S^{2-}/S_n^{2-}) and Co^{2+}/Co^{3+} were introduced.

A QDSSC containing a novel sequential inorganic ZnS/SiO_2 double layer to reduce interfacial recombination and to increase charge collection efficiency

onto the $CdSe_xTe_{1-x}$QD-sensitized TiO_2 photoanode and employing the S^{2-}/S_n^{2-} redox couple in aqueous solution exhibited the highest conversion efficiency of 8.21% [169]. In order to improve the stability of QDSSCs for outdoor applications, the volatile liquid electrolytes can be replaced more stable polymer-based electrolytes. Yu *et al.* reported a quasi-solid state polysulfide electrolyte containing chemically cross-linked polyacrylamide as polymer matrix for CdS/CdSe cosensitized solar cells and achieved efficiency of 4% [170]. Yang *et al.* synthesized graphene implanted polyacrylamide (PAAm) conducting gel electrolyte by immersing the polymer films in a liquid electrolyte containing polysulfide redox couple [171]. Graphene is used with the aim of accelerating the reduction reaction of redox species in the DSSCs. The use of these electrolytes in quasi-solid state QDSSCs containing CdS sensitizer resulting in power conversion efficiency of 2.34% for electrolyte containing 7 wt-% graphene compared to 1.36% for pure PAAm electrolytes.

In 2013, Chen *et al.* [172] reported a highly conductive hydrogel polysulfide quasi-solid-state using dextran as gelator used in quantum dot-sensitized solar cells (QDSSCs). The electrolyte with 15 wt-% gelator showed conductivity comparable with LE and QDSSC efficiency of 3.23% under one sun (AM 1.5, 100 mW cm^{-2}) illumination, which is slightly lower than that of QDSSCs based on LE (3.69%). Kim *et al.* reported a stable QDSSC using a ZnO photoanode, a carbon-based counterelectrode with gel type polysulfide redox electrolyte [173]. The electrolyte consists of poly(ethylene glycol) dimethylether (PEGDME), 0.5 M Na_2S, 2 M S, 0.2 M KCl, and fumed silica nanoparticles as filler in a 7:3 (v/v) mixture of methanol and distilled water. The optimized cell exhibited 5.45% photoelectric conversion efficiency, comparable with liquid electrolyte (5.69%) and long-term stability of over 5000 seconds.

Feng *et al.* in 2016 constructed a quasi-solid-state QDSSC using gel electrolyte prepared by solidifying a polysulfide aqueous solution using sodium carboxymethylcellulose (CMC-Na) with the impressive efficiency of 9.21% with CdSeTe as the photosensitizer and Cu_2S as the counterelectrode [174]. The electrolyte provided satisfactory conductivity compared to liquid-based polysulfide electrolytes. Also, the gel electrolytes possesses good contact with the surfaces of mesoporous photoanodes due to the presence of strong coordination between carboxylate groups on CMC–Na polymer chains with the metal ions of the photoanode surface. More recently, in 2017 a gel electrolyte containing a natural polymer, agar, was developed for quasi-solid state QDSSCs using $CuInS_2$ or CdS as sensitizer and a various counter electrolytes, such as reduced graphene oxide (RGO)–Cu_2S, RGO-brass, and Cu_xS thin films. Among the fabricated cells the QDSSC containing CdS sensitizer, agar-based gel electrolyte, and (RGO)–Cu_2S counterelectrode has shown a maximum efficiency of 2.21% [175].

It should be noted that the quantum dots have been used in different photovoltaic devices, such as by forming a Schottky junction cells with a metal or

with other semiconductor materials in the heterojunction structure [176]. Recently, a certified solar cell power conversion efficiency of 10.6% has been obtained by using a dispersion of hydrophobic PbS quantum dots in the methyl ammonium iodide organic–inorganic hybrid material [177]. Additionally, the quantum dots show great promise for fabrication of hybrid bulk heterojunction solar cells with enhanced power conversion efficiency, yet controlling the morphology and interface structure on the nanometer length scale is challenging [178–180].

5.5 Perovskite-Sensitized Solar Cells (PSSC)

Perovskites are a group of a compound having a specific crystal structure (Figure 5.9a) with the general formula ABX_3 (X = oxygen, halogen). In the crystal structure of perovskites the larger cation A occupies the cubooctahedral sites and smaller cation B occupies the octahedral sites. There are thousands of compounds that adapt the perovskite structure. Organometallic halide such as $CH_3NH_3PbX_3$ (the A-site cation is $CH_3NH_3^+$ and the B-site cation is Pb^{2+}, as shown in Figure 5.9b) with perovskite structure has attracted attention due to the changes in electrical properties and bandgap with increasing dimensionality from 2D to 3D [181].

In literature, several authors have observed that an increase of the electron-hole diffusion length, a longer charge carrier lifetime, and smaller trap density are attributed to the growth of grain size of the perovskite material from polycrystalline to single crystal thin films [182, 183]. In addition, the perovskites exhibit radiation hardness and withstand proton doses that exceed the damage threshold of crystalline silicon by almost three orders of magnitude [184, 185].

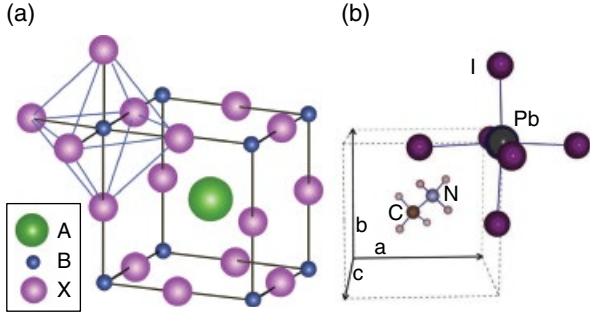

Figure 5.9 (a) ABX_3 perovskite structure showing BX_6 octahedral and larger A cation occupied in cubooctahedral site. (b) The unit cell of cubic $CH_3NH_3PbI_3$ perovskite. Original figure in (b) was reprinted from Reference [187]. Reproduced with permission of American Chemical Society.

To date, the power conversion efficiency of the perovskite-based solar cell shows an increase in value from 3.8% to greater than 20%, reached in less than seven years [186].This made perovskite suitable for solar cell applications.

In 2009, Miyasaka *et al.* reported the application of 3D perovskite $CH_3NH_3PbX_3$ (X = Br, I) as an inorganic sensitizer to replace dye in dye-sensitized solar cells [188]. The cells containing $CH_3NH_3PbX_3$-sensitized TiO_2 anode, platinum counterelectrode, and, respectively, lithium halide and halogen as redox couple yielded an efficiency of 3.13% for $CH_3NH_3PbBr_3$ and of 3.81% for $CH_3NH_3PbI_3$. Park *et al.* reported a perovskite $(CH_3NH_3)PbI_3$ nanocrystal sensitized solar cell with an efficiency of 6.5% under 1 sun irradiation, much higher compared to N719 ($\eta = 3.89\%$) [189]. The higher efficiency is due to the higher absorption coefficient of $(CH_3NH_3)PbI_3$, which is 10 times higher than that of ruthenium-based dyes.

As perovskite is ionic in nature, it will dissolve easily in a polar solvent. Thus, use of liquid electrolytes in PSSCs will affect the stability of the cells. These instability issues can be solved by substituting liquid electrolyte with polymer electrolytes or solid-state hole transport material. In 2016, Ragul *et al.* reported perovskite sensitized solar cells (PSSC) comprising methyl ammonium tri-lead iodide ($CH_3NH_3PbI_3$) and ethyl ammonium tri-lead iodide ($CH_3CH_2NH_3PbI_3$) with solid polymer electrolyte consisting of PEO, KI, and I_2 in methanol [190, 191]. The fabricated PSSC with $CH_3NH_3PbI_3$ has shown an efficiency of 0.53% whereas $CH_3CH_2NH_3PbI_3$ shows the efficiency of 0.75%.

5.6 Conclusion

Solar energy is one the promising renewable energy sources. Among various generations of solar cells, thin film based solar cells are more cost effective and environmentally friendly. In thin film based solar cells, electrolyte part plays a vital role in deciding the cell performance and stability of the cells. Using conventional liquid electrolytes, a conversion efficiency of 13% was achieved. But, the issues of liquid electrolytes, such as poor stability and corrosive nature, can be resolved by replacing the conventional liquid electrolyte with a more stable noncorrosive electrolyte, such as RTILs, HTMs, polymer electrolytes, etc. In the midst of other electrolytes, polymer electrolytes attained attention due to stability, low cost, and nontoxic nature. Gel polymer electrolyte containing additives has attained efficiency up to 10% in the case of dye-sensitized solar cells and up to 6% in the case of quantum dot sensitized solar cell. Further, studies on understanding the interactions of polymer electrolytes with electrodes and sensitizer to enhance charge transfer efficiency and to decrease recombination losses will improve the cell performance and stability of DSSCs, QDSSCs, and PSSCs.

Acknowledgements

The research work was financially supported by Solar Energy Research Initiative-DST, New Delhi (DST/TM/SERI/2k12/109(C).

References

1 Smalley RE, Bush W, Mansfield S. Future Global Energy Prosperity : The Terawatt Challenge, Fall Meeting, Materials Research Society, Boston, 2004.
2 Lewis NS, Nocera DG. Powering the planet : Chemical challenges in solar energy utilization. *Proc Natl Acad Sci USA*, 2006; **103**: 15729–15736.
3 Wetstone G, Thornton K, Hinrichs-rahlwes R, *et al*. *Renewables 2016 Global Status Report*, 2016, REN21. ISBN 978-3-9818107-0-7.
4 Würfel P. Physics of Solar Cells: From Principles to New Concepts, 2005, Wiley-VCH. doi: 10.1002/9783527618545
5 Ellabban O, Abu-rub H, Blaabjerg F. Renewable energy resources : Current status, future prospects and their enabling technology. *Renew Sustain Energy Rev*, 2014; **39**: 748–764. doi: 10.1016/j.rser.2014.07.113
6 Becquerel AE. Comptes Rendus de l'Academie des Sciences. *Comptes Rendus l'Academie Des Sci*, 1839; **9**: 561–569.
7 Kibria MT, Ahammed A, Sony SM, *et al*. A review : Comparative studies on different generation solar cells technology. *Proceedings of 5th International Conference on Environmental Aspects of Bangladesh [ICEAB 2014]*, 2014: 51–53.
8 Chapin DM, Fuller CS, Pearson GL. A New Silicon pn Junction Photocell for Converting Solar Radiation into Electrical Power. *J Appl Phys*, 1954; **676**: 22–24. doi:10.1063/1.1721711
9 Nozik A. Quantum dot solar cells. *Phys E (Amsterdam, Neth)*, 2002;**14**:115–120. doi:10.1016/S1386-9477(02)00374-0
10 König D, Casalenuovo K, Takeda Y, *et al*. Hot carrier solar cells: Principles, materials and design. *Phys E (Amsterdam, Neth)*, 2010; **42**: 2862–2866. doi:10.1016/j.physe.2009.12.032
11 King RR, Bhusari D, Larrabee D, *et al*. Solar cell generations over 40% efficiency. *Prog Photovoltaics Res Appl*, 2012; **20**: 801–815. doi: 10.1002/pip.1255
12 Fonash S. *Solar Cell Device Physics*, 2nd edn, Elsevier, 2010.
13 Luque A, Martí A, Stanley C. Understanding intermediate-band solar cells. *Nat Photonics*, 2012; **6**: 146–152. doi: 10.1038/nphoton.2012.1
14 Marsen B, Klemz S, Landi G, *et al*. Phases in copper–gallium–metal–sulfide films (metal = titanium, iron, or tin). *Thin Solid Films*, 2011; **519**: 7284–7287. doi:10.1016/j.tsf.2011.01.137

15 Renno C, Petito F, Landi G, Neitzert HC. Experimental characterization of a concentrating photovoltaic system varying the light concentration. *Energy Convers Manag*, 2017; **138**: 119–130. doi:10.1016/j.enconman.2017.01.050

16 Krossing I, Reisinger A. Chemistry with weakly-coordinating fluorinated alkoxyaluminate anions: Gas phase cations in condensed phases? *Coord Chem Rev*, 2006; **250**: 2721–2744. doi:10.1016/j.ccr.2005.10.023

17 Mathew S, Yella A, Gao P, *et al*. Dye-sensitized solar cells with 13% efficiency achieved through the molecular engineering of porphyrin sensitizers. *Nature Chem.*, 2014; **6**. doi:10.1038/nchem.1861

18 Pan Z, Mora-sero I, Shen Q, *et al*. High efficiency "green" quantum dot solar cells. *J Am Chem Soc*, 2014; **136**(25): 9203–9210. doi:10.1021/ja504310w

19 Im J, Lee C, Lee J, *et al*. 6.5% efficient perovskite quantum-dot-sensitized solar cell. *Nanoscale*, 2011; **2**: 4088–4093. doi:10.1039/c1nr10867k

20 Li B, Wang L, Kang B, Qui Y. Review of recent progress in solid-state dye-sensitized solar cells. *ChemInform*, 2006; **90**: 549–573. doi:10.1016/j.solmat.2005.04.039

21 Rogers RD. Chemistry: Ionic liquids – solvents of the future? *Science*, 2003; **302**: 792–793. doi:10.1126/science.1090313

22 Papageorgiou N. The performance and stability of ambient temperature molten salts for solar cell applications. *J Electrochem Soc*, 1996; **143**: 3099. doi:10.1149/1.1837171

23 Ku S-Y, Lu S-Y. Inexpensive room temperature ionic liquids for low volatility electrolytes of dye-sensitized solar cells. *Int J Electrochem Sci*, 2011; **6**: 5219–27

24 Bai Y, Cao Y, Zhang J, *et al*. High-performance dye-sensitized solar cells based on solvent-free electrolytes produced from eutectic melts. *Nat Mater*, 2008; **7**: 626–30. doi:10.1038/nmat2224

25 Jovanovski V, González-Pedro V, Giménez S, *et al*. A sulfide/polysulfide-based ionic liquid electrolyte for quantum dot-sensitized solar cells. *J Am Chem Soc*, 2011; **133**: 20156–20159. doi:10.1021/ja2096865

26 Tennakone K, Kumara GRRA, Kumarasinghe AR, *et al*. A dye-sensitized nano-porous solid-state photovoltaic cell. *Semicond Sci Technol*, 1995; **10**: 1689–1693. doi:10.1088/0268-1242/10/12/020

27 Li D, Qin D, Deng M, *et al*. Optimization the solid-state electrolytes for dye-sensitized solar cells. *Energy Environ Sci*, 2009; **2**: 283–291. doi:10.1039/B813378F

28 Meng Q-B, Takahashi K, Zhang X-T, *et al*. Fabrication of an efficient solid-state dye-sensitized solar cell. *Langmuir*, 2003; **19**: 3572–3574. doi:10.1021/la026832n

29 Kumara GRA, Konno A, Shiratsuchi K, *et al*. Dye-sensitized solid-state solar cells: use of crystal growth inhibitors for deposition of the hole collector. *Chem Mater*, 2002; **14**: 954–955. doi:10.1021/cm011595f

30 Perera VPS, Tennakone K. Recombination processes in dye-sensitized solid-state solar cells with CuI as the hole collector. *Sol Energy Mater Sol Cells*, 2003; **79**: 249–255. doi:10.1016/S0927-0248(03)00103-X

31 O'Regan B, Lenzmann F, Muis R, Wienke J. A solid-state dye-sensitized solar cell fabricated with pressure-treated P25–TiO_2 and CuSCN: Analysis of pore filling and iv characteristics. *Chem Mater*, 2002; **14**: 5023–5029. doi:10.1021/cm020572d

32 Chung I, Lee B, He J, Chang RPH, Kanatzidis MG. All-solid-state dye-sensitized solar cells with high efficiency. *Nature*, 2012; **485**: 486–489. doi:10.1038/nature11067

33 Chander N, Chandrasekhar PS, Komarala VK. Solid state plasmonic dye sensitized solar cells based on solution processed perovskite $CsSnI_3$ as the hole transporter. *RSC Adv*, 2014; **4**: 55658–55665. doi:10.1039/C4RA09719J

34 Karthikeyan CS, Thelakkat M. Key aspects of individual layers in solid-state dye-sensitized solar cells and novel concepts to improve their performance. *Inorganica Chim Acta*, 2008; **361**: 635–655. doi:10.1016/j.ica.2007.04.033

35 Grätzel M, Bach U, Lupo D, *et al*. Solid-state dye-sensitized mesoporous TiO_2 solar cells with high photon-to-electron conversion efficiencies. *Nature*, 1998; **395**: 583–585. doi:10.1038/26936

36 Xu B, Tian H, Lin L, *et al*. Integrated design of organic hole transport materials for efficient solid-state dye-sensitized solar cells. *Adv Energy Mater*, 2015; **5**: 1401185. doi:10.1002/aenm.201401185

37 Burschka J, Dualeh A, Kessler F, *et al*. Tris(2-(1 H -pyrazol-1-yl)pyridine) cobalt(III) as p-type dopant for organic semiconductors and its application in highly efficient solid-state dye-sensitized solar cells. *J Am Chem Soc*, 2011; **133**: 18042–18045. doi:10.1021/ja207367t

38 Fenton DE, Parker JM, Wright P V. Complexes of alkali metal ions with poly(ethylene oxide). *Polymer (Guildf)*, 1973; **14**: 589.

39 Wright P V. Electrical conductivity in ionic complexes of poly(ethylene oxide). *Br Polym J*, 1975; **7**: 319–327. doi:10.1002/pi.4980070505

40 Vashishta P, Mundy JN, Shenoy GK. Fast ion transport in solids : electrodes, and electrolytes. *Proceedings of the International Conference on Fast Ion Transport in Solids, Electrodes, and Electrolytes*, Lake Geneva, WI, USA, 21–25 May, 1979. North Holland; 1979.

41 Sapp SA, Sotzing GA, Reynolds JR. High contrast ratio and fast-switching dual polymer electrochromic devices. *Chem Mater*, 1998; **10**: 2101–2108. doi:10.1021/cm9801237

42 Meyer WH. Polymer electrolytes for lithium-ion batteries. *Adv Mater*, 1998; **10**: 439–448. doi:10.1002/(SICI)1521-4095(199804)10:6<439::AID-ADMA439>3.0.CO;2-I.

43 Opekar F, Štulík K. Electrochemical sensors with solid polymer electrolytes. *Anal Chim Acta*, 1999; **385**: 151–162. doi:10.1016/S0003-2670(98)00583-2

44 Saikia D, Pan Y-C, Wu C-G, *et al*. Synthesis and characterization of a highly conductive organic–inorganic hybrid polymer electrolyte based on amine terminated triblock polyethers and its application in electrochromic devices. *J Mater Chem C*, 2014; **2**: 331–343. doi:10.1039/C3TC31555J

45 Ratner MA, Shriver DF. Ion transport in solvent-free polymers. *Chem Rev*, 1988; **88**: 109–124. doi:10.1021/cr00083a006

46 Druger S, Ratner M, Nitzan A. Polymeric solid electrolytes: Dynamic bond percolation and free volume models for diffusion. *Solid State Ionics*, 1983; **9–10**: 1115–1120. doi:10.1016/0167-2738(83)90139-X

47 Druger SD, Nitzan A, Ratner MA. Dynamic bond percolation theory: A microscopic model for diffusion in dynamically disordered systems. I. Definition and one-dimensional case. *J Chem Phys*, 1983; **79**: 3133–142. doi:10.1063/1.446144

48 Dzulkurnain N, Ahmad A, Mohamed N. P(MMA-EMA) random copolymer electrolytes incorporating sodium iodide for potential application in a dye-sensitized solar cell. *Polymers (Basel)*, 2015; **7**: 266–280. doi:10.3390/polym7020266

49 Singh VK, Bhattacharya B, Shukla S, Singh PK. New solid-polymer-electrolyte material for dye-sensitized solar cells. *Mater Tehnol*, 2015; **49**: 123–127.

50 Manuel Stephan A. Review on gel polymer electrolytes for lithium batteries. *Eur Polym J*, 2006; **42**: 21–42. doi:10.1016/j.eurpolymj.2005.09.017

51 Xue Z, He D, Xie X. Poly(ethylene oxide)-based electrolytes for lithium-ion batteries. *J Mater Chem A*, 2015; **3**: 19218–19253. doi:10.1039/C5TA03471J

52 Bhattacharya B, Nagarale RK, Singh PK. Effect of sodium-mixed anion doping in PEO-based polymer electrolytes. *High Perform Polym*, 2010; **22**: 498–512. doi:10.1177/0954008309104931

53 Call F, Stolwijk NA. Impact of I_2 additions on iodide transport in polymer electrolytes for dye-sensitized solar cells: Reduced pair formation versus a Grotthuss-like mechanism. *J Phys Chem Lett*, 2010; **1**: 2088–2093. doi:10.1021/jz100644z

54 Srivastava N, Tiwari T. New trends in polymer electrolytes: a review. *E-Polymers*, 2009; **9**: 1738–1754.

55 Armand M. Polymers with ionic conductivity. *Adv Mater*, 1990; **2**: 278–286. doi:10.1002/adma.19900020603

56 Golodnitsky D, Strauss E, Peled E, Greenbaum S. Review – On order and disorder in polymer electrolytes. *J Electrochem Soc*, 2015; **162**: A2551–2566. doi:10.1149/2.0161514jes

57 Dey A, Karan S, Dey A, De SK. Structure, morphology and ionic conductivity of solid polymer electrolyte. *Mater Res Bull*, 2011; **46**: 2009–2015. doi:10.1016/j.materresbull.2011.07.008

58 Xia J, Li F, Huang C, *et al*. Improved stability quasi-solid-state dye-sensitized solar cell based on polyether framework gel electrolytes. *Sol Energy Mater Sol Cells*, 2006; **90**: 944–952. doi:10.1016/j.solmat.2005.05.021

59 Zhou DY, Wang GZ, Li WS, *et al*. Preparation and performances of porous polyacrylonitrile–methyl methacrylate membrane for lithium-ion batteries. *J Power Sources*, 2008; **184**: 477–480. doi:10.1016/j.jpowsour.2008.05.027

60 Saikia D, Han CC, Chen-Yang YW. Influence of polymer concentration and dyes on photovoltaic performance of dye-sensitized solar cell with P(VdF-HFP)-based gel polymer electrolyte. *J Power Sources*, 2008; **185**: 570–576. doi:10.1016/j.jpowsour.2008.06.063

61 Vincent CA. Polymer electrolytes. *Prog Solid State Chem*, 1987; **17**: 145–261. doi:10.1016/0079-6786(87)90003-3

62 Dey A. Thermal and electric properties of CeO_2 nanoparticles dispersed in polyethylene oxide:NH_4ClO_4 complex. *Solid State Ionics*, 2008; **178**: 1963–1968. doi:10.1016/j.ssi.2007.12.063

63 Scrosati B, Croce F, Appetecchi GB, Persi L. Nanocomposite polymer electrolytes for lithium batteries. *Nature*, 1998; **394**: 456–458. doi:10.1038/28818

64 Landi G, Sorrentino A, Fedi F, *et al*. Cycle stability and dielectric properties of a new biodegradable energy storage material. *Nano Energy*, 2015; **17**: 348–355. doi:10.1016/j.nanoen.2015.09.006

65 Landi G, Sorrentino A, Iannace S, Neitzert HC. Differences between graphene and graphene oxide in gelatin based systems for transient biodegradable energy storage applications. *Nanotechnol*, 2017; **28**: 54005. doi:10.1088/1361-6528/28/5/054005

66 Gray F. M. *Polymer Electrolyte Reviews*. Elsevier Applied Science; 1987, p. 139.

67 Gerischer H, Michel-Beyerle ME, Rebentrost F, Tributsch H. Sensitization of charge injection into semiconductors with large band gap. *Electrochim Acta*, 1968; **13**: 1509–1515. doi:10.1016/0013-4686(68)80076-3

68 Tsubomura H, Matsumura M, Nomura Y, Amamiya T. Dye sensitised zinc oxide: aqueous electrolyte: platinum photocell. *Nature*, 1976; **261**: 402–403. doi:10.1038/261402a0

69 Matsumura M, Matsudaira S, Tsubomura H, *et al*. Dye sensitization and surface structures of semiconductor electrodes. *Ind Eng Chem Prod Res Dev*, 1980; **19**: 415–421. doi:10.1021/i360075a025

70 Desilvestro J, Graetzel M, Kavan L, *et al*. Highly efficient sensitization of titanium dioxide. *J Am Chem Soc*, 1985; **107**: 2988–2990. doi:10.1021/ja00296a035

71 O'Regan B, Grätzel M. A low-cost, high-efficiency solar cell based on dye-sensitized colloidal TiO_2 films. *Nature*, 1991; **353**: 737–740. doi:10.1038/353737a0

72 Hagfeldt A, Boschloo G, Sun L, *et al*. Dye-sensitized solar cells. *Chem Rev*, 2010; **110**: 6595–6663. doi:10.1021/cr900356p

73 Wu J, Lan Z, Hao S, *et al*. Progress on the electrolytes for dye-sensitized solar cells. *Pure Appl Chem*, 2008; **80**: 2241–2258.

74 Sima C, Grigoriu C, Antohe S. Comparison of the dye-sensitized solar cells performances based on transparent conductive ITO and FTO. *Thin Solid Films*, 2010; **519**: 595–597. doi:10.1016/j.tsf.2010.07.002

75 Vomiero A, Galstyan V, Braga A, *et al*. Flexible dye sensitized solar cells using TiO_2 nanotubes. *Energy Environ Sci*, 2011; **4**: 3408. doi:10.1039/c0ee00485e

76 Kang MG, Park N-G, Ryu KS, *et al*. A 4.2% efficient flexible dye-sensitized TiO_2 solar cells using stainless steel substrate. *Sol Energy Mater Sol Cells*, 2006; **90**: 574–581. doi:10.1016/j.solmat.2005.04.025.

77 Sommeling PM, Späth M, Kroon J, *et al*. Flexible dye-sensitized nanocrystalline TiO_2 solar cells. *Proceedings of 16th Eur. Photovolt. Sol. Energy Conf.*, 2000, pp. 1–5.

78 Keis K, Magnusson E, Lindström H, *et al*. A 5% efficient photoelectrochemical solar cell based on nanostructured ZnO electrodes. *Sol Energy Mater Sol Cells*, 2002; **73**: 51–58. doi:10.1016/S0927-0248(01)00110-6

79 Green ANM, Palomares E, Haque SA, *et al*. Charge Transport versus Recombination in Dye-Sensitized Solar Cells Employing Nanocrystalline TiO_2 and SnO_2 Films. *J Phys Chem B*, 2005; **109**: 12525–12533. doi:10.1021/jp050145y

80 Qin P, Zhu H, Edvinsson T, *et al*. Design of an organic chromophore for p-type dye-sensitized solar cells. *J Am Chem Soc*, 2008; **130**: 8570–8571. doi:10.1021/ja8001474

81 Ke L, Dolmanan S Bin, Shen L, *et al*. Degradation mechanism of ZnO-based dye-sensitized solar cells. *Sol Energy Mater Sol Cells*, 2010; **94**: 323–326. doi:10.1016/j.solmat.2009.10.007

82 Barbé CJ, Arendse F, Comte P, *et al*. Nanocrystalline titanium oxide electrodes for photovoltaic applications. *J Am Ceram Soc*, 2005; **80**: 3157–3171. doi:10.1111/j.1151-2916.1997.tb03245.x

83 Lindström H, Holmberg A, Magnusson E, *et al*. A new method for manufacturing nanostructured electrodes on plastic substrates. *Nano Lett*, 2001; **1**: 97–100. doi:10.1021/nl0055254

84 Lindström H, Holmberg A, Magnusson E, *et al*. A new method to make dye-sensitized nanocrystalline solar cells at room temperature. *J Photochem Photobiol A Chem*, 2001; **145**: 107–112. doi:10.1016/S1010-6030(01)00564-0

85 Galoppini E. Linkers for anchoring sensitizers to semiconductor nanoparticles. *Coord Chem Rev*, 2004; **248**: 1283–1297. doi:10.1016/j.ccr.2004.03.016

86 Grätzel M. Photovoltaic performance and long-term stability of dye-sensitized meosocopic solar cells. *Comptes Rendus Chim*, 2006; **9**: 578–583. doi:10.1016/j.crci.2005.06.037

87 Mishra A, Fischer MKR, Bäuerle P. Metal-free organic dyes for dye-sensitized solar cells: from structure: Property relationships to design rules. *Angew Chemie Int Ed*, 2009; **48**: 2474–2499. doi:10.1002/anie.200804709

88 Martineau D, Beley M, Gros PC, *et al*. Tuning of ruthenium complex properties using pyrrole- and pyrrolidine-containing polypyridine ligands. *Inorg Chem*, 2007; **46**: 2272–2277. doi:10.1021/ic062042f

89 Yella A, Lee H-W, Tsao HN, *et al*. Porphyrin-sensitized solar cells with cobalt (II/III)-based redox electrolyte exceed 12 percent efficiency. *Science*, 2011; **334**: 629–634. doi:10.1126/science.1209688

90 Kuciauskas D, Monat JE, Villahermosa R, *et al*. Transient absorption spectroscopy of ruthenium and osmium polypyridyl complexes adsorbed onto nanocrystalline TiO_2 photoelectrodes. *J Phys Chem B*, 2002; **106**: 9347–5938. doi:10.1021/jp014589f

91 Hasselmann GM, Meyer GJ. Diffusion-limited interfacial electron transfer with large apparent driving forces. *J Phys Chem B*, 1999; **103**: 7671–7675. doi:10.1021/jp992086s

92 Ferrere S. New photosensitizers based upon $Fe(L)_2(CN)_2$. and $Fe(L)_3$. (L = substituted 2,2′-bipyridine): Yields for the photosensitization of TiO_2 and effects on the band selectivity. *Chem Mater*, 2000; **12**: 1083–1089. doi:10.1021/cm990713k

93 Nazeeruddin MK, Péchy P, Renouard T, *et al*. Engineering of efficient panchromatic sensitizers for nanocrystalline TiO_2-based solar cells. *J Am Chem Soc*, 2001; **123**: 1613–1624. doi:10.1021/ja003299u

94 Nazeeruddin MK, De Angelis F, Fantacci S, *et al*. Combined experimental and DFT-TDDFT computational study of photoelectrochemical cell ruthenium sensitizers. *J Am Chem Soc*, 2005; **127**: 16835–16847. doi:10.1021/ja052467l

95 Selopal GS, Wu H-P, Lu J, *et al*. Metal-free organic dyes for TiO_2 and ZnO dye-sensitized solar cells. *Sci Rep*, 2016; **6**: 18756. doi:10.1038/srep18756

96 Mehmood U, Rahman S, Harrabi K, *et al*. Recent advances in dye sensitized solar cells. *Adv Mater Sci Eng*, 2014; **2014**: 1–12. doi:10.1155/2014/974782

97 Wang Z-S, Koumura N, Cui Y, *et al*. Hexylthiophene-functionalized carbazole dyes for efficient molecular photovoltaics: Tuning of solar-cell performance by structural modification. *Chem Mater*, 2008; **20**: 3993–4003. doi:10.1021/cm8003276

98 Koumura N, Wang Z-S, Miyashita M, *et al*. Substituted carbazole dyes for efficient molecular photovoltaics: long electron lifetime and high open circuit voltage performance. *J Mater Chem*, 2009; **19**: 4829. doi:10.1039/b905831a

99 Joly D, Pellejà L, Narbey S, *et al*. A robust organic dye for dye sensitized solar cells based on iodine/iodide electrolytes combining high efficiency and outstanding stability. *Sci Rep*, 2015; **4**: 4033. doi:10.1038/srep04033

100 Wu J, Lan Z, Lin J, Huang M, Huang Y, Fan L, *et al*. Electrolytes in dye-sensitized solar cells. *Chem Rev*, 2015; **115**: 2136–2173. doi:10.1021/cr400675m

101 Wang M, Grätzel C, Zakeeruddin SM, Grätzel M. Recent developments in redox electrolytes for dye-sensitized solar cells. *Energy Environ Sci*, 2012; **5**: 9394. doi:10.1039/c2ee23081j

102 Hamann TW, Ondersma JW. Dye-sensitized solar cellredox shuttles. *Energy Environ Sci*, 2011; **4**: 370–381. doi:10.1039/C0EE00251H

103 Boschloo G, Hagfeldt A. Characteristics of the iodide/triiodide redox mediator in dye-sensitized solar cells. *Acc Chem Res*, 2009; **42**: 1819–1826. doi:10.1021/ar900138m

104 Teng C, Yang X, Yuan C, *et al*. Two novel carbazole dyes for dye-sensitized solar cells with open-circuit voltages up to 1 V based on Br^-/Br_3^- electrolytes. *Org Lett*, 2009; **11**: 5542–5545. doi:10.1021/ol9022936

105 Gorlov M, Pettersson H, Hagfeldt A, Kloo L. Electrolytes for dye-sensitized solar cells based on interhalogen ionic salts and liquids. *Inorg Chem*, 2007; **46**: 3566–3575. doi:10.1021/ic062244b

106 Wang P, Zakeeruddin SM, Moser J-E, *et al*. A solvent-free, $SeCN^-/(SeCN)_3^-$ based ionic liquid electrolyte for high-efficiency dye-sensitized nanocrystalline solar cells. *J Am Chem Soc*, 2004; **126**: 7164–7165. doi:10.1021/ja048472r

107 Nusbaumer H, Moser J-E, Zakeeruddin SM, *et al*. Co II $(dbbip)_2^{2+}$ complex rivals tri-iodide/iodide redox mediator in dye-sensitized photovoltaic cells. *J Phys Chem B*, 2001; **105**: 10461–10464. doi:10.1021/jp012075a

108 Papageorgiou N. An iodine/triiodide reduction electrocatalyst for aqueous and organic media. *J Electrochem Soc*, 1997; **144**: 876. doi:10.1149/1.1837502

109 Nazeeruddin MK, Kay A, Rodicio I, *et al*. Conversion of light to electricity by cis-X_2bis(2,2′-bipyridyl-4,4′-dicarboxylate)ruthenium(II) charge-transfer sensitizers ($X = Cl^-$, Br^-, I^-, CN^-, and SCN^-) on nanocrystalline titanium dioxide electrodes. *J Am Chem Soc*, 1993; **115**: 6382–6390. doi:10.1021/ja00067a063

110 Lee S, Jun Y, Kim K-J, Kim D. Modification of electrodes in nanocrystalline dye-sensitized TiO_2 solar cells. *Sol Energy Mater Sol Cells*, 2001; **65**: 193–200. doi:10.1016/S0927-0248(00)00095-7

111 Jeong H, Pak Y, Hwang Y, *et al*. Enhancing the charge transfer of the counter electrode in dye-sensitized solar cells using periodically aligned platinum nanocups. *Small*, 2012; **8**: 3757–3561. doi:10.1002/smll.201201214

112 Kay A, Grätzel M. Low cost photovoltaic modules based on dye sensitized nanocrystalline titanium dioxide and carbon powder. *Sol Energy Mater Sol Cells*, 1996; **44**: 99–117. doi:10.1016/0927-0248(96)00063-3

113 Nogueira AF, Alonso-Vante N, De Paoli M-A. Solid-state photoelectrochemical device using poly(*o*-methoxy aniline) as sensitizer and an ionic conductive elastomer as electrolyte. *Synth Met*, 1999; **105**: 23–27. doi:10.1016/S0379-6779(99)00078-8

114 Singh PK, Kim K-W, Rhee H-W. Development and characterization of ionic liquid doped solid polymer electrolyte membranes for better efficiency. *Synth Met*, 2009; **159**: 1538–1541. doi:10.1016/j.synthmet.2009.04.012

115 Buraidah MH, Teo LP, Majid SR, *et al*. Characterizations of chitosan-based polymer electrolyte photovoltaic cells. *Int J Photoenergy*, 2010; **2010**: 1–7. doi:10.1155/2010/805836

116 Imperiyka M, Ahmad A, Hanifah SA, Bella F. A UV-prepared linear polymer electrolyte membrane for dye-sensitized solar cells. *Phys B Condens Matter*, 2014; **450**: 151–154. doi:10.1016/j.physb.2014.05.053

117 Su'ait MS, Ahmad A, Badri KH, *et al*. The potential of polyurethane bio-based solid polymer electrolyte for photoelectrochemical cell application. *Int J Hydrogen Energy*, 2014; **39**: 3005–3017. doi:10.1016/j.ijhydene.2013.08.117

118 Anandan S, Sivakumar R. Effect of loaded TiO_2 nanofiller on heteropolyacid-impregnated PVDF polymer electrolyte for the performance of dye-sensitized solar cells. *Phys Status Solidi*, 2009; **206**: 343–350. doi:10.1002/pssa.200824276

119 Singh PK, Kim K-W, Park N-G, Rhee H-W. Mesoporous nanocrystalline TiO_2 electrode with ionic liquid-based solid polymer electrolyte for dye-sensitized solar cell application. *Synth Met*, 2008; **158**: 590–593. doi:10.1016/j.synthmet.2008.04.003

120 Anandan S, Sivakumar R, Tharani P. Solid-state dye-sensitized solar cells constructed with an electrochrome impregnated elastomeric electrolyte. *Synth Met*, 2008; **158**: 1067–1071. doi:10.1016/j.synthmet.2008.04.030

121 Sivakumar R, Akila K, Anandan S. New type of inorganic–organic hybrid (heteropolytungsticacid–polyepichlorohydrin) polymer electrolyte with TiO_2 nanofiller for solid state dye sensitized solar cells. *Curr Appl Phys*, 2010; **10**: 1255–1260. doi:10.1016/j.cap.2010.03.003

122 Kim JH, Kang M-S, Kim YJ, *et al*. Dye-sensitized nanocrystalline solar cells based on composite polymer electrolytes containing fumed silica nanoparticles. *Chem Commun*, 2004: **1662**. doi:10.1039/b405215c

123 Nogueira VC, Longo C, Nogueira AF, *et al*. Solid-state dye-sensitized solar cell: Improved performance and stability using a plasticized polymer electrolyte. *J Photochem Photobiol A Chem*, 2006; **181**: 226–232. doi:10.1016/j.jphotochem.2005.11.028

124 Bhattacharya B, Lee JY, Geng J, *et al*. Effect of cation size on solid polymer electrolyte based dye-sensitized solar cells. *Langmuir*, 2009; **25**: 3276–3281. doi:10.1021/la8029177

125 Nei de Freitas J, Longo C, Nogueira AF, De Paoli M-A. Solar module using dye-sensitized solar cells with a polymer electrolyte. *Sol Energy Mater Sol Cells*, 2008; **92**: 1110–1114. doi:10.1016/j.solmat.2008.03.022

126 Cao F, Oskam G, Searson PC. A solid state, dye sensitized photoelectrochemical cell. *J Phys Chem*, 1995; **99**: 17071–17073. doi:10.1021/j100047a003

127 Wang P, Zakeeruddin SM, Moser JE, *et al*. A stable quasi-solid-state dye-sensitized solar cell with an amphiphilic ruthenium sensitizer and polymer gel electrolyte. *Nat Mater*, 2003; **2**: 402–407. doi:10.1038/nmat904

128 Chen C-L, Teng H, Lee Y-L. Preparation of highly efficient gel-state dye-sensitized solar cells using polymer gel electrolytes based on poly(acrylonitrile-co-vinyl acetate). *J Mater Chem*, 2011; **21**: 628–632. doi:10.1039/C0JM03597A

129 Park SJ, Yoo K, Kim J-Y, *et al*. Water-based thixotropic polymer gel electrolyte for dye-sensitized solar cells. *ACS Nano*, 2013; **7**: 4050–4056. doi:10.1021/nn4001269

130 Kim D-W, Jeong Y-B, Kim S-H, *et al*. Photovoltaic performance of dye-sensitized solar cell assembled with gel polymer electrolyte. *J Power Sources*, 2005; **149**: 112–116. doi:10.1016/j.jpowsour.2005.01.058

131 Bella F, Ozzello ED, Sacco A, *et al*. Polymer electrolytes for dye-sensitized solar cells prepared by photopolymerization of PEG-based oligomers. *Int J Hydrogen Energy*, 2014; **39**: 3036–3045.

132 Priya ARS, Subramania A, Jung Y-S, Kim K-J. High-performance quasi-solid-state dye-sensitized solar cell based on an electrospun PVdF–HFP membrane electrolyte. *Langmuir*, 2008; **24**: 9816–9819. doi:10.1021/la801375s

133 Wang L, Fang S, Lin Y, *et al*. A 7.72% efficient dye sensitized solar cell based on novel necklace-like polymer gel electrolyte containing latent chemically cross-linked gel electrolyte precursors. *Chem Commun*, 2005: 5687. doi:10.1039/b510335e

134 Yang H, Ileperuma OA, Shimomura M, Murakami K. Effect of ultra-thin polymer membrane electrolytes on dye-sensitized solar cells. *Sol Energy Mater Sol Cells*, 2009; **93**: 1083–1086. doi:10.1016/j.solmat.2008.12.019

135 Chen J-G, Chen C-Y, Wu C-G, Ho K-C. In situ low temperature polymerization of bismaleimide for gel-type electrolyte for dye-sensitized solar cells. *J Phys Chem C*, 2010; **114**: 13832–13837. doi:10.1021/jp101859r

136 Hong SC, Nguyen-Thai NU, Hong SB, Kang P-H. UV-cross-linked block copolymers for initiator-free, controlled in situ gelation of electrolytes in dye-sensitized solar cells. *J Mater Chem*, 2012;**22**:18854. doi:10.1039/c2jm32526h

137 Lee K-M, Hsu C-Y, Chiu W-H, *et al*. Dye-sensitized solar cells with a micro-porous TiO_2 electrode and gel polymer electrolytes prepared by in situ cross-link reaction. *Sol Energy Mater Sol Cells*, 2009; **93**: 2003–2007. doi:10.1016/j.solmat.2009.07.017

138 Kumar M, Sekhon S. Role of plasticizer's dielectric constant on conductivity modification of PEO–NH_4F polymer electrolytes. *Eur Polym J*, 2002; **38**: 1297–1304. doi:10.1016/S0014-3057(01)00310-X

139 Nogueira AF, Longo C, De Paoli M-A. Polymers in dye sensitized solar cells: overview and perspectives. *Coord Chem Rev*, 2004; **248**: 1455–1468. doi:10.1016/j.ccr.2004.05.018

140 Yusuf SNF, Azzahari AD, Yahya R, *et al*. From crab shell to solar cell: a gel polymer electrolyte based on N-phthaloylchitosan and its application in dye-sensitized solar cells. *RSC Adv*, 2016; **6**: 27714–27724. doi:10.1039/C6RA04188D

141 Li Q, Chen X, Tang Q, *et al*. Enhanced photovoltaic performances of quasi-solid-state dye-sensitized solar cells using a novel conducting gel electrolyte. *J Power Sources*, 2014; **248**: 923–930. doi:10.1016/j.jpowsour.2013.10.025

142 Pavithra N, Asiri AM, Anandan S. Fabrication of dye sensitized solar cell using gel polymer electrolytes consisting poly(ethylene oxide)-acetamide composite. *J Power Sources*, 2015; **286**: 346–353. doi:10.1016/j.jpowsour.2015.03.160

143 Pavithra N, Velayutham D, Sorrentino A, Anandan S. Poly(ethylene oxide) polymer matrix coupled with urea as gel electrolyte for dye sensitized solar cell applications. *Synth Met*, 2017; **226**: 62–70. doi:10.1016/j.synthmet.2017.01.014

144 Chatzivasiloglou E, Stergiopoulos T, Kontos AG, *et al*. The influence of the metal cation and the filler on the performance of dye-sensitized solar cells using polymer-gel redox electrolytes. *J Photochem Photobiol A Chem*, 2007; **192**: 49–55. doi:10.1016/j.jphotochem.2007.05.003

145 Zebardastan N, Khanmirzaei MH, Ramesh S, Ramesh K. Novel poly(vinylidene fluoride-co-hexafluoro propylene)/polyethylene oxide based gel polymer electrolyte containing fumed silica (SiO_2) nanofiller for high performance dye-sensitized solar cell. *Electrochim Acta*, 2016; **220**: 573–580. doi:10.1016/j.electacta.2016.10.135

146 Khannam M, Nath BC, Mohan KJ, Dolui SK. Development of quasi-solid-state dye-sensitized solar cells based on a poly(vinyl alcohol)/poly(ethylene glycol)/functionalized multi-walled carbon nanotubes gel electrolyte. *ChemistrySelect*, 2017; **2**: 673–679. doi:10.1002/slct.201601766

147 Huang K-C, Chen P-Y, Vittal R, Ho K-C. Enhanced performance of a quasi-solid-state dye-sensitized solar cell with aluminum nitride in its gel polymer electrolyte. *Sol Energy Mater Sol Cells*, 2011; **95**: 1990–1995. doi:10.1016/j.solmat.2010.02.047

148 Wang M, Yin X, Xiao XR, *et al*. A new ionic liquid based quasi-solid state electrolyte for dye-sensitized solar cells. *J Photochem Photobiol A Chem*, 2008; **194**: 20–26. doi:10.1016/j.jphotochem.2007.07.009

149 Nadia SR, Khanmirzaei MH, Ramesh S, Ramesh K. Quasi-solid-state agar-based polymer electrolytes for dye-sensitized solar cell applications using imidazolium-based ionic liquid. *Ionics (Kiel)*, 2017; **23**: 1585–1590. doi:10.1007/s11581-016-1946-0

150 Ng HM, Ramesh S, Ramesh K. Efficiency improvement by incorporating 1-methyl-3-propylimidazolium iodide ionic liquid in gel polymer electrolytes for dye-sensitized solar cells. *Electrochim Acta*, 2015; **175**: 169–175. doi:10.1016/j.electacta.2015.01.076

151 Suryanarayanan V, Lee K-M, Ho W-H, *et al*. A comparative study of gel polymer electrolytes based on PVDF-HFP and liquid electrolytes, containing imidazolinium ionic liquids of different carbon chain lengths in DSSCs. *Sol Energy Mater Sol Cells*, 2007; **91**: 1467–1471. doi:10.1016/j.solmat.2007.03.008

152 Ye T, Wang J, Dong G, *et al*. Recent progress in the application of polyoxometalates for dye-sensitized/organic solar cells. *Chinese J Chem*, 2016; **34**: 747–756. doi:10.1002/cjoc.201600231

153 Hatakeyama K, Sakaguchi H, Ogawa K, *et al*. Solid-state metal-hydride batteries using heteropolyacid hydrate as an electrolyte. *J Power Sources*, 2003; **124**: 559–563. doi:10.1016/S0378-7753(03)00741-9

154 Chen D, Zhang Q, Wang G, *et al*. A novel composite polymer electrolyte containing room-temperature ionic liquids and heteropolyacids for dye-sensitized solar cells. *Electrochem Commun*, 2007; **9**: 2755–2759. doi:10.1016/j.elecom.2007.09.013

155 Nagaraj P, Sambandam A. Silicotungustic acid incorporated gel polymer electrolyte as efficient redox mediator for dye sensitized solar cells. *Synth Met*, 2016; **219**: 93–100. doi:10.1016/j.synthmet.2016.05.014

156 Ikeda N, Miyasaka T. A solid-state dye-sensitized photovoltaic cell with a poly(N-vinyl-carbazole) hole transporter mediated by an alkali iodide. *Chem Commun*, 2005:**1886**. doi:10.1039/b416461j

157 Bisquert J. Photovoltaics: The two sides of solar energy. *Nat Photonics*, 2008; **2**: 648–649. doi:10.1038/nphoton.2008.212

158 Ito S, Zakeeruddin SM, Comte P, *et al*. Bifacial dye-sensitized solar cells based on an ionic liquid electrolyte. *Nat Photonics*, 2008; **2**: 693–698. doi:10.1038/nphoton.2008.224

159 Tai Q, Chen B, Guo F, *et al*. In situ prepared transparent polyaniline electrode and its application in bifacial dye-sensitized solar cells. *ACS Nano*, 2011; **5**: 3795–3799. doi:10.1021/nn200133g

160 Duan Y, Tang Q, Liu J, *et al*. Transparent metal selenide alloy counter electrodes for high-efficiency bifacial dye-sensitized solar cells. *Angew Chemie Int Ed*, 2014; **53**: 14569–14574. doi:10.1002/anie.201409422

161 Yang P, Tang Q. Bifacial quasi-solid-state dye-sensitized solar cells with metal selenide counter electrodes. *Electrochim Acta*, 2016; **188**: 560–565. doi:10.1016/j.electacta.2015.12.066

162 Pugliese D, Lamberti A, Bella F, *et al*. TiO_2 nanotubes as flexible photoanode for back-illuminated dye-sensitized solar cells with hemi-squaraine organic dye and iodine-free transparent electrolyte. *Org Electron*, 2014; **15**: 3715–22. doi:10.1016/j.orgel.2014.10.018

163 Pavithra N, Velayutham D, Sorrentino A, Anandan S. Thiourea incorporated poly(ethylene oxide) as transparent gel polymer electrolyte for dye sensitized solar cell applications. *J Power Sources*, 2017; **353**: 245–253. doi:10.1016/j.jpowsour.2017.04.011

164 Chang J-Y, Su L-F, Li C-H, *et al*. Efficient "green" quantum dot-sensitized solar cells based on Cu_2S–$CuInS_2$–ZnSe architecture. *Chem Commun*, 2012; **48**: 4848. doi:10.1039/c2cc31229h

165 Chen C-L, Teng H, Lee Y-L. In situ gelation of electrolytes for highly efficient gel-state dye-sensitized solar cells. *Adv Mater*, 2011; **23**: 4199–4204. doi:10.1002/adma.201101448

166 Sargent EH. Infrared photovoltaics made by solution processing. *Nat Photonics*, 2009; **3**: 325–331. doi:10.1038/nphoton.2009.89

167 Hanna MC, Nozik AJ. Solar conversion efficiency of photovoltaic and photoelectrolysis cells with carrier multiplication absorbers. *J Appl Phys*, 2006; **100**: 74510. doi:10.1063/1.2356795

168 Ogermann D, Wilke T, Kleinermanns K. CdS_xSe_y/TiO_2 Solar cell prepared with sintered mixture deposition. *Open J Phys Chem*, 2012; **2**: 47–57. doi:10.4236/ojpc.2012.21007

169 Zhao K, Pan Z, Mora-Seró I, *et al*. Boosting power conversion efficiencies of quantum-dot-sensitized solar cells beyond 8% by recombination control. *J Am Chem Soc*, 2015; **137**: 5602–5609. doi:10.1021/jacs.5b01946

170 Yu Z, Zhang Q, Qin D, *et al*. Highly efficient quasi-solid-state quantum-dot-sensitized solar cell based on hydrogel electrolytes. *Electrochem Commun*, 2010; **12**: 1776–1779. doi:10.1016/j.elecom.2010.10.022

171 Duan J, Tang Q, Li R, *et al*. Multifunctional graphene incorporated polyacrylamide conducting gel electrolytes for efficient quasi-solid-state quantum dot-sensitized solar cells. *J Power Sources*, 2015; **284**: 369–376. doi:10.1016/j.jpowsour.2015.03.060

172 Chen H-Y, Lin L, Yu X-Y, *et al*. Dextran based highly conductive hydrogel polysulfide electrolyte for efficient quasi-solid-state quantum dot-sensitized solar cells. *Electrochim Acta*, 2013; **92**: 117–123. doi:10.1016/j.electacta.2013.01.025

173 Kim H, Hwang I, Yong K. Highly durable and efficient quantum dot-sensitized solar cells based on oligomer gel electrolytes. *ACS Appl Mater Interfaces*, 2014; **6**: 11245–11253. doi:10.1021/am501407m

174 Feng W, Zhao L, Du J, *et al*. Quasi-solid-state quantum dot sensitized solar cells with power conversion efficiency over 9% and high stability. *J Mater Chem A*, 2016; **4**: 14849–14856. doi:10.1039/C6TA05894A

175 Raphael E, Jara DH, Schiavon MA. Optimizing photovoltaic performance in $CuInS_2$ and CdS quantum dot-sensitized solar cells by using an agar-based gel polymer electrolyte. *RSC Adv*, 2017; **7**: 6492–6500. doi:10.1039/C6RA27635K

176 Carey GH, Abdelhady AL, Ning Z, *et al*. Colloidal quantum dot solar cells. *Chem Rev*, 2015; **115**: 12732–12763. doi:10.1021/acs.chemrev.5b00063

177 Lan X, Voznyy O, García de Arquer FP, *et al*. 10.6% Certified colloidal quantum dot solar cells via solvent-polarity-engineered halide passivation. *Nano Lett*, 2016; **16**: 4630–4634. doi:10.1021/acs.nanolett.6b01957

178 Ren S, Chang L-Y, Lim S-K, *et al*. Inorganic–organic hybrid solar cell: Bridging quantum dots to conjugated polymer nanowires. *Nano Lett*, 2011; **11**: 3998–4002. doi:10.1021/nl202435t

179 Landi G, Henninger M, De Girolamo del Mauro A, *et al*. Investigation of the optical characteristics of a combination of InP/ZnS-quantum dots with MWCNTs in a PMMA matrix. *Opt Mater (Amst)*, 2013; **35**: 2490–2495. doi:10.1016/j.optmat.2013.07.007

180 Shauddin SM. Comparison among various emerging PV cells with history, current status and future challenges. *Energy Power*, 2013; **3**: 91–105.
181 Mitzi DB, Feild CA, Harrison WTA, Guloy AM. Conducting tin halides with a layered organic-based perovskite structure. *Nature*, 1994; **369**: 467–469. doi:10.1038/369467a0
182 Barone C, Lang F, Mauro C, *et al*. Unravelling the low-temperature metastable state in perovskite solar cells by noise spectroscopy. *Sci Rep*, 2016; **6**: 34675. doi:10.1038/srep34675
183 Stranks SD, Eperon GE, Grancini G, *et al*. Electron-hole diffusion lengths exceeding 1 micrometer in an organometal trihalide perovskite absorber. *Science*, 2013; **342**: 341–344. doi:10.1126/science.1243982
184 Lang F, Nickel NH, Bundesmann J, *et al*. Radiation hardness and self-healing of perovskite solar cells. *Adv Mater*, 2016; **28**: 8726–8731. doi:10.1002/adma.201603326
185 Brus VV., Lang F, Bundesmann J, *et al*. Defect dynamics in proton irradiated $CH_3NH_3PbI_3$ perovskite solar cells. *Adv Electron Mater*, 2017:1600438. doi:10.1002/aelm.201600438
186 Zuo C, Bolink HJ, Han H, *et al*. Advances in perovskite solar cells. *Adv Sci*, 2016; **3**: 1500324. doi:10.1002/advs.201500324
187 Giorgi G, Fujisawa J-I, Segawa H, Yamashita K. Small photocarrier effective masses featuring ambipolar transport in methylammonium lead iodide perovskite: A density functional analysis. *J Phys Chem Lett*, 2013; **4**: 4213–4216. doi:10.1021/jz4023865
188 Kojima A, Teshima K, Shirai Y, Miyasaka T. Organometal halide perovskites as visible-light sensitizers for photovoltaic cells. *J Am Chem Soc*, 2009; **131**: 6050–6051. doi:10.1021/ja809598r
189 Im J-H, Lee C-R, Lee J-W, *et al*. 6.5% efficient perovskite quantum-dot-sensitized solar cell. *Nanoscale*, 2011; **3**: 4088. doi:10.1039/c1nr10867k
190 Rahul, Bhattacharya B, Singh PK. Stable perovskite sensitized solar cell using PEO-based polymer electrolyte in ambient environment condition. *Curr Nanomater*, 2017; **1**: 171–175. doi:10.2174/2405461502666161209162815
191 Rahul, Bhattacharya B, Singh PK, *et al* Perovskite sensitized solar cell using solid polymer electrolyte. *Int J Hydrogen Energy*, 2016; **41**: 2847–2852. doi:10.1016/j.ijhydene.2015.12.093

6

Rational Screening Strategies for Counter Electrode Nanocomposite Materials for Efficient Solar Energy Conversion

Prabhakarn Arunachalam

Electrochemistry Research Group, King Saud University, Saudi Arabia

6.1 Introduction

One of the most essential issues for human society in this century is the increasing demand for low cost, clean, and abundant sources of energy with nominal impact to the environment. In fact, solar energy with its limitless quantity is projected to offer a source of cleaner and low cost renewable energy. The solar power reaching the earth's surface is equivalent to that provided by 130 million power plants of 500 MW [1–6]. However, the use of solar energy in the future as a main source depends on the success of vital factors of fundamental and technological concern. The devices used for solar energy conversion and for storage and distribution of solar energy must be friendly to the environment. Devices with lower production cost and great efficiency are, therefore, a requirement for light capture and solar energy conversion. The solar cell is an auspicious renewable energy storage device that converts solar energy into electrical energy; it is a major prospect to provide a solution to the upcoming energy related issues that humanity faces [7–9]. Currently, solar energy based technology is attaining great acceptance due to its several benefits, which comprise its proficiency to function with noiselessly and without toxicity or greenhouse gas release. Among available solar cells, dye-sensitized solar cells (DSSCs) exhibit numerous benefits, due to their greater efficiency, relatively low cost, convenient manufacturing procedures, eco-friendliness, flexibility, transparency, and good plasticity. The DSSC, invented by Professor M. Gratzel in 1991, is a most favorable route to harvest solar energy [10]. Nevertheless, DSSCs work well in research laboratory circumstances compared to other available solar cells; parameters such as power conversion efficiency (PCE), lifetime, and production cost control their commercial usage.

Rational Design of Solar Cells for Efficient Solar Energy Conversion, First Edition.
Edited by Alagarsamy Pandikumar and Ramasamy Ramaraj.

Over the last few decades, alterations to DSSCs are continuing to enhance their photovoltaic activities. Nanocomposite materials play a vital part in the advancement of DSSCs [11, 12]. Overall, a DSSC comprises a nanocrystalline oxide semiconductor such as TiO_2 (photoanode), a dye sensitizer, an electrolyte containing a redox couple (e.g. I_3^-/I^-), and a platinum-coated transparent fluorine-doped tin oxide (FTO) substrate as counterelectrode (CE) [13]. Moreover, the light absorption of dye and semiconductor charge collection process imitate the harvesting of natural light in photosynthesis [14, 15]. Of the available numerous kinds of solar cells, quantum dotsensitized solar cells (QDSSCs) have specific unique benefits, such as a great absorption extinction coefficient, great intrinsic dipole moments, the production of multiple excitons, bandgap tunability by quantum dots (QDs), and simple synthetic processes [16–18]. By considering these distinctive benefits, QDSSCs have been recognized to be an auspicious type of next generation solar cells. Principally, a QDSSC is an altered version of a DSSC. Mostly, QDSSCs have assemblies and working phenomenon that are identically parallel to those of DSSCs; the QDs substitute the organic dyes. The photovoltaic behavior of DSSCs is assessed in terms of the PCE, which is really the ratio between the power output (P_{out}) and power input (P_{in}) (Equation 6.1). However, this factor is reliant on the short-circuit photocurrent density (Jsc), the open-circuit photovoltage (Voc), and the fill factor (FF) (Equation 6.1). Power input is reliant on the incident light flux (I_o). The J_{SC} is illustrated as the ratio of I_{SC} versus the area of device.

$$PCE = P_{out}/P_{in} \times 100 = J_{SC}V_{OC}FF/I_o \times 100 \tag{6.1}$$

As a crucial material of DSSCs, the major part of the CE is to catalyze the reduction of I_3^- to I^-. A platinum-based electrocatalyst serves as a CE in DSSCs mostly for two aims: (i) it acts as an electrocatalyst that aids in the restoration of I^- from I_3^-, and (ii) the collection of electrons from the outer load to the redox electrolyte. Though platinum is one of the most suitable candidates for catalytic reduction due to its larger electrocatalytic behavior, stability, and conductivity, as a scarce noble metal its higher production cost limits the scale up for use in DSSCs. Therefore, it is necessary to focus on the nonplatinized CE that is able to substitute for platinum as catalyst. The PCE of DSSCs does not increase in percentage with an increase in the thickness of the platinum film, and it is possible to attain a higher PCE with a thin platinum film 2 nm in thickness. These effects indicate that the construction costs of CE materials can be slightly reduced by decreasing the quantity of platinum used.

Nevertheless, a new viable approach to decrease the production cost of DSSCs is to discover other kinds of CE that have good catalytic performances but are based on low-cost materials [19]. The common necessity of a CE

materials is that it must have good optical behavior to capture the solar light energy in the visible light area with a great electrocatalytic ability. However, the electrocatalytic behavior of the CE materials can be enhanced by improving the specific surface area, thus the CE materials must be fabricated with nanoscale dimensions. Moreover, these nanosized CE materials display different physical and chemical activities related to their corresponding bulk materials [20]. To overcome this problem, many research works are focusing on CE electrocatalytic materials, comprising carbonaceous materials, metallic compounds (nitrides, carbides, and sulfides), polymers, and metal oxides [21–24], with a superior electronic conductivity, large specific surface area, and a good electrocatalytic ability [25, 26]. For instance, carbon-based materials are attaining extensive consideration owing to their amazing multifunctional properties [27–29]. Dissimilar carbonaceous structures such as activated charcoal (AC) [30, 31], carbon black (C_b) [32, 33], graphite [34, 35], grapheme [36, 37], and carbon nanotubes (CNT) [38] have been fabricated and have revealed amazing performance abilities as CE material in solar energy conversion.

In this chapter, recent advancement in screening strategies in the selecting the CE materials in an efficient solar energy conversion system are examined. Moreover, the electrocatalytic activity of efficient nonplatinum CE materials for solar cell applications is discussed. This CE material contains carbon-based materials, polymers, metal sulfides, metal nitrides and carbides, and composites materials. Furthermore, various efficient CE materials established via this procedure are discussed. In addition, the role of these nanocomposite materials for DSSCs, QDSSCs, and PSCs is discussed.

6.2 Principles of Next Generation Solar Cells

"Next generation" solar cells, such as solid state DSSCs, QDSSCs, and PSCs, have developed as the most auspicious technologies for low cost substitutes to replace silicon-based solar cells in the last decades. The principles of next generation solar cells need to be discussed.

6.2.1 Dye-sensitized Solar Cells

A DSSC includes a set of various layers of components arranged in serial, comprising transparent conducting substrate, TiO_2 nanoparticles, dyes, redox electrolyte, and CE enclosed with sealing gasket. The representative arrangement is presented in Figure 6.1.

The working principle of DSSCs varies considerably from that of the first and second generation solar cells and is carefully associated with natural photosynthetic process, whereas the light absorption and charge carrier migration are supported by other constituents. Briefly, the essential constituents and basic

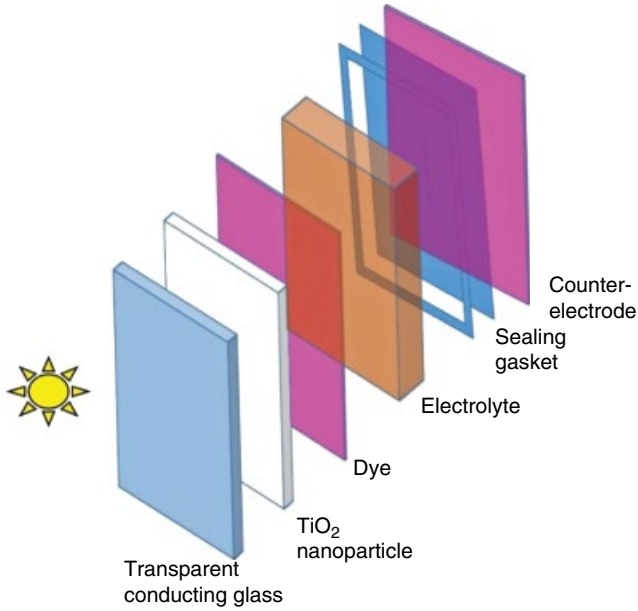

Figure 6.1 Representative arrangement of a DSSC.

working procedures of DSSCs are systematically demonstrated in Figure 6.2. The basic working procedures include [39–42]:

i) upon illumination of the cell, photoexcitation of sensitizer to generate excited dye;
ii) electron addition into the conduction band (CB) of TiO_2, ensuing in the creation of oxidized dye;
iii) electron migration to the photoanode and flow to the CE via outer circuit;
iv) oxidized dye restoration by collecting electron carrier from the reduced redox couple;
v) oxidized redox couple restoration at the photocathode by collecting electrons;
vi) electron recombination by providing electron carriers to oxidized dye;
vii) electron recombination by giving electron carriers to the oxidized redox couple;
viii) relaxation of the excited dye to its ground state.

In this chapter, low-cost CE materials for DSSCs applications are discussed in detail. Exhaustive review articles on the specific constituents of DSSCs and an indication of the energetics of the electron transfer mechanism involved in DSSCs have previously been discussed [43–49].

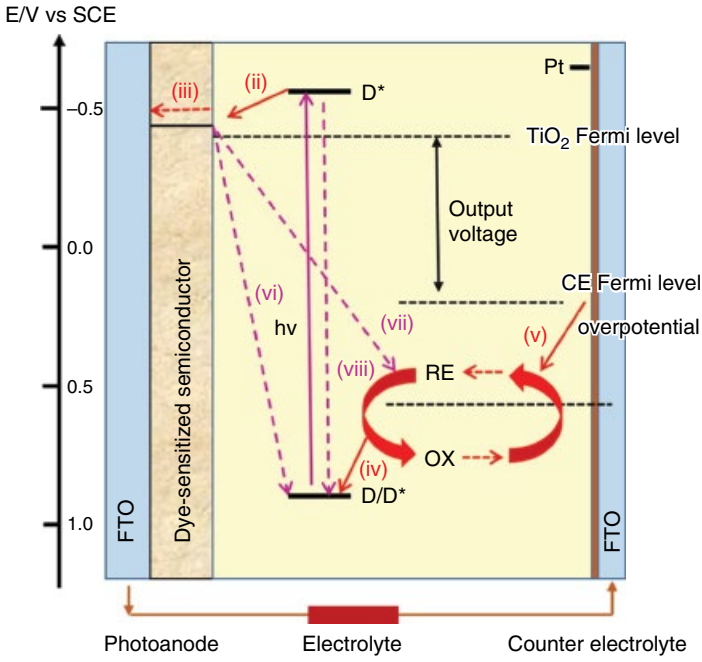

Figure 6.2 Basic working processes and constituent components of a DSSC.

6.2.2 Principles of Quantum Dot Sensitized Solar Cells

QDSSCs have been recognized to be an auspicious type of next generation solar cell. Principally, a QDSSC is an altered type of DSSCs. Mostly in QDSSCs, constructions and working procedures are identical behavior to DSSCs, and the QDs substitute the organic dyes. The basic principles and working processes of a QDSSC have been described in detail elsewhere [50–54]. Figure 6.3 demonstrates the working processes of functioning QDSSCs under irradiation of the cell. If the cell is open to visible light, QD sensitizers capture light energy in a definite range of wavelengths depending on its bandgap energy. The absorbed sunlight stimulates electrons in the valence band (VB) of the QDs to the CB. The excited electron carriers in the CB of the QDs migrate to the conduction band (CB), which contains conducting oxide as anodes (typically TiO_2 or ZnO), and this gives them with superior electroconductivity. The photoanode is linked to the CEs with outer circuit so that the electrons produced can move along the outer circuit to the CEs materials. Moreover, simulated charges are created by opposed effects instigated by electron carrier excitation, and holes are created in the VB of the QDs and migrate to the redox electrolyte via oxidizing the redox electrolyte. Moreover, the oxidized redox electrolyte is diminished at the CEs via the outer circuit. At this level, the entire cell is

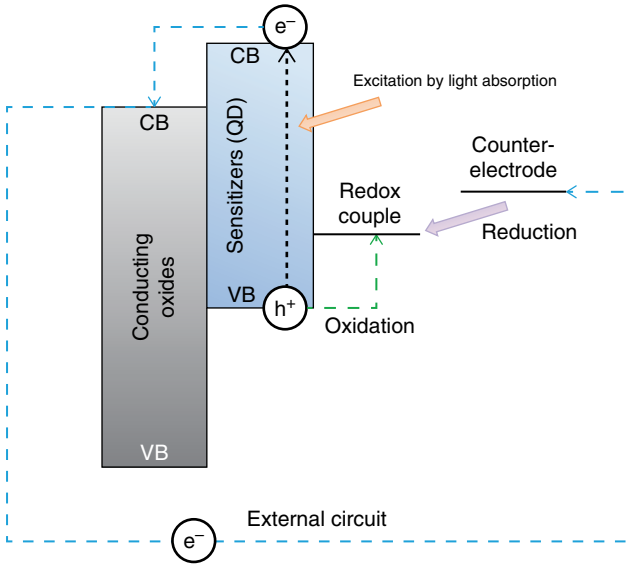

Figure 6.3 Working processes of a QDSSCs, with energy band levels, flow of charge carriers.

provided without any change in the internal condition. These make it more likely for the electron carrier to flow inside the cell for several periods or infinitely. The main motivating force of the electron movement is credited to the energy-level arising among the altered Fermi levels at the QDs/conducting metal oxides and the redox applied bias of the electrolyte solution.

6.2.3 Principles of Perovskite Solar Cells

In recent years, organo-metal perovskite solar cells (PSCs) have garnered excessive consideration among the researchers. Most recently, much research efforts has been dedicated to examining various kinds of PSCs and advancing the performance of the cell [55–57]. In comparison with conventional solar cells, the PSC has the potential to attain higher efficiency with an economical and convenient fabrication process. Particularly for the hole-conductor-free PSCs, the use of costly organic/polymeric hole-transporting candidates are not necessary, which can reduce materials costs significantly [58, 59]. CE materials play a major part in PSCs [60, 61]. For most PSC described so far, gold is the most effective and extensively used CE candidate. Conversely, gold is costly and increases the overall production cost of the PSC. Inexpensive metal CEs like silver works well in a PSC with HTM layer, but it remains unstable in a HTM-free PSC [62]. In view of the aggressive rivalry in the world photovoltaic technology, to assemble this type of solar cell economically as a marketable

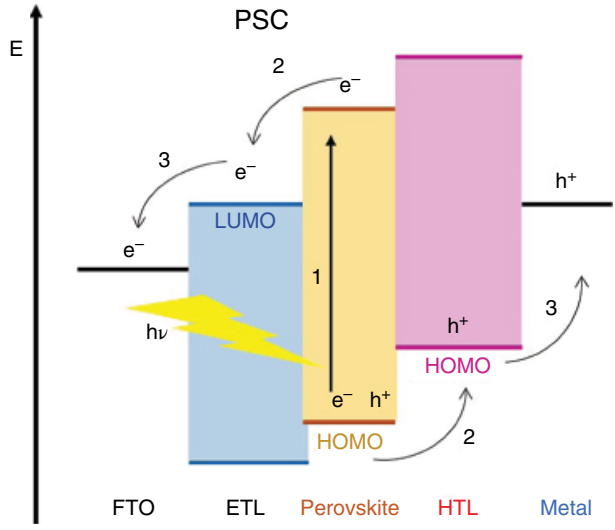

Figure 6.4 Band diagram and main processes for a PSC: 1 absorption of photon and free charge generation; 2 charge transport; 3 charge extraction [62]. Reproduced with permission of Nature Publishing Group.

product, low-cost CEs with satisfactorily efficient cells need to be established. The basic components of a PSC are displayed in Figure 6.4. It illustrates that the absorption of photons in perovskite materials within PSCs does not lead to the creation of a long lifetime exciton. The most commonly used candidates for the active layer in PSCs is the methylammonium lead iodide perovskite, ($MAPbI_3$), which is located amid an electron transporting layer (ETL), usually mesoporous but also planar TiO_2, and a hole transporting layer (HTL).

6.3 Platinum-free Counterelectrode Materials

6.3.1 Carbon-based Materials for Solar Energy Conversion

Carbonaceous materials have been verified to be an appropriate material to replace the platinum CE in solar cells; this is credited to their superior electronic conductivity, large specific surface area, good corrosion resistance towards electrolyte, high thermal stability, and low cost. These materials include activated carbon (C_a), carbon black (C_b), conductive carbon (C_c), carbonfiber (C_f), mesoporous carbon (C_m), CNTs, fullerene, and graphene have been effectively engaged as CEs [63–66].

For DSSCs, Kay and Gratzel first discovered a graphite and C_b as a CE materials and attained a PCE of 6.7% [67]. Since then, exhaustive investigation

works have been focused on carbonaceous materials. Similar to C_a, C_b, C_f, C_m, CNTs, and graphene-based CE materials have been used in DSSCs and shown promising activity [68–73]. The PCE and the fill factor of DSSCs are mostly reliant on the carbon layer thickness. It is well known that the fill factor increases as the thickness of the carbon layer increases up to 10 mm [74]. Glassy carbon with a lower crystalline nature displays superior catalytic performance for the regeneration of I^- from I_3^- in the redox system. The photovoltaic results show enhanced electrocatalytic performances can be credited to an upsurge in graphene stacks and active reaction sites in glassy carbon [75]. Ma and coworkers carried out detailed research works on various kinds of carbon-based materials of C_a, C_b, C_c, C_d, C_f, CNTs, ordered C_m, discarded toner (C_p), andC_{60}. The photovoltaic investigation illustrated that ordered C_m and carbon dye displayed the superior electrocatalytic performance and the DSSCs provided a high PCE of 7.5%. Conventional carbonaceous candidates (C_a, C_b, C_c, CNTs, and C_f) exhibited decent electrocatalytic performances, and the PCE of the DSSCs varied from 6.3 to 7.0% [76]. Lee *et al*. reported DSSCs with nano-sized carbon materials as a CE and photovoltaic studies illustrated a PCE of 7.56%. Moreover, electrocatalytic activity suggested that, after keeping the fabricated solar devices in the dark for 60 days, the carbon CE attained 84% of its initial efficiency [77]. Quite recently, Fang and coworkers fabricated porous-based carbon NPs on the titanium film substrate as CEs, and the DSSCs displayed a PCE of 6.6% [78].

Among the available various kinds of carbon-based materials; CNTs and graphene have tremendous potential in comparison with the carbonaceous materials and are widely considered to be hotter research topics among the researchers. Peng and coworkers prepared DSSCs using CNT fibers with numerous diameters (25–100 μm). The photovoltaic results indicated that the CNT fiber (diameter = 60 μm) had the greatest catalytic performances and achieved a maximum PCE of 7.33% [79]. Lin *et al*. fabricated vertically arranged single walled CNTs onto FTO substrate via contact transfer process which was employed as CE catalyst in DSSCs [80]. Veerapan and coworkers have engaged colloidal graphite as an CE [81] and spray-coated carbon CE for regeneration of I^- from I_3^- in DSSCs. The photovoltaic performance of spray-coated carbon CE materials attained a superior PCE of 6.2% [82]. Chen *et al*. have developed a C_b-coated graphite CE (thickness = 0.2 mm) by a spin-coating method; it displays a maximal PCE of 6.46%, which is superior than the efficiency (6.37%) of a thermally deposited Pt/FTO CE [83]. Kilic and coworkers fabricated a MWCNT/mesoporous TiO_2 network and demonstrated it as a substitute to conventional FTO/TiO_2 mesoporous based DSSCs. The MWCNT/mesoporous TiO_2 photoanodes with iron pyrite (FeS_2) achieved a PCE of 7.27% [84].

Graphene CEs were anticipated to be a gifted candidate for DSSCs due to their exceptional electronic conductivity, which can reduce charge transfer resistance (R_{ct}). Kaniyoor and coworkers described that the R_{ct} of thermally

exfoliated graphene films is 11.7 Ωcm^2, which is closer to that of a platinum CE (6.5 Ωcm^2) [85]. Graphene films for DSSCs CE have been designed by various methods, thermal exfoliation from graphite oxide [83], the oxidative exfoliation of graphite followed by chemical reduction [86], the chemical reduction of graphene oxide [87], and electrophoretic deposition followed by a thermal process [88]. Znai *et al.* developed a two-stage process of microwave-exfoliated graphite flakes via a thermal treatment process. Consequently, the graphene/C_3N_4 hybrid CE materials were thermally annealed at 900 °C, resulting in the creation of crumbled N-doped graphene. The usage of the hybrid nanostructures as CE in DSSCs attained a promising PCE of 7.2% [89]. Pang *et al.* have effectively engaged a network structure of graphene as an efficient CE for DSSCs. The charge transfer resistance and DSSC performances illustrates that FTO-free solar cells may be established using graphene; this is schematically presented in Figure 6.5. The economical FTO-free graphene-based CE optimized showed a PCE of 9.33% [90].

For QDSSCs, carbon-based materials must be astonishing applicants for CE materials in that they are available at economical prices and display good electrocatalytic behaviors relative to other kinds of CEs. Various research efforts have been carried out on different types of carbon CEs to progress the optimal CE [91, 92]. To obtain the greater PCE with carbon-based CEs in QDSSCs, the CEs must satisfy two vital necessities: firstly, large specific surface area to reimburse the sluggish intrinsic reaction kinetics; secondly, adequate infiltration of the electrolyte into the carbon layer of the CEs. Seol and coworkers concentrated on these factors and developed an ordered mesocellular carbon foam as the CE materials [93]. Du *et al.* reported the mesoporous carbon supported on titanium mesh CEs that delivers an efficient three-dimensional electrical tunnel with improved electroconductivity than state-of-art Cu_2S/FTO CEs. The photovoltaic results indicate that the PCE of MC/Ti CEs show a PCE of 11.6% [94].

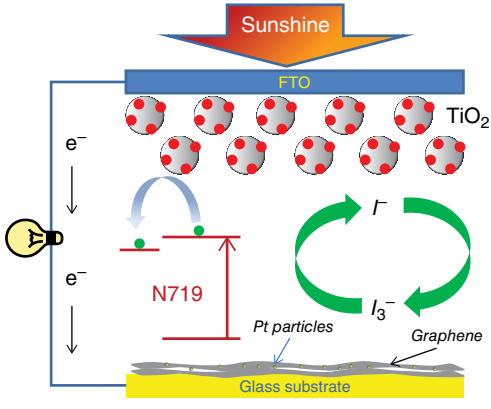

Figure 6.5 Schematic diagram of DSSCs developed with graphene-based counterelectrode [90]. Reproduced with permission of Royal Society of Chemistry.

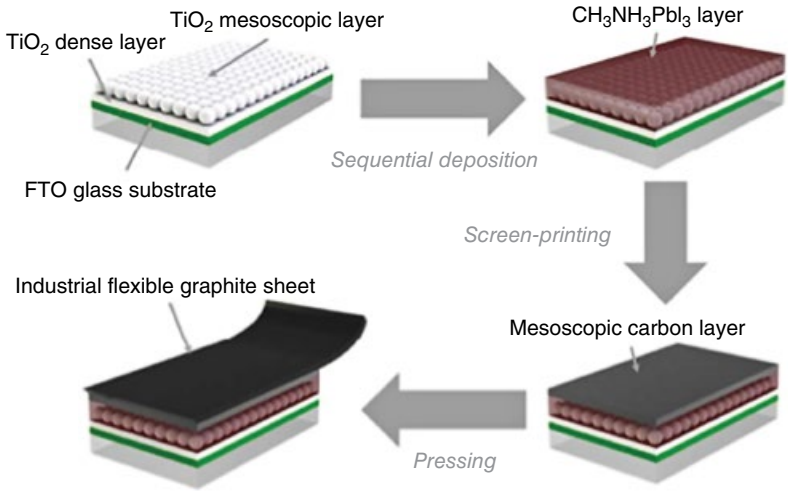

Figure 6.6 Graphic diagram of the fabrication steps of all-carbon flexible CE based HTM-free PSCs [98]. Reproduced with permission of Royal Society of Chemistry.

For perovskite solar cells (PSCs), carbon-based materials are successfully employed as CEs similar to DSSC and QDSSCs. The approximate 5.0 eV work function creates carbon materials that are suitable CE candidates for PSCs [95]. Quite recently, several carbon-based materials have been successfully employed in PSCs, indicating that the carbon materials are potential materials for hole-conductor-free PSCs [95–97]. Yang *et al.* employed various kinds of carbon-based materials for hole-conductor-free PSCs by a convenient low-temperature process (Figure 6.6). The photovoltaic results suggest that a PCE of 10.2% has been attained by a hole-conductor-free mesoscopic $CH_3NH_3PbI_3/TiO_2$ heterojunction PSC with the CE comprising the composition of graphite and C_b [98].

6.3.2 Metal Nitride and Carbide Materials

Transition metal nitrides and carbides, termed interstitial compounds, have a tendency to imitate platinum-like catalytic behavior as earlier studies verified [99, 100]. The potential use of these materials has been generally recognized in materials chemistry owing to their exceptional physical and chemical properties, that is their superior electrochemical stability, electroconductivity, and magnetic properties. As substitutes to the noble metal-based CE metals, metal nitride and carbide materials have been commonly engaged in ammonia synthesis, dehydrosulfurization, hydrogenation and dehydrogenation, the methanol oxidation reaction, supercapacitors, and they display respectable photocatalytic performance [101–103]. Since 2009, these materials have been employed in DSSCs as CE candidates as substitutes for platinum CEs. Wu *et al.*

have investigated various metallic compounds in DSSCs as CE electrocatalysts [14]. Systematic comparative studies of the PCE of DSSCs and the *J-V* curve of metal carbide and nitride based catalysts have been carried out. Moreover, transition metal carbides, such as molybdenum carbides (Mo_2C) and tungsten carbides (WC), are also a probable alternative for platinum CEs in DSSCs. Moreover, there is evidence that the electrocatalytic behavior can be improved by the loading of P25 into Mo_2C and WC particles [104]. Similarly, highly active Mo_2N and W_2N have been fabricated and engaged as CEs in DSSCs systems for the regeneration of iodide. Mo_2N and W_2N CEs can attain PCEs of 6.38 and 5.81%, respectively; these efficiencies are comparatively similar to the photovoltaic activities of DSSCs synthesized by using a platinum CE [105].

For QDSSCs, Seol *et al*. effectively unified the advantages of both molybdenum compounds and carbon-based materials by fabricating molybdenum-based compound/CNT-RGO heterostructures and engaged them as CE materials [106]. The photovoltaic performance of these heterostructures attained a PCE of greater than 5%.The molybdenum-based compound/CNT-RGO composites were fabricated via a convenient modified urea-glass route [107]. Mo_2N and Mo_2C attached onto the CNT/RGO morphological structure might be fabricated from the reaction by adjusting the ratio of the urea to molybdenum precursor. These types of heterostructures are loaded on FTO substrates and engaged as CEs for QDSSCs comprising CdS/CdSe-sensitized ZnO photoanodes and polysulfide electrolyte. The electrostability of the Mo_2N and Mo_2C CE materials is credited to be mainly due to their noble-metal-like nature, as earlier described [108, 109]. Furthermore, other specific materials, such as NiN, TiN, and TiC, have also been researched as CEs in DSSCs [110–113]. In particular, TiN and TiC NPs were engaged as CEs in CdS QDSSCs, and then TiC NPs displayed the maximal efficiency (2.11%) in comparison with TiN NPs (1.97%) [111].

6.3.3 Metal Sulfide Materials

The creation of an effective photocathode is very vital for all kinds of electrochemical reactions. Metal sulfides are recognized to be appropriate candidates, as these electrocatalyst are loaded on conductive FTO substrates and are generally investigated in energy conversion applications. In recent years, transition metal sulfides like molybdenum disulfide (MoS_2) have gradually attracted much consideration for a wide range of uses like supercapacitors, batteries, hydrogen evolution reaction, DSSCs, and so on [114, 115]. For DSSCs, cobalt sulfide (CoS) loaded FTO substrate tends to have better electrocatalytic performance than the bulk platinum electrode for the regeneration of I^- from I_3^-. CoS and copper sulfide (CuS) have been employed as CE in DSSCs. A maximal PCE of 2.7% is attained with a CuS CE, while the platinum CE displays an efficiency of only 0.51% in polysulfide electrolytes [116]. Wang *et al*. have revealed

that CoS is highly efficient in regeneration of I^- from I_3^- in DSSCs; moreover, it retains significant electrochemical stability and thermal stress, which create an exceptionally remarkable material as a substitute for platinum in DSSCs [117]. Wu *et al.* have employed MoS_2 and WS_2 in DSSC cell systems as CE electrocatalysts these sulfides shown exceptional catalytic for the creation of the classical I^-/I_3^- redox couple. These CEs attain a high PCE of 7.59 and 7.73%, respectively, which are near to the photovoltaic behavior of DSSCs with a platinum CE [118]. MoS_2 has an equivalent structural morphology to graphene, which has received considerable interest as a candidate substitute to platinum-free CE materials. Moreover, the electrocatalytic behavior and the electronic conductivity of the CE materials have a great influence in the photovoltaic behavior of DSSCs. Conversely, a pure inorganic-based CE candidate will hinder the commercial use due to sluggish charge carrier transport efficiency among the metal nanoparticles and the conducting substrate, resulting in nanoparticles aggregation [119]. Thereafter, many research works have been devoted to enhancing an electrical conductivity and also catalytic regeneration of I^- by combining carbonaceous CE materials and metallic compounds. The pure MoS_2 with well dispersed carbon-based materials can probably deliver a combined effect regarding the electrocatalytic reduction of triiodide [120, 121]. Recently, various kinds of carbon materials incorporating flower-like MoS_2 microspheres were fabricated via a simple single-step hydrothermal method; a schematic representation of DSSCs is displayed in Figure 6.7. The DSSCs

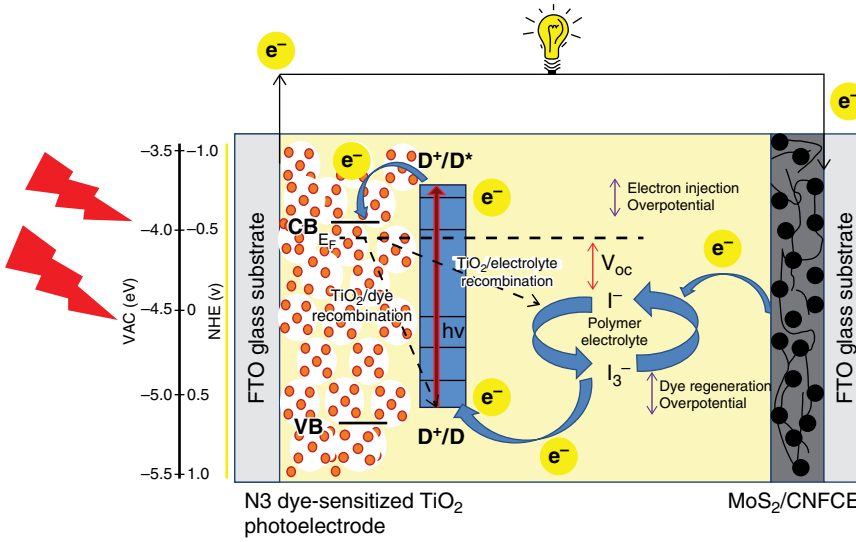

Figure 6.7 The schematic illustration of DSSCs based on MoS_2/CNF CE in visible-light illumination [122]. Reproduced with permission of Springer Nature.

fabricated with MoS_2/CNF CEs and phthaloylchitosan polymer based electrolyte displayed a PCE of 3.17%, whereas unmodified MoS_2CE displayed only 1.04% [122]. The photovoltage and PCE curve for DSSCs fabricated with various kinds of carbon incorporated flower-like MoS_2 are displayed in Figure 6.8. These works validate the use of carbon incorporated MoS_2 as a probable CE candidate in DSSCs.

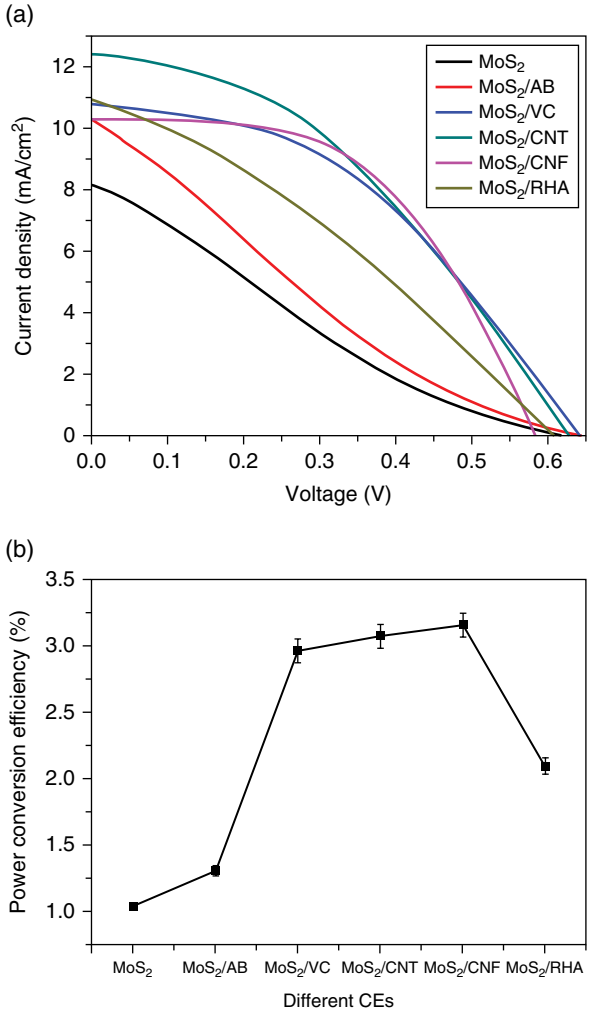

Figure 6.8 Photocurrent–voltage curves of DSSCs fabricated with MoS_2, MoS_2/AB, MoS_2/VC, MoS_2/CNT, MoS_2/CNF, and MoS_2/RHA CEs [122]. Reproduced with permission of Springer Nature.

For QDSSCs, pure platinum is not an appropriate applicant as a CE candidate due to its corrosion nature in the presence of the polysulfide electrolyte. For to this reason, sulfide materials might be a potential substitute to platinum CEs due to their electrochemical stability towards the polysulfide electrolyte. The various QDs, such as CdSe, CdTe, CuS, CdS, PbS, and InAs, have been engaged as sensitizers of crystalline TiO_2 [123, 124]. Different kinds of sulfide-based materials, including CoS [125, 126, CuS [127, 128], Cu_2S [129, 130], PbS [131, 132], NiS [133, 134], and copper zinc tin sulfide [135], have been stated as potential applicants for the CE materials. Unlike metal-based CEs, sulfide CE materials work in a dissimilar way, as they have their specific bandgap energies. Among these, CuS CE tends to have improved redox behavior concerning the reduction of the polysulfide electrolyte couple, and the enhanced Jsc, FF, and PCE as well [136, 137]. Savariraj *et al.* fabricated CuS nanoflakes and nanoplatelets via facile chemical bath deposition and employed them as CE materials in QDSSCs. The photovoltaic performance of QDSSCs with a CuS CE showed a PCE of 4.02% [138].These covalently bonded CE materials with sulfur enhancement have been stated to have improved electrocatalytic performance due to poorer interlayer van der Waals forces, displaying graphite-like structures [139].

6.3.4 Composite Materials

Composite materials usually comprising two or more component, which combine the benefits of each constituent into one, have been extensively recognized as effective CEs in DSSCs. In recent years, some platinum-based composite materials such as platinum/CNT, platinum/graphene, and platinum/polymer have been employed as CE electrocatalysts in DSSCs; these composites display greater electrocatalytic behavior than the conventional platinum CE [140, 141]. The transition metal based materials TiC, WO_2, and VN have been combined with platinum and engaged as CE electrocatalysts for DSSCs. The photovoltaic performance of these materials is almost 20% superior to that of the individual materials [142]. Conversely, to fabricate economical DSSCs requires searching new kinds of cheaper CE materials with superior electrocatalytic activity to substitute for platinum and platinum-based composite catalysts. Joshi and coworkers have employed an efficient DSSCs by using economical carbon/TiO_2 composite as an substitute to the platinum CE electrode for regeneration of iodide [143]. Since 2006, graphene-based composite materials have been considered as CE in DSSCs, when the primary research works on graphene materials with CP was described by Stankovich*et al.* [144]. Generally, in graphene–polymer composite CEs, the polymer performs as conducting support and the graphene is accountable for the high electrocatalytic performance for the regeneration of I^- from I_3^-. Moreover, graphene sheets can be engaged as a polymeric support and it can be achieved

by diffusing the polymer materials over the graphene. Wang *et al.* fabricated a composite CE material with polyaniline (PANI)–graphene sheets via an *in situ* polymerization method, with PANI well dispersed on the graphene sheets. The photovoltaic performances of DSSCs with graphene–PANI composites materials provide a PCE of nearly 6.09%, which is very closer to bulk platinum CEs [145]. Likewise, the CE fabricated by Lee *et al.*, comprising a poly(3,4-ethylenedioxythiophene)–graphene nanocomposite CE material, gave a PCE of 6.26%, mostly credited to the higher amount of loading graphene into the poly(3,4-ethylenedioxythiophene) (PEDOT), superior electronic charge transfer and electrochemical performance [146]. Moreover, nickel (Ni) and cobalt (Co) metals can be united with graphene to create a nanocomposite CE materials. Dou and coworkers fabricated $Ni_{12}P_5$–graphene composites as CE materials for DSSCs via a hydrothermal process. This composite material displays a reasonable electrocatalytic performance concerning the regeneration of I^- from I_3^-, providing a PCE of 5.7% [147]. The major benefit of engaging a metal–graphene based nanocomposite as a CE is to enhance the electron transfer rate at the CE, which behaves as a reactive site for the electrocatalytic reaction and also behaves as a spacer amid the graphene sheets. Moreover, the use of graphene delivers a fast diffusion pathway for the electrolyte by generating an excellent electrode–electrolyte contact, which increases the electron transfer rate at the electrolyte–CE interface [148].

For QDSSCs, various kinds of the above mentioned CE materials have been employed and all of these CE materials tends to have their individual ups and downs, which makes it hard to regulate which materials would be the appropriate selection for their application in CEs. In this feature, some heterostructures comprising of more than two dissimilar types of CEs have been receiving attention as novel candidates for efficient CEs in QDSSCs. As a consequence, numerous research works have been described on heterostructured CEs, such as Cu_2S/Pt [149], Cu_2S/RGO [150], CoS/graphene [151], PbS/graphene [152], gold/reduced graphene [153], $CuInS_2$/carbon composite [154], and MoX/CNT CEs [106].

6.3.5 Metal Oxide Materials

For DSSCs, metal oxides are also recognized to be suitable candidates to substitute for the platinum CE; this is credited to their cheaper cost, good thermal properties, and superior catalytic performances. Unlike metallic compounds (carbides, nitrides, sulfides), transition metal oxides are infrequently used as electrocatalysts to substitute for platinum. Moreover, the metal oxide and its hydroxide-based materials tend to possess good electrochemical properties for energy related application [155–161]. In particular; few semiconductor oxides have a tendency to enhance the catalytic performance for the regeneration of I^- from I_3^-. Wang *et al.* have investigated the catalytic performance of zinc

oxide (ZnO) with a CP that displays exceptional photovoltaic activity with a supreme PCE of 8.17% [162]. Tantalum oxide (TaO) displays remarkable platinum-like electrocatalytic performance for iodide regeneration in DSSCs. The photovoltaic behavior displayed a high PCE of about 6.48%, which is superior to the PCE of the platinum CE [163]. Ma *et al*. fabricated WO_2 nanorods, which provide exceptional catalytic performance, and the iodide electrolyte based DSSCs using WO_2 CE displayed a high PCE of 7.25%, near to the PCE of platinum CE based DSSCs (7.57%) [164]. DSSCs fabricated using V_2O_3,Nb_2O_5 and TaO_x displayed reasonable PCE values of 5.40, 4.84, and 6.79% [165]. However, metal oxides such asTiO_2, ZrO_2, Cr_2O_3, and MoO_2 gave poor electrocatalytic performances. DSSCs fabricated using niobium oxide CEs displayed PCE values of 5.68 (hexagonal Nb_2O_5), 4.55 (orthorombic Nb_2O_5), and 5.82% (monoclinic Nb_2O_5). Furthermore, another niobium oxide, NbO_2, was fabricated which displayed the superior catalytic performances, attaining a PCE of 7.88%, exceeding the DSSCs using a platinum CE (7.65%) [166]. Wang *et al*. fabricated RuO_2 nanocrystals through hydrothermal treatment and sintering processes, and successfully employed them as CE catalyst in DSSCs [167]. The photovoltaic investigation shown PCE of 7.22% was attained, more than the platinum-based DSSCs (7.17%).

6.3.6 Polymer Counterelectrodes

Apart from the well-investigated CE materials, such as the metal oxides, carbon-based materials, metallic compounds, and composite materials debated above, there could be other viable candidates for CE materials. Over the last decades, research works have been focused on CP credited to their probable benefits as conducting glass substrates, hole conductors, and CE candidates for DSSCs. For DSSCs, to highlight the advantages of transparency and flexibility, it is vital to fabricate transparent and flexible CEs. Till now, there are various types of CPs that can be engaged as CEs in DSSCs; PEDOT/PSS, polythiophene (PT), polypyrrole (PPy), PANI can be potential candidate due to their higher conductivities, which are created by the existence of sp_2 orbital bonds. CPs have the benefits of easy, convenient preparation procedure and flexibility. As early as 2003, Hayase and coworkers employed PEDOT/PSS CEs for quasi-solid DSSCs, with the verdict that these CEs exhibited superior qualities to platinum for an ionic liquid electrolyte (ILE) [168]. Yanagida *et al*. specified that the greater viscosity and sluggish conductivity of ILE demanded high I_2 concentration; hence, the porous PEDOT/PSS CEs were more appropriate than platinum for an ILE [169]. Li and coworkers described that the enhancement in the specific surface area of the PANI photoelectrode enhanced its electrocatalytic performance. Moreover, a PANI electrode tends to have sluggish R_{ct} and a superior electrocatalytic performance for the I^-/I_3^- redox reaction than the platinum CE and the PCE of DSSCs is 7.15%, which is superior to

the platinum CE (6.90%) [170]. Xiao *et al*. have employed PANI nanofibers as a substitute for the platinum CE in DSSCs; they display brilliant electrocatalytic behavior for the redox reaction of the electrolyte. A PCE of 6.21% can be attained by employing the PANI nanofiber CE; it is near to the PCE of a platinum CE (6.39%) [171]. Li *et al*. have explored the influence of doping various kinds anions, such as SO_4^{2-}, ClO_4^-, BF_4^-,Cl^-, and TsO^- (Ts = tosyl) into the PANI film. Between them, the SO_4^{2-}-doped PANI film displays a superior reduction current for the electrocatalytic reduction and a lesser R_{ct} than the platinum CE. The PANI–SO_4 CE in DSSCs shows a PCE of 5.6% [172]. The sodium dodecyl sulfate (SDS)-doped PANI film reveals the maximum conductivity, and this leads to a superior electrocatalytic regeneration of I^-. DSSCs fabricated with PANI-SDS as a CE display a PCE of 7.0%,which is close to classical platinum CE (7.4%) [173]. Wu *et al*. have fabricated PPy/FTO nanoparticles to assemble a PPy CE for DSSCs and obtain a PCE for DSSCs of 7.66%, which is superior to that of the platinum CE (6.90%) [174]. Pringle *et al*. fabricated PEDOT film on an ITO/PEN flexible substrate via an electrodeposition method through various deposition intervals (5–45 s). The results indicated that the small deposition duration of 5 s, was sufficient to attain an extremely efficient and transparent PEDOT film. The DSSCs consuming this CE material and an organic liquid electrolyte attained a maximal PCE of about 8.0% [175].

For QDSSCs, little investigation has been carried out on the use of these CPs in CEs for QDSSCs to date [176–178]. Yeh and coworkers used PEDOT, PT, and PPy as CE candidates and testifed the photovoltaic activities and features of these CEs in QDSSCs [179]. A CdS-sensitized mesoporous TiO_2 was employed as the photoanode, while an aqueous polysulfide was used as the electrolyte solution in the QDSSCs. The conducting polymer films were fabricated via electrochemical polymerization. The photovoltaic performance investigation reveals the better electrochemical behavior of PEDOT; the QDSSCs comprising the PEDOT CE created the maximal PCE of 1.16%. Though the PCE of the QDSSC comprising the PEDOT CE was not sufficient enough, the other CP-based CEs revealed even more unsatisfactory results. However, this research work proposed the promising use of CP as CE materials in QDSSC and further detailed investigation able to submit new visions for innovative and efficient CEs.

6.4 Summary and Outlook

Over the last decades, DSSCs are gaining more consideration due to their capacity to transform sunlight into electricity in an economical manner. A DSSCs is comprised of an electrode (photoanode, usually a TiO_2-coated FTO plate engaged as the photoanode and photocathode), a dye as the sensitizer, and I_3^-/I^-redox electrolytes. The PCE of DSSCs is reaching the efficiency level

required for commercialization. This chapter reviewed the recent developments in the mechanistic investigation of the interfacial electrocatalytic reaction on CE candidates, as well as the creation of a rational screening criteria for efficient CEs in DSSCs, QDSSCs, and PSCs. Moreover, various efficient CE materials developed via this procedure have been discussed. An exceptional CE candidate must possess (i) impeccable stability and (ii) high electrocatalytic activity; platinum satisfies these two requirements has the title of the best CE material. Currently, the major target for DSSCs is to reduce the production cost of the materials and enhance the photo-to-current conversion efficiency. In terms of production cost, the dye and CE are the main attention. Advancement of nonplatinum-based CE electrocatalysts can make DSSCs more modest among numerous photovoltaic devices. A nonplatinum-based CE electrocatalyst not only reduces the cost of the materials but is more appropriate for the regeneration of I^- from I_3^-, which, in turn, is valuable for attaining maximum efficiency. In recent years, the nonplatinum-based CE catalysts have been established rapidly, and the wide range of the electrocatalysts widened from the costly platinum to lower cost electrocatalysts, such as carbon-based materials, polymers, metallic compounds, metal oxides, metal sulfides, and composite materials. Similarly, various CEs for QDSSCs and PSCs have been introduced. There are various kinds evolving and directions for selecting CE catalysts: (i) employing a commercially available substrate to produce CEs; (ii) create multiple nanocomposite materials based on multiple compounds; (iii)explore convenient processing methods to synthesize flexible CEs; (iv) apply nonplatinum-based electrocatalysts in commercial modules; (v) perform an electrochemical stability test in harsh conditions.

References

1 S. Lewis, G. Crabtree, *Basic Research Needs for Solar Energy Utilization*, Office of Science, US Department of Energy, Washington, DC, 2005.
2 P. Arunachalam, S. Zhang, T. Abe, *et al.*, *Appl. Catal., B*, **193**, 2016, 240–247.
3 S. Zhang, P. Arunachalam, T. Abe, *et al.*, *J. Photochem. Photobiol., A*, **244**, 2012, 18–23.
4 P. Arunachalam, A. Al-Mayouf, M.A. Ghanem, *et al.*, *Int. J. Hydrogen Energy*, **41**, 2016, 11644–11652.
5 P. Arunachalam, M.S. Amer, M.A. Ghanem, *et al.*, *Int. J. Hydrogen Energy*, **42**, 2017, 11346–11355.
6 S.M. AlShehri, J. Ahmed, T. Ahamad, *et al.*, *RSC Adv.*, **7**, 2017, 45615–45623.
7 I. Chung, B. Lee, J. He, *et al.*, *Nat. Lett.*, **485**, 2012, 486–490.
8 A. Malathi, P. Arunachalam, A.N. Grace, *et al.*, *Appl. Surf. Sci.*, **412**, 2017, 85–95.
9 A. Malathi, V. Vasanthakumar, P. Arunachalam, *et al.*, *J. Colloid. Interface Sci.*, **506**, 2017, 553–563.

10 B. Oregan, M. Gratzel, *Nature*, **353**, 1991, 737–740.
11 A. Kongkanand, R. Martine-Dominguez, P.V. Kamat, *Nano Lett.*, **7**, 2007, 676–680.
12 P. Brown, K. Takeuchi, P.V. Kamat, *J. Phys. Chem. C*, **112**, 2008, 4776–4782.
13 J.H. Wu, Z. Lan, J.M. Lin, *et al*., *Chem. Rev.*, **115**, 2015, 2136–2173.
14 M. Wu, X. Lin, Y. Wang, *et al*., *J. Am. Chem. Soc.*, **134**, 2012, 3419–3428.
15 A. Fakharuddin, R. Jose, T.M. Brown, *et al*., *Energy Environ. Sci.*, **7**, 2014, 3952–3981.
16 W.W. Yu, L. Qu, W. Guo, X. Peng, *Chem. Mater.*, **15**, 2003, 2854–2860.
17 R. Vogel, P. Hoyer, H. Weller, *J. Phys. Chem.*, **98**, 1994, 3183–3188.
18 J.M. Luther, M.C. Beard, Q. Song, *et al*., *Nano Lett.*, **7**, 2007, 1779–1784.
19 Y. Wang, M. Wu, X. Lin, *et al*., *Eur. J. Inorg. Chem.*, 2012, 3557–3561.
20 E. Ramasamy, C. Jo, A. Anthonysamy, *et al*., *Chem. Mater.*, **24**, 2012, 1575–1582.
21 Z.Q. Li, F. Gong, G. Zhou, Z. S. Wang, *J. Phys. Chem. C*, **117**, 2013, 6561–6566.
22 H.C. Sun, D. Qin, S.Q. Huang, *et al*., *Energy Environ. Sci.*, **4**, 2011, 2630–2637.
23 G.T. Yue, P. Li, F.M. Li, C. Chen, *RSC Adv.*, **6**, 2016, 61278–61283.
24 P. Arunachalam, M.A. Ghanem, A.M. Al-Mayouf, M. Al-shalwi, *Mater. Lett.*, **196**, 2017, 365–368.
25 Y.J. Li, Q.W. Tang, L.M. Yu, *et al*., *Power Sources*, **305**, 2016, 217–224.
26 G.T. Yue, X.P. Ma, W.F. Zhang, *et al*., *Nanoscale Res. Lett.*, **10**, 2015, 1–9.
27 I.A. Sahito, K.C. Sun, A.A. Arbab, *et al*., *Carbohydr. Polym.*, **130**, 2015, 299–306.
28 I.A. Sahito, K.C. Sun, A.A. Arbab, *et al*., *J. Power Sources*, **319**, 2016, 90–98.
29 B. Fang, S.-Q. Fan, J.H. Kim, *et al*., *Langmuir*, **26**, 2010, 11238–11243.
30 S.Q. Fan, B. Fang, J.H. Kim, *et al*., *Langmuir*, **26**, 2010, 13644–13649.
31 A.A. Arbab, K.C. Sun, I.A. Sahito, *et al*., *J. Mater. Chem. A*, **4**, 2016, 1495–1505.
32 Z.A. Akbar, J.S. Lee, H.I. Joh, *et al*., *J. Phys. Chem. C*, **119**, 2015, 2314–2321.
33 B. Zhao, H. Huang, P. Jiang, *et al*., *J. Phys. Chem. C*, **115**, 2011, 22615–22621.
34 G. Veerappan, K. Bojan, S.-W. Rhee, *ACS Appl. Mater. Interfaces*, **3**, 2011, 857–862.
35 Y.Y. Li, C.T. Li, M.H. Yeh, *et al*., *Electrochim. Acta*, **179**, 2015, 211–219.
36 Y. Li, H. Wang, Q. Feng, *et al*., *ACS Appl. Mater. Interfaces*, **5**, 2013, 8217–8224.
37 J. Theerthagiri, K. Premnath, P. Arunachalam, *et al*., *Int. J. Hydrogen Energy*, **42**, 2017, 13020–13030.
38 J.-Z. Chen, C. Wang, C.-C. Hsu, I.C. Cheng, *Carbon*, **98**, 2016, 34–40.
39 J. Wu, Z. Lan, J. Lin, *et al*., *Chem. Rev.*, **115**, 2015, 2136–2173
40 B. O'Regan, M. Gratzel, *Nature*, **353**, 1991, 737–740.
41 M. Gratzel, *Nature*, **414**, 2001, 338–344.
42 A. Hagfeldtt, M. Gratzel, *Chem. Rev.*, **95**, 1995, 49–68
43 A.K. Chandiran, M. Abdi Jalebi, M.K. Nazeeruddin, M. Gratzel, *ACS Nano*, **8**, 2014, 2261–2268.
44 M. Liang, J. Chen, *Chem. Soc. Rev.*, **42**, 2013, 3453–3488.

45 A. Mishra, M.K.R. Fischer, P. Bauerle, *Angew. Chem. Int. Ed.*, **48**, 2009, 2474–2499.
46 J. Wu, Z. Lan, J. Lin, *et al*., *Chem. Rev.*, **115**, 2015, 2136–2173.
47 P. Poudel, Q. Qiao, *Nano Energy*, **4**, 2014, 157–175.
48 S. Thomas, T.G. Deepak, G.S. Anjusree, *et al*., *J. Mater. Chem. A*, **2**, 2014, 4474–4490.
49 S. Hwang, M. Batmunkh, M.J. Nine, *et al*., *ChemPhysChem*, **16**, 2015, 53–65.
50 F.T. Kong, S.Y. Dai, *Prog. Chem.*, **18**, 2006, 1409–1424.
51 P.V. Kamat, *J. Phys. Chem. Lett.*, **4**, 2013, 908–918
52 I. Hod, A. Zaban, *Langmuir*, **30**, 2013, 7264–7273
53 P.V. Kamat, K. Tvrdy, D.R. Baker, J.G. Radich, *Chem. Rev.*, **110**, 2010, 6664–6688.
54 I. Hwang, K. Yong, *Chemelectrochem*, **2**, 2015, 634–653.
55 A. Kojima, K. Teshima, Y. Shirai, T. Miyasaka, *J. Am. Chem. Soc.*, **131**, 2009, 6050.
56 M.M. Lee, J. Teuscher, T. Miyasaka, *et al*., *Science*, **338**, 2012, 643.
57 Q. Chen, H.P. Zhou, Z.R. Hong, *et al*., *J. Am. Chem. Soc.*, **136**, 2014, 622.
58 L. Etgar, P. Gao, Z.S. Xue, *et al*. *Am. Chem. Soc.*, **134**, 2012, 17396
59 W. Abu Laban and L. Etgar, *Energy Environ. Sci.*, **6**, 2013, 3249.
60 J. Mandelkorn, J.H. Lamneck Jr, *J. Appl. Phys.*, **44**, 1973, 4785
61 T. Wada, N. Kohara, S. Nishiwaki, T. Negami, *Thin Solid Films*, **387**, 2001, 118.
62 T. Leijtens, G.E. Eperon, S. Pathak, A. *et al*., *Nat. Commun.*, **4**,2013, 2885.
63 L. Wang, H. Liu, R.M. Konic, *et al*., *Chem. Soc. Rev.*, **42**, 2013, 8134–8156.
64 R.D. Costa, F. Lodermeyer, R. Casillas, D.M. Guldi, *Energy Environ. Sci.*, **7**, 2014, 1281–1296.
65 M. Gratzel, *J. Photochem. Photobiol. C*, **4**, 2003, 145–153.
66 H.M. Upadhyaya, S. Senthilarasu, M.H. Hsu, D. Kishore Kumar, *Sol. Energy Mater. Sol. Cells*, **119**, 2013, 291–295.
67 A. Kay, M. Gratzel, *Sol. Energy Mater. Sol. Cells*, **44**, 1996, 99–117.
68 K. Imoto, K. Takahashi, T. Yamaguchi, *et al*., *Sol. Energy Mater. Sol. Cells*, **79**, 2003, 459–469.
69 T.N. Murakami, S. Ito, Q. Wang, *et al*., *J. Electrochem. Soc.*, **153**, 2006, A2255–A2261.
70 S. Hou, X. Cai, Y. Fu, *et al*., *J. Mater. Chem.*, **21**, 2011, 13776–13779.
71 W.J. Lee, E. Ramasamy, D.Y. Lee, J.S. Song, *ACS Appl. Mater. Interfaces*, **1**, 2009, 1145–1149.
72 G. Wang, W. Xing, S. Zhuo, *J. Power Sources*, **1**, 2009, 568–573.
73 L. Kavan, J.H. Yum, M. Gratzel, *ACS Nano*, **5**, 2011, 165–172.
74 N. Murakami, S. Ito, Q. Wang, *et al*., *J. Electrochem. Soc.*, **153**, 2006, A2255–A2261.
75 S. Xu, Y. Luo, W. Zhong, *Solar Energy*, **85**, 2011, 2826–2832.
76 M. Wu, X. Lin, T. Wang, *et al*., *Energy Environ. Sci.*, **4**, 2011, 2308–2315.
77 W.J. Lee, E. Ramasamy, D.Y. Lee, J. S. Song, *Sol. Energy Mater. Sol. Cells*, **92**, 2008, 814–818.
78 W. Zeng, G. Fang, T. Han, *et al*., *J. Power Sources*, **239**, 2014, 456–462.

79 S. Pan, Z. Yang, H. Li, *et al*., *J. Am. Chem. Soc.*, **135**, 2013, 10622–10625.
80 F. Hao, P. Dong, J. Zhang, *et al*., *Sci. Rep.*, **2**, 2012, 368.
81 G. Veerappan, K. Bojan, S. W. Rhee, *ACS Appl. Mater. Interfaces*, **3**, 2011, 857–862.
82 G. Veerappan, K. Bojan, S.W. Rhee, *Renewable Energy*, **41**, 2012, 383–388.
83 J. Chen, K. Li, Y. Luo, *et al*., *Carbon*, **47**, 2009, 2704–2708.
84 B. Kilic, S. Turkdogan, A. Astam, *et al*., *Sci. Rep.*, **6**, 2016, 27052.
85 A. Kaniyoor, S. Ramaprabhu, *J. Appl. Phys.*, **109**, 2011, 124308.
86 D.W. Zhang, X.D. Li, H.B. Li, *et al*., *Carbon*, **49**, 2011, 5382–5388.
87 C.T. Hsieh, B.H. Yang and J.Y. Lin, *Carbon*, **49**, 2011, 3092–3097.
88 H. Choi, S. Hwang, H. Bae, *et al*., *Electron. Lett.*, **47**, 2011, 4.
89 P. Zhai, T.C. Wei, Y.H. Chang, *et al*., *Small*, **10**, 2014, 3347–3353.
90 B. Pang, L. Dong, S. Ma, *et al*., *RSC Adv.*, **6**, 2016, 41287–41293.
91 B. Fang, M. Kim, S.-Q. Fan, *et al*., *J. Mater. Chem.*, **21**, 2011, 8742–8748.
92 F. Hao, P. Dong, J. Zhang, *et al*., *Sci. Rep.*, **2**, 2012, 368.
93 M. Seol, E. Ramasamy, J. Lee, K. Yong, *J. Phys. Chem. C*, **115**, 2011, 22018–22024.
94 Z. Du, Z. Pan, F. Fabregat-Santiago, *et al*., *J. Phys. Chem. Lett.*, **7**, 2016, 3103–3111.
95 Z.L. Ku, Y.G. Rong, M. Xu, *et al*., *Sci. Rep.*, **3**, 2013, 3132.
96 Z. Li, S.A. Kulkarni, P.P. Boix, *et al*., *ACS Nano*, **8**, 2014, 6797.
97 M. Xu, Y. Rong, Z. Ku, *et al*., *J. Mater. Chem. A*, **2**, 2014, 8607.
98 Y. Yang, J. Xiao, H. Wei, *et al*., *RSC Adv.*, **4**, 2014, 52825–52830.
99 R.B. Levy, M. Boudart, *Science*, **181**, 1973, 547–549.
100 S.T. Oyama, *Catal. Today*, **15**, 1992, 179–200.
101 L.N. Skvortsova, L.N. Chukhlomina, G.M. Mokrousov, *et al*., *Russ. J. Appl. Chem.*, **85**, 2012, 41–45.
102 A.M. Alexander, J.S.J. Hargreaves, *Chem. Soc. Rev.*, **39**, 2010, 4388–4401.
103 M.K. Neylon, S. Choi, H. Kwon, *et al*., *Appl. Catal. A*, **183**, 1999, 253–263.
104 M. Wu, X. Lin, A. Hagfeldt, T. Ma, *Angew. Chem. Int. Ed.*, **50**, 2011, 3520–3524.
105 M. Wu, Q. Zhang, J. Xiao, *et al*., *J. Mater. Chem.*, **21**, 2011, 10761–10766.
106 M. Seol, D.H. Youn, J.Y. Kim, *et al*., *Adv.Energy Mater.*, **4**, 2014, 1300775.
107 C. Giordano, C. Erpen, W. Yao, M. Antonietti, *Nano Lett.*, **8**, 2008, 4659–4663.
108 D. Ham, J. Lee, *Energies*, **2**, 2009, 873–899.
109 S. Li, J.S. Lee, *J. Catal.*, **178**, 1998, 119–136.
110 J. Soo Kang, M.-A. Park, J.-Y. Kim, *et al*., *Sci. Rep.*, **5**, 2015, 10450–10450.
111 M.-H. Yeh, L.-Y. Lin, C.-P. Lee, *et al*., *J. Power Sources*, **237**, 2013, 141–148.
112 D.H. Youn, M. Seol, J.Y. Kim, J.-W. Jang, *et al*., *Chemsuschem*, **6**, 2013, 261–267.
113 R.A. Senthil, J. Theerthagiri, J. Madhavan, *et al*., *J. Solid State Chem.*, **242**, 2016, 199–206.
114 G. Yue, J.Y. Lin, S.Y. Tai, *et al*., *Electrochim. Acta*, **85**, 2012, 162–168.
115 K.J. Huang, L. Wang, J.Z. Zhang, K. Xing, *J. Electroanal. Chem.*, **752**, 2015, 33–40.

116 N. Balis, V. Dracopoulos, K. Bourikas, P. Lianos, *Electrochim. Acta*, **91**, 2013, 246–252.
117 M. Wang, A.M. Anghel, B. Marsan, *et al*., *Am. Chem. Soc.*, **131**, 2009, 15976–15977.
118 M. Wu, Y. Wang, X. Lin, *et al*., *Phys. Chem. Chem. Phys.*, **13**, 2011, 19298–19301.
119 H.C. Hung, Y J. Lin, Z.Y. Ke, *J. Mater. Sci.: Mater. Electron.*, **27**, 2016, 5059–5063.
120 G. Yue, J. Wu, Y. Xiao, *et al*., *J. Mater. Chem. A*, **1**, 2013, 1495–1501.
121 S.Y. Tai, C.J. Liu, S.W. Chou, *et al*., *J. Mater. Chem.*, **22**, 2012, 24753–24759.
122 J. Theerthagiri, R.A. Senthil, P Arunachalam, *et al*., *J Solid State Electrochem.*, **21**, 2017, 581–590.
123 P.P. Boix, G. Larramona, A. Jacob, *et al*., *J. Phys. Chem. C*, **116**, 2012, 1579–1587.
124 S. Ruhle, M. Shalom, A. Zaban, *ChemPhysChem*, 2010, **11**, 2290–2304.
125 M.S. Faber, K. Park, M. Caban-Acevedo, *et al*., *J. Phys. Chem. Lett.*, **4**, 2013, 1843–1849.
126 Y. Shengyuan, A.S. Nair, Z. Peining, S. Ramakrishna, *Mater. Lett.*, **76**, 2012, 43–46.
127 Z. Yang, C.-Y. Chen, C.-W. Liu, *et al*., *Adv. Energy Mater.*, **1**, 2011, 259–264.
128 H. Lee, M. Wang, P. Chen, *et al*., *Nano Lett.*, **9**, 2009, 4221–4227.
129 K. Meng, P.K. Surolia, O. Byrne, K.R. Thampi, *J. Power Sources*, **248**, 2014, 218–223.
130 Q. Shen, A. Yamada, S. Tamura, T. Toyoda, *Appl. Phys. Lett.*, **97**, 2010, 123107.
131 Z. Tachan, M. Shalom, I. Hod, *et al*., *J. Phys.Chem. C*, **115**, 2011, 6162–6166.
132 J.B. Zhang, F.Y. Zhao, G.S. Tang, Y. Lin, *J. Solid State Electrochem.*, **17**, 2013, 2909–2915.
133 G. Hodes, J. Manassen, D. Cahen, *J. Appl. Electrochem.*, **7**, 1977, 181–182.
134 J. Theerthagiri, R.A. Senthil, P. Arunachalam, *et al*., *Ionics*, **23**, 2017, 1017–1025.
135 X. Zeng, D. Xiong, W. Zhang, *et al*., *Nanoscale*, **5**, 2013, 6992–6998.
136 H. Flaisher, R. Tenne, G. Hodes, *J. Phys. D*, **17**, 1984, 1055.
137 P.V. Kamat, *J. Phys. Chem. C*, **112**, 2008, 18737.
138 A.D. Savariraj, K.K. Viswanathan, K. Prabakar, *Electrochim. Acta*, **149**, 2014, 364–369.
139 H.S.S. Ramakrishna Matte, A. Gomathi, A.K. Manna, *et al*., *Angew. Chem., Int. Ed.*, **49**, 2010, 4059.
140 K.C. Huang, Y.C. Wang, P.Y. Chen, *et al*., *J. Power Sources*, **203**, 2012, 274–281.
141 M.Y. Yen, C.C. Teng, M.C. Hsiao, *et al*., *J. Mater. Chem.*, **21**, 2011, 12880–12888.
142 Y. Wang, C. Zhao, M. Wu, *et al*., *Electrochim. Acta*, **105**, 2013, 671–676.
143 P. Joshi, Y. Xie, M. Ropp, *et al*., *Energy Environ. Sci.*, **2**, 2009, 426–429.

144 S. Stankovich, D.A. Dikin, G.H.B. Dommett, *et al*., *Nature*, **442**, 2006, 282–286.
145 G. Wang, S. Zhuo, W. Xing,*Mater. Lett.*, **69**, 2012, 27–29.
146 K.S. Lee, Y. Lee, J.Y. Lee, *et al*., *ChemSusChem*, **5**, 2012, 379–382.
147 Y.Y. Dou, G.R. Li, J. Song, X.P. Gao, *Phys. Chem. Chem. Phys.*, **14**, 2012, 1339–1342.
148 R. Bajpai, S. Roy, N. Kulshrestha, *et al*., *Nanoscale*, **4**, 2012, 926–930.
149 C.J. Raj, K. Prabakar, A.D. Savariraj, H.J. Kim, *Electrochim. Acta*, **103**, 2013, 231–236.
150 J.G. Radich, R. Dwyer, P.V. Kamat, *J. Phys. Chem. Lett.*, **2**, 2011, 2453–2460.
151 H. Hu, J. Ding, J. Qian, *et al*., *Mater. Lett.*, **114**, 2014, 7–10.
152 P. Parand, M. Samadpour, A. Esfandiar, A.I. Zad, *ACS Photonics*, **1**, 2014, 323–330.
153 G. Zhu, L. Pan, H. Sun, *et al*., *ChemPhysChem.*, **13**, 2012, 769–773.
154 X. Zhang, X. Huang, Y. Yang, *et al*., *ACS Appl. Mater. Interfaces*, **5**, 2013, 5954–5960.
155 R.A. Senthil, A. Selvi, P. Arunachalam, *et al*., *J Mater. Sci: Mater. Electron.*, **28**, 2017, 10081.
156 M.A. Ghanem, A.M. Al-Mayouf, P. Arunachalam, T. Abiti, *Electrochim. Acta*, **207**, 2017, 177–186.
157 A.K. Das, S. Sahoo, P. Arunachalam, S. Zhang, *RSC Adv.*, **6**, 2017, 107057–107064.
158 M.A. Ghanem, P. Arunachalam, A.M. Almayouf, M.T. Weller, *J. Electrochem. Soc.*, **163**, 2017, H450–H458.
159 J. Theerthagiri, K. Thiagarajan, B. Senthilkumar, *et al*., *ChemistrySelect*, **2**, 2017, 201–210.
160 P. Arunachalam, M.N. Shaddad, A.S. Alamoudi, *et al*., *Catalysts*, **7**, 2017, 119.
161 M.A. Ghanem, A.M. Al-Mayouf, J.P. Singh, P. Arunachalam, *Electrocatalysis*, **8**, 2017, 16–26.
162 H. Wang, W. Wei, Y.H. Hu, *J. Mater. Chem. A*, **1**, 2013, 6622–6628.
163 S. Yun, L. Wang, W. Guo, T. Ma, *Electrochem. Commun.*, **24**, 2012, 69–73.
164 M. Wu, X. Lin, A. Hagfeldt, T. Ma, *Chem. Commun.*, **47**, 2011, 4535–4537
165 S. Yun, M. Wu, Y. Wang, J *et al*., *ChemSusChem*, **6**, 2013, 411–416.
166 X. Lin, M. Wu, A. Hagfeldt, T. Ma, *Chem. Commun.*, **47**, 2011, 11489–11491.
167 Y. Hou, Z. Chen, D. Wang, *et al*., *Small*, **10**, 2013, 484–492.
168 Y. Shibata, T. Kato, T. Kado, *et al*., *Chem. Commun.*, 2003, 2730–2731.
169 Y. Saito, W. Kubo, T. Kitamura, *et al*., *J. Photochem. Photobiol. A*, **164**, 2004, 153–157.
170 Q. Li, J. Wu, Q. Tang, *et al*., *Electrochem. Commun.*, **10**, 2008, 1299–1302.
171 Y. Xiao, G. Han, Y. Li, *et al*., *J. Mater. Chem. A*, **2**, 2014, 3452–3460.
172 Z. Li, B. Ye, X. Hu, *et al*., *Electrochem. Commun.*, **11**, 2009, 1768–1771.
173 Y. Qiu, S. Lu, S. Wang, *et al*., *J. Power Sources*, **253**, 2014, 300–304.
174 J. Wu, Q. Li, L. Fan, *et al*., *J. Power Sources*, **181**, 2008, 172–176.

175 J.M. Pringle, V. Armel, D.R. MacFarlane, *Chem. Commun.*, **46**, 2010, 5367–5369.
176 S. Abdul Al Mohsin, J. Armstrong, J. B. Cui, *J. Renewable Sustainable Energy*, **4**, 2012, 043108.
177 L. Chen, C.X. Guo, Q. Zhang, *et al*., *ACS Appl. Mater. Interfaces*, **5**, 2013, 2047–2052.
178 T. Shu, Z.-L. Ku, *J. Alloys Compd.*, **586**, 2014, 257–260.
179 M.H. Yeh, C.P. Lee, C.Y. Chou, *et al*., *Electrochim. Acta*, **57**, 2011, 277–284.

7

Design and Fabrication of Carbon-based Nanostructured Counter Electrode Materials for Dye-sensitized Solar Cells

Jayaraman Theerthagiri[1,2], Raja Arumugam Senthil[1], and Jagannathan Madhavan[1]

[1] *Solar Energy Laboratory, Thiruvalluvar University, India*
[2] *Centre of Excellence for Energy Research, Sathyabama Institute of Science and Technology, India*

7.1 Photovoltaic Solar Cells – An Overview

Photovoltaic (PV) is the collective name for devices that directly convert sunlight into electricity. Among all the sustainable energy technologies, such as wind, tide, hydro, geothermal, and biomass, PV technology is the most elegant method of producing electricity without pollution, sound or moving parts [1–5]. The history of PV dates back to the first discovery of the "photovoltaic effect" by French physicist Edmond Becquerel in 1839. He noticed the generation of an electric current while experimenting with a silver-coated platinum electrode placed in an electrolyte [6, 7]. This preliminary result opened the way for developing a variety of concepts and devices to convert sunlight into electricity in order to explore clean and renewable energy.

The spectral distribution of the solar spectrum was first described by Max Planck in 1901 through his Planck's law [8]. In 1905, Albert Einstein described how "light quanta" absorption causes the photoelectric effect and, hence, was awarded the Nobel Prize in 1921. This is the theoretical basis for all PV devices. Modern application of PV devices was initiated in 1954. A research team at Bell Labs, USA, discovered that a voltage was produced by the p-n junction diodes under room light. In the same year, it announced the production of silicon (p-n junction) solar cells with over 6% efficiency [3], which is considered as a milestone in the development of a PV device. Soon after, solar energy conversion was applied to power space satellites and smaller items like calculators, watches, etc. Nowadays, solar cells have occupied markets in a variety of applications. For example, people power their homes and businesses with individual solar photovoltaic systems.

Rational Design of Solar Cells for Efficient Solar Energy Conversion, First Edition.
Edited by Alagarsamy Pandikumar and Ramasamy Ramaraj.

The strong advances in PV technology in the past decade mean it is recognized as an important contributor in future energy generation applications. Photovoltaics are usually divided into different categories called generations. The generation of PV devices turned out to be advantageous in production cost with respect to silicon devices. Today we have crossed almost four generations of solar cells, because of which we can now use different types of solar cells according to our needs and preferences. Some famous types are described here.

7.1.1 First Generation Solar Cells

The first generation solar cells are also known as silicon wafer-based solar cells. These cells are typically made with crystalline silicon wafer and had large areas. This generation of silicon solar cell is still ruling the commercial market because of its dominant quality of high efficiency. However, very pure silicon is needed to achieve high efficiency and its price is high when compared to the power output due to the energy required manufacturing process.

7.1.2 Second Generation Solar Cells

The second generation of PV materials is based on the use of thin film deposits of semiconductors. In this generation, four types of solar cell were established. These include amorphous silicon cells, in which hydrogen is introduced to the silicon to make it possible to dope the silicon with boron and phosphorus. The cells are built up in this sequence from bottom to top. Polycrystalline silicon, which is made of pure silicon grains, work better than the previous designs because of their mobility feature. This can be achieved by using a material with a textured surface on both the front and back of the cell, rather than a flat surface. Examples include copper indium gallium selenide (CIGS) alloy cells, deposited on glass or stainless steel, and are complex in design. Cadmium telluride (CdTe) cells are formed with cadmium and tellurium mixed with a zinc cubic crystal structure. The second generation of thin film technology allows fewer materials to be used, so that the manufacturing cost is significantly reduced. But the efficiencies of thin-film solar cells are comparatively low compared to the previous generation solar cells.

7.1.3 Third Generation Solar Cells

Third generation solar cells are very different from the previous generations because of the use of innovative semiconductors. This generation of solar cells does not rely on traditional p-n junction to separate photogenerated charge carriers. There are several technologies in this generation, which includes

photoelectrochemical cells, nanocrystal solar cells, and dye-sensitized solar cells (DSSCs). Nanocrystal solar cells are based on a silicon substrate with a coating of nano crystals. Among all the technologies of this generation, DSSCs are the promising area for academic research. DSSCs have received considerable interest as a potential alternative to the conventional p-n junction silicon solar cells in recent years.

7.1.4 Fourth Generation Solar Cells

Fourth generation solar cells use composite PV technology, in which polymers with nano particles are mixed together to make a single multispectrum layer that can help electrons and protons to move, so producing better voltage and good quality of direct current.

The detailed elucidation of solar cells showed the first generation of silicon wafer-based solar cells having high efficiency, but relatively expensive to produce, whereas the second generation thin film deposits of semiconductors have lower efficiency, but are much cheaper to produce, so that the cost per watt is lower than in first generation cells. However, the third generation of photoelectrochemical cells are very efficient, with a special mention of DSSCs, the most successful type of solar cell in this generation. Among various solar cells, DSSCs demonstrate specific advantages over other PV devices because of their high efficiency, low cost, simple fabrication procedures, environmental friendliness, transparency, and good plasticity. There are lot of research findings reported in this field. Their goal is to make DSSCs with inexpensive production costs, high power conversion efficiency, and high stability. This chapter gives a detailed illustration on DSSCs and their applications.

7.2 Dye-sensitized Solar Cells

DSSCs are the most prominent third generation solar cell, exhibiting several features that are not available in any other types of solar cell. Also, it is a potential candidate for the traditional silicon-based solar cells in different aspects, such as simple fabrication procedure, low cost, high flexibility, good plasticity, ease of building combination, environmental friendliness, etc. [9–13]. Since the outstanding report of O'Regan and M. Gratzel in 1991 [14], DSSCs have become a turning point in the area of research and have been given much attention by the international research community. The history of DSSCs begins in the early 1870s with the discovery of panchromatic film, which was a building stone in the field of photography and photoelectrochemistry. They used dyes with silver halide in a gelatine medium, which showed a good sensitivity to UV light for which the panchromatic film was able to

render an image; this was followed by James Moser in 1887, who discovered the first "sensitization photoelectrode". In 1991, O'Regan and M. Gratzel described a low cost, high-efficiency solar cell based on dye-sensitized colloidal TiO_2 films. The device was fabricated using 10 μm thick, optically transparent film of nanometer-sized TiO_2 particles coated with a monolayer of charge-transfer dye (ruthenium dye) to sensitize the film for light harvesting. This was the first report on the efficient solar cell with an overall light-to-electric conversion efficiency value of 7.1–7.9% in simulated solar light conditions [14]. Henceforth, the typical DSSC is commonly referred to as the Gratzel cell by researchers. Since the exploration of DSSCs, great efforts have been devoted towards the modification of DSSCs in order to make these devices more efficient and stable.

7.2.1 Major Components of DSSCs

It is very important to identify the components of DSSCs to know its working mechanism. A typical conventional DSSC comprises four major parts: nanocrystalline semiconductor oxide (photoanode), dye as sensitizer, redox electrolyte, and counterelectrode (CE). The schematic structure of a typical DSSC is shown in Figure 7.1 [15]. A clear understanding of each component in a DSSC is essential to achieve high power conversion efficiency and stability.

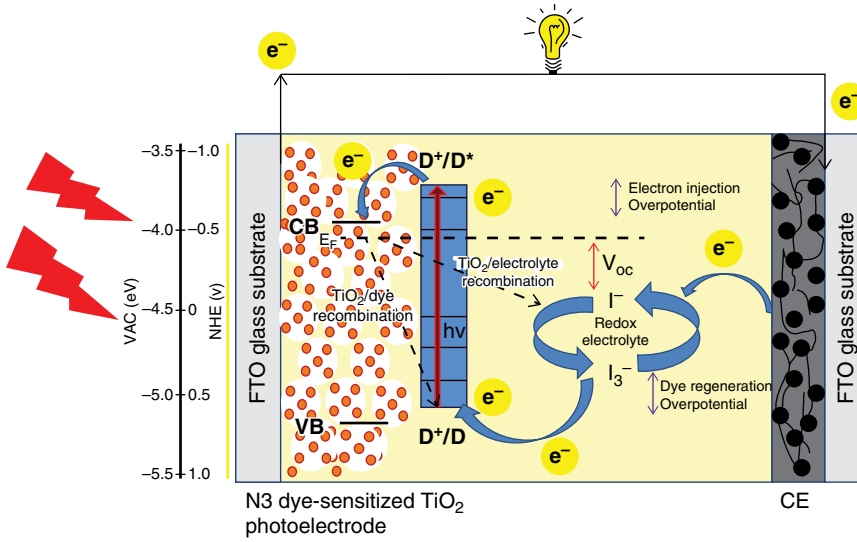

Figure 7.1 Typical schematic structure of a DSSC [15]. Reproduced with permission of Springer.

7.2.1.1 Transparent Conducting Glass Substrate

The photoelectrode and CE of standard DSSCs are prepared on a transparent conducting glass substrate. Transparent conducting glass substrate is used not only in PV devices but also in other optoelectronic devices. The conducting glass substrate must be highly transparent to allow the maximum passage of solar light to the active area and should have high electrical conductivity. Mostly, fluorine-doped tin oxide (FTO) or indium-doped tin oxide (ITO) glass substrate is commonly used in DSSCs. Even though ITO exhibits better optical transparency and electrical conductivity, FTO is the most preferred because of its stability. The stability of ITO diminishes at a temperature above 300 °C and the production of conventional DSSCs requires a firing temperature above 450 °C in order to form a nanoporous structure of the TiO_2. Further, the limited supply of indium, its high cost, and the weak flexibility of the ITO layer also hinder the application of ITO in DSSCs.

7.2.1.2 Photoelectrode

The photoelectrode (photoanode) is a key component in the DSSC; it consists of a nanoporous layer of a semiconductor metal oxide attached to a transparent conducting FTO glass substrate. The main function of a photoanode is to optimize light harvesting by providing high internal surface area in which dyes are adsorbed. The oxide film holds the dye molecules and collects the photogenerated electron from the LUMO level of the dye molecules, providing a path for the transport of the electrons to the conducting glass substrate. The photoanode material must satisfy several requirements regarding morphology, chemical and electronic structure [16].

- The photoanode material should have high surface area, porosity to load a large amount of dye molecules.
- It must be transparent to visible light, possess high density of states to quickly accept electrons from the photoexcited dye, and should have suitable conduction band position.
- It should have a large bandgap (3 eV) of the semiconductor oxide materials that make them suitable for absorption of large portion of the solar spectrum.
- The conduction band edge of the photoanode material should lie slightly below the excited state energy level of dye (sensitizer), which is an important condition for the efficient electron injection.
- The photoelectrode must allow transport of injected electrons to the FTO glass substrate faster than they can recombine with either oxidized dye molecules or the oxidized redox species.
- It must also be chemically and mechanically stable to achieve long lifetimes.
- It should possess high electron mobility.

With all these qualities, TiO_2, which has a large bandgap, is highly preferred for use as photoanode material in DSSCs. TiO_2 is a stable, nontoxic oxide that

has a bandgap of 3.2 eV and does not absorb high solar light. Three crystal forms of TiO_2 occur naturally: rutile, anatase, and brookite. Rutile is thermodynamically more stable and has a bandgap of 3.0 eV with an absorption edge of 413 nm. Anatase is the preferred structure in DSSCs, because it has a larger bandgap, 3.2 eV, with an absorption edge of 388 nm. It has a conduction band position below the LUMO level of many dyes. The empty d-orbital has a high density of states to accept electrons from the dye on the picosecond time scale. In addition to TiO_2, other semiconductors have also been used as photoelectrode materials in DSSCs; these include ZnO, WO_3, SnO_2, CeO_2, ZrO_2, Nb_2O_5, and Ta_2O_5. However, TiO_2 and ZnO are still the best semiconductors for the photoelectrode in DSSCs.

7.2.1.3 Dye Sensitizer

The dye sensitizer can be regarded as one of the crucial parts in DSSCs. The sensitizer role in DSSCs is to absorb the solar light and to generate electrons that are subsequently injected into the conduction band of the semiconductor electrode on which the dye is anchored. Some essential characteristics of the sensitizer are [17, 18]:

- The absorption spectrum of the dye should cover the whole visible region and near-infrared portion of the solar spectrum.
- The excited state level of the dye should be higher in energy than the conduction band edge of n-type semiconductor, so that an efficient electron transfer process between the excited dye and conduction band of the semiconductor take place.
- Dye should be very stable when exposed to constant light irradiation.
- The dye must bind strongly to the semiconductor oxide material and should have good solubility.
- For the strong binding of dye on the surface of semiconductor oxide, it should have anchoring groups, namely –COOH, $–H_2PO_3$, $–SO_3H$.
- The dye should not aggregate on the surface to avoid nonradiative decay of the excited state to the ground state.

Generally, metal–organic and organic dyes are used in DSSCs, although metal-free organic dyes could present several advantages, such as easy availability, cost effectiveness, synthetic approach, and high molar extinction coefficient [19, 20]. Despite certain limitations of metal-based organic dyes, such as expensive synthesis process and low molar extinction coefficient in the visible region, they exhibit higher power conversion efficiency than the organic dyes, because the organic dyes tend to aggregate on the surface of semiconductor and have narrow light absorption bands in the visible region. The most common high performing dyes reported so far are the ruthenium centered polypyridyl complexes such as N3, N719, and N749 (black dye). The chemical structures of N3, N719, and N749 dyes are shown in Figure 7.2.

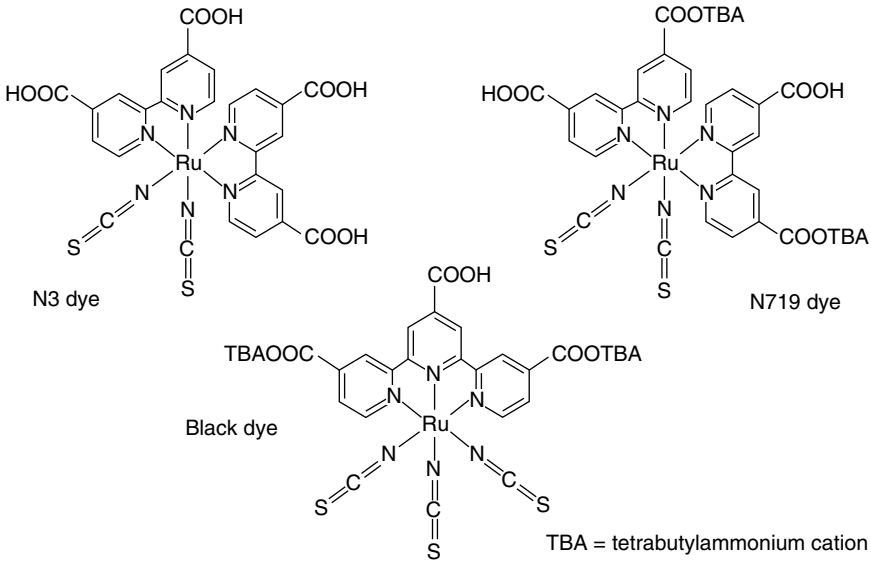

Figure 7.2 The chemical structures of N3, N719, and N749 (black) dyes.

7.2.1.4 Redox Electrolytes

The function of the redox electrolyte in DSSCs is to regenerate the oxidized dye sensitizer, transport in DSSCs, and completion of the external electrical circuit. The stability of DSSCs is highly dependent on the redox electrolytes. In order to regenerate the oxidized dye sensitizer, the redox potential of the electrolyte should be positioned slightly more negative than the HOMO level of the dye. A variety of redox couples are employed in the electrolytes, such as I^-/I_3^-, Co(II)/Co(III), SCN^-/SCN_3^- and Br^-/Br_3^-. Among these redox couples, I^-/I_3^- is the most widely used in electrolytes for DSSCs, not only because it exhibits a suitable electrochemical redox potential to reduce several oxidized dyes but also along with its best kinetic properties. Kinetics of two charge transfer steps are reported to be important for device performance [16]:

1) The oxidized dye molecule must be regenerated by the redox species much faster than the dye recombines with an electron in the oxide.
2) Recombination between the oxidized redox species and an electron in the oxide must be slow compared to electron transport to the substrate.

The electrolytes used in DSSCs are classified based on their viscosity, such as liquid electrolyte, quasi-solid electrolyte or solid polymer electrolyte. The liquid electrolyte is being used nowadays to achieve high power conversion efficiency; it usually constitutes a redox couple dissolved in a high dielectric constant organic solvent. In order to increase the device performance, some additives can

also be added. Although DSSCs achieve high power conversion efficiency while employing liquid electrolytes (I^-/I_3^- redox couple), they do have certain disadvantages, such as poor long-term stability due to the leakage and evaporation of liquids, corrosion of electrode, sealing problem, etc. All these factors affect the stability of DSSCs. In order to overcome these disadvantages, researchers focused on alternatives like gelation of solvent or polymer incorporating I^-/I_3^- redox couple [13, 21–23]. The important criteria considered for a polymer selection are that it should possess good conductivity and stability. The conductivity of an electrolyte mainly depends upon the concentration of salt containing the mobile species as well as the extent to which the salt is dissociated, thus making all dissociated ions available for conduction. But the dissociation of salts depends on parameters such as dissociation constant of the salt, donor number of the solvent, dielectric constant of the solvent, and nature of the salt. However, in polymer electrolytes, the conductivity arises from the rapid segmental motion and the interaction between the cation and the donor atom of the main structure.

7.2.1.5 Counterelectrode

The CE is one of the most important components in the DSSC; it consists of an electrocatalytic material coated on the conducting side of the transparent FTO glass substrate. The main function of the CE is that it acts as an electrocatalyst by reducing the redox species, which are the mediators for recombination of the dye sensitizer after the electron injection, and for collecting the hole from the hole-transporting materials in a solid state DSSC [24]. A CE with high electrocatalytic activity for triiodide reduction has low internal resistance, which results in a high fill factor. The CE material in DSSCs should possess high electrocatalytic activity towards the reduction of I_3^- into I^- ions and good stability towards the electrolyte used in the device, low charge resistance, and low cost. Generally, a platinum (Pt) deposited FTO or ITO glass substrate is the most commonly used CE in DSSCs due to its superior electrocatalytic activity and stability. However, platinum as a noble metal is easily corroded by I^-/I_3^- electrolyte and the cost of platinum CE is over 40% of the whole device fabrication cost. These factors strongly hinder the large scale production and commercial application of the DSSCs. This promoted numerous studies to develop an alternative material to the platinum CE to reduce the cost and simultaneously keep the effectiveness of the DSSCs. The alternative CE materials includes carbon materials, conducting polymers, metal oxides, sulfide materials, transition metal nitrides, carbides, and composite materials.

7.2.2 Working Mechanism of DSSCs

DSSCs typically comprise electrodes (anode and cathode), dye as sensitizer, and an I^-/I_3^- redox couple containing the electrolytes (Figure 7.1). When the cell is illuminated, an electron generated by the sensitizer is transferred to the

conduction band of the semiconductor oxide wherein the sensitizer is anchored. Then, the sensitizer is regenerated by the iodide ions from the electrolyte (I^-/I_3^- redox couple dissolved in an organic solvent) and I_3^- in the electrolyte is reduced by the electron reaching the CE through back contact. The cycle is completed by the electron migration between the TiO_2 semiconductor and the CE [25, 26].

Photoexcitation	$D + hv \longrightarrow D^*$
Electron injection	$D^* \longrightarrow D^+ + e^-_{CB}$
Dye regeneration	$2D^+ + 3I^- \longrightarrow I_3^- + 2D$
Regeneration of iodide	$I_3^- + 2e^- \longrightarrow 3I^-$

For the efficient regeneration of electrolyte, the charge-transfer resistance of the catalyst in the CE and the diffusion constant of triiodide are very important.

7.3 Carbon-based Nanostructured CE Materials for DSSCs

Carbon-based nanostructures are quite striking to replace platinum CE in DSSCs due to their large surface area, high conductivity, high reactivity for the reduction of triiodide, corrosion resistance towards iodine, and low cost. Numerous carbon materials such as graphene, carbon nanotubes, carbon nanofibers, activated carbon, graphite, and carbon black have been effectively used as a CE [27–30]. As a first report, Kay and Gratzel investigated a graphitic-carbon black mixture as a CE electrocatalyst for DSSCs and obtained a power conversion efficiency of 6.7% [31]. Subsequently, exhaustive research efforts have been expended on carbon-based materials as a CE in DSSCs. The photovoltaic parameters (power conversion efficiency and fill factor) of DSSCs are powerfully dependent on the thickness of the carbon layer [32].

Wu *et al.* prepared carbon black thin films using a doctor blade process and employed them as CEs of DSSCs [33]. These carbon black films, when heat treated at 350 °C, showed a low electrocatalytic activity, high charge transfer resistance, and poor performance. These results are attributed to the presence of residual PVDF. By elevating the treating temperature to 450 °C, PVDF was completely removed and the electrochemical properties of the resultant carbon black films resemble closely those of platinum film. The DSSCs using these carbon black CEs achieved significant power conversion efficiencies of 8.27–8.35%, which could be comparable to the DSSC fabricated with conventional platinum CE (8.29%). Zhu *et al.* prepared platinum/carbon sphere (Pt/CS) composites as electrocatalyst for the reduction of triiodide in Co^{3+}/Co^{2+} redox

electrolytes [34]. The excellent electrocatalytic performance of Pt/CS can fundamentally be attributed to the low apparent activation energy (Ea) of the redox reaction between Co^{3+} and Co^{2+}. Using the Pt/CS CE a high power conversion efficiency of 9.02% under 100 $mWcm^{-2}$ of simulated sunlight illumination was achieved. Nagaraju *et al.* synthesized honeycomb-like activated porous carbon (HPC) powder with meso/macropore structures via chemical activation and pyrolysis processes under inert gas atmosphere [35]. The morphology of the synthesized HPC is shown in Figure 7.3. The synthesized HPC was successfully employed as a cost-effective CE in DSSC. The fabricated DSSCs with HPC-based CE exhibited an excellent power conversion efficiency of 4.98%, which was attributed to the high specific surface area and hierarchical porous property of the HPC sample.

Susmitha *et al.* developed single wall carbon nanohorns (SWCNH) and graphene nanoplatelets (GNP) decorated CEs for DSSC application [36]. SWCNH-loaded DSSC showed higher photovoltaic conversion efficiency (4.09%) than the GNP (3.13%), which can be attributed to higher average surface roughness area, lower series, charge transfer resistance and electrolyte diffusion. In addition, the power conversion efficiencies increase with higher load of SWCNH up to

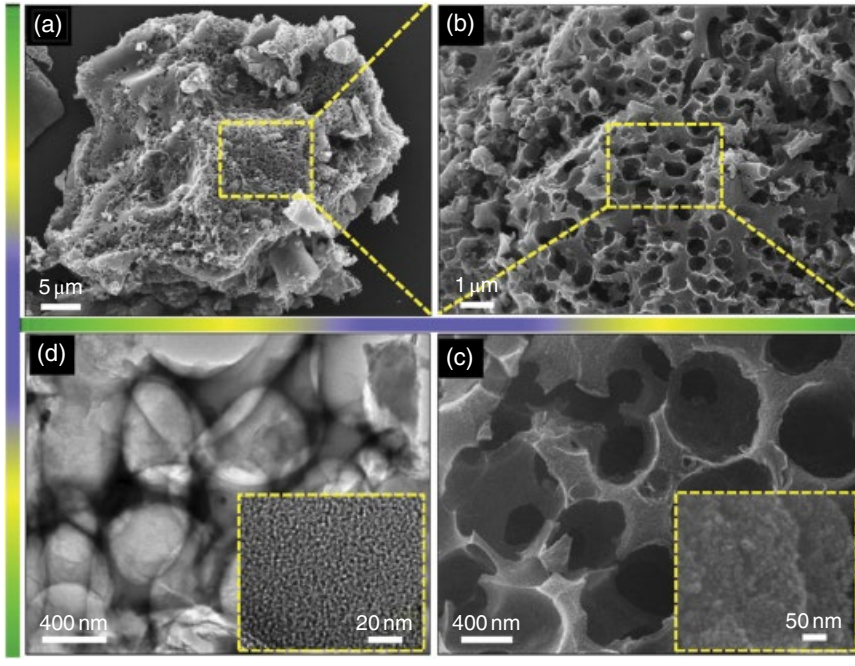

Figure 7.3 (a–c) FE-SEM images and (d) TEM images of the carbonized HPC sample under inert gas atmosphere [35]. Reproduced with permission of Elsevier.

3.0 mg. Therefore, their reports have proved that the SWCNH material has got great potential to function as low-cost CE material for reduction of iodide/triiodide redox couple in DSSCs. Wang *et al*. prepared g-C_3N_4/MWCNTs composite by a two-step method of refluxing and heating polymerization processes [37]. The prepared g-C_3N_4/MWCNTs composite was applied as CE in DSSCs. Under illumination of 100 mWcm^{-2}, the fabricated DSSC using g-C_3N_4/MWCNTs composite CE has achieved a power conversion efficiency of 6.34%. The reason for the enhanced power conversion efficiency might be due to the enhanced electrocatalytic activity of the triiodide reduction. The observed charge-transfer resistance of g-C_3N_4/MWCNTs composite electrode is 2.1 Ω cm^2, which was much lower than the individual g-C_3N_4 and MWCNT electrodes

Hou *et al*. developed polypyrrole/MWCNT CEs by electropolymerization of the polypyrrole (PPy) on the MWCNT-coated FTO glass using a cyclic voltammetry technique [38]. The DSSC based on the PPy/MWCNT composite CE showed an excellent photoelectric conversion efficiency of 7.15% under full sunlight illumination (100 mW cm^{-2}, AM 1.5 G), which was much higher than that of the MWCNT (1.72%) and PPy (5.72%) based DSSCs, and that of the platinum-based DSSC (7.76%). The corresponding *J-V* curves are shown in Figure 7.4. The higher performances of composite CEs was achieved due to the

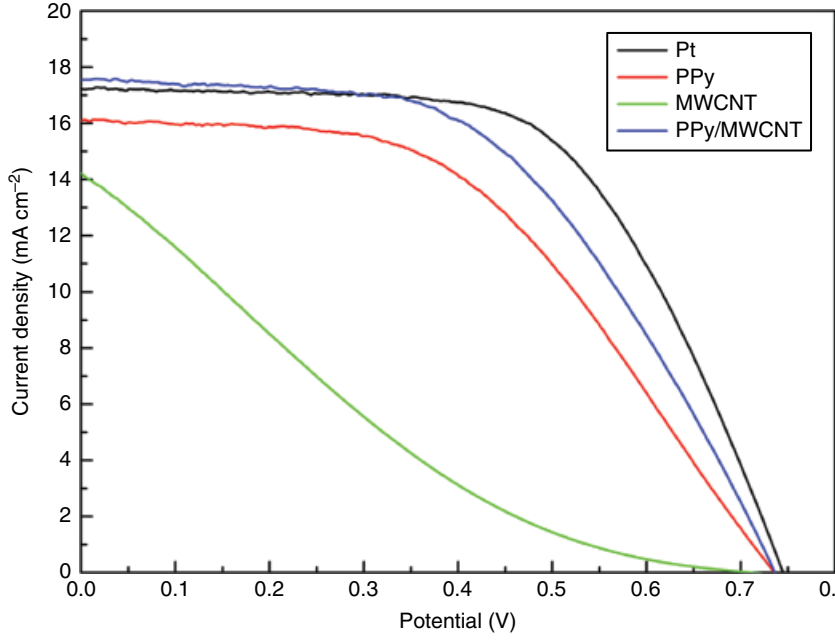

Figure 7.4 *J-V* curves of fabricated DSSCs based on the platinum, PPy, MWCNT, and PPy/MWCNT CEs [38]. Reproduced with permission of Elsevier.

synergistic effect of MWCNT and PPy, which led to more advantages like high surface area, good conductivity of the MWCNT, and good catalytic activity of the PPy towards the reduction of triiodide to iodide, providing fast electron transport and diffusion channels and ample availability of interfacial catalytic active sites. Wu *et al.* prepared nitrogen-doped carbon materials by direct pyrolysis of nanostructured Prussian blue analogue (metal hexacyanoferrates) without any other additional carbon sources and metal catalysts [39]. The as prepared N-CNTs were employed as CE for DSSCs. The fabricated DSSC using N-CNTs CE was shown to achieve a power conversion efficiency of 7.48%, which was higher than a platinum CE (7.12%). The enhanced power conversion efficiency of DSSC employing a metal-free NCNT counterelectrode was primarily attributed to the significantly reduced diffusion and charge transfer resistances in the porous NCNT catalyst layer. Thuy *et al.* developed graphene coated alumina-modified polypyrrole (PPy/GCA) composite as CE for DSSCs; the assembled device was reported to exhibit an efficiency of 7.33% and was comparable to that of using a conventional platinum CE (7.57%) [40].

Guo *et al.* synthesized nickel sulfide/conductive carbon composite by a simple hydrothermal process and employed it as CE in DSSCs [41]. This synthesized electrocatalyst illustrated excellent electrocatalytic performances towards the triiodide reduction and exhibited a high power conversion efficiency of 8.15%, which was comparable with that of a platinum CE (8.29%). He *et al.* fabricated porous graphene-doped copper indium disulfide/carbon (p-GN@$CuInS_2$/C) composite nanofibers via electrospinning, *in situ* synthesis, and a carbonization process [42]. A schematic illustration of the formation mechanism for p-GN@$CuInS_2$/C composite nanofibers is shown in Figure 7.5. The fabricated DSSC using the p-GN@$CuInS_2$/C nanofibers as a CE was shown to achieve a power conversion efficiency of 7.23%, which was higher than the efficiencies of DSSCs assembled using the samples without graphene (6.48%), with the $CuInS_2$/C nanofibers (5.45%), and the conventional platinum CE (6.34%). The excellent photovoltaic performance of the p-GN@$CuInS_2$/C CE was attributed to its special hierarchical porous structure, which provided additional active catalytic sites for the reduction of triiodide. The doping of the reduced graphene oxide (RGO) resulted in a well-dispersed growth of $CuInS_2$ nanocrystals in the carbon nanofibers, which, in turn, increased the number of active catalytic sites and promoted active electron and ion transfer. Wu *et al.* fabricated various transition metal ion doped MWCNT-PANI composites as CEs in DSSCs [43]. The nickel and cobalt doped MWCNT-PANI composite showed an excellent electrocatalytic activity towards the triiodide reduction and the fabricated DSSCs achieved a power conversion efficiency of 6.0 and 5.75%, respectively. Bagavathi *et al.* prepared Fe_3O_4–carbon black nanocomposite by a simple solution mixing process and applied as CE in DSSCs [44]. The *J-V* characteristics of the DSSCs fabricated with a Fe_3O_4–carbon black CE was measured at a light intensity of 80 $mWcm^{-2}$. The DSSC assembled with

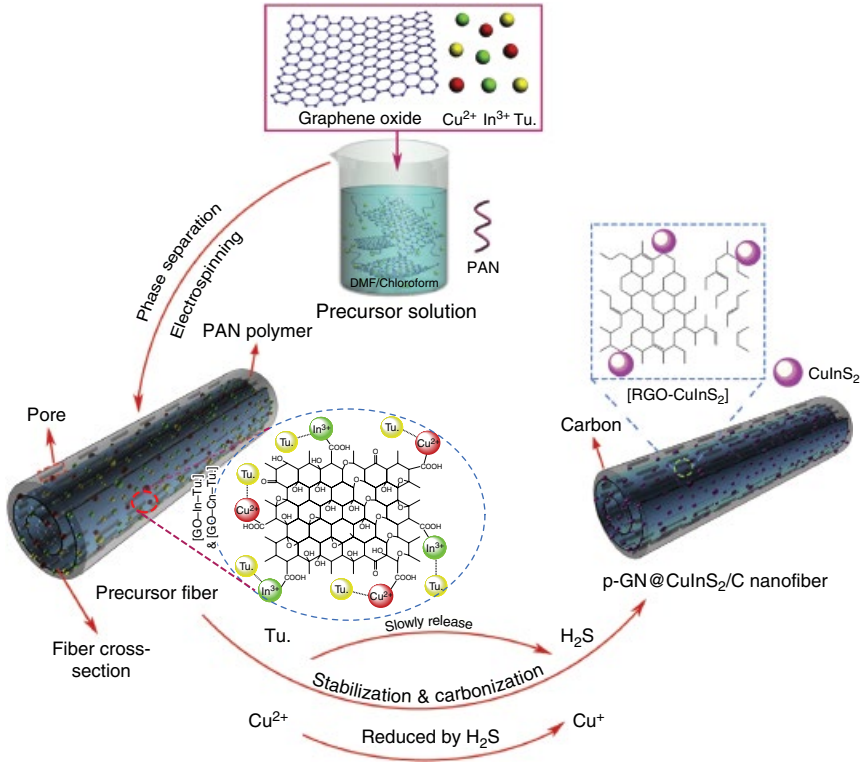

Figure 7.5 Schematic illustration of the formation mechanism for p-GN@$CuInS_2$/C composite nanofibers [42]. Reproduced with permission of Elsevier.

this nanocomposite exhibited an excellent power conversion efficiency of 6.1%, which was superior to that of a conventional platinum CE (4.1%).

Sun *et al.* developed a Sb_2S_3@carbon nanoparticle hybrid electrocatalyst by introducing a mesoporous carbon nanoparticle film (CNP) for *in situ* growth of Sb_2S_3 to construct a Sb_2S_3@CNP hybrid electrocatalyst [45]. A CNP matrix was developed to support Sb_2S_3. The Sb_2S_3@CNP electrocatalyst demonstrated a lower charge transfer resistance at the electrode/electrolyte interface and higher electrocatalytic activity towards the reduction of triiodide. The fabricated DSSC with Sb_2S_3@CNP CE generated a fill factor of 67.6%, which was significantly higher than that of using pristine Sb_2S_3 (52.8%). The power conversion efficiency of the fabricated DSSC with Sb_2S_3@CNP CE was calculated as 6.69%, which was quite comparable with a platinum CE (6.74%). Li *et al.* synthesized cobaltosic sulfide/electrospun carbon nanofibers (Co_3S_4/ECs) by combining the versatility of the electrospinning process following a hydrothermal method [46]. The synthesized Co_3S_4/ECs was used as CE in fabricated

DSSCs that showed a high power conversion efficiency of 9.23%, and was increased by 10.1% compared to the DSSCs based on a platinum CE (8.38%).

Xiao *et al.* synthesized Pt_3Ni alloy supported by carbon nanofiber (CN) composites (Pt_3Ni/CNs) by a simple solvothermal method and employed in DSSCs as CE [47]. The fabricated DSSCs based on Pt_3Ni/CNs CE achieved a power conversion efficiency of 8.34%. Further, to increase the electrocatalytic activity of Pt_3Ni/CNs composites, transition metal chrome (Cr) was doped in Pt_3Ni/CNs to fabricate the composites of Cr-Pt_3Ni/CNs using the same method. The electrocatalytic performances towards triiodide reduction of the fabricated CEs in I^-/I_3^- redox couple is shown in Figure 7.6. The results revealed that Cr-Pt_3Ni/CNs CE exhibited a higher current density and lower peak-to-peak separation (Epp), which confirmed the high catalytic performances of Cr-Pt_3Ni/CNs CE than the other electrodes. Due to the high electrocatalytic activity and rapid charge transfer ability, the power conversion efficiency of the DSSC employing Cr-Pt_3Ni/CNs as CE was increased to 8.76%, which was much higher than that of the platinum CE (7.04%) employed under the same condition. Lu *et al.* prepared reduced graphene oxide (rGO) nanoflakes in a nickel cobalt sulfide (NCS) to form NCS/rGO hybrids and introduced them into DSSCs as CE [48]. It was found that the rGO acted bifunctionally including a cocatalyst in accelerating the triiodide reduction for the main NCS

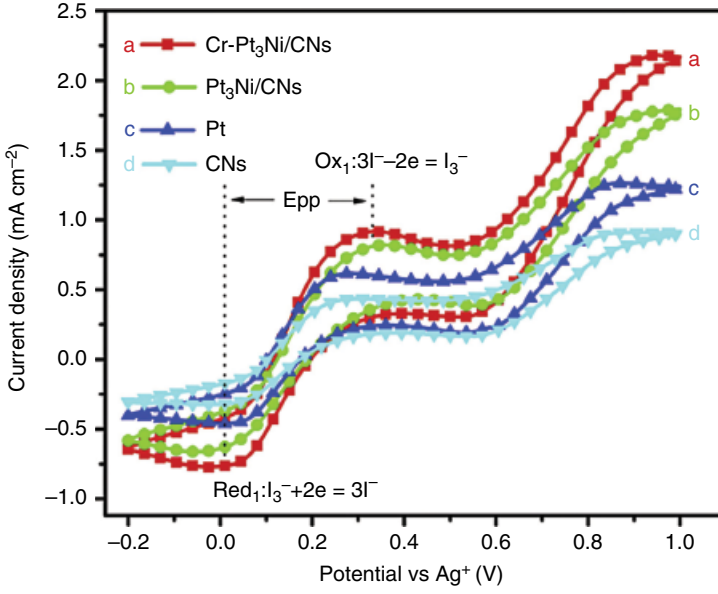

Figure 7.6 CV curves of Cr-Pt_3Ni/CNs, Pt_3Ni/CNs, Pt, and CNs CEs towards the I^-/I_3^- redox couple [47]. Reproduced with permission of Elsevier.

catalysts, conductivity promotor to decrease the series resistance of the CE. Addition of carbonaceous materials into the transition metal sulfide CE of a DSSC is a common method to improve the performance of the CE and consequent photovoltaic performance. Based on this concept, Zhang *et al*. developed 3D nitrogen-doped graphene/reduced hydroxylated carbon nanotube composite aerogel (NG/CNT-OH) with unique hierarchical porosity using a two-step hydrothermal process [49]. NG/CNT-OH exhibited great electrocatalytic performances towards triiodide reduction, high ionic conductivity, and good flexibility, thus generating high-performance flexible CE for DSSCs. This flexible NG/CNT-OH CE showed good stability in the fabricated DSSCs achieving a power conversion efficiency of 6.36%, which was higher than that of using a platinum CE (5.74%). Increasing the ratio of CNT-OH to the GO in the reactant has led to lower content of doped N but better diffusion of electrolyte in the CEs because of more complete GO etching reaction.

Lee *et al*. synthesized graphene-modified vanadium pentoxide nanobelts (GVNBs) using a facile one-step hydrothermal process and used as CE in DSSC applications [50]. The GVNBs were found to show an excellent electrocatalytic activity towards the reduction of triiodide to iodide due to the synergetic effect between the one-dimensional shape of vanadium pentoxide nanobelts and the reduced graphene oxide. The DSSCs based on the GVNBs CEs have reached a high power conversion efficiency of 6.17%, which was comparable to that of the conventional platinum-based CEs (7.98%). Chen *et al*. prepared nitrogen and phosphorus codoped carbon nanosheets by a simply direct pyrolysis method using amino tris(methylene phosphonic acid) as carbon source and introduced them into DSSCs as CE [51]. As a consequence, the DSSC based on NPC-800 (NPC carbonized at 800 °C) CE achieved a power conversion efficiency of 6.74%, which was higher than that of the cell with a platinum CE (5.76%). The exhibited higher power conversion efficiency of DSSC with NPC-800, might be due to rapid electrolyte diffusion. Yu *et al*. synthesized 3D N/S codoped graphene (NS-GN) networks through a simple one-step hydrothermal route and used them as CE for the reduction of triiodide into iodide in the DSSCs [52]. The schematic representation of the synthesis of the NS-GN is shown in the Figure 7.7. The nitrogen and sulfur codoping strategy significantly enhances the electrocatalytic activity towards triiodide reduction. The fabricated DSSC with N/S codoped graphene CE was found to exhibit an efficiency of 9.40%. This superior electrochemical performance can be attributed to the synergistic effect of sulfur and nitrogen atoms in graphene, the conductive 3D graphene networks with a large surface area, and an interconnected porous structure. Chiu *et al*. synthesized $CoSe_2$/carbon composite film as CE for DSSCs using a two-step process via pulse-potential electrodeposition followed by an annealing process [53]. The assembled DSSC with this $CoSe_2$/C composite CE achieved a high power conversion efficiency of 8.92%, which was found to be higher than that of using a conventional platinum CE (8.25%).

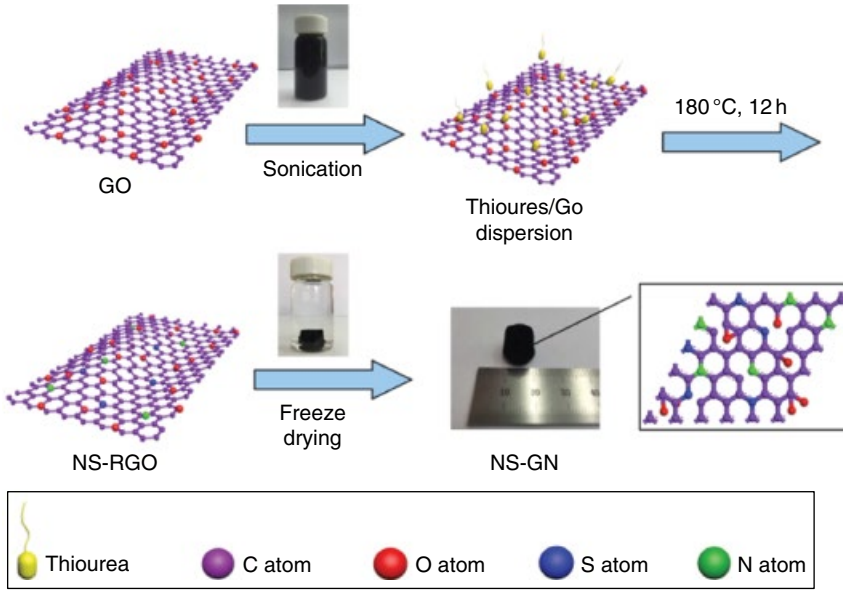

Figure 7.7 The schematic representation of the synthesis of the NS-GN [52]. Reproduced with permission of Elsevier.

Zhou *et al.* developed a hierarchical graphene-beaded carbon nanofiber with incorporated nickel nanoparticles (G/CNFs–Ni) as used as a low-cost CE for DSSCs [54]. The introduction of graphene nanosheets and nickel nanoparticles in CNF networks was found to significantly increase the cell stability and decrease the charge-transfer resistance at the interface between CE/electrolyte, which led to high electrocatalytic performances towards triiodide reduction. The fabricated DSSC using G/CNFs–Ni CE was reported to exhibit a high power conversion efficiency of 7.14%, which was quite comparable to that of a platinum CE (7.59%).

Zhu *et al.* fabricated N-doped carbon microspheres using a microwave-assisted method followed by thermal treatment under an ammonia atmosphere and used them as CEs for DSSCs [55]. The assembled DSSC with N–C microspheres exhibited a maximum power conversion efficiency of 6.28%, which was higher than that of pristine carbon microspheres CE (5.52%) and comparable to that the DSSC assembled with a conventional platinumCE (6.95%). Leu *et al.* fabricated boron-doped MWCNT (BCNT) film as a low-cost platinum-free CE for DSSCs and employed it towards the reduction of triiodide to iodide ions [56]. The fabricated DSSC based on a BCNT CE has showed an excellent energy conversion efficiency of 7.91%, which was higher than that of the DSSC assembled with pristine MWCNT CE (6.02%) and was quite close to that of a platinum CE (8.03%). Chen *et al.* synthesized Co-imbedded ordered

mesoporous carbon (Co-OMC) materials by a facile low-temperature hydrothermal process of phenolic resin-F127 composites with various amounts of cobalt nitrate, and followed it by carbonization [57]. The Co-OMCs are used as CEs in DSSCs towards the electrocatalytic reduction of triiodide. The enhanced electrocatalytic activity and electrical conductivity was exhibited due to the synergistic effect between OMC and the appropriate amount of cobalt nanoparticles. The DSSCs based on Co-OMC CEs exhibited a power conversion efficiency of 7.02%, which was higher than that of the pristine OMC CE (6.18%), and comparable to that of the conventional platinum CE (7.10%).

Mahalingam *et al.* fabricated Pt/rGO using a chemical bath deposition method and employed it as a CE for In_2O_3-based DSSC [58]. The fabricated DSSC with Pt/rGO CE exhibited a good photovoltaic performance with high photocurrent density of 8.1 mA cm^{-2} and power conversion efficiency of 1.68%. Sigdel *et al.* prepared an electrospun carbon nanofiber (ECN)/TiO_2 composite CE for DSSCs by spray-coating an ECN/TiO_2 (1:1 by weight) mixture on a FTO glass substrate [59]. DSSCs fabricated with ECN/TiO_2 CEs were found to show a power conversion efficiency of 7.25%, which was comparable to that of DSSC based on a thermally deposited platinum CE (7.57%). Xu *et al.* synthesized a nitrogen-doped carbon and Fe_3C CE for DSSCs using a simple carbothermal reduction of iron(II) oxalate (FeC_2O_4) nanowires in the presence of cyanamide (NH_2CN) at 600 °C [60]. The fabricated DSSC using an Fe_3C@N-C CE showed an energy conversion efficiency of 7.36%, which was found to be higher than that of the DSSC with a platinum CE (7.15%). This increase in electrocatalytic activity was attributed to the synergistic effect of N–C and Fe_3C along with the one-dimensional configuration, which endowed the nanocomposites with more interfacial active sites and improved electron transfer efficiency for the triiodide reduction.

Choi *et al.* prepared graphene-based multiwalled carbon nanotubes (GMWNTs) and employed them as CE instead of a platinum to fabricate DSSCs [61]. The detailed schematic illustration for the fabrication of a DSSC based on GMWNTs is presented in the Figure 7.8. The fabricated DSSC was found to show a power conversion efficiency of 3.0%. Ahmad *et al.* prepared different kind of CEs by dispersing the various combinations of MWCNTs and GNPs into PEDOT:PSS aqueous solution for DSSCs applications [62]. They have observed that the addition of GNPs into a MWCNTs composite resulted in an increase in the electrical conductivity and a reduction in the R_{ct} value of the CE in DSSCs. Among various combinations, the 44 wt-% of WCNTs and 22 wt-% of GNPs mixed PEDOT:PSS film CE based DSSC has exhibited the best power conversion efficiency of 4.10%, which was higher than that of a standard platinum-based CE based (3.90%). Kumar *et al.* achieved carbide synthesis by carbonization at high temperature in flowing argon [63]. The synthesized carbon material had a surface area of 5 m^2/g with the particle size of 816 nm. Furthermore, they have also reported on the graphitic nature of these carbon

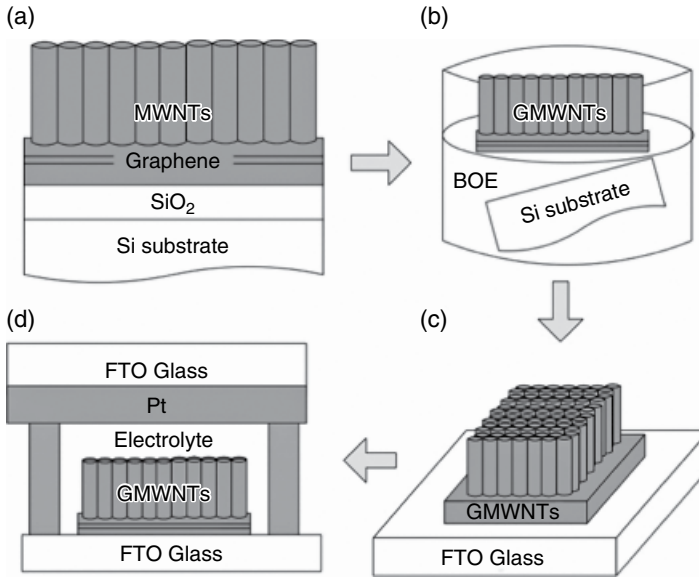

Figure 7.8 Schematic illustration of device process: (a) synthesis of GMWNTs on SiO_2/Si, (b) lift-off process of GMNTs, (c) transplant to FTO glass, and (d) half cell without TiO_2 and dye. [61]. Reproduced with permission of Elsevier.

material exhibiting good electrocatalytic property with a power conversion efficiency of 6.72%, which was comparable with the conventional platinum CE (8.19%) under the same experimental conditions. Yue *et al*. synthesized a highly porous MoS_2–C hybrid film via an *in situ* hydrothermal route [64]. This synthesized MoS_2-C hybrid film was used as a low-cost CE in DSSCs. The DSSC fabricated with this novel MoS_2-C CE showed a high power conversion efficiency of 7.69%, which was higher than that of a platinum CE (6.74%). This may be due to its low charge transfer resistance on the electrolyte/electrode interface, high electrocatalytic activity, and fast reaction kinetics towards the reduction of triiodide to iodide.

Wang *et al*. synthesized 3D honeycomb-like structured graphene sheets (HSG) by reaction between Li_2O and CO; these were used as a CE instead of platinum to fabricate DSSCs [65]. This HSG CE based DSSC was found to exhibit a power conversion efficiency of 7.8%, which was quite comparable to that of DSSCs with an expensive platinum CE. Gong *et al*. prepared activated graphene nanoplatelets (aGNPs) by a hydrothermal method using KOH as activating agent [66]. Further, this aGNPs was used as a CE to fabricate DSSCs. The fabricated DSSC was shown to achieve a power conversion efficiency of 7.7%, which was comparable with the conventional platinum CE based DSSC (8.0%). This may be to its excellent electrocatalytic activity for triiodide

reduction at the interface between the electrolytes and the CE. Kim *et al*. fabricated DSSCs using three different carbon-based CEs such as graphene, SWNTs, and graphene-SWNT composites via an electrophoretic deposition method [67]. The results of the DSSC assembled with the graphene-deposited CE showed a highest power conversion efficiency of 5.87% under AM 1.5 and 1 sun conditions. Hence, it was reported and used for a low cost, high-throughput process for DSSCs. This work clearly states that the graphene is a most suitable CE material for DSSC applications. In a similar study, Barberio *et al*. fabricated the DSSCs with four different carbon-based CEs like graphene, multiwalled carbon nanotubes, and nanocomposites of MWCNTS and metal nanoparticles [68]. They have also compared the photovoltaic performance of these CEs with those of classical electrodes (amorphous carbon and platinum). Among these four different CEs, the graphene and Ag/CNT electrode based DSSCs were found to show the best power conversion efficiency of 5.4 and 5.9%, respectively. The efficiency values obtained were reported to be 50% higher than that of a graphite CE and 25% higher than that of a platinum CE.

In another study, Erten-Ela *et al*. prepared poly(3,4-ethylenedioxythiophene) (PEDOT), polyaniline (PANI), and polythiophene (PTh) based MWCNT composites by a RF-rotating plasma grafting method [69]. The prepared MWCNT composites were used as CE materials instead of platinum in DSSCs. Among these composites, PANI/MWCNT composites were reported to have higher electrocatalytic activity than others. Furthermore, a power conversion efficiency value of 2.07% was also reported in the study. Guo *et al*. synthesized a $CoCr_2O_4$/carbon nanotubes ($CoCr_2O_4$/CNTs) nanocomposite via a facile solution route and used it as the CE in DSSCs [70]. The DSSC fabricated with this $CoCr_2O_4$/CNTs nanocomposite-based CE was found to exhibit a power conversion efficiency of 8.40%, which was almost close to platinum-based DSSCs (8.68%). The observed results have proved that the $CoCr_2O_4$/CNTs composites can be used as an efficient electrocatalytic material for DSSC applications. A research team of Joshi *et al*. developed a low cost carbon/TiO_2 composite and used it as a CE in DSSCs [71]. The surface morphology of the fabricated carbon/TiO_2 composite on FTO glass substrate is shown in the Figure 7.9. The DSSC fabricated with this nanoscale carbon/TiO_2 composite CE has been shown to achieve a power conversion efficiency of 5.5%, which is comparable to that of a platinum CE based DSSC (6.4%) under similar conditions. Hence, the carbon/TiO_2 composite was reported as a good low cost alternative CE material for the platinum electrode in DSSCs. In an another study, Kouhnavard *et al*. prepared a new type of CE by mixing of hydrophilic carbon (HC) particles and TiO_2 colloid (HC/TiO_2) deposited on a fluorine-doped tin oxide substrate using a doctor blade technique [72]. The DSSC fabricated with a HC/TiO_2 CE showed a power conversion efficiency of 1.9%; this compares to a platinum electrode (3.6%) under same experimental conditions. This may be due to the high surface

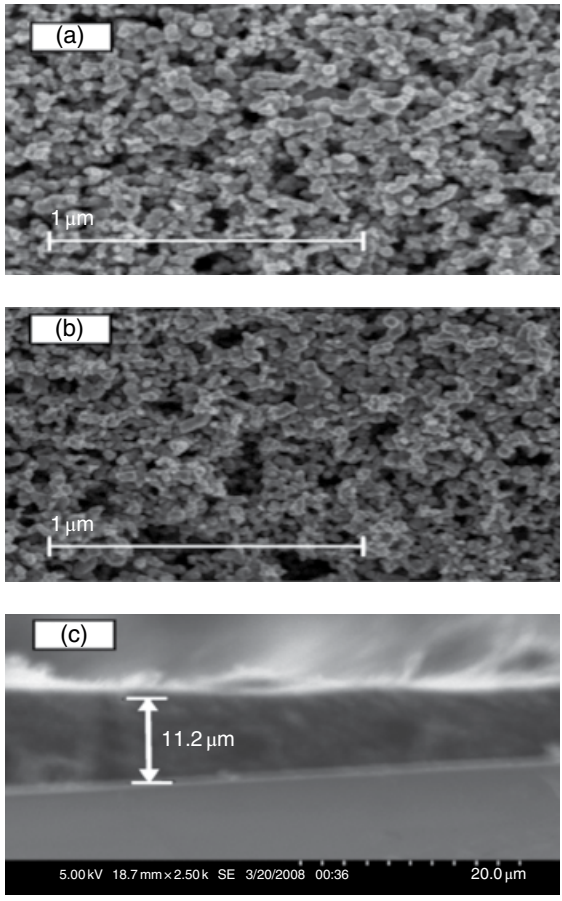

Figure 7.9 Top view SEM images of (a) a 11.2 μm thick carbon/TiO_2 composite layer and (b) a pure TiO_2 nanoparticle layer on a FTO substrate. (c) Cross-section SEM image of a carbon/TiO2 composite layer [71]. Reproduced with permission of the Royal Society of Chemistry.

roughness of the HC/TiO_2 that has increased the electrocatalytic activity facilitating the diffusion of triiodide ions.

Leu *et al*. synthesized a boron-doped multiwalled carbon nanotube (BCNT) using a simple two-step post-growth substitution reaction route under atmospheric pressure [73]. The synthesized BCNT was found to exhibit a good electrical conductivity and catalytic ability on comparison with pure CNT. The DSSC assembled with a BCNT CE has also showen a higher power conversion efficiency (7.91%) than that of pure a CNT CE (6.02%) and was quite close to that of a platinum CE (8.03%). In another report, Li *et al*. fabricated a DSSC

using mesoporous carbon (MC)-imbedded tungsten carbide (W_2C) composite used as a flexible CE and an iodide electrolyte [74]. It showed a power conversion efficiency of 7.61%. In addition, the W_2C/MC composite was found to be a suitable CE for an organic sulfide redox couple electrolyte based DSSC and exhibited a higher power conversion efficiency (5.96%) than that of pure W_2C (5.08%) and MC (4.38%). Another research team, Murakami *et al*. fabricated a DSSC using carbon black as a CE for triiodide reduction [75]. This fabricated DSSC showed an enhanced power conversion efficiency of 9.1%. In a similar study, Du *et al*. synthesized two-dimensional porous Co_3O_4 nanoflakes anchored on reduced graphene oxide nanosheets by a hydrothermal reduction process and used them as CE in DSSCs [76]. They observed an enhanced photovoltaic performance in DSSCs after the addition of RGO into the 2D porous Co_3O_4 nanoflakes. The DSSCs assembled with a Co_3O_4@RGO CE showed a power conversion efficiency of 5.79%, which was much higher than that of a pure Co_3O_4 CE (1.2%) and a pure RGO CE (2.2%). Apart from that, the observed efficiency value was quite comparable with the conventional platinum CE (6.16%). Additionally, the Co_3O_4@RGO nanohybrids also exhibited a good electrochemical stability.

Pan *et al*. assembled the DSSCs using CNT fiber, core-sheath CNT/reduced graphene oxide nanoribbon (RGONR), CNT/RGO composite fiber, and RGO fiber based CE for DSSC applications [77]. They have also compared the photovoltaic performances of the fabricated DSSCs using two different electrolytes of I^-/I_3^- and T^-/T_2^-. Among these different CEs, core-sheath CNT/RGONR fiber CE has achieved the highest power conversion efficiency of 5.64% in the I^-/I_3^- electrolyte, whereas the bare CNT fiber CE showed the highest power efficiency of 4.78% in the T^-/T_2^- electrolyte. Roy-Mayhew *et al*. fabricated a DSSC with functionalized graphene sheets (FGS) as CE and achieved a power conversion efficiency of 4.99%, which was comparable to that of a platinum CE (5.48 %) [78]. The FGS CE was found to exhibit low R_{CT} value of 0.64 Ωcm^2 when compared with the platinum CE (0.79 Ωcm^2). This lower charge-transfer resistance was reported to be useful in achieving the best photovoltaic performance of DSSCs. In a similar study, Yang *et al*. synthesized the Pt–MWCNT composite and used it as a CE material to fabricate highly efficient DSSCs [79]. These fabricated DSSCs have shown a power conversion efficiency of 8.62%, which was much higher than that of a conventional platinum CE (7.56%). This increased trend was the significant due to increase in the cell fill factor from 0.57 to 0.65 after addition of MWCNT to the platinum. Hence, the Pt–MWCNT composite was established as a useful CE material to enhance the photovoltaic performance of the DSSCs.

Joshi *et al*. assembled a DSSC using a nickel incorporated carbon nanotube/nanofiber composite (Ni-CNT-CNF) as a low cost platinum-free CE to reduced the cost of the DSSC [80]. The DSSC based on the Ni-CNT-CNF composite CE showed a power conversion efficiency of 7.96%, which was comparable

with the platinum CE (8.32%). Wu *et al*. introduce nine kinds of carbon material, such as well-ordered mesoporous carbon (Com), activated carbon (Ca), carbon black (Cb), conductive carbon (Cc), carbon dye (Cd), carbon fiber (Cf), carbon nanotube (Cn), discarded toner of a printer (Cp), and fullerene (C60), as CE materials towards triiodide reduction in the DSSCs system [81]. The SEM images of all the nine kinds of carbon materials are shown in the Figure 7.10. They have compared the electrochemical catalytic activity of these carbon materials with a standard platinum CE in their study. All these carbon materials were found to possess electrochemical catalytic activity for triiodide reduction. However, Com was found to exhibit an outstanding electrochemical catalytic activity when compared with other CEs and the platinum CE. Also, the Cd and Com CE based DSSCs recorded the highest power conversion efficiency of 7.5%, which was equal to a platinum CE based DSSC (7.5%). Therefore, the results obtained supported that the carbon materials will, hopefully, be the substitutes for the expensive platinum for DSSC applications.

The large scale commercial applications of DSSCs will require a lot of platinum, which is highly expensive and, moreover, not abundantly available. In this regard, carbon materials could be seen as a promising option to replace platinum CEs in DSSCs. However, the fundamental disadvantage of pristine

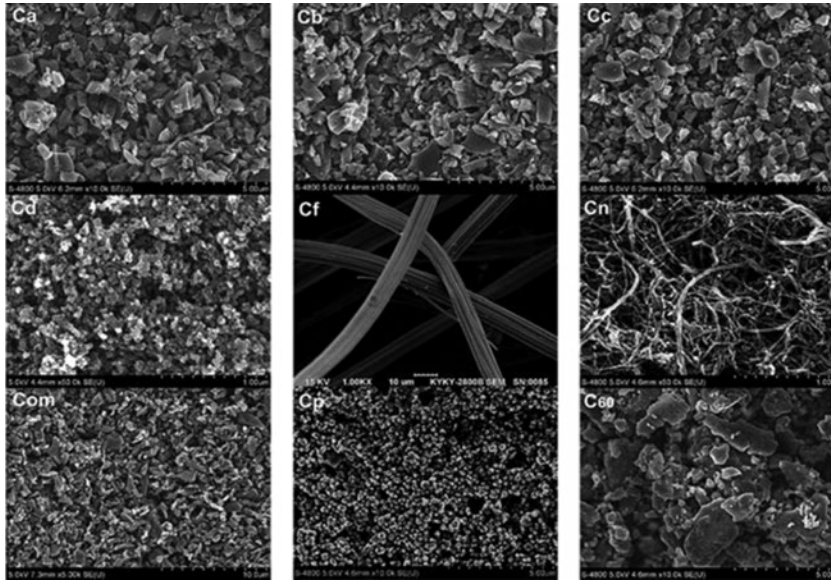

Figure 7.10 SEM morphological images of various carbon materials such as Ca – activated carbon, Cb – carbon black, Cc – conductive carbon, Cd – carbon dye, Cf – carbon fiber, Cn – carbon nanotube, Com – mesoporous carbon, Cp – discarded toner of a printer, C60 – fullerene [81] Reproduced with permission of the Royal Society of Chemistry.

Table 7.1 Photovoltaic characteristics of DSSCs using different carbon-based nanostructured CEs.

Sample	V_{oc} (V)	J_{sc} (mA cm^{-2})	FF	H (%)	References
SWCNH	0.68	14.48	0.42	4.09	[36]
g-C_3N_4/MWCNT	0.72	14.200	0.62	6.34	[37]
PPy/MWCNT	0.74	17.56	0.55	7.15	[38]
NCNT	0.72	14.35	0.71	7.48	[39]
PPy/GCA	0.71	16.54	0.61	7.33	[40]
NiS/Cc	0.76	18.18	0.59	8.15	[41]
P-GN@$CuInS_2$/C	0.69	17.53	0.59	7.23	[42]
MWCNT-PANI-Ni^{2+}	0.70	14.25	0.60	6.0	[43]
MWCNT-PANI-Co^{2+}	0.69	13.75	0.60	5.75	[43]
Fe_2O_3/CB	0.66	14.00	0.51	6.10	[44]
Sb_3S_3@CNP	0.68	14.6	0.67	6.69	[45]
Co_3S_4/ECs	0.77	16.57	0.72	9.23	[46]
Pt_3Ni/CNS	0.76	15.19	0.71	8.34	[47]
Cr-Pt_3Ni/CNS	0.77	15.80	0.72	8.76	[47]
Graphene-V_2O_5-nanobelts	0.79	14.20	0.55	6.17	[50]
N/P-carbon nanosheet	0.74	14.50	0.63	6.74	[51]
N/S-graphene	0.74	16.86	0.74	9.40	[52]
$CoSe_2$/C	0.73	18.03	0.67	8.92	[53]
G/CNFs-Ni	0.84	14.31	0.6	7.14	[54]
N-C microsphere	0.71	14.40	0.60	6.28	[55]
B-MWCNT	0.72	17.30	0.63	7.91	[56]
Co-OMC	0.70	17.98	0.55	7.02	[57]
ECN/TiO_2	0.84	13.69	0.63	7.25	[59]
Fe_3C@N-C	0.74	14.97	0.66	7.36	[60]
GMWNT	0.76	5.60	0.70	3.0	[61]
WCNT-GNP/PEDOT:PSS	0.70	11.35	0.51	4.10	[62]
MoS_2–C hybrid	0.75	15.07	0.68	7.69	[64]
HSG	0.77	27.2	0.371	7.80	[65]
aGNPs	0.73	22.54	0.47	7.7	[66]
Graphene	0.7	13.10	0.636	5.87	[67]
Ag/CNT	0.58	26.24	0.382	5.9	[68]

(*Continued*)

Table 7.1 (Continued)

Sample	V_{oc} (V)	J_{sc} (mA cm^{-2})	FF	H (%)	References
PANI/MWCNT	0.55	11.19	0.33	2.07	[69]
$CoCr_2O_4$/CNTs	0.75	18.98	0.59	8.40	[70]
Carbon/TiO_2	0.70	12.53	0.57	5.5	[71]
HC/TiO_2	0.71	4.00	0.622	1.9	[72]
BCNT	0.72	17.3	0.63	7.91	[73]
W_2C/MC	0.62	14.19	0.671	5.96	[74]
Carbon black	0.79	16.8	0.685	9.1	[75]
Co_3O_4@RGO	0.79	11.91	0.615	5.79	[76]
CNT/RGONR fiber	0.713	11.30	0.70	5.64	[77]
Pt–MWCNT	0.750	17.7	0.65	8.62	[79]
Ni-CNT-CNF	0.80	15.83	0.63	7.96	[80]

carbon nanostructures based CEs is that these materials require a large dosage to accomplish focused synergistic action. A poor association between the carbon film and the substrate largely limits the long-term utilization of carbon-based nanostructures as CEs. In order to overcome these drawbacks, composites of carbon-based nanostructures are advisable, as highlighted in this chapter. The carbon composites are made of combining two or more materials that could be used as an efficient CE for DSSCs. These carbon-based composite materials were found to show excellent performances compared to the conventional platinum CE, as reported in various studies discussed so far. The photovoltaic characteristics of DSSCs using various carbon-based nanostructured CEs are shown in Table 7.1.

7.4 Conclusions

DSSCs have gained recent research attention because of their capacity to convert sunlight into electricity at a low cost. Platinum is a common CE used in most of the DSSC studies, despite issues of costliness and low abundancy restricting it to large scale application. This chapter has exclusively discussed the use of alternatives to the expensive platinum-based CE in DSSCs. Also highlighted have been the applications of various composites of carbon-based nanostructures, such as graphene, carbon nanotubes, carbon nanofibers, activated carbon, graphite, and carbon black, for use as platinum-free CEs towards enhanced power conversion efficiency and to meet the cost effectiveness options

of the device. While designing a new electrocatalytic material a researcher should always remember in choosing materials low cost, eco-friendliness and that it should cover a wide range of applications,. Further, a detailed investigation should be undertaken to develop novel CEs for DSSCs, as many new concepts and design strategies are required in this field.

References

1 J. Theerthagiri, R.A. Senthil, P. Arunachalam, *et al*., *Solid State Electrochem.*, **21** (2017), 581–590.
2 J. Theerthagiri, R.A. Senthil, M.H. Buraidah, *et al*., *J. Mater. Chem. A*, **4** (2016), 16119–16127.
3 N.A. Ludin, A.M.Al-A. Mahmoud, A.B. Mohamad, *et al*., *Renew. Sust. Energ. Rev.*, **31** (2014), 386–396.
4 J. Theerthagiri, R.A. Senthil, M.H. Buraidah, *et al*., *J. Mater. Sci. Technol.*, **32** (2016), 1339–1344.
5 C.P. Lee, R.Y.Y. Lin, J. Theerthagiri, *et al*., *RSC Adv.*, **5** (2015), 23810–23825.
6 E. Bequerel, *C.R. Acad. Sci.*, **9** (1839), 145–149.
7 R. Williams, *J. Chem. Phys.*, **32** (1960), 1505–1514.
8 M. Planck, *Ann. Phys.*, **4** (1901), 553 (1–6).
9 M. Gratzel, *J. Photochem. Photobiol. C: Photochem. Rev.*, **4** (2003), 145–153.
10 J. Theerthagiri, R.A. Senthil, M.H. Buraidah, *et al*., *J. Solid State Chem.*, **238** (2016), 113–120.
11 J. Theerthagiri, R.A. Senthil, M.H. Buraidah, *et al*., *Mater. Today Proceeding*, **3** (2016), S65–S72.
12 J. Theerthagiri, R.A. Senthil, M.H. Buraidah, *et al*., *Mater. Focus*, **5** (2016), 355–361.
13 J. Theerthagiri, R.A. Senthil, M.H. Buraidah, *et al*., *Ionics*, **21** (2015), 2889–2896.
14 O'Regan, M. Gratzel, *Nature*, **353** (1991), 737–740.
15 J. Theerthagiri, R.A. Senthil, P. Arunachalam, *et al*., *J. Solid State Electrochem.*, **21** (2017), 581–590.
16 J.B. Baxter, *J. Vac. Sci. Technol. A*, **30** (2012), 020801–020819.
17 A. Hagfeldt, G. Boschloo, L. Sun, *et al*., *Chem. Rev.*, **110** (2010), 6595–6663.
18 H. Lin¸ W.L. Wang, Y.Z. Liu, *et al*., *Front. Mater. Sci. China*, **3** (2009), 345–352.
19 J.A. Mikroyannidis, P. Suresh, M.S. Roy, G.D. Sharma, *Electrochim. Acta*, **56** (2011), 5616–5623.
20 T. Ono, T. Yamaguchi, H. Arakawa, *Sol. Energy Mater. Sol. Cells*, **93** (2009), 831–835.
21 R.A. Senthil, J. Theerthagiri, M.A. Madhavan, *J. Non-Cryst. Solids*, **406** (2014), 133–138.
22 J. Theerthagiri, R.A. Senthil, M.H. Buraidah, *et al*., *J. Appl. Polym. Sci.*, **132** (2015), 42489.

23 R.A. Senthil, J. Theerthagiri, J. Madhavan, A.K. Arof, *Ionics*, **22** (2016), 425–433.
24 S. Thomas, T.G. Deepak, G.S. Anjusree, *et al*., *J. Mater. Chem. A*, **2** (2014), 4474–4490.
25 Theerthagiri J, Senthil RA, Madhavan J, Maiyalagan T, *ChemElectroChem*, **2** (2015), 928–945.
26 G. Smestad, C. Bignozzi, R. Argazzi, *Sol. Energy Mater. Sol. Cells*, **32** (1994), 259–272.
27 R.D. Costa, F. Lodermeyer, R. Casillas, D.M. Guldi, *Energy Environ. Sci.*, **7** (2014), 1281–1296.
28 L. Wang, H. Liu, R.M. Konic, *et al*., *Chem. Soc. Rev.*, **42** (2013), 8134–8156.
29 H.G. Shiraza, F.R. Astaraie, *J. Mater. Chem. A*, **3** (2015), 20849–20862.
30 M. Janani, P. Srikrishnarka, S.V. Nair, A.S. Nair, *J. Mater. Chem. A*, **3** (2015), 17914–17938.
31 A. Kay, M. Gratzel, *Sol. Energy Mater. Sol. Cells*, **44** (1996) 99–117.
32 T.N. Murakami, S. Ito, Q. Wang, *et al. J. Electrochem. Soc.*, **153** (2006), A2255–A2261.
33 C.S. Wu, T.W. Chang, H. Teng, Y.L. Lee, *Energy*, **115** (2016), 513–518.
34 Y. Zhu, C. Gao, Q. Han, *et al*., *J. Catal.*, **346** (2017), 62–69.
35 G. Nagaraju, J.H. Lim, S.M. Cha, J.S. Yu, J. Alloys *Compd*, **693** (2017), 1297–1304.
36 K. Susmitha, M. Mamata Kumari, A. Joseph Berkmans, *et al*. *Solar Energy*, **133** (2016), 524–532.
37 G. Wang, S. Kuang, J. Zhang, *et al*., *Electrochim. Acta*, **187** (2016), 243–248.
38 W. Hou, Y. Xiao, G. Han, H. Zhou, *Electrochim. Acta*, **190** (2016), 720–728.
39 M.S. Wu, Z.Z. Ceng, *Electrochim. Acta*, **191** (2016), 895–901.
40 C.T.T. Thuy, J.H. Jung, S. Thogiti, *et al*. *Electrochim. Acta*, **205** (2016), 170–177.
41 M. Guo, F. Zhao, Y. Yao, *et al*., *Electrochim. Acta*, **205** (2016), 15–19.
42 J. He, M. Zhou, L. Wang, *et al*., *Electrochim. Acta*, **215** (2016), 626–636.
43 K. Wu, L. Chen, C. Duan, *et al*., *Mater. Des.*, **104** (2016), 298–302.
44 M. Bagavathi, A. Ramar, R. Saraswathi, *Ceram. Int.*, **42** (2016), 13190–13198.
45 P. Sun, M. Zhang, C. Ai, *et al*., *J. Power Sources*, **319** (2016), 219–226.
46 L. Li, J. Xiao, H. Sui, *et al*., *J. Power Sources*, **326** (2016), 6–13.
47 J. Xiao, M. Cui, M. Wang, *et al*., *J. Power Sources*, **328** (2016), 543–550.
48 M.N. Lu, J.Y. Lin, T.C. Wei, *J. Power Sources*, **332** (2016), 281–289.
49 J. Zhang, M. Yu, S. Li, *et al*., *J. Power Sources*, **334** (2016), 44–51.
50 M. Lee, S.K. Balasingam, Y. Ko, *et al*., *Synth. Met.*, **215** (2016), 110–115.
51 M. Chen, L.L. Shao, Y.X. Guo, X.Q. Cao, *Chem. Eng. J.*, **304** (2016), 303–312.
52 Z. Yu, Y. Bai, Y. Wang, *et al*., *Chem. Eng. J.*, **311** (2017), 302–309.
53 I.T. Chiu, C.T. Li, C.P. Lee, *et al*., *Nano Energy*, **22** (2016), 594–606.
54 Z. Zhou, S. Sigdel, J. Gong, B. *et al*., *Nano Energy*, **22** (2016), 558–563.
55 G. Zhu, H. Wang, H. Xu, *et al*., *RSC Adv.*, **6** (2016), 58064–58068.
56 Y.A. Leu, M.H. Yeh, L.Y. Lin, *et al*., *ACS Sustainable Chem. Eng.*, **5** (2017), 537–546.
57 M. Chen, L.L. Shao, X. Qian, *et al*., *J. Mater. Chem. C*, **2** (2014), 10312–10321.

58 S. Mahalingam, H. Abdullah, S. Shaari, A. Muchtar, *Ionics*. doi 10.1007/s11581-016-1759-1.
59 S. Sigdel, A. Dubey, H. Elbohy, *et al*., *J. Mater. Chem. A*, **2** (2014), 11448–11453.
60 H. Xu, C. Zhang, Z. Wang, *et al*., *J. Mater. Chem. A*, **2** (2014), 4676–4681.
61 H. Choi, H. Kim, S. Hwang, *et al*., *Solar Energ. Mater. Solar Cells*, **95** (2011), 323–25.
62 Ahmad, J.E. McCarthy, M. Bari, Y.K. Gunko, *Solar Energy*, **102** (2014), 152–161.
63 R. Kumar, S.S. Nemala, S. Mallick, P. Bhargava, *Solar Energy*, **144** (2017), 215–220.
64 G. Yue, J. Wu, Y. Xiao, *et al*., *J. Mater. Chem. A*, **1** (2013), 1495–1501.
65 H. Wang, K. Sun, F. Tao, *et al*., *Angew. Chem,*. **125** (2013), 9380–9384.
66 J. Gong, Z. Zhou, K. Sumathy, *et al*., *J. Appl. Phys.*, **119** (2016), 135501.
67 H. Kim, H. Choi, S. Hwang, *et al*., *Nanoscale Res. Lett.*, **7** (2012), 53.
68 M. Barberio, A. Imbrogno, D. RGrosso, *et al*., *Mater. Res. Express*, **2** (2015), 075502.
69 S. Erten-Ela, S. Cogal, G.C. Cogal, A.U. Oksuz, *Fullerenes, Nanotubes, Carbon Nanostruct,*, **24** (2016), 380–384.
70 M. Guo, B. Tang, H. Zhang, *et al*., *Chem. Commun.*, **50** (2014), 7356–7358.
71 P. Joshi, Y. Xie, M. Ropp, *et al*., *Energy Environ. Sci.*, **2** (2009), 426–429.
72 M. Kouhnavard, N.A. Ludin, B.V. Ghaffari, *et al*., *J. Appl. Electrochem.*, **46** (2016), 259–266.
73 Y.A. Leu, M.H. Yeh, L.Y. Lin, *et al*., *ACS Sustainable Chem. Eng.*, **5** (2017), 537–546.
74 L. Li, H. Sui, W. Zhang, *et al*., *J. Mater. Chem. C*, **4** (2016), 6778–6783.
75 T.N. Murakami, S. Ito, Q. Wang, *et al*., *J. Electrochem. Soc.*, **153** (2006), A2255–A2261.
76 F. Du, X. Zuo, Q. Yang, *et al*., *J. Mater. Chem. C*, **4** (2016), 10323–10328.
77 S. Pan, Z. Yang, P. Chen, *et al*., *J. Phys. Chem. C*, **118** (2014), 16419–16425.
78 J.D. Roy-Mayhew, D.J. Bozym, C. Punckt, I.A. Aksay, *ACS Nano*, **4** (2010), 6203–6211.
79 X.H. Yang, J.W. Guo, S.Y.Y. Hou, *et al*., *J. Mater. Chem. A*, **2** (2014) 614–619.
80 P. Joshi, Z. Zhou, P. Poudel, *et al*., *Nanoscale*, **4** (2012), 5659–5664.
81 M. Wu, X. Lin, T. Wang, *et al*., *Energy Environ. Sci.*, **4** (2011), 2308–2315.

8

Highly Stable Inverted Organic Solar Cells Based on Novel Interfacial Layers

Fang Jeng Lim[1] *and Ananthanarayanan Krishnamoorthy*[2]

[1] *Solar Energy Research Institute of Singapore (SERIS), National University of Singapore, Singapore*
[2] *SRM Research Institute and Department of Chemistry, SRM University, India*

8.1 Introduction

Organic solar cells (OSC) based on solution-processed semiconducting polymers have been a hot topic of research since the 1980s [1, 2]. The evolution of the OSC devices started from single organic layer [1, 3], bilayer planar heterojunction [4] to bulk heterojunction (BHJ) [5, 6] designs. BHJ structure has been widely adopted to produce more efficient devices with a record efficiency of 10.8% using thieno[3,4-b]thiophene/benzodithiophene (PTB7), [6, 6]-phenyl C_{71} butyric acid methyl ester ($PC_{71}BM$), and an IR-absorbing diketopyrrolopyrrole based porphyrin small molecule (DPPEZnP-TEH) [7].

Organic solar cells present several advantages over conventional inorganic counterparts: lightweight, flexibility, semi-transparent, easy color-tuning, positive temperature coefficient, low energy intensive fabrication protocols, and sensitivity to low-light condition [8]. As a result, they can be used in several niche applications where it is not possible to use conventional silicon solar cells. For instance, their flexible, lightweight, and semi-transparent nature enables them to be integrated easily onto a variety of surfaces, such as fabrics, mobile electronics, and windows in buildings. Apart from that, organic semiconductors, which have variety of colors, are also suitable for aesthetically significant applications like building-integrated photovoltaics (BIPV). Furthermore, due to the nature of charge hopping transport in organic semiconductors, it has a positive temperature coefficient, i.e. device efficiency increases as the surrounding temperature gets higher. Most importantly, they also have a superior performance in low-light (diffused-light) conditions [9, 10], which makes them suitable for indoor power generation. Therefore, without

Rational Design of Solar Cells for Efficient Solar Energy Conversion, First Edition.
Edited by Alagarsamy Pandikumar and Ramasamy Ramaraj.

directly competing with conventional silicon solar cells, OSCs can potentially fill in the areas where silicon solar cells cannot be used.

Even though OSCs have several advantages over silicon solar cells, they fall short on two important factors: the device efficiency and the device lifetime. The commercialization of organic solar cells is still largely hampered because of these factors. To ensure the feasibility of OSC modules, the costs involving manufacture, packaging, installation, and maintenance have to be covered by the revenue proportional to its power output. Thus, it is vital for the cell efficiency to exceed 10% before it can be considered commercially viable [11]. Tandem architecture could push the potential over 10%, giving an efficiency of 10.6% using a low bandgap polymer [12]. However, to fully achieve a cost-effective OSC, a high-efficiency single junction device is desired. In 2016, the National Renewable Energy Laboratory (NREL) updated the solar cell efficiency chart with a breakthrough efficiency exceeding 11% for organic solar cells with morphologically optimized PffBT4T-C_9C_{13}:$PC_{71}BM$ [13–16]. These recent improvements in the efficiency value suggest good prospects for OSCs. From the industry aspect, a breakthrough in device efficiency of 13.2% was announced by Heliatek GmbH in 2016 on multijunction vacuum-processed small molecules based OSCs [17]. Some of the market players who are involved in the production of organic photovoltaics are Heliatek, Sono-tek, and Solarmer [8, 18, 19].

8.2 Research Areas in Organic Solar Cells

The research into OSCs can be classified into three main overlapping areas: (i) efficiency; (ii) stability and; (iii) scalability, as shown in Figure 8.1. Each area triggers a series of research directions.

Firstly, boosting the efficiency of OSCs towards and surpassing 10% is an always-prevalent challenge. According to the NREL, the efficiency of OSCs has grown since 1980s from 0.8 to 11.5% in 2015 [14]. The enhancement of device efficiency is achieved primarily by developing novel photoactive layers. A continuous development of low bandgap conjugated semiconductor materials, tailoring of donor-acceptor morphology, and adopting new device architecture are a few of the directions taken by the research community. Achieving the goal may also require an alternative design on the device architecture. Tandem architecture was adopted to harvest a broader spectrum of sunlight with an effectively thicker device and a larger open-circuit voltage [20]. However, this design is limited by the effective short-circuit current, which is limited by the absorber layer with the lower current. Various device optimization and material selection options are needed in order for the device to deliver its highest capability.

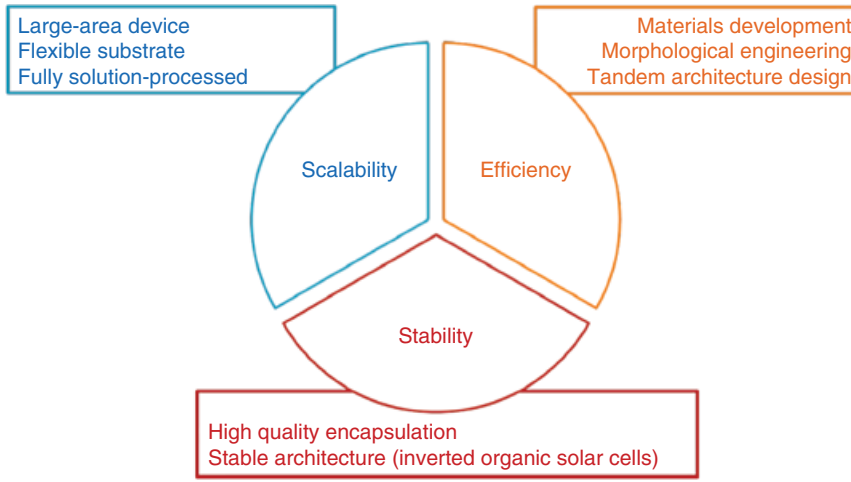

Figure 8.1 Research areas for organic solar cells.

Secondly, the scalability of the device is important to eventually fabricate organic solar cells or solar modules in a large-scale, roll-to-roll, and solution-processed way. To do so, the conventional spin coating and thermal evaporation methods on a rigid substrate have to be abandoned, as they give low throughput and are incompatible to large area, flexible devices [11, 21]. A continuous roll-to-roll processing method has to be devised for a high throughput and large area compatible capability on flexible substrates. However, the implementation of this method often requires a lot of optimization steps, which generally account for the observed lower efficiency [22]. The realization of the processability of OSCs is vital to take them one step closer on the road of product manufacturing.

Lastly, apart from achieving high efficiency and roll-to-roll processability in OSCs, device stability must not be overlooked. Søndergaard *et al.* have proposed a goal of 10-10 (10% efficiency and 10 years of stability) as the point when OSCs transcend from laboratory scale research to industrial scale production [21]. This goal is, in the authors' opinion, extremely important for the device practicality because the inherent poor stability of the device severely hampers their practical value. The degradation of organic semiconductors in oxygen and moisture remains a key point to be addressed by the research community [23]. These materials degrade rapidly in the presence of oxygen and moisture, hindering the energy harvesting capability of the device. Poly(3,4-ethylene dioxythiophene):poly(styrene sulfonate) (PEDOT:PSS) on top of the indium-doped tin oxide (ITO) is highly sensitive to moisture, only capable of functioning for one hour without proper encapsulation [24]. Due to the acidity

of PEDOT:PSS, it will often etch into ITO substrate when wet, causing degraded contact [25]. Furthermore, the presence of low work function metals such as aluminum, which oxidizes easily in air, as cathode will also cause reduced longevity of the device lifetime [26]. Thus, to safeguard the stability of the device, high-cost encapsulation techniques are mandatory. Though glass–glass type encapsulation results in the best device lifetime, it eliminates the flexible characteristics of an OSC. Research efforts on developing proper device encapsulations have been carried out [27]. However, tackling the problem from the root, i.e. ITO etching by PEDOT:PSS and low-work function aluminum, is a better strategy.

To this end, an inverted organic solar cell (IOSC), which "inverts" the sequencing of layers, was adopted to address these root causes. The adoption of such architecture could effectively contribute to a significant improvement in device lifetime [28]. In this chapter, the focus is mainly on the stability aspect of the organic solar cells.

Firstly, the fundamentals, advantages, and properties of IOSCs are presented. A summary of recent developments using various charge transport layers will also be outlined. Secondly, two unique inherent issues of IOSC, i.e. wettability and light-soaking issues, are discussed. Thirdly, strategies to overcome such issues by adopting electron and hole transport layer modifications to produce a solution-processed, light-soaking free IOSC are illustrated by using specific examples. The versatility of such solution-processed, light-soaking free devices using a different photoactive layer, such as low bandgap polymer and small molecule based photoactive layers, is presented as well. Lastly, the chapter concludes with a brief conclusion and outlook to the future of IOSCs.

8.3 An Overview of Inverted Organic Solar Cells

IOSCs are gaining attention from the research community due to their superior device stability. Since 2006, device efficiency of at least 3% was successfully achieved using P3HT:$PC_{61}BM$ [29, 30]. A stable, solution-processable IOSC on a flexible substrate with an efficiency of 3.3% was also achieved [28]. In fact, the record high OSC efficiency of 10.8% using PffBT4T-2OD:$TC_{71}BM$ as photoactive layer has been realized with the inverted architecture [13]. Table 8.1 shows a summary of development of inverted organic solar cells with various other photoactive layers.

Many results have indeed proven that IOSCs have longer device stability than conventional devices [28, 31–35]. Yang *et al*. reported an inverted bulk heterojunction (BHJ) device based on PBDTTT-C-T/$PC_{71}BM$ blend with gold nanoparticles and nanograting design with an efficiency of 8.8% [36]. Hau *et al.* demonstrated an inverted flexible OSC device using ZnO as an interfacial

Table 8.1 Summary of recent development in device efficiency for inverted organic solar cells using various photoactive layer materials.

ETL	Donor[a]	Acceptor[a]	HTL	Metal	V_{oc} (mV)	j_{sc} (mA cm^{-2})	FF (%)	η (%)	Year	Ref.
PFN	PTB-7	$PC_{71}BM$	MoO_3	Ag	740	17.2	72	9.2	2012	[40]
ZnO	PTB-7	$PC_{71}BM$	MoO_3	Al	710	13.5	67	6.5	2013	[41]
			WO_3		720	14.3	64	6.7		
Zn-C_{60}	PTB7-Th	$PC_{71}BM$	MoO_3	Ag	800	15.7	74	9.4	2013	[42]
ZnO-CsSt	PTB-7	$PC_{71}BM$	MoO_3	Al	730	15.9	62	7.0	2014	[43]
					740	17.1	69	8.7		
ZnO	PNTz4T	$PC_{61}BM$	MoO_x	Ag	729	18.2	74	9.6	2015	[44]
		$PC_{71}BM$			708	19.4	73	9.8		
ZnO	PffBT4T-2OD	$TC_{71}BM$	MoO_x	Al	770	18.8	75	10.8	2015	[13]
ZnO-HBPA	PffBT4T-2OD	$PC_{71}BM$	MoO_x	Ag	700	15.2	68	7.6	2016	[45]
ZnO	FBT	$PC_{71}BM$	MoO_x	Ag	720	19.0 [40]	66	8.9	2017	[46]

[a] For full chemical names of the photoactive layer materials and solvents, please refer to the respective journals.

layer that could retain 80% of the initial device performance after 40 days of exposure in air [28]. McGehee *et al.* reported a PCDTBT polymer based OSC with an inverted architecture that shows a shelf life of seven years under encapsulation in ambient conditions [37]. Park *et al.* developed a dynamic annealed ZnO electron transport layer with 94% of device efficiency retained after exposure in air for 50 days [38]. Lima *et al.* have also conducted an outdoor stability study of an IOSC with V_2O_5 as a hole transport layer that is able to retain 80% of its initial device efficiency for 900 hours [35]. In fact, preliminary testing of a conventional and inverted architecture based on P3HT:PC_{61}BM in air without encapsulation in our laboratory also shows similar enhancements in device lifetime (Figure 8.2).

There are two major modifications in the device structure of inverted OSCs: (i) "inversion" of the transport layers and (ii) the change of metal with higher work function. Firstly, the PEDOT:PSS hole transport layer (HTL) is shifted upwards between the photoactive layer and the metal contact. It is found that the acidity of PEDOT:PSS upon contact with moisture and oxygen could be the major cause for the instability of the cell as it etches the ITO [24, 39]. Thus, shifting the PEDOT:PSS layer to the top of the photoactive layer prevents the etching of ITO. Instead of low work function metal, an air-stable high work function metal such as silver or gold is used as the metal electrode. As a result, the direction of carrier extraction is "inverted" with respect to the conventional architecture. The electrons are now extracted at ITO while holes are extracted at the metal electrode (Figure 8.3).

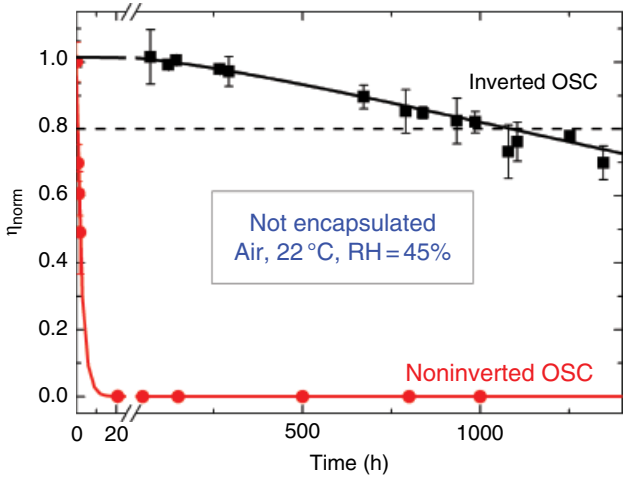

Figure 8.2 Comparison of the lifetime of conventional and inverted P3HT:PC_{61}BM OSC under exposure to ambient condition without encapsulation.

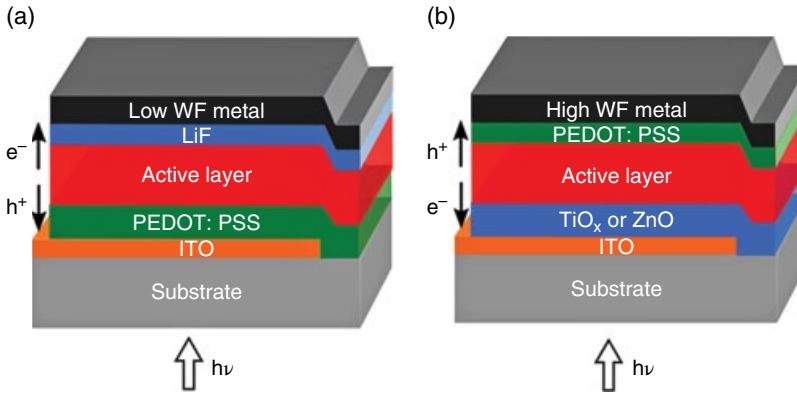

Figure 8.3 Schematic representation for (a) conventional OSC cell structure and (b) an inverted OSC. Note the direction of charge collections between the two types of devices.

8.3.1 Transport Layers in Inverted Organic Solar Cells

Similar to its noninverted counterpart, IOSCs require electron transport layers (ETLs) and hole transport layers (HTLs) for an effective charge extraction. Efficient charge extraction would lead to a minimal recombination loss and low leakage current. Several n-type metal oxides, such as TiO_x [32, 47], ZnO [45, 48] and Cs_2CO_3 [48, 50], were generally used as ETLs. Materials such as poly(3,4-ethylene dioxythiophene):poly(styrene sulfonate) (PEDOT:PSS) [31, 51, 52], p-type metal oxides [35, 41, 53], and nanoparticles [54] were normally used as HTLs. Charge transport layers play an extremely vital role in IOSC devices, as they affect the energy alignment between the transport layer and photoactive layer interface, tailoring the built-in field, improving charge selectivity, and improving device stability.

8.3.2 PEDOT:PSS Hole Transport Layer

Among the wide range of materials available for the HTL in IOSC, PEDOT:PSS is often preferred due to its ease of solution-processing. This is because a metal oxide based HTL is generally deposited by means of thermal evaporation; while PEDOT:PSS can be easily deposited by printing or coating methods (Table 8.2). As a result, PEDOT:PSS is the main material for the HTL in IOSCs used in this work. PEDOT is a conductive polymer that adopts 3,4-dialkoxy-thiophene structures. Its conductive nature originates from the polymerization of the bicyclic 3,4-ethylenedioxythiophene (EDOT) and its derivatives. From the structure of the polymer, the presence of oxygen atoms adjacent to the thiophene ring stabilizes the positively charged EDOT during polymerization. As a result, a conductive PEDOT polymer is formed [55]. Due to the inherent

Table 8.2 IOSC device performance with various hole transport layer materials and deposition methods.

Photoactive material	HTL (formulation)	Additives (for PEDOT:PSS only)	HTL deposition method	Film thickness (nm)	η (%)	Year	Ref.
P3HT:$PC_{61}BM$	PEDOT:PSS (CPP 105 D)	Dynol	Spin coat	250	1.4	2005	[56]
P3HT:$PC_{61}BM$	PEDOT:PSS (unspecified)	Triton X-100	Spin coat	40	4.0	2010	[57]
P3HT:$PC_{61}BM$	PEDOT:PSS (Clevios PH)	Isopropanol	Doctor blade	120	2.4	2011	[58]
P3HT:$PC_{61}BM$	PEDOT:PSS (PVP AI 4083)	Unspecified surfactant	Spin coat	50	3.0	2011	[59]
P3HT:$PC_{61}BM$	PEDOT:PSS (PVP AI 4083)	Not reported	Spin coat	30	3.6	2011	[60]
P3HT:$PC_{61}BM$	VO_x	n/a	Spin coat	25	3.9	2011	[60]
P3HT:$PC_{71}BM$	MoO_x	n/a	Thermal evaporation	2	4.0	2011	[50]
P3HT:$PC_{61}BM$	PEDOT:PSS (PVP AI 4083)	Capstone FS-31	Spin coat	80	3.1	2012	[30]
P3HT:$PC_{61}BM$	PEDOT:PSS	Surfynol 104 PA	Spin coat	40	4.0	2013	[61]
PTB7:$PC_{71}BM$	MoO_x	n/a	Thermal evaporation	10	6.5	2013	[41]
PTB7:$PC_{71}BM$	WO_x	n/a	Thermal evaporation	5	6.7	2013	[41]
P3HT:$PC_{61}BM$	CoO_x	n/a	Thermal evaporation	10	2.7	2015	[62]
P3HT:$PC_{61}BM$	ITO nanoparticle	n/a	Spin coat	16	3.0	2016	[54]

chemical structure and the hydrophilicity of the material, PEDOT:PSS is intrinsically an acidic and hygroscopic compound. Typical conductivity of PEDOT is in the range of 500 S cm^{-1}. However, such high conductivity is not suitable for hole transport action because large lateral conductivity will occur, leading to unwanted device interconnections. When coupled with PSS at various ratios, its conductivity can be tuned to as low as 10^{-3} S cm^{-1} [55]. PEDOT:PSS with a lower conductivity (Clevios™ P VP AI 4083) is normally used as the hole transport layer for organic solar cells.

8.3.3 Titanium Oxide Electron Transport Layer

In IOSCs, the electron transport layer (ETL) aids the device in transporting the dissociated electrons to the electron-collecting contacts, i.e. ITO. Table 8.3 shows a summary the efficiencies of IOSC devices fabricated with various electron transport layer materials. P3HT:PC_{61}BMIOSC based on ZnO as electron transport layer could achieve a device efficiency of 3.6% with proper annealing control [63] and even 4.2% using atomic layer deposition (ALD) [64]. In fact, SnO_2 and Nb_2O_5 were also reported to be a decent electron transport layer in IOSCs [65, 66]. Devices based on solution-processed TiO_x as electron transport layer could also achieve an efficiency of 3.7% by using sol-gel spin coating and chemical bath deposition [67, 68]. In this work, TiO_x is used as the ETL in IOSC devices because of its transparent, high mobility, and stable properties. Apart from these attributes, a thickness of ~100 nm can also serve as a UV protective layer for the device to improve the device lifetime [51].

There are various methods in which these metal oxide ETLs can be deposited onto transparent conducting substrates (TCOs) for IOSC applications, a few of which are spin coating, chemical vapor deposition (CVD), atomic layer deposition (ALD), doctor blading (DB), spray pyrolysis, and chemical bath deposition (CBD) (Table 8.3). ALD and CVD techniques require vacuum conditions and high temperature environments that could deteriorate the quality of the substrates and also incur high manufacturing cost. Spin coating and spray pyrolysis are difficult to manufacture when the OSC expands into a larger area. CBD seems to be the most suitable coating method among all because it is a facile, scalable, low temperature, solution processed, and low-cost aqueous deposition method. A comprehensive overview on the theory and development of chemical bath deposition has been reported by Lokhande [69]. This method has been used to deposit thin film metal oxides on various conducting or nonconducting substrates (Table 8.4).

Oxide thin films can be deposited by immersing a substrate into a chemical bath at ambient conditions, without being subjected to a harsh deposition environment [69]. A straightforward thickness control in the range of 20 nm to several microns under a low temperature, solution processed, and facile set-up can be relatively easily realized by this method [68, 70, 71]. Chemical bath

Table 8.3 IOSC device performance with various metal oxides and coating methods.

ETL	Precursor solutions	Coating technique	Heat treatment (°C)	Thickness (nm)	η (%)	Photoactive layer	Year	Ref.
ZnO	Diethyl zinc	ALD*	45	36	3.8	P3HT:$PC_{61}BM$	2010	[64]
TiO_2	Titanium oxysulfate ($TiOSO_4$)	CBD*	*In situ*	20	3.8	P3HT:bis-$PC_{61}BM$	2010	[68]
ZnO (AZO)	Zinc acetate Aluminium hydroxide acetate	Doctor blade	260	100	2.4	P3HT:$PC_{61}BM$	2011	[58]
TiO_x	$TiCl_4$	Doctor blade	—	38	2.6	P3HT:$PC_{61}BM$	2011	[80]
Nb_2O_5	Niobium ethoxide	Spin coat	450	10	2.7	P3HT:$PC_{61}BM$	2011	[66]
Cs_2CO_3	Commercial powder	Spin coat	150	n/a	4.0	P3HT:$PC_{61}BM$	2011	[50]
TiO_x	Titanium (IV) isopropoxide (TTIP)	Spin coat	180	130	2.9	P3HT:$PC_{61}BM$	2012	[30]
ZnO	Zinc acetate	Spray Pyrolysis	n/a	350	3.2	P3HT:$PC_{61}BM$	2013	[81]
ZnO	$(Zn(OH)_2(NH_3)_x)$	Spin coat	150	10	3.6	P3HT:$PC_{61}BM$	2013	[63]
TiO_2	Titanium (IV) isopropoxide (TTIP) Ti metal foil	Spin coat Sputtering	460 200	50 40	3.7 2.9	P3HT:$PC_{61}BM$	2013	[67]
TiO_2-Au NPs	TiO_2 nanoparticles	Spin coat	150	20	8.7	PTB7:$PC_{71}BM$	2013	[82]
TiO_x/PEI	Ti metal plate	Magnetron Sputtering	No anneal	82	8.7	PTB7:$PC_{71}BM$	2014	[83]

SnO_x	Tetrakis(dimethylamino) tin(IV) (TDMASn)	ALD	80	60	5.7	PCDTBT:$PC_{61}BM$	2015	[84]
F-TiO_x	Ammonium hexafluorotitanate Boric acid	CBD	180	80	7	PTB7:$PC_{71}BM$	2015	[33]
ZnO-HBPA	Zinc acetate Hyperbranched poly(amino acid)	Spin coat	100	50	7.6	PffBT4T–2OD:$PC_{71}BM$	2016	[45]
Al-ZnO	ZnO nanoparticles	Spin coat	70	10	7.9	PTB7:$PC_{71}BM$	2016	[85]
TiO_2-TOPD	TiO2/TIPD dispersion	Spin coat	155	20	10.2	PTB7-Th:$PC_{71}BM$	2017	[86]
F-TiO_x	Ammonium hexafluorotitanate Boric acid	CBD	180	80	3.0	SMDPPEH:$PC_{61}BM$	2016	[34]

* CBD: Chemical Bath Deposition; ALD: Atomic Layer Deposition

Table 8.4 List of chemical bath deposited oxide films on various substrates.

	Precursor(s)	Deposition rate (nm/h)	Substrate	Bath temperature (°C)	Year	Ref.
SnO_2	$SnCl_2 \cdot 5H_2O$ HCl	9	SiO_2	80	2000	[74]
SnO_2	$SnCl_2 \cdot 2H_2O$ KNO_3	4	Glass	60	2002	[75]
ZnO	$Zn(NO_3)_2$ $(CH_3)_2NH \cdot BH_3$	800	SiO_2	60	2006	[76]
TiO_2	$(NH_4)_2TiF_6$ H_3BO_3	100	FTO	50	2008	[70]
TiO_x	$TiCl_3$	470	FTO	80	2008	[71]
ZnO	$Zn(NO_3)_2$ $Na_3C_6H_5O_7$	1200	Glass	50	2008	[77]
TiO_x	$TiOSO_4$ H_2O_2	200	FTO	80	2010	[68]
F-TiO_x	$(NH_4)_2TiF_6$ H_3BO_3	43	ITO	40	2011	[78]
SnO_x	$SnCl_2 \cdot 5H_2O$	300	Glass	55	2012	[79]
F-TiO_x	$(NH_4)_2TiF_6$ H_3BO_3	50	ITO	40	2014	[32]

deposited titanium oxide (CBD-TiO_x) thin films on transparent conducting oxide (TCO) substrates have been widely studied [70–72]. In solar cell applications, the CBD technique has been used to fabricate well-controlled TiO_x layers [68, 73].

8.4 Issues in Inverted Organic Solar Cells and Respective Solutions

Although an IOSC provides an excellent way to tackle the poor device stability in organic solar cells, it is not yet completely feasible to be used in large-scale manufacturing and practical energy harvesting applications. The main source of the problem stems from the charge transport layers in the device. The configuration and material used for the charge transport layers give rise to two serious issues: (i) the wettability issue of the PEDOT:PSS hole transport layer on photoactive layers and (ii) the light-soaking issue due to the use of metal

oxide electron transport layer. In this section, these issues are discussed further, with the proposal for modifications of these transport layers to overcome the inherent difficulties associated with them.

8.4.1 Wettability Issue of PEDOT:PSS in Inverted Organic Solar Cells

Coating of the PEDOT:PSS onto the photoactive layer remains to a serious technical challenge in in the fabrication of these devices. The hydrophobic nature of the underlying photoactive layer (such as P3HT:$PC_{61}BM$) produces high surface tension upon contact with hydrophilic PEDOT:PSS, causing a serious wettability issue. Without the aid of additives, PEDOT:PSS can hardly be coated onto the photoactive layer. Upon contact, PEDOT:PSS solution would form a high surface angle on the photoactive layer surface (Figure 8.4, left). Consequently, this will lead to poor film morphology and inferior device performance. Removal of PEDOT:PSS as a hole transport layer (HTL) is not an option to resolve this issue, as this will render the photoactive layer susceptible to oxygen and moisture, causing detrimental effects to the device performance. Furthermore, the absence of HTL will also result in poor device performance.[87] Replacement of PEDOT:PSS with other p-type oxides is undesired because that would make the device incompatible for solution-processing (Table 1.2). Therefore, use of additives is necessary to circumvent this wettability issue.

To lower the surface energy of PEDOT:PSS, a nonionic additive should be used. On one hand, anionic additives such as sodium dodecyl sulfate (SDS) could significantly enhance the conductivity by substituting PSS anion by the anions [88]. High conductivity PEDOT:PSS is not a suitable HTL, as it will cause undesired lateral device connections. On the other hand, cationic additives would neutralize the PSS anion by forming a stable complex that could affect the morphology of the PEDOT:PSS film. The addition of nonionic surfactant neither alters its conductivity significantly, nor affects its morphology to an undesired state. As a result, nonionic additives are generally used to modify the wettability of PEDOT:PSS [56, 57, 89].

In Table 8.2, an overview of the additives that are commonly added into PEDOT:PSS before coating onto the photoactive layer is presented. Isopropyl alcohol (IPA) is the most commonly used additive for PEDOT:PSS to reduce

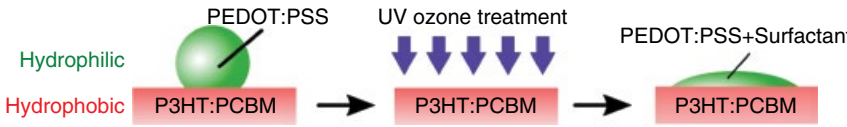

Figure 8.4 Schematic showing the necessity of UV ozone treatment on photoactive layers prior to coating PEDOT:PSS with conventional surfactant modification.

the surface energy [58]. Other alternatives such as Dynol [56], Triton X-100 [57], and Zonyl FS-300 [89] were also used previously. The use of fluorosurfactants such as Zonyl FS-300 is more beneficial than the use of hydrocarbon-based surfactants (Triton X-100) in reducing the surface tension between the two organic layers. This is attributed to the lipophobic nature of the C–F tail, which tends to concentrate at the liquid–air interface, contrary to the lipophilic C–H tail that concentrates in condensed phase interfaces [90]. In the fabrication of inverted OSCs, Zonyl FS-300 is often used together with IPA because Zonyl FS-300 or IPA alone is insufficient for PEDOT:PSS to lie within the wetting envelope of P3HT:$PC_{61}BM$ [22]. An undesirable and detrimental UV ozone surface treatment of the photoactive layer prior to PEDOT:PSS coating is often required to increase its surface energy (Figure 8.4).Therefore, a study to investigate an alternative additive to PEDOT:PSS to resolve the wettability issue for inverted organic solar cells would be a valuable contribution.

8.4.2 Light-soaking Issue of TiO_x-based Inverted Organic Solar Cells

Apart from the wettability issue, there is another inherent issue in IOSCs, i.e. the necessity of a mandatory "light-soaking" treatment. Generally, an IOSC device requires continuous exposure to light in order to active its full potential [91]. This phenomenon is observed especially in IOSCs with n-type metal oxides (TiO_x, ZnO) as the ETL. The as-prepared IOSC would show S-shaped *J-V* characteristics with a low short circuit current and a low fill factor during the initial illumination [91–95]. After prolonged illumination, the device efficiency gradually improves and saturates at its highest value. A typical device with TiO_x as an electron transport layer requires approximately 10 minutes under AM 1.5G illumination to reach its maximum efficiency [32] A light-soaking time of 10 minutes was needed when Al-doped ZnO (AZO) is used as the electron transport layer [95]. The light-soaking behavior in an IOSC seems to originate from the filling of the oxygen and moisture induced trap sites in the metal oxide by photoelectrons generated by the UV component ($\lambda \leq 400$ nm) under AM 1.5G illumination (1000 W m^{-2}) [91, 96]. Such trap-filling action consequently lowers the work function of the ETL and improves its electron selectivity [97].

The severity of the light-soaking effect lies in its reversible property [98–100]. As a result, the device must be newly activated at each light–dark cycle (every morning when used for outdoor applications) before it can function at full capacity. To roughly estimate the light-soaking time required to fully activate an IOSC device in outdoor applications, the following assumptions were made: (i) the device was illuminated under a sunny day in Singapore; (ii) 100% conversion of photons to electrons in solar cells; (iii) irradiance intensity is proportional to the photon density, and proportional to the light-soaking time, i.e. intensity $\propto$ photon density $\propto$ electron density $\propto$ light-soaking time; (iv) identical irradiance wavelength spectrum between indoor and outdoor light sources; (v) devices with the same device area were used. If a typical IOSC

device requires 10 minutes to complete its light-soaking treatment under a solar simulator (AM 1.5G, 1000 W m^{-2}), a light-soaking of at least an hour is required under the sun every morning (Figure 8.5). This requirement greatly hinders the practicality of the device, especially in outdoor applications. Therefore, it is mandatory to address this issue by significantly reducing the light-soaking time in inverted organic solar cells.

8.5 Overcoming the Wettability Issue and Light-soaking Issue in Inverted Organic Solar Cells

8.5.1 Fluorosurfactant-modified PEDOT:PSS as Hole Transport Layer

Lim *et al*. have adopted a type of nonionic fluorosurfactant: Capstone® Dupont™ FS-31 (herein referred to as CFS-31) as a substitute to common additives such as Zonyl FS-300 in the fabrication of IOSC. CFS-31 is capable of providing

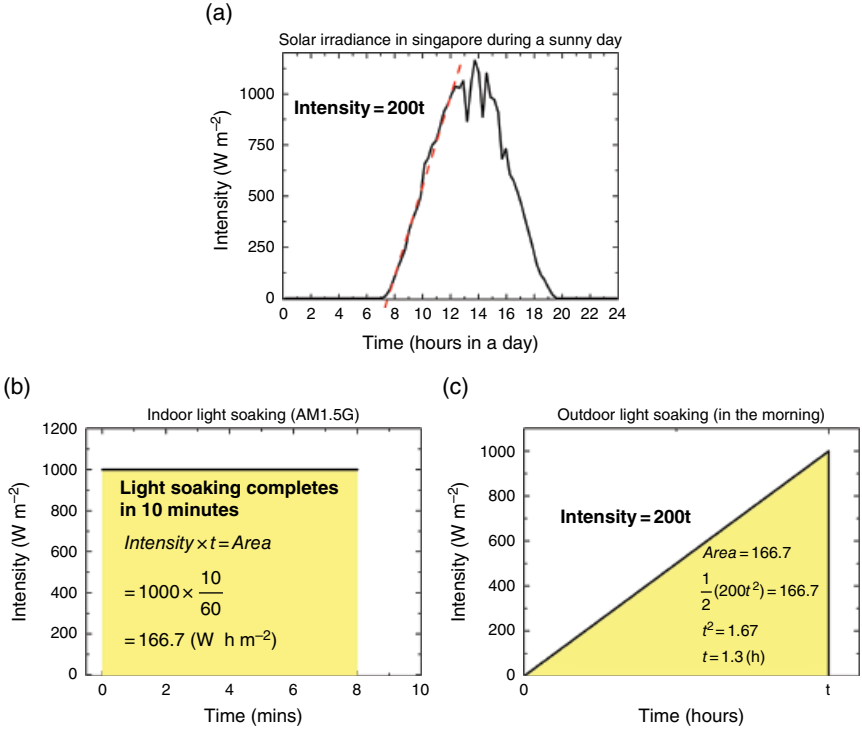

Figure 8.5 (a) Typical solar irradiance as a function of time for a typical sunny day in Singapore; (b) light-soaking calculation with assumption of 10 minutes under the solar simulator; (c) the corresponding light-soaking estimation under the sun by equating the energy densities (area under the curves in (b) and (c)).

remarkably low surface tension (~15 mN/m) compared to Zonyl FS-300 (~23 mN/m) in aqueous or solvent-based products (ideal for PEDOT:PSS) that could enable better wetting. The use of this fluorosurfactant is capable of resolving the wettability issue while retaining the device efficiency [30]. Through the improvement of surface wettability, this work aims to highlight that the presence of CFS-31 (i) improves the device performance of solution-processed IOSCs; (ii) enables proper PEDOT:PSS coating onto P3HT:$PC_{61}BM$ without additional surface treatments; (iii) provides invariant optimal device parameters, such as thickness of TiO_x ETL; and (iv) forms better energy alignment that results in an stable device performance for at least 1000 hours when exposed to the ambient atmosphere.

The unique feature of CFS-31 is that it provides an optimal region between 4–8 v/v% (CFS-31 to PEDOT:PSS ratio), as shown in Figure 8.6, which greatly simplifies the fabrication process. Studies have shown that when the surfactant is at its optimal concentration region (4–8 v/v%), the device has its most optimal PEDOT conduction pathway, resulting in a device with low defects, high uniformity (shown in high fill factor near predicted theoretical maximum of P3HT:PCBM devices [101]), better charge carrier transport with minimal bimolecular and interfacial recombination (shown by high j_{sc}), and good ohmic

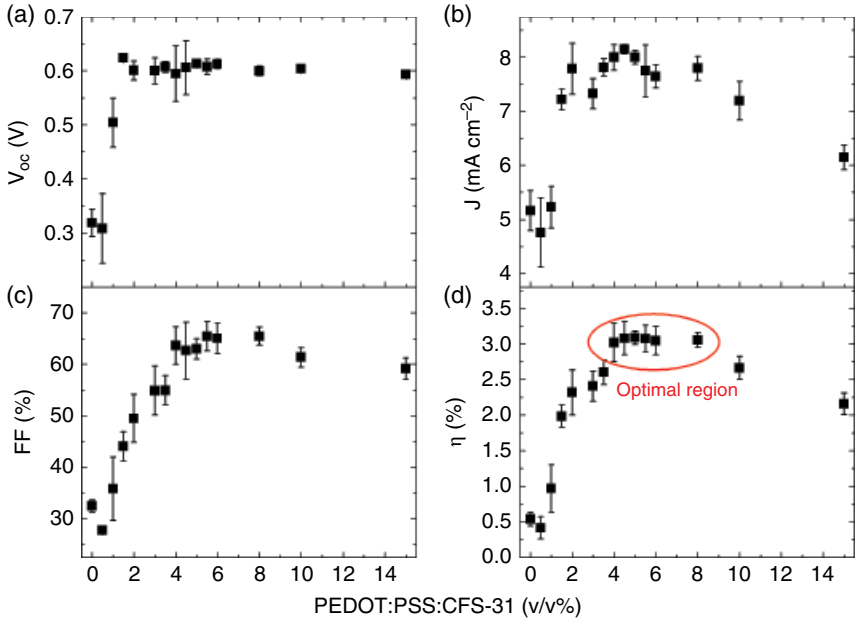

Figure 8.6 Device performance showing (a) V_{oc}, (b) j_{sc}, (c) fill factor, and (d) efficiency of ITO/TiO_x/P3HT:$PC_{61}BM$/PEDOT:PSS:CFS-31/Ag IOSC with various CFS-31 concentrations (ranging from 0 to 15 v/v%).

Table 8.5 Device performance of inverted organic solar cells with device architecture ITO/TiO_x/P3HT:PC_{61}BM/(PEDOT:PSS + additives)/Ag using various types of additives at TiO_x thickness of about 100 nm.

PEDOT:PSS formulation	V_{oc} (mV)	j_{sc} (mA cm^{-2})	FF (%)	η (%)	Reference
PEDOT:PSS + IPA	580	6.3	55	2.1	[50]
PEDOT:PSS + Zonyl FS300	560	7.9	48	2.2	[22]
PEDOT:PSS + CFS-31	610	7.8	65	3.1	[30]

contact (shown by a V_{oc} value close to the LUMO offset of P3HT [102]). When such an HTL is used in P3HT:PC_{61}BM-based IOSC at the optimal range, the device could achieve 3.1%, significantly better compared to other conventional surfactants (Table 8.5).

As shown in Figure 8.7, there is a strong correlation between the surfactant concentration and the electrical properties of the device. In the absence of surfactant, almost no PEDOT:PSS was coated on P3HT:PC_{61}BM and, as a consequence, a high barrier between the HOMO of P3HT and silver is formed. This results in a large leakage current ($R_{sh}A$ = 0.15 kΩ·cm^2) and large series resistance (r_sA = 42.8 Ω·cm^2) (the device active area is 0.09 cm^2). A thick and nonuniform PEDOT:PSS layer was formed in a low surfactant concentration regime (0.5–1 v/v%); this has direct influence on the series resistance of the device. As evidenced in Figure 8.7b, there is an increase in the series resistance of the device in this regime and also a large leakage current (low shunt resistance, $R_{sh}A$ = 0.11 kΩ·cm^2). This high leakage current is due to the huge number of defects present in the film. Furthermore, the inferior PEDOT:PSS film formation on P3HT:PC_{61}BM caused by poor adhesion is an issue for lateral conduction (r_sA = 54.5 Ω·cm^2). When the surfactant concentration increases beyond 1.0 v/v%, a sharp increase in the shunt resistance and a decrease in series resistance were observed. The PEDOT:PSS film slowly becomes more uniform and less defective as the surfactant concentration increases, giving rise to high shunt resistance, which stabilizes at around 1–1.4 kΩ·cm^2. Correspondingly, the series resistance also decreases from 69.8 to 12.6 Ω·cm^2. The series resistance indeed increases slowly when the concentration of the surfactant increases beyond 5.5 v/v% and this leads to a decrease in the J_{sc} and fill factor of the device. This phenomenon can be explained with occurrence of more phase segregation at PEDOT:PSS due to blockage of conduction pathways by the surfactant molecules (Figure 8.7viii). The blocking effect is especially evident in a device with 15 v/v% surfactant concentration by the formation of maze-like networks that are formed on the PEDOT:PSS film; the cause for the reduced device performance is still attributed predominantly to the reduction in J_{sc}.

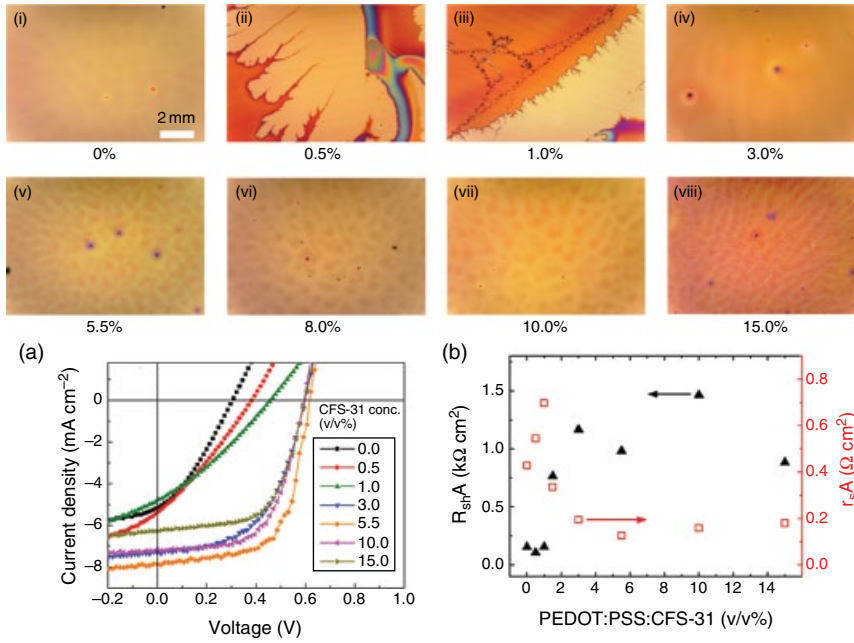

Figure 8.7 Optical microscopy images showing P3HT:$PC_{61}BM$/PEDOT:CFS-31 with (i–viii) 0, 0.5, 1.0, 3.0, 5.5, 8.0, 10.0, and 15.0%, respectively. The dark orange region is PEDOT:PSS, while the light yellow region is P3HT:$PC_{61}BM$. (a) Illuminated *J-V* characteristics of representative devices with various CFS-31 surfactant concentration; (b) shunt and series resistance of corresponding devices extracted from (a), the lines connecting the data points only serves as guidance. The images were extracted from [30]. Reproduced with permission of Royal Society of Chemistry.

The addition of the new surfactant into PEDOT:PSS shows no detrimental effects on the stability of the inverted device (Figure 8.8). The device has superior stability over nonencapsulated noninverted devices, which degraded to 50% of their initial value less than three hours after exposure to air (Figure 8.8, inset). The device was able to retain almost 75% of its initial device performance even after 400 hours when exposed to ambient air without encapsulation. This reveals that the Capstone® FS-31 has no detrimental effect to the photoactive layer. The observed degradation of the device efficiency is caused mainly by the continual decrease in J_{sc}. This is attributed to the change in both chemical and physical morphology of the active layer components of the device [103].

A new type of fluorosurfactant for PEDOT:PSS, Capstone® Dupont™ FS-31 (CFS-31), was used as an alternative for conventional additives in IOSCs to overcome the fabrication issue. Smooth and uniform films that lie within the wetting envelope of P3HT:$PC_{61}BM$ were achieved by CFS-31 alone without the

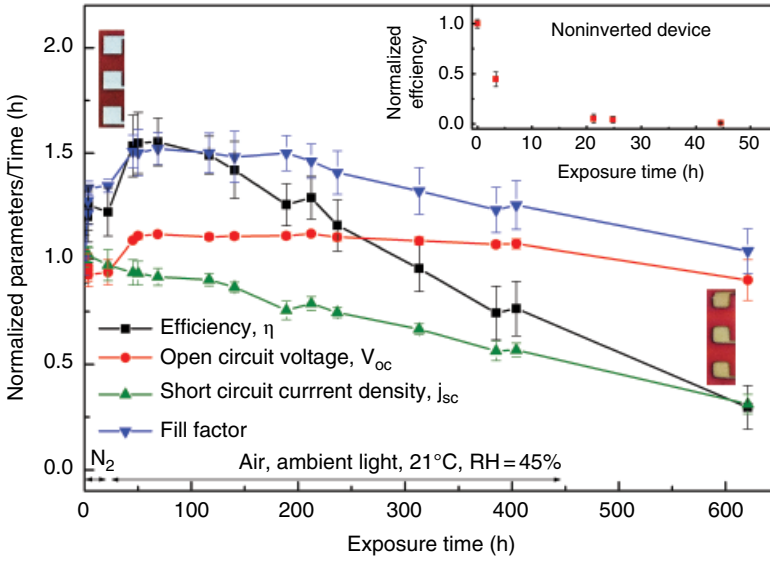

Figure 8.8 Normalized V_{oc}, J_{sc}, fill factor, and efficiency of ITO/TiO_x/P3HT:PC_{61}BM/PEDOT:PSS: CFS-31/Ag with 5.5 v/v% CFS-31 concentration under exposure in N_2 (first 24 hours) and in air (subsequent exposure time) without encapsulation. The parameters were normalized by their respective maximum values. The pictures on the left show the freshly exposed IOSC while the ones on the right shows the same device exposed to air after 600 hours. The graph was extracted from [30]. Reproduced with permission of Royal Society of Chemistry.

need of detrimental UV ozone treatment on P3HT:PC_{61}BM prior to coating. Furthermore, addition of CFS-31 to PEDOT:PSS exhibits no detrimental effect on the device hole transport behavior. This work has demonstrated that solution-processed IOSCs using a CFS-31 modified PEDOT:PSS hole transport layer exhibit an efficiency up to 3.1%, higher than that of the existing additives reported previously. At least 75% of the initial performance was preserved after a 400-hour exposure in air without encapsulation. All these attributes of CFS-31 highlight its advantages over many other additives. In conclusion, the Capstone® Dupont™ FS-31 seems to be a good candidate for overcoming the wettability issues encountered in the fabrication of solution-processed inverted organic photovoltaic devices.

8.5.2 Fluorinated Titanium Oxide as Electron Transport Layer

Impurity-modified metal oxides have been adopted by various groups to address the light-soaking issue. Strontium and barium doped ZnO and aluminum doped ZnO onto TiO_x (AZO-TiO_x) were already used as ETLs to address this issue in IOSCs [93, 97]. Kim *et al.* have also reported a nitrogen-doped TiO_x

electron transport layer to reduce the light-soaking time in a PTB7-th:$PC_{70}BM$ IOSC [104]. Therefore, in this work, fluorinated titanium oxide (F-TiO_x), deposited by solution-processed chemical bath deposition (CBD), was proposed as a functionalized ETL in IOSCs to address this issue. This material has been applied extensively in various applications, such as electrochromic [78], anticorrosion of metal [105], photocatalytic applications [106], and solar cells [107]. The presence of fluorine in TiO_x could significantly reduce its dangling bonds by passivation [78]. In CdS and CdSe quantum dot solar cells (QDSCs), F-TiO_x was used to enhance the cell efficiency [108]. Based on the passivation property of fluorine in TiO_x, it can be used to reduce the trap states to accelerate the trap-filling action during the light-soaking. As discussed in Section 8.3.3, chemical bath deposition (CBD) is a routinely employed coating technique to fabricate metal oxide thin films [79, 108]. Most importantly, fluorine in TiO_x can be incorporated intrinsically by CBD onto TCO substrates [78, 105]. In this section, a brief overview of a specific example adopting a F-TiO_x electron transport layer in an inverted organic solar cell is discussed.

Thin (80 nm) F-TiO_xETL, deposited on tin-doped indium oxide (ITO) via chemical bath deposition using the hydrolysis reaction of ammonium hexafluorotitanate and boric acid, was shown to significantly reduce the device light-soaking time almost tenfold compared to a conventional sol-gel coated TiO_x ETL, without affecting the device efficiency of 3% in P3HT:$PC_{61}BM$ device [32]. However, a significant difference in the light-soaking behavior was observed between these two devices, as shown in Figure 8.9. Figures 8.9a and 8.9b show the *J-V* characteristics for sol-gel TiO_x and F-TiO_x based IOSC devices, respectively, under AM 1.5G conditions (light-soaking treatments). S-shape characteristics, a typical phenomenon that occurs due to suppression of electron transport in TiO_x [109], were observed at the initial stage of illumination. However, the F-TiO_x device reaches its saturated efficiency (50 s) much faster compared than the sol-gel TiO_x device (350 s).

Furthermore, F-TiO_x was reported to be sufficiently versatile to be integrated into various photoactive layer material combinations, including polymers, low bandgap polymers, and small molecules. Figures 8.9c and 8.9d show the time evolution of the device efficiencies using P3HT:$PC_{61}BM$, PTB-7:$PC_{71}BM$ and SMDPPEH:$PC_{61}BM$ under AM 1.5G illumination in a N_2 atmosphere. Sol-gel TiO_x based devices require approximately 5–8 minutes for the efficiency to saturate. For F-TiO_x, the efficiency saturates after approximately 30–60 seconds of illumination (Table 8.6). It is noteworthy that such light-soaking duration under indoor laboratory conditions would mean at least one hour of light-soaking at outdoor conditions every morning (see Section 8.4.2), a reduction from eight minutes to 30 seconds means saving 75% of activation time in actual outdoor operation. Thus, F-TiO_x ETL IOSCs allow a more light-soaking free device to be potentially implemented on a commercial scale.

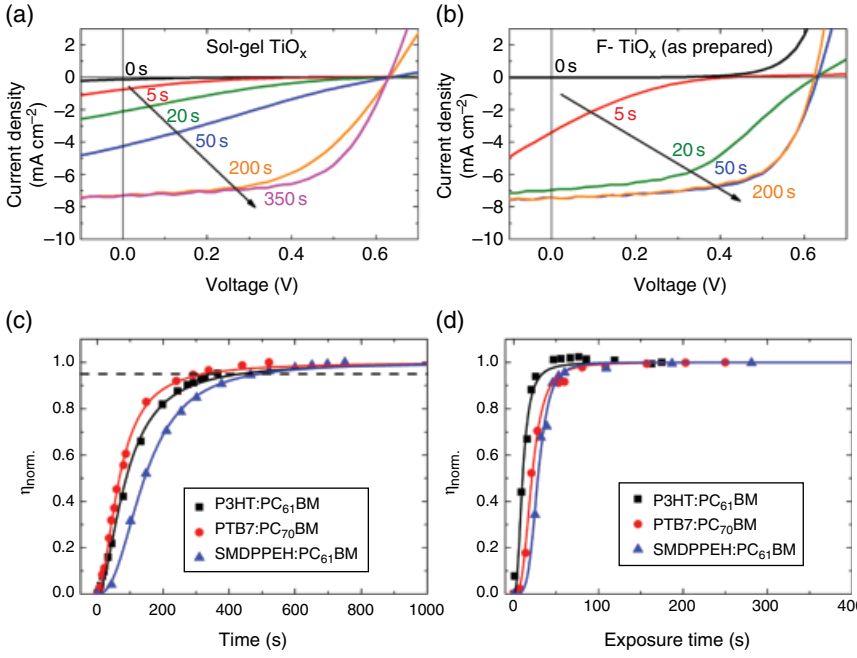

Figure 8.9 Current-voltage (*J-V*) characteristics of inverted organic solar cells with (a) sol-gel TiO_x and (b) F-TiO_x as electron transport layer when subjected to light-soaking treatments; the illumination time are shown (guided by arrows). (c) Light-soaking effect on the efficiency of sol-gelTiO_x layers upon AM 1.5G illumination in P3HT:PC_{61}BM, PTB7:PC_{71}BM and SMDPPEH:PC_{61}BM devices. (d) Light-soaking effect on the efficiency of F-TiO_x layers upon AM 1.5G illumination in P3HT:PC_{61}BM, PTB7:PC_{71}BM and SMDPPEH:PC_{61}BM devices The symbols represent experimental data while the solid lines are fitted data. The figures were extracted from [32] and [34].

Table 8.6 Summary of light-soaking time (τ_{soak}) of P3HT:PC_{61}BM, PTB-7:PC_{71}BM and SMDPPEH:PC_{61}BM IOSC using (a) sol-gel TiO_x and (b) F-TiO_x as electron transport layer.

	τ_{soak} [a] (s)		
Photoactive layer	**sol-gel TiO_x**	**F-TiO_x**	**Reference**
P3HT:PC_{61}BM	434	34	[32]
PTB-7:PC_{71}BM	326	56	[33]
SMDPPEH:PC_{61}BM	491	57	[34]

[a] Light-soaking time: time required to reach 95% of maximum efficiency.

Several reports have suggested that the light-soaking behavior of an IOSC device with metal oxide ETL originates from at least two different perspectives. Firstly, the light-soaking originates from the filling of trap states, which decreases the work function of the ETL and enables electron extraction through the ITO/metal oxide interface [91]. Secondly, the induced interface dipole between the metal oxide/organic interface may also determine the formation of an extraction barrier for the dissociated excitons in the device [97]. Thus, a light-soaking experiment with various ETL configurations of sol-gel, TiO_x (80 nm), F-TiO_x(80 nm), bilayer sol-gel TiO_x (40 nm)/F-TiO_x (40 nm), and F-TiO_x (40 nm)/sol-gel TiO_x (40 nm), was conducted to investigate which interface contributes to the light-soaking behavior. The device architectures are depicted in Figure 8.10. The results in Figure 8.11 show that the F-TiO_x based device has the shortest light-soaking time (about 30 s), followed by the sol-gel TiO_x/F-TiO_x (about 150 s), F-TiO_x/sol-gelTiO_x (about 170 s), and sol-gel TiO_x (about 450 s). This observation suggests that both ITO/TiO_x and TiO_x/organic interfaces contribute to the light-soaking behavior, as seen from the intermediate timings compared to pure sol-gel TiO_x. In this chapter, the focus is on the effect of trap-filling at the ITO/metal oxide interface on the light-soaking behavior.

The necessity of light-soaking seems to originate from the active unfilled electron traps caused by dangling bonds [84, 91, 93, 97]. These dangling bonds are susceptible to the adsorption of oxygen in air and form active trap sites, which could be removed by UV photons [96]. Ultraviolet photoelectron

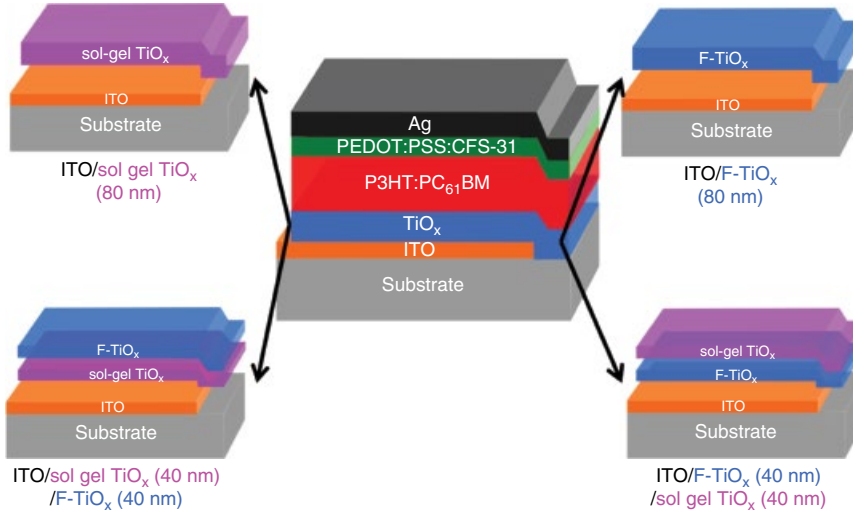

Figure 8.10 Schematic showing various combinations of TiO_x used for studying the contribution of different interfaces to the light-soaking effect.

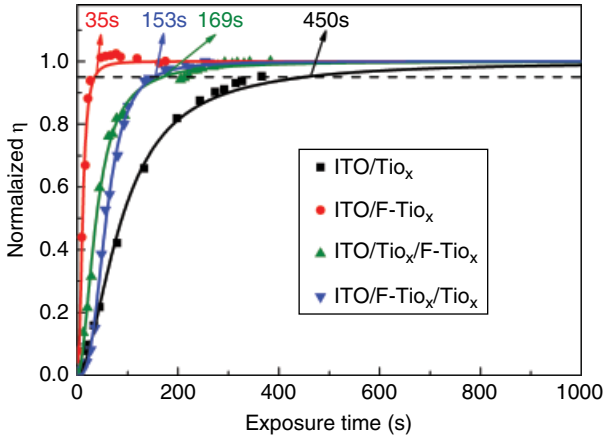

Figure 8.11 Light-soaking control experiment of fresh inverted organic solar cells with sol-gel TiO_x (80 nm), F-TiO_x (80 nm), sol-gel TiO_x (40 nm)/F-TiO_x(40 nm), and F-TiO_x(40 nm)/sol-gel TiO_x (40 nm) as electron transport layers upon AM 1.5G illumination. The symbols represent experimental data while the solid lines are fitted data by logistic function. The indicated time represents the corresponding light-soaking time (τ_{soak}) for each sample as defined in the main text.

spectroscopy (UPS) and UV photoconductivity measurements show that F-TiO_x has a lower work function compared to sol-gel TiO_x, primarily due to lower trap state density caused by passivation of fluorine onto TiO_x dangling bonds (Figures 8.12a and 8.12b). As a result, it accelerates the trap filling action to desorb the oxygen atoms on the F-TiO_x surface (Figure 8.12c) [32, 96].

Combining the findings of the UPS spectra and the UV photoconductivity response, an explanation for the improvement in the light-soaking characteristics of the device with F-TiO_x electron transport layer from the perspective of ITO/TiO_x interface is suggested. Figure 8.12d shows the resulting energy level diagrams of the interface for sol-gel TiO_x and F-TiO_x before light-soaking. In sol-gel TiO_x, due to the lower ΔE_{vac} (0.4 eV) and higher work function (4.5 eV), the Fermi level (E_F) is further away from the conduction band. Since there are more trap states existing in sol-gel TiO_x, the shift of E_F suggests the material has a lower overall carrier concentration due to these unfilled trap states. This phenomenon would influence its barrier width at ITO/TiO_x interface, causing a longer Debye length (L_D), thus forming a larger barrier width between ITO and sol-gel TiO_x (Figure 8.12d). In F-TiO_x, due to the higher ΔE_{vac} (0.5 eV) and the lower work function (4.4 eV), E_F now shifts closer to the conduction band compared to sol-gel TiO_x. Since the trap state density of F-TiO_x is lower than sol-gel TiO_x, the shift of E_F suggests an increase in overall carrier concentration, due to partial filling of the electron trap sites by fluorine atoms in the TiO_x. The increased carrier

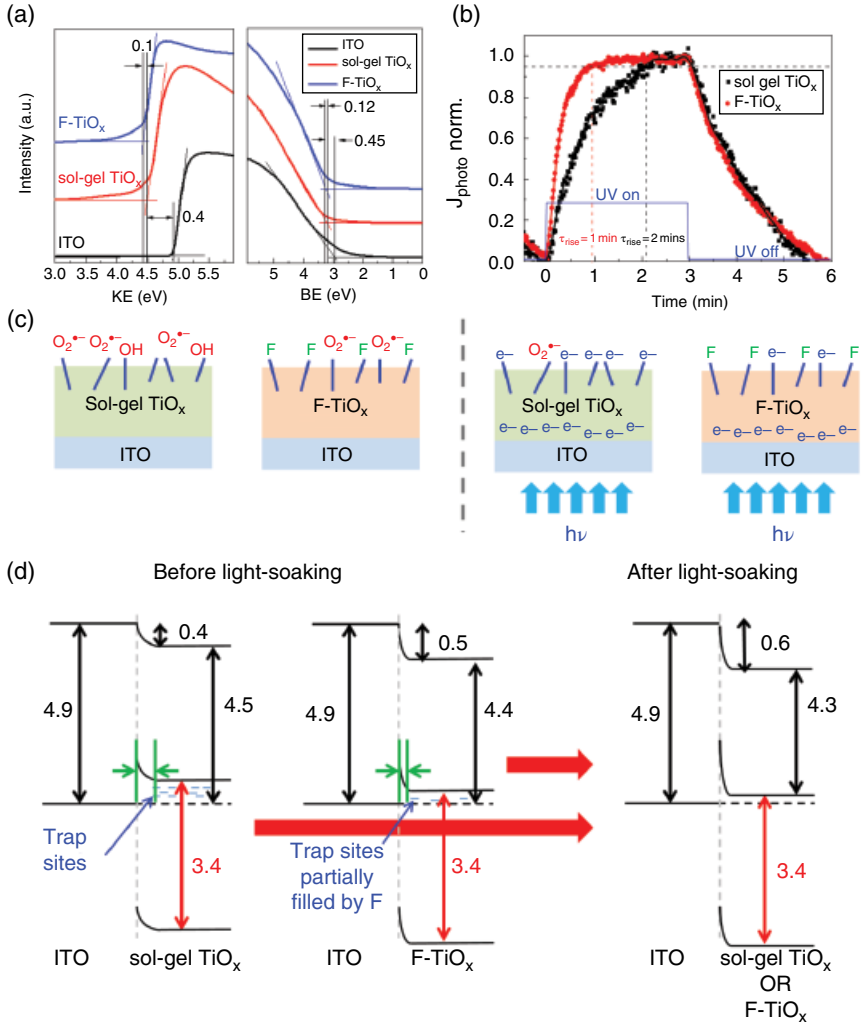

Figure 8.12 (a) Ultraviolet photoelectron spectroscopy (UPS) secondary cut-off spectra of ITO, ITO/sol-gel TiO_x, and ITO/F-TiO_x before light-soaking. (b) Normalized photocurrent of sol-gel TiO_x (O at%) /Ag (■) and F-TiO_x(1.3 F at%)/Ag (•) under UV illumination; the step (—) indicates UV light ON/OFF state. (c) A proposed model for trap-filling phenomenon of sol-gel TiO_x and F-TiO_x before and after light-soaking treatment. (d) Resulting energy band diagrams at ITO/TiO_x interface before light-soaking treatment. All values were obtained from UPS measurements, the bandgaps were estimated by their respective absorption spectra and the arrows at the ITO/TiO_x interface represent the resulting barrier width due to the Fermi level realignment. The evolution behavior of light-soaking effect was adopted from [91]. The figures were adapted from [32]. Reproduced with permission of Royal Society of Chemistry.

concentration will decrease the L_D and narrows the barrier width between ITO and F-TiO_x (Figure 8.12d). This result also corroborate with a previous study that shows a significant increase in carrier concentration of TiO_2 after doping with fluorine [110]. All these phenomena are observed in the ITO/TiO_x interface before light-soaking treatment. When the device is illuminated, the ΔE_{vac} of both TiO_x and F-TiO_x samples would increase and could converge towards a common value after light-soaking. Given the initial ΔE_{vac} value of F-TiO_x (0.5 eV) is nearer to the light-soaked condition (0.6 eV as observed by Kim *et al*. [91]), the time taken to fully fill the trap sites in F-TiO_x is significantly shortened compared to sol-gel TiO_x, as illustrated in Figure 8.12d. Hence, such findings provide a possible explanation to the significant reduction in the light-soaking time in F-TiO_x inverted organic solar cells.

In summary, the F-TiO_x electron transport layer can be used to fabricate a light-soaking free IOSC without affecting the device efficiency. As illustrated in this chapter, it is also versatile enough to be integrated with a wide range of photoactive materials, including conjugated polymer (P3HT), low bandgap (PTB-7) polymer, and small molecule systems (SMDPPEH).

8.6 Conclusions and Outlook

In the development of a more stable organic solar cell, inverted organic solar cells (IOSCs) are normally adopted. However, two serious issues are often encountered while fabricating inverted organic solar cells: the wettability issue and the light-soaking issue. These issues arise from the respective transport layers. The hydrophilic PEDOT:PSS hole transport layer cannot be directly coated onto the hydrophobic P3HT:$PC_{61}BM$ photoactive layer. The conventional n-type metal oxide (TiO_x) electron transport layer, filled with defective trap states, is the cause of the light-soaking issue in the device. Therefore, the strategy of transport layer modification was adopted using unique examples of fluorosurfactant-modified PEDOT:PSS and fluorinated titanium oxide.

In Section 8.5.1, a new type of nonionic fluorosurfactant – Capstone® Dupont™ FS-31 – was proposed as an additive for the PEDOT:PSS hole transport layer for IOSC fabrication. This study was conducted with P3HT:$PC_{61}BM$ in IOSCs with a CFS-31 modified PEDOT:PSS hole transport layer. The modified PEDOT:PSS provided the following attributes: (i) improved device efficiency from 2.1 to 3.1% compared to conventional additives; (ii) uniform coating of PEDOT:PSS onto P3HT:$PC_{61}BM$ without additional additives and surface treatments; (iii) invariant optimal thickness of TiO_x electron transport layers; and (iv) a stable device lifetime that could maintain 80% of its initial efficiency for 400 hours in ambient atmosphere without encapsulation.

In Section 8.5.2, a chemical bath deposited fluorinated titanium oxide (F-TiO_x) electron transport layer was used to address the light-soaking issue in IOSCs for the first time. This study was conducted by comparing the light-soaking characteristics of P3HT:$PC_{61}BM$ based IOSCs using conventional sol-gel TiO_x and F-TiO_x as electron transport layer. Studies on the chemical composition, morphology, and band structures have shown that the presence of fluorine in TiO_x seems to reduce the trap state density in the ETL by partially filling the states prior to light-soaking. The resultant effect greatly shortens the time required for trap filling when the device is illuminated. Without affecting the device efficiency, the light-soaking time was reduced significantly compared to conventional sol-gel coated TiO_x as electron transport layer. Such an electron transport layer has also shown consistent characteristics in a wide range of photoactive layer materials, including low bandgap polymers and small molecules (P3HT, PTB-7, and SMDPPEH). This new device design has the potential to be incorporated into both polymer and small molecule systems, which makes it easily adopted in future high-efficiency materials. This new device design is believed to open up a door of possibility in the development of organic solar cells.

In conclusion, charge transport layer modification is one effective strategy to further pave the way to the realization of air-stable, efficient, and solution-processable organic solar cells. In future new material design and modification, it is important for researchers to gauge potential through the aspects of efficiency, solution-processability, and versatility.

Acknowledgements

SERIS is sponsored by the National University of Singapore (NUS) and Singapore's National Research Foundation (NRF) through the Singapore Economic Development Board (EDB). Fang Jeng Lim expresses his sincere gratitude to the Singapore National Research Foundation (Energy Innovation Programme Office) for providing a PhD scholarship. The authors sincerely acknowledge the Royal Society of Chemistry for permitting use of the figures provided in this chapter. They also gratefully acknowledge Dupont, through MegaChem Limited, Singapore, for supplying Capstone FS-31.

References

1 G.A. Chamberlain, Organic solar cells: a review, *Solar Cells*, **8**, 1983, 47–83.
2 T. Benanti, D. Venkataraman, Organic solar cells: an overview focusing on active layer morphology, *Photosynthesis Research*, **87**, 2006, 73–81.
3 D. Wöhrle, D. Meissner, Organic solar cells, *Advanced Materials*, **3**, 1991, 129–138.

4 C.W. Tang, Two-layer organic photovoltaic cell, *Applied Physics Letters*, **48**, 1986, 183–185.
5 J.J.M. Halls, C.A. Walsh, N.C. Greenham, *et al*., Efficient photodiodes from interpenetrating polymer networks, *Nature*, **376**, 1995, 498–500.
6 G. Yu, J. Gao, J.C. Hummelen, *et al*., Polymer photovoltaic cells: enhanced efficiencies via a network of internal donor-acceptor heterojunctions, *Science*, **270**, 1995, 1789–1790.
7 L. Nian, K. Gao, F. Liu, *et al*., 11% Efficient ternary organic solar cells with high composition tolerance via integrated near-IR sensitization and interface engineering, *Advanced Materials*, **28**, 2016, 8184–8190.
8 Unique - HeliaFilm® perfectly combines design and functionality, 2015. http://www.heliatek.com/en/solar-films; last accessed 29 April 2018.
9 J. You, L. Dou, K. Yoshimura, *et al*., A polymer tandem solar cell with 10.6% power conversion efficiency, *Nature Communications*, **4**, 2013, 1446.
10 S. Guo, C. Brandt, T. Andreev, *et al*., First step into space: performance and morphological evolution of P3HT:PCBM bulk heterojunction solar cells under AM 0 illumination, *ACS Applied Materials & Interfaces*, **6**, 2014, 17902–17910.
11 R.R. Søndergaard, M. Hösel, F.C. Krebs, Roll-to-roll fabrication of large area functional organic materials, *Journal of Polymer Science Part B Polymer Physics*, **51**, 2013, 16–34.
12 G. Li, R. Zhu, Y. Yang, Polymer solar cells, *Science*, **6**, 2012, 153–161.
13 Y. Liu, J. Zhao, Z. Li, *et al*., Aggregation and morphology control enables multiple cases of high-efficiency polymer solar cells, *Nature Communications*, **5**, 2014, 5293. doi: 10.1038/ncomms6293.
14 NREL, Best Research-Cells Efficiencies, 2017. https://www.nrel.gov/pv/assets/images/efficiency-chart.png; last accessed 29 April 2018.
15 J. Zhao, Y. Li, G. Yang, *et al*., Efficient organic solar cells processed from hydrocarbon solvents, *Nature Energy*, **1**, 2016, 15027.
16 M.A. Green, K. Emery, Y. Hishikawa, *et al*., Solar cell efficiency tables (version 49), *Progress in Photovoltaics: Research and Applications*, **25**, 2017, 3–13.
17 Heliatek sets new organic photovoltaic world record efficiency of 13.2%, 2016, http://www.heliatek.com/en/press/press-releases/details/heliatek-sets-new-organic-photovoltaic-world-record-efficiency-of-13-2; last accessed 23 April 2018.
18 Sono-Tek Corporation, 2015, http://www.sono-tek.com/; last accessed 23 April 2018.
19 Solarmer, 2015, http://solarmer.com/; last accessed 23 April 2018.
20 S. Sista, Z. Hong, L.M. Chen, Y. Yang, Tandem polymer photovoltaic cells – current status, challenges and future outlook, *Energy & Environmental Science*, **4**, 2011, 1606–1620.
21 R. Søndergaard, M. Hösel, D. Angmo, *et al*., Roll-to-roll fabrication of polymer solar cells, *Materials Today*, **15**, 2012, 36–49.

22 M.M. Voigt, R.C.I. Mackenzie, C.P. Yau, *et al.*, Gravure printing for three subsequent solar cell layers of inverted structures on flexible substrates, *Solar Energy Materials and Solar Cells*, **95**, 2011, 731–734.

23 N. Espinosa, R. García-Valverde, A. Urbina, *et al.*, Life cycle assessment of ITO-free flexible polymer solar cells prepared by roll-to-roll coating and printing, *Solar Energy Materials and Solar Cells*, **97**, 2012, 3–13.

24 K. Kawano, R. Pacios, D. Poplavskyy, *et al.*, Degradation of organic solar cells due to air exposure, *Solar Energy Materials and Solar Cells*, **90**, 2006, 3520–3530.

25 H. Kim, S. Nam, H. Lee, *et al.*, Influence of controlled acidity of hole-collecting buffer layers on the performance and lifetime of polymer: fullerene solar cells, *The Journal of Physical Chemistry C*, **115**, 2011, 13502–13510.

26 W. Gaynor, J.-Y. Lee, P. Peumans, Fully solution-processed inverted polymer solar cells with laminated nanowire electrodes, *ACS Nano*, **4**, 2009, 30–34.

27 J. Ahmad, K. Bazaka, L.J. Anderson, *et al.*, Materials and methods for encapsulation of OPV: a review, *Renewable and Sustainable Energy Reviews*, **27**, 2013, 104–117.

28 S.K. Hau, H.-L. Yip, N.S. Baek, *et al.*, Air-stable inverted flexible polymer solar cells using zinc oxide nanoparticles as an electron selective layer, *Applied Physics Letters*, **92**, 2008, 253301–253303.

29 M.S. White, D.C. Olson, S.E. Shaheen, *et al.*, Inverted bulk-heterojunction organic photovoltaic device using a solution-derived ZnO underlayer, *Applied Physics Letters*, **89**, 2006, 143517–143513.

30 F.J. Lim, A. Krishnamoorthy, J. Luther, G.W. Ho, Influence of novel fluorosurfactant modified PEDOT:PSS hole transport layer on the performance of inverted organic solar cells, *Journal of Materials Chemistry*, **22**, 2012, 25057–25064.

31 A. Kanwat, J. Jang, Extremely stable organic photovoltaic incorporated with WO_x doped PEDOT: PSS anode buffer layer, *Journal of Materials Chemistry C*, **2**, 2014, 901–907.

32 F.J. Lim, Y.T. Set, A. Krishnamoorthy, *et al.*, Addressing the light-soaking issue in inverted organic solar cells using chemical bath deposited fluorinated TiO_x electron transport layer, *Journal of Materials Chemistry A*, **3**, 2015, 314–322.

33 F.J. Lim, A. Krishnamoorthy, G.W. Ho, Device stability and light-soaking characteristics of high-efficiency benzodithiophene–thienothiophene copolymer-based inverted organic solar cells with F-TiO_x electron-transport layer, *ACS Applied Materials & Interfaces*, **7**, 2015, 12119–12127.

34 F.J. Lim, A. Krishnamoorthy, G.W. Ho, All-in-one solar cell: stable, light-soaking free, solution processed and efficient diketopyrrolopyrrole based small molecule inverted organic solar cells, *Solar Energy Materials and Solar Cells*, **150**, 2016, 19–31.

35 F.A.S. Lima, M.J. Beliatis, B. Roth, T *et al.*, Flexible ITO-free organic solar cells applying aqueous solution-processed V_2O_5 hole transport layer: an outdoor stability study, *APL Materials*, **4**, 2016, 026104.

36 X. Li, W.C.H. Choy, L. Huo, *et al.*, Dual plasmonic nanostructures for high performance inverted organic solar Cells, *Advanced Materials*, **24**, 2012, 3046–3052.

37 C.H. Peters, I.T. Sachs-Quitana, J.P. Kastrop, *et al.*, High efficiency polymer solar cells with long operating lifetimes, *Advanced Energy Materials*, **1**, 2011, 491–494.

38 H.-Y. Park, D. Lim, K.-D. Kim, S.-Y. Jang, Performance optimization of low-temperature-annealed solution-processable ZnO buffer layers for inverted polymer solar cells, *Journal of Materials Chemistry A*, **1**, 2013, 6327–6334.

39 K. Norrman, M.V. Madsen, S.A. Gevorgyan, F.C. Krebs, Degradation patterns in water and oxygen of an inverted polymer solar cell, *Journal of the American Chemical Society*, **132**, 2010, 16883–16892.

40 Z. He, C. Zhong, S. Su, *et al.*, Enhanced power-conversion efficiency in polymer solar cells using an inverted device structure, *Nature Photonics*, **6**, 2012, 593–597.

41 R. Lampande, G.W. Kim, J. Boizot, *et al.*, A highly efficient transition metal oxide layer for hole extraction and transport in inverted polymer bulk heterojunction solar cells, *Journal of Materials Chemistry A*, **1**, 2013, 6895–6900.

42 S.-H. Liao, H.-J. Jhuo, Y.-S. Cheng, S.-A. Chen, Fullerene derivative-doped zinc oxide nanofilm as the cathode of inverted polymer solar cells with low-bandgap polymer (PTB7-Th) for high performance, *Advanced Materials*, **25**, 2013, 4766–4771.

43 G. Wang, T. Jiu, G. Tang, *et al.*, Interface modification of ZnO-based inverted PTB7:PC71BM organic solar cells by cesium stearate and simultaneous enhancement of device parameters, *ACS Sustainable Chemistry & Engineering*, **2**, 2014, 1331–1337.

44 V. Vohra, K. Kawashima, T. Kakara, *et al.*, Efficient inverted polymer solar cells employing favourable molecular orientation, *Nature Photonics*, **9**, 2015, 403–408.

45 T.-Y. Juang, Y.-C. Hsu, B.-H. Jiang, C.-P. Chen, Highly efficient inverted organic photovoltaics containing aliphatic hyperbranched polymers as cathode modified layers, *Macromolecules*, **49**, 2016, 7837–7843.

46 C. Zhou, G. Zhang, C. Zhong, *et al.*, Toward high efficiency polymer solar cells: influence of local chemical environment and morphology, *Advanced Energy Materials*, **7**, 2017, 1601081.

47 K.-L. Ou, D. Tadytin, K.X. Steirer, *et al.*, Titanium dioxide electron-selective interlayers created by chemical vapor deposition for inverted configuration organic solar cells, *Journal of Materials Chemistry A*, **1**, 2013, 6794–6803.

48 S. Trost, T. Becker, A. Polywka, *et al.*, Avoiding photoinduced shunts in organic solar cells by the use of tin oxide (SnO_x) as electron extraction material instead of ZnO, *Advanced Energy Materials*, 2016.

49 H.-H. Liao, L.-M. Chen, Z. Xu, *et al.*, Highly efficient inverted polymer solar cell by low temperature annealing of Cs_2CO_3 interlayer, *Applied Physics Letters*, **92**, 2008, 173303–173303.

50 Y.I. Lee, J.H. Youn, M.S. Ryu, *et al*., Electrical properties of inverted poly (3-hexylthiophene): Methano-fullerene 6, 6.-phenyl C71-butyric acid methyl ester bulk hetero-junction solar cell with Cs_2CO_3 and MoO_3 layers, *Solar Energy Materials and Solar Cells*, **95**, 2011, 3276–3280.

51 H. Sun, J. Weickert, H.C. Hesse, L. Schmidt-Mende, UV light protection through TiO_2 blocking layers for inverted organic solar cells, *Solar Energy Materials and Solar Cells*, **95**, 2011, 3450–3454.

52 J. Ouyang, "Secondary doping" methods to significantly enhance the conductivity of PEDOT:PSS for its application as transparent electrode of optoelectronic devices, *Displays*, **34**, 2013, 423–436.

53 C. Stenta, Study and characterization of ZnPc:C_{60}/MoO_x interface in organic solar cells by means of photoelectron spectroscopy, Masters thesis, Universidade Nova de Lisboa, Portugal, 2013.

54 T. Wahl, S. Zellmer, J. Hanisch, *et al*., Thin indium tin oxide nanoparticle films as hole transport layer in inverted organic solar cells, *Thin Solid Films*, **616**, 2016, 419–424.

55 C.J. Brabec, V. Dyakonov, U. Scherf, *Organic Photovoltaics: Materials, Device Physics, and Manufacturing Technologies*, Wiley-VCH, 2008.

56 M. Glatthaar, M. Niggemann, B. Zimmermann, *et al*., Organic solar cells using inverted layer sequence, *Thin Solid Films*, **491**, 2005, 298–300.

57 W.H. Baek, M. Choi, T.S. Yoon, *et al*., Use of fluorine-doped tin oxide instead of indium tin oxide in highly efficient air-fabricated inverted polymer solar cells, *Applied Physics Letters*, **96**, 2010, 133506.

58 T. Stubhan, H. Oh, L. Pinna, *et al*., Inverted organic solar cells using a solution processed aluminum-doped zinc oxide buffer layer, *Organic Electronics*, **12**, 2011, 1539–1543.

59 P.P. Boix, J. Ajuria, R. Pacios, G. Garcia-Belmonte, Carrier recombination losses in inverted polymer: fullerene solar cells with ZnO hole-blocking layer from transient photovoltage and impedance spectroscopy techniques, *Journal of Applied Physics*, **109**, 2011, 074514. doi: 10.1063/1.3561437.

60 C.-P. Chen, Y.-D. Chen, S.-C. Chuang, High-performance and highly durable inverted organic photovoltaics embedding solution-processable vanadium oxides as an interfacial hole-transporting layer, *Advanced Materials*, **23**, 2011, 3859–3863.

61 S.W. Heo, K.H. Baek, T.H. Lee, *et al*., Enhanced performance in inverted polymer solar cells via solution process: Morphology controlling of PEDOT:PSS as anode buffer layer by adding surfactants, *Organic Electronics*, **14**, 2013, 1629–1635.

62 W. Xiangdong, P. Qing, Z. Weiguo, L. Gangtie, High performance of inverted polymer solar cells with cobalt oxide as hole-transporting layer, *Semiconductor Science and Technology*, **30**, 2015, 055001.

63 Y. Ka, E. Lee, S.Y. Park, *et al*., Effects of annealing temperature of aqueous solution-processed ZnO electron-selective layers on inverted polymer solar cells, *Organic Electronics*, **14**, 2013, 100–104.

64 J.-C. Wang, W.-T. Weng, M.-Y. Tsai, *et al*., Highly efficient flexible inverted organic solar cells using atomic layer deposited ZnO as electron selective layer, *Journal of Materials Chemistry*, **20**, 2010, 862–866.
65 S. Trost, K. Zilberberg, A. Behrendt, T. Riedl, Room-temperature solution processed SnOx as electron extraction layer for inverted organic solar cells with superior thermal stability, *Journal of Materials Chemistry*, **22**, 2012, 16224–16229.
66 O. Wiranwetchayan, Z. Liang, Q. Zhang, *et al*., The role of oxide thin layer in inverted structure polymer solar cells, *Materials Sciences and Applications*, **2**, 2011, 1697–1701.
67 E. Berner, T. Jager, T. Lanz, *et al*., Influence of crystalline titanium oxide layer smoothness on the performance of inverted organic bilayer solar cells, *Applied Physics Letters*, **102**, 2013, 4.
68 T. Kuwabara, H. Sugiyama, M. Kuzuba, *et al*., Inverted bulk-heterojunction organic solar cell using chemical bath deposited titanium oxide as electron collection layer, *Organic Electronics*, **11**, 2010, 1136–1140.
69 C.D. Lokhande, Chemical deposition of metal chalcogenide thin films, *Materials Chemistry and Physics*, **27**, 1991, 1–43.
70 Y. Masuda, K. Kato, Anatase TiO_2 films crystallized on SnO_2:F substrates in an aqueous solution, *Thin Solid Films*, **516**, 2008, 2547–2552.
71 A.M. More, T.P. Gujar, J.L. Gunjakar, *et al*., Growth of TiO_2 nanorods by chemical bath deposition method, *Applied Surface Science*, **255**, 2008, 2682–2687.
72 C. Xu, D. Gao, Two-stage hydrothermal growth of long ZnO nanowires for efficient TiO_2 nanotube-based dye-sensitized solar cells, *The Journal of Physical Chemistry C*, **116**, 2012, 7236–7241.
73 H. Han, P. Sudhagar, T. Song, *et al*., Three dimensional-TiO_2 nanotube array photoanode architectures assembled on a thin hollow nanofibrous backbone and their performance in quantum dot-sensitized solar cells, *Chemical Communications*, **49**, 2013, 2810–2812.
74 S. Supothina, M.R. De Guire, Characterization of SnO_2 thin films grown from aqueous solutions, *Thin Solid Films*, **371**, 2000, 1–9.
75 H. Unuma, H. Takabatake, K. Watanabe, *et al*., Preparation of SnO_2 thin films by the oxidative-soak-coating method, *Journal of Materials Science Letters*, **21**, 2002, 1241–1243.
76 H.-C. Cheng, C.-F. Chen, C.-C. Lee, Thin-film transistors with active layers of zinc oxide (ZnO) fabricated by low-temperature chemical bath method, *Thin Solid Films*, **498**, 2006, 142–145.
77 Z.Y. Wu, J.H. Cai, G. Ni, ZnO films fabricated by chemical bath deposition from zinc nitrate and ammonium citrate tribasic solution, *Thin Solid Films*, **516**, 2008, 7318–7322.
78 M.-K. Lee, C.-H. Fan, H.-C. Wang, C.-Y. Chang, Fluorine passivation of titanium oxide films on ito/glass grown by liquid phase deposition for electrochroism, *Journal of The Electrochemical Society*, **158**, 2011, D511–D514.

79 H. Khallaf, C.-T. Chen, L.-B. Chang, *et al*., Chemical bath deposition of SnO_2 and Cd_2SnO_4 thin films, *Applied Surface Science*, **258**, 2012, 6069–6074.

80 H. Oh, J. Krantz, I. Litzov, *et al*., Comparison of various sol-gel derived metal oxide layers for inverted organic solar cells, *Solar Energy Materials and Solar Cells*, **95**, 2011, 2194–2199.

81 Y.-J. Noh, S.-I. Na, S.-S. Kim, Inverted polymer solar cells including ZnO electron transport layer fabricated by facile spray pyrolysis, *Solar Energy Materials and Solar Cells*, **117**, 2013, 139–144.

82 D. Zhang, W.C.H. Choy, F. Xie, *et al*., Plasmonic electrically functionalized TiO_2 for high-performance organic solar cells, *Advanced Functional Materials*, **23**, 2013, 4255–4261.

83 D. Yang, P. Fu, F. Zhang, *et al*., High efficiency inverted polymer solar cells with room-temperature titanium oxide/polyethylenimine films as electron transport layers, *Journal of Materials Chemistry A*, **2**, 2014, 17281–17285.

84 S. Trost, A. Behrendt, T. Becker, *et al*., Tin oxide (SnO_x) as universal "light-soaking" free electron extraction material for organic solar cells, *Advanced Energy Materials*, **5**, 2015, 1500277.

85 B. Wu, Z. Wu, Q. Yang, *et al*., Improvement of charge collection and performance reproducibility in inverted organic solar cells by suppression of ZnO subgap states, *ACS Applied Materials & Interfaces*, **8**, 2016, 14717–14724.

86 Y. Yan, F. Cai, L. Yang, *et al*., Light-soaking-free inverted polymer solar cells with an efficiency of 10.5% by compositional and surface modifications to a low-temperature-processed TiO_2 electron-transport layer, *Advanced Materials*, **29**, 2017, 1604044.

87 J.D. Servaites, M.A. Ratner, T.J. Marks, Organic solar cells: a new look at traditional models, *Energy & Environmental Science*, **4**, 2011, 4410–4422.

88 B. Fan, Y. Xia, J. Ouyang, Novel ways to significantly enhance the conductivity of transparent PEDOT: PSS, *Proceedings of SPIE*, **7415**, 2009, 74151Q.

89 D.J. Lipomi, B.C.K. Tee, M. Vosgueritchian, Z. Bao, Stretchable organic solar cells, *Advanced Materials*, **23**, 2011, 1771–1775.

90 N.M. Kovalchuk, A. Trybala, V. Starov, *et al*., Fluoro- vs hydrocarbon surfactants: Why do they differ in wetting performance? *Advances in Colloid and Interface Science*, **210**, 2014, 65–71.

91 J. Kim, G. Kim, Y. Choi, *et al*., Light-soaking issue in polymer solar cells: Photoinduced energy level alignment at the sol-gel processed metal oxide and indium tin oxide interface, *Journal of Applied Physics*, **111**, 2012, 114511.

92 T. Kuwabara, C. Iwata, T. Yamaguchi, K. Takahashi, Mechanistic insights into UV-induced electron transfer from PCBM to titanium oxide in inverted-type organic thin film solar cells using AC impedance spectroscopy, *ACS Applied Materials & Interfaces*, **2**, 2010, 2254–2260.

93 O. Pachoumi, C. Li, Y. Vaynzof, *et al*., Improved performance and stability of inverted organic solar cells with sol–gel processed, amorphous mixed metal

oxide electron extraction layers comprising alkaline earth metals, *Advanced Energy Materials*, **3**, 2013, 1428–1436.

94 W. Wei, C. Zhang, D. Chen, *et al.*, Efficient "light-soaking"-free inverted organic solar cells with aqueous solution processed low-temperature ZnO electron extraction layers, *ACS Applied Materials & Interfaces*, **5**, 2013, 13318–13324.

95 M. Dusza, W. Strek, F. Granek, Significance of light-soaking effect in proper analysis of degradation dynamics of organic solar cells, *Journal of Photonics for Energy*, **6**, 2016, 035503–035503.

96 F.C. Krebs, T. Tromholt, M. Jørgensen, Upscaling of polymer solar cell fabrication using full roll-to-roll processing, *Nanoscale*, **2**, 2010, 873–886.

97 S. Trost, K. Zilberberg, A. Behrendt, *et al.*, Overcoming the "light-soaking" issue in inverted organic solar cells by the use of Al:ZnO electron extraction layers, *Advanced Energy Materials*, **3**, 2013, 1437–1444.

98 M.R. Lilliedal, A.J. Medford, M.V. Madsen, *et al.*, The effect of post-processing treatments on inflection points in current–voltage curves of roll-to-roll processed polymer photovoltaics, *Solar Energy Materials and Solar Cells*, **94**, 2010, 2018–2031.

99 Z. Lin, C. Jiang, C. Zhu, J. Zhang, Development of inverted organic solar cells with TiO_2 interface layer by using low-temperature atomic layer deposition, *ACS Applied Materials & Interfaces*, **5**, 2013, 713–718.

100 H. Schmidt, K. Zilberberg, S. Schmale, *et al.*, Transient characteristics of inverted polymer solar cells using titanium oxide interlayers, *Applied Physics Letters*, **96**, 2010, 243305–243301.

101 R. Mauer, I.A. Howard, F. Laquai, Effect of nongeminate recombination on fill factor in polythiophene/methanofullerene organic solar cells, *Journal of Physical Chemistry Letters*, **1**, 2010, 3500–3505.

102 F. Zhang, X. Xu, W. Tang, *et al.*, Recent development of the inverted configuration organic solar cells, *Solar Energy Materials and Solar Cells*, **95**, 2011, 1785–1799.

103 N. Grossiord, J.M. Kroon, R. Andriessen, P.W.M. Blom, Degradation mechanisms in organic photovoltaic devices, *Organic Electronics*, **13**, 2012, 432–456.

104 G. Kim, J. Kong, J. Kim, *et al.*, Overcoming the light-soaking problem in inverted polymer solar cells by introducing a heavily doped titanium sub-oxide functional layer, *Advanced Energy Materials*, **5**, 2015, 1401298.

105 C.X. Lei, H. Zhou, Z.D. Feng, *et al.*, Liquid phase deposition (LPD) of TiO_2 thin films as photoanodes for cathodic protection of stainless steel, *Journal of Alloys and Compounds*, **513**, 2012, 552–558.

106 Y. Wang, H. Zhang, P. Liu, *et al.*, Nature of visible-light responsive fluorinated titanium dioxides, *Journal of Materials Chemistry A*, **1**, 2013, 12948–12953.

107 M. Samadpour, P.P. Boix, S. Gimnez, *et al*., Fluorine treatment of TiO_2 for enhancing quantum dot sensitized solar cell performance, *The Journal of Physical Chemistry C*, **115**, 2011, 14400–14407.

108 S.M. Pawar, B.S. Pawar, J.H. Kim, *et al*., Recent status of chemical bath deposited metal chalcogenide and metal oxide thin films, *Current Applied Physics*, **11**, 2011, 117–161.

109 B. Ecker, H.-J. Egelhaaf, R. Steim, *et al*., Understanding S-shaped current–voltage characteristics in organic solar cells containing a TiO_x interlayer with impedance spectroscopy and equivalent circuit analysis, *The Journal of Physical Chemistry C*, **116**, 2012, 16333–16337.

110 W.Q. Fang, X.L. Wang, H. Zhang, *et al*., Manipulating solar absorption and electron transport properties of rutile TiO_2 photocatalysts via highly n-type F-doping, *Journal of Materials Chemistry A*, **2**, 2014, 3513–3520.

9

Fabrication of Metal Top Electrode via Solution-based Printing Technique for Efficient Inverted Organic Solar Cells

Navaneethan Duraisamy[1], Kavitha Kandiah[2], Kyung-Hyun Choi[3], Dhanaraj Gopi[1], Ramesh Rajendran[4], Pazhanivel Thangavelu[4], and Maadeswaran Palanisamy[5]

[1] *Department of Chemistry, Periyar University, India*
[2] *Department of Microbiology, Periyar University, India*
[3] *Department of Mechatronics Engineering, Jeju National University, Republic of Korea*
[4] *Department of Physics, Periyar University, India*
[5] *Department of Energy Studies, Periyar University, India*

9.1 Introduction

Increasing global warming and extreme weather changes with respect to excessive use of fossil fuels and carbon dioxide (CO_2) emissions tend to concentrate research efforts on renewable energy sources. Numerous impressive renewable energy sources are exist, such as wind energy, hydropower, solar cells, solar thermal, wave, and tidal power. Among these energy sources, solar energy based photovoltaic (PV) technologies are subject to extensive attention to fulfill the future energy needs [1–4]. The sun is the main source of energy for our planet, providing total radiation of approximately 3×10^{24} J/year. Whereas, 1.7×10^5 TW energy reaches the earth's surface, about 600 TW is available for practical application and 60 TW could be produced via solar granges, which have an efficiency of 10% [5]. These records tend to clear the possibility of using PV technology as a solution for the global energy demand [2]. The production of electricity from renewable energy sources could be increased due to the improvement of renewable energy installed capacity, as shown in Figure 9.1. Moreover, India alone set the goal up to 2022 to produce solar power. In this respect, India will add 15 and 16 GW of solar power capacity in the years 2018 and 2019, respectively (Figure 9.2).

Generally, PV cells are classified into three types: first, second, and third generation devices, with respect to their technology. First generation devices

Rational Design of Solar Cells for Efficient Solar Energy Conversion, First Edition.
Edited by Alagarsamy Pandikumar and Ramasamy Ramaraj.

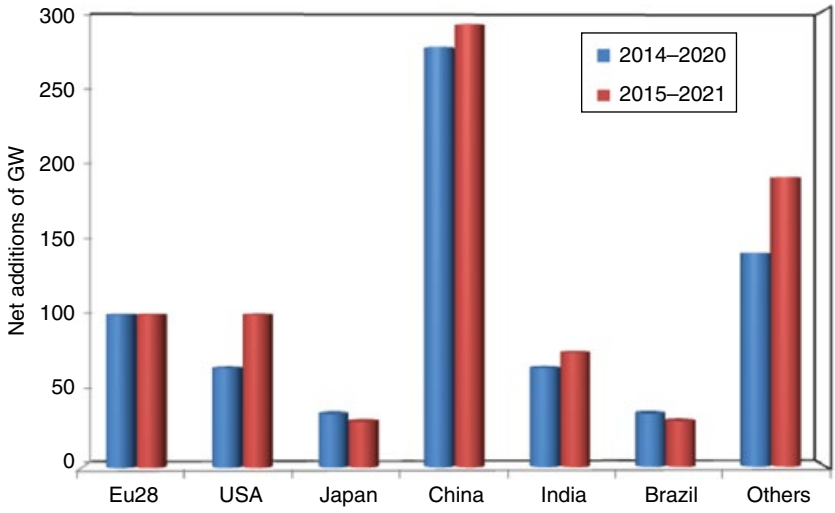

Figure 9.1 Renewable electricity capacity growth (GW).

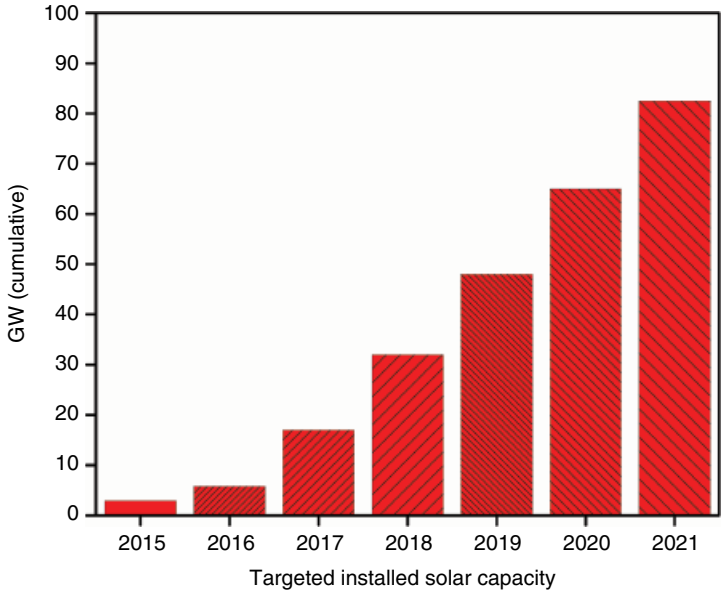

Figure 9.2 India sets targets to reach ambitious 2021 solar goal.

are single- or multicrystalline silicon-based solar cells (p-n junction) for harvesting energy and represent about 85% of total market share in PV technology. Silicon-based PV devices achieve around 20% efficiency [6]. However, these devices have some drawbacks, such as high fabrication temperatures, high cost, they occupy a large space, high purity requirements for silicon crystals, and the negative environmental impact of the processing technologies, which need be resolved for the large scale commercial production of low cost PV devices [7]. Inorganic thin film based solar cells are second generation PV devices (roughly 15% market share). Cadmium telluride (CdTe) and copper indium (gallium) diselenide (CI(G)S) are mostly used in inorganic thin film solar cells. Thin film cell structures mainly include single, double, or multiple junctions, i.e. the difference between p-i-n junction layers in the device structures. To improve cell efficiencies, several fabrication processes would be involved to achieve uniform thin layers with different bandgaps, which lead to increased fabrication cost. Compared with first generation PV devices, second generation PV devices are less efficient (about 14%). Numerous experts have an eye on the development of thin film devices with improved efficiency and reduced fabrication costs [8].

In order to develop low cost PV devices there has been in-depth research over the last few decades. The next (third-) generation PV devices are receiving considerably more attention than first and second generation PV devices due to their cost-effective fabrication process, flexibility, and easy-to-optimize device efficiency. Third generation PV devices, such as dye-sensitized solar cells (DSSCs), polymer or organic solar cells (OSCs), quantum dot solar cells, and hetero junction cells, have not been commercialized so far [9, 10]. In this regards, organic solar cells or organic photovoltaic cells (OPV) are considered of unique interest for efficient conversion of visible light into electricity.

9.2 Organic Photovoltaic Cells

Organic photovoltaic cells deal with conductive organic polymers or small organic molecules. They have an ability to convert low energy infrared (IR) or high energy ultraviolet (UV) into electricity with respect to the bandgap of the light absorbing material (active layer). OPVs have several advantages, such as light weight, low cost, flexibility, semitransparency, solution-processability, and they are feasible for large area production at low temperature. In general, OPVs materials have a conjugated π bond (alternating single and double bond structure), which is formed via sp^2-hybridized carbon atoms. The energy bandgap for π–π^* transitions provides two energy states, the highest occupied molecular orbital (HOMO) and the lowest unoccupied molecular orbital (LUMO) for π and π^* orbitals, respectively. This energy separation plays a vital

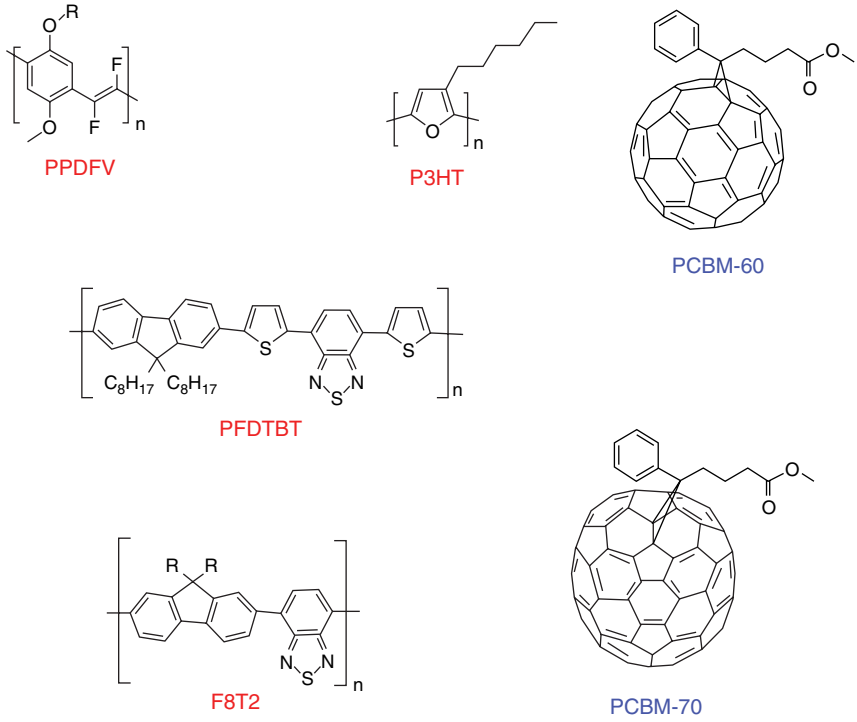

Figure 9.3 Organic conducting materials (donor and acceptor) for OPVs devices.

role in determining the energy bandgap of corresponding materials (typically, organic materials have an energy bandgap of 1–4 eV). Figure 9.3 illustrated several organic conducting materials (donor and acceptor) for OPVs.

9.3 Working Principle

The working principle of OPVs is mainly consists of five consecutive steps: (i) an electron-hole pair (exciton) is created by absorption of light radiation; (ii) diffusion of the exciton into active interfaces within its lifetime; (iii) separation of free charge carriers from the electron-hole pair; (iv) charge carrier transport into the electrodes interface; and (v) charge collections at the respective electrodes, which are illustrated in Figure 9.4.

The absorption of light can stimulate an electron from the HOMO to the LUMO level. In organic materials, it is not so easy to produce free charge carriers. Therefore, organic semiconducting materials first generate an exciton (bound electron-hole pair), which leads to further diffusion into donor–acceptor interfaces within its lifetime (in nanoseconds) [11, 12]. Excitons

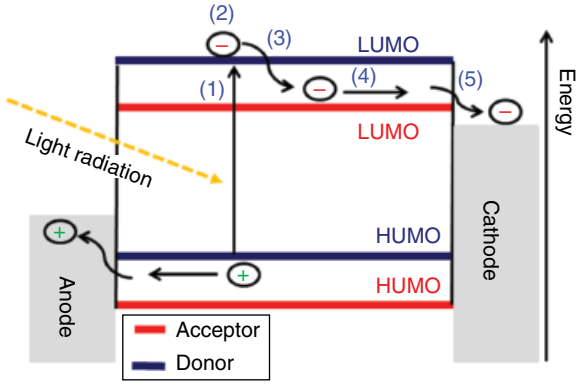

Figure 9.4 Mechanism of photocurrent generation in an OPV device.

travel for a certain distance before they are recombined through conjugated chain segments. This diffusion length is determined by the exciton migration as given by:

$$L_D = \sqrt{D \times \tau} \tag{9.1}$$

where D is the exciton diffusivity and τ is the natural lifetime of the exciton. The exciton diffusion length (L_D) is usually much lower than the optical absorption length of organic materials 1/α [13]. To improve the exciton diffusion efficiency, bulk heterojunctions (with a large interfacial area) are generally used to shorten the exciton travel distance [14]. Moreover, the low dielectric constant of organic material needs excess energy to overcome the coulombic attraction for the separation of the exciton (strong binding energy) into free charge carriers. This can be overcome using heterojunction materials because its potential drop compensates exciton binding energy, allowing for exciton separation [15, 16]. Further, the charge carriers (electrons and holes) tend to reach the device external contacts via conducing materials. The charge transport efficiency is measured by the material mobility (μ) (defined as the velocity of average particle with respect to an electric force per unit electric field (E) [17]). In OPVs, a continuous pathway is essential in each conducting material to transport the charge carriers to the external contacts. The relationship between electric field, mobility, and the charge carrier transport length ($L_{e,h}$) is defined as:

$$L_{e,h} = \mu_{e,h} \tau_{e,h} E \tag{9.2}$$

where $\tau_{e,h}$ is the charge carrier lifetime and $\mu_{e,h}$ is the mobility of charge lifetime.

9.4 Device Architecture

OPV performance not only depends on the electrical properties of the organic conducting materials but also on device architecture and the surface morphology of the active layer [18]. In general, normal OPV devices are of the sandwich type – an active layer (conducting polymers) interfaced between two metal electrodes; they are classified into four major types: monolayer, planar heterojunction, bulk heterojunction, and order bulk heterojunction devices.

9.4.1 Single Layer or Monolayer Device

Monolayer OPVs are made up of single organic conducting polymer (active layer) sandwiched between two asymmetric metal electrodes with different work functions (Figure 9.5a). The formation of an exciton (absorption of light by active layer) tends to split into charge carriers due to the influence of potential generated by the asymmetric electrodes work function. This further drives the electrons and holes into the respective electrodes. Monolayer OPVs commonly frail performance is due to poor exciton dissociation.

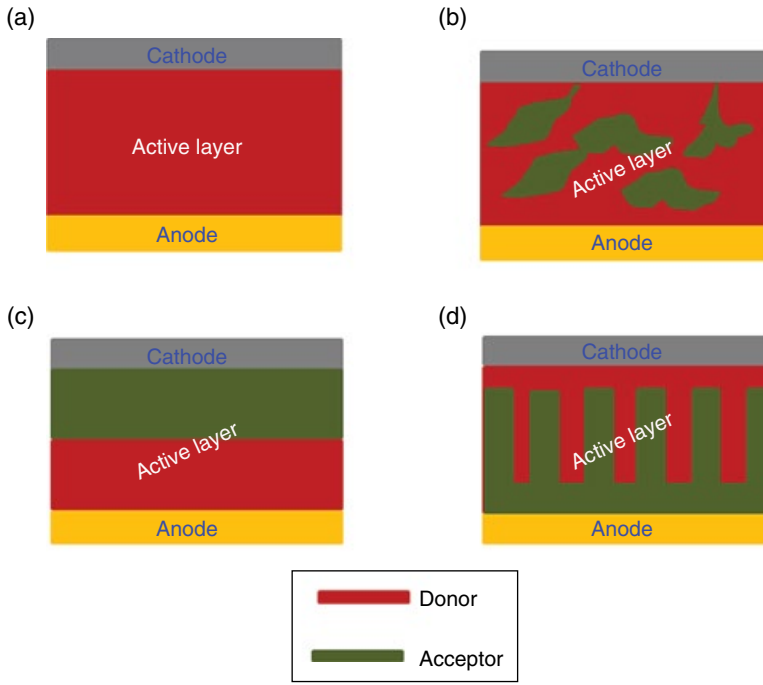

Figure 9.5 OPV device architectures: (a) single layer, (b) planar heterojunction, (c) bulk heterojunction, and (d) ordered bulk heterojunction.

9.4.2 Planar Heterojunction Device

This type of device uses two different organic conducting materials stacked in layers between two different metal electrodes (Figure 9.5b). These two organic layers (different electron affinity and ionization energy) significantly increase the exciton splitting efficiency compared to that of a single layer device. The diffusion length of the exciton is in the order of 10 nm. In the OPV device, the organic conducting polymer film thickness required for adequate light absorption is several tens of nanometers; this significantly diminishes the excitons (electrons and hole) reaching the hetrojunction interface before electron-hole recombination, which severely reduces device efficiency.

9.4.3 Bulk Heterojunction Device

This type of device is prepared by blending of donor and acceptor materials in a layer of several tens of nanometer uniformly distributed between two different electrodes (Figure 9.5c). This allow excitons to readily reach an active layer interface within short period of time, resulting in an enhanced power conversion efficiency, over 5% more than the previous type devices. However, inherently random interpenetrating network morphology and the isolation of the donor and acceptor type phases lead to poor charge carrier transport and weak charge collection efficiency of the respective electrodes due to noncontinuous pathways in the bulk heterojunction device.

9.4.4 Ordered Bulk Heterojunction Device

In this device, conducting donor and acceptor materials are interlocked like the fingers of two clasped hands on a nanometer scale, while directly contacting their corresponding electrodes (Figure 9.5d). This type of architecture severely improves the exciton splitting rate because of the massive interfaces within close proximity to the diffusion length. Further, it affords a suitable conducting pathway for the charge carriers to travel towards the respective electrodes. This also has some limitations, such as weak hole mobility, allowing recombination of electrons because exciton diffusion length in organic conducting materials is <20 nm. Therefore, space between the nanostructures should be reduced to promote charge separation and also buffer layers (hole or electron selecting layer) introduced in between active layers and current collector for further enhancement of carrier separation and fast charge transfer to the respective electrodes. In this respect, a typical OPV device consists of the following layers: transparent conductive electrode, hole selecting layer, active layer, and top contact electrode. The normal architecture of an OPV device is shown in Figure 9.6a.

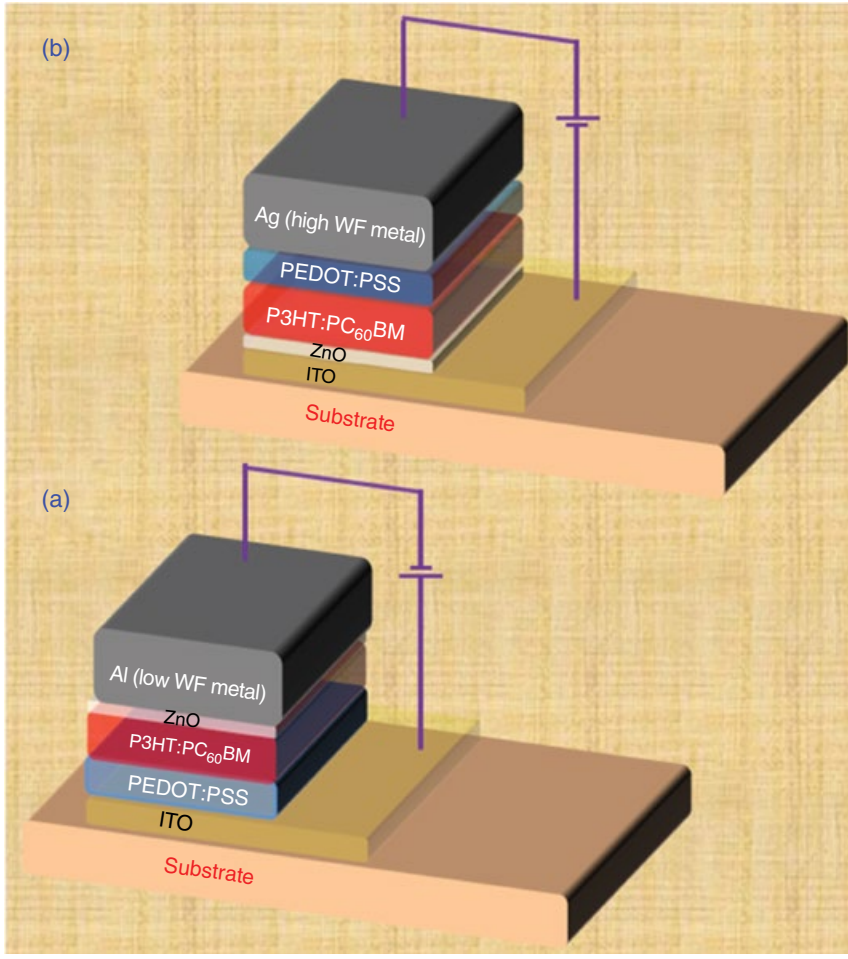

Figure 9.6 Schematic illustration of an OPV device: (a) conventional structure and (b) inverted structure.

9.4.5 Inverted Organic Solar Cells

A typical OPV device uses poly(3,4-ethylenedioxythiophene):poly(styrenesulfonate) (PEDOT:PSS) as the anodic buffer layer and indium tin oxide (ITO) as an anode. The acidic nature of PEDOT:PSS may destroy the bottom ITO layer [19, 20]. In addition, the deposition of metal top contact aluminum may penetrate into the active layer, resulting in alteration of the physicochemical properties of the active layers; also, the top contact readily undergoes oxidation in the presence of atmospheric air [21, 22]. All these phenomena seriously affect the device stability and lifetime. To avoid these issues, buffer layers may be used on

both sides of the active layers but in reverse manner; this is known as an inverted type organic device, as shown in Figure 9.6b.

Inverted organic solar cells significantly improve the device stability and lifetime due to the influence of less air sensitive metals (silver or gold) used as a hole collecting electrode and ITO as an electron collecting electrode. In addition, the metal oxide layers, such as zinc oxide (ZnO), titanium oxide (TiO_2,) and organic conducting polymer of PEDOT:PSS, introduced act as buffer layers between the electrodes and active layers. These layers play a vital role in reducing or controlling oxygen and metal diffusion into the active layer and also prevent the corrosion of the ITO electrode [23–25].

9.5 Fabrication Process

Numerous research groups have reported the solution-based spin coating, dip coating, and nonvacuum printing techniques of screen printing, doctor blading, ink jet printing, and spray coating for the deposition of the active layer and buffer layer in OPV device fabrication [26–29]. These efforts are significantly focused on the large-scale production of organic (active) layers, except for the top electrode. The vacuum-based thermal evaporation method has been extensively used for the deposition of metal top electrode [26, 30, 31]. These methods face some severe limitations, such as use of complex processes, expensive vacuum system, and well-ordered atmosphere, and may cause thermal destruction to predeposited organic layers [32, 33]. These issues can be overcome by introducing solution-based techniques for top electrode preparation in an inverted OPV device. But the solution-based deposition of metal nanoparticles is not so easy because of solvent influence on the predeposited organic layer [34]. This limitation can be controlled using the advanced printing technique of hybrid electrohydrodynamic atomization (Hybrid-EHDA).

9.5.1 Hybrid-EHDA Technique

The Hybrid-EHDA method is the most auspicious technique for printing (patterns and thin film) of functional materials [35–37]. It affords low cost, high processing speed, less material wastage, and printing of a wide area in a very short period [36, 38]. The basic principle of this technique is the atomization of starting precursors under pneumatic pressure and electric potential, which overcome the liquid surface tension and produce surface charged droplets with a diameter range from submicron to nanoscale. A random distribution of small droplets is deposited on the respective substrate. The main advantage of this method is the ability to cover a broad area with the rapid drying of fine droplets (in the order of microseconds), resulting in the control of the solvent effect on the underlying organic layers. Additionally, printed layers required a very low

temperature for annealing compared with other solution-based process [34, 36]. A schematic illustration of Hybrid-EHDA technique is shown in Figure 9.7. A plastic syringe is filled with precursor solution or ink and the ink flow is controlled by a piston pump. The syringe is directly connected to a capillary nozzle holder.

A metallic nozzle is fixed at the bottom of nozzle holder for the purpose of spraying or atomization. The electric potential is applied between the metallic nozzle and the substrate via a high voltage power supply (0–21 kV). The substrate holder is grounded. The applied potential is used to control the spray process, with the further influence of the pneumatic pressure (pump pressure range 0–5 bar). The substrate and nozzle holder movements are controlled in the x-, y- and z-axes (interfaced with computer software). The overall spray process is observed via CCD camera, which is interfaced with PC. In the Hybrid-EHDA technique, the homogeneous spray can be achieved by optimizing the following parameters [39–42]:

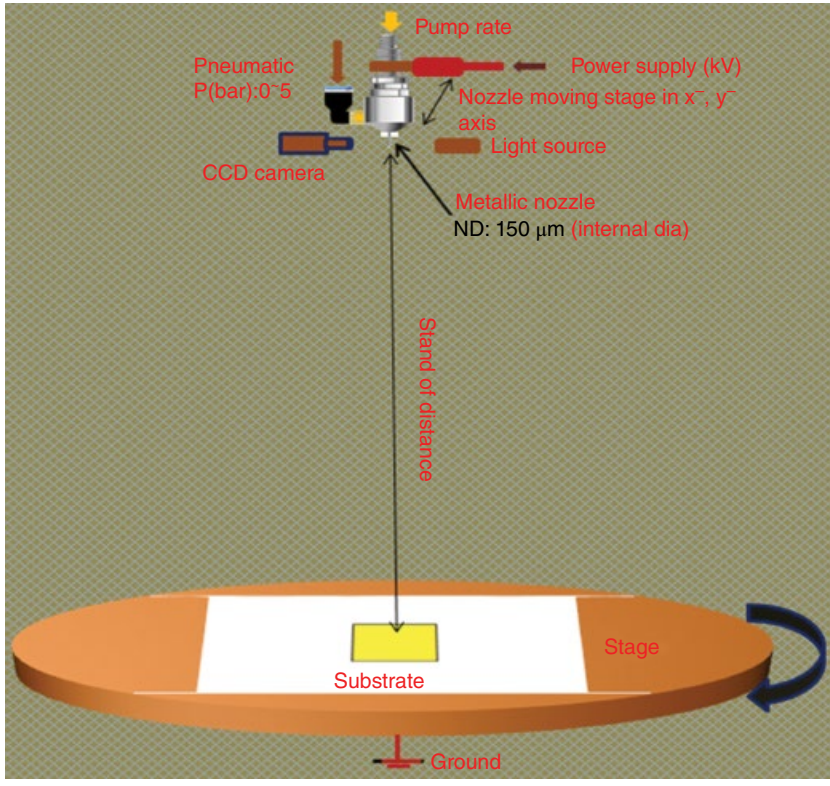

Figure 9.7 Schematic illustration of the Hybrid-EHDA set-up.

1) Flow rate.
2) Applied potential.
3) Pneumatic pressure.
4) Stand-off distance.
5) Nozzle diameter.
6) Precursor solution or ink properties

9.5.1.1 Flow Rate

Flow rate has an important role in achieving the desired charged droplets of ink or precursor solution with constant physicochemical properties. When the flow rate increases, the applied potential and pneumatic pressure on the liquid need to be increased to achieve an homogeneous spray. At high flow rate, the ejection of charged droplets with a larger diameter occurs due to the larger droplet diameter and the increase in the kinetic energy of the charged droplets; these severely affect the film uniformity. The formation of an homogeneous spray with appropriate charged droplets is difficult to achieve at minimum flow rate. Therefore, it is very important to use the optimum ink flow rate to achieve atomized droplets (charged small size droplets) under controlled applied potential and pneumatic pressure in the deposition of functional thin films using the Hybrid-EHDA technique.

9.5.1.2 Applied Potential

The applied potential (electric field) is an essential parameter in the spray process. The homogeneous spray is obtained through the influence of applied potential at constant flow rate and ink properties. However, the applied potential has less effect on the spray than the flow rate. The applied potential is varied with respect to the flow rate to achieve an homogeneous spray.

9.5.1.3 Pneumatic Pressure

Pneumatic pressure is also an important parameters in the spray process. Generally, with water-based precursor solution or inks it is not easy to achieve uniform spray by controlling the flow rate and applied potential due to the influence of high surface tension. In this case, an additional, force, pneumatic pressure, is employed to achieve an homogeneous spray. Therefore, both applied potential and pneumatic pressure play a vital role for homogeneous spray in thin film deposition.

9.5.1.4 Stand-off Distance

The distance between the nozzle tip and the substrate is called the stand-off distance. The flying time of monodispersed droplets and the rate of solvent evaporation are periodically controlled by stand-off distance. The solvent evaporation rate is very important in achieving homogeneous thin films. Low boiling point solvents, such as methanol, ethanol, and isopropanol, are very

easy to evaporate at a minimum stand-off distance. However, high boiling point solvents, such as dichlorobenzene, dimethyl sulfoxide, and N-methyl-2-pyrrolidone, are very difficult to evaporate at minimum stand-off distance. So, the stand-off distance should be increased. Therefore, the stand-off distance mainly depends on the nature of the ink.

9.5.1.5 Nozzle Diameter

Nozzle diameter has a role in determining the shape and diameter of the spray, together with flow rate, applied potential, and pneumatic pressure. A nozzle with a small diameter ejects smaller droplets during the spray process and also limits flow rate. Achieving a homogeneous spray with a smaller diameter nozzle is very easy compared with larger diameter at minimum applied potential and pneumatic pressure. The nozzle diameters are varied according to the spray area or patterns for diverse thin films and device applications.

9.5.1.6 Ink Properties

Apart from the above parameters, the physicochemical properties of the ink also play a role in achieving uniform thin film deposition. Moreover, the process parameters are mostly dependent on the ink's electrical conductivity, viscosity, and surface tension.

9.5.1.6.1 Electrical Conductivity

The electrical conductivity is an important parameter during the atomization process. It can affect both the liquid shape and spray homogeneity because of the charge density on liquid surface. It is easy to achieve a spray with liquid that has high electrical conductivity. However, when using liquid with very low conductivity it is not as easy to achieve a spray by applying an electric field. Thus, low conductivity liquid tends to be sprayed with the help of pneumatic pressure. The choice is simply based on the nature of the precursor or inks [40–44].

9.5.1.6.2 Viscosity

The viscosity of the precursor solution or inks has a little influence on the atomization process. The jet length increases with an increase in the viscosity. However, the formation of monodispersed droplets is slow with respect to ink viscosity. The high viscosity based cone-jet is more suitable for patterns due to longer jet [45, 46] but, in the case of the spray process, low viscosity of inks are more suitable for thin film deposition due to jet breakup at smaller distance.

9.5.1.6.3 Surface Tension

The atomization process occurs when the electrical forces overcome the surface tension on the apex of the meniscus with the additional help of pneumatic pressure. The required applied voltage and pneumatic pressure will be increased as the surface tension of the ink increases.

The above mentioned properties of the precursor solution or ink are periodically influenced by the chemical structure of desired materials and solvents. The chemical structures, such as molecular geometry, electronic structure, crystal structure of molecules, and solvents nature (polar, semipolar, and nonpolar), are directly influence the ink properties.

9.5.2 Mode of Atomization

The atomization mode is determined by the need to achieve an homogeneous thin film; there are three types of mode: dripping mode, stable spray mode, and unstable spray mode.

9.5.2.1 Dripping Mode

The first step appearing in the Hybrid-EHDA technique is a dripping mode. The dripping mode is observed only at given flow rate without electric potential and pneumatic pressure on the liquid. The size of the droplets is almost the same or larger than that of the nozzle tip. The drops are observed as regular spheres detaching from the nozzle capillary as the weight of the drop overcomes the capillary forces.

9.5.2.2 Unstable Spray Mode

An unstable spray mode is exhibited when the applied potential and pneumatic pressure are not enough to permanently overcome the liquid surface tension. If the spray is unstable due to insufficient applied potential and pneumatic pressure, the droplets are not monodispersed in nature and this severely affects the homogeneity of the thin film. Moreover, if the applied potential and pneumatic pressure are increased beyond certain limits (above the stable spray), spray instability is again observed. The values of these parameters are mainly based on the nature of the inks.

9.5.2.3 Stable Spray Mode

This is the most important atomization mode in the Hybrid-EHDA process. Stable spray can be achieved by adjusting the applied potential and pneumatic pressure values to overcome the unstable spray mode. This is further disintegrated into monodispersed charged droplets to achieve an homogeneous thin film. The stable spray mode is shown in Figure 9.8(f2) (highlighted by the yellow circle – highly uniform stable mode).

9.6 Fabrication of Inverted Organic Solar Cells

The organic device is fabricated by two methods: spin coating and the electrospray technique. We have fabricated organic solar cells with following architecture: ITO/ZnO/P3HT:PCBM/PEDOT:PSS/Ag. A patterned ITO was used as conductive substrate (MerckDisplayTechnologies, 15 Ω/sq,).

9.6.1 Deposition of Zinc Oxide (ZnO) on ITO Substrate

Zinc oxide (ZnO) nanoparticles are synthesized via a simple sol-gel technique. Zinc acetate dihydrate ($Zn(CH_3COO)_2.H_2O$), 2-methoxy ethanol ($C_3H_8O_2$), and monoethanolamine (C_2H_7NO) as a starting precursor, solvent, and stabilizing agent. These are stirred for one hour at 60 °C. 0.05 M concentration zinc acetate dihydrate is homogeneously dissolved in 2-methoxy ethanol. Then, a few drops of stabilizing agent are added into the solution and followed by stirring. The stirring is continued for two hours at 60 °C. Finally, the precipitate is washed and centrifuged and dried at 90 °C for one day. The obtained sample is calcinated at 450 °C for three hours in an electric furnace.

As prepared zinc oxide nanoparticles are uniformly dispersed in 2-methoxy ethanol under continues stirring. A few drops of N-methyl ethanol amine are added into the above solution as a stabilizing agent to achieve a homogeneous dispersion of ZnO solution [47, 48]. Freshly prepared ZnO is deposited on ITO-coated substrate via spin coating [49]. Before the deposition process, the substrates are cleaned using acetone, isopropanol, and deionized water, then further dried under UV chamber for10 minutes. The deposited ZnO thin film is achieved at a rotational speed of 1500 rpm for 20 seconds under ambient conditions and it is annealed at150°C for two hours [42]. The deposited ZnO acts as a buffer layer.

9.6.2 Deposition of P3HT:PCBM

Poly(3-hexylthiophene):poly(6,6-phenyl C61-butyric acid methyl ester) P3HT:PCBM solution (ink) is prepared by dissolving P3HT and PCBM in a molar ratio of 1:1 in dichlorobenzene as a solvent. In order to achieve an homogeneous solution, the entire solution is continuously stirred for 24 hours at 60 °C [50,51].

As prepared P3HT:PCBM ink is uniformly coated on ZnO/ITO substrate via spin coating. The homogeneous thin film is achieved at a rotational speed of 1000 rpm for 30 seconds, which is annealed at 120 °C for 30 minutes under a nitrogen atmosphere.

9.6.3 Deposition of PEDOT:PSS

PEDOT:PSS ink is prepared by diluting (2.3 wt-%) PEDOT:PSS paste with isopropanol (2:1 weight ratio) under constant stirring for 20 minutes at 1500 rpm. Further, 2 ml of deionized water is added drop by drop and stirring is continued for two hours under ambient conditions. The obtained solution is filtered through the polymeric filter (PTFE – 0.45 μm) to achieve homogeneous dispersion of PEDOT:PSS ink.

As prepared PEDOT:PSS aqueous solution is used as a buffer layer in organic solar cells. Before the deposition, the hydrophobic nature (occurred from predeposited P3HT:PCBM) is reduced by oxygen (O_2) plasma treatment, which leads to enhanced hydrophilic surface property [28, 34]. Then, PEDOT:PSS film is deposited on a P3HT:PCBM layer via spin coating. The PEDOT:PSS thin film is achieved at 300 rpm for 30 seconds and then annealed at 140 °C for 10 minutes.

9.6.4 Deposition of Silver as a Top Electrode

A nanostructured silver top electrode on predeposited PEDOT:PSS/P3HT:PCBM/ZnO/ITO substrate is deposited through the Hybrid-EHDA technique [42]. The deposition of nanostructured silver thin films is addressed by the influence of applied voltage and pneumatic pressure at constant flow rate (10 ml/h) and stand-off distance (100 mm). These two parameters significantly control the atomization process. A uniform atomization of silver ink with respect to applied voltage and pneumatic pressure is shown in Figures 9.8a–9.8d. Initially, dripping mode is observed at 0 kV without applying pressure, which is maintained until 9 kV. At 9 kV, the dripping mode deforms into unstable spray mode, which is observed to be maintained until stable spray or atomization mode. The stable mode is observed at 18 kV with 0.0 bar but the spray is not in homogeneity (Figure 9.8a). The pneumatic pressure is increased up to 0.3 bar and is maintained throughout the experiment by changing the applied voltage, as shown in Figure 9.8b.

At 0.0 kV with constant pressure (0.3 bar), the unstable spray is observed and is maintained until 15 kV. At 15 kV, the stable spray is ejected, which is the most important spray process for achieving uniform thin films. Beyond this voltage, the stability of spray is disturbed due to the influence of higher charge density. Figure 9.8c shows the atomization of silver ink at 0.5 bar of pneumatic pressure with respect to applied voltage. At 0.0 kV, the dripping mode deforms into unstable spray mode and is further influenced by increasing applied potential. The stable spray is ejected at 15 kV. The droplet density is much high in the center of the spray, as shown in the brighter region in Figure 9.8(c6). While increasing the applied voltage, the spray mode tends to disintegrate at the nozzle tip, which directly affects the spray homogeneity. The spray homogeneity and atomization process of silver ink examined further at a constant pneumatic pressure of 0.7 bar with different applied potential are shown in Figure 9.8d. The vigorous spray is observed until 6 kV, which is significantly controlled by increasing the applied potential; a stable spray mode is achieved at 15 kV. The stability is maintained until 18 kV. At 18 kV, the spray area is reduced by the influence of higher potential.

Figure 9.8e represents the spray process that occurs at one bar pneumatic pressure with different applied potential. At 0.0 kV, unstable spray is observed

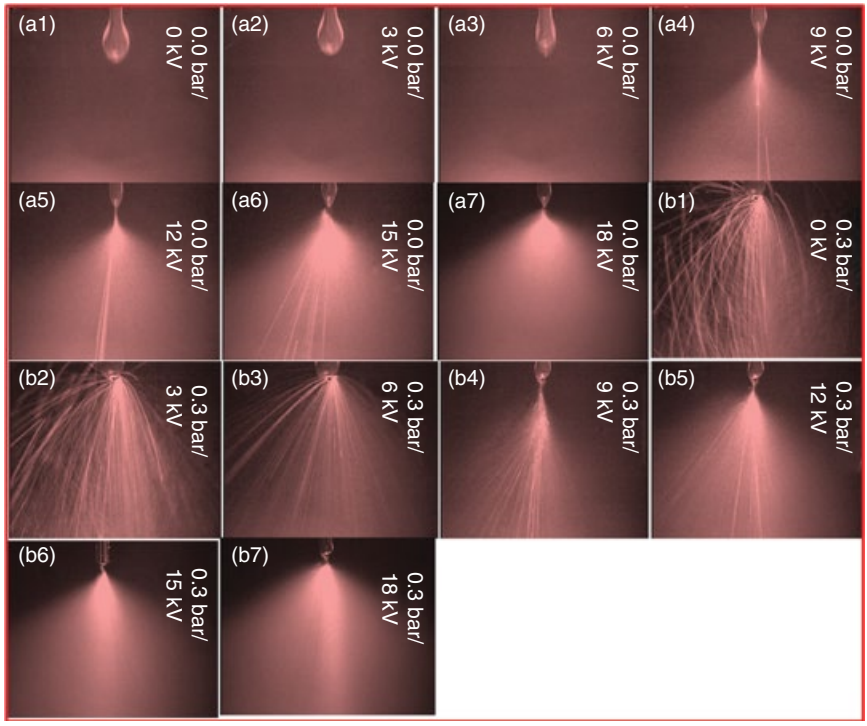

Figure 9.8(a–b) Influence of applied potential on spray or atomization mode of silver ink at constant pneumatic pressure: (a) 0.0 bar and (b) 0.3 bar.

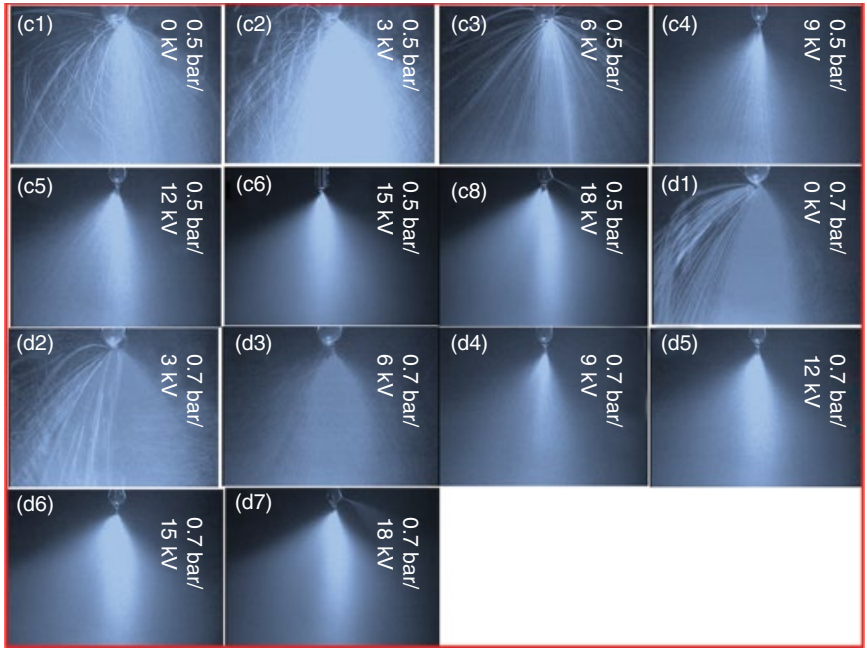

Figure 9.8(c–d) Influence of applied potential on spray or atomization mode of silver ink at constant pneumatic pressure: (c) 0.5 bar and (d) 0.7 bar.

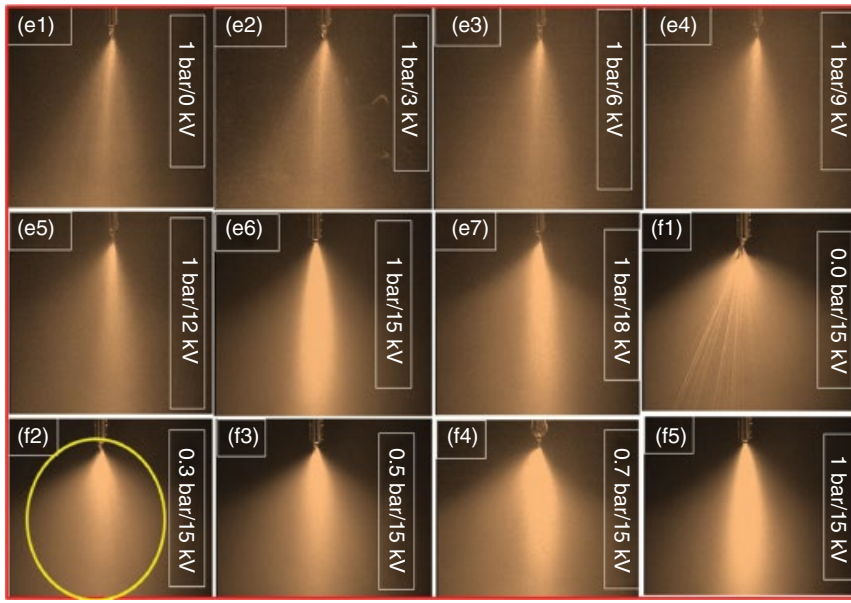

Figure 9.8(e–f) (e) Influence of applied potential on spray or atomization mode of silver ink at constant pneumatic pressure of 1 bar and (f) influence of pneumatic pressure on spray at constant applied potential (15 kV)

and is maintained until stable spray is ejected from the metallic nozzle tip. At 15 kV, the stable spray is observed but the spray area is smaller compared with 0.3 bar due to the influence of pneumatic pressure (1 bar). The overall spray deposition with respect to the pneumatic pressure and applied voltage tends to attain the uniform and large area spray at 0.3 bar of pneumatic pressure and 15 kV of applied potential, which leads to an homogeneous thin film. Further, the atomization process is stabilized by varying pneumatic pressure at constant applied potential of 15 kV (confirmed from the previous discussion) as shown in Figure 9.8f. Initially, nonuniform spray is observed at 0 bar pressure. With the pneumatic pressure increased at a constant applied potential, the shape of the spray is reformed, resulting in a stable or homogeneous spray mode at 0.3 bar (Figure 9.8(f2)). If the pressure is increased above 0.3 bar, the spray stability is severely disturbed to form unstable spray. Therefore, this result clearly confirmed that the homogeneous deposition of the silver top electrode is achieved at constant pneumatic pressure (0.3 bar) and applied potential (15 kV). In addition, there are four different spray times (2, 4, 6, and 8 min) used to achieve the silver top electrode with different film thickness, which are annealed at 160 °C for 20 min.

9.7 Device Morphology

The device architecture is clearly investigated via focused ion beam (FIB). The cross-sectional image of the device (top electrode obtained at spray time of 8 min) revealed a layer sequence of silver (top electrode)/PEDOT:PSS/P3HT:PCBM/ZnO/ITO (bottom electrode) (Figure 9.9). The silver top electrode consistently spread over the PEDOT:PSS layer with uniform film thickness, which enhances the charge transport into the outer circuit. The film thickness of buffer layer (in-between the active layer and top electrode) was found to be about 520 nm. It prevents silver diffusion into the active layer. The silver nanoparticle grain growth and pore formation at the bottom side of silver film are reduced (near PEDOT:PSS layer) compared with the top side silver film. A series of microstructural (particle necking, grain growth, and pore formation) developments during thermal sintering are clearly shown in the FIB image. The buffer layer (ZnO) and active layer (P3HT:PCBM) are revealed to have a film thickness of about 69 and about 207 nm, respectively. Top electrode thickness based electrical conductivity and device performance is explained in the next sections.

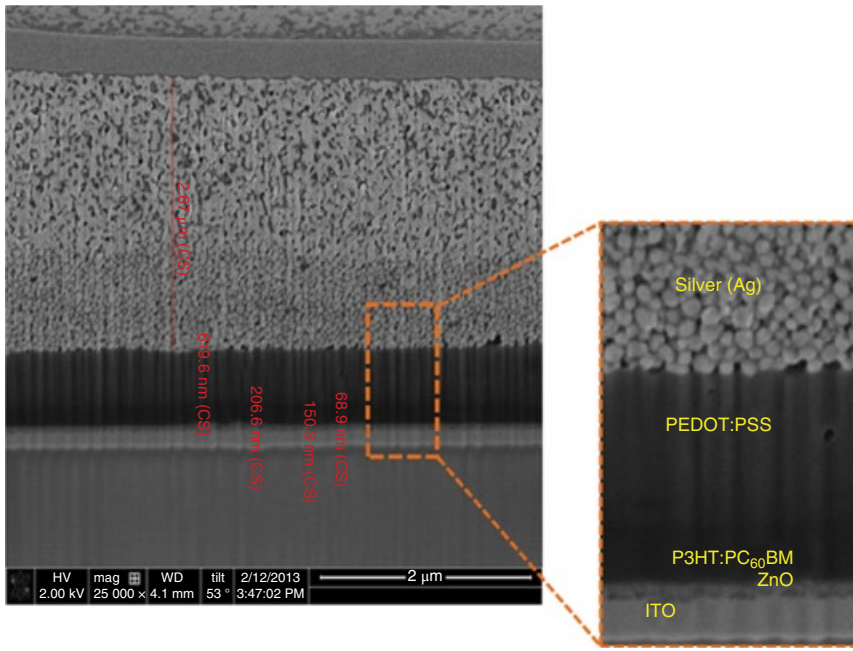

Figure 9.9 The cross-sectional view of the organic device.

9.8 Device Performance

The film thickness and sheet resistance of top electrode play an important role in fabricating the solar cell device. Therefore, the physicochemical properties of top electrode, especially film thickness and sheet resistance, must be examined before superior performance organic solar cells can be fabricated. The film thickness varies significantly with respect to spray time, stand-off distance, flow rate, and material concentration [28, 42]. The thickness of thin films (top electrode) varies with respect to spray times (2, 4, 6, and 8 min), resulting in changes in the sheet resistances, as shown in Figures 9.10a and 9.10b.

The average film thickness of the deposited layers is taken into account, corresponds to the average values measured at similar spray times. The sheet resistance of silver film decreased (from 9.13 Ω/sq to 0.07 Ω/sq) with increasing film thickness (from 0.8 μm to 2.6 μm). The result confirmed that the lowest sheet resistance of 0.07 Ω/sq is achieved at a spray time of eight minutes.

The device performances are investigated by measuring device efficiency with respect to different thickness of silver top electrode. The photovoltaic (PV) characterization of the devices is measured under 100 mW cm^{-2} AM 1.5 global solar illumination in a nitrogen atmosphere [52]. In the device (ITO/ZnO/P3HT:PCBM/PEDOT:PSS/Ag) structure, the active layer of P3HT:PCBM is sandwiched between two buffer layers (PEDOT:PSS and ZnO films). The PEDOT:PSS acts as an effective hole transport layer; ZnO acts as a hole blocking layer and also as a good electron transport layer. The charge transport mechanisms of the inverted organic solar cells are illustrated in Figure 9.11.

The current density vs voltage (*J*–*V*) measurement of the devices is displayed in Figure 9.12. The device short circuit current density (Jsc), open-circuit voltage (V_{oc}), fill factor (FF), and power conversion efficiency (PCE) are given in Table 9.1.

The results confirmed the maximum fill factor (FF) and superior power conversion efficiency at a spray time of eight minutes (for silver deposition time). This is because of the lower sheet resistance with prominent charge transport compared to the minimum spray time (2 min). In general, increasing power conversion efficiency is dependent upon the active layer, buffer layer, and top and bottom electrodes, but here we have an eye on the increasing power conversion efficiency through the influence of the silver top electrode (other materials parameters remains constant). The deposited silver top electrode has ohmic behavior with the PEDOT:PSS thin film [28], which acts as a hole selecting interlayer as well as providing smoother surface for silver top electrode [24, 28, 53–55]. Furthermore, the device stability is improved by the reverse nature of charge collection (using a less air sensitive, high work function based metal (Ag) as the back electrode) as well as by the deposited ZnO also providing the electron selective contact at the ITO interface [56–59].

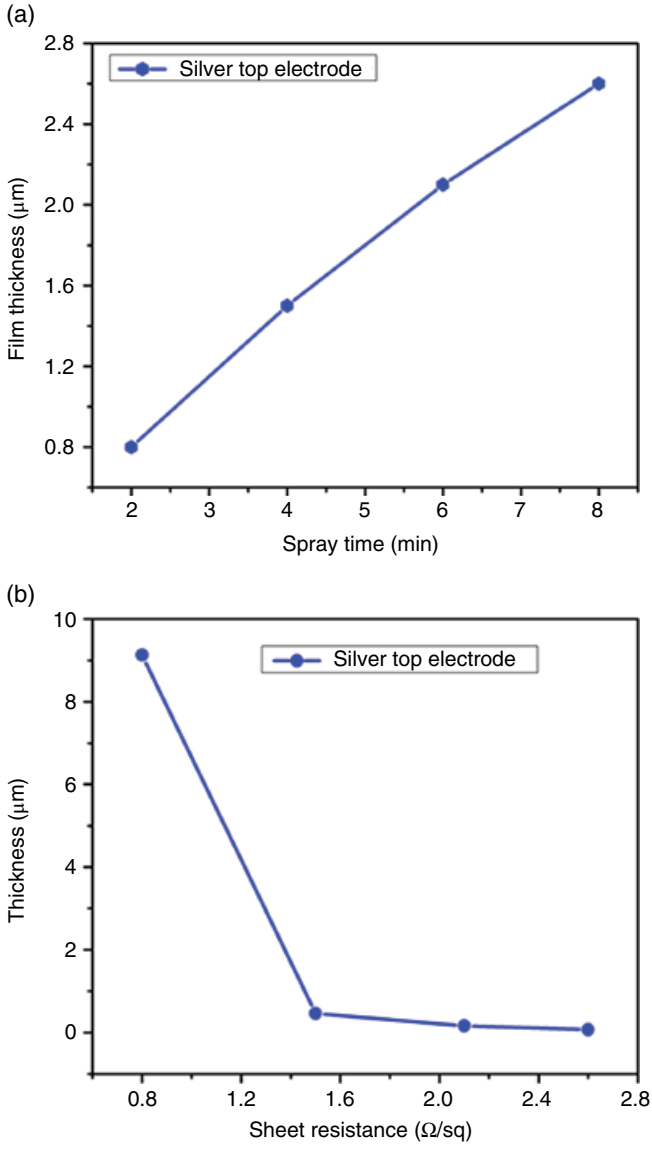

Figure 9.10 (a) Thickness of silver thin films with respect to spray times; (b) sheet resistance of silver films with respect to film thickness (in both figures, the error bars represents the standard deviation).

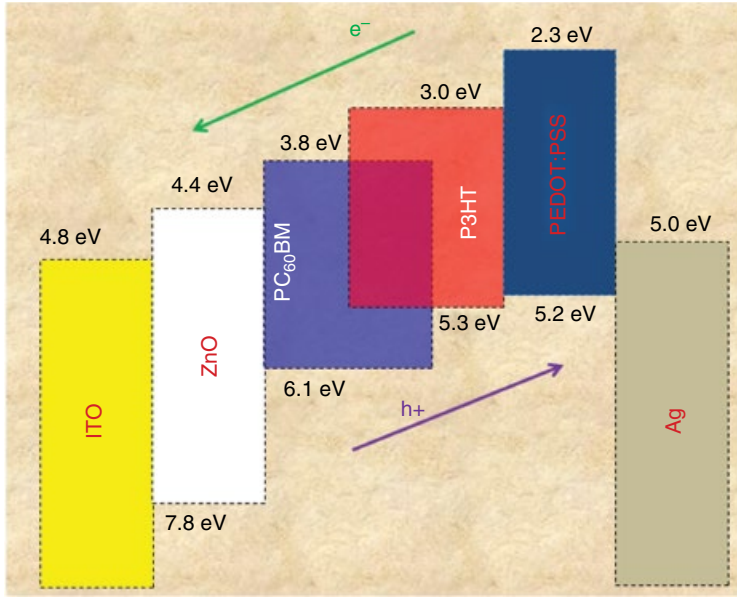

Figure 9.11 Energy level diagram of inverted organic solar cells.

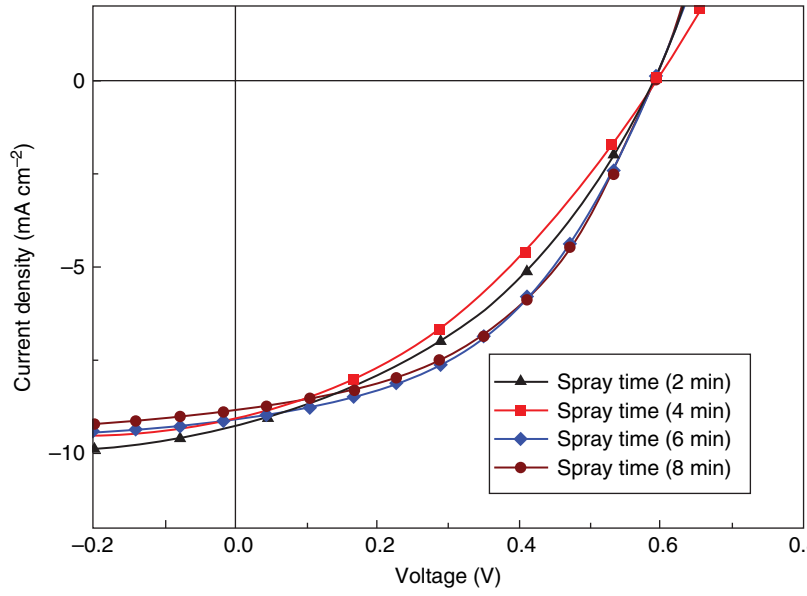

Figure 9.12 The current density–voltage characteristics of inverted organic solar cells produced with silver top contact via the Hybrid-EHDA process.

Table 9.1 Photovoltaic parameters of inverted organic solar cells with respect to the spray time of silver top electrode.

Spray time of the nanostructured silver top electrode (min)	Sheet resistance (Ω/sq)	V_{oc} (V)	J_{sc} (mA cm^{-2})	FF (%)	PCE (%)
2	9.13	0.59	9.03	37.38	2.00
4	0.46	0.58	9.28	39.69	2.16
6	0.16	0.59	9.08	45.0	2.42
8	0.07	0.59	8.85	46.60	2.44

Girotto *et al.* and Junwoo *et al.* stated that the voids at the interface between the PEDOT:PSS and the silver causes a reduction in electrical contact between the two successive layers. In addition, few metal particles are found in the PEDOT:PSS buffer layer, confirming that the buffer layer tends to prevent silver diffusion into the active layer, where it act as a quenching center for charge carriers and excitons [34, 42]. Anderasen *et al.* and Hau *et al.* stated that PEDOT:PSS works as a barrier to prevent oxygen diffusion into the organic layers [24, 25]. Norrman *et al.* and Chen *et al.* stated that employing interfacial layers (buffer layers) between the active layer and metal electrode are found to enhance the charge collection efficiency, which is due to control in the electron-hole recombination at the active layer/top electrode interface [58, 60].

The power conversion efficiencies and fill factors of organic devices are illustrated in Table 9.1. The lowest fill factor is observed at a spray time of two minutes because of the high sheet resistance. While increasing the spray time, the device fill factor is increased by decreasing sheet resistance. The maximum fill factor is attained at a spray time of eight minutes. On the other hand, the power conversion efficiency is significantly influenced by the top electrode properties, especially sheet resistance. Device efficiencies are increased by reducing the top electrode sheet resistance due to the increase in film thickness. The power conversion efficiency of the fabricated organic device through solution-processed nanostructured silver is closer to other organic devices [24, 34, 61]. The maximum power conversion efficiency of the inverted organic solar cell is found to be 2.44 % at a spray time of eight minutes. The Hybrid-EHDA process offers the ability to deposit a relatively large area through solution-based atomization and reduces the solvent influence on underlying organic layers. Therefore, this technique has great potential for use in fabrication of large area electronic devices.

The future research trends will focus on the fabrication of large scale printed inverted organic photovoltaic devices with prominent device efficiency and good life time.

9.9 Conclusion

In OPV devices, the solution-based nanostructured silver top electrode is deposited via the Hybrid-EHDA technique. The homogeneous spray mode is achieved with respect to applied potential and pneumatic pressure and the silver top electrode achieved with four different spray times. The homogeneous deposition of a thin film is achieved with porous free morphology. The sheet resistance of silver film is significantly reduced by increasing film thickness. The observed power conversion efficiency of the invert OPVs device is found to be 2.44% at a spray time of eight minutes (top electrode deposition with sheet resistance of 0.07 Ω/sq). The Hybrid-EHDA technique provides the ability to deposit a large area relatively quickly via solution-based atomization under controlled solvent influence on the underlying organic layers. Therefore, this technique has a great potential in the field of printed electronic devices.

Acknowledgements

Dr. Navaneethan Duraisamy and Kavitha Kandiah acknowledge UGC-Dr. D.S. Kothari Postdoctoral Fellowship (Ref no: No.F.4-2/2006 (BSR)/EN/15-16/0031) and (Ref. no: No.F.4-2/2006 (BSR)/BL/15-16/0225), UGC, New Delhi.

References

1 M. Kouhnavard, S. Ikeda, N.A. Ludin, *et al*., A review of semiconductor materials as sensitizers for quantum dot-sensitized solar cells, *Renew. Sust. Energ. Rev.*, **37**, 2014, 397–407.
2 P.V. Kamat, Meeting the clean energy demand: nanostructure architectures for solar energy conversion, *J. Phys. Chem. C*, **111**, 2007, 2834–2860.
3 K.W.J. Barnham, M. Mazzer, B. Clive, Resolving the energy crisis: nuclear or photovoltaics, *Nat. Mater.*, **5**, 2006, 161–164.
4 G.J. Meyer, Molecular approaches to solar energy conversion with coordination compounds anchored to semiconductor surfaces, *Inorg. Chem.*, **44**, 2005, 6852–6864.
5 M.A.M. Al-Alwani, A.B. Mohamad, *et al*., Dye-sensitised solar cells: Development, structure, operation principles, electron kinetics, characterisation, synthesis materials and natural photosensitisers, *Renew. Sust. Energ. Rev.*, **65**, 2016, 183–213.
6 T. Saga, Advances in crystalline silicon solar cell technology for industrial mass production, *NPG Asia. Mater.*, **2**, 2010, 96–102.
7 Y. Ooyama, Y. Harima, Molecular designs and syntheses of organic dyes for dye-sensitized solar cells, *Eur. J. Org. Chem.*, **18**, 2009, 2903–2934.

8 M.T. Bhatti, A.M. Rana, A.F. Khan, M.I. Ansari, Effect of annealing on electrical properties of Indium Tin Oxide (ITO) thin films, *J. Appl. Sci.*, **2**, 2002, 570–573.

9 P. Ramasamy, D.H. Lim, J. Kim, J. Kim, A general approach for synthesis of functional metal oxide nanotubes and their application in dye sensitized solar cells, *RSC Adv.*, **4**, 2014, 2858–2864.

10 A. Keawprajak, P. Piyakulawat, A. Klamchuen, *et al.*, Influence of crystallizable solvent on the morphology and performance of P3HT:PCBM bulk-heterojunction solar cells, *Sol. Energ. Mat. Sol. Cells*, **94**, 2010, 531–536.

11 L.W. Barbour, R.D. Pensack, M. Hegadorn, *et al.*, Excitation transport and charge separation in an organic photovoltaic material: Watching excitations diffuse to interfaces, *J. Phys. Chem. C*, **112**(10), 2008, 3926–3934.

12 A. Jannat, M.F. Rahman, M.S.H. Khan, A review study of organic photovoltaic cell, *IJSER*, **4**, 2013, 1–6

13 S.R. Forrest, The limits to organic photovoltaic cell efficiency, *MRS Bulletin*, **30**(01), 2005, 28–32.

14 G. Yu, J. Gao, J.C. Hummelen, *et al.*, Polymer photovoltaic cells: enhanced efficiencies via a network of internal donor-acceptor heterojunctions, *Science*, **270**(5243), 1995, 1789–1791.

15 M.D. Archer, R. Hill, *Clean Electricity from Photovoltaics*, Photoconversion of Solar Energy Series, vol. **1**, Imperial College Press, London, 2001.

16 V. Mihailetchi, L.J. Koster, J.C. Hummelen, P.W. Blom, Photocurrent generation in polymer-fullerene bulk heterojunctions, *Phy. Rev. Lett.*, **93**(21), 2004, 216601(1–4)

17 A.J. Mozer, N.S. Sariciftci, Negative electric field dependence of charge carrier drift mobility in conjugated, semiconducting polymers, *Chem. Phys. Lett.*, **389**(4), 2004, 438–442.

18 J. Liu, Y. Shi, Y. Yang, Solvation-induced morphology effects on the performance of polymer-based photovoltaic devices, *Adv. Funct. Mater.*, **11**(6), 2001, 420–424.

19 K.W. Wong, H.L. Yip, Y. Luo, *et al.*, Blocking reactions between indium-tin oxide and poly(3,4-ethylene dioxythiophene):poly(styrene sulphonate) with a self-assembly monolayer, *Appl. Phys. Lett.*, **80**, 2002, 2788–2790.

20 Y. Sahin, S. Alem, R. deBettignies, J. M. Nunzi, Development of air stable polymer solar cells using an inverted gold on top anode structure, *Thin Solid Films*, **476**, 2005, 340–343.

21 K. Kawano, R. Pacios, D. Poplavskyy, *et al.*, Degradation of organic solar cells due to air exposure, *Sol. Energ. Mat. Sol. Cells*, **90**, 2006, 3520–3530.

22 M. Boman, S. Stafstrom, J.L. Bredas, Theoretical investigations of the aluminum/polythiophene interface, *J. Chem. Phys.*, **97**, 1992, 9144–9153.

23 J. Birgerson, M. Fahlman, P. Brijms, W.R. Salaneck, Conjugated polymer surfaces and interfaces: a mini-review and some new results, *Synth. Metals*, **80**1996, 125–130.

24 S.K. Hau, H.L. Yip, N.S. Baek, *et al*., Air-stable inverted flexible polymer solar cells using zinc oxide nanoparticles as an electron selective layer, *Appl. Phys. Lett.*, **92**, 2008, 253301–253303.

25 M. Andersen, J.E. Carle, N.C. Bagger, *et al*., Transparent anodes for polymer photovoltaics: oxygen permeability of PEDOT, *Sol. Energy Mater. Sol. Cells*, **91**, 2007, 539–543.

26 J.W. Kang, Y.J. Kang, S. Jung, *et al*., Fully spray- coated inverted organic solar cells, *Sol. Energy Mater. Sol. Cells*, **103**, 2012, 76–79.

27 S.E. Shaheen, R. Radspinner, N. Peyghambarian, G.E. Jabbour, Fabrication of bulk heterojunction plastic solar cells by screen printing, *Appl. Phys. Lett.*, **79**, 2001, 2996–2998.

28 N. Duraisamy, N.M. Muhammad, A. Ali, *et al*., Characterization of poly(3,4-ethylenedioxythiophene):poly(styrenesulfonate) thin film deposited through electrohydrodynamic atomization technique, *Mater. Lett.*, **83**, 2012, 80–83.

29 S.E. Park, J.Y. Hwang, K. Kim, *et al*., Spray deposition of electrohydrodynamically atomized polymer mixture for active layer fabrication in organic photovoltaics, *Sol. Energy Mater. Sol. Cells*, **95**, 2011, 352–356.

30 P. Kumar, A. Gaur, Model for the J–V characteristics of degraded polymer solar cells, *J. Appl. Phys.*, **113**, 2013, 0945051–0945058.

31 A. Keawprajak, P. Piyakulawat, A. Klamchuen, *et al*., Influence of crystallizable solvent on the morphology and performance of P3HT:PCBM bulk-heterojunction solar cells, *Sol. Energy Mater. Sol. Cells*, **94**, 2010, 531–536.

32 C. Sene, M.E. Calixto, K.D. Dobson, R.W. Birkmire, Electrodeposition of $CuInSe_2$ absorber layers from pH buffered and non-buffered sulfate-based solutions, *Thin Solid Films*, **516**, 2008, 2188–2194.

33 C. Eberspacher, C. Fredric, K. Pauls, J. Serra, Thin-film CIS alloy PV materials fabricated using non-vacuum, particles-based techniques, *Thin Solid Films*, **387**, 2001, 18–22.

34 C. Girotto, B.P. Rand, S. Steudel, *et al*., Nanoparticle-based, spray-coated silver top contacts for efficient polymer solar cells, *Org. Electron.*, **10**, 2009, 735–740.

35 Y. Li, Y. Wu, B.S. Ong, Facile synthesis of silver nanoparticles useful for fabrication of high-conductivity elements for printed electronics, *J. Am. Chem. Soc.*, **127**, 2005, 3266–3267.

36 K. Barton, S. Mishra, K.A. Shorter, *et al*., A desktop electrohydrodynamic jet printing system, *Mechatronics*, **20**, 2010, 611–616.

37 K. Shigeta, Y. He, E. Sutanto, *et al*., Functional protein microarrays by electrohydrodynamic jet printing, *Anal. Chem.*, **84**(22), 2012, 10012–10018.

38 N. Duraisamy, N.M. Muhammad, H.C. Kim, *et al*., Fabrication of TiO_2 thin film memristor device using electrohydrodynamic ink jet printing, *Thin Solid Films*, **520**, 2012, 5070–5074.

39 N. Duraisamy, G. Ponniah, J. Jo, K.H. Choi, Structural and electrical properties of Ag Grid/Poly(3, 4-ethylenedioxythiophene):Poly(styrene sulfonate) coatings for diode application through advanced printing technology, *J. Nanosci. Nanotechnol.*, **13**, 2013, 5957–5963

40 N.M. Muhammad, N. Duraisamy, H.W. Dang, *et al*., Solution processed Al doped ZnO film fabrication through electrohydrodynamic atomization, *Thin Solid Films*, **520**, 2012, 6398–6403

41 N. Duraisamy, S.J. Hong, K.H. Choi, Deposition and characterization of silver nanowires embedded PEDOT:PSS thin films via electrohydrodynamic atomization, *Chem. Eng. J.*, **225**, 2013, 887–894

42 J. Kim, N. Duraisamy, T.M. Lee, *et al*., Hybrid electrohydrodynamic atomization of nanostructured silver top contact for inverted organic solar cells, *Sol. Energy Mater. Sol. Cells*, **130**, 2014, 156–162

43 N. Duraisamy, A. Numan, K. Ramesh, *et al*., Investigation on structural and electrochemical properties of binder free nanostructured nickel oxide thin film, *Mater. Lett.*, **161**, 2015, 694–697

44 M. Zubair, N. Duraisamy, K.H. Choi, M.T. Hyun, Conductivity enhancement of PEDOT:PSS thin film using roll to plate technique and its characterization as a Schottky diode, *J. Mater. Sci.: Mater. Electron.*, **25**, 2014, 1033–1039.

45 D.S. Kim, K. Rahman, A. Khan, K. H. Choi, Direct fabrication of copper nanoparticle patterns through electrohydrodynamic printing in cone-jet mode, *Mater. Manuf. Process*, **27**, 2012, 1295–1299.

46 K. H. Choi, K. Ali, K. Rahman, A study of the dependence of electrohydrodynamic jetting on the process parameters and liquid physical properties, *Chin. J. Phys.*, **52**, 2014, 799–815.

47 N. Duraisamy, K. R. Kwon, J. Jo, K.H. Choi, Development of nanostructured ZnO thin film via electrohydrodynamic atomization technique and its photoconductivity characteristics, *J. Nanosci. Nanotechnol.*, **14**, 2014, 5849–5855.

48 H.J. Park, K.H. Lee, B. Kumar, *et al*., Inverted organic solar cells with ZnO thin films prepared by sol–gel method, *J. Nanoelectron. Optoelectron.*, **5**, 2010, 1–4.

49 K.H. Choi, N. Duraisamy, M.N. Awais, *et al*., Investigation on switching behavior of ZrO_2 thin film for memory device applications, *Mater. Sci. Semicond. Process*, **16**, 2013, 1285–1291.

50 M. Reinhard, R. Eckstein, A. Slobodskyy, *et al*., Solution-processed polymer–silver nanowire top electrodes for inverted semi-transparent solar cells, *Org. Electron.*,**14**, 2013, 273–277.

51 N. Duraisamy, N.M. Muhammad, M.T. Hyun, K.H. Choi, Structural and electrical properties of P3HT:PCBM/PEDOT:PSS thin films deposited through electrohydrodynamic atomization technique, *Mater. Lett.*, **92**, 2013, 227–230.

52 B. Yin, L. Yang, Y. Liu, *et al*., Solution-processed bulk heterojunction organic solar cells based on an oligothiophene derivative, *Appl. Phys. Lett.*, **97**, 2010, 023303(1–3).

53 R. Steim, S.A. Choulis, P. Schilinsky, C.J. Brabec, Interface modification for highly efficient organic photovoltaics, *Appl. Phys. Lett.*, **92**, 2008, 0933031–0933033.

54 G.K. Mor, K. Shankar, M. Paulose, *et al*., High efficiency double heterojunction polymer photovoltaic cells using highly ordered TiO_2 nanotube arrays, *Appl. Phys. Lett.*, **91**, 2007, 1521111–1521113.

55 C. Waldauf, M. Morana, P. Denk, *et al*., Highly efficient inverted organic photovoltaics using solution based titanium oxide as electron selective contact, *Appl. Phys. Lett.*, **89**, (006, 2335171–2335173.

56 T.B. Yang, K. Sun, X.L. Liu, *et al*., Zinc oxide nanowire as an electron-extraction layer for broad band polymer photo detectors with an inverted device structure, *J. Phys. Chem. C*, **116**, 2012, 13650–13653.

57 S. Lattante, Electron and hole transport layers: their use in inverted bulk hetero junction polymer solar cells, *Electronics*, **3**, 2014, 132–164.

58 C. Chen, F. Li, Improving the efficiency of ITO/nc-TiO_2/CdS/P3HT:PCBM/PEDOT:PSS/Ag inverted solar cells by sensitizing TiO_2 nanocrystalline film with chemical bath-deposited CdS quantum dots, *Nanoscale Res. Lett.*, **8**, 2013, 1–7.

59 M.S. White, D.C. Olson, S.E. Shaheen, *et al*., Inverted bulk-hetero junction organic photovoltaic device using a solution-derived ZnO under layer, *Appl. Phys. Lett.*, **89**, 2006, 1435171–1435173.

60 K. Norrman, M.V. Madsen, S.A. Gevorgyan, F.C. Krebs, Degradation patterns in water and oxygen of an inverted polymer solar cell, *J. Am. Chem. Soc.*,**132**, 2010, 16883–16892.

61 J.B. Kim, C.S. Kim, Y.S. Kim, Y.L. Loo, Oxidation of silver electrodes induces transition from conventional to inverted photovoltaic characteristics in polymer solar cells, *Appl. Phys. Lett.*, **95**, 2009, 1833011–1833013.

10

Polymer Solar Cells – An Energy Technology for the Future

Alagar Ramar and Fu-Ming Wang

Graduate Institute of Applied Science and Technology, National Taiwan University of Science and Technology, Taiwan, R.O.C.

10.1 Introduction

Today solar cell research is enriched with novel materials, methods, and design concepts with the major goal of producing high efficiency devices. The discovery of the photovoltaic effect by Edmund Becquerel in 1839 led to serious research by scientists all over the world that blossomed into so-called photovoltaic technology [1, 2]. Commercial silicon solar cells were developed in the 1950s and commercialized in the 1960s for use in the space industry. Even though the inorganic solar cells entered the market, the high cost and the related environmental issues necessitated that alternatives were explored to help supply worldwide energy need. After the fundamental studies on the optical and electronic properties of pentacene in the 1960s, Tang successfully fabricated the first organic photovoltaic device where the concept of the generation of excitons at donors and their separation at a donor–acceptor interface was introduced [3]. It was a major breakthrough in organic photovoltaic devices.

Later, the photo-induced charge transfer from the conjugated polymer poly[2-methoxy-5-(2-ethylhexyloxy)]-1,4-phenylenevinylene (MEH-PPV) to fullerene was first observed by Sariciftci *et al*., which suggested that the conjugated polymer could be used as the electron donor and fullerene could be used as the electron acceptor in polymer solar cells (PSCs) [4]. The well-known polymer–fullerene bulk-heterojunction (BHJ) concept was introduced by Yu and Heeger in 1995 to avoid certain limitations of the donor–acceptor bilayer device [5].

In order to increase the efficiency, research was focused on materials design. One of the achievements in material design is the covalent grafting of fullerene

Rational Design of Solar Cells for Efficient Solar Energy Conversion, First Edition.
Edited by Alagarsamy Pandikumar and Ramasamy Ramaraj.

moieties onto the donor-polymer backbone, the so-called double-cable polymers, which can be regarded as a molecular heterojunction (MHJ). This means that a single molecule can act as a p-n type material, being capable of transporting both electrons and holes. After photoinduced electron transfer, the double-cable polymer creates two ideal channels for both hole transporting along the polymer chain and electron hopping between the pendant acceptor units [6–8]. The MHJ ensures a large interfacial area between donor and acceptor and also a promising strategy to prevent donor/acceptor phase separation.

In addition to the materials development, parallel evolution of novel device architectures to combat the problems of light absorption, charge separation, and device stability through the concepts of inverted and tandem structures made this field not only very promising for photovoltaic energy conversion but also competitive to the thin film inorganic solar cells. Even though the polymers have low bandgap for absorbing more visible light, experimental parameters such as concentration of the active materials, thickness of the active layer, annealing temperature, and processing additives also influence the device performance. This chapter updates the progress made in materials and novel design in the device structure for the improved photovoltaic performance of PSCs.

10.2 Materials Developments for Bulk Heterojunction Solar Cells

10.2.1 Conjugated Polymer–Fullerene Solar Cells

Polymers had been considered to be insulating materials before the discovery of high conductivity in doped polyacetylene in 1977 by Shirakawa *et al.* [9]. After Shirakawa, many research groups started to work on conducting polymers due to their interesting electrical, electrochemical, and optical properties. Then the conjugated polymers became a prime constituent in organic electronics.

The general principle of a PSC can be described as follows. Upon illumination by light, the donor forms bound electron-hole pairs, namely excitons, which arise from the excitation of an electron from the highest occupied molecular orbital (HOMO) to lowest unoccupied molecular orbital (LUMO). In the absence of any interface to dissociate the excitons into free charge carriers, the excitons will undergo decay to the ground state by either radiative or nonradiative deacy. The interface between the two layers, the donor/acceptor heterojunction, is responsible for efficient exciton dissociation. The electrons and holes created at the interface can be transported through the acceptor and donor layers, respectively, and collected at two electrodes, thereby contributing to an electrical current in an external circuit. The difference between the

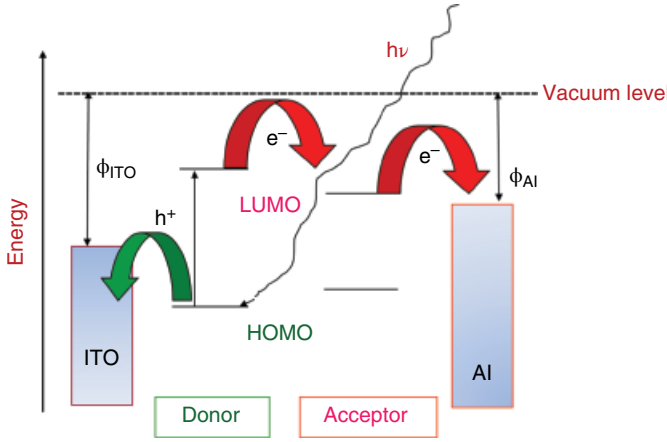

Figure 10.1 General operating principle of a polymer solar cell.

ionization potential of the donor and the electron affinity of the acceptor determines the maximum open circuit voltage (V_{oc}) under illumination (Figure 10.1).

Since conjugated polymers are solution-processable, they can be coated by spin coating, inkjet printing, roller casting, etc. [10]. They are also lightweight and the bandgap can be tuned by simple functionalization with electron releasing and electron withdrawing groups. There are several conjugated polymers that have been used extensively for polymer–fullerene BHJ solar cells. However, the basic skeleton will mainly rely on polythiophene, polyfluorene, polycarbazole, poly(phenylene vinylene), etc. In almost all cases the fullerene derivative [6,6]-phenyl-C61-butyric acid methyl ester ($PC_{61}BM$) has been used as the premier electron acceptor (Figure 10.2). The power conversion efficiency reached between 4 and 5% with poly(3-hexylthiophene) (P3HT)/PCBM in the last decade [11].

In order to commercialize PSCs, a reasonable efficiency (10%) is required. So numerous efforts have been made to understand the concept more clearly and to improve the performance with various type of conjugated polymers. Interestingly, the bandgap tuning was handled by the researchers to enhance the absorption, so that it can produce more excitons. The position of the HOMO and LUMO has an impact on the open-circuit voltage, i.e. the energy difference between the HOMO of the electron donor polymer and the LUMO of the electron acceptor fullerene derivative is found to be associated with the open-circuit voltage. The next main factor governing the efficiency is morphology. Even though the donor and acceptors have ideal energy positions the physical interaction is very important. A primary condition for a polymer–fullerene BHJ solar cell is an interface between donor and acceptor, which forms a bicontinuous network for the hole and electron transport [12, 13].

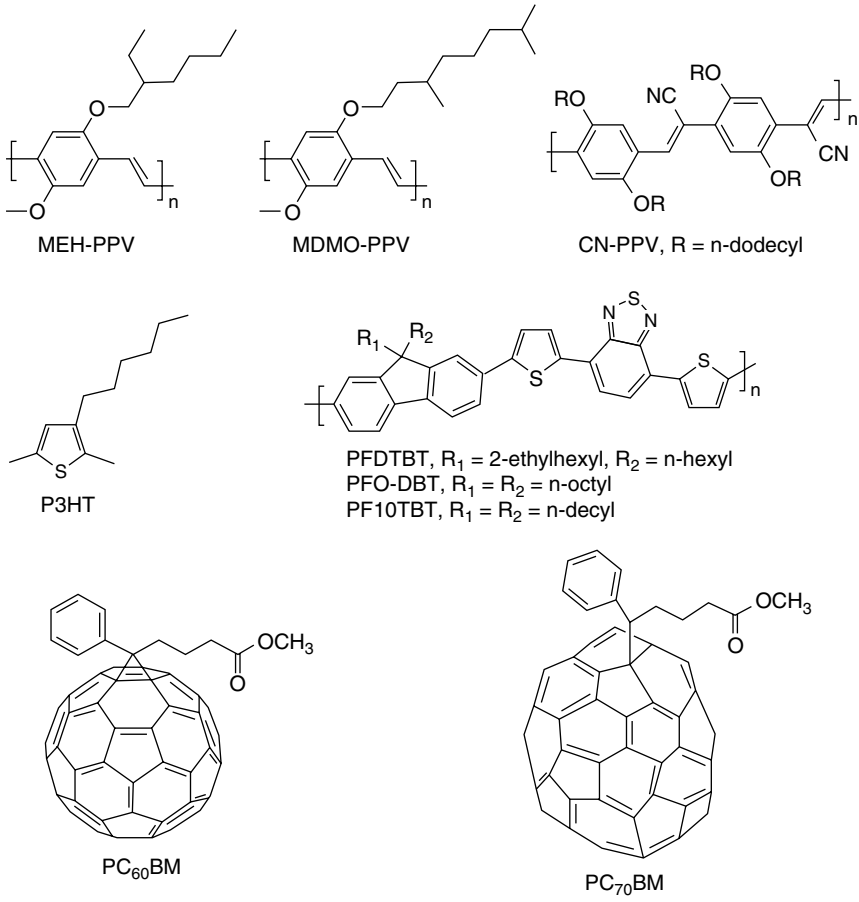

Figure 10.2 Structures of commonly used polymer donors and fullerene acceptors.

Poly(3-hexylthiophene) was one of the most studied conducting polymer until some of new interesting polymers, such as poly[N-9′-heptadecanyl-2,7-carbazole-*alt*-5,5-(4′,7′-di-2-thienyl-2′,1′,3′-benzothiadiazole)] (PCDTBT), PTB7, and PCDTTBD, arrived [14]. A broad-bandgap conjugated polymer PBDTTTZ, a copolymer of 2-alkylthiophene-substituted BDT and 2,5-bis(thiophen-2-yl) thiazolo[5,4-d]thiazole, connected with $PC_{71}BM$ in a PSC configuration showed 5.22% efficiency [15]. A new copolymer based on alternating spirobifluorene, thiophene, and benzothiadiazole units (PSFDTBT) has been synthesized and a PSC demonstrated an efficiency of 4.6% and a high V_{oc} of 0.94 V with the ideal electron acceptor $PC_{71}BM$ [16]. Heeger *et al.* reported that PCDTBT with a $PC_{71}BM$-based BHJ solar cell displayed an efficiency of 7.5% [17]. A conjugated polymer (FBT-DThDT-TT-H), using 5,6-difluoro-2,1,3-thiadiazole (FBT) as the

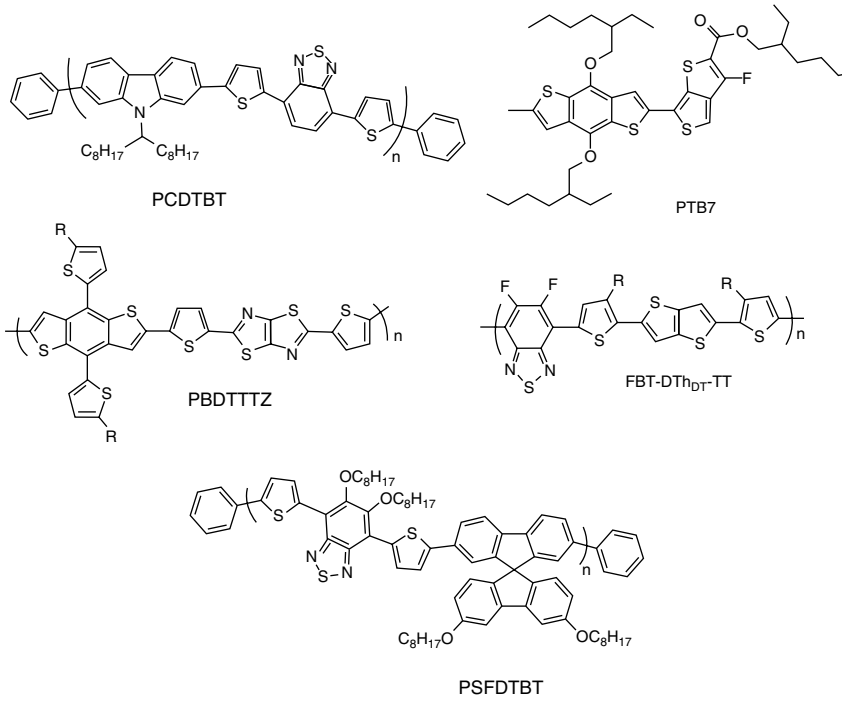

Figure 10.3 Structures of widely investigated conjugated polymers.

electron-accepting unit and terthiophene or 2,5-di(thiophen-2-yl)thieno[3,2-b] thiophene as the electron-donating unit, was synthesized by Cai *et al*. They cast the active layer using the polymer FBT-DThDT-TT-H with $PC_{71}BM$ in a hot (80 °C) solution containing *o*-dichlorobenzene solvent and chloronaphthalene as additive and achieved a power conversion efficiency of 7.78% [18]. Some of the conjugated polymers showing high performance are given in Figure 10.3.

Instead of sulfur as the heteroatom in the main backbone of the polymer there are also some other atoms, such as silicon and germanium based polymers, have been studied for their photovoltaic property (Figure 10.4). For example, a silicon containing polymer, poly(4-(5-(9,9-dioctyl-9H-dibenzosilole-2-yl)thiophen-2-yl)-5,6-bis(octyloxy)-7-(thiophen-2-yl) benzo[*c*][1, 2, 5]thiadiazole) with $PC_{71}BM$ produced a 6.02% efficient device. Here, TiO_x was used as the hole-blocking layer while 1,8-diiodooctane was used as additive in the active layer [19]. Selenium-containing donor–acceptor low-bandgap polymer (P3SDTQ) combined with PCBM showed a reasonable photovoltaic response [20]. In addition to that, a low-bandgap alternating copolymer containing dithienosilole and thienopyrrolodione (PDTSTPD) has been used as donor with $PC_{71}BM$ as acceptor to show an

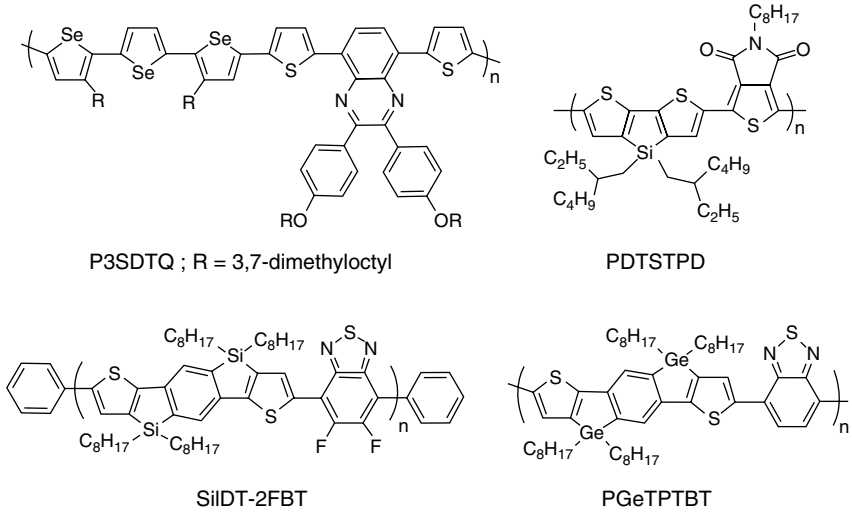

Figure 10.4 Chemical structures of heteroatoms such as Se, Si and Ge present in the core structure of donor polymers.

efficiency of 7.5% [21]. Silaindacenodithiophene (SiIDT) copolymerized with 5,6-difluorobenzo[*c*][1, 2, 5]thiadiazole (2FBT) and 5,6-difluoro-4,7-di(thiophen-2-yl) benzo[*c*][1, 2, 5]thiadiazole (2FDTBT) were studied for their photovoltaic performance and also displayed 4.5% efficiency [22]. Z. Fei *et al*. reported that germaindacenodithiophene and benzodithiazole coupled conjugated polymer (PGeTPTBT) blended with $PC_{71}BM$ in dichorobenzene and fabricated with the usual device structure of ITO/PEDOT:PSS/PGeTPTBT:$PC_{71}BM$/Ca/Al exhibited 5.02% power conversion efficiency [23].

The side chain of the polymer backbone has also played an important role in solubility and good interaction between the donor and acceptor, etc.. A pronounced orientation of side chains leads to highly ordered crystallites and gives rise to higher molecular weight of the polymer and, hence, high mobility [24]. Also, longer and less bulky side chains make the planarization better and give a closely packed polymer backbone, which leads to absorption of the photons to a lower energy [25]. Not only that, even the space between the main backbone and the side chain has shown an impact on the device performance. For example, semiconducting polymers containing benzodithiophene with decylphenylethynyl substituents and spacing alkyl groups have been synthesized. The spacing between the benzodithiophene and decylphenylethynyl has a strong impact on the photovoltaic performance. An increase in space between the side chains means an increase the polymer to fullerene ratio is needed to achieve the same power conversion efficiency [26].

The conjugated polymer showing the highest photovoltaic performance among all those reported here is poly[(5,6-difluoro-2,1,3-benzothiadiazol-4,7-diyl)-*alt*-(3,3‴-di(2-nonyltridecyl)-2,2′;5′,2′;5″,2‴-quaterthiophen-5,5‴-diyl)] (PffBT4T-C_9C_{13}). The usual solvent and additives in PSCs were *o*-dichlorobenzene and 1,8-diiodooctane. But here 1,2,4-trimethylbenzene is used as solvent while 1-phenylnaphthalene is used as additive. The solvent enables highly oriented polymer–fullerene interfaces while the additive changes the polymer backbone orientation relative to the substrate from edge-on to face-on, reduces the domain size, and increases the domain purity of the BHJ films. Finally, the device with the configuration ITO/ZnO/PffBT4T-C_9C_{13}:$PC_{71}BM$/V_2O_5/Al shows the best proven efficiency of 11.7% with V_{oc} of 784 V, J_{sc} of 19.8 mA cm^{-2}, and relatively good fill factor of about 73% for single polymer-fullerene BHJ solar cell [27]. Researchers are still trying to understand the relationship between the structure of various functional groups and core repeating unit present in the polymers to provide useful information for the development of PSCs.

10.2.2 Non-Fullerene Polymer Solar Cells

Even though fullerene derivatives based acceptor materials are dominant in BHJ PSCs, they also have some disadvantages. They do not absorb light as do polymers, in addition to which their production and purification costs are high. To address these limitations, researchers introduced non-fullerine acceptor materials. Organic materials are very cheap compared to fullerene and they can be chemically modified simply, so the tuning of absorption in both directions, namely blue shift and red shift, is possible. Until 2010 there was not much progress on these issues. In 2011, notably, Blocking *et al.* reported an efficiency of 2.5% with a naphthalimide-vinyl-benzothiadiazole based small molecule acceptor blended with poly(3-hexylthiophene) (P3HT) [28]. Perylenediimide (PDI) based acceptor materials were extensively used for fullerene-free PSCs (Figure 10.5). They are sufficiently stable to light, heat, and chemicals. Also, they have both n-type semiconducting and light absorbing behaviors. These properties made them leading electron acceptors in fullerene-free PSCs [29]. An alternative copolymer (PBDD4T-2F) based on 1,3-bis(4-(2-ethylhexyl)-thiophen-2-yl)-5,7-bis(2-ethylhexyl)benzo[1,2-c:4,5-c′]-dithiophene-4,8-dione (BDD) and 3,3′-difluoro-2,2′-bithiophene (T-T-2F) mixed with non-fullerene derivative ITIC shows an 8.13% efficiency [30].

Poly[(2,6-(4,8-bis(5-(2-ethylhexyl)thiophen-2-yl)-benzo[1,2-b:4,5-b']dithiophene))-*alt*-(5,5-(1',3'-di-2-thienyl-5',7'-bis(2-ethylhexyl)benzo[1',2'-c:4',5'-c']dithiophene-4,8-dione))]) as the donor and 3,9-bis(2-methylene-(3-(1,1-dicyanomethylene)-indanone))-5,5,11,11-tetrakis(4-hexylphenyl)-dithieno[2,3-d:2',3'-d']-s-indaceno[1,2-b:5,6-b']dithiophene) (ITIC) as the acceptor in an inverted PSC configuration shows an efficiency of

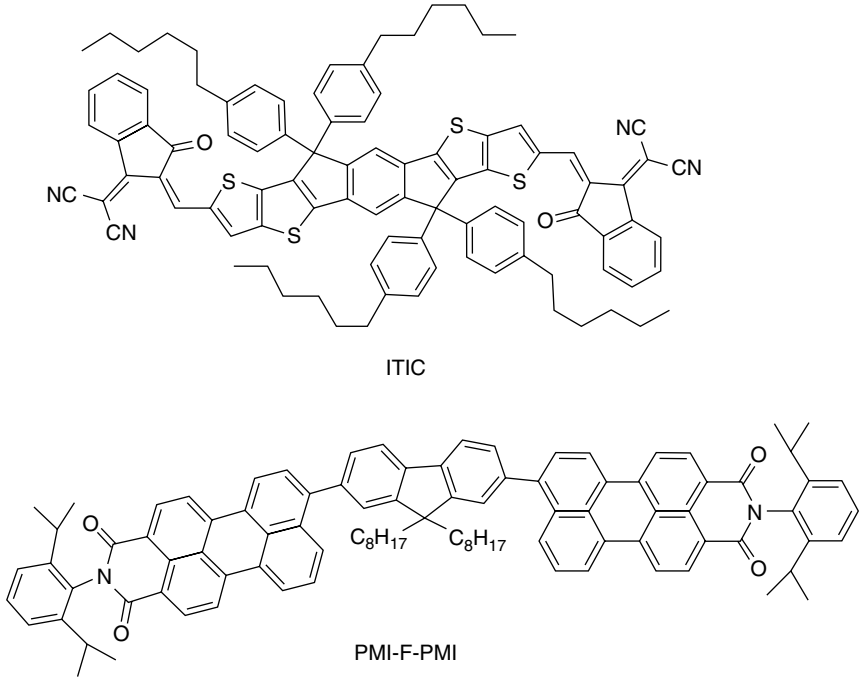

Figure 10.5 Chemical structures of non-fullerene electron acceptors ITIC and PMI-F-PMI.

11.21% with good fill factor of 74% [31]. More recently, the non-fullerene acceptor perylene monoimide (PMI-F-PMI) with bithienyl-benzodithiophene-based wide-bandgap copolymer (PTZ1) as donor produced a high open-circuit voltage of 1.3 V and a power conversion efficiency of 6% [32].

10.2.3 All-Polymer Solar Cells

All-polymer solar cells also have same the device configurations as conventional PSCs. However, they have the special property that both donor and acceptor materials absorb light and transport the charge carriers in their semiconducting structure (Figure 10.6), so they become a potential and cost-effective alternate to the fullerene-based BHJ solar cells. Kim *et al*. fabricated all-polymer solar cells using poly[4,8-bis(5-(2-ethylhexyl)thiophen-2-yl) benzo[1,2-b:4,5-b′]dithiophene-*alt*-1,3-bis(thiophen-2-yl)-5-(2-hexyldecyl)-4H-thieno[3,4-c]pyrrole-4,6(5H)-dione] (PBDTTTPD) as the electron donor and poly[[N,N′-bis(2-hexyldecyl)-naphthalene-1,4,5,8-bis(dicarboximide)-2,6-diyl]-*alt*-5,5′-thiophene] (P(NDI2HD-T)) as the electron acceptor; the device exhibited 6.64% efficiency [33].

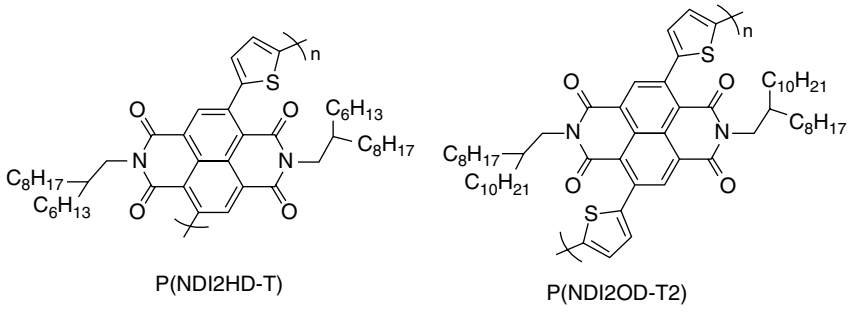

Figure 10.6 Structures of non-fullerene polymer electron acceptor materials.

A very high-mobility crystalline naphthalene diimide (NDI)–selenophene copolymer acceptor (PNDISHD) and a small band gap benzodithiophene (BDT)-thieno[3,4-b]thiophene (TT) copolymer donor (PBDTT-FTTE) were used to fabricate PSCs at room temperature and thermally annealed at 170 °C. The photovoltaic device fabricated at room temperature showed an impressive efficiency of 7.7% with a current density of 18.80 mA cm^{-2}, which was a twofold improvement compared with that annealed at high temperature [34]. Sun *et al*. synthesized benzodithiophene-quinoxaline-thiophene based polymers with various side chains and fluorine substitutions; they were fabricated with a general structure of ITO/PEDOT-PSS (45 nm)/polymer: poly{[N, N′-bis(2-octyldodecyl)-naphthalene- 1,4,5,8-bis(dicarboximide)-2,6-diyl]- *alt* -5,5′ -(2,2′-bithiophene)} (P(NDI2OD-T2)/Al. Finally the difluoro-substituted polymer (P2F-DO) exhibited an efficiency of 5.35% with the relatively high fill factor of 0.67 [35].

10.3 Materials Developments for Molecular Heterojunction Solar Cells

10.3.1 Double-cable Polymers

Devices made of materials having both donor (p-type) and acceptor (n-type) represent the most efficient configuration to realize organic photovoltaic cells with high power conversion efficiency. Currently research focus is on the synthesis of active electronic materials that combine the p-type semiconducting properties of conjugated polymers with the n-type fullerenes. Even though BHJ solar cells have many advantages, the control of phase separation is very difficult. One way of controlling a bicontinuous phase separation to ensure a large interfacial area between donor and acceptor is to covalently graft fullerene moieties onto the donor-polymer backbone, the so-called charm-bracelet type double-cable polymers, which can be regarded as a MHJ. The covalent fixation of fullerene units onto the conjugated backbone is a promising strategy

to prevent donor/acceptor phase separation and to maximize the interfacial area. After photoinduced electron transfer, the double-cable polymer creates two ideal channels for both hole transport along the polymer chain and electron hopping between the pendant acceptor units [6–8].

The double-cable polymers have been synthesized by two different approaches. One is the direct reaction of C_{60} with specifically functionalized soluble conjugated polymers [36–38]. Alternatively, they can be produced through the copolymerization of two monomers, one carrying the fullerene moiety and another one designed to improve the solubility [39–41]. The presence of an alkyl spacer between the polymer and the fullerene gives a better solubility and prevents the ground state interaction between the donor and acceptor.

There are many reports based on the synthesis and characterization of double-cable polymers for photovoltaic applications. In all the examples the basic polymer backbone has been made mainly with thiophene [42–45] or carbazole [46–48] because of their favorable photophysical properties towards photovoltaic applications. Sometimes the double-cable polymer has been synthesized with a combination of both thiophene and carbazole as the polymer chain [49]. Research on the design for new materials is underway to achieve a high efficiency. In order to achieve a high efficiency the following requirements should be fulfilled: the materials should be designed in such a way that they have a controlled nanoscale morphology for optimizing the charge generation and transport; a good synthetic effort is required to prepare materials with high purity, adequate content of fullerene, solubility, light-harvesting ability, and so on [7]. The realization of effective double-cable polymers will bring the donor–acceptor heterojunction at a molecular level.

The first conjugated polymeric material bearing fullerene side groups was described in 1996 by Benincori *et al.* [50]. The direct grafting of C_{60} at the bridging carbon of cyclopentadithiophene led to a compound suitable for electropolymerization. Yassar *et al.* reported the synthesis of a double-cable polymer with a repeat unit consisting of bithiophene carrying a fullerene group through a flexible alkyl chain spacer [51].

Ramos *et al.* used double-cable polymers for photovoltaic application for the first time in 2001 [52]. They synthesized a conjugated backbone, a hybrid of poly(*p*-phenylene vinylene) and poly(*p*-phenylene ethynylene), with pending methanofullerene moieties (PPV-C_{60}). They fabricated the molecular heterojunction solar cell using the synthesized double-cable polymer and observed a photocurrent of 0.42 mA cm^{-2} under AM 1.5 conditions. Later, Otero *et al.* reported a polythiophene based double-cable polymer with an alkyl spacer to improve the solubility of the polymer [53]. The double-cable polymer with 14% of fullerene showed a power conversion efficiency of 0.6% under irradiation of monochromatic light at 505 nm.

Thereafter, during 2007, Tan *et al*. reported an efficiency of 0.52% with a soluble polythiophene based double-cable polymer [40]. The efficiency was five times higher than the same polymer blended with the usual electron acceptor, $PC_{61}BM$. The photoluminescence quenching of polythiophene in the double-cable polymer was more effective than the polythiophene blended with $PC_{61}BM$. These results ensured the effective charge transfer in the double-cable structure of polymer. The well-known P3HT bearing pendant fullerene showed a low efficiency, in the order of 10^{-2}–10^{-5}% [38]. The reason for the very low efficiency is cited to be the inefficient electron hopping from one fullerene to another fullerene. A MHJ solar cell based on poly{3-hexylthiophene-*co*-3-[6-(1-oxy-4-*N*-methylfulleropyrrolidinephenyl)hexyl]thiophene} double-cable polymer showed an efficiency of 1.55% [41]. Good control of the nanophase separation ensured it achieved a higher efficiency than the blended one. A MHJ solar cell based on a fullerene attached diblock copolymer P3HT-*b*-(P3HT-*co*-(P3HT-*graft*-phenyl C_{61}butyric propargyl ester)) (D3) has been reported to show a power conversion efficiency of 2.46% [54]. Recently a polythiophene–fullerene double-cable polymer, poly[3-hexylthiophene-co-3-(6-fullerenylhexyl)thiophene] (COP2) has been synthesized; its photovoltaic behavior under optimal condition was 4.19 ± 0.18%, which is the highest value reported so far among the double-cable polymer based PSCs. The fullerene loading was 46 wt-% in the double-cable polymer and dissolved in *o*-dichlorobenzene with a concentration of 13 mg/ml; the thickness of the active layer was 150 nm [55]. Chemical structures of some of the selected donor-acceptor double-cable polymers are given in Figure 10.7.

10.4 Developments in Device Structures

The device architecture of the photoactive layer has a strong impact on charge carrier separation and transport, and, therefore, plays a major role in improving the efficiency. In a way, the rapid developments in this field can be attributed to the advancements made in the design of the cells with multilayer configurations that occurred parallel to the realization of new conjugated molecules/polymers and composites. Single layer solar cells, one of the device structures first introduced, were a metal-insulator-metal model with a single organic material sandwiched between a low-work-function metal (Al) and a high-work-function metal (Au) [56]. Here the photoexcitons generated are close to the depletion region of the Schottky contact, which leads to the separation of charge carriers as a result of the limited exciton diffusion length. Therefore, only a small region – denoted the active zone – contributes to photocurrent generation. Bilayer devices, introduced by Tang in 1986, led the organic solar cells in a particular direction, which is based on the donor–acceptor concept [3]. Here the exciton is dissociated at the donor–acceptor interface,

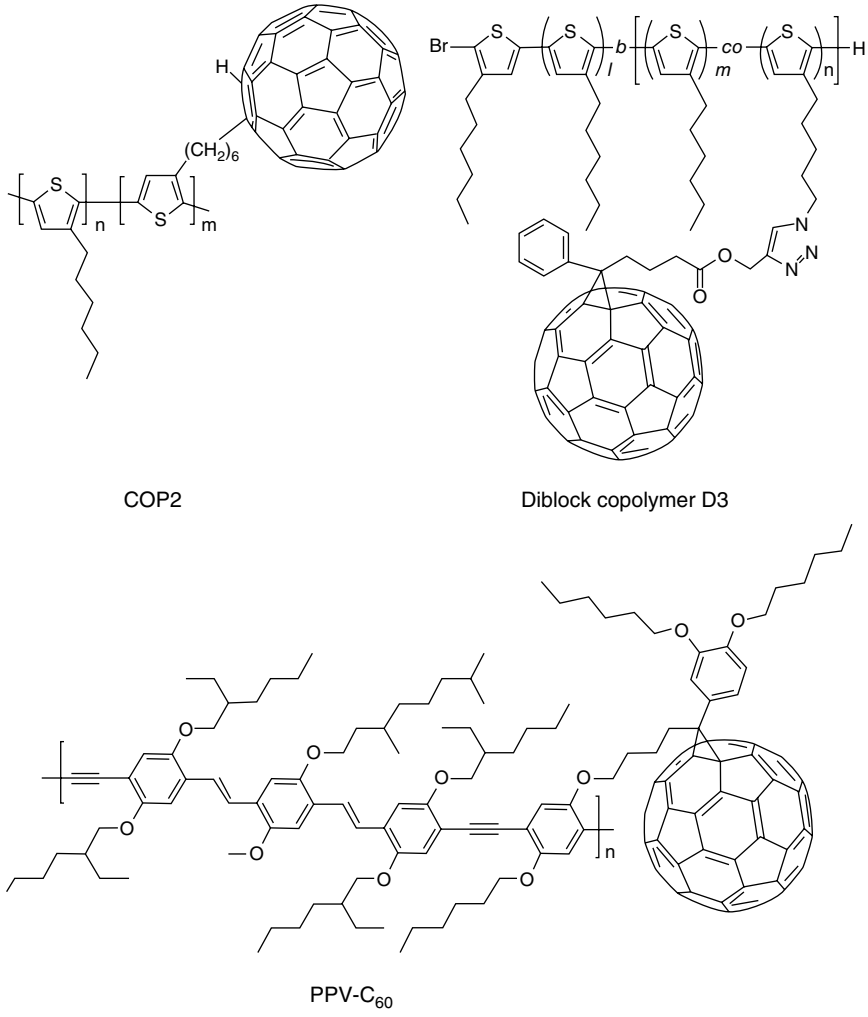

Figure 10.7 Structures of the charm-bracelet type double-cable polymers COP2, D3, and PPV-C_{60}.

leading to the separation of holes on the donor side and electrons on the acceptor side. Thus, the charge carriers may travel independently within separate materials and bimolecular recombination is largely suppressed.

To overcome the limitations of bilayer devices and increase the interfacial area, the BHJ concept was introduced where the donor and acceptor materials are intimately mixed throughout the bulk. The first polymer/C_{60} BHJ device was introduced by Sariciftci *et al.* in 1993; poly

[2-methoxy-5-(2-ethylhexyloxy)-1,4-phenylenevinylene] (MEH-PPV), a conjugated polymer, blended with C_{60} was used as the active layer [57]. The exciton diffusion length was 10–20 nm. Here the excitons need not travel long distances, as in the case of the bilayer structure, to reach the donor/acceptor interface and charge separation can take place everywhere in the photoactive layer [58]. Further developments have been made to improve the performance of BHJ solar cells. One of the methods involves coating a conducting PEDOT:PSS layer, which enables efficient charge transport, acts as electron-blocking layer, and also smoothens the rough ITO surface [59]. In 2011, a report showed an efficiency of 8.37% for a device with an active layer consisting of thieno[3,4-*b*]-thiophene/benzodithiophene:[6,6]-phenyl C_{71}-butyric acid methyl ester ($PC_{71}BM$) and poly [(9,9-bis(3′-(*N*,*N*-dimethylamino)propyl)-2,7-fluorene)-alt-2,7-(9,9-dioctylfluorene)] as cathode interlayer. Here the cathode interlayer simultaneously enhanced the open-circuit voltage, short circuit current density, fill factor, and efficiency [60]. Further developments in the device structure are described detail in the following section.

10.4.1 Tandem Solar Cells

Tandem structure in PSCs has been introduced to increase light absorption. Hadipour *et al.* fabricated a polymer-based tandem solar cell by stacking two single cells in series using an all-solution-processed technique [61]. In general, the subcells have completely different absorption spectra: high energy photons are absorbed in the bottom cell and low energy photons are absorbed in the top cell; the whole visible part of the solar spectrum can be covered. A composite middle electrode is applied that serves both as a charge recombination center and as a protecting layer for the first cell during spin coating of the second cell. In 2007, Kim *et al.* reported an efficiency of 6.5% using a tandem configuration in which P3HT:$PC_{71}BM$ and poly[2,6-(4,4-bis-(2-ethylhexyl)-4H-cyclopenta[2,1-b;3,4-b']dithiophene)-alt-4,7-(2,1,3-benzothiadiazole)]:PC61BM coated with TiO_2 acted as the electron transport layer [62].

An efficiency of 8.9% has been reported for a triple-junction tandem cell based on PCDTBT:$PC_{71}BM$ and PMDPP3T:$PC_{61}BM$, where PCDTBT is poly[[9-(1-octylnonyl)-9H-carbazole-2,7-diyl]-2,5-thiophenediyl-2,1,3-benzothiadiazole-4,7-diyl-2,5-thiophenediyl]andPMDPP3Tispoly[[2,5-bis(2-hexyldecyl-2,3,5,6-tetrahydro-3,6-dioxopyrrolo[3,4-*c*]pyrrole-1,4-diyl]-alt-[3,3-dimethyl-2,2:5,2-terthiophene]-5,5-diyl] [63]. The addition of another photoactive layer (PMDPP3T:$PC_{61}BM$) in the above tandem structure has been effected and the triple junction device has shown an improved efficiency of 9.6%. There is one other triple-junction tandem solar cell showing very high efficiency greater than 11%; the device structure is ITO/ZnO/P3HT:ICBA/PEDOT:PSS/ZnO/PTB:$PC_{71}BM$/WO_3/PEDOT:PSS/ZnO/LBG:$PC_{71}BM$/WO_3/Al [64]. The tandem structure of the PSC is shown in Figure 10.8.

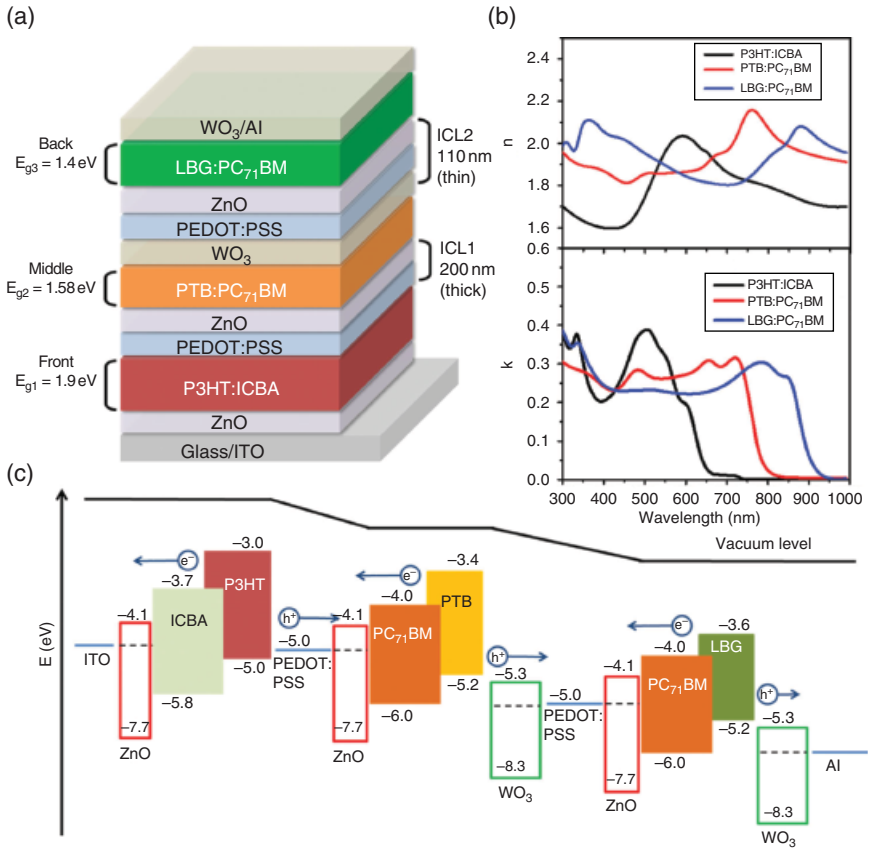

Figure 10.8 (a) Layer stacks of the triple-junction tandem solar cell in the inverted architecture. (b) Optical parameters n and k for P3HT:ICBA, PTB:$PC_{71}BM$, and LBG:$PC_{71}BM$ structures used in the simulations. (c) Energy levels of the materials investigated in this study. Reproduced with permission of John Wiley and Sons [64].

A high power conversion efficiency of 11.3% with a V_{oc} of 1.54 V has been achieved by Heeger's research group using a homo-Tandem structure i.e. The device structure is ITO/PEDOT:PSS/PTB7-Th:$PC_{71}BM$/ZnO/CPE-K or CPEPh-Na/PTB7-Th:$PC_{71}BM$/Al. They stacked the two identical cells with same donor material poly[4,8-bis(5-(2-ethylhexyl)thiophen-2-yl) benzo[1, 2-b:4, 5-b']dithiophene-co-3-fluorothieno[3,4-b]thiophene-2-carboxylate] (PTB7-Th) and the acceptor material [6, 6]-phenyl C71-butyric acid methyl ester ($PC_{71}BM$) [65]. Recently, in 2016 Zhang *et al.*, published an article in which PBDD4T-2F:PC61BM have been used as the front cell while the PDPP4T:$PC_{71}BM$ blend have been used as rear cell. The tandem cell showed an efficiency of 10.12% with a V_{oc} of 1.53 V while the front and rear cells showed 7.80% and 6.57% respectively [30].

All-polymer tandem solar cells have been reported by Yuan *et al.* [66]. They claim that benzodithiophene-quinoxaline-thiophene based polymer P2F-DO as donor and poly{[N, N'-bis(2-octyldodecyl)-naphthalene- 1,4,5,8-bis(dicarboximide)-2,6-diyl]- *alt* -5,5' -(2,2'-bithiophene)}(P(NDI2OD-T2) as acceptor gives 6.70% efficiency in a tandem structure while that of the same in single junction solar cells gave 4.68% efficiency, which is 43% less than the tandem one. It is noteworthy to mention that the open-circuit voltage of single cell is about 0.80 V while that of the tandem cell is 1.58 V. At the same time, the current density of the tandem cell is 7.31 mA cm^{-2} whereas the single cell has a high value of 10.08 mA cm^{-2}.

10.4.2 Inverted Polymer Solar Cells

The concept of an inverted configuration was first reported by Rostalski and Meissner [67] for a bilayer p-n type organic solar cells. They inverted the position of the cathode and anode materials, i.e. air-stable high-work-function metals, typically, silver or gold, were used as the anode and ITO was used as the cathode. Later the concept was developed by Xahin *et al.* for PSCs [68]. In the inverted PSCs, the anode, such as silver (or gold), can be formed using coating or printing technology from silver (or gold) pastes to simplify and lower the cost of manufacturing. The inverted structure show better long-time stability compared to the normal structure. In the inverted PSCs, n-type metal oxides, such as TiO_2, ZnO, and Cs_2CO_3, have been used to modify the cathode, leading to power conversion efficiencies ranging from 3 to 7% [69]. The metal oxides serve as electron transport layers. The performance of inverted PSCs is predominantly influenced by the optical transparency and electrical conductivity of these electron transport layers; it is also influenced by the interfacial contact between the electron transport layer and the BHJ active layer [70]. There are some ladder-type multifused polymers with thienyl-phenylene-thienylene-phenylene-thienyl (TPTPT) as the core unit that show 4.3% efficiency in a normal PSC configuration while in the inverted structure they exhibit a higher 5.1% efficiency [71].

In 2012, Yang *et al.* obtained an efficiency value of 8.4% for the inverted configuration structure ITO/ZnO/PFN-Br/PBDT-DTNT:$PC_{71}BM$/MoO_3/Ag. Here PBDT-DTNT is the donor while PFN-Br is the conjugated polyelectrolyte [72]. A power conversion efficiency of 9.21% under AM 1.5G illumination has been achieved for the inverted PSCs with a device configuration ITO/PFN/poly[(9,9-bis(3′-(*N*,*N*-dimethylamino)propyl)-2,7-fluorene)-alt-2,7-(9,9-dioctylfluorene)]/thieno[3,4-b]-thiophene/benzodithiophene:$PC_{71}BM$/MoO_3/Ag [73]. The architecture of the latest inverted PSC is shown in the Figure 10.9.

A novel dipole layer has been introduced by Nam *et al.* to improve the efficiency. They did this by introducing a neutral polymer, poly(2-ethyl-2-oxazoline) (PEOz) between the electron collecting buffer layer (ZnO) and the BHJ

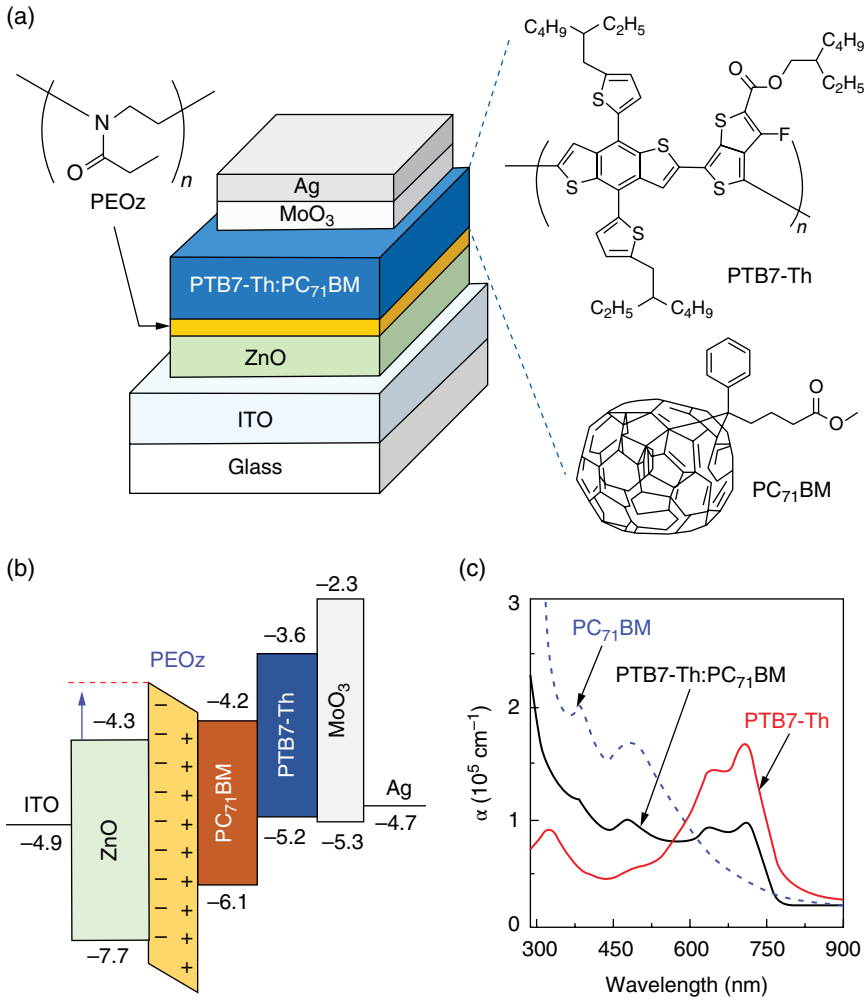

Figure 10.9 (a) Solar cell device stack and chemical structures for PTB7-Th, $PC_{71}BM$, and PEOz. (b) Flat energy band diagram for PTB7-Th:$PC_{71}BM$ BHJ solar cells with ZnO/PEOz ECBL/interlayer. The blue arrow denotes the shift in ZnO work function caused by the PEOz. (c) Absorption coefficient (α) spectra for pristine films of PTB7-Th and PC71BM, and for a BHJ PTB7-Th:$PC_{71}BM$ blend film. Reproduced with permission of Nature Publishing Group [74].

photoactive layer. The photoactive layer consists of poly[4,8-bis(5-(2-ethylhexyl) thiophen-2-yl)benzo[1,2-b:4,5-b']dithiophene-alt-3-fluorothieno[3,4-b]thiophene-2-carboxylate] as donor and [6,6]-phenyl-C71-butyric acid methyl ester as acceptor. The dipole layer greatly improved the photovoltaic efficiency of the inverted type PSC to 10.74%, a high record value [74].

Table 10.1 The maximum efficiency attained for each type of polymer solar cell.

Development	Type of polymer solar cell	Type of configuration	Efficiency (%)	Ref
Material	Polymer–fullerene BHJ	ITO/ZnO/PffBT4T-C_9C_{13}:$PC_{71}BM$/V_2O_5/Al	11.70	27
	Non-fullerene or fullerene-free BHJ	ITO/ZnO/PEI/PNDIS-HD:PBDTT-FTTE/MoO_3/Ag	11.21	31
	All polymer BHJ	ITO/ZnO/PEI/PNDIS-HD:PBDTT-FTTE/MoO_3/Ag	7.73	34
	Double-cable polymer MHJ	ITO/PEDOT:PSS/COP2/Al	4.19	55
Device	Tandem (Homo)	ITO/PEDOT:PSS/PTB7-Th:$PC_{71}BM$/ZnO/CPEPh-Na/PTB7-Th:$PC_{71}BM$/Al	11.30	65
	Tandem (Hetero)	ITO/PFN/PBDD4T-2 F:$PC_{61}BM$/MoO_3/Ag/PFN/PDPP4T:$PC_{71}BM$/MoO_3/Al	10.12	30
	Tandem (Triple junction)	ITO/ZnO/P3HT:ICBA/PEDOT:PSS/ZnO/PTB:$PC_{71}BM$/WO_3/PEDOT:PSS/ZnO/LBG:$PC_{71}BM$/WO_3/Al	11.55	64
	Tandem (All polymer)	ITO/ZnO/P2F-DO:N2200/M-PEDOT:PSS/ZnO/P2F-DO:N2200/MoO_3/Al	6.70	66
	Inverted	ITO/ZnO/ PEOz/PTBT-Th:$PC_{71}BM$/MoO_3/Ag	10.74	74

More recently a binary acceptor system based on a small molecule and fullerene derivative has been introduced in inverted PSCs. The small molecule, RTCN in the device structure ITO/ZnO/PTB7-Th:PC71BM:RTCN/MoO_3/Ag, not only enhanced the dye adsorption but also provide additional exciton dissociation at the PTB7–Th:RTCN interface. This binary system has enriched the performance of single acceptor system from 8.50 to 9.55% [75]. Studies of other materials for the development of device configuration are continuing.

The literature updates for the maximum efficiency achieved for all types of PSCs are given in Table 10.1 [76–78]. The table clearly exposes the changes in material or device that resulted in different power conversion efficiency. In addition, the nature of materials, such as polymer–fullerene, non-fullerene or fullerene free, all polymer, and double-cable polymer, reflected a variable efficiency. The device configuration itself produced a dramatic change. Even a small introduction to the modification layer would give rise to noticeable change in their solar energy conversion.

10.5 Conclusions

In this chapter a brief history of polymer solar cells has been given as an introduction. An overview of the materials developed for polymer-fullerene, non-fullerene, all polymer, and double-cable polymer solar cells has been provided along with their power conversion efficiencies. Also, the progress made in device configuration to improve photovoltaic performance from the preliminary stage has been described. The advantage of the polymer solar cells is that solution-processable coating techniques can be used to manufacture the solar cells in a roll-to-roll fashion. They are economically cheap, lightweight, and portable. As they are solid state cells, no electrolyte or water is needed to maintain its life. New materials with different functionalities and device structures are being developed by various researchers worldwide to improve the efficiency and stability of polymer solar cells. It is believed that the information provided here will help researchers attain molecular, material, and device level control for complete optimization of solar energy conversion technology. Polymer solar cells will soon enter the market for solving our energy problems. Everyone can have printed solar cells on bags, umbrella, and cars as portable and rollable format.

Acknowledgements

Alagar Ramar and Fu-Ming Wang acknowledge the Ministry of Science and Technology, Taiwan, for the financial support.

References

1 A.E. Becquerel, Recherches Sur Les Effets De La Radiation Chimique De La Lumiere Solaire Au Moyen Des Courants Electriques, *Compt. Rend. Acad. Sci.*, **9**, 1839, 145–149.

2 A.E. Becquerel, Memoire Sur Les Effects d'Electriques Produits Sous 1'Influence Des Rayons Solaires, *Annalen der Physick und Chemie*, **54**, 1841, 35–42.

3 C.W. Tang, Two-layer organic photovoltaic cell, *Appl. Phys. Lett.*, **48**, 1986, 183–185.

4 N.S. Sariciftci, L. Smilowitz, A.J. Heeger, and F. Wudl, Photoinduced electron transfer from a conducting polymer to buckminsterfullerene, *Science*, **258**, 1992, 1474–1476.

5 G. Yu and A.J. Heeger, Charge separation and photovoltaic conversion in polymer composites with internal donor/acceptor heterojunctions, *J. Appl. Phys.*, **78**, 1995, 4510–4515.

6 A. Cravino and N.S. Sariciftci, Double-cable polymers for fullerene based organic optoelectronic applications, *J. Mater. Chem.*, **12**, 2002, 1931–1943.

7 A. Cravino, Conjugated polymers with tethered electron-accepting moieties as ambipolar materials for photovoltaics, *Polym. Int.*, **56**, 2007, 943–956.

8 N. Martin and F. Giacalone (eds), *Fullerene Polymers*, Wiley-VCH, Weinheim, 2009.

9 H. Shirakawa, E.J. Louis, A.G. MacDiarmid, *et al*., Synthesis of electrically conducting organic polymers: halogen derivatives of polyacetylene, $(CH)_x$, *J. Chem. Soc. Chem. Commun.*, 1977, 578–580.

10 F.C. Krebs, Fabrication and processing of polymer solar cells: a review of printing and coating techniques, *Sol. Energy Mater. Sol. Cells*, **93**, 2009, 394–412.

11 H. Hoppe and N.S. Sariciftci, Polymer solar cells, *Adv. Polym. Sci.*, **214**(1), 2007, 1–86.

12 B.C. Thompson and J.M.J. Frechet, Polymer-fullerene composite solar cells, *Angew. Chem., Int. Ed.*, **47**, 2008, 58–77.

13 M.A. Brady, G.M. Su, and M.L. Chabinyc, Recent progress in the morphology of bulk heterojunction photovoltaics, *Soft Matter*, **7**, 2011, 11065–11077.

14 S. Beaupre' and M. Leclerc, PCDTBT: En route for low cost plastic solar cells, *J. Mater. Chem. A*, **1**, 2013, 11097–11105.

15 L. Huo, X. Guo, S. Zhang, *et al*., PBDTTTZ: A broad band gap conjugated polymer with high photovoltaic performance in polymer solar cells, *Macromolecules*, **44**, 2011, 4035–4037.

16 M. Wang, C. Li, A. Lv, *et al*., Spirobifluoroene-Based Conjugated Polymers for Polymer Solar Cells with High Open-Circuit Voltage, *Macromolecules*, **45**, 2012, 3017–3022.

17 D.H. Wang, J.K. Kim, J.H. Seo, *et al*., Transferable graphene oxide by stamping nanotechnology: electron-transport layer for efficient bulk-heterojunction solar cells, *Angew. Chem., Int. Ed.*, **52**, 2013, 2874–2880.

18 P. Cai, Z. Chen, L. Zhang, *et al*., An extended π–conjugated area of electron-donating units in d-a structured polymers towards high-mobility field-effect transistors and highly efficient polymer solar cells, *J. Mater. Chem. C*, **5**, 2017, 2786–2793.

19 J. Song, C. Du, C. Li, and Z. Bo, Silole-containing polymers for high-efficiency polymer solar cells, *J. Pol. Sci., Part A: Polym. Chem.*, **49**, 2011, 4267–4274.

20 W.-H. Lee, S. K. Son, K. Kim, *et al*., Synthesis and characterization of new selenophene-based donor-acceptor low-bandgap polymers for organic photovoltaic cells, *Macromolecules*, **45**, 2012, 1303–1312.

21 T.-Y. Chu, J. Lu, S. Beaupré, *et al*., Effects of the molecular weight and the side-chain length on the photovoltaic performance of dithienosilole/thienopyrrolodione copolymers, *Adv. Funct. Mater.*, **22**, 2012, 2345–2351.

22 B.C. Schroeder, Z. Huang, R.S. Ashraf, *et al*., Silaindacenodithiophene-based low band gap polymers – the effect of fluorine substitution on device performances and film morphologies, *Adv. Funct. Mater.*, **22**, 2012, 1663–1670.

23 Z. Fei, R.S. Ashraf, Z. Huang, *et al*., Germanindacenodithiophene based low band gap polymers for organic solar cells, *Chem. Commun.*, **48**, 2012, 2955–2957.

24 M.H. Tong, S. Cho, J.T. Rogers, *et al*., Higher molecular weight leads to improved photoresponsivity, charge transport and interfacial ordering in a narrow bandgap semiconducting polymer, *Adv. Funct. Mater.*, **20**, 2010, 3959–3965.

25 C. Piliego, T.W. Holcombe, J.D. Douglas, *et al*., Synthetic control of structural /order in *N*-Alkylthieno[3,4-*c*]pyrrole-4,6-dione-based polymers for efficient solar cells, *J. Am. Chem. Soc.*, **132**, 2010, 7595–7597.

26 P. Sista, B. Xue, M. Wilson, *et al*., Influence of the alkyl substituents spacing on the solar cell performance of benzodithiophene semiconducting polymers, *Macromolecules*, **45**, 2012, 772–780.

27 J. Zhao, Y. Li, G. Yang, *et al*., Efficient organic solar cells processed from hydrocarbon solvents, *Nat. Energy*, **1**, 2016, 15027 (1–7).

28 J.T. Bloking, X. Han, A.T. Higgs, *et al*., Solution-processed organic solar cells with power conversion efficiencies of 2.5% using benzothiadiazole/imide-based acceptors, *Chem. Mater.*, **23**, 2011, 5484–5490.

29 C. Zhan, X. Zhang and J. Yao, New advances in non-fullerene acceptor based organic solar cells, *RSC Adv.*, **5**, 2015, 93002–93026.

30 S. Zhang, Y. Qin, M.A. Uddin, *et al*., A fluorinated polythiophene derivative with stabilized backbone conformation for highly efficient fullerene and non-fullerene polymer solar cells, *Macromolecules*, **49**, 2016, 2993–3000.

31 W. Zhao, D. Qian, S. Zhang, *et al*., Fullerene-free polymer solar cells with over 11% efficiency and excellent thermal stability, *Adv. Mater.*, **28**, 2016, 4734–4739.

32 Y. Zhang, X. Guo, B. Guo, *et al*., Nonfullerene polymer solar cells based on a perylene monoimide acceptor with a high open-circuit voltage of 1.3 V, *Adv. Funct. Mater.*, **27**, 2017, 1603892 (1–8).

33 T. Kim, J.-H. Kim, T.E. Kang, *et al*., Flexible, highly efficient all-polymer solar cells, *Nat. Commun.*, **6**, 2015, 8547 (1–7).

34 Y.-J. Hwang, B.A.E. Courtright, A.S. Ferreira, *et al*., 7.7% Efficient all-polymer solar cells, *Adv. Mater.*, **27**, 2015, 4578–4584.

35 J. Sun, J. Gu, J. Yuan, *et al*., High performance all-polymer solar cells employing systematically tailored donor polymers, *Org. Electron.*, **33**, 2016, 227–234.

36 R. N. Thomas, Acid catalyzed fullerenation of carbazole polymer, *J. Polym. Sci. Part A: Polym. Chem.*, **32**, 1994, 2727–2737.

37 Y. Chen, Z-E. Huang, and R-F. Cai, The synthesis and characterization of C_{60} chemically modified poly(*N*-vinycarbazole), *J. Polym. Sci., Part B: Polym. Phys.*, **34**, 1996, 631–640.

38 B. Gholamkhass, T. J. Peckham and S. Holdcroft, Poly(3-hexylthiophene) bearing pendant fullerenes: aggregation vs self-organization, *Polym. Chem.*, **1**, 2010, 708–719.

39 F. Zhang, M. Svensson, M. R. Andersson, *et al*., Soluble polythiophenes with pendant fullerene groups as double cable materials for photodiodes, *Adv. Mater.*, **13**, 2001, 1871–1874.

40 Z. Tan, J. Hou, Y. He, *et al*., Synthesis and photovoltaic properties of a donor-acceptor double-cable polythiophene with high content of C_{60} pendant, *Macromolecules*, **40**, 2007, 1868–1873.

41 M. Lanzi, L. Paganin, and F. Errani, Synthesis, characterization and photovoltaic properties of a new thiophne-based double-cable polymer with pendant fullerene group, *Polymer*, **53**, 2012, 2134–2145.

42 A. Cravino, G. Zera, H. Neugebauer, *et al*., Electropolymerization and spectroscopic properties of a novel double-cable polythiophene with pendant fullerenes for photovoltaic applications, *Synth. Met.*, **121**, 2001, 1555–1556.

43 A. Cravino, G. Zerza, H. Neugebauer, *et al*., Electrochemical and photophysical properties of a novel polythiophene with pendant fulleropyrrolidine moieties: toward "double cable" polymers for optoelectronic devices, *J. Phys. Chem. B*, **106**, 2002, 70–76.

44 Y. He, J. Hou, Z. Tan and Y. Li, Synthesis and photovoltaic properties of polythiophene derivatives with side chains containing C_{60} end group, *J. Appl. Polym. Sci.*, **115**, 2010, 532–539.

45 A. Ramar and R. Saraswathi, Synthesis and characterization of a novel poly(isothianaphthene)-C_{60} double-cable polymer, *J. Mater. Sci.: Mater. Electron.*, **27**, 2016, 852–861.

46 Y. Chen, Z-E. Huang, and R-F. Cai, The synthesis and characterization of C_{60} chemically modified poly(*N*-vinylcarbazole), *J. Polym. Sci., Part B: Polym. Phys.*, **34**, 1996, 631–640.

47 T.X. Lava, F. Tran-Vanb, P.H. Aubert, and C. Chevrota, Elaboration and characterization of donor-acceptor polymer through electropolymerization of fullerene substituted N-alkylcarbazole, *Synth. Met.*, **162**, 2012, 1923–1929.

48 A. Ramar and R. Saraswathi, Synthesis and characterization of a charm-bracelet-type poly(*N*-vinylcarbazole)-C_{60} double-cable polymer, *J. Mater. Sci.*, **50**, 2015, 3740–3749.

49 N. Berton, I. Fabre-Francke, D. Bourrat, *et al.*, Poly(bisthiophene-carbazole-fullerene) double-cable polymer as new donor-acceptor material: preparation and electrochemical and spectroscopic characterization, *J. Phys. Chem. B*, **113**, 2009, 14087–14093.

50 T. Benincori, E. Brenna, F. Sannicolo, *et al.*, The first "charm bracelet" conjugated polymer: an electroconducting polythiophene with covalently bound fullerene moieties, *Angew. Chem.*, **35**, 1996, 648–651.

51 A. Yassar, M. Hmyene, D.C. Loveday, and J.P. Ferraris, Synthesis and characterization of polythiophenes functionalized by buckminsterfullerene, *Synth. Met.*, **84**, 1997, 231–232.

52 A.M. Ramos, M.T. Rispens, J.K.J. van Duren, *et al.*, Photoinduced electron transfer and photovoltaic devices of a conjugated polymer with pendant fullerenes, *J. Am. Chem. Soc.*, **123**, 2001, 6714–6715

53 M. Otero, T. Dittrich, J. Rappich, *et al.*, Photoinduced charge separation in organic-inorganic hybrid sytem: C_{60}-containing electropolymer/CdSe-quantum dots, *Electrochim. Acta*, **173**, 2015, 316–322.

54 S. Miyanishi, Y. Zhang, K. Hashimoto, and K. Tajima, Controlled synthesis of fullerene-attached poly(3-alkylthiophene)-based copolymers for rational morphological design in polymer photovoltaic devices, *Macromolecules*, **45**, 2012, 6424–6437.

55 M. Lanzi, E. Salatelli, T. Benelli, *et al.*, A regioregular polythiophene-fullerene for polymeric solar cells, *J. Appl. Polym. Sci.*, **132**, 2015, 42121 (1–10).

56 P.J. Reucroft, P.L. Kronick and E.E. Hillman, Photovoltaic effects in tetracene crystals, *Mol. Cryst. Liq. Cryst.*, **6**, 1969, 247–254.

57 N.S. Sariciftci, L. Smilowitz, A.J. Heeger, and F. Wudl, Semiconducting polymers (as donors) and buckminsterfullerene (as acceptor): photoinduced electron transfer and heterojunction devices, *Synth. Met.*, **59**, 1993, 333–352.

58 M. Hiramoto, H. Fukusumi, and M. Yokoyama, Three-layered organic solar cell with a photoactive interlayer of codeposited pigments, *Appl. Phys. Lett.*, **58**, 1991, 1062–1064.

59 R. Po, M. Maggini, and N. Camaioni, Polymer solar cells: recent approaches and achievements, *J. Phys. Chem. C*, **114**, 2010, 695–706.

60 Z. He, C. Zhong, X. Huang, *et al*., Simultaneous enhancement of open-circuit voltage, short-circuit current density and fill factor in polymer solar cells, *Adv. Mater.*, **23**, 2011, 4636–4643.

61 A. Hadipour, B. de Boer, J. Wildeman, *et al*., Solution-processed organic tandem solar cells, *Adv. Funct. Mat.*, **16**, 2006, 1897–1903.

62 J.Y. Kim, K. Lee, N.E. Coates, *et al*., Efficient tandem polymer solar cells fabricated by all-solution processing, *Science*, **317**, 2007, 222–225.

63 W. Li, A. Furlan, K.H. Hendriks, *et al*., Efficient tandem and triple-junction polymer solar cells, *J. Am. Chem. Soc.*, **135**, 2013, 5529–5532.

64 C.-C. Chen, W.-H. Chang, K. Yoshimura, *et al*., An efficienct triple-junction polymer solar cell having a power conversion efficiency exceeding 11%, *Adv. Mater.*, **26**, 2014, 5670–5677.

65 H. Zhou, Y. Zhang, C.-K. Mai, *et al*., Polymer homo-tandem solar cells with best efficiency of 11.3%, *Adv. Mater.*, **27**, 2015, 1767–1773.

66 J. Yuan, J. Gu, G. Shi, *et al*., High efficiency all-polymer tandem solar cells, *Sci. Rep.*, **6**, 2016, 26459 (1–7).

67 J. Rostalski and D. Meissner, Photocurrent spectroscopy for the investigation of chaarge carrier generation and transport mechanisms in organic p/n-junction solar cells, *Sol. Energy Mater. Sol. Cells*, **63**, 2000, 37–47.

68 Y. Xahin, S. Alem, R. de Bettignies, and J.-M. Nunzi, Development of air stable polymer solar cells using an inverted gold on top structure, *Thin Solid Films*, **476**, 2005, 340–343.

69 L-M. Chen, Z. Hong, G. Li, and Y. Yang, Recent progress in polymer solar cells: manipulation of polymer:fullerene morphology and the formation of efficient inverted polymer solar cells, *Adv. Mater.*, **21**, 2009, 1434–1449.

70 H. Oh, J. Krantz, I. Litzov, *et al*., Comparison of various sol-gel derived metal oxide layers for inverted organic solar cells, *Sol. Energy Mater. Sol. Cells*, **95**, 2011, 2194–2199.

71 C.-H. Chen, Y.-J. Cheng, C.-Y. Chang, and C.-S. Hsu, Donor-acceptor random copolymers based on a ladder-type nonacyclic unit: synthesis, characterization and photovoltaic applications, *Macromolecules*, **44**, 2011, 8415–8424

72 T. Yang, M. Wang, C. Duan, *et al*., Inverted polymer solar cells with 8.4% efficiency by conjugated polyelectrolyte, *Energy Environ. Sci.*, **5**, 2012, 8208–8214.

73 Z. He, C. Zhong, S. Su, *et al*., Enhanced power-conversion efficiency in polymer solar cells using an inverted device structure, *Nat. Photon.*, **6**, 2012, 591–595.

74 S. Nam, J. Seo, S. Woo, *et al*., Inverted polymer fullerene solar cells exceeding 10% efficiency with poly(2-ethyl-2-oxazoline) nanodots on electron-collecting buffer layers, *Nat. Commun.*, **6**, 2015, 8929 (1–9).

75 Y. Wang, W.-D. Xu, J.-D. Zhang, *et al*., A small molecule/fullerene binary acceptor system for high-performance polymer solar cells with enhanced

light-harvesting properties and balanced carrier mobility, *J. Mater. Chem. A*, **5**, 2017, 2460–2465.

76 Y.-J. Cheng, S.-H. Yang, and C.-S. Hsu, Synthesis of conjugated polymers for organic solar cell applications, *Chem. Rev.*, **109**, 2009, 5868–5923.

77 Y. Wang, W. Wei, X. Liu, and Y. Gu, Research progress on polymer heterojunction solar cells, *Sol. Energy Mater. Sol. Cells*, **98**, 2012, 129–145.

78 K. Zhang, Z. Hu, C. Sun, *et al.*, Toward solution-processed high-performance polymer solar cells: from material design to device engineering, *Chem. Mater.*, **29**, 2017, 141–148.

11

Rational Strategies for Large-area Perovskite Solar Cells: Laboratory Scale to Industrial Technology

Arunachalam Arulraj[1] *and Mohan Ramesh*[2]

[1] *University College of Engineering-Bharathidasan, Institute of Technology (BIT) campus, Anna University, India*
[2] *CSIR-Central Electrochemical Research Institute, India*

11.1 Introduction

The earth receives almost 2.9×10^{15} kW of energy every day in the form of electromagnetic radiation from the sun, which is about one hundred times the total energy consumption of the globe in a year [1]. The conversion of solar energy into electrical energy is called photovoltaic technology or solar technology. Solar technology is not new, its history spans from the seventh century B.C, when we started out of using solar radiation with glass and mirrors to light fires. At present, we have everything from solar-powered bags to solar-powered buildings [2]. In 1954, Bell telephone research laboratories reported 4% efficiency using silicon solar cells, which later improved to attain 11% efficiency. During this era the cost of generation of one watt was about $77/watt. However, to date the efficiency of silicon-based solar cells has not crossed 18–20% and the costs of production are about $5–6/watt.

The journey of perovskite structured materials started in the nineteenth century, when there were research studies of inorganic lead halides [3]; organic–inorganic halides were studied in the early twentieth century [4]. The first reports of perovskite-structured hybrid halide compounds – methyl ammonium lead [$(CH_3NH_3Pb)\ X_3$] (X = Cl, I, Br) and methyl ammonium tin bromine iodide [$CH_3NH_3SnBr_{1-x}I_x$] alloy – were by Weber in 1978 [5, 6]. In subsequent decades researchers started to study its context of unusual physics and chemistry in earnest [7–9]. After lead halide compounds were first suggested for photovoltaic applications in the 1980s [10, 11], one had to wait until 2009 for Kojima *et al*. to report first on perovskite for solar cells [12]; the rapid

Rational Design of Solar Cells for Efficient Solar Energy Conversion, First Edition.
Edited by Alagarsamy Pandikumar and Ramasamy Ramaraj.

improvement in performance has made it the rising star of the photovoltaic world within a short span of years.

11.2 Perovskite

The word "perovskite" refers to any kind of material with same type of crystal structure as calcium titanium oxide ($CaTiO_3$). The mineral was discovered in the Ural mountains of Russia by Gustav Rose in 1839 and is named after Russian mineralogist Lev Perovski [13]. It adopts a three-dimensional crystal structure consisting of a corner-sharing TiO_6 octahedral, with Ca occupying the cubo-octahedral cavity in each unit cell. The same crystal structure is also found for broad range of materials with ABX_3 stoichiometry, in which A and B are cations, where A is a large cation compared to B; X is an anion, which could be oxygen, nitrogen, carbon, or a halogen (chlorine, bromine, or iodine). The schematic representation of the ABX_3 crystal structure is represented in Figure 11.1 [14]. Perovskite materials are archetypal system for phase transitions with accessible cubic, orthorhombic, tetragonal, trigonal, and monoclinic polymorphs depending on the tilting and rotation of the BX_3 polyhedral in the lattice [15]. Reversible phase changes can be induced by a range of external stimuli, including temperature, pressure, and magnetic or electric fields. To keep the perovskite crystal structure stable, the size of the three ions is strictly confined by the tolerance factor [16]:

$$T = \frac{R_B + R_X}{\sqrt{2}\left(R_A + R_X\right)}$$

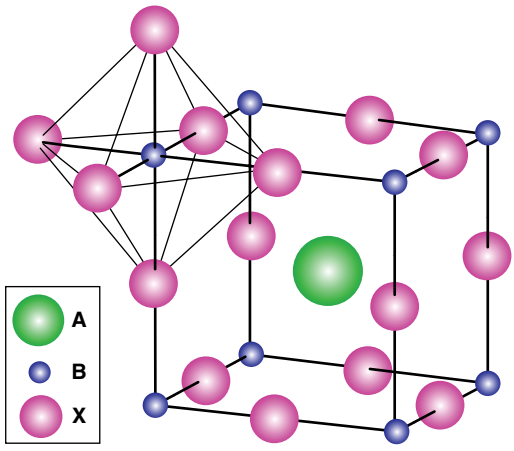

Figure 11.1 ABX_3 crystal structure [14]. *Source:* Zhao. http://www.mdpi.com/2304-6732/2/4/1139/htm. Licensed under CC BY 4.0.

where R_A, R_B and R_X are ionic radii of A, B and X site elements, respectively. The tolerance factor is applicable at room temperature to the empirical ionic radii. For an ideal cubic structure the t-value appears to be within the limit of 0.75 to 1 (i.e. $0.75 > t > 1$) due to different distortions; in some cases it is found to be very close to unity. These distortions play a crucial role in perovskite, particularly in the electronic, magnetic, and dielectric properties, which are most significant in the case of diverse applications.

11.3 Perovskite Solar Cells

Until 1980 there were no reports relating halide perovskite materials as a solar absorber; Salau reported a new perovskite alloy having a direct bandgap (between 1.4 and 2.2 eV). Organometal halide perovskite as a light absorber in solar cells has amazed everyone by its performance. It receives a special attention in the scientific community and industry because of its low cost, ease of fabrication, and high photoconversion efficiency (PCE). Some perovskites, like $CH_3NH_3PbI_3$, $CH_3NH_3PbIxCl_{3-x}$, and formamidinium lead iodide [$FAPbI_3$], have broad absorption spectra with a bandgap of about 1.5–1.6 eV and are used as light absorbers in perovskite solar cells (PSCs). In addition to its absorption properties, a perovskite should have appropriate dielectric constant (ε), Bohr radius, exciton binding energy (E_b), and diffusion length of charge carriers. These factors are strongly correlated with the photophysical, photoelectrical properties and solar cell device performance. The electron hole pairs generated by photons in the organic–inorganic perovskites can exist as free charge carriers or excitons, with E_b based on the excitons, and can be classified as Frenkel-type or Wannier-type. Many researchers have reported an E_b of 29–50 meV for $CH_3NH_3PbI_3$ [17–20] and 35–98 meV for $CH_3NH_3PbCl_{3-x}I_x$ [21, 22]. Recently, there was a report with an E_b of 2 meV for $CH_3NH_3PbI_3$ perovskite; this is very low compared to inorganic semiconductors like Si (15.0 meV), GaAs (4.2 meV), and CdTe (10.5 meV) [23]. Based on these excellent capabilities of light absorption and photophysical/photoelectrical properties, perovskites are considered as promising materials for solar cell devices.

In early 2009, organometal halide perovskites were first employed as visible-light "sensitizers" in photoelectrochemical cells [24]. In this work, performed by Miyasaka *et al.*, the solar cells were based on mesoporous TiO_2 photoanodes that were sensitized with $CH_3NH_3PbX_3$. However, the resulting PCE was not up to the levels obtained for triiodide (about 3.81%) and for tribromide (about 3.13%) and the cell stabilities were poor in a liquid electrolyte. Park *et al.* in 2011 fabricated dye-sensitized solar cells (DSSCs) using $CH_3NH_3PbI_3$ ($MAPbI_3$) nanocrystals with a thickness of 2–3 nm, which increased the PCE to 6.54% at one sun condition by means of nanocrystals with iodide redox shuttle [25]. In both cases the perovskite materials were applied in quantum dots (QDs)

deposited on TiO_2, but these sensitizers decomposed or dissolved in liquid electrolyte and the cells became rapidly degraded within few minutes.

The breakthrough in PSCs came in 2012, when Professor Gratzel and his coworkers collaborated with Park *et al*. They used $MAPbI_3$ as a light harvester in combination with conducting polymer as hole conductor, 2,20,7,7,0-tetrakis-(N,N-dimethoxyphenyl-amine)-9,90-spirobi-fluorene (spiro-MeOTAD) on mesoporous TiO_2 producing the PCE of 9.7% [26]. During the same period, Snaith, in collaboration with Miyasaka, reported solar cells based on a "meso-superstructured" scaffold, which revealed that an inert scaffold such as Al_2O_3 can replace the n-type semiconducting materials in the device fabrication. By employing this superstructure technique, device performance was boosted to 10.9 %. This result also established that perovskite materials can behave as n-type semiconductors [27]. Later on it was reported that perovskite has an ambipolar property and can transport both electrons and holes, and that a solid perovskite film few hundred nanometers thick can sustain charge generation and transport [28]. The evolution of PSCs and the various types based on their configuration are shown in Figure 11.2 [29]. The outstanding achievements in device performance from both materials science and device engineering promise further breakthroughs in this field of study. However, the perception of the mechanisms underlying such exceptional performance has not grown at the same pace [30–34].

11.3.1 Architecture

The first perovskite-based photovoltaic system was, in fact, a mimic of DSSCs, in which dye molecules had been replaced by perovskite nanoparticles and the liquid electrolyte had been replaced with a solid-state hole transporting layer [35]. The architecture of perovskite solar cells evolved from mesoscopic sensitized configuration, super-mesostructured scaffold, to thin film planar configuration. The structure of organo-lead halides based hybrid solar cells basically categorized into mesoscopic architecture (Figures 11.3a and 11.3c) or planar architecture (Figures 11.3b and 11.3d). For either mesoscopic or planar, the devices can be constructed with n-i-p (Figures 11.3a and 11.3b) or p-i-n heterojunctions (Figure 11.3c and 11.3d), depending on which polarity of contact is applied as substrate layer. These four structures of PSCs are schematically shown in Figure 11.3 [36].

11.3.1.1 Mesoporous PSCs

In this type of architecture, mesoscopic semiconducting materials have been used as an electron transporting layer (ETL) (typically TiO_2) and the perovskite materials serve as a light harvester. Upon absorption of photons by perovskite materials, the bands are excited and the electrons are transferred into the neighboring ETL while the holes move towards the adjacent hole

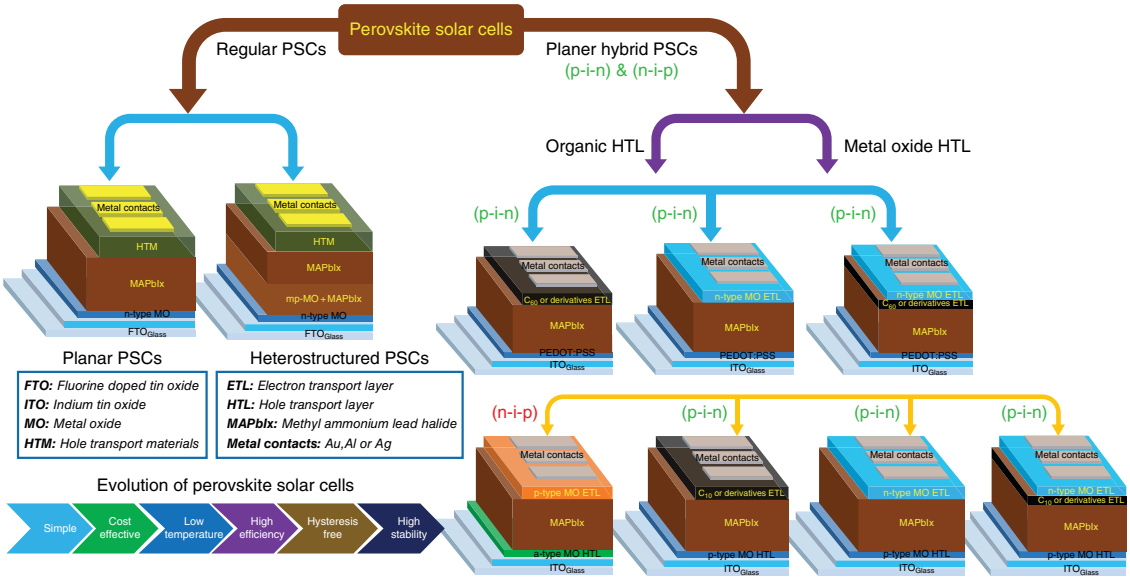

Figure 11.2 Evolution of PSCs [29]. Reproduced with permission of Royal Society of Chemistry.

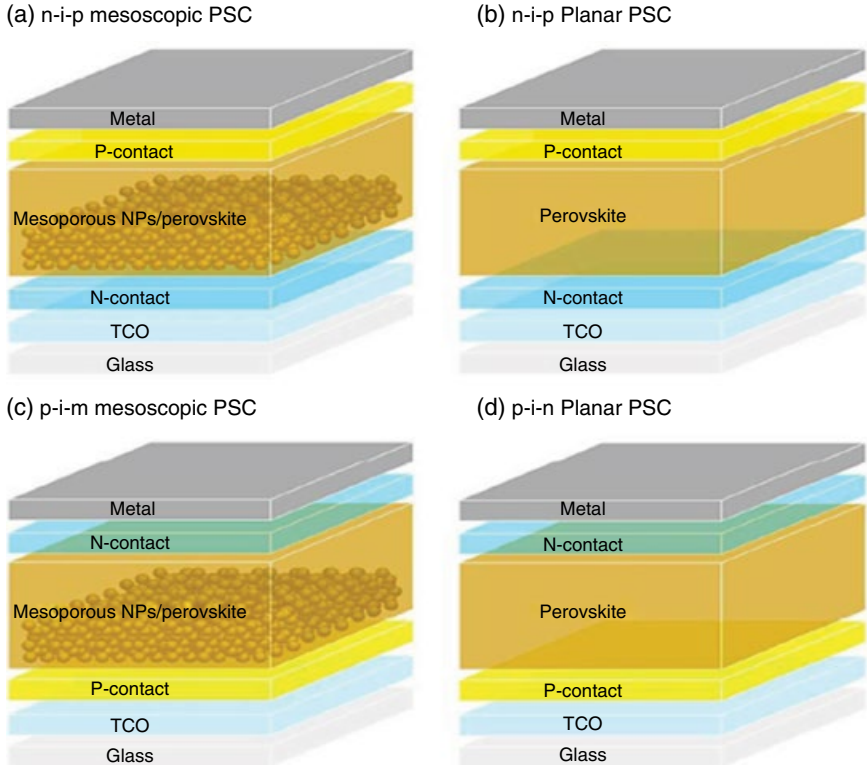

Figure 11.3 A schematic representation of (a) and (b) n-i-p mesoporous and planar, (c) and (d) p-i-n n-i-p mesoporous and planar structures [36]. Reproduced with permission of Royal Society of Chemistry.

transporting layer (HTL). A compact film of TiO_2 (C-TiO_2) is deposited beneath the scaffold as a hole-blocking layer [37, 38]. The active and buffer layers are sandwiched between the transparent conducting substrate and the metal contact electrode [37]. To enhance the performance of the device, this type of configuration was first urbanized by coating the facet of the scaffold by perovskite precursor solutions invading the scaffold pores [39]. The pitfall in this kind of configuration is that deposition of the mesoporous layer implies high temperature processing and thus makes it an extortionate process. Also, the mesoporous layer may not be structurally homogeneous, causing fragmented padding of perovskite materials in the pores, which results in suppression of the of the device's performance [27, 40, 41]. Due to this issue, the pilot scaling of devices may not be possible when employing this kind of configuration.

11.3.1.2 Planar PSCs

To overcome this issue novel device architecture, called planar configuration, has been developed that can be fabricated at low temperature. This kind of architecture does not make use of mesoporous architecture and high temperature processes, which is a practical option for scaling-up the devices. Based on its layer stacking sequences it is subdivided into two: (i) the conventional n-i-p structure, in which ETL is deposited over the bottom cathode, HTL is deposited beneath the top anode layer, and the perovskite light harvester has been sandwiched between the ETL and HTL; and (ii) the p-i-n structure, which is the inverse of the n-i-p [42]. The n-i-p configuration was first introduced in 2003 with a modification of meso-superstructured PSCs by incorporating Al_2O_3 as a scaffold on the c-TiO_2 layer [43]. This kind of architecture has the advantage that the perovskite materials can fulfil both the roles of light absorption and efficient charge transport with the minimal recombination [44–47]. Similarly, the planar configuration with the p-i-n type was first developed in 2013 by Guo *et al.* following the work reported by Etgar *et al*., who reported that perovskite materials can act as both absorber and hole conductor [48, 49]. In this first kind of p-i-n architecture, poly(3, 4-ethylenedioxythiophene) polystyrene sulfonate (PEDOT:PSS) was employed as a HTL, a fullerene-based molecule as an acceptor, and perovskite materials as a donor. Recently, there have been several kinds of inorganic p-type layer, such as nickel oxide (NiO_x), grapheme-based materials, CuSCN, etc., that have been used effectively in the fabrication of perovskite solar cells [50–53]. The p-i-n planar architecture finds a path in transferring smaller scale devices into larger scale devices towards commercialization owing to its ease of fabrication and relatively small hysteresis [54–56].

11.4 Device Processing

It is not an easy task to transfer a process from the research scale to a commercial scale. It must pass through many stages that tackle each step to transform the device into a commercial one. Considering these aspects for device processing is a significant tool that plays a role in pilot-scaling of devices. There are several strategies involving in up- scaling the devices starting from synthesizing of materials to fabrication of devices. Some of the important aspects for transferring technology towards commercialization are discussed here.

11.4.1 Solvent Engineering

Solvent engineering technology has proven to be an efficient way for producing dense perovskite layers by controlling the grain size. To improve the quality of the perovskite films both polar and nonpolar solvents have been used in

solvent engineering process [57]. A few steps need to be considered for an effective solvent engineering process: (i) the ratio of solvent and the precursor solution taken because the stretching of perovskite crystal depends on the solvent concentration; (ii) how the solvent forms the complexes with the perovskite precursor solution; (iii) what intermediate phase is formed during the solvent treatment plays a critical role in drastically reducing the energy barrier in perovskite formation; and (iv) how to remove the remnant solvent [58]. By considering all these facts an effective PSC can be fabricated with solvent engineering technology. Seok *et al.* demonstrated a cosolvent method by mixing DMSO in gamma–butyrolactone for a one-step spin coating process, which enabled the dissolubility of the precursor to be enhanced and dense perovskite films formed [59]. Park *et al.* demonstrated the solvent engineering technique using diethyl ether as a superfluous solvent and concluded the device fabricated using diethyl ether possesses good thermal stability with better PCE [60]. Even though solvent engineering technology is a very constructive experimental methodology, two major challenges remain. Firstly, the mechanism of the nonpolar solvent on the precursor adducts, which further governs the perovskite formation, has not been systematically studied yet. Secondly, the reason why the CH_3NH_3-PbI_2-DMSO adduct plays a more important role in the crystallization process than CH_3NH_3-PbI_2-dimethylformamide (DMF) is unclear.

11.4.2 Compositional Engineering

Compositional engineering plays a vital role in the formation of high quality perovskite films for device fabrication. The design of high performance PSCs using mixed perovskite ($MAPbI_3$) and ($MAPbBr_3$) was first reported as material engineering [61]. From this successful formation the bandgap energy and lattice parameters of the phase structure were determined. The Goldschmidt tolerance factor with the value of unity can be achieved by tuning the composition of cations and anions in the PSCs, which favors stability of perovskite halides and reduces charge trap density [62, 63]. Researchers developed various compositions for fabricating the PSCs starting from the ETL to HTL to improve the stability and the performance of the device. The highest PCE of PSCs to date was mostly achieved using compositional engineering [64]. Recently, Shi Tang *et al.* employed cesium and bromine ions in the perovskite solution and fabricated the devices and achieved a stabilized photoconversion efficiency of about 19.3% [65].

11.4.3 Interfacial Engineering

The self-assembly crystallization performance of organic–inorganic hybrid perovskite materials is more beneficial in fabrication of perovskite crystals by solution processing at low temperature, but it also possess some

drawbacks in the controlled formation of compact and flat thin film. In the case of high performance PSCs with a thin-film type architecture, it is very crucial to achieve the self-assembly crystallization. Despite the recent unprecedented achievement in reaching a PCE of 22.1% using mesoscopic PSCs [60, 66–68], this is still far from the predicted efficiency limit (about 31%) [69]. Notably, losses occurring due to interfacial recombination were a negative influence in the charge injection at the perovskite/transport layer interface [70]. Similarly, deprived charge transport of electrons and holes in ETL and HTL severely limits charge collection at the electrodes [71–73], which leads to a reduction of both J_{sc} and FF, thus reducing the PCE [74]. Hence, a fine-tuning of interface and interlayer properties is obligatory to enhance the charge transport and extraction at the perovskite/transport layer interface. Moreover, the prospect to tune the perovskite/transport layer interface to allow reduction in JV hysteresis sweep, meanwhile helps in improving the charge collection [75, 76]. The first solvent engineering process was reported by Seok *et al*. with DMSO as mediator, which acts as both solvent and reactant for PbI_2 [59]. The schematic representation is shown in Figure 11.4a. By employing DMSO as intermediate in the PSCs, the substrate results in the formation of flat crystalline and more compact film. The film formation will be:

$$MAI - PbI_2 - DMSO \rightarrow MAPbI_3 + DMSO \uparrow$$

The intermediate phase film will be successfully converted into crystalline perovskite film by subject it to annealing treatment. By removing the intermediate DMSO in the film, the compact and flat morphology formed will remain the same. This successful approach opens a path for controlling the rapid crystallization kinetics of perovskite films. Following this research there is a tremendous interest in applying interfacial engineering in the fabrication of PSCs. Recently Lee *et al*. developed a large area substrate of over 18.4 cm^2 by introducing an amphiphilic conjugated polymer electrolyte as an interfacial compatibilizer and achieved a PCE of 17 % [77]. Similarly, 2D materials like graphene find application in interfacial engineering in PSCs. di Carlo *et al*. demonstrated the fabrication of PSCs using graphene as an interfacial layer to develop an active area of over 50 cm^2 and achieved a PCE of 12.6 % [78]. Recently, Nazeeruddin *et al*. demonstrated $10 \times 10\ cm^2$ PSCs delivering about 11% with zero losses for one year stability using 2D/3D interfacial engineering [79]. In this article the first principle calculation on interface engineering has been done and reported. The density of states (DOS) function for the interface structure with its 2D interface has been reported, as shown in Figure 11.4b. Thus, it opens a gateway for scaling-up and stabilizing the device and transferring technology towards commercialization.

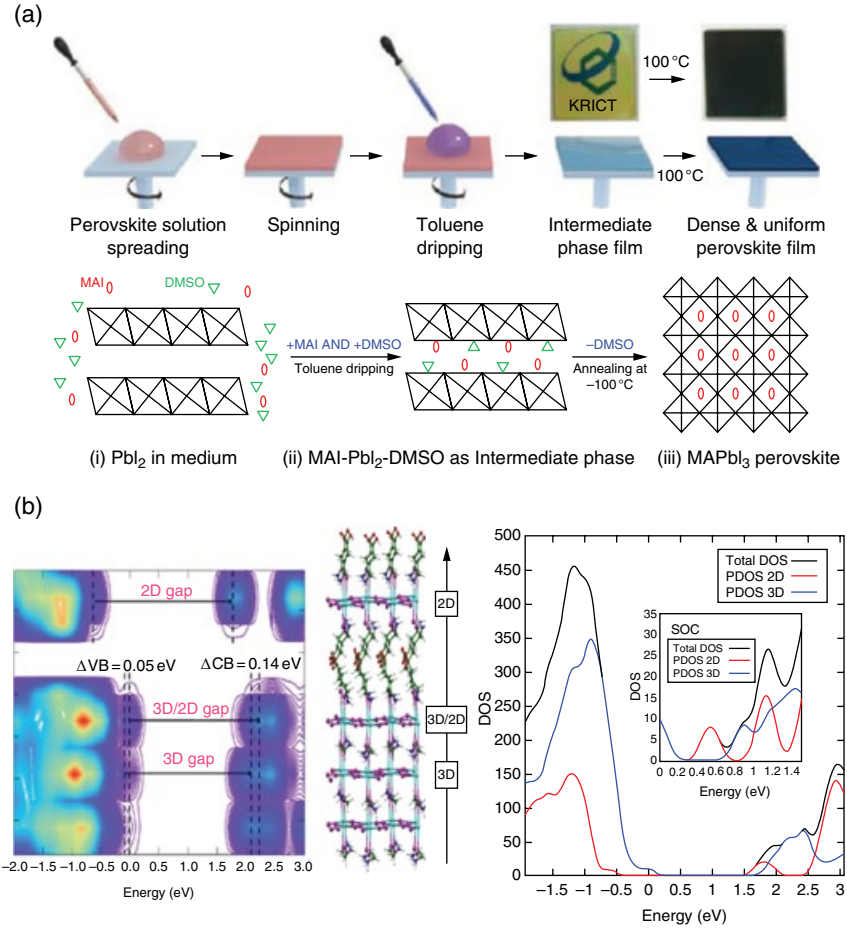

Figure 11.4 (a) Schematic representation of interfacial engineering using DMSO as solvent [59]. Reproduced with permission of Nature Publishing Group. (b) First principle studies on 2D/3D interface using simulation [79]. *Source:* Grancini https://www.nature.com/articles/ncomms15684. Licensed under CC BY 4.0.

11.5 Enhancing the Stability of Devices

The stability of the device is a main concern when considering commercialization. As discussed previously, the performance of the device has increased drastically in terms of efficiency. But the stability of the device still lagging behind, even in the smaller area devices. Long-term stability is mainly affected by the inherent vulnerability of the light absorbers (i.e. perovskite materials) to heat and moisture. Degradation of perovskite materials due to moisture and

heat can be traced in several ways. A few of the best observable examples are the change in color from dark brown to yellow, decreased intensity in light absorption, and changes in the XRD peaks [80–82]. Stability can be improved by encapsulating the whole device, preventing exposure of the perovskite film to moisture. The encapsulation should be done in a careful manner so that it does not allow/include any trace of moisture present in atmosphere [83]. Besides encapsulation, material engineering has to be considered to prevent the perovskite film from decomposition. Tai *et al.* demonstrated the fabrication of PSCs with long-term stability by careful design of materials engineering. The authors used lead (II) thiocyanate as precursor for preparing the perovskite film with a relative humidity of 70% and achieved a maximum PCE of about 15% [84].

11.5.1 Deposition Techniques

The morphology and crystallinity of the perovskite materials play an important role in the device performance. In smaller scale devices, the crystallinity of the perovskite materials can be attained easily by controlling the parameters. In the case of large area device fabrication it is difficult to control the crystallinity and the morphology of the materials used. Crystallization of the materials is strictly related to the deposition technique and the substrate surface used. Similarly, the roughness of the layer is strongly impacted by the manufacturing process and each technique has need of its own frame for film optimization to avoid in homogeneity and the presence of pin-holes. Some of the techniques used for small area devices are not appropriate for pilot scaling the devices, because of their complexity or large amount of materials waste, etc. Some of the materials used in the device fabrication are toxic, so manufacturing must take account of process safety. This section gives a brief discussion on some of the pilot scaling-up processing techniques employed for developing effective module manufacturing.

11.5.1.1 Spin Coating

A main objective for pilot scaling-up of the devices is to ensure highly uniform deposition of the various layers. The most widely used technique at the laboratory scale for device fabrication is spin coating. It delivers good uniformity and thickness with reproducibility of the film. The quality of the film can be controlled by controlling parameters such as deposition time and the ink formulation with the rotational speed. Laboratory-scale devices (typically with the dimension of about 0.1 cm^2) have obtained a recorded efficiency of about 22.1% by using this technique [71, 85]. However, when the device is scaled up from 0.1 cm^2 to 1 cm^2 there will be drop in PCE of about 10–15% in comparative terms [86, 87]. Cheng *et al.* reported on planar device architecture comprising glass/FTO/NiMgLiO/$CH_3NH_3PbI_3$/PCBM/Ti(Nb)Ox/Ag deposited using

spin coating. In this work a PCE of 16.2% for the active area of about 1.02 cm^2 was reported. The certified efficiency of perovskite solar cells over an area > 1 cm^2 was held by the National Institute of Materials Science (NIMS), Japan, up to 2015; it fabricated perovskite solar cells with an area of 1.02 cm^2 with a recorded efficiency of 15.6% [88]. In 2016, Li *et al.* employed a vacuum-flash solution technique for developing perovskite solar cells. In this method spin coated film was placed in a vacuum chamber for few seconds to amplify solvent removal and improve rapid crystallization before an annealing treatment. By employing this method Li and the research group fabricated a device with an active area of 1.44 cm^2 and achieved a PCE of 20.5% and a certified PCE of 19.6% [89].

Even if active areas of about 1 cm^2 are larger than most laboratory scale reported devices, the areas to be considered for pilot scaling-up of devices needs to be at least an order of magnitude larger. Matteocci *et al.* reported perovskite solar cell modules comprising five subcells connected in series, as shown in Figure 11.5a, with a PCE of 5.1%; the authors also described how the

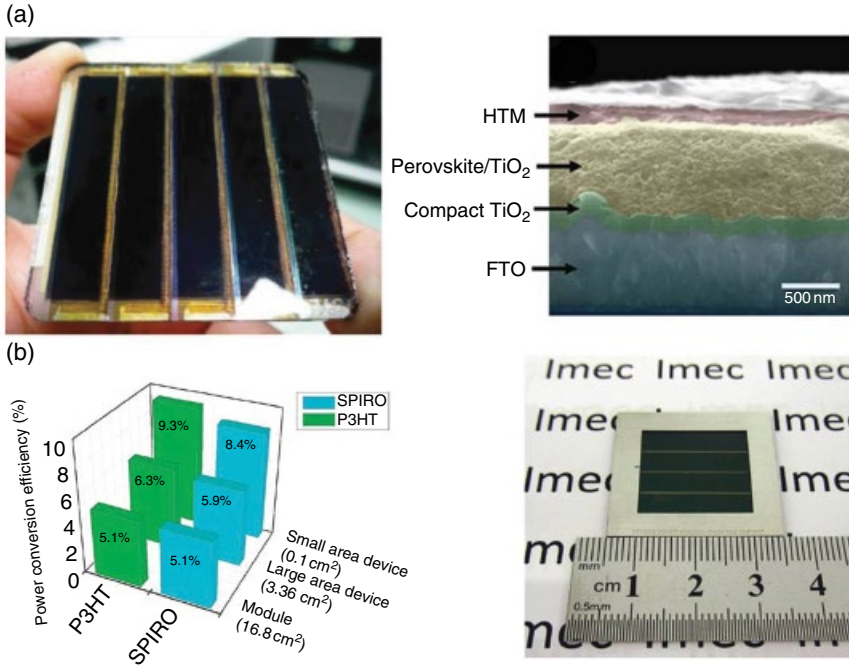

Figure 11.5 (a) Series connected five subcells and cross-section FESEM images with the variation of effect in solvent [90]. Reproduced with permission of Royal Society of Chemistry. (b) pictorial representation of four subcells with active area of 4 cm^2 [91]. Reproduced with permission of Royal Society of Chemistry.

efficiency varied with dimension [90]. Qiu *et al*., in 2016, developed a module with four series-connected cells over an aperture area of 4 cm^2, as shown in Figure 11.5b. With this series connected module, the Qi research group achieved PCE of 13.6% [91]. Matteocci *et al*., following their own previous research work, fabricated modules over the larger dimension of 10 cm^2 and achieved a PCE of 9.1% on the aperture area and 13% on the active area [92]. So far by employing this method, Heo *et al*. have fabricated a perovskite solar module with the larger area of 40 cm^2 with an inverted planar structure and a PCE of 12.9% [93]. Even though the efficiencies of the modules developed using the spin coating technique achieved high leves, in actual fact it does not represent an effective method for up-lifting perovskite solar cell manufacturing, because this method of deposition involves huge volume of waste in solution during fabrication, which increases manufacturing cost and exposure to potentially harmful chemicals. To address this drawback, an alternative technique called "blade coating" has been developed.

11.5.1.2 Blade Coating

Blade coating is one of the printing techniques that offers an option for developing solar modules for processing on a larger scale in a cost effective and simple manner [39]. In general, blade coating has a simple fabrication setup with a micrometer screw, which, in turn, makes it possible to adjust the height of the substrate surface by adjusting the screw. Furthermore, it enables the user to adopt a divergent approach to control the thickness and morphology. The crystallization of perovskite greatly depends on the deposition time and temperature; hence, it is mandatory to control the solvent evaporation rate to achieve a good quality of film. The evaporation rate of the deposited solvent can be controlled by a handful of methods, such as raising the temperature of substrates up to the boiling point of the solvent used or by dribbling air over the surfaces during the coating.

In 2016, Mallajosyula *et al*. reported large area hysteresis-free perovskite solar cells with an active area of 1 cm^2 using the doctor blade technique as shown in Figure 11.6a. The authors reported the effect of controlling the substrate temperature, volume of the solution, and the acceleration speed of the blade. By controlling all these parameters the authors achieved a PCE of 7.32% [94]. In 2015, Razza *et al*. demonstrated fabricating series-connected modules in several dimensions over the larger area of 100 cm^2, in which the patterning of the perovskite was achieved by laser ablation of PbI_2. The larger area module is show in Figure 11.6b. By pattering and controlled deposition of perovskite and HTL, an efficiency of 10.4 % was recorded for an active area of 10 cm^2 and 4.3% for 100 cm^2 active areas [95]. The same research group has achieved a PCE of 9% over 100 cm^2 active areas by optimizing the deposition rate of Spiro-meOTAD by blade coating [96. Yang *et al*. demonstrated fully printable perovskite devices using a blade coating applicator on both glass and flexible

(a)

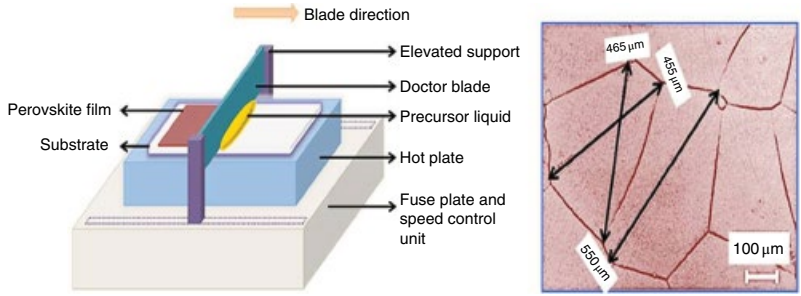

(b)

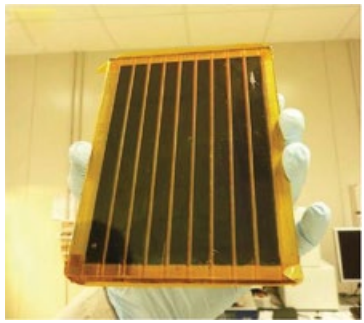

Figure 11.6 (a) Pictorial representation of doctor blade instrument with its growth of grain size [94]. (b) Image of large area module of 100 cm^2 fabricated using doctor blade method [95]. Reproduced with permission of Elsevier Publishing.

substrates, concluding that this is one of the promising scalable techniques of the simplest manner [97]. Yet to increase the reproducibility, an automatic deposition technique called "slot die" coating was developed; it is based on a similar principle to the blade coating technique.

11.5.1.3 Slot Die Coating

Slot die coating is one of the significant printing methods used to deposit the solvent in a large scale manner by controlling the amount of solvent used in a precise manner and of acquiring patterned layout. It works on the same principle employed in the blade coating method. As with the blade coating technique, this method also requires controlled evaporation of solvent to yield a film with a better crystallinity and morphology. Vak *et al.* demonstrated the fabrication of perovskite devices fully using slot die coating. The authors used a 3D printer for deposition in which acceleration and speed can be controlled in all three dimensions of *x, y, z*. Since the device fabrication is fully controlled by the system no hardware is required. The research group reported

deposition of 10 cm^2 with series interconnection of five cells with an active area of 0.1 cm^2 [98].

Jung *et al.* demonstrated fabrication of reliable perovskite films using a printing process through synergetic effects of binary processing additives, N-cyclohexyl-2-pyrrolidone (CHP), and dimethyl sulfoxide (DMSO). Notably, these perovskite films are deposited by facile one-step processing under a room temperature and ambient atmosphere, as shown in Figure 11.6c [99]. Hwang *et al.*, who employed the same 3D printer setup and reported in more detail about the influence of gas quenching, the device configuration, and the film, quenched using gas. The authors reported the possibility of controlling the crystallization temperature aid in terms of reproducibility and morphology control. By varying the temperatures, the PCE of the cells differs; a maximum PCE of 11.96% has been recorded for 70 °C, representing a hopeful result for cells composed of all printed layers except for the electrodes [100]. Similarly, Ming He *et al.* reported the solution printing method and studies of its crystallization kinetics, which is represented in Figure 11.6d [101]. Solliance *et al.* demonstrated a perovskite module with the aperture area of 168 cm^2 using slot die coating with laser pattering that achieved a PCE of 10%. Hence, to improve the perovskite solar cells in the pilot scale, slot die coating is one of the most significant methods, and can be keener in roll-to-roll manufacturing.

11.5.1.4 Screen Printing

Screen printing is one of the artistic techniques that espouse a mesh made of steel or a screen made of synthetic fibers that is used to transfer the ink or emulsion onto a substrate. A desired design called a pattern is made on the mesh and by means of moving a blade or squeegee across the screen it is possible to transfer the emulsion to the substrate through the pattern. The screen printing technique is mainly acquired from the field of DSSCs, in which it is being used for depositing the nanocrystalline materials uniformly on the substrates and modules. The schematic representation of the screen printing technique is shown in Figure 11.7a. Similarly in the case of PSCs, it is used to print the nanocrystalline scaffold in the mesoporous structure for both the cells and module fabrication [102]. Mei *et al.*, in 2014 reported fully screen printed PSCs without employing a hole conducting layer. The research group fabricated PSCs using two mesoporous layers, TiO_2 and ZrO_2, as scaffold into which the perovskite solution had been been infiltrated. The fabricated cells achieved a PCE of 12.8% and were stable for a period of over 1000 hours in ambient full sunlight conditions [56]. More recently, in 2016, Solaronix developed PSCs with a 500 cm^2 large solar module by employing this technique in a quadruple stacked manner. This work transposed laboratory scale cells about 1 cm^2 to a more significant area, a hundred times larger, without a drop in the performance of the devices. The company achieved a PCE of 12%; the cells operated for more than 5000 hours with a thermal stress ideally in the range 50–70 °C.

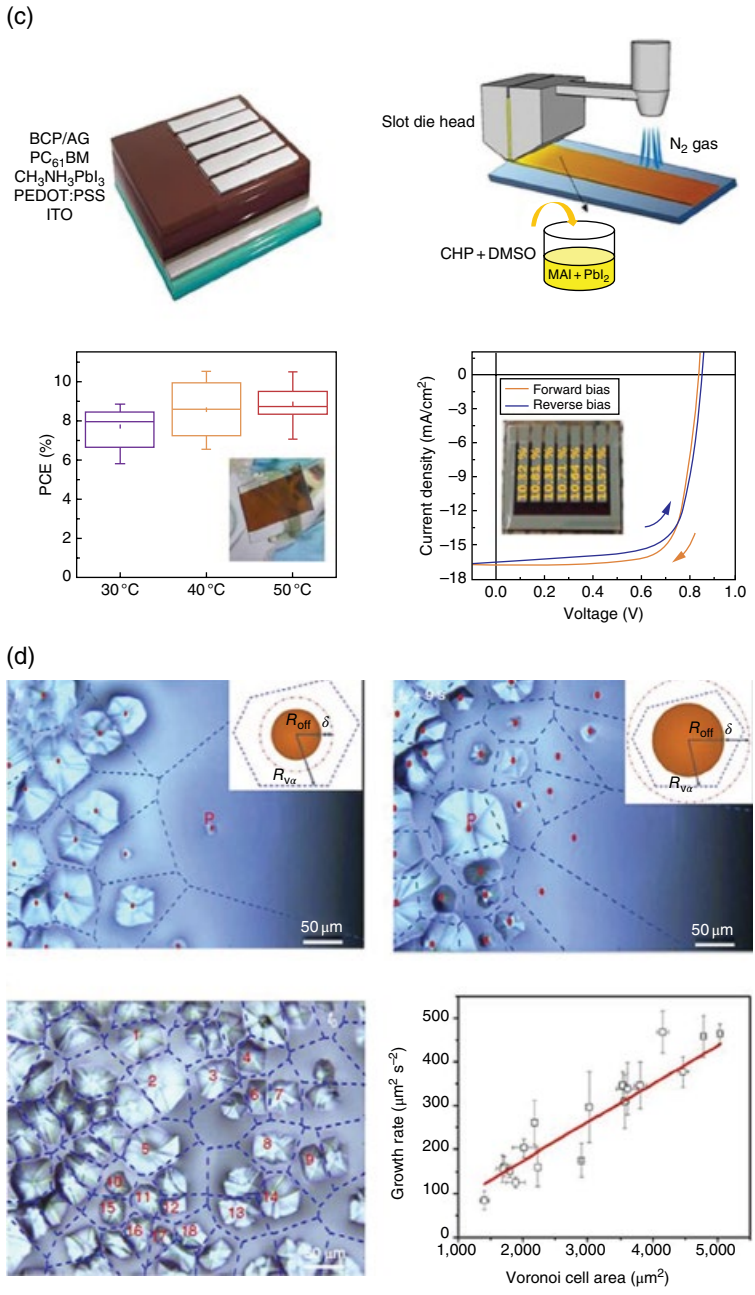

Figure 11.6 (c) Schematic representation of the facile one-step processing of perovskite film using a slot die coater [99]. (d) Kinetic growth study of perovskite crystal. Figure adapted from [101]. *Source:* He. https://www.nature.com/articles/ncomms16045. Licensed under CC BY 4.0.

(a)

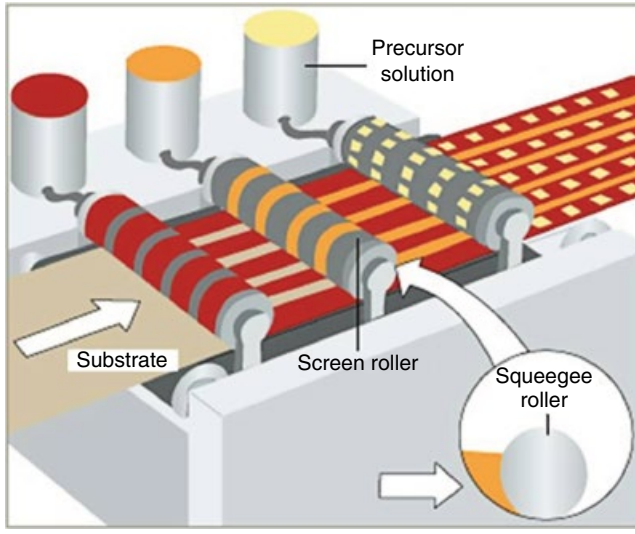

(b)

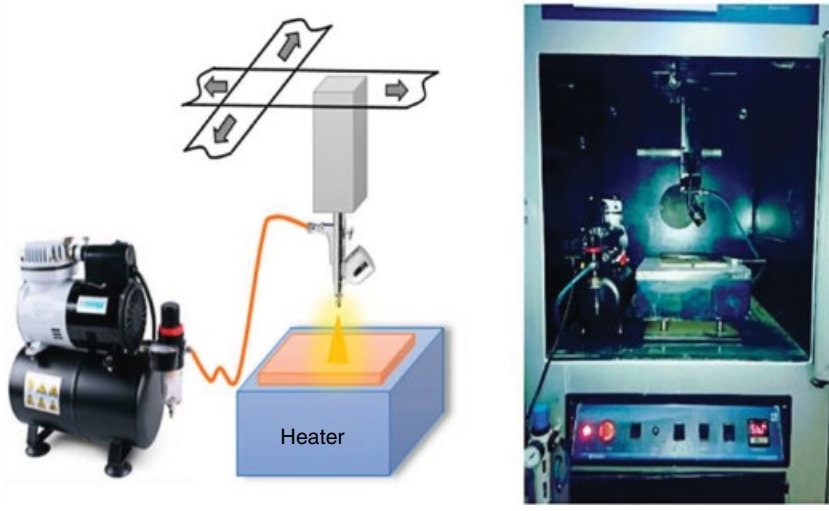

Figure 11.7 (a) Schematic representation of the screen printing method. (b) Pictorial representation of the spray coating method for PSCs. Figure adapted from [105]. *Source:* Habibi. http://www.mdpi.com/2079-6412/7/3/42/htm. Licensed under CC BY 4.0.

Thus, this technique is one of the most significant tools for pilot scaling-up device technology.

11.5.1.5 Spray Coating

Spray coating is an alternative deposition technique widely used in industrial production and it is the best method for polymer solution coating. As early as 2007, the spray painting method was surveyed as a cost-effective technique for fabricating large area OPVs. Seven years later, Barrows *et al*. employed a similar method for depositing PSCs and achieved a PCE of 11% by controlling parameters such as substrate temperatures, annealing treatments, gas carrier, etc. [103]. Kai *et al*. demonstrated flexible PSCs using an ultrasonic spray coating method. In this method, photonic curing technology was used for annealing treatments and achieved a PCE of 13% [104]. Even though the work demonstrated flexible PSCs with a high PCE and its mechanical stress, the results were not obtained for large area devices. The roughness of the film plays a key role along with the number of pin-holes; both these factors should be low to obtain high-efficiency PSCs. After optimization and research Morteza *et al*. reported large area (about 25 cm^2) defect-free PSCs using this deposition technique. The research group demonstrated scalable spray deposition using automated spray coating and by controlling the film roughness and thickness, solution concentration, and annealing treatments, as shown in Figure 11.7b. They also reported the surface tension, contact angle, and viscosity of the solution [105].

11.5.1.6 Laser Patterning

Some of the deposition techniques, such as blade coating or screen coating, are not self-patterned. To create the required layout it is necessary to use masks and/or etching but quite often it results in excluding uniform deposition of materials. Moreover, the masks used are thermoplastic and not suitable for high temperatures and use of strong solvents, while the use of metallic masks is not easy [92]. Pattern formation is used not only to improve the performance of the devices but also to help in transferring/scaling-up the device for manufacturing purposes. In general, PSCs are designed by stacking multiple layers with a thickness in the order of a few hundred nanometers. Laser processing is focused on preventing damage to each underlying layer or the substrate used during patterning. It is also used to remove the previously deposited layers for contact (i.e. interconnection), which is more helpful in fabricating large area modules. Removal of several materials, layer by layer or all at once, is made possible by choosing different wavelengths of the laser used. The use of different laser wavelength is highly associated with the different deposition techniques used [95]. Patterning and framing using lasers have several benefits, such as a high precision, intense selectivity and automation, processing speed, resolution, and cost-effective approach. It also helps in reducing the dead areas and making use of those areas as contacts in large area perovskite modules [106].

In general, laser patterning consists of three sequential laser processes, namely P1, P2, and P3 [107, 108]. In the sequential laser process, the P1 process mainly focuses on the insulation of photoanodes, such that they can be easily connected to neighboring cells in modules by means of series connection. Typically, the P2 process involves removing the entire stack – ETL/perovskite/HTL – in order to connect the two adjacent cells in series and by removing the entire stack contact resistance will be reduced [92]. The final P3 process relates to the insulation of the counterelectrode; it also involves reducing the parallel resistance by removing the ETL/perovskite/HTL stack [109]. As discussed earlier, Mettocci *et al.* used laser pattering to remove excess perovskite and HTL to achieve interconnection of devices. They used two different kind of lasers, CO_2 and Nd:YVO_4, to remove perovskite and HTL. By employing this kind of technique, a PCE of about 13% was obtained for an active are of about 10 cm^2 [92]. Similarly, many researchers have used laser for patterning along with their different deposition techniques. Palma *et al.* demonstrated a fully laser processed perovskite solar cell module over a larger area of 14.5 cm^2. The authors used the entire three lasers patterning process (P1-P2-P3) for device fabrication and focused mainly on improving the aperture ratio of the device [110].

11.5.1.7 Roll-to-Roll Deposition

The roll-to-roll (R-R) deposition technique has the potential of pilot-scaling the technology by means of manufacturing in a large scale manner with high throughput, flexible, and reproducibility [100, 111–113]. It also overcomes some of the limitations, such as continuous deposition over larger area for a long duration irrespective of substrate materials and size used. This is one of the successful methods in manufacturing solar cells, especially in the field of DSSCs and organic solar cells [114–117]. Furthermore, it is also more compatible with other printing techniques on glass, such as inkjet, bade coating, and slot die. The deposition parameters optimized for glass are not suitable for flexible substrates; hence, a new optimization has to be developed for depositing on flexible substrates. Hwang *et al.* demonstrated fabrication of perovskite solar cells on PET/ITO substrates using a printing technique through the slot die method. They reported the optimized ETL, perovskite, and HTL deposition on flexible substrates and the back electrode was deposited using vacuum evaporation [100]. Kerbs *et al.* reported a fully fabricated perovskite solar cells using R-R along with slot die coating on PET/ITO substrates. The authors demonstrated two kinds of geometry, (i) one-step normal and (ii) two-step inverted geometry [118].

Lyn Zee *et al.* reported a facile roll-printing method with a geometrically confined lateral crystal growth for the fabrication of large-scale single-crystal perovskite thin films. The research group fabricated single-crystal perovskite in the form of a patterned thin film in a three inch wafer with a high carrier mobility of 45.64 $cm^2 V^{-1} s^{-1}$ [119]. The schematic representation of lateral crystal growth and the large fabrication of R-R printing is shown in Figure 11.7c [119, 120]

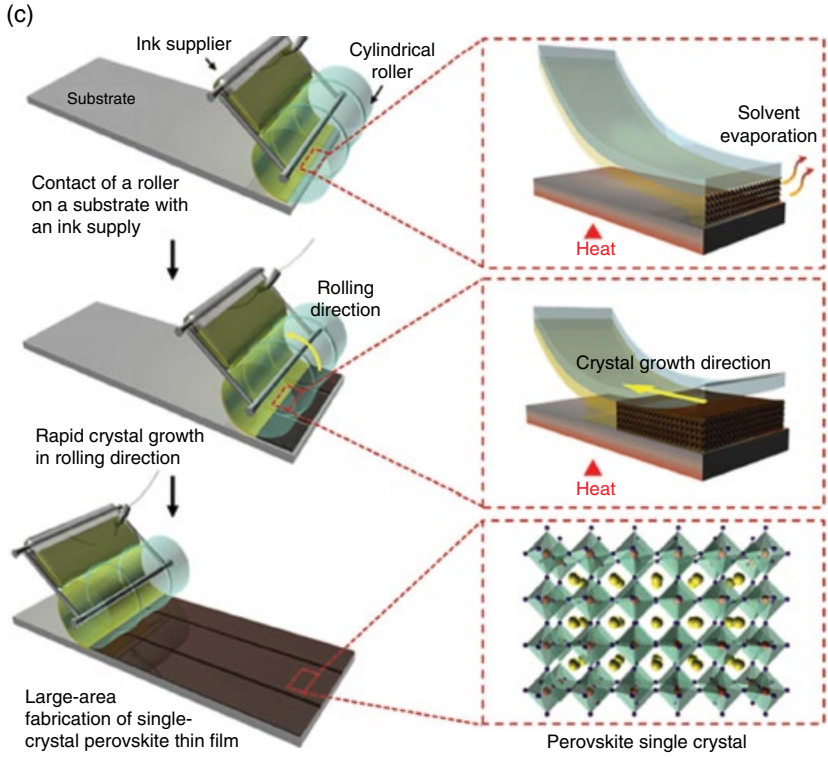

Figure 11.7 (c) Schematic representation of lateral crystal growth fabricated using R-R. Figure adapted from [119]. *Source:* Lee. https://www.nature.com/articles/ncomms15882. Licensed under CC BY 4.0.

11.5.1.8 Other Large Area Deposition Techniques

Several other methods are available for fabrication of PSCs in a large scale manner in addition to those techniques just mentioned. Some of the techniques include chemical vapour deposition (CVD), flexographic, gravure printing, airbrush painting, inkjet printing, and so on. The excellent results obtained with small scale devices using these techniques can be considered promising for fabricating modules on the large scale. Tavakoli *et al*. reported fabrication of small scale PSCs using CVD for depositing perovskite materials; its schematic representation is shown in Figure 11.8a [121]. Leyden *et al*. demonstrated fabrication of perovskite using the CVD method with the series interconnection of five cells and six cells with active areas of 8.8, 12, and 15.4 cm^2, as shown in Figure 11.8b [122].

Inkjet printing is a flexible method for fabricating several layers from colloidal ink solutions. It is operated on the principle of the ejection of a fixed

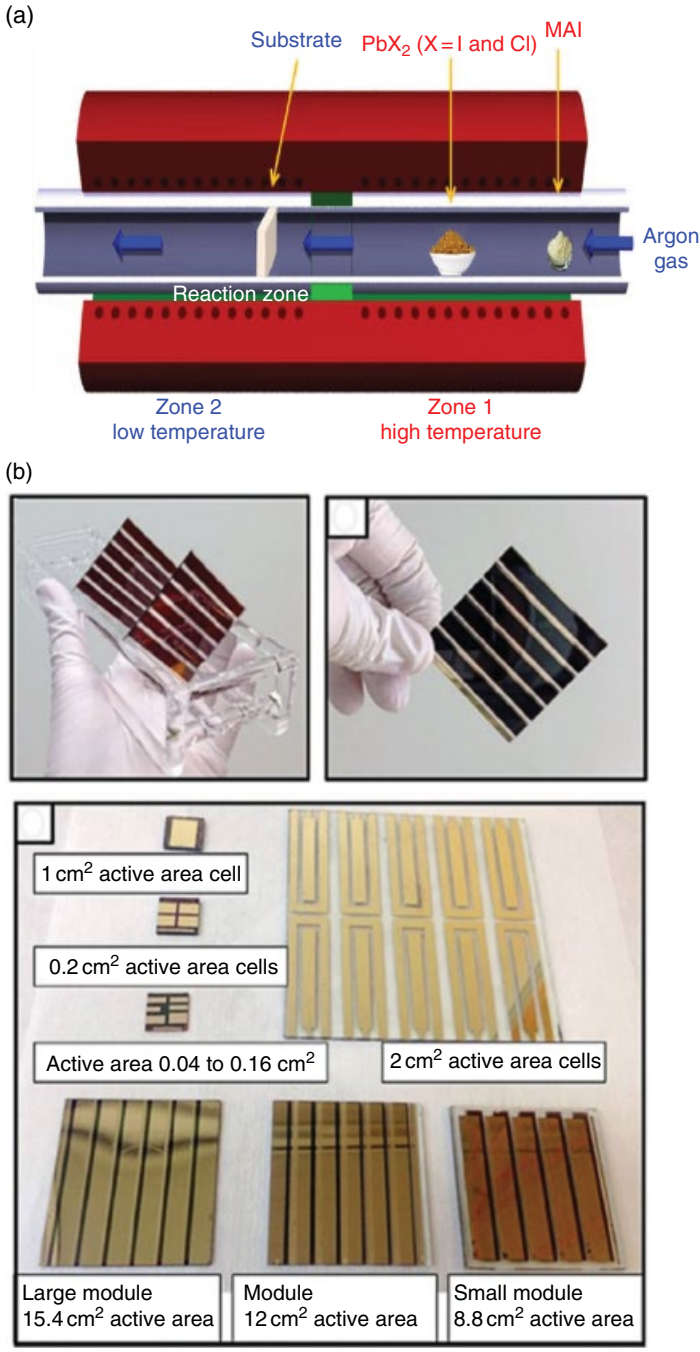

Figure 11.8 (a) Schematic representation of the CVD setup. Figure adapted from [121]. *Source:* Tavakoli. https://www.nature.com/articles/srep14083. Licensed under CC BY 4.0. (b) Pictorial representation of smaller module with 1 cm^2 to larger module of 8.8 cm^2 grown using CVD [122]. *Source:* Leyden. http://pubs.rsc.org/en/content/articlelanding/2016/ta/c6ta04267h#!divAbstract. Licensed under CC BY 3.0.

amount of solution through a nozzle in the form of droplets. The main advantage of using this technique is that there will not be any critical spacing between the nozzle and the substrate, resulting in reducing the losses [123]. Ramesh *et al*. reported an air brush technique for the deposition of perovskite materials in PSCs for active areas of 1, 6, and 34.2 cm^2 with PCEs of 9.70, 6.88, and 4.66% [124].

In addition to existing deposition techniques a new deposition technique called soft-cover deposition (SCD) was developed by Ye *et al*. By employing this method the surface wettability, thermal crystallization, and solution viscosity are controlled to grow large grain sized perovskite crystal without any pin-holes. A large area of over 51 cm^2 has been fabricated by their research group with rough-border-free films, as shown in Figure 11.8c [125]. The same research group followed its earlier work to develop a low temperature SCD and fabricated a device with active areas of 5 and 12 cm^2 with a PCE of 15.3% [126].

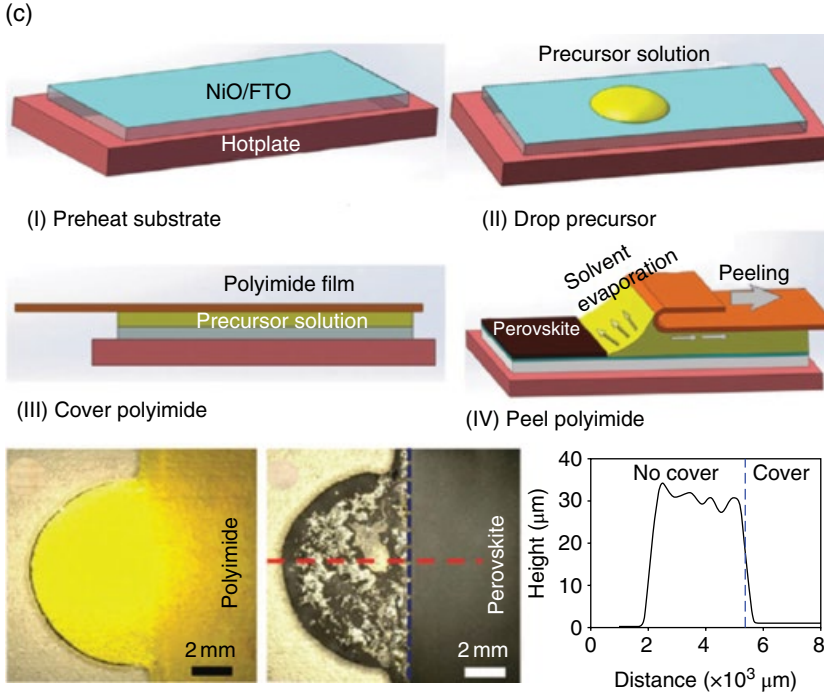

Figure 11.8 (c) Schematic representation of the SCD method for fabricating PSCs [125]. Reproduced with permission of Royal Society of Chemistry.

11.6 Summary

In summary, this chapter has reviewed the field of organic–inorganic halide perovskites from its evolution to technological applications. It is keenly focused on rational strategies involved in transferring small scale devices into large area devices. The properties and structural analysis of pervoskite-based materials have been discussed in briefly. The role of pervoskite in solar cells, its configuration, and various strategies involved in the processing of device fabrication (PSCs) are stated. Moreover, it gives a deep insight into the different fabrication techniques available for fabricating the perovskite solar cells in a laboratory as well as transferring of technology into commercial use by achieving large area fabrication of devices.

Acknowledgement

Dr. M. Ramesh expresses sincere thanks to the Department of Science and Technology, India [DST/INSPIRE/04/2015/002860] for financial support. Mr. Arunachalam Arulraj gratefully acknowledges his supervisor, Dr G Senguttuvan, Associate Professor, University College of Engineering – BIT campus, Tiruchirappalli for his constant encouragement and support.

References

1 US Department of Energy: Energy Efficiency and Renewable Energy, The History of Solar. https://www1.eere.energy.gov/solar/pdfs/solar_timeline.pdf; last accessed 1 May 2018.
2 R.S. Rohella, S.K. Panda, and P. Das, Perovskite solar cell – a source of renewable green power, *International Journal of Scientific and Research Publications*, **5**, 2015, 2250–3153.
3 J.M. Frost and A. Walsh, Molecular motion and dynamic crystal structures of hybrid halide perovskites, In: N.-G.Park, M. Grätzel, and T. Miyasaka (eds), Organic-Inorganic Halide Perovskite Photovoltaics, Springer, 2016, 1–17.
4 R. Wyckoff, The crystal structures of monomethyl ammonium chlorostannate and chloroplatinate, *American Journal of Science*, **16**, 1928, 349–359.
5 D. Weber, $CH_3NH_3SnBrxI_3$-x (x = 0–3), a Sn(II)-system with the cubic perovskite structure, *Zeitschrift für Naturforschung B*, **33**, 1978, 862–865.
6 D. Weber, $CH_3NH_3PbX_3$, a Pb(II)-system with cubic perovskite structure, *Zeitschrift für Naturforschung B*, **33**, 1978, 1443–1445.

7 A. Poglitsch and D. Weber, Dynamic disorder in methylammonium trihalogenoplumbates (II) observed by millimeter-wave spectroscopy, *The Journal of Chemical Physics*, **87**, 1987, 6373–6378.

8 N. Onoda-Yamamuro, T. Matsuo, and H. Suga, Calorimetric and IR spectroscopic studies of phase transitions in methylammonium trihalogenoplumbates, *Journal of Physics and Chemistry of Solids*, **51**, 1990, 1383–1395.

9 R.E. Wasylishen, O. Knop, and J.B. Macdonald, Cation rotation in methylammonium lead halides, *Solid State Communications*, **56**, 1985, 581–582.

10 A. Salau, Fundamental absorption edge in PbI_2:KI alloys, *Solar Energy Materials*, **2**, 1980, 327–332.

11 P. Gao, M. Grätzel, and M.K. Nazeeruddin, Organohalide lead perovskites for photovoltaic applications, *Energy & Environmental Science*, **7**, 2014, 2448–2463.

12 J.H. Heo, S.H. Im, J.H. Noh, *et al*., Efficient inorganic-organic hybrid heterojunction solar cells containing perovskite compound and polymeric hole conductors, *Nature Photonics*, **7**, 2013, 486–491.

13 H.-R. Wenk and A. Bulakh, Minerals: *Their Constitution and Origin*, Cambridge University Press, 2016.

14 X. Zhao and N.-G. Park, Stability issues on perovskite solar cells, *Photonics*, **2**, 2015, 1139– 1151.

15 E. Edri, S. Kirmayer, A. Henning, *et al*., Why lead methylammonium tri-iodide perovskite-based solar cells require a mesoporous electron transporting scaffold (but not necessarily a hole conductor), *Nano Letters*, **14**, 2014, 1000–1004.

16 V. Goldschmidt, Geochemische Verteilungsgesetze der Elemente, *Akad. Oslo I. Mat-Nat.* **K1**, 8, 1926, 112–117.

17 K. Tanaka, T. Takahashi, T. Ban, *et al*., Comparative study on the excitons in lead-halide-based perovskite-type crystals $CH_3NH_3PbBr_3$ $CH_3NH_3PbI_3$, *Solid State Communications*, **127**, 2003, 619–623.

18 M. Hirasawa, T. Ishihara, T. Goto, *et al*., Magnetoabsorption of the lowest exciton in perovskite-type compound $(CH_3NH_3)PbI_3$, *Physica B: Condensed Matter*, **201**, 1994, 427–430.

19 T. Ishihara, Optical properties of PbI-based perovskite structures, *Journal of Luminescence*, **60**, 1994, 269–274.

20 I. Koutselas, L. Ducasse, and G.C. Papavassiliou, Electronic properties of three- and low-dimensional semiconducting materials with Pb halide and Sn halide units, *Journal of Physics: Condensed Matter*, **8**, 1996, 1217.

21 W. Zhang, M. Saliba, S.D. Stranks, *et al*., Enhancement of perovskite-based solar cells employing core-shell metal nanoparticles, *Nano Letters*, **13**, 2013, 4505–4510.

22 V. D'Innocenzo, G. Grancini, M.J. Alcocer, *et al*., Excitons versus free charges in organo-lead tri-halide perovskites, *Nature Communications*, **5**, 2014, 3586.

23 Q. Lin, A. Armin, R.C.R. Nagiri, *et al.*, Electro-optics of perovskite solar cells, *Nature Photonics*, **9**, 2015, 106–112.

24 A. Kojima, K. Teshima, Y. Shirai, and T. Miyasaka, Organometal halide perovskites as visible-light sensitizers for photovoltaic Cells, *Journal of the American Chemical Society*, **131**, 2009, 6050–6051.

25 J.-H. Im, C.-R. Lee, J.-W. Lee, *et al.*, 6.5% efficient perovskite quantum-dot-sensitized solar cell, *Nanoscale*, **3**, 2011, 4088–4093.

26 H.-S. Kim, C.-R. Lee, J.-H. Im, *et al.*, Lead iodide perovskite sensitized all-solid-state submicron thin film mesoscopic solar cell with efficiency exceeding 9%, *Scientific Reports*, **2**, 2012, 591.

27 M.M. Lee, J. Teuscher, T. Miyasaka, *et al.*, Efficient hybrid solar cells based on meso-superstructured organometal halide perovskites, *Science*, **338**, 2012, 643–647.

28 Y.-C. Hsiao, T. Wu, M. Li, *et al.*, Fundamental physics behind high-efficiency organo-metal halide perovskite solar cells, *Journal of Materials Chemistry A*, **3**, 2015, 15372–15385.

29 S.S. Mali and C.K. Hong, p-i-n/n-i-p type planar hybrid structure of highly efficient perovskite solar cells towards improved air stability: synthetic strategies and the role of p-type hole transport layer (HTL) and n-type electron transport layer (ETL) metal oxides, *Nanoscale*, **8**, 2016, 10528–10540.

30 W. Zhang, M. Anaya, G. Lozano, *et al.*, Highly efficient perovskite solar cells with tunable structural color, *Nano Letters*, **15**, 2015, 1698–1702.

31 Y.-Y. Sun, M. L. Agiorgousis, P. Zhang, and S. Zhang, Chalcogenide perovskites for photovoltaics, *Nano Letters*, **15**, 2015, 581–585.

32 M. Zhang, M. Lyu, H. Yu, *et al.*, Stable and low-cost mesoscopic $CH_3NH_3PbI_2Br$ perovskite solar cells by using a thin poly (3-hexylthiophene) layer as a hole transporter, *Chemistry – A European Journal*, **21**, 2015, 434–439.

33 R. Sheng, A. Ho-Baillie, S. Huang, *et al.*, Methylammonium lead bromide perovskite-based solar cells by vapor-assisted deposition, *The Journal of Physical Chemistry C*, **119**, 2015, 3545–3549.

34 Z. Xiao, Y. Yuan, Y. Shao, *et al.*, Giant switchable photovoltaic effect in organometal trihalide perovskite devices, *Nature Materials*, **14**, 2015, 193–198.

35 M. Grätzel, The light and shade of perovskite solar cells, *Nature Materials*, **13**, 2014, 838–842.

36 M.-H. Li, P.-S. Shen, K.-C. Wang, *et al.*, Inorganic p-type contact materials for perovskite-based solar cells, *Journal of Materials Chemistry A*, **3**, 2015, 9011–9019.

37 J. Troughton, D. Bryant, K. Wojciechowski, *et al.*, Highly efficient, flexible, indium-free perovskite solar cells employing metallic substrates, *Journal of Materials Chemistry A*, **3**, 2015, 9141–9145.

38 P.P. Boix, K. Nonomura, N. Mathews, and S.G. Mhaisalkar, Current progress and future perspectives for organic/inorganic perovskite solar cells, *Materials Today*, **17**, 2014, 16–23.

39 J. Burschka, N. Pellet, S.-J. Moon, *et al.*, Sequential deposition as a route to high-performance perovskite-sensitized solar cells, *Nature*, **499**, 2013, 316–319.

40 G.E. Eperon, V.M. Burlakov, P. Docampo, *et al.*, Morphological control for high performance, solution-processed planar heterojunction perovskite solar cells, *Advanced Functional Materials*, **24**, 2014, 151–157.

41 P. Docampo, J.M. Ball, M. Darwich, *et al.*, Efficient organometal trihalide perovskite planar-heterojunction solar cells on flexible polymer substrates, *Nature Communications*, **4**, 2013, 2761.

42 H. Kim, K.-G. Lim, and T.-W. Lee, Planar heterojunction organometal halide perovskite solar cells: roles of interfacial layers, *Energy & Environmental Science*, **9**, 2016, 12–30.

43 J.M. Ball, M.M. Lee, A. Hey, and H.J. Snaith, Low-temperature processed meso-superstructured to thin-film perovskite solar cells, *Energy & Environmental Science*, **6**, 2013, 1739–1743.

44 J. Lee, M. M. Menamparambath, J.Y. Hwang, and S. Baik, Hierarchically structured hole transport layers of spiro-OMeTAD and multiwalled carbon nanotubes for perovskite solar cells, *ChemSusChem*, **8**, 2015, 2358–2362.

45 C.-Y. Chang, C.-Y. Chu, Y.-C. Huang, *et al.* Perovskite morphology by polymer additive for high efficiency solar cell, *ACS Applied Materials & Interfaces*, **7**, 2015, 7, 4955–4961.

46 L. Zuo, Z. Gu, T. Ye, *et al.*, Enhanced photovoltaic performance of $CH_3NH_3PbI_3$ perovskite solar cells through interfacial engineering using self-assembling monolayer, *Journal of the American Chemical Society*, **137**, 2015, 2674–2679.

47 K. Wang, Y. Shi, Q. Dong, *et al.*, Low-temperature and solution-processed amorphous WOX as electron-selective layer for perovskite solar cells, *Journal of Physical Chemistry Letters*, **6**, 2015, 755–759.

48 J.Y. Jeng, Y.F. Chiang, M.H. Lee, *et al.*, $CH_3NH_3PbI_3$ perovskite/fullerene planar-heterojunction hybrid solar cells, *Advanced Materials*, **25**, 2013, 3727–3732.

49 L. Etgar, P. Gao, Z. Xue, *et al.*, Mesoscopic $CH_3NH_3PbI_3/TiO_2$ heterojunction solar cells, *Journal of the American Chemical Society*, **134**, 2012, 17396–17399.

50 K.-C. Wang, J.-Y. Jeng, P.-S. Shen, *et al.*, p-type Mesoscopic nickel oxide/organometallic perovskite heterojunction solar cells, *Scientific Reports*, **4**, 2014, 4756.

51 S. Ye, W. Sun, Y. Li, *et al.*, CuSCN-based inverted planar perovskite solar cell with an average PCE of 15.6%, *Nano Letters*, **15**, 2015, 3723–3728.

52 Z. Wu, S. Bai, J. Xiang, *et al.*, Efficient planar heterojunction perovskite solar cells employing graphene oxide as hole conductor, *Nanoscale*, **6**, 2014, 10505–10510.

53 J.-S. Yeo, R. Kang, S. Lee, *et al.*, Highly efficient and stable planar perovskite solar cells with reduced graphene oxide nanosheets as electrode interlayer, *Nano Energy*, **12**, 2015, 96–104.

54 J.H. Heo, H. J. Han, M. Lee, *et al.*, Stable semi-transparent $CH_3NH_3PbI_3$ planar sandwich solar cells, *Energy & Environmental Science*, **8**, 2015, 2922–2927.

55 J.H. Park, J. Seo, S. Park, *et al.*, Efficient $CH_3NH_3PbI_3$ perovskite solar cells employing nanostructured p-type NiO electrode formed by a pulsed laser deposition, *Advanced Materials*, **27**, 2015, 4013–4019.

56 A. Mei, X. Li, L. Liu, *et al.*, A hole-conductor-free, fully printable mesoscopic perovskite solar cell with high stability, *Science*, **345**, 2014, 295–298.

57 P.W. Liang, C.Y. Liao, C.C. Chueh, *et al.*, Additive enhanced crystallization of solution-processed perovskite for highly efficient planar-heterojunction solar cells, *Advanced Materials*, **26**, 2014, 3748–3754.

58 W. Li, J. Fan, J. Li, *et al.*, High performance of perovskite solar cells via catalytic treatment in two-step process: the case of solvent engineering, *ACS Applied Materials & Interfaces*, **8**, 2016, 30107–30115.

59 N.J. Jeon, J.H. Noh, Y.C. Kim, *et al.*, Solvent engineering for high-performance inorganic-organic hybrid perovskite solar cells, *Nature Materials*, **13**, 2014, 897–903.

60 N. Ahn, D.-Y. Son, I.-H. Jang, *et al.*, Highly reproducible perovskite solar cells with average efficiency of 18.3% and best efficiency of 19.7% fabricated via Lewis base adduct of lead(II) iodide, *Journal of the American Chemical Society*, **137**, 2015, 8696–8699.

61 J.H. Noh, S.H. Im, J.H. Heo, *et al.*, Chemical management for colorful, efficient, and stable inorganic-organic hybrid nanostructured solar cells, *Nano Letters*, **13**, 2013, 1764–1769.

62 N.J. Jeon, J.H. Noh, W.S. Yang, *et al.*, Compositional engineering of perovskite materials for high-performance solar cells, *Nature*, **517**, 2015, 476–480.

63 A. Binek, F.C. Hanusch, P. Docampo, and T. Bein, Stabilization of the trigonal high-temperature phase of formamidinium lead iodide, *The Journal of Physical Chemistry Letters*, **6**, 2015, 1249–1253.

64 D. Bi, C. Yi, J. Luo, *et al.*, Polymer-templated nucleation and crystal growth of perovskite films for solar cells with efficiency greater than 21%, *Nature Energy*, **1**, 2016, 16142.

65 S. Tang, Y. Deng, X. Zheng, *et al.*, Composition engineering in doctor-blading of perovskite solar cells, *Advanced Energy Materials*, **7**, 2017, 1700302.

66 W. Ke, G. Fang, Q. Liu, *et al.*, Low-temperature solution-processed tin oxide as an alternative electron transporting layer for efficient perovskite solar cells, *Journal of the American Chemical Society*, **137**, 2015, 6730–6733.

67 W.S. Yang, J.H. Noh, N.J. Jeon, *et al.*, Solar cells: high-performance photovoltaic perovskite layers fabricated through intramolecular exchange, *Science*, **348**, 2015, 1234–1237.

68 M. Saliba, T. Matsui, J.-Y. Seo, *et al.*, Cesium-containing triple cation perovskite solar cells: improved stability, reproducibility and high efficiency, *Energy & Environmental Science*, **9**, 2016, 1989–1997.

69 W.E. Sha, X. Ren, L. Chen, and W.C. Choy, The efficiency limit of $CH_3NH_3PbI_3$ perovskite solar cells, *Applied Physics Letters*, **106**, 2015, 221104.

70 J.M. Marin-Beloqui, L. Lanzetta, and E. Palomares, Decreasing charge losses in perovskite solar cells through mp-TiO_2/MAPI interface engineering, *Chemistry of Materials*, **28**, 2016, 207–213.

71 A. Agresti, S. Pescetelli, S. Casaluci, *et al.*, Device architectures with nanocrystalline mesoporous scaffolds and thin compact layers for flexible perovskite solar cells and modules, *Nanotechnology* (IEEE-NANO), 2015, 381–384.

72 Y. Wang, H.-Y. Wang, M. Yu, *et al.*, Trap-limited charge recombination in intrinsic perovskite film and meso-superstructured perovskite solar cells and the passivation effect of the hole-transport material on trap states, *Physical Chemistry Chemical Physics*, **17**, 2015, 29501–29506.

73 E.M. Hutter, G.E. Eperon, S.D. Stranks, and T.J. Savenije, Charge carriers in planar and meso-structured organic–inorganic perovskites: mobilities, lifetimes, and concentrations of trap states, *Journal of Physical Chemistry Letters*, **6**, 2015, 3082–3090.

74 A. Listorti, E.J. Juarez-Perez, C. Frontera, *et al.*, Effect of mesostructured layer upon crystalline properties and device performance on perovskite solar Cells, *Journal of Physical Chemistry Letters*, **6**, 2015, 1628–1637.

75 M. Abdi-Jalebi, M.I. Dar, A. Sadhanala, *et al.*, Impact of a mesoporous titania-perovskite interface on the performance of hybrid organic-inorganic perovskite solar cells, *Journal of Physical Chemistry Letters*, **18**, 2016, 3264–3269.

76 J. Shi, X. Xu, D. Li, and Q. Meng, Interfaces in perovskite solar cells, *Small*, **11**, 2015, 2472–2486.

77 J. Lee, H. Kang, G. Kim, *et al.*, Achieving large-area planar perovskite solar cells by introducing an interfacial compatibilizer, *Advanced Materials*, **29**, 2017. doi: 10.1002/adma.201606363.

78 A. Agresti, S. Pescetelli, A.L. Palma, *et al.*, Graphene Interface engineering for perovskite solar modules: 12.6% power conversion efficiency over 50 cm^2 active area, *ACS Energy Letters*, **2**, 2017, 279–287.

79 G. Grancini, C. Roldán-Carmona, I. Zimmermann, *et al.*, One-year stable perovskite solar cells by 2D/3D interface engineering, *Nature Communications*, **8**, 2017, 15684.

80 S.N. Habisreutinger, T. Leijtens, G.E. Eperon, *et al.*, Carbon nanotube/polymer composites as a highly stable hole collection layer in perovskite solar cells, *Nano Letters*, **14**, 2014, 5561–5568.

81 G. Niu, W. Li, F. Meng, *et al.*, Study on the stability of $CH_3NH_3PbI_3$ films and the effect of post-modification by aluminum oxide in all-solid-state hybrid solar cells, *Journal of Materials Chemistry A*, **2**, 2014, 705–710.

82 Y. Han, S. Meyer, Y. Dkhissi, *et al.*, Degradation observations of encapsulated planar CH3NH3PbI3 perovskite solar cells at high temperatures and humidity, *Journal of Materials Chemistry A*, **3**, 2015, 8139–8147.

83 C. Qin, T. Matsushima, T. Fujihara, *et al.*, Degradation mechanisms of solution-processed planar perovskite solar cells: thermally stimulated current measurement for analysis of carrier traps, *Advanced Materials*, **28**, 2016, 466–471.

84 Q. Tai, P. You, H. Sang, *et al.*, Efficient and stable perovskite solar cells prepared in ambient air irrespective of the humidity, *Nature Communications*, **7**, 2016, 11105.

85 Y. Zhou and K. Zhu, Perovskite solar cells shine in the "Valley of the Sun", *ACS Energy Letters*, **1**, 2016, 64–67.

86 W. Chen, Y. Wu, Y. Yue, *et al.*, Efficient and stable large-area perovskite solar cells with inorganic charge extraction layers, *Science*, **350**, 2015, 944–948.

87 M. Yang, Y. Zhou, Y. Zeng, *et al.*, Square-centimeter solution-processed planar $CH_3NH_3PbI_3$ perovskite solar cells with efficiency exceeding 15, *Advanced Materials*, **27**, 2015, 6363–6370.

88 M.A. Green, K. Emery, Y. Hishikawa, *et al.*, Solar cell efficiency tables (Version 45), *Progress in Photovoltaics: Research and Applications*, **23**, 2015, 1–9.

89 X. Li, D. Bi, C. Yi, *et al.*, A vacuum flash-assisted solution process for high-efficiency large-area perovskite solar cells, *Science*, **353**, 2016, 58–62.

90 F. Matteocci, S. Razza, F. Di Giacomo, *et al.*, Solid-state solar modules based on mesoscopic organometal halide perovskite: a route towards the up-scaling process, *Physical Chemistry Chemical Physics*, **16**, 2014, 3918–3923.

91 W. Qiu, T. Merckx, M. Jaysankar, *et al.*, Pinhole-free perovskite films for efficient solar modules, *Energy & Environmental Science*, **9**, 2016, 484–489.

92 F. Matteocci, L. Cinà, F. Di Giacomo, *et al.*, High efficiency photovoltaic module based on mesoscopic organometal halide perovskite, *Progress in Photovoltaics: Research and Applications*, **24**, 2016, 436–445.

93 J.H. Heo, H.J. Han, D. Kim, *et al.*, Hysteresis-less inverted $CH_3NH_3PbI_3$ planar perovskite hybrid solar cells with 18.1% power conversion efficiency, *Energy & Environmental Science*, **8**, 2015, 1602–1608.

94 A.T. Mallajosyula, K. Fernando, S. Bhatt, A. *et al.*, Large-area hysteresis-free perovskite solar cells via temperature controlled doctor blading under ambient environment, *Applied Materials Today*, **3**, 2016, 96–102.

95 S. Razza, F. Di Giacomo, F. Matteocci, *et al.*, Perovskite solar cells and large area modules (100 cm^2) based on an air flow-assisted PbI_2 blade coating deposition process, *Journal of Power Sources*, **277**, 2015, 286–291.

96 S. Razza, S. Castro-Hermosa, A. Di Carlo, and T.M. Brown, Research update: large-area deposition, coating, printing, and processing techniques for the upscaling of perovskite solar cell technology, *APL Materials*, **4**, 2016, 091508.

97 Z. Yang, C.C. Chueh, F. Zuo, *et al.*, High-performance fully printable perovskite solar cells via blade-coating technique under the ambient condition, *Advanced Energy Materials*, **5**, 2015, 1500328.

98 D. Vak, K. Hwang, A. Faulks, *et al.*, 3D Printer based slot-die coater as a lab-to-fab translation tool for solution-processed solar cells, *Advanced Energy Materials*, **5**, 2015, 1401539.

99 Y.-S. Jung, K. Hwang, Y.-J. Heo, *et al.*, One-step printable perovskite films fabricated under ambient conditions for efficient and reproducible solar cells, *ACS Applied Materials & Interfaces*, **9**, 2017, 27832–27838.

100 K. Hwang, Y.S. Jung, Y.J. Heo, *et al.*, Toward large scale roll-to-roll production of fully printed perovskite solar cells, *Advanced Materials*, **27**, 2015, 1241–1247.

101 M. He, B. Li, X. Cui, *et al.*, Meniscus-assisted solution printing of large-grained perovskite films for high-efficiency solar cells, *Nature Communications*, **8**, 2017, 16045.

102 F. Di Giacomo, V. Zardetto, A. D'Epifanio, *et al.*, Flexible perovskite photovoltaic modules and cells rased on atomic layer deposited compact layers and UV-irradiated TiO_2 scaffolds on plastic substrates., *Advanced Energy Materials*, **5**, 2015, 1401808.

103 A.T. Barrows, A.J. Pearson, C.K. Kwak, *et al.*, Efficient planar heterojunction mixed-halide perovskite solar cells deposited via spray-deposition, *Energy & Environmental Science*, **7**, 2014, 2944–2950.

104 D. Sanjib, B. Yang, G. Gu, *et al.*, High-performance flexible perovskite solar cells by using a combination of ultrasonic spray-coating and low thermal budget photonic curing, *ACS Photonics*, **2**, 2015, 680–686.

105 M. Habibi, A. Rahimzadeh, I. Bennouna, and M. Eslamian, Defect-free large-area (25 cm^2) light absorbing perovskite thin films made by spray coating, *Coatings*, **7**, 2017, 42.

106 Y. Gupta, H. Liers, S. Woods, *et al.*, Optimization of a Si solar cell current collection, *Photovoltaic Specialists Conference*, 1982, 1092–1101.

107 H. Booth, Laser Processing in industrial solar module manufacturing, *Journal of Laser Micro/Nanoengineering*, **5**, 2010, 183–191.

108 S. Haas, Untersuchung und Optimierung der Serienverschaltung von Silizium-Dünnschicht-Solarmodulen, *Forschungszentrum Jülich*, **91**, 2010, 202.

109 S. Haas, A. Gordijn, and H. Stiebig, High speed laser processing for monolithical series connection of silicon thin-film modules, *Progress in Photovoltaics: Research and Applications*, **16**, 2008, 195–203.

110 A.L. Palma, F. Matteocci, A. Agresti, *et al.*, Laser-patterning engineering for perovskite solar modules with 95% aperture ratio, *IEEE Journal of Photovoltaics*, **7**(6), 2017, 1674–1680.

111 J.H. Kim, S.T. Williams, N. Cho, *et al.*, Enhanced enivronmental stability of planar heterojunction perovsite solar cells based on blade-coating, *Advanced Energy Materials*, **5**, 2015, 1401229.

112 R. Søndergaard, M. Hösel, D. Angmo, *et al.*, Roll-to-roll fabrication of polymer solar cells, *Materials Today*, **15**, 2012, 36–49.

113 B. Susrutha, L. Giribabu, and S.P. Singh, Recent advances in flexible perovskite solar cells, *Chemical Communications*, **51**, 2015, 14696–14707.

114 T. Brown, F. De Rossi, F. Di Giacomo, *et al.*, Progress in flexible dye solar cell materials, processes and devices, *Journal of Materials Chemistry A*, **2**, 2014, 10788–10817.

115 S.A. Gevorgyan, M.V. Madsen, H.F. Dam, *et al.*, Interlaboratory outdoor stability studies of flexible roll-to-roll coated organic photovoltaic modules: Stability over 10,000 h, *Solar Energy Materials and Solar Cells*, **116**, 2013, 187–196.

116 R. Rösch, F.C. Krebs, D.M. Tanenbaum, and H. Hoppe, Quality control of roll-to-roll processed polymer solar modules by complementary imaging methods, *Solar Energy Materials and Solar Cells*, **97**, 2012, 176–180.

117 F.C. Krebs, T. Tromholt, and M. Jørgensen, Upscaling of polymer solar cell fabrication using full roll-to-roll processing, *Nanoscale*, **2**, 2010, 873–886.

118 T.M. Schmidt, T.T. Larsen-Olsen, J.E. Carlé, *et al.*, Upscaling of perovskite solar cells: fully ambient roll processing of flexible perovskite solar cells with printed back electrodes, *Advanced Energy Materials*, **5**, 2015, 1500569.

119 L. Lee, J. Baek, K.S. Park, *et al.*, Wafer-scale single-crystal perovskite patterned thin films based on geometrically-confined lateral crystal growth, *Nature Communications*, **8**, 2017, 15882.

120 B. Leung, J. Song, Y. Zhang, and J. Han, Evolutionary selection growth: towards template-insensitive preaparation of single-crystal layers, *Advanced Materials*, **25**, 2013, 1285–1289.

121 M.M. Tavakoli, L. Gu, Y. Gao, *et al.*, Fabrication of efficient planar perovskite solar cells using a one-step chemical vapor deposition method, *Scientific Reports*, **5**, 2015, 14083.

122 M.R. Leyden, Y. Jiang, and Y. Qi, Chemical vapor deposition grown formamidinium perovskite solar modules with high steady state power and thermal stability, *Journal of Materials Chemistry A*, **4**, 2016, 13125–13132.

123 X. Peng, J. Yuan, S. Shen, *et al.*, Perovskite and organic solar cells fabricated by inkjet printing: progress and prospects, *Advanced Functional Materials*, **27**, 2017, 1703704.

124 M. Ramesh, K.M. Boopathi, T.-Y. Huang, *et al.*, Using an airbrush pen for layer-by-layer growth of continuous perovskite thin films for hybrid solar cells, *ACS Applied Materials & Interfaces*, **7**, 2015, 2359–2366.

125 F. Ye, H. Chen, F. Xie, *et al.*, Soft-cover deposition of scaling-up uniform perovskite thin films for high cost-performance solar cells, *Energy & Environmental Science*, **9**, 2016, 2295–2301.

126 F. Ye, W. Tang, F. Xie, *et al.*, Low temperature soft-cover deposition of uniform large-scale perovskite films for high-performance solar cells, *Advanced Materials*, **29**, 2017, 1701440.

12

Hot Electrons Role in Biomolecule-based Quantum Dot Hybrid Solar Cells

T. Pazhanivel[1], G. Bharathi[2], D. Nataraj[2], R. Ramesh[3], and D. Navaneethan[3]

[1] *Department of Physics, Periyar University, India*
[2] *Department of Physics, Bharathiyar University, India*
[3] *Department of chemistry, Periyar University, India*

12.1 Introduction

Solar cells are devices that convert solar light into electrical energy via a photovoltaic effect. The development of novel solar cells is being promoted by the increasing awareness that available energy reserves are running out. A major energy shortage is expected in the near future unless renewable energy can cover the deficit. On the other hand, the supply of energy from the sun is 3×1024 joules per year, about 10 000 times more than current annual consumption. In other words, covering 0.1% of the earth's surface with solar cells with an efficiency of 10% would satisfy our present needs. Crystal silicon based solar cells are the mainstream of the current photovoltaic industry. But the relatively thick layer of silicon required for reasonable photon capture rates and the high expense of crystal silicon fabrication is a heavy burden. Other approaches including changes in the material side (amorphous silicon) and the device side (thin film, multiple junctions) still cannot satisfy the requirement of high efficiency and low cost simultaneously. In one word, solar cells cannot be employed as the main power source for human beings until a significant breakthrough happens.

A number of novel solar cells have been investigated, including photoelectrochemical cells, polymer solar cells, and nanocrystal cells. They have been named the third generation of solar cells to differentiate them from previous ones (first generation crystal silicon cells and second generation thin film cells). In the last few decades, various plastic solar cells, which are based on

Rational Design of Solar Cells for Efficient Solar Energy Conversion, First Edition.
Edited by Alagarsamy Pandikumar and Ramasamy Ramaraj.

interpenetrating polymer works [1], polymer/fullerene blends [2], and halogen-doped organic crystals [3], have also been developed. Compared to silicon-based devices, plastic solar cells are light in weight, disposable, inexpensive to fabricate, flexible, and designable on the molecular level. Plastic solar cells with different device architectures have been developed, e.g. single layer diode [4–6] bilayer acceptor/donor heterojunctions [1, 7–9] bulk heterojunction [2, 10, 11], and tandem organic photovoltaic cells [12–14].

One drawback of solar cells based on small organic molecules is the inability to fabricate them in large areas or on flexible substrates due to the evaporation technique limit. Polymer solar cells based on spin casting techniques, on the other hand, are no longer restricted by such problems. One important limitation of organic semiconductors is the extremely low electron mobility. This can be solved by either introducing electron transporting fullerene or combining polymer with semiconductor nanocrystal quantum dots in nanoscales. The latter approach is named hybrid polymer/nanocrystal or quantum dot solar cells. Due to their similarity to the conjugated polymer/fullerene solar cell, they are sometimes considered as a subcategory of organic photovoltaic devices. Quantum dots (QDs) have superior properties for solar cell applications, including the multiple exciton production from one photon and an extended absorption into infrared.

In silicon, one photon of light frees one electron from its atomic orbit. In the late 1990s, Arthur Nozik, a senior research fellow at the National Renewable Energy Laboratory in Golden, postulated that quantum dots of certain semiconductor materials could release two or more electrons when struck by high-energy photons, such as those found toward the blue and ultraviolet end of the spectrum [15]. In 2004, Victor Klimov of Los Alamos National Laboratory in New Mexico provided the first experimental proof for Nozik's postulation: he showed quantum dots of PbSe could produce up to seven electrons per photon when exposed to high-energy ultraviolet light [16]. Nozik's team soon demonstrated the effect in dots made of other semiconductors, such as PbS [17] and PbTe [18]. The fact that quantum dots can produce multiple excitons upon receiving a single photon favors today's photovoltaic cells, which can only manage one exciton per high-energy photon, with high kinetic energy carriers losing their energy as heat. This would not result in a sevenfold increase in final output, however, but could significantly boost the maximum theoretical efficiency. Besides that, quantum dot photovoltaics would theoretically be cheaper to manufacture, as they can be made using simple chemical reactions like colloidal synthesis.

The effective use of the solar spectrum is another important benefit of QD over organic semiconductors. All the previuosly mentioned solar cells could only absorb the visible part of the solar spectrum, leaving the infrared part unused. A QD-based photovoltaic device with the ability of absorbing infrared light would be expected to significantly improve the power conversion

efficiency, thus bring significant progress in solar cell research. And this is just the driving force of our research. Still the QD-based solar are cells have only 7% efficiency, because of faster recombination and energy loss as heat. Shen *et al.* [19] have investigated the effect of a ZnS coating on the photovoltaic properties of CdSe quantum dot-sensitized solar cells. CdSe quantum dots were adsorbed onto nanostructured TiO_2 films for different times by using a chemical bath deposition method to produce QD-sensitized solar cells. The device performance was analyzed under a solar illumination of 100 mW cm^{-2}; the maximum efficiency of the sample was increased from 1.16% to as high as 2.02% when the electrodes were coated with ZnS.

By reducing the energy loss and increasing the excited state electrons lifetime, the efficiency can be increased. Some research groups are working to reduce the energy loss from QDs through the hot electron concept with suitable capping molecules. Gao *et al.* [20] have prepared PbSe quantum dot solids with high charge carrier mobilities using layer-by-layer dip-coating with 1, 2-ethanediamine as substitute capping ligands. Using a time and energy resolved transient absorption spectroscopy, they observed that in QD solids hot carrier cooling becomes faster with increased electronic coupling and was significantly enhanced compared to the cooling rate for QDs in dispersion. This suggested that strong electronic coupling was an issue of concern for hot carrier QD solar cells. So if one wants to use hot electrons to improve solar cell performance then the first and far most important step is to find a solution to reduce the ultrafast cooling rate of higher energy state (hot electron) carriers. The second important requirement is extraction of hot carrier for their effective usage. However, realization of both of the requirements is challenging to the scientific community. Only recently, Pandey *et al.* [21] observed hot electrons in core/shell CdSe/ZnSe colloidal quantum dots. The hot electrons, in the first excited conduction state 1Pe of the CdSe core, were efficiently extracted by tunneling through the ZnSe shell. Electron extraction times are temperature-independent and the range from about 100 ps for approximately 3 nm ZnSe shell thickness. The hot electron extraction leads to quenching of the visible photoluminescence. This was the first step toward infrared detection, as well using the intraband transitions of colloidal quantum dots.

12.2 Classifications of Solar Cells

In general, the solar cell types are categorized as first, second, third, and fourth generation. First generation cells consists of a large area, single layer p-n junction diode, which is capable of generating usable electrical energy from light sources with the wavelengths of sunlight. These cells are typically made using a silicon wafer. Second generation cells are based on the use of thin-film deposits of semiconductors. These devices were initially designed to be high-efficiency,

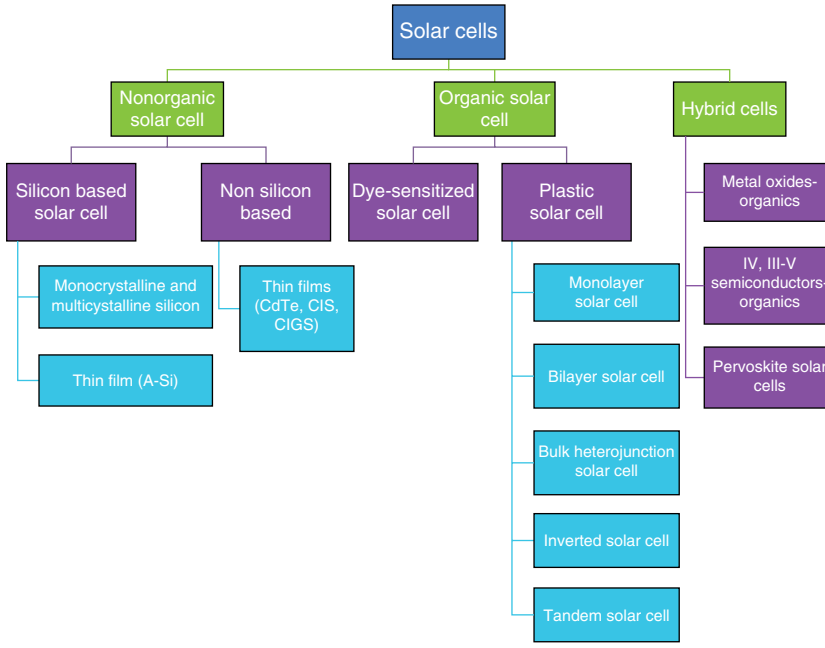

Figure 12.1 Classification of solar cells.

multiple junction photovoltaic cells. Third generation cells are very different from the previous semiconductor devices, as they do not rely on a traditional p-n junction to separate photogenerated charge carriers. These new devices include photoelectrochemical cells, polymer solar cells, and nanocrystal solar cells. Dye-sensitized solar cells and quantum dot sensitized solar cells are now in production. Examples include amorphous silicon, polycrystalline silicon, microcrystalline silicon, cadmium telluride, copper indium selenide/sulfide. Fourth generation is a composite photovoltaic technology with the use of polymers and nano particles mixed together to make a single multispectral layer.

Depending on the materials used for fabrication, solar cells are further classified into three types: firstly, nonorganic or inorganic based solar cells; secondly, organic based solar cells; and, finally, hybrid solar cells, which are made by the mixture of organic and inorganic materials. The classification of solar cells is given in Figure 12.1.

12.2.1 Inorganic Solar Cells

Solar cells based on silicon are most important because of their higher efficiency and portability [22]. For the manufacturing of silicon-based solar cells pure silicon crystals, either single or multicrystals, are used.

Though theoretical efficiency of single crystalline solar cells is a little higher than that of multicrystalline cells, in practice the performances of both are same. They are used in the street lamps, satellites, space shuttles, defense, and various industrial applications [23]. As to second generation solar cells, first generation solar cells are considered to have higher lifetime [24]. Nonorganic solar cells are classified into two types:

i) **Single crystal Si solar cells**. The first generation of solar cells are single crystal Si solar cells and they have a vital role in practical application since they possess higher power conversion efficiency (PCE) than other types. Although single crystal solar cells have advantages they have some drawbacks, which pull down their markets; some of the drawbacks are manufacturing cost and the high energy needed for production of good quality single crystals without any imperfections [25].
ii) **Thin film solar cells**. Second generation solar cells are based on thin films; they have the major advantages of light weight and affordabilit, but the performances of these devices are comparatively very low compared to crystalline solar cells because of their imperfections [26]. This type of cell is prepared by coating transparent and conducting, supporting material, such as steel, glass, plastic, etc., with thin film layers of silicon. The major practical application of this type of solar cell is in the field of scientific calculators and street lamps. Compared with individual solar cells, the efficiency of amorphous solar panels is low. Cadmium telluride (CdTe), copper indium gallium diselenide (CIGS), amorphous thin-film silicon, etc., are commercially available thin film solar cells [27]. To overcome the above shortcomings the main focus of research is focused on the improvement of efficiency; as a result, experimental efficiency for CdTe and CIGS is approaching 21%, overtaking m-Si solar cells, the dominant material currently used in most solar PV panels [28].

12.2.2 Organic Solar Cells (OSCs)

The latest emerging field of third generation photovoltaic cells is made up of organic electronics. The materials used in fabrication of this type of solar cells are solution-processable at high throughput and are low cost, resulting in cost-effective material. Third generation cells are classified into several types such as, dye-sensitized solar cells (DSSCs), plastic or polymer based organic solar cells.

i) **Dye sensitized solar cells (DSSCs)**. Third generation type solar cells are dye-sensitized solar cells (DSSCs), which are hybrid organic–inorganic solar cells. The most dominant characteristic feature of the device is a mesoporous film of titanium dioxide (TiO_2) in the nanometer range. This is deposited with a single layer of dye that is sensitive to the radiation in the

range of visible region. The mechanism of the dye involved here is similar to the mechanism of chlorophyll in plants; it harvests solar light and transfers the energy via electron transfer to a suitable material (here ZnO) to produce electricity as opposed to chemical energy in plants. Since DSSCs are manufactured from abundant and cost-effective materials by inexpensive processes (e.g. doctor blade), they are expected to be a major contributor to the future commercial PV technology [29].

ii) **Polymer or plastic solar cells (PSC)**. Based on conjugated polymers and molecules there emerged a new photovoltaic technology called plastic solar cell technology. In this type of cell, higher efficiencies are achieved by mixing electron ± donor-type polymers with suitable electron acceptors. On the basis of device fabrication methods, plastic or polymer based OSCs are classified into the following types:

- monolayer solar cells;
- bilayer solar cells;
- bulk heterojunction BHJ solar cells;
- inverted solar cells;
- tandem solar cells.

12.2.3 Hybrid Solar Cells

An alternative to silicon solar cells is third generation excitonic photovoltaic devices. Hybrid solar cells are a combination of a polymer and nano organic or inorganic semiconductor materials. They combines the excellent electronic properties of inorganic molecules with flexibility of amorphous substrates with affordable price [30].

i) **Perovskite solar cells** are an (organic–inorganic) type of solar cell that has gained much attention within five years, due to steady improvement of power conversion ability and low processing costs. Significant aspects of perovskite are its synthetic feasibility, strong optical absorption, charge recombination rate, and ease of fabrication. Moreover, hybrid perovskites can be fabricated by simple synthetic methods and are easy to capitalize when compared to the existing excitonic photovoltaic technologies such as dye-sensitized solar cells (DSSC) and organic solar cells (OSC). Another important aspect is high charge-carrier mobility, which is highly desirable for developing high-performance solar cell devices [31].

12.3 Main Losses in Solar Cells

The energy conversion loss is the main factor to affect the efficiency of the solar cell. The two most important power loss mechanisms in single-band gap photovoltaic cells are (i) the inability to absorb photons with energy less than the band gap and (ii) ***thermalization loss*** of photon energy exceeding the gap

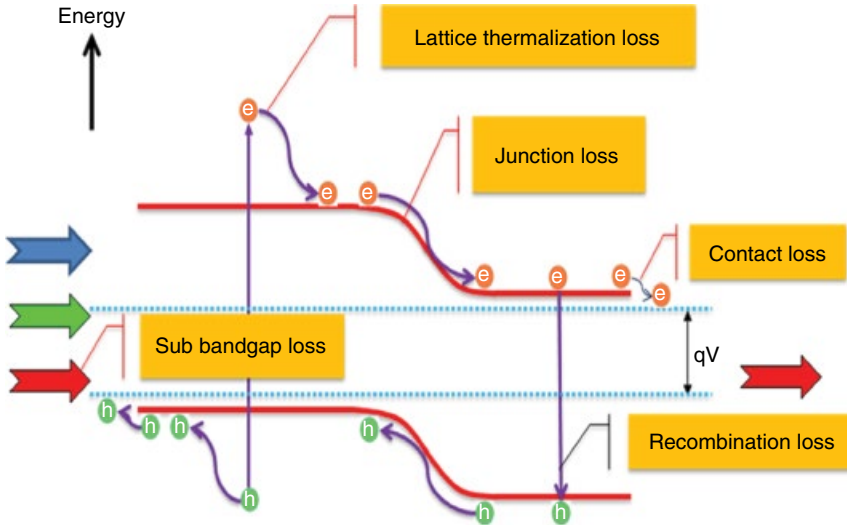

Figure 12.2 Energy conversion loss process in standard solar cells.

(Figure 12.2). Longer wavelengths are not absorbed by the solar cell material. Shorter wavelength generates an electron-hole pair greater than the band gap of the p-n junction material. The excess energy is lost as heat because the electron (hole) relaxes to the conduction (valence) band edges. The amounts of the losses, due to these two reasons, are around 23 and 33% of the incoming solar energy, respectively [32].

12.3.1 Recombination Loss

Recombination loss most commonly occurs at impurities or defects of the crystal structure, but it occurs also at the surface of the semiconductor. In the latter case, energy levels may be introduced inside the energy gap, which encourages the electrons to fall back into the valence band and recombine with holes. In the recombination process energy is released in one of the following ways:

- Nonradiative recombination – phonons, lattice vibrations.
- Radiative recombination – photons, light or EM-waves.
- Auger recombination – which is releasing kinetic energy to another free carrier.

12.3.2 Contact Losses

In a solar cell, the electrons have to flow from one side of the cell to the other through an external circuit. The bottom can be covered with a metal, allowing for good conduction, but if the top is completely covered, then photons cannot

get through the opaque conductor and all of the current is lost (in some cells, transparent conductors are used on the top surface, but not in all). If contacts are put only at the sides of the cell, then the electrons have to travel an extremely long distance to reach them. Remember, silicon or CdTe or CdSe are semiconductors, they are not nearly as good as a metal for transporting current. Its internal resistance (series resistance) is fairly high, which means higher conduction losses. To minimize these losses, cells are typically covered by a metallic contact grid that shortens the distance that electrons have to travel while covering only a small part of the cell surface.

12.4 Hot Electron Concept in Materials

Higher energy conduction band (CB) electrons are known as "hot electrons". Hot electrons usually relax to the bottom of the conduction band and lose their excess energy as heat (Figure 12.3a); because of this, the higher energy state excited electron lifetime is very short in bulk material. In QD, the energy levels are discrete in nature (absence of phonon bottleneck effect, Figure 12.3b), so the excess energy loss is expected to be minimized. When the hot carriers spend a relatively long time in the higher energy state, then their extraction towards the acceptor is maximized.

However, in contrast to this expectation, the hot electron cooling process in QDs is still occurs in ultrafast time and this means that their extraction before cooling is a challenging process [20, 21, 33]. In the absence of a phonon bottleneck effect in QDs [34], an "Auger like" [35, 36] process and 'trap states' [37] are the pathways of cooling and, in fact, dominate at higher excitation energies, as reported elsewhere.

Recently, Anshu Pandey and Philippe Guyot-Sionnest [21] have extracted hot electrons from CdSe/ZnSe core shell QDs by simply exciting the sample with two different energy sources. A resonant 4 μm intraband pulse was irradiated, subsequent to an interband excitation pulse, so that the valence band edge electrons were promoted to above the CB edge state ($1p_e$) of CdSe QDs and from there they were tunneled out through the ZnSe outer layer as hot electrons. A similar extraction process was also made possible from PbSe QDs. The team, led by Aydil, prepared PbSe QDs with a range of diameter (3.3–6.7 nm) and deposited a layer of it on to a TiO_2 precoated surface to demonstrate hot electron extraction. Hot electron extraction was possible because of the nature of the interface between PbSe QDs and TiO_2. The interface was such that only the higher energy state CB electrons from PbSe QDs can be transfer into the CB levels of TiO_2.

In our case, CdSe–β-carotene hybrids, the photoexcited higher energy state electrons (of CdSe QDs) do not relax down to the CB edge state of the QDs. Instead they are extracted out of quantum dot into the carotene's LUMO level as hot electrons; this observation was very clear in our excitation energy dependent PL studies.

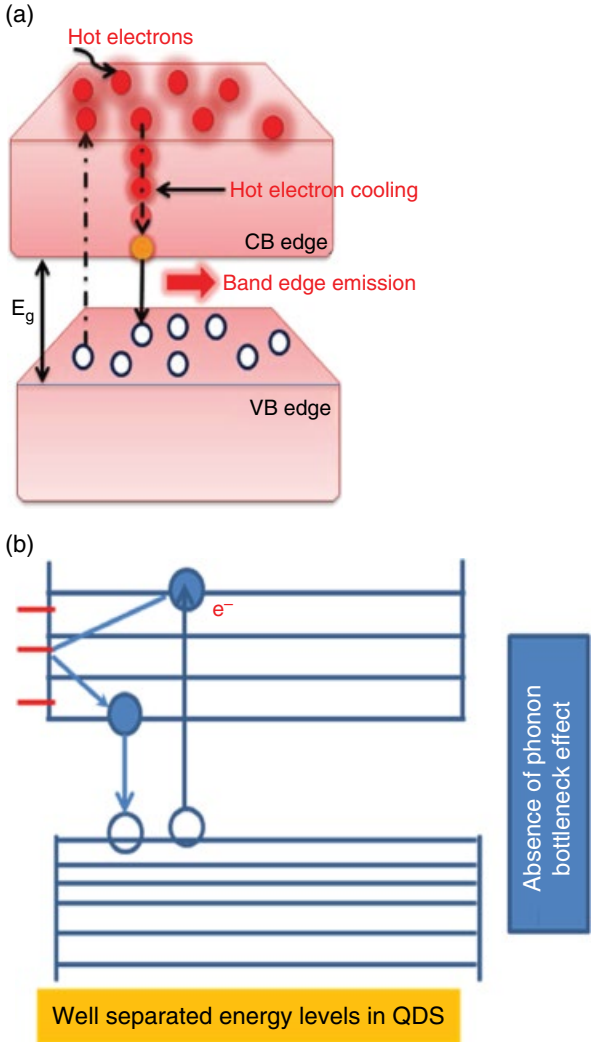

Figure 12.3 (a) The bulk band structure of a semiconductor. Here the photoexcited higher energy state of electrons relaxes through the continuous states of CB and reaches CB edge state. (b) Energy band structure of QD. Here the photoexcited electrons relax through the defect levels (hence in both the systems, slowing down of cooling process is challenging one).

12.5 Methodology

QDs are produced from variety of physical and chemical methods such as lithographic patterning, molecular beam epitaxial, and colloidal synthesis. Among them, colloidal synthesis is one of the leading techniques for synthesizing high quality QDs. The main limitations of physical methods are the cost of

fabrication and the difficulty in controlling the position of individual dots. Foremost advantages of chemical synthesis are: (i) size-tunable QDs are achieved by controlling the reaction conditions and precursor ratios; and (ii) by manipulating surface chemistry it is easy to passive the surface atoms to obtain high quality QDs with high quantum yield. Here, the focus is on the colloidal based hot injection method for QD preparation.

12.5.1 Hot Injection Method

The hot injection or organometallic synthesis method is one of the most versatile methods for the synthesis of QDs. At first Murray *et al*. [38] used the hot injection method to synthesize nanocrystals of cadmium chalcogenides with nonionic (organometallic) cadmium and selenium (or sulfur or tellurium) precursors in a high boiling polar coordinating solvents, namely, trioctylphosphine oxide (TOPO), trioctylphosphine (TOP), and oleic acid (OA). This method affords luminescent nanocrystals with tunable size and shape, and stepping-down of defects can be achieved by proper selection of capping ligands and controlling the other experimental parameters.

In this method, a group of CdSe nanocrystals is grown by injecting appropriate high boiling solvents like TOPO, TOP, and OA (OA coordinates with the Cd^{2+}, OA forming an OA-Se complex). One room temperature precursor (OA-Se) solution was injected into another hot precursor, which allowed the reactions to continue at high temperature (about 200 °C). The fast injection of the precursor induces a high degree of super saturation, resulting in a short burst of nucleation. During the nucleation process the precursor concentration in the solution decreases abruptly. The drop in temperature, due to the injection of the "cold" reactants and the low concentration of unreacted precursors, prevents any further nucleation events. In the next step, the temperature is carefully increased to a value that allows the slow growth of the nuclei to larger nanoparticles while suppressing further nucleation. The separation of nucleation and growth is a prerequisite to synthesize monodispersed nanoparticles, and therefore the hot injection method generally leads to nanoparticles with a narrow size distribution of about 5%. The final size of the QDs is determined by the growth temperature, atmospheric conditions, and concentration of the capping molecules. QDs are sanitarily stabilized by the long alkyl chain of the capping molecules, which slow down the growth of nanocrystals at higher temperature and produce well passivated (defect free) nanocrystals.

After preparation, nanocrystals can easily be separated from the growth solution by adding an appropriate solvent and redissolving them in a suitable organic solvent to form stable colloidal suspensions. The TOPO molecules remain attached to the surface of the cadmium atoms and the suspensions are sanitarily stabilized. In our experimental setup, we are using a conical flask, heating mantel, and nitrogen cylinder to synthesize the high quality QDs.

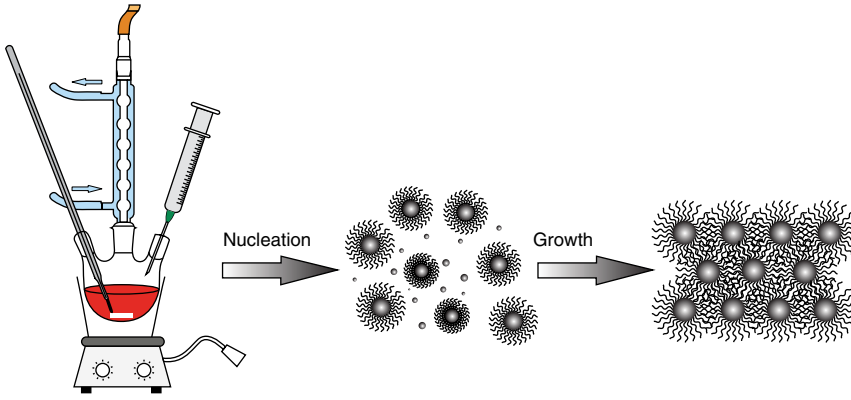

Figure 12.4 Hot injection method experimental setup and QD nucleation. Reproduced with permission of Royal Society of Chemistry.

The experimental setup for the hot injection method is shown in Figure 12.4. The entire reaction was done under a nitrogen atmosphere to dehydrate and remove of air [39]. Monodispersed CdTe, CdSe/ZnS, CdTe/ZnS QDs are also prepared by adopting the same procedure. For hybrid material preparation the respective QD samples are physically mixed with the biomolecule.

12.5.1.1 Nucleation and Growth Stages

In this synthesis method, the size dispersion of the CdSe nanocrystals is remarkably small and later adaptations have led to even smaller size dispersions. One of the reasons for this might be that nucleation and further growth of the nanocrystals occur in separate timeframes. Hot injection leads to instantaneous nucleation, quenched by fast cooling of the reaction mixture and because supersaturation is relieved by the nucleation burst. Further growth of the nuclei into mature nanocrystals occurs at a relatively lower temperature, such that new nucleation events do not occur. The classic nucleation and growth model is applied to quantum dot synthesis. Formation of nanocrystals is divided into three different stages. Firstly, the precursors decompose and form the monomers. The concentration of the monomer increases until supersaturation (which produces the energetic nucleation) occurs. Due to the nucleation burst, the monomer concentration decreases the supersaturation.

A higher concentration of precursors ensures the nanocrystal growth is onto the existing nuclei. Over the first few minutes of the reaction, the average size of the QD increases rapidly and the size distribution decreases, this is called "focusing of size distribution". When the monomer concentration is extremely low, the growth of nanocrystal become slower; the smaller nanocrystals are dissolved and are redeposited on the larger nanocrystals, thus the overall average size of the QDs increases and the size distribution broadens, this is called

"defocusing" or "Ostwald ripening process". In order to attain monodispersed samples, QD growth is sterically controlled in a focusing region and can be achieved by controlling the precursor, growth time, and multiple injections to keep the concentration of monomer high.

12.5.1.2 Merits of this Method

- High boiling point and organometallic coordinating precursors facilitate nanocrystal growth to some extent slowly at high temperature, which results in well passivated nanocrystals.
- QD size mainly depends on the reaction mixture heating time, so pulling successive aliquots out of the reaction vessel easily produces the ranges of QD size.
- The final product obtained from the synthesis reaction is in a liquid form, the QDs are in a colloidal suspension rather than a solution; it looks like the protein and fat molecules in a glass of milk. In a structure the outermost atoms of the nanocrystal are coordinated to organic ligand molecules; these ligands facilitate the interaction of the QDs with the solvent without precipitating.
- This colloidal growth allows the direction of the QDs into optically clear solutions or polymer films, as well as the possible attachment to a metal surface or various template structures [40, 41].
- The nature of precursor, mineralizer, and the reaction conditions like aging temperature and time required for the controlled synthesis of size controlled QDs.

12.6 Material Synthesis

A composite of CdSe intercalated β-carotene (βC) hybrid material is synthesized via two successive steps.

12.6.1 CdSe QD Preparation

CdSe QDs were prepared by a well-known method, as reported elsewhere [42]. Firstly, 0.2 mmole of selenium stock solution was prepared by dissolving selenium powder in 5 ml octadecene and keeping the solution at 180 °C for one hour. Then cadmium solution was prepared by taking CdO powder as precursor in a mixture solution of 1 ml oleic acid and 9 ml of octadecene, which was then heated to 180 °C for one hour until a clear solution was formed. The temperature of CdO containing solution was increased to 220 °C, 5 ml selenium stock solution was added, and the reaction was allowed 15 minutes to obtain large-size CdSe QDs. The as-prepared colloidal QD solution, after repeated washing with ethanol, was subjected to structural and optical characterization.

12.6.2 QD–βC Hybrid Formation

To prepare the CdSe QD–βC hybrid, a known amount of hexane solutions of CdSe QD and β-carotene were prepared separately and then mixed together in a vial to prepare the hybrid sample.

12.7 Identification of Hot Electrons

Identification of hot electrons can be identified by:

- photoluminescence (PL) spectrum;
- TCSPC;
- transient absorption (TC).

12.7.1 Photoluminescence (PL) Spectrum

The PL spectrum was recorded from the CdSe QD after the addition of the βC solution with different concentration (0.01 mmol solution of βC, prepared with hexane, was added to bare QD solution, in steps of 1 ml). Because of the addition of βC, the emission intensity from the CdSe QD was increased. Furthermore, a gradual shift in the emission peak maximum towards the higher energy side, as shown in Figure 12.5, has also been noticed. The PL intensity was increased much better and reached a maximum value with a βC concentration of 5 ml. The increased quantum yield corresponding to this emission maximum is about 47.12%, which is about 2.39 times higher than that of the bare CdSe QD system. The molecule is believed to be surface passivating the defect states of CdSe QDs and, therefore, an emission enhancement was noticed. Because of surface passivation, nonradiative relaxation pathways are

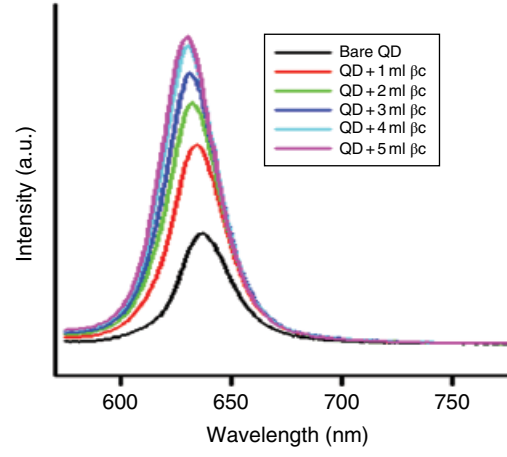

Figure 12.5 Emission spectra of CdSe QD with different βC concentration in comparison with bare CdSe QD.

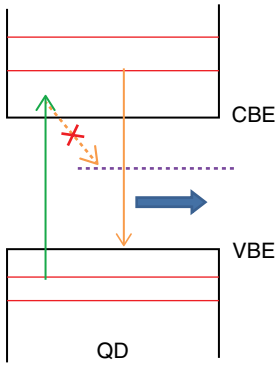

Figure 12.6 Schematic representation of arrested nonradiative relaxation of CdSe QD.

arrested (Figure 12.6) and, therefore, naturally, the radiative emission yield from QDs is increased with a blue shift.

Excitation energy dependent emission measurement on bare CdSe QD has resulted in a constant yield of 5%, as shown in Figure 12.7. Here the PL emission intensity was "gradually" decreased with the increase of excitation energy; the reason for this is reported elsewhere [43]. Unpassivated surface states associated with the surface atoms of colloidal QDs provide a nonradiative relaxation pathway or channel to the highly excited charge carriers and, therefore, the higher energy excited charge carriers are either inhibited or deviated from reaching the band edge states (from where radiative recombination is resulted); consequently, a reduced PL intensity results [44].

A careful investigation of the PL emission behavior of a hybrid sample conducted at different excitation energies, in steps of 1 nm from 545 down to 500 nm, has shown that the quantum yield was almost quenched completely down to 0.25 % at 500 nm (Figure 12.8). In this hybrid sample the maximum yield point is at (or up to) 545 nm, which means that the excited state of CdSe QD at 585 nm is confined well by the carotene. When the hybrid sample was

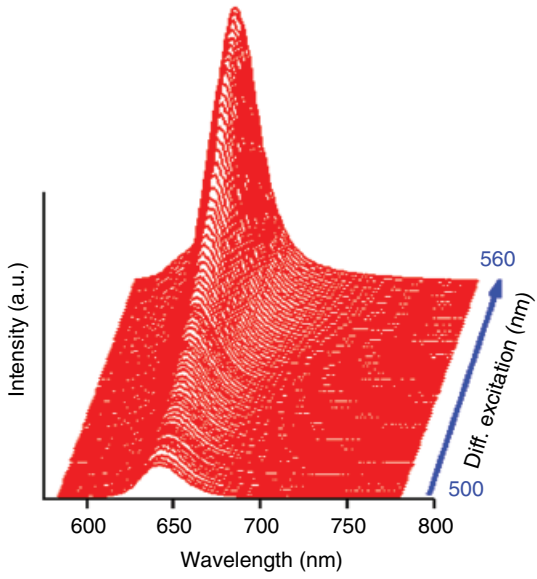

Figure 12.7 Three dimensional plot showing the excitation energy dependent PL behavior for a bare CdSe QD sample.

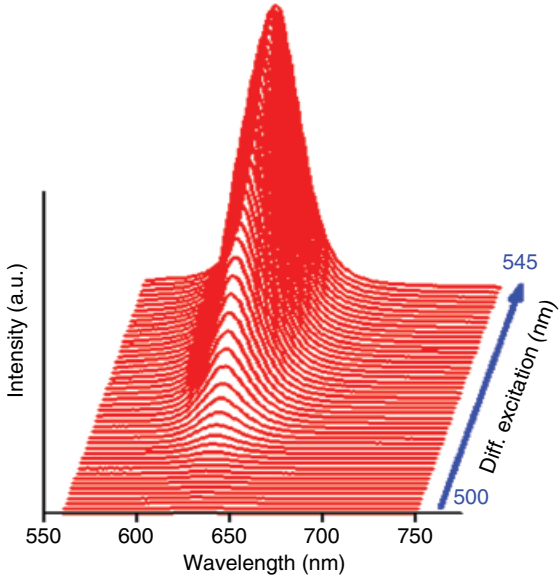

Figure 12.8 Three dimensional plot showing the excitation energy dependent PL behavior for a CdSe QD-βC hybrid sample.

excited at higher excitation energies, for example well above the second absorption maximum at 545 nm, then CdSe QD's emission yield was started decreasing, "suddenly"; this can be noticed visibly, as shown in Figure 12.9 (curve b). This sudden decrease in the PL must be due to the transfer of hot electrons from the QD to βC, which has been proved by laser flash photolysis experiments (to be discussed later).

In most of the reported hybrid systems either conduction band edge electron transfer (Scheme I in Figure 12.10) or hole transfer (Scheme II in Figure 12.10) assisted charge carrier separation becomes responsible for the observed fluorescence quenching. But, in our case, the higher energy state CB electron or hot electron transfer becomes responsible for the fluorescence quenching (Scheme III in Figure 12.10), and excitation energy dependent PL investigation has shown this clearly. Both the CB edge excited electrons and valence band (VB) edge created holes are not transferred to the molecular energy levels, which means that the nature of interface between the CdSe QD (of size about 4 nm) and carotene molecule is type I in nature, as shown in Scheme III of Figure 12.10. Our hybrid structure is, thus, different from other hybrids such as CdSe-Rhodamine B [45], CdSe-methylene blue [46], and CdSe-methyl viologen [47], where the molecule's LUMO level was just below the CB edge level of the CdSe QD. Type I band alignment between the QD and molecule (with respect to vacuum level) with an experimental CB_{offset} value of 0.30 eV.

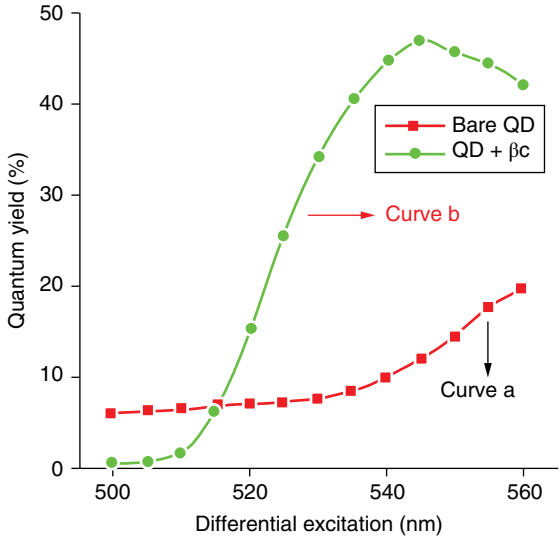

Figure 12.9 The calculated quantum yield as a function of excitation energy for the bare (curve a) and CdSe QD-βC hybrid (curve b) samples.

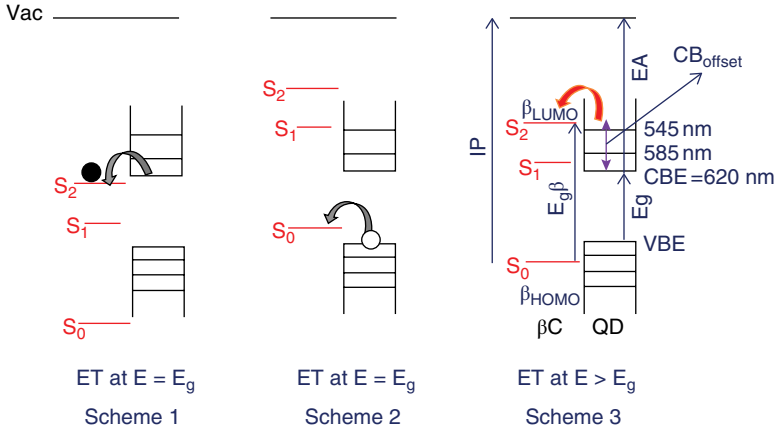

Figure 12.10 Interfacial energy level diagram between a CdSe QD and beta-carotene explaining various possible quenching mechanisms.

The experimental CB_{offset} is nothing but the difference in energy between the PL quenching point (at approximately 540 nm) and the CB edge state of CdSe QD (optical absorption maximum at 620 nm or energy gap of CdSe QD (E_{gQD})). Using this experimental CB_{offset} value in Equation 12.1, obtained from the interfacial energy diagram,

$$CB_{offset} = EA_{QD} - EA_{\beta C} \tag{12.1}$$

where EA_{QD} and $EA_{\beta C}$, respectively, correspond to the electron affinity values of CdSe QD and βC, we have calculated EA_{QD}. Before that the $EA_{\beta C}$ was obtained from Equation 12.2. For this, the experimental energy band gap ($E_{g\beta}$) of βC (which is 2.74 eV) and the reported ionization potential (I_P) energy (–5.84 eV) [33] values of βC were used.

$$EA_{\beta C} = I_p - E_{g\beta} \tag{12.2}$$

The obtained electron affinity value of CdSe QD is –3.40 eV, which closely matches the reported experimental and theoretical EA value of a CdSe QD of similar size [48]. Matching of the as obtained EA value of CdSe QDs with that of reported values has indirectly confirmed the experimental conduction band offset value between these two hybridizing systems.

12.7.2 Time-correlated Single Photon Counting (TCSPC)

To validate the experimental observations such as "luminescence enhancement" and "luminescence quenching", which are due, respectively, to the surface passivation effect and

$$y = a_1 \cdot e^{-\frac{t}{\tau_1}} + a_2 \cdot e^{-\frac{t}{\tau_2}} + a_3 \cdot e^{-\frac{t}{\tau_3}} \tag{12.3}$$

electron transfer to the βC, lifetime measurements were conducted at the CB edge and higher energy CB state. Figure 12.11 compares the time resolved PL decay behavior at 500 nm and 620 nm, which were recorded from both bare and hybrid samples, after exciting the samples at 400 nm. The emission decay curves of the bare and hybrid samples have been analyzed using the triexponential decay fit [49] shown in Equation 12.3 and fitting parameters such as "a" and "τ" were obtained. By substituting the values of a_1, a_2, a_3 and τ_1, τ_2, τ_3 into Equation 12.4, the average lifetime values of electrons in that energy level were then calculated.

$$\langle \tau \rangle = \frac{\sum_{i=1}^{n} a_i \tau_i^2}{\sum_{i=1}^{n} a_i \tau_i} \tag{12.4}$$

Table 12.1 summarizes all of the fitting parameters and calculated average lifetime values. The calculated the average lifetime, at the CB edge state of CdSe QDs (620 nm), when it is hybridized with βC is 13.76 ns, which is high in magnitude when compared to the value of 7.58 ns measured from the CB edge

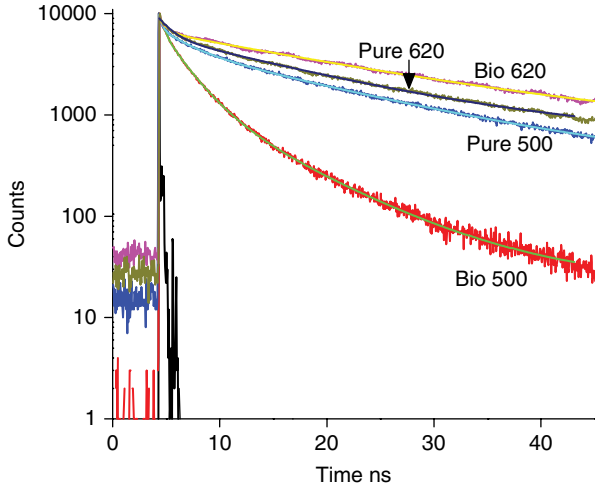

Figure 12.11 PL decay curves for bare and CdSe QD-βC hybrid samples recorded at 620 nm and 500 nm.

Table 12.1 Fitting parameters for the fluorescent decay of pure and βC capped CdSe QDs.

Sample	Decay spectrum at (nm)	Lifetime value τ_1 (ns)	Lifetime value τ_2 (ns)	Lifetime value τ_3 (ns)	Average lifetime τ (ns)
Pure QDs	500	0.2 (8%)	2.5 (45%)	8 (47%)	6.67
	620	0.26 (8%)	2.5 (37%)	8.6 (55%)	7.58
QDs with Bio	500	0.47 (20%)	1.5 (33%)	5.8 (47%)	4.92
	620	0.27 (3%)	2.2 (11%)	14 (86%)	13.76

state of bare CdSe QDs. The reason for the longer lifetime value may be due to the surface passivation effect of βC on CdSe QDs. A similar increase in $<\tau>$ was also noticed from the type I CdSe/ZnS core shell QD system, which was attributed to the surface passivation effect [50]. The $<\tau>$ at 500 nm of the hybrid sample is much shorter (4.92 ns) and this is because of the transfer of electrons to the LUMO level of the molecule. The average lifetime value of the bare and hybrid systems at 520 nm were used to calculate the charge transfer rate (K_{et}) using Equation 12.5. The calculated electron transfer rate is $5.35 \times 10^7\,s^{-1}$, which is similar to the reported transfer rate between CdSe and TiO_2 [51]. However, because of the experimental limitation in measuring the shortest lifetime components at the higher energy level, the calculated rate constant is an approximate value only.

$$\kappa_{et} = \frac{1}{<\tau>_{\beta c-CdSe}} - \frac{1}{<\tau>_{CdSe}} \tag{12.5}$$

12.7.3 Transient Absorption

Finally, to confirm the charge separated state, with electrons in the LUMO level of the βC and holes in the valence band edge state of the CdSe QD, nanosecond transient absorption (TA) spectra were recorded. The wavelength of the laser source was 355 nm. Figure 12.12 shows the TA spectra of hybrid sample with two negative bleach minima at 450 and 620 nm. As these bleach positions are matching with the absorption edge values of βC and CdSe QD at 450 and 620 nm, respectively, their origin is expected to come from these two respective systems.

Remember, this could not be due to the direct excitation of either βC or CdSe QDs because their respective individual bleach profiles recover at much faster rates. For example, in the case of pure βC the excited state electrons in the S_2 state undergo a fast internal conversion down to the S_1 state within 200 fs. Again, from there the electrons undergo a downward transition to the S_0 state in a few tens of picoseconds [52–54]. In the case of CdSe QDs, the band edge bleach profile recovers within a few nanoseconds, as reported elsewhere [55]. Therefore, the slow recovering negative bleach at 450 nm must be due to the transferred electrons from the CdSe QD to the LUMO level of the βC. As the excitation energy used in this TA experiment is well above 550 nm, photoexcited CdSe QD's VB electrons are transferred to the LUMO level of the βC molecule (Figure 12.13). Transferred electrons exist there as hot

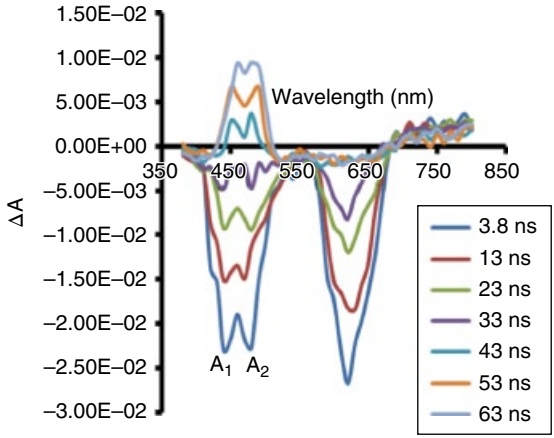

Figure 12.12 Transient absorption spectra recorded from a βC-CdSe QD hybrid sample.

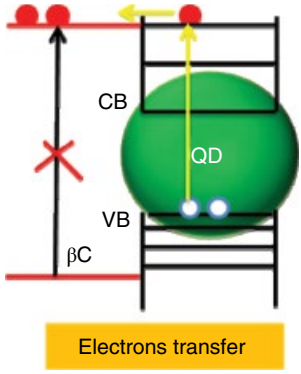

Figure 12.13 Schematic representation of the electron transfer process.

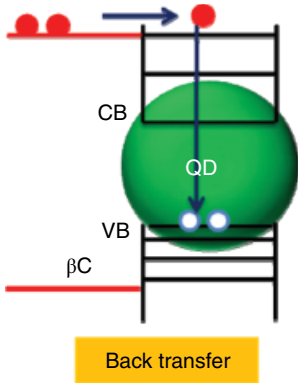

Figure 12.14 Schematic representation of the back transfer process.

electrons for a few tens of nanoseconds; therefore, any further transition to this molecular level (followed by the excitation of molecule (HOMO to LUMO)) is blocked and, as a consequence, negative bleach is obtained at 450 nm. To make sure that this 450 nm negative bleach is from teh βC, the difference between two peak positions at A_1 and A_2 has been measured; it is 45 nm, agreeing with the vibrational level separation of the βC. The other slow recovering negative bleach spectra at 620 nm is due to "holes" in the VB edge state of the CdSe QD. This 620 nm bleach appears until the holes in the VB edge state of the CdSe QD are depleted by the back transferred electrons from the LUMO level of the βC (Figure 12.14).

Hot electrons in the molecular LUMO level back transfer to the CB edge state of the CdSe QD, from where they recombine with the holes in the VB level of the CdSe QD, and by this process (cooling process) both the molecule and QD are brought back to their respective neutral state. Figure 12.15 shows the time dependent absorption profiles measured at 450 and 620 nm peak positions of the bleach spectra. To know the average lifetime values, respectively, associated with this back transferring process and cooling of charge carriers, we have fitted the absorption curve measured at 450 and 620 nm. A value of about 24.44 ns was obtained from the absorption curve at 450 nm and this could correspond to the average lifetime value for the back transferring of hot electrons into the CB edge state of the CdSe QD. A similar average lifetime value measured from the absorption curve at 620 nm has resulted in a value of about 30.05 ns, which is nothing but the time taken by the back transferred electrons to recombine with the holes in the valence band of CdSe QDs (cooling process). The average lifetime value measured at 620 nm is higher in magnitude than that of the value measured at 450 nm because the recombination process is possible after the arrival of back transferred electrons to the CB edge state of CdSe QDs. This difference in the average lifetime value has, thus, suggested a fact that the back transferring mechanism or pathway of electrons is via the CB edge state of CdSe QDs.

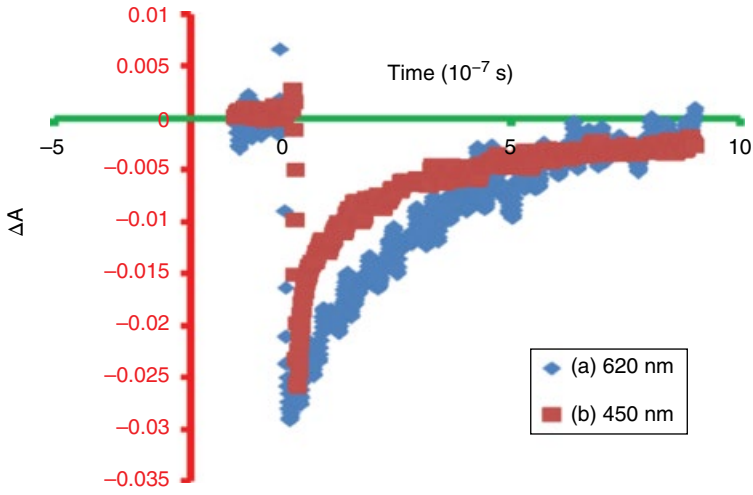

Figure 12.15 Time dependent absorption profiles of CdSe QDs at 620 nm (a) and beta-carotene at 450 nm (b).

The slow recovering negative bleaches at 450 and 620 nm are direct evidence to the existence of hot electrons.

Type I core shell structures, like CdSe/ZnS, are well known for enhanced emission yield [56], and when their outer surface is attached to electron accepting molecules like benzoquinone or surrounded by metal oxide nanocrystals (TiO_2), then the photoexcited charge carriers are separated out of the CdSe QD and the emission yield from the core QD is quenched down [57]. In this type I core shell QDs, the photoexcited electrons are thermalized to the CB edge state of CdSe QD and, from there, they tunnel out to the electron accepting system (molecule or metal oxide). It is because of this thermalization process that the excess energy possessed by the electrons is lost in the core QD itself (when it is excited with higher excitation energy). Interestingly, our hybrid system, which is also type I in nature, has behaved differently. It has exhibited both fluorescence enhancement and quenching, and one can tune the sample between these two states by just varying the excitation energy. At lower excitation energies, because of the confinement effect, PL yield was enhanced similar to that of a CdSe/ZnS core shell structure. But once the excitation energy was used above a threshold value of 550 nm then the electrons were transferred to the LUMO level of the molecule, leading to the PL quenching. We believe that the electron wave function overlapping at the molecular level is high for the higher energy state CB electrons and, therefore, they are extracted out of CdSe QDs in the presence of the βC.

12.8 Quantum Dot Sensitized Solar Cells

In 1991, O'Regan and Grȁtzel [58] first reported a new architecture for the dye-sensitized solar cell (DSSC). It has attracted much attention throughout the world from both academic and industrial fields as a promising alternative to silicon-based solar cells [59]. Currently, 11% is the highest efficiency recorded by DSSCs and their long-term stability has improved by using hydrophobic dyes and robust electrolytes [60, 61]. For further improvement of the overall efficiency in DSSCs, various dye molecules have been designed and prepared as a key material for absorbing incident solar radiation, transferring charges over porous metal oxide layers with high surface areas [62]. Inorganic semiconducting materials can be well suited for solar cell sensitization [63, 64] because they are robust, band gaps can be effectively tuned, and they are easy to process. Hence, they are ideal candidates for the optimization of a solar cell to achieve a maximum efficiency. Recently, sensitization of mesoporous metal oxide layers with various quantum dots (CdSe [65], CdTe [66], etc.) has been proposed, and their photovoltaic properties have been tested. However, QD-sensitized solar cells (QDSSCs) have shown comparatively lower efficiencies than the values expected. QD-sensitized cells have been attracting much attention especially because of the recent popularity in the preparation of well-defined colloidal QDs by wet chemical synthesis [67] and the demonstration of multiple exciton generation from single-photon absorption in colloidal QDs through impact ionization (an inverse Auger process) [16]. Therefore, progress in this field requires a breakthrough to understand the working mechanism of QDSSCs and the realization of multiple exciton-extracted devices.

12.8.1 Working Principle

The basic structure of the QDSSC is shown in Figure 12.16. It mainly consists of three parts: working electrode, electrolyte, and counterelectrode [68]. The working electrode, that is a photoelectrode or photoanode, is generally fabricated through deposition of a layer of mesoporous nanocrystalline semiconductor (TiO_2 or ZnO) on a conductive substrate (e.g. FTO and ITO glass), and then the absorption of QDs onto the mesoporous semiconductor. The electrolyte is normally a liquid, containing a redox couple (S^{2-}/S_x^{2-}), filling in between the working electrode and the counterelectrode to transport carriers. The counterelectrode, also named a cathode, is a passive electrode, normally a conductive glass coated with a layer of catalyst (platinum, gold), for charge exchange between the counterelectrode and electrolyte. From Figure 12.16, it is seen that the QDs generate excitons under illumination with sunlight and then the excited electrons are injected from the CB of the QDs into the CB of TiO_2. At the same time, the photogenerated holes are donated to the

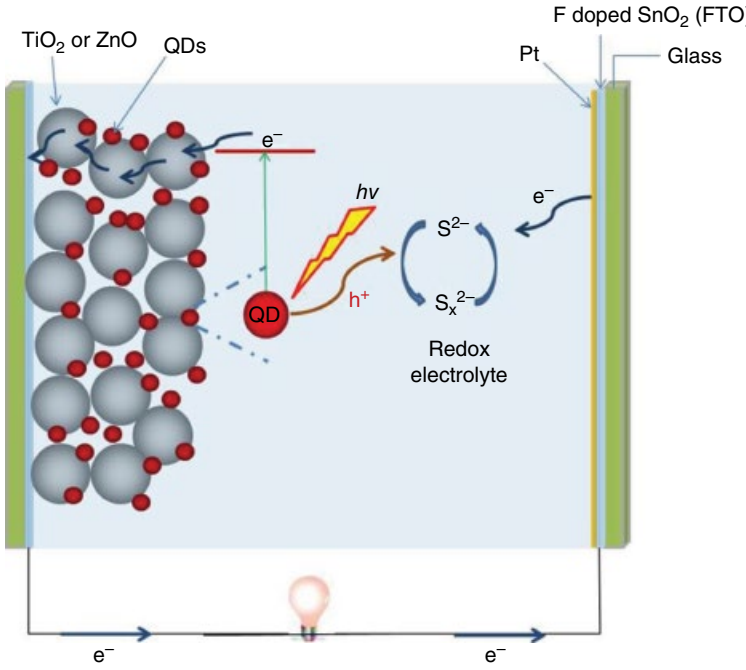

Figure 12.16 General schematic structure of the QD sensitized solar cell showing all the components and a process of excited electron transfer under illumination.

electrolyte and, thus, the QDs are restored. The oxidation species of electrolyte diffuses to the counterelectrode and is reduced by the migrating electrons from the external circuit. The above process can be expressed as [65, 69, 70]:

$$\mathrm{QDs} + \mathrm{h}\nu \longrightarrow \mathrm{QDs}(\mathrm{e} + \mathrm{h})$$

$$\mathrm{QDs}(\mathrm{e}) + \mathrm{TiO_2} \longrightarrow \mathrm{QDs} + \mathrm{TiO_2}(\mathrm{e})$$

$$\mathrm{QDs}(\mathrm{h}) + \mathrm{S}(\mathrm{e}) \longrightarrow \mathrm{QDs} + \mathrm{S}$$

12.8.2 Device Preparation

12.8.2.1 Preparation of TiO_2 Nanoparticle Electrode

A semitransparent TiO_2 (20 nm in size) nanoparticulate layer 8 μm in thickness was prepared by screen printing a paste of TiO_2 nanoparticles (Ti-Nanoxide HT/SP from Solaronix) onto the ultrasonically cleaned fluorine doped tin oxide (FTO, 8 Ω/sq) glass substrates. The thickness of coating was controlled

by repeating the screen printing. Before depositing the next layer, each layer was dried at 120°C for 10 minutes, and then finally sintered at 500°C for 30 minutes.

12.8.2.2 QDs Deposition on TiO_2 Nanoparticle

A colloidal solution of QDs/β-carotene was prepared by mixing an equal weight (0.01 g) of QDs and β-carotene in a common solvent (2 ml of chloroform). As prepared hybrid solution was then drop cast onto a TiO_2 precoated FTO substrate that acted as photoelectrode.

12.8.2.3 Counterelectrode and Assembly of QDSSC

A counterelectrode was prepared by depositing gold on an FTO substrate. The as prepared photo and counterelectrodes were joined together with a spacer (SX-1170-60, Solaronix SA) of thickness 120 μm between them and a polysulfide electrolyte composed of 0.5 M Na_2S, 2 M S, 0.2 M KCl in methanol/water (7:3 by volume) was injected through the hole on the counterelectrode to complete the cell structure. A black mask (8 × 8 mm) was used in the subsequent photovoltaic studies.

12.8.3 Performance

The QD sensitized solar cell device structure is schematically represented in Figure 12.17. The magnitude of the photocurrent from the hybrid coated solar cell device is high when compared with that of the bare CdSe QD coated device; the reason for this could be due to the transfer of photo generated electrons from the CdSe QD into the CB of TiO_2 through β-carotene energy levels. The electrons in the LUMO level of the β-carotene are relatively free from the influence of CdSe QDs (exciton binding force) and, therefore, can move towards the

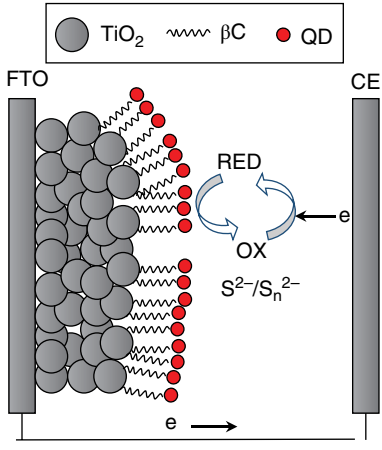

Figure 12.17 Schematic representation of a QD sensitized solar cell device structure.

TiO_2 coated electrode as hot electrons. However, because there is no anchoring group with β-carotene, the molecule is not well connected with the TiO_2 surface, thus providing an interfacial resistance to the flow of electrons into the oxide material. But because of the existing driving force in the device, electrons are able to move into the TiO_2 conduction band energy levels and constitute a photocurrent across the external circuit. While crossing the interface, hot electrons may lose their energy. Even after moved into the conduction band levels of TiO_2, because of the continuum nature of band states. the electrons relax down to the band edge state, losing their extra energy.

As a consequence it becomes difficult to see the real "hot electron effect" in this device. But still β-carotene has helped to increase the magnitude of the photocurrent by extracting electrons away from CdSe QDs. Here we have to point out that the possibilities for the transfer of photo-generated electrons from β-carotene into the CB of TiO_2 cannot be ruled out, because the molecule has shown weak absorption at around 350 nm (450 nm absorption level is reduced by the supply of electrons from CdSe QDs), but its magnitude will be very low. In general, though this molecule has strong absorption in the visible region, the magnitude of the photocurrent generated by this molecule is very low. Lack of surface anchoring groups in this molecule and its preference to make energy transfer induced type interactions are the reasons for the poor photocurrent efficiency.

12.9 Conclusion

A QDSSC device has been fabricated, using CdSe, QDs, and their hybrids with beta carotene as an active material. The performance of the device can be improved further by covalently attaching β-carotene with the TiO_2 surface and, by doing so, the resistance for the flow of electrons into the metal oxide can be reduced. Also, by using oleic acid free CdSe QDs, it is possible to reduce the resistance for the flow of electrons between QD layers, which, in turn, could help to harvest more photogenerated electrons across the metal oxide. Even by using a still wider bandgap metal oxide in the place of TiO_2, if it is possible to directly inject hot electrons into electrode material, then an enhanced open circuit voltage is possible.

References

1 J.J.M. Halls, K. Pickler, R.H. Friend, *et al*., Efficient photodiodes from interpenetrating polymer networks, *Nature*, **376**, 1995, 498–500.

2 G. Yu, J. Gao, J.C. Hummelen, *et al*., Polymer photovoltiac cells – Enhanced efficiencies via a network of internal donor-acceptor heterojunctions, *Science*, **270**, 1995, 1789.

3 J.H. Schon, C. Kloc, E. Bucher, and B. Batlogg, Efficient organic photovoltaic diodes based on doped pentacene, *Nature*, **403**, 2000, 408–410.
4 A.K. Ghosh and T. Feng, Merocyanine organic solar cells, *Journal of Applied Physics*, **49**, 1978, 5982–5989.
5 G.A. Chamberlain, P.J. Cooney, and S. Dennison, Photovoltaic properties of merocyanine solid-state photocells, *Nature*, **289**, 1981, 45.
6 T. Moriizumi and L. Kudo, Merocyanine-dye photovoltaic cell on a plastic film, *Applied Physics Letters*, **38**, 1981, 85–86.
7 C.W. Tang, Two-layer organic photovoltaic cell, *Applied Physics Letters*, **48**, 1986, 183–185.
8 L.C. Chen, D. Godovsky, O. Inganas, *et al*., Polymer photovoltaic devices from stratified multilayers of donor–acceptor blends, *Advanced Materials*, **12**, 2000, 1367–1370.
9 M. Granstrom, K. Petritsch, A.C. Arias, *et al*., Laminated fabrication of polymeric photovoltaic diodes, *Nature*, **395**, 1998, 257–260.
10 S.E. Shaheen, C.J. Brabec, and N.S. Sariciftci, 2.5% efficient organic plastic solar cells, *Applied Physics Letters*, **78**, 2001, 841–843.
11 R.A.J. Janssen, J.C. Hummelen, and N.S. Sariciftci, Polymer–fullerene bulk heterojunction solar cells, *MRS Bulletin*, **30**, 2005, 33–36.
12 P. Sullican, S. Heutz, S.M. Schultes, and T.S. Jones, Influence of codeposition on the performance of CuPc–C60 heterojunction photovoltaic devices, *Applied Physics Letters*, **84**, 2004, 1210–1212.
13 J. Xue, S. Uchida, B.P. Rand, S.R. Forrest, Asymmetric tandem organic photovoltaic cells with hybrid planar-mixed molecular heterojunctions, *Applied Physics Letters*, **85**, 2004, 5757–5759.
14 A. Hadipour, B. de Boer, J. Wildeman, *et al*., Solution-processed organic tandem solar cells, *Advanced Functional Materials*, **16**, 2006, 1897–1903.
15 A.J. Nozik, Quantum dot solar cells, *Physica E Low-dimensional Systems and Nanostructures*, **14**, 2002, 115–120.
16 R.D. Schaller and V.I. Klimov, High efficiency carrier multiplication in PbSe nanocrystals implications for solar energy conversion, *Physical Review Letters*, **92**, 2004, 186–601.
17 R.J. Ellingson, M.C. Beard, J.C. Johonson, *et al*., Highly efficient multiple exciton generation in colloidal PbSe and PbS quantum dots, *Nano Letters*, **5**, 2005, 865–871.
18 J.E. Murphy, M.C. Beard, A.G. Norman, *et al*., PbTe colloidal nanocrystals: synthesis, characterization, and multiple exciton generation, *Journal of the American Chemical Society*, **128**, 2006, 3241–3247.
19 Q. Shen, J. Kobayashi, L.J. Diguna, and T. Toyoda, Effect of ZnS coating on the photovoltaic properties of CdSe quantum dot-sensitized solar cells, *Journal of Applied Physics*, **103**, 2008, 084304.
20 Y. Gao, E. Talgorn, M. Aerts, *et al*., Enhanced hot-carrier cooling and ultrafast spectral diffusion in strongly coupled PbSe quantum-dot solids, *Nano Letters*, **11**, 2011, 5471–5476.

21 A. Pandey and P. Guyot-Sionnest, Hot electron extraction from colloidal quantum dots, *The Journal of Physical Chemistry Letters*, **1**, 2009, 45–47.
22 S. Binetti, M. Acciarri, A. Le Donne, *et al*., Key success factors and future perspective of silicon-based solar cells, *International Journal of Photoenergy*, 2013, 1–6.
23 S. Mekhilef, R. Saidur, A. Safari, A review on solar energy use in industries, *Renewable and Sustainable Energy Reviews*, **15**, 2011, 1777–1790.
24 D.C. Jordan, S.R. Kurtz, Photovoltaic degradation rates – an analytical review, *Progress in Photovoltaics: Research and Applications*, **21** (2013) 12–29.
25 W.A. Badawy, A review on solar cells from Si-single crystals to porous materials and quantum dots, *Journal of Advanced Research*, **6**, 2015, 123–132.
26 R.W. Miles, G. Zoppi, I. Forbes, Inorganic photovoltaic cells, *Materials Today*, **10**, 2007, 20–27.
27 S. Sharma, K.K. Jain, A. Sharma, Solar cells: in research and applications – a review, *Materials Sciences and Applications*, **6**, 2015, 1145–1155.
28 T. Saga, Advances in crystalline silicon solar cell technology for industrial mass production, *NPG Asia Materials*, **2**, 2010, 96–102.
29 S. Mathew, A. Yella, P. Gao, *et al*., Dye-sensitized solar cells with 13% efficiency achieved through the molecular engineering of porphyrin sensitizers, *Nature Chemistry*, **6**, 2014, 242–247.
30 S. Prasanthkumar and L. Giribabu, Recent advances in perovskite-based solar cells, *Current Science*, **111**, 2016, 1173–1181.
31 T.B. Song, Q. Chen, H. Zhou, *et al*., Perovskite solar cells: film formation and properties, *Journal of Materials Chemistry A*, **3**, 2015, 9032–9050.
32 J. Nelson, *The Physics of Solar Cells*, Imperial College Press, London, 2003.
33 A. Pandey and S. Philippe, Slow electron cooling in colloidal quantum dots, *Science*, **322**, 2008, 929–932.
34 W.A. Tisdale, K.J. Williams, B.A. Timp, *et al*., Hot-electron transfer from semiconductor nanocrystals, *Science*, **328**, 2010, 1543–1547.
35 A.L. Efros, V.A. Kharchenko, M. Rosen, Breaking the phonon bottleneck in nanometer quantum dots: Role of Auger-like processes, *Solid State Communications*, **93**, 1995, 281–284.
36 L.W. Wang, M. Califano, A. Zunger and A. Franceschetti, Pseudopotential theory of Auger processes in CdSe quantum dots, *Physical Review Letters*, **91**, 2003, 056404.
37 D.F. Schroeter, D.J. Griffiths and P.C. Sercel, Defect-assisted relaxation in quantum dots at low temperature, *Physical Review B*, **54**, 1996, 1486.
38 C.B. Murray, D.J. Norris, and M.G. Bawendi. Synthesis and characterization of nearly monodisperse CdE (E = S, Se, Te) semiconductor nanocrystallites, *Journal of the American Chemical Society*, **115** 1993, 8706–8715.
39 C.J. Jia and F. Schuth, Phys. Colloidal metal nanoparticles as a component of designed catalyst, *Physical Chemistry Chemical Physics*, **13**, 2011, 2457–2487.

40 A.A. Guzelian, U. Banin, A.V. Kadacanich, *et al.*, Colloidal chemical synthesis and characterization of InAs nanocrystal quantum dots, *Applied Physics Letters*, **69**, 1996, 1432–1434.

41 L. Manna, E.C. Scher and A.P. Alivisatos, Shape control of colloidal semiconductor nanocrystals, *Journal of Cluster Science*, **13**, 2002, 521–532.

42 H. Shen, H. Wang, Z. Tang, *et al.*, High quality synthesis of monodisperse zinc-blende CdSe and CdSe/ZnS nanocrystals with a phosphine-free method, *CrystEngComm*, **11**, 2009, 1733–1738.

43 R.J. Ellingson, J.L. Blackburn, P. Yu, *et al.*, Excitation energy dependent efficiency of charge carrier relaxation and photoluminescence in colloidal InP quantum dots, *The Journal of Physical Chemistry B*, **106**, 2002, 7758–7765.

44 H. Kandori, H. Sasabe, and M. Mimuro, Direct determination of a lifetime of the S2 state of beta-carotene by femtosecond time-resolved fluorescence spectroscopy, *Journal of the American Chemical Society*, **116**, 1994, 2671–2672.

45 A. Boulesbaa, Z. Huang, D. Wu, and T. Lian, Competition between energy and electron transfer from CdSe QDs to adsorbed rhodamine B, *The Journal of Physical Chemistry C*, **114**, 2010, 962–969.

46 J. Huang, Z. Huan, Y. Yang, *et al.*, Multiple exciton dissociation in CdSe quantum dots by ultrafast electron transfer to adsorbed methylene blue, *Journal of the American Chemical Society*, **132**, 2010, 4858–4864.

47 V.V. Matylitsky, L. Dworak, V.V. Breus, *et al.*, Ultrafast charge separation in multiexcited CdSe quantum dots mediated by adsorbed electron acceptors, *Journal of the American Chemical Society*, **131**, 2009, 2424–2425.

48 J. Jasieniak, M. Califano, and S.E. Watkins, Size-dependent valence and conduction band-edge energies of semiconductor nanocrystals, *ACS Nano.* **5**, 2011, 5888–5902.

49 D.R. James, Y.S. Liu, P. De Mayo, and W.R. Ware, Distributions of fluorescence lifetimes: consequences for the photophysics of molecules adsorbed on surfaces, *Chemical Physics Letters*, **120**, 1985, 460–465.

50 H.M. Gong, Z.K. Zhou, H. Song, *et al.*, The influence of surface trapping and dark states on the fluorescence emission efficiency and lifetime of CdSe and CdSe/ZnS quantum dots, *Journal of Fluorescence*, **17**, 2007, 715–720.

51 I. Robel, M. Kuno, and P.V. Kamat, Size-dependent electron injection from excited CdSe quantum dots into TiO_2 nanoparticles, *Journal of the American Chemical Society*, **129**, 2007, 4136–4137.

52 T. Ritz, A. Damjanovic, K. Schulten, *et al.*, Efficient light harvesting through carotenoids, *Photosynthesis Research*, **66**, 2000, 125–144.

53 H.H. Billsten, D. Zigmantas, V. Sundstrom, and T. Polivka, Dynamics of vibrational relaxation in the S_1 state of carotenoids having 11 conjugated C=C bonds, *Chemical Physics Letters*, **355**, 2002, 465–470.

54 E. Papagiannakis, J.T.M. Kennis, I.H.M. Van Stokkum, *et al*., An alternative carotenoid-to-bacteriochlorophyll energy transfer pathway in photosynthetic light harvesting, *Proceedings of the National Academy of Sciences*, **99**, 2002, 6017–6022.

55 J.H. Bang and P. V. Kamat, CdSe quantum dot-fullerene hybrid nanocomposite for solar energy conversion: electron transfer and photoelectrochemistry, *ACS Nano*, **5**, 2011, 9421–9427,

56 P. Reiss, M. Protiere, and L. Li, Core/shell semiconductor nanocrystals, *Small*, **5**, 2009, 154–168.

57 A. Makhal, H. Yan, P. Lemmens, and S.K. Pal, Light harvesting semiconductor core-shell nanocrystals: Ultrafast charge transport dynamics of CdSe-ZnS quantum dots, *The Journal of Physical Chemistry C*, **114**, 2010, 627–632.

58 B.O. Regan and M. Gratzel, A low-cost, high-efficiency solar cell based on dye-sensitized colloidal TiO_2 films, *Nature*, **353**, 1991, 737–740.

59 A. Hagfelt and M. Gratzel, Molecular photovoltaics, *Accounts of Chemical Research*, **33**, 2000, 269–277.

60 M.K. Nazeeruddin, F. De Angelis, S. Fantacci, *et al*. Combined experimental and DFT-TDDFT computational study of photoelectrochemical cell ruthenium sensitizers, *Journal of the American Chemical Society*, **127**, 2005, 16835–16847.

61 P. Wang, S.M. Zakeeruddin, J.E. Moser, *et al*., A stable quasi-solid-state dye-sensitized solar cell with an amphiphilic ruthenium sensitizer and polymer gel electrolyte, *Nature Materials*, **2**, 2003, 402–407.

62 M.K. Nazeeruddin and M. Gratzel, Dyes for semiconductor sensitization. In: S. Licht (ed.) *Encyclopedia of Electrochemistry. Volume 6. Semiconductor Electrodes and Photoelectrochemistry*. Wiley-VCH, 2002, 407.

63 K. Taretto and U. Rau, Modeling extremely thin absorber solar cells for optimized design, *Progress in Photovoltaics: Research and Applications*, **12**, 2004, 573–591.

64 A.J. Nozik, Quantum dot solar cells, *Physica E: Low-dimensional Systems and Nanostructures*, **14**, 2002, 115–120.

65 I. Robel, V. Subramanian, M. Kuno, and P.V. Kamat, Quantum dot solar cells. Harvesting light energy with CdSe nanocrystals molecularly linked to mesoscopic TiO_2 films, *Journal of the American Chemical Society*, **128**, 2006, 2385–2393.

66 K. Ernst, R. Engelhardt, K. Ellmer, *et al*., Contacts to a solar cell with extremely thin CdTe absorber, *Thin Solid Films*, **387**, 2001, 26–28.

67 C.B. Murray, D.J. Norris, and M.G. Bawendi, Synthesis and characterization of nearly monodisperse CdE (E = S, Se, Te) semiconductor nanocrystallites, *Journal of the American Chemical Society*, **115**, 1993, 8706–8715.

68 Z. Yang, C.Y. Chen, P. Roy, and H.T. Chang, Quantum dot-sensitized solar cells incorporating nanomaterials, *Chemical Communications*, **47**, 2011, 9561–9571.

69 Y.L. Lee and Y.S. Lo, Highly efficient quantum-dot-sensitized solar cell based on co-sensitization of CdS/CdSe, *Advanced Functional Materials*, **19**, 2009, 604–609.

70 A. Kongkanand, K. Tvrdy, K. Takechi, *et al*., Quantum dot solar cells. Tuning photoresponse through size and shape control of CdSe-TiO_2 architecture, *Journal of the American Chemical Society*, **130**, 2008, 4007–4015.

Index

a

absorber 79, 82
acceptor 17–19, 283–298, 300
ACI 125
activated charcoal 172
active layer 284, 287, 293, 295, 297–298
additive 88, 100, 101
adsorption 64, 80, 242
Ag *see* silver
aggregation 18–20, 29, 50
algae 72, 82
alignment 64, 66
AlN 147
AM 17
AM 1.5G 240
amine 89, 91
amorphous silicon 15
anchoring 67, 69, 71, 72, 80, 82
anthocyanin 64–72, 74, 75, 80, 82, 89, 90, 92–95, 97
antioxidant 70, 71
applied potential 264, 265
architecture of perovskite solar cells 310
atomization modes 267
Au *see* gold
auger recombination 345
autoclave 65, 68, 77

b

back transferring 358
bandgap 1, 2, 63, 75, 77, 86
B4Br 144
betalains 70, 71
bicontinuous network 285
bifacial 1, 48, 149
bilayer 4
bimolecular recombination 236
biocompatible 89, 98
biodegradable 89, 98
biopolymer 88, 91
BL (γ- butyrolactone) 145
black dye 17, 27–30, 35, 136
blade coating 319
blend 88
blocking layer 95, 99
BMII (1-butyl-3-methyl-methyl-imidazolium iodide) 89, 90, 92, 93, 97, 98, 101, 104–108, 141
bromide 139
BTD (Benzothiadiazole) 137

Rational Design of Solar Cells for Efficient Solar Energy Conversion, First Edition.
Edited by Alagarsamy Pandikumar and Ramasamy Ramaraj.

buffer 72–77, 79, 80, 82
buffer layer 262, 297
bulk-heterojunction (BHJ) 224, 283, 285–286, 289–291, 294–295, 297–299
bulk heterojunction device 261

c

C.Pulcherrima 62, 65, 70, 71, 74, 77, 82
cadmium selenide 179, 182
cadmium telluride 15, 182
Calvin cycle 62, 70
Capstone FS-31 228
carbazole 26, 33, 35, 51
carbon 134, 147, 148, 151
carbon black 171, 175
carbon dye 214
carbon nanofiber 206, 209, 213, 216
carbon nanoparticle 205
carbonyl 96, 98, 106
carboxyl 71
carotenoid 70, 71, 107
carrier 2, 3, 90
cathode 86, 87
CB (conduction band) 135, 142
CDCA (chenodeoxycholic acid) 31, 32, 35, 39, 40, 135
CdTe/CdS 122, 123
CE 86, 87, 90, 91, 95, 97, 98, 106, 109, 125, 140, 149, 169–186
charge 2, 3, 6, 10, 11
charge resistance 200
charge separation 284, 295
charge transfer 206
charge transfer resistance 176, 177
charm-bracelet 291, 294
chemical bath deposition 229, 239–245
chemical vapor deposition 326, 327
chemisorption 17
chitin 88
chitosan (Ch) 88–91, 95, 98
chlorophyll 62, 63, 70, 72, 74, 93–95, 96, 100–103, 105–107
CIGS *see* copper indium gallium selenide (CIGS)
citric acid 70–72, 74, 77, 82
c-MWCNTs 147
CNT 171, 175, 176, 179, 181, 182
coadsorbent 24, 29, 35, 49
cobalt sulfide 179, 183
cocktail sensitization 19, 41, 46, 48
compact 90, 95, 99, 100, 108
compact layer 19, 32, 51
complementary absorption 18, 21, 41, 47, 49
compositional engineering 314
conducting polymers 182, 184, 185
conduction band 17, 19, 29, 172, 173, 186
conductivity 86, 88, 90, 91, 95–97, 100, 101, 106, 108, 109
conjugated polymer 283–289, 291–292, 295
conjugated semiconductor 222
contact angle 324
cooling process 358
copper indium gallium selenide (CIGS) 15, 122
copper sulfide 179, 182
counter electrode 16, 17, 44, 51, 86, 193, 200, 204
CPE 129, 130, 144, 145, 148
crystallization kinetics 321, 322
crystal Structure 308
Cs_2CO_3 227
current 6

d

DEC (diethyl carbonate) 129, 145
degradation 237, 316
deoxycholic acid 29, 30, 35, 38, 40, 43, 49
deposition techniques 317
device efficiency 273

device processing 313
dielectric 88, 97, 99, 101, 105, 109
diffusion 2, 6
1,8-diiodooctane 287, 289
diketopyrrolopyrrole 35, 221
DME (1,2-dimethoxyethane) 145
doctor blade 228
doctor blade instrument 320
donor 17, 18, 26, 35, 46, 283–298
double-cable 292–294, 299–300
DSSCs 1–13, 15, 16, 18–20, 27, 31, 33, 41, 45, 47, 49–51, 61–72, 74, 75, 77, 85, 87, 92, 105, 162, 169–171, 175–180, 182–186, 195
dye 1–10, 12, 86, 89, 90, 95, 97, 101–109, 124–127, 130–140
Dynol 228

e

efficiency 61, 62, 64, 68, 73–75, 77, 79, 82, 90, 95–101, 105, 106, 108, 109, 122–127, 131, 134–145, 147–153, 222
EG 125
electrical conductivity 266
electrocatalyst 200, 204, 205
electrocatalytic activity 209, 210, 212
electrolyte 1–3, 5, 6, 62–65, 68, 69, 77, 79, 82
electron 1–6, 8, 13, 62–67, 69, 70, 81
electron lifetime 20, 23, 26, 30
electron transporting layer (ETL) 175, 227, 310, 311, 313, 315
electron trap 242
electropolymerization 203
EMImTFO^{-} 141
encapsulation 224, 317
energy 61, 62, 71, 74, 75
enhancing stability 316
enzyme 62, 71
eosin-Y 4, 10–12
etching 324
evaporation rate 319
evolution of Perovskite Solar cells 310, 311
exciton 242, 283–285, 300
exciton binding force 362
exciton diffusion length 293, 295
extraction 64–72, 77, 80, 82

f

fabrication 62, 64, 65, 70, 74, 82
Fermi 3, 5, 11, 97
Fermi level 243
FF 141, 144
fill factor 170, 176, 289–291, 295
filler 88
film thickness 273
flavonoids 70
flexible 325
flower 62, 65, 71, 77, 80, 82
flow rate 265
fluorinated titanium oxide 239
fluorosurfactant 234
focusing of size distribution 349
formic acid 25
Frenkel-type 309
F-TiOx 239–245
FTO (fluorine-doped tin oxide) 65–69, 77, 80, 86, 95, 97, 98, 106, 109, 133, 140, 142, 170, 175–180, 185
fullerene 283–286, 288–293, 299–300

g

general principle 284
geometry 325
glass transition 88
gold 3–9, 11, 12
GPE (gel polymer electrolyte) 129, 130, 142–150
graphene nanoplatelets 51
graphite oxide 177
GuSCN 125, 143

h

HCl 65, 67, 71, 75
heteroatom 287, 288
hetero-Tandem 299
highest occupied molecular orbital (HOMO) 17, 86, 132, 175, 199, 284, 285
hole transport layer (HTL) 175, 227, 310, 311, 313, 315
HOMO *see* highest occupied molecular orbital (HOMO)
homo-tandem 296, 299
hot electrons 346
hot injection method 348
HPA 141, 142, 148
HTM 123, 126, 127, 153
Hybrid-EHDA 263
hybrid polymer 340
hydrophilic 233
hydrophilic carbon 211
hydrophobic 233
hydrothermal 2, 6, 8, 12
hydrothermal method 62, 65, 70, 73, 75, 82
hydroxyl 89, 91, 95, 98

i

IL (Ionic liquid) 90
impact ionization 360
impedance 140
indole 18, 35
indoline 29, 30, 48, 49
inkjet printing 326
ink properties 266
inorganic Solar Cells 342
in situ 143, 144, 149
interface 3, 4, 6
interfacial contact 88
interfacial engineering 314, 316
interfacial layers 221
interfacial recombination 236
intermediate phase film 315
inverted organic solar cells 221, 224, 262
in vitro 71
iodate 91
iodide 87, 96, 106, 108, 109, 125–129, 131, 137, 139, 141–149, 151–153, 201, 204, 210, 213
iodine 89, 106, 125, 131, 137, 145, 149, 150
ionic liquid electrolyte 184
ions 62, 63, 65, 75, 77
IPCE 18, 20, 21, 23, 24, 27–30, 32, 33, 41, 46, 49, 51
iron pyrite 176
isopropanol 228
ITO (indium-doped tin oxide) 90, 95, 100, 133, 134, 223

j

J-V characteristics 240

k

KI 93, 96, 97, 99–105, 108–110, 129, 142, 147, 149, 153

l

large area deposition techniques 326
large area perovskite module 319, 320
laser patterning 324
lattice 88, 90, 96, 106
LE (liquid electrolytes) 123–125, 144, 151
lead sulfide 182. 183
leakage 69, 77, 79, 82
LiBOB 106
lifetime 222
light 2–4, 7, 8
light-soaking 224, 234, 242
LiI 92, 97, 107, 108, 126, 142, 144–146, 148, 149
lipophobic 234

low cost 195, 196, 200, 203, 208, 210, 216
lowest unoccupied molecular orbital (LUMO) 17, 86, 132, 175, 197, 198, 284, 285
LUMO *see* lowest unoccupied molecular orbital (LUMO)

m

masks 324
measures 62, 64, 68, 79, 82
MEH-PPV 283, 295
mesoporous 90, 95
mesoporous carbon 175, 176
mesoporous perovskite solar cells 310
metal oxide 2
metallic nozzle 264
methylammonium lead iodide perovskite 175, 178
miscible 91
MK 37, 138
MLCT (metal-to-ligand charge transfer) 135
molar extinction coefficient 17, 19, 21, 33, 41, 46
molecular heterojunction (MHJ) 284, 291, 293, 299
molybdenum carbides 179
morphology 64, 66, 70
MPN (3-methoxypropionitrile) 143
Murray, C.B. 348
MWCNT (multiwalled carbon nanotubes) 176, 208, 209, 211, 215

n

N3 16, 27, 28, 38, 92–94, 96–101, 103–105, 107–109, 131, 136, 139, 145
N719 5, 6, 10–12, 17, 26–29, 31–33, 35, 38–40, 92, 96, 97, 99, 104, 109, 126, 133, 145, 153
NADP+ 62, 63
NaI 129, 140–143, 146, 147, 149
nanofillers 141, 142, 145, 146
nanoflowers 4, 8, 9, 11, 77, 82
nanoparticles 2–13, 64, 67, 81, 83
nanorods 2, 4, 6–8, 10, 11, 13, 64–68, 70, 72, 75, 77, 82
nanowires 2, 4, 8, 9, 11
natural dye 61, 62, 64, 65, 67–72, 74, 77
Nb2O5 229
niobium oxide 184
n-i-p configuration 313
NIR (near-infrared) 135
nozzle diameter 266
N-phthaloylation 91
nucleation 348

o

o-dichlorobenzene 287, 289, 293
open-circuit photovoltage 170, 180
open circuit voltage (Voc) 285
organic dyes 198
organic photovoltaic cells 257
organic solar cells 15, 221
organometal halide perovskite 309
Ostwald ripening process 350
oxide 87
oxygen 242

p

PAN 88, 96, 99, 105–108, 110
panchromatic 18, 31, 41, 46
panchromatic film 195
PANI 149, 183, 184,, 185
PAN–VA 143
PBDTTT-C-T 224
PBMI 144
PCA 67, 69, 70, 82
PC61BM 224
PC71BM 221
PCDTBT 286–287, 295
PCE (power conversion efficiency) 18, 21, 28, 29, 31–33, 35, 45–51, 169, 170, 175–185

PEDOT (poly(3,4-ethylenedioxythiophene) 183, 185
PEDOT:PSS 223, 288, 295–296, 299
PEG (poly(ethylene glycol) 127, 142, 145
PEN 134
PEO 89–91, 93–98, 101, 104, 108, 127–129, 141, 142, 145, 146, 149, 153
PEODME 141
perovskite 124, 126, 130, 152, 153, 308
perovskite Solar Cells 309
PET (poly(ethylene terephthalate) 133
PffBT4T-2OD 224
PGeTPTBT 288
PhCh (phthaloylchitosan) 88, 91–98, 110
phenothiazine 24, 26, 50
phenyl-C61-butyric acid methyl ester (PC61BM) 285, 293, 295–296, 299
phenyl-C71-butyric acid methyl ester (PC71BM) 286–289, 295–300
phosphazene 90
photoactive layer 224
photoanode 1–6, 8, 10–13, 86, 89, 91, 95, 97–100, 106, 108, 109, 124, 132–134, 137, 140–142, 149, 151, 176, 179
photocatalytic 67, 69
photoelectrode 2, 3, 8, 11, 62–67, 69, 70, 75, 77, 79, 80, 82, 196–198
photoexcitation 201
photoluminescence (PL) spectrum 351
photonic curing 324
photons 67, 69–72, 80, 82
photosensitizer 16, 17, 87, 127, 131, 135, 151
photostability 69, 70, 82
photosynthesis 61, 62, 64, 70
photovoltaic 11, 61–64, 71, 74, 77, 79, 82, 85, 89, 91, 92, 99, 102, 109, 122–124, 135, 142, 143, 148, 149, 151
photovoltaic cell 15
P3HT 224
phthalocyanine 19–21, 51
pigment 62, 63, 67, 69–71, 74, 81
p-i-n configuration 313
planar heterojunction device 261
planar perovskite solar cells 313
plasmon 3, 4, 6–11, 13
plasmonic 97
plastic solar cells 344
plasticizer 88, 90, 98, 101, 130, 141, 142, 145, 146, 148, 149
platinum 65, 68, 80, 82, 97, 131, 133, 134, 140, 149, 153, 170, 171, 175, 177–180, 182–186, 200, 203–205
PMII 141, 143
PMMA 127
pneumatic pressure 265
p-n junction 194
PoAni-TSA 140
polar 105, 106
poly(3,4-ethylene dioxythiophene):poly(styrene sulfonate) 223
poly(3-hexylthiophene) (P3HT) 285
polymers 240
polypyrrole 184, 185, 203, 204
polysaccharide 88
polythiophene 184, 185
porosity 63, 64
porphyrin 25, 135, 137, 139
power loss mechanisms 344
PPO (phenyl propoxidase) 71, 129
Principle of Hybrid-EHDA 263
PSCs (perovskite solar cells) 124, 125, 152, 153, 175, 178, 186
PTB7 221, 286–287, 296, 298, 299
PVA 88, 98–105, 110
PV cells 255

PVDF (poly(vinylidene fluoride) 88, 109, 110, 127, 142
PVDF–HFP 143, 144, 146, 147
PV technology 193–195
pyridine 30, 91, 100

q
QD (Quantum dots) 170
QDSSCs 124–126, 150, 151, 153, 170, 171, 173, 177–179, 182–186, 360
QS-DSSC (quasi-solid-state dye sensitized solar cells) 142, 143
quantum dot sensitized solar cells *see* QDSSCs

r
recombination 3, 6, 8, 18, 19, 24, 29, 32, 33, 35, 45–48, 50, 63, 64, 81, 95, 96, 99, 100, 109, 126, 127, 133, 134, 137, 139, 144, 148, 150, 152, 233
redox 1–3, 65, 77, 80, 82, 86, 87, 106, 124, 125, 128, 131, 133, 135, 137, 138 139, 140, 143–146, 148–151, 153
redox couple 16, 24, 49
redox electrolyte 16–18, 22, 51, 199
reduced graphene oxide 179, 183, 204, 207, 213
regeneration 196, 201
resonance 3, 4, 6–8
rhodamine 4
RK-1 137
roll-to-roll deposition 325, 326
rose 62, 64, 65, 70, 71, 74, 77, 82
RTIL (room temperature ionic liquid) 125, 126, 147–149, 153
ruthenium 6, 99
ruthenizer 99

s
scalability 222
scattering 64, 77
scheme of mesoporous and planar perovskite solar cells 312
Schottky 3, 4, 6, 7, 10, 87, 98
SCN 139
screen printing 321, 323
SeCN 139
second generation PV devices 257
segmental motion 88
semiconductor 1–4, 8, 11, 15–17
sensitization 67–71, 74, 77
sensitizer 1, 5, 10, 12, 13, 61, 62, 64, 68, 70, 71, 86, 95, 96, 99, 125–127, 131–133, 135–137, 140, 143, 149–151, 153, 196–198, 309
sequential laser process 325
sheaf 10–12
sheet resistance 2, 73, 274
short circuit current 87, 109
short-circuit photocurrent density 170, 182
silicon solar cells 283
silver 3, 4, 6, 7, 10, 11
silver thin film 269
single crystal Si solar cells 343
single layer device 260
slot die coating 320, 322
small molecules 240
SMDPPEH 245
SnO_2 229, 232
sodium 75–77, 79, 82
sodium alginate 72–74
sodium dodecyl sulfate 185
soft cover deposition 328
sol-gel TiOx 239–245
solubility 91
solution printing method 321
solution-processed 224
solvent 67–71, 74, 77, 82, 88, 91, 98, 109, 110
solvent engineering 313
SPE 129, 140–142
Spin caoting 317
Spin coat 228
spin coating 285, 295
spiro-MeOTAD 127, 310

spirulina 72–74
spray coating 324
spray pyrolysis 230
spray time 271, 273
squaraine 18, 27, 28, 46, 47, 49, 50
SS-DSSCs 127, 140
STA (silicotungustic acid) 148
stability 61, 64, 65, 68–72, 74, 82, 222
stable spray mode 2, 67, 269
stand-off distance 265
stepwise sensitization 19, 24, 27, 30–33, 35, 41
sulfide 87, 97
surface tension 233, 236, 266, 324
surfactants 233, 236, 237
surfynol 104 PA 228

t
TBAI (tetrabutylammonium iodide) 92, 96, 97, 100, 101, 103–105
TBP (4-tertbutyl pyridine) 125, 143, 145
TC71BM 224
TCO (transparent conducting oxide) 134, 135, 140
thermal evaporation 228, 263
thermalization loss 344
thin film solar cells 343
third generation type solar cells 343
TiO_2 2, 4, 6, 11–13, 61, 63–75, 77, 82
TiOx 227
titanium dioxide 61, 65, 69
tolerance factor 308, 309
TPAI 92–94, 96–109
transient absorption 357
transparent conducting substrate 229
trap sites 242
trap state 346
trap state density 243
triiodide 6, 62, 63, 65, 86, 87, 91, 106, 108, 139, 143, 146, 148, 204–208
triphenylamine 49
triple junction 295, 299
Triton X-100 228
TTIP (titanium tetra isopropoxide) 65, 75
tungsten carbide 179, 213
type I core shell 359

u
ultraviolet photospectroscopy 243
UV ozone 234, 238
UV photoconductivity 243

v
valence band 173, 186
viscosity 266, 324

w
wettability 233
work function 242, 243
working principal of OPV 258

x
xanthophyll 71, 72, 74

y
YD2-O-C8 137

z
Z-907 136
zinc oxide (ZnO) 1–13, 173, 179, 184, 224, 227, 268, 289, 295–300
Z-scheme of photosynthesis 61, 62, 64, 70